MEGA QUAKES: CASCADING EARTHQUAKE HAZARDS AND COMPOUNDING RISKS

EDITED BY: Katsuichiro Goda, Tiziana Rossetto, Nobuhito Mori and Solomon Tesfamariam

PUBLISHED IN: Frontiers in Built Environment

frontiers Research Topics

Frontiers Copyright Statement

© Copyright 2007-2016 Frontiers Media SA. All rights reserved.

All content included on this site, such as text, graphics, logos, button icons, images, video/audio clips, downloads, data compilations and software, is the property of or is licensed to Frontiers Media SA ("Frontiers") or its licensees and/or subcontractors. The copyright in the text of individual articles is the property of their respective authors, subject to a license granted to Frontiers.

The compilation of articles constituting this e-book, wherever published, as well as the compilation of all other content on this site, is the exclusive property of Frontiers. For the conditions for downloading and copying of e-books from Frontiers' website, please see the Terms for Website Use. If purchasing Frontiers e-books from other websites or sources, the conditions of the website concerned apply.

Images and graphics not forming part of user-contributed materials may not be downloaded or copied without permission.

Individual articles may be downloaded and reproduced in accordance with the principles of the CC-BY licence subject to any copyright or other notices. They may not be re-sold as an e-book.

As author or other contributor you grant a CC-BY licence to others to reproduce your articles, including any graphics and third-party materials supplied by you, in accordance with the Conditions for Website Use and subject to any copyright notices which you include in connection with your articles and materials.

All copyright, and all rights therein, are protected by national and international copyright laws.

The above represents a summary only. For the full conditions see the Conditions for Authors and the Conditions for Website Use.

ISSN 1664-8714
ISBN 978-2-88945-454-9
DOI 10.3389/978-2-88945-454-9

About Frontiers

Frontiers is more than just an open-access publisher of scholarly articles: it is a pioneering approach to the world of academia, radically improving the way scholarly research is managed. The grand vision of Frontiers is a world where all people have an equal opportunity to seek, share and generate knowledge. Frontiers provides immediate and permanent online open access to all its publications, but this alone is not enough to realize our grand goals.

Frontiers Journal Series

The Frontiers Journal Series is a multi-tier and interdisciplinary set of open-access, online journals, promising a paradigm shift from the current review, selection and dissemination processes in academic publishing. All Frontiers journals are driven by researchers for researchers; therefore, they constitute a service to the scholarly community. At the same time, the Frontiers Journal Series operates on a revolutionary invention, the tiered publishing system, initially addressing specific communities of scholars, and gradually climbing up to broader public understanding, thus serving the interests of the lay society, too.

Dedication to quality

Each Frontiers article is a landmark of the highest quality, thanks to genuinely collaborative interactions between authors and review editors, who include some of the world's best academicians. Research must be certified by peers before entering a stream of knowledge that may eventually reach the public - and shape society; therefore, Frontiers only applies the most rigorous and unbiased reviews.
Frontiers revolutionizes research publishing by freely delivering the most outstanding research, evaluated with no bias from both the academic and social point of view.
By applying the most advanced information technologies, Frontiers is catapulting scholarly publishing into a new generation.

What are Frontiers Research Topics?

Frontiers Research Topics are very popular trademarks of the Frontiers Journals Series: they are collections of at least ten articles, all centered on a particular subject. With their unique mix of varied contributions from Original Research to Review Articles, Frontiers Research Topics unify the most influential researchers, the latest key findings and historical advances in a hot research area! Find out more on how to host your own Frontiers Research Topic or contribute to one as an author by contacting the Frontiers Editorial Office: **researchtopics@frontiersin.org**

MEGA QUAKES: CASCADING EARTHQUAKE HAZARDS AND COMPOUNDING RISKS

Topic Editors:
Katsuichiro Goda, University of Bristol, Bristol, United Kingdom
Tiziana Rossetto, University College London, United Kingdom
Nobuhito Mori, Kyoto University, Japan
Solomon Tesfamariam, The University of British Columbia, Canada

Aftermath of the 2011 Tohoku earthquake and tsunami in Otsuchi, Iwate, Japan.

Image: Nobuhito Mori.

Large-scale earthquake hazards pose major threats to modern society, generating casualties, disrupting socioeconomic activities, and causing enormous economic loss across the world. Events, such as the 2004 Indian Ocean tsunami and the 2011 Tohoku earthquake, highlighted the vulnerability of urban cities to catastrophic earthquakes. Accurate assessment of earthquake-related hazards (both primary and secondary) is essential to mitigate and control disaster risk exposure effectively. To date, various approaches and tools have been developed in different disciplines. However, they are fragmented over a number of research disciplines and underlying assumptions are often inconsistent. Our society and infrastructure are subjected to multiple types of cascading earthquake hazards; therefore, integrated hazard assessment and risk management strategy is needed for mitigating potential consequences due to multi-hazards. Moreover, uncertainty modeling and its impact on hazard prediction and anticipated consequences are essential parts of probabilistic earthquake hazard and risk assessment. The Research Topic is focused upon modeling and impact assessment of cascading earthquake hazards, including mainshock ground shaking, aftershock, tsunami, liquefaction, and landslide.

Citation: Goda, K., Rossetto, T., Mori, N., and Tesfamariam, S., eds. (2018). Mega Quakes: Cascading Earthquake Hazards and Compounding Risks. Lausanne: Frontiers Media. doi: 10.3389/978-2-88945-454-9

Table of Contents

Editorial

Preface

05 ***Editorial: Mega Quakes: Cascading Earthquake Hazards and Compounding Risks***

Katsuichiro Goda, Tiziana Rossetto, Nobuhito Mori and Solomon Tesfamariam

Mega Quakes - Damage Observations and Lessons for Disaster Risk Reduction

08 ***An Analysis of Fatality Ratios and the Factors That Affected Human Fatalities in the 2011 Great East Japan Tsunami***

Anawat Suppasri, Natsuki Hasegawa, Fumiyasu Makinoshima, Fumihiko Imamura, Panon Latcharote and Simon Day

21 ***The 2015 Gorkha Nepal Earthquake: Insights from Earthquake Damage Survey***

Katsuichiro Goda, Takashi Kiyota, Rama Mohan Pokhrel, Gabriele Chiaro, Toshihiko Katagiri, Keshab Sharma and Sean Wilkinson

36 ***Ground Motion Characteristics of the 2015 Gorkha Earthquake, Survey of Damage to Stone Masonry Structures and Structural Field Tests***

Rishi Ram Parajuli and Junji Kiyono

48 ***The 2016 Kumamoto Earthquakes: Cascading Geological Hazards and Compounding Risks***

Katsuichiro Goda, Grace Campbell, Laura Hulme, Bashar Ismael, Lin Ke, Rebekah Marsh, Peter Sammonds, Emily So, Yoshihiro Okumura, Nozar Kishi, Maki Koyama, Saki Yotsui, Junji Kiyono, Shuanglan Wu and Sean Wilkinson

71 ***Losses Associated with Secondary Effects in Earthquakes***

James E. Daniell, Andreas M. Schaefer and Friedemann Wenzel

Assessing Hazards and Risks due to Strong Ground Motions

85 ***Empirical Assessment of Non-Linear Seismic Demand of Mainshock–Aftershock Ground-Motion Sequences for Japanese Earthquakes***

Katsuichiro Goda, Friedemann Wenzel and Raffaele De Risi

102 ***Overview of Ground-Motion Issues for Cascadia Megathrust Events: Simulation of Ground-Motions and Earthquake Site Response***

Hadi Ghofrani, Gail M. Atkinson and Sheri Molnar

120 ***Seismic Performance Evaluation Framework Considering Maximum and Residual Inter-Story Drift Ratios: Application to Non-Code Conforming Reinforced Concrete Buildings in Victoria, BC, Canada***

Solomon Tesfamariam and Katsuichiro Goda

140 ***Energy-Based Seismic Risk Evaluation of Tall Reinforced Concrete Building in Vancouver, BC, Canada, under M_w9 Megathrust Subduction Earthquakes and Aftershocks***

Solomon Tesfamariam and Katsuichiro Goda

157 ***Estimation of Seismic Loss for a Portfolio of Buildings under Bidirectional Horizontal Ground Motions due to a Scenario Cascadia Event***

Taojun Liu and Hanping Hong

Assessing Hazards and Risks due to Massive Tsunamis

167 ***Tsunami Hazard Analysis of Future Megathrust Sumatra Earthquakes in Padang, Indonesia Using Stochastic Tsunami Simulation***

Ario Muhammad, Katsuichiro Goda and Nicholas Alexander

186 ***Probabilistic Tsunami Hazard Analysis of the Pacific Coast of Mexico: Case Study Based on the 1995 Colima Earthquake Tsunami***

Nobuhito Mori, Ario Muhammad, Katsuichiro Goda, Tomohiro Yasuda and Angel Ruiz-Angulo

202 ***Tsunami-Driven Debris Motion and Loads: A Critical Review***

Ioan Nistor, Nils Goseberg and Jacob Stolle

213 ***Estimating Tsunami-Induced Building Damage through Fragility Functions: Critical Review and Research Needs***

Ingrid Charvet, Joshua Macabuag and Tiziana Rossetto

235 ***Possible Failure Mechanism of Buildings Overturned during the 2011 Great East Japan Tsunami in the Town of Onagawa***

Panon Latcharote, Anawat Suppasri, Akane Yamashita, Bruno Adriano, Shunichi Koshimura, Yoshiro Kai and Fumihiko Imamura

New Approaches for Reducing Catastrophic Impact due to Mega Quakes

253 ***Probabilistic Earthquake–Tsunami Multi-Hazard Analysis: Application to the Tohoku Region, Japan***

Raffaele De Risi and Katsuichiro Goda

272 ***Probabilistic Seismic and Tsunami Hazard Analysis Conditioned on a Megathrust Rupture of the Cascadia Subduction Zone***

Hyoungsu Park, Daniel T. Cox, Mohammad Shafiqual Alam and Andre R. Barbosa

291 ***A Framework for Seismic Design of Items in Safety-Critical Facilities for Implementing a Risk-Informed Defense-in-Depth-Based Concept***

Tatsuya Itoi, Yuki Iita and Naoto Sekimura

300 ***Application of High Performance Computing to Earthquake Hazard and Disaster Estimation in Urban Area***

Muneo Hori, Tsuyoshi Ichimura, Lalith Wijerathne, Hideyuki Ohtani, Jiang Chen, Kohei Fujita and Hiroyuki Motoyama

frontiers in Built Environment

EDITORIAL
published: 16 February 2018
doi: 10.3389/fbuil.2018.00008

Editorial: Mega Quakes: Cascading Earthquake Hazards and Compounding Risks

Katsuichiro Goda[1], Tiziana Rossetto[2], Nobuhito Mori[3] and Solomon Tesfamariam[4]*

[1] University of Bristol, Bristol, United Kingdom, [2] University College London, London, United Kingdom, [3] Kyoto University, Kyoto, Japan, [4] The University of British Columbia, Okanagan Campus, Kelowna, BC, Canada

Keywords: earthquakes, tsunamis, hazards, risks, risk management

Editorial on the Research Topic

Mega Quakes: Cascading Earthquake Hazards and Compounding Risks

Mega quakes pose major threats to modern society, generating casualties and fatalities, disrupting socioeconomic activities, and causing enormous economic loss across the world. Recent major disasters, such as the 2004 Indian Ocean tsunami, the 2011 Tohoku Japan earthquake and tsunami, and the 2015 Gorkha Nepal earthquake, are vivid reminders that complex risk cascades drive most earthquake crises. Examples of cascading chains of geological events are as follows: earthquake rupture generating tsunami; strong shaking triggering large-scale landslide and liquefaction; and mainshock inducing a sequence of damaging aftershocks.

Our society and infrastructures are subjected to multiple types of cascading earthquake hazards; therefore, integrated hazard assessment and risk management strategies are needed for mitigating potential consequences due to multiple concurrent hazards. For effective disaster risk reduction, accurate risk assessments of earthquake-related hazards are the fundamental requirements. Moreover, uncertainty modeling and its impact on hazard prediction and anticipated consequences are essential parts of earthquake risk management decision-making.

The *Mega Quakes Research Topic* collects the cutting-edge research contributions from 84 leading researchers and professionals around the world, who are actively involved with modeling, assessment, mitigation, and management of earthquake hazards and risks. It contains 19 articles that cover a wide range of cascading earthquake-triggered hazards and risks in various geographical regions, including Cascadia (Pacific Northwest), Indian Ocean, Japan, Mexico, and Nepal.

MEGA QUAKES—DAMAGE OBSERVATIONS AND LESSONS FOR DISASTER RISK REDUCTION

After each major earthquake disaster, we learn new lessons as to what was not effective, what worked well, and what needs to be improved for future. Observing damage patterns from historical events and analyzing gathered data to create new knowledge and practice for enhanced disaster preparedness and risk reduction are the key to achieve sustainable and resilient urban cities and rural communities.

Along this line, Suppasri et al. present a new analysis of human fatality ratios in the 2011 Tohoku Japan tsunami to overcome the limitations of previous investigations of the fatality ratios for global tsunami disasters. This study identifies that tsunami hazard awareness is the key factor influencing human loss consequences.

OPEN ACCESS

Edited and Reviewed by:
Izuru Takewaki,
Kyoto University, Japan

****Correspondence:***
Katsuichiro Goda
katsu.goda@bristol.ac.uk

Specialty section:
This article was submitted to Earthquake Engineering, a section of the journal Frontiers in Built Environment

Received: *22 January 2018*
Accepted: *02 February 2018*
Published: *16 February 2018*

Citation:
Goda K, Rossetto T, Mori N and Tesfamariam S (2018) Editorial: Mega Quakes: Cascading Earthquake Hazards and Compounding Risks. Front. Built Environ. 4:8. doi: 10.3389/fbuil.2018.00008

Goda et al. and Parajuli and Kiyono report post-earthquake damage survey results after the 2015 Gorkha earthquake in Nepal. Both studies highlight significant challenges related to mainshock shaking, aftershock risks, and landslides in remote mountainous areas. Sound structural design and construction of reinforced concrete (RC) and masonry (brick and stone) buildings are the key to reduce the earthquake risk in Nepal.

Furthermore, Goda et al. present an earthquake reconnaissance work for the 2016 Kumamoto Japan earthquake sequences. The investigation highlights the complex patterns of earthquake damage and loss due to the major mainshock-aftershock ground shaking sequence, ground deformation, landslide, and liquefaction, affecting a wide range of buildings and infrastructure in Kumamoto.

On the other hand, Daniell et al. investigate the aggregate effects of the secondary hazards (e.g., landslide, liquefaction, tsunami, fire, flooding, and surface rupture) on overall earthquake loss by analyzing various sources of earthquake damage and loss data reported in the literature. Their analysis provides a useful empirical evidence regarding how important to account for cascading hazards and compounding risks in earthquake impact assessment.

ASSESSING HAZARDS AND RISKS DUE TO STRONG GROUND MOTIONS

Ground shaking is the primary cause of earthquake damage and loss. Assessing seismic hazards and risks accurately is a formidable task because of large uncertainties associated with earthquake rupture processes, seismic wave propagation, near-surface site effects, and seismic vulnerability of buildings and infrastructure. This is particularly the case for mega quakes, where earthquake rupture is very complex and triggers numerous aftershocks over a prolonged period and buildings are excited by long-duration strong ground motions.

Goda et al. develop an extensive dataset of real mainshock–aftershock sequences for Japanese earthquakes. To evaluate the structural damage potential of major aftershocks quantitatively, the study carries out an empirical assessment of peak and residual ductility demands of numerous inelastic systems having different vibration periods, yield strengths, and hysteretic characteristics.

Ghofrani et al. present a recent development of the stochastic finite-fault method for the Cascadia subduction earthquake scenarios in the Pacific Northwest by accounting for uncertainties of the key model parameters, such as stress drop, regional attenuation, and local site effects. The study highlights the challenges that need to be overcome in future studies to obtain more accurate estimates of strong ground motions that might be experienced in the next mega-thrust event in Cascadia.

Tesfamariam and Goda propose a novel seismic performance evaluation framework based on maximum and residual inter-story drift ratios, rather than a single structural response parameter. The developed framework is applied to evaluate the potential impact to non-ductile RC buildings in Victoria, BC, Canada, due to the Cascadia subduction earthquakes. Furthermore, Tesfamariam and Goda extend the above framework by considering an energy-based damage index as performance indicator. Both new methodologies are particularly suitable for conducting seismic risk analyses of buildings in major subduction environments, where long-period ground motions with repeated major aftershocks are anticipated.

Liu and Hong present a seismic loss estimation study for buildings in Vancouver, BC, Canada by simulating multi-component ground motion records due to the possible Cascadia subduction events using a stochastic finite-fault method. The study considers structural responses under bidirectional seismic excitations and is a novel extension of the past seismic loss estimation studies for building portfolios.

ASSESSING HAZARDS AND RISKS DUE TO MEGA TSUNAMIS

Tsunamis that are triggered by mega-thrust subduction earthquakes are highly destructive, and are typical examples of low-probability high-consequence events. As exemplified during the recent mega tsunami disasters in Indian Ocean, Chile, and Japan, numerous coastal cities and towns around the world might be devastated. Assessing tsunami hazards for future scenarios require proper treatment of uncertain earthquake rupture characteristics. On the other hand, tsunami risk assessments should consider various wave effects, such as non-hydrostatic, local amplification, macro roughness by artificial structures, and debris impact forces, acting on buildings and infrastructure in high-risk coastal areas. To quantify the expected damage or losses due to tsunamis, empirical tsunami fragility and vulnerability functions can be used.

By adopting a novel stochastic tsunami simulation method, Muhammad et al. conduct a probabilistic tsunami hazard analysis in Padang by considering stochastic rupture scenarios in the Mentawai-Sunda subduction zone off Sumatra Island, Indonesia, whereas Mori et al. carry out a probabilistic tsunami hazard assessment for the Pacific coast of Mexico. Both studies generate probabilistic estimates of anticipated tsunami wave profiles at several shallow-water wave recording locations. They highlight strong sensitivity of maximum tsunami height to major earthquake slip locations, thus indicating the importance of accounting for earthquake source rupture uncertainties in future probabilistic tsunami hazard and risk studies.

Nistor et al. present a state-of-the-art research review on debris loads, i.e., solid objects entrained within the inundating flows impacting on structures. This is of critical importance in the design of tsunami-resistant infrastructure. The article summarizes recent advancements in the determination of debris dynamics using an experimental setting, which have enabled to improve the assessment of mechanisms of the debris load as well as of the potential maximum impact loads.

Charvet et al. present a comprehensive review of empirical tsunami fragility modeling, which employs sophisticated statistical methods to develop a correlation between observed tsunami damage and experienced tsunami hazard parameters. The article emphasizes how to assess the quality of current estimations of

tsunami fragility. The study also introduces the best practice when developing new fragility functions, which is particularly useful for future studies of tsunami fragility modeling.

Latcharote et al. present an intriguing investigation to examine the possible failure mechanisms of six buildings in Onagawa, Miyagi, Japan that were overturned during the 2011 Tohoku tsunami. These failures are caused by combinations of hydrodynamic and buoyancy forces acting on submerged buildings during the tsunami, but also affected by damage to building foundation due to liquefaction prior to the tsunami. The case studies discussed in the article are good exemplars of building collapse due to cascading hazards and compounding risks.

NEW APPROACHES FOR REDUCING CATASTROPHIC IMPACT DUE TO MEGA QUAKES

To enhance disaster risk preparedness and management against earthquake catastrophes, new multi-hazard approaches are needed by considering the risks due to both primary and secondary hazards. The new assessment methods and tools will improve the current practice of preparing individual hazard-specific maps, which are developed separately and are based on different methods, data, assumptions, and scenarios. Moreover, advances in "high performance computing (HPC)" and "big data" sciences open new avenues to evaluate catastrophic earthquake hazards and risks more rigorously and accurately.

De Risi and Goda develop a novel simulation-based procedure for estimating the likelihood that seismic intensity and tsunami inundation will exceed given hazard levels. The procedure accounts for a common physical rupture process for shaking and tsunami; therefore, cascading multi-hazard impact can be evaluated. The presented work is a first step toward an earthquake-tsunami multi-hazard performance-based engineering framework.

Park et al. develop a new methodology for integrated probabilistic seismic and tsunami hazard analysis (PSTHA), and apply it to the Cascadia subduction zone in the U.S. Pacific Northwest. The method adopts a logic tree approach to quantify the epistemic uncertainties associated with earthquake-tsunami hazard and risk predictions. In future, the proposed PSTHA can be adopted as the basis for a probabilistic multi-hazard damage and loss assessment.

Inspired by the Fukushima Daiichi nuclear power plant crisis aftermath the 2011 Tohoku earthquake and tsunami in Japan, Itoi et al. propose a risk-informed defense-in-depth-based framework. The new method addresses the issues related to treating residual risks and cliff-edge effects in safety-critical facilities more robustly. It provides additional seismic margin by preventing common cause failures.

Hori et al. develop an integrated earthquake simulator (IES) by taking advantages of HPC and a system of automated model construction. The IES enables a seamless simulation of analyzing all processes of earthquake hazard and disaster. The study presents an illustration of quantitative seismic risk assessment for Tokyo Metropolis, which involves more than 100 billion degree-of-freedoms in the simulation. This is a future computational platform of evaluating the earthquake impact to urban cities in an active seismic region.

AUTHOR CONTRIBUTIONS

KG, TR, NM, and ST handled manuscripts and edited the Research Topic.

Conflict of Interest Statement: The authors declare that the research was conducted in the absence of any commercial or financial relationships that could be construed as a potential conflict of interest.

The handling editor declared a shared affiliation, though no other collaboration, with one of the authors, NM.

Copyright © 2018 Goda, Rossetto, Mori and Tesfamariam. This is an open-access article distributed under the terms of the Creative Commons Attribution License (CC BY). The use, distribution or reproduction in other forums is permitted, provided the original author(s) and the copyright owner are credited and that the original publication in this journal is cited, in accordance with accepted academic practice. No use, distribution or reproduction is permitted which does not comply with these terms.

frontiers in Built Environment

ORIGINAL RESEARCH
published: 22 December 2016
doi: 10.3389/fbuil.2016.00032

An Analysis of Fatality Ratios and the Factors That Affected Human Fatalities in the 2011 Great East Japan Tsunami

Anawat Suppasri[1], Natsuki Hasegawa[2], Fumiyasu Makinoshima[2], Fumihiko Imamura[1], Panon Latcharote[1] and Simon Day[3]*

[1] International Research Institute of Disaster Science (IRIDeS), Tohoku University, Sendai, Japan, [2] Department of Civil Engineering, Graduate School of Engineering, Tohoku University, Sendai, Japan, [3] Institute for Risk and Disaster Reduction, University College London, London, UK

This study presents a new analysis of spatial variation in fatality ratios in the 2011 Great East Japan tsunami, in order to overcome the limitations of previous studies that tended to underestimate the fatality ratios. In addition, this analysis was performed in a manner that allows the results to be compared to those from analyses of fatality ratios in other historical tsunamis. To do this, it uses population and fatality data at the village scale in areas of less than 3 km^2 where the inundation ratio was greater than 70%, rather than the lower resolution data used in previous studies. The median value of the tsunami inundation depth at each location was extracted at the original 5-m grid resolution. All of the data were obtained from the Reconstruction Support Survey Archive. Based on the results, a strong correlation between the fatality ratio and inundation depth was found only in some areas of the Sendai Plain, whereas no strong correlation was observed along the Sanriku ria coastline. Fatality ratios in Sanriku were likely related not only to the force of the tsunami but also to other factors, such as the ria topography and the population's experience of past historical tsunamis. Data from other tsunamis in regions where tsunamis frequently occur also indicate that historical tsunami experience is a key factor in reducing fatality ratios. In contrast, the Sendai Plain shows smaller variation in local tsunami amplification effect compared to that of the Sanriku ria coastline as well as fewer coastal defense structures. Therefore, the fatality ratio in that region was predominantly affected by the force of the tsunami and the residents' individual characteristics. On the Sendai Plain, Ishinomaki City exhibited a strong correlation between the fatality ratio and inundation depth as well as between fatality ratio and building damage, because its low evacuation ratio meant that many fatalities occurred in victims' homes. Therefore, the fatality ratio in Ishinomaki City was higher than those in other areas at the same inundation depth. Simple empirical formulas were developed for estimation of human fatalities based on inundation depths and building damage ratios.

Keywords: the 2011 Great East Japan tsunami, human fatalities, fatality ratio, building damage, Ishinomaki City

OPEN ACCESS

Edited by:
Katsuichiro Goda, University of Bristol, UK

Reviewed by:
Nick Horspool, GNS Science, New Zealand
Lucinda Jane Leonard, University of Victoria, Canada

****Correspondence:***
Anawat Suppasri
suppasri@irides.tohoku.ac.jp

Specialty section:
This article was submitted to Earthquake Engineering, a section of the journal Frontiers in Built Environment

Received: *23 September 2016*
Accepted: *06 December 2016*
Published: *22 December 2016*

Citation:
Suppasri A, Hasegawa N, Makinoshima F, Imamura F, Latcharote P and Day S (2016) An Analysis of Fatality Ratios and the Factors That Affected Human Fatalities in the 2011 Great East Japan Tsunami. Front. Built Environ. 2:32. doi: 10.3389/fbuil.2016.00032

INTRODUCTION

The 2011 Great East Japan Tsunami was generated by a magnitude 9.0 earthquake with a rupture length that spanned the entire Tohoku region (Satake et al., 2013). Direct damage from the earthquake shaking and coseismic landslides was limited, with few reports of fatalities; however, the tsunami caused a large number of fatalities, as well as damage to buildings and other property (Suppasri et al., 2012). In general, the primary parameters that affect earthquake-related fatality ratios are the magnitude of the earthquake and the shaking intensities of different building types (Jaiswal et al., 2011). After severe damage caused by the 1978 Miyagi-oki earthquake, new building design codes and retrofitting procedures were widely implemented in the area. Therefore, despite the 2011 earthquake's large magnitude and strong ground motion, relatively little damage was caused by the earthquake itself, and the tsunami was responsible for most of the damage.

Some studies of fatality models were conducted prior to the 2011 tsunami. Endoh and Takahashi (1995) performed a full-scale prototype experiment to quantify the balance of the human body subjected to overtopping waves and proposed an empirical formula to evaluate the wave height and human dangers. Sugimoto et al. (2003) presented a method to determine the loss of life following a tsunami that utilized numerical calculations and GIS coordinates based on the Nankai tsunami in Japan. Koshimura et al. (2006) developed a method for estimating the number of casualties that may occur during evacuation from an inundation zone after a tsunami has inundated an area. The method is based on a simple model that considers the effects of hydrodynamic forces on the human body. Marchand et al. (2009) developed a model based on sea defense measures to quantify the potential damages and casualties associated with the 2004 Indian Ocean tsunami in Banda Aceh, Indonesia. Yeh (2010) introduced the use of anthropometric data in a tsunami casualty model. Muhari et al. (2011) further enhanced the human casualty model developed by Koshimura et al. (2006) by adding the human fall mechanism based on experiments by Endoh and Takahashi (1995). Yeh (2014) proposed a new casualty estimation model by incorporating temporal parameters, namely, tsunami arrival time, time of maximum run-up, tsunami warning time, time required for people to evacuate after the warning, and evacuee travel time. The fatality ratios of some historical tsunamis in Japan are summarized and discussed in Section "Historical Tsunamis" before the analysis of the 2011 tsunami.

This study examines the factors that affected human fatalities in the case of the 2011 tsunami based on the fatality ratio for the population and the tsunami inundation in each affected area. Fatality data for this tsunami were collected by national and local government agencies. As discussed below (see 2011 Great East Japan Tsunami), several previous studies have analyzed these fatality data, but they either used scales that were too large for the exposure data or mixed large- and small-scale data. This approach leads to the underestimation of the fatality ratio and yields results that are not comparable to the fatality ratios determined based on data from historical tsunamis. To overcome this problem, the areas and data investigated in this study were carefully selected to ensure the accuracy of the fatality ratios, as explained in Section "The 2011 Great East Japan Tsunami: Reconsidering the Spatial Scale." In Section "Factors That Affect Human Casualties during Tsunami Events," the factors that affected human fatalities are elucidated in detail based on the calculated fatality ratio of each target region. Additionally, a statistical analysis was performed, and several empirical formulas for estimating the fatality ratio were developed for this specific case study, as shown in Section "Factors That Affect Human Casualties during Tsunami Events." The results of this study can improve the estimation of human casualties associated with future tsunamis with similar characteristics.

HISTORICAL TSUNAMIS

This section reviewed the human fatalities caused by historical tsunamis both inside and outside Japan, as reported in previous studies. The factors that affected human fatalities during historical tsunamis are introduced, and the relationships between these factors and the fatality ratio are discussed, with a focus on the 2011 tsunami provided in Section "Factors That Affect Human Casualties during Tsunami Events." **Figure 1** and **Table 1** present data from the following studies and summarize the historical tsunamis that have occurred in Japan, including the 1741 Oshima-Oshima tsunami (Tsuji et al., 2002), the 1771 Meiwa tsunami (Miyazawa et al., 2012), the 1896 Meiji Sanriku and 1933 Showa Sanriku tsunamis (Yamashita, 2008), and the 1944 Showa Tonankai and 1993 Okushiri tsunamis (Kawata, 1997). It should be noted that only events in 1896, 1933, and 2011 impact the east coast of Japan. **Figure 2** presents a plot of the maximum tsunami run-up heights and fatality ratios of these historical tsunamis using data from these previous studies. In these studies, the fatality ratio was defined as the percentage of the number of dead or missing persons to the total population of the inundation zones before the tsunami. This definition is acceptable because the settlements were small and on the shore, hence the historical sizes of settlements were equal or nearly equal to the number of tsunami-exposed residents within them. However, more recently settlements have merged and extended inland, so that their residential areas are large compared to the actual tsunami inundation area in the case of the 2011 tsunami (see The 2011 Great East Japan Tsunami: Reconsidering the Spatial Scale). The relationships between these parameters are discussed in the following sections.

It is also useful to compare the 2011 event in Japan to historical tsunamis in countries with high frequencies of destructive tsunamis (as high as 1/50 years on some coastlines). These countries have correspondingly high levels of tsunami awareness and readiness to evacuate in response to the slightest sign that a tsunami may occur, particularly in traditional coastal communities that have long been established on vulnerable coastlines.

1741 Oshima-Oshima Tsunami, 1771 Meiwa Tsunami, and 1896 Meiji Sanriku Tsunami

These three tsunamis occurred more than 100 years ago at a time when no large tsunamis had recently occurred on the affected coastlines. Additionally, no coastal defense structures or warning systems above the local level existed in the period. These three

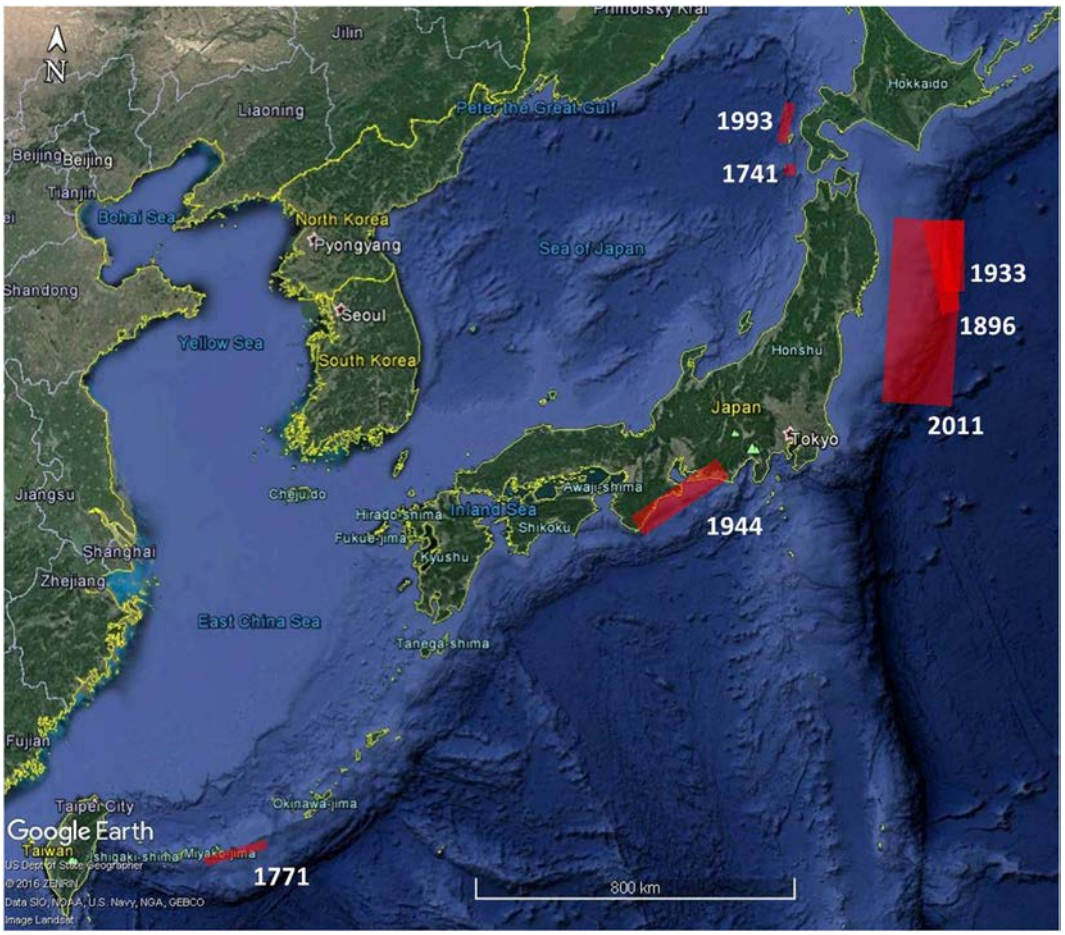

FIGURE 1 | **Approximate source areas of historical tsunamis in Japan for which detailed tsunami heights and fatality ratios are available**.

TABLE 1 | Times of earthquake occurrence and earliest tsunami arrival times to the nearest coastlines for the historical tsunamis plotted in Figure 2.

Event name	Occurrence time	Earliest arrival time (min)	Additional information regarding the tsunami source
1741 Oshima-Oshima	05:00	5	Tsunami generated by volcanic eruption
1771 Meiwa	08:00	10	Associated with submarine landslide
1896 Meiji Sanriku	19:32	30	Tsunami earthquake, little ground motion
1933 Showa Sanriku	02:30	22	Outer-rise earthquake
1944 Showa Tonankai	13:35	10	Typical interplate earthquake
1993 Okushiri	22:17	3	Epicenter was near the island
2011 Great East Japan	14:46	29	Large rupture area

tsunamis were much larger than other historical tsunamis in these regions. The 1741 Oshima-Oshima tsunami was generated by a volcanic eruption (Tsuji et al., 2002), the 1771 Meiwa tsunami was associated with a submarine landslide (Miyazawa et al., 2012), and the 1896 Meiji Sanriku tsunami was triggered by a tsunami earthquake, an earthquake with little ground shaking that nevertheless generated a large tsunami (Satake and Tanioka, 1999). These events resulted in very high fatality ratios, especially in the case of the 1771 tsunami. For these three tsunamis, the time of event occurrence and the earliest tsunami arrival time (**Table 1**) had no influence on the fatality ratio because the residents were not alerted by the source events of the tsunamis and so would only have been alerted by seeing or hearing the incoming tsunami wave minutes before its impact.

1933 Showa Sanriku Tsunami, 1944 Tonankai Tsunami, and 1946 Nankai Tsunami

The 1933 Showa Sanriku tsunami occurred just 37 years after the 1896 Meiji Sanriku tsunami. The two tsunamis affected a similar area of the Sanriku Coast. Although the earthquake occurred in the middle of the night, it was associated with strong ground motions that provided an alert for the population exposed to the tsunami. Thus, the warning provided by the strong shaking and

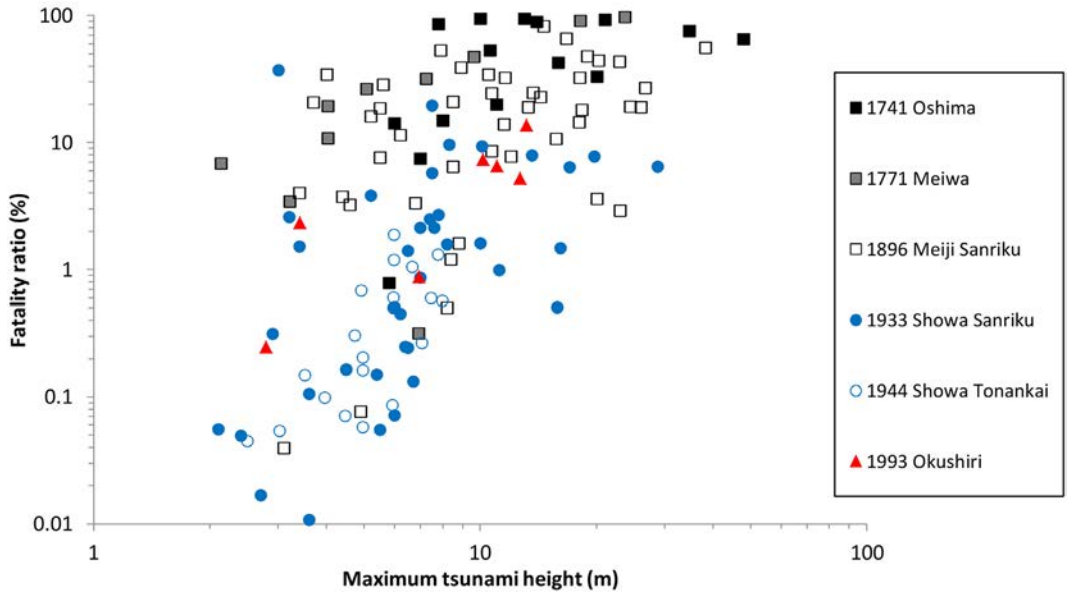

FIGURE 2 | **Relationship between the maximum tsunami heights and fatality ratios of historical tsunamis in Japan**. Previously published 2011 Tohoku data are not shown for reasons discussed in Section "2011 Great East Japan Tsunami."

the experience of the previous tsunami reduced the number of human casualties, in this case, from a fatality ratio as high as 80% in the 1896 tsunami to a fatality ratio of less than 10% in 1933, even though the latter occurred in the middle of the night. The low fatality ratios characteristic of the 1944 Tonankai earthquake and tsunami (less than 2% even at tsunami heights of nearly 10 m), which occurred 90 years after the 1854 Ansei Tokai and Nankai tsunamis, can be similarly explained.

1993 Okushiri Tsunami

In contrast to the events discussed above, the 1993 Okushiri tsunami struck the coastal community within a few minutes of the source earthquake (faster than the official warning), and with larger than expected waves. Hence, it was difficult for the population to respond effectively to the shaking, and the fatality ratio was as high as 10%.

2011 Great East Japan Tsunami

The 2011 tsunami caused a large number of human casualties in two regions on the eastern coast of Japan, namely, on the Sanriku Coast, where there is high tsunami awareness and many structural countermeasures have been implemented, and on the Sendai Plain and other areas with lower awareness and fewer structural countermeasures. The Sanriku Coast had relatively recently experienced two major tsunamis in 1896 and 1933; however, these two tsunamis had almost no impact on the Sendai Plain and other areas. Using regression analysis to determine the controlling factors, Ueda (2012) considered human fatalities at the village, town, and city scales, whereas Yun and Hamada (2015) considered human fatalities associated with a combination of city and street-level scales. Aldrich and Sawada (2015) used a similar statistical regression approach that combined a mixture of data at the town and village scales; however, they found that a political indicator [level of support for the governing Liberal Democratic Party of Japan (LDP)] and a social indicator (pre-disaster crime rates) exhibited the strongest correlations with the fatality rate, apart from the size of the tsunami itself. They suggest that these two indicators are indicators of investment in pre-disaster community preparedness and of social cohesion and argue that these factors enabled efficient evacuation. We discuss their interpretations of their data in Section "Conclusion."

Together with Suppasri et al. (2013), these previous studies identified different fatality ratio characteristics based on different geographical settings, historical backgrounds, and disaster countermeasures on the Sanriku Coast vs. those on the Sendai Plain. The fatality ratios calculated in these previous studies were less than 20% in areas where the tsunami run-up height was less than 20 m. However, because the scales used in these previous studies differ from (are larger than) those used to evaluate other historical events, their results are not strictly comparable; thus, it is not appropriate to include the previously published results for the 2011 tsunami in **Figure 2**.

2004 Indian Ocean Tsunami, 2007 Solomon Islands Tsunami, and 2010 Chile Tsunami

In this section, we review examples from other countries with high occurrence frequencies of damaging tsunamis, where effective self-warning and evacuation plans, even at the last minute, have led to large reductions in fatalities in some affected communities compared to other communities affected by the same tsunamis.

This effect was first noted in the 2004 Sumatra tsunami, during which traditional communities on Simeulue and the Andaman and Nicobar Islands were self-evacuated in response to earthquake shaking; consequently, they experienced much lower fatality rates than did non-indigenous communities in the same areas (e.g., Sieh, 2006). The first quantitative study of the effect was conducted during a post-tsunami damage survey after the 2007 Solomon Islands tsunami, in which the fatality ratios of traditional Solomon Islands communities were much less than those of immigrant communities who had moved to the Solomon Islands from Kiribati in the central Pacific (Fritz and Kalligeris, 2008; McAdoo et al., 2008). Testimony from these communities strongly indicated that the traditional communities were alerted by the earthquake shaking followed by sea-level drawdown. They responded with a rapid evacuation initiated and led by the village elders, resulting in a lower fatality ratio. By contrast, in the immigrant communities, many people, including many children, did not evacuate since their arrival in the Solomon Islands between 1955 and 1962 postdated the previous large tsunamis in the area (McAdoo et al., 2009). Notably, children from the immigrant communities explored the reefs exposed by the drawdown, and many perished when the tsunami swept across the reefs. A subsequent study (McAdoo et al., 2009) found that the fatality ratios in the traditional or indigenous communities were less than 1% overall and were dominated by fatalities in a single village where the tsunami run-up height (12 m) was twice as high as it was anywhere else. The fatality ratios in the immigrant villages were approximately 4% overall, several times the average fatality ratio in the traditional communities.

Similarly, during the 2010 Chile tsunami, prompt and effective evacuations occurred in coastal fishing communities that had previously been affected by the 1960 tsunami and other earlier tsunamis. In contrast, much higher fatalities occurred among transient groups of tourists at coastal campsites (Fritz et al., 2011). Other recent examples of effective self-evacuations in long-established coastal communities have been reviewed by Okal (2015). These studies emphasize the role of community-based education and awareness programs in promoting self-warning and voluntary evacuations as effective measures in near-field areas where strong earthquake shaking provides sufficient warning.

THE 2011 GREAT EAST JAPAN TSUNAMI: RECONSIDERING THE SPATIAL SCALE

Spatial Scale

The spatial scale in Japan can be classified as follows: Level 1, prefectures; Level 2, cities/towns/villages; Level 3, village sections; and Level 4, streets (1×2 km^2), as shown in **Figure 3A**. However, as noted in the previous section, previous studies of the 2011 tsunami event have been based on large-scale population data or both large- and small-scale data. For example, Ueda (2012) used Level 2 data, whereas Yun and Hamada (2015) used a mixture of data from Levels 2–4 in their analysis. Therefore, the fatality ratios calculated by these authors are underestimates for the fatality ratios in the areas actually inundated, because they include in their calculations many people resident in parts of Level 2 domains outside the inundation areas. Their results cannot be compared to those from different areas for the same event or to those from the same areas for historical events where many communities were small and on the shore hence totally inundated. Therefore, the fatality ratios were recalculated in this study using a spatial scale as fine as Level 3 to investigate the factors that affect human fatalities and accurately compare the characteristics of the 2011 tsunami to those of other historical tsunamis.

Data

In this study, areas affected by the 2011 tsunami (**Figure 3B**) distinguished at the street level were selected from the Reconstruction Support Survey Archive (2016) based on two criteria: (1) the areas were required to be smaller than 3 km^2 to ensure that they only reflected the characteristics of one area and (2) the tsunami inundation ratios (the ratio of the area that is inundated) were required to be larger than 70% to ensure that the calculated fatality ratios were those of the actual exposed population (or as close as possible) to avoid including the non-exposed population, as shown in **Figure 3C**. Tsunami inundation depths at a resolution of 5 m × 5 m were also obtained from the Reconstruction Support Survey Archive (2016). In this study, the fatality ratio was defined as the ratio of the number of dead or missing persons to the total population before the 2011 tsunami, as illustrated in Eq. 1. A limitation should be noted when using the resident or nighttime population in this study. This event occurred in the afternoon, and retired or self-employed persons were home, while others may have been working outside of the village in which they lived: although equally, people resident outside the inundation area may have been working or at school in the inundation zone. Both the total number of people in the inundation zone at the time of the tsunami and the age distribution of that population are therefore subject to a degree of uncertainty given the data used.

$$\text{Fatality ratio (FR)}(\%) = \frac{\text{no. of dead} + \text{missing}}{\text{population before the tsunami}} \times 100 \quad (1)$$

Method of Calculation

Sets of inundation depths and fatality ratios at the village level (Level 3) from the Reconstruction Support Survey Archive (2016), Pearson's product-moment correlation coefficients (Pearson's R), and statistical data at each city/town/village level (Level 2) were computed in both Sanriku Coast and Sendai Plain study areas (**Figure 3A**). The Pearson's R values provide the basis for the discussion presented in Section "Factors That Affect Human Casualties during Tsunami Events," in which three different regions are examined separately: the Sanriku Coast, Sendai Plain, and Ishinomaki City. Finally, empirical formulas were proposed based on previously proposed fatality prediction models used by the central and local governments in Japan. Additional details regarding the determination of the empirical formulas are given in Section "Comparisons with Existing Empirical Equations for Human Fatality Estimation and Proposed New Equations."

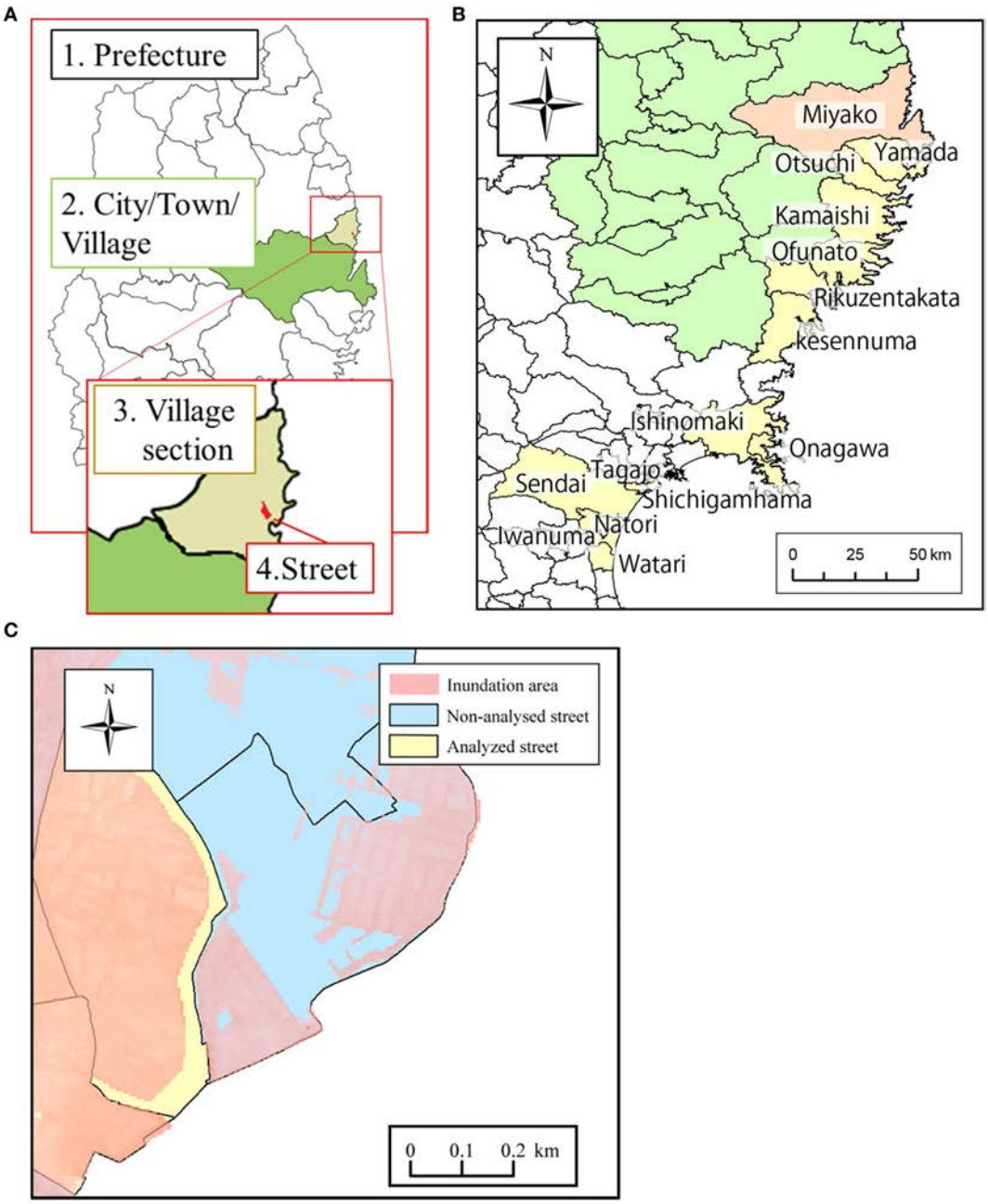

FIGURE 3 | **(A)** Spatial scale used in this study, **(B)** study areas, and **(C)** inundation area selected for this study.

FACTORS THAT AFFECT HUMAN CASUALTIES DURING TSUNAMI EVENTS

Many factors have been identified in previous studies [i.e., Aldrich and Sawada (2015) and Yun and Hamada (2015)], both quantitative and qualitative, that affect human fatality ratios during tsunami events. Their effects vary with the different characteristics of each event, which can be divided into four categories: (a) characteristics of the tsunami itself, such as arrival time, inundation depth, peak wave, and impact forces; (b) characteristics of the topography such as slope, land elevation, and coastal types; (c) characteristics of tsunami mitigation measures in the impacted region, such as evacuation routes and facilities, warning systems and disaster awareness programs, and extent of constructed barriers or tsunami defenses; and (d) personal characteristics of individuals in the population of the inundation zone, such as disaster awareness and knowledge of effective mitigation actions, mental and physical ability to gather and interpret information, mental ability to make evacuation decisions, and physical ability to implement these decisions. More details about the variables of each factor are summarized in **Table 2**.

TABLE 2 | Summary of variables for each factor that affect human fatality ratios.

Factor			
(a) Tsunami characteristics	**(b) Topographical characteristics**	**(c) Regional characteristics**	**(d) Personal characteristics**
High inundation depth (+)	Ria coast (+)	Defense structure (–)	High awareness (–)
High wave force (+)	High slope (+)	Warning system (–)	High knowledge (–)
Fast arrival time (+)	Low elevation (+)	Evacuation facility (–)	High decision-making capacity (–)

(+), positive contributor to fatality ratio; (–), negative contributor to fatality ratio.

The characteristics in the first two categories are widely known to strongly affect the fatality rate, and as a result numerous studies have been devoted to ensuring that tsunami models correctly represent the interactions between tsunami waves and topography to produce the resulting inundation and flow fields. Similarly, characteristics in the last two categories are co-dependent and also depend on the history of tsunamis in the region. Data from survivor interviews in the aftermath of the Tohoku 2011 tsunami (Ando et al., 2013), as well as video records of the disaster, strongly indicate that the actions of many were influenced by their expectations of likely tsunamis and the capacities of official tsunami warning systems, coastal defenses, and tsunami refuge areas. Failures of these defenses and refuges to protect against the tsunami resulted in significantly increased casualties in some places (Ando et al., 2013; Day and Fearnley, 2015). When interpreting the results of statistical approaches to understanding the importance of different characteristics based on the factors that influence fatality rates, it is important to recognize the complexities that may be associated with the interactions between characteristics.

Factors That Affect Human Fatality Ratios on the Sanriku Coast

The Sanriku Coast has a distinctive coastal topography, namely, that of a so-called ria coastline, where tsunamis can be easily amplified (Suppasri et al., 2013). The local communities there have experienced with historically recent tsunami disasters (the 1896 Meiji Sanriku and 1933 Showa Sanriku tsunamis). Thus, the human fatality ratios on the Sanriku Coast were affected by the factors shown in Eq. 2 and **Table 3**. There is a weak correlation between inundation depth and fatality ratio in this region [**Figure 4A**; $R \leq 0.32$ (**Figure 4D**)], with large scatter and a strong negative correlation in Onagawa, likely due to personal characteristic factors such as an expectation of safety in areas not expected to be inundated.

$$\begin{aligned}\text{Human fatalities} \propto\ & \text{(a) Tsunami characteristics} \\ & +\text{(b) Topographical characteristics} \\ & +\text{(c) Regional characteristics} \\ & +\text{(d) Personal characteristics}\end{aligned} \tag{2}$$

Factors That Affect Human Fatality Ratios on the Sendai Plain

The Sendai Plain has low relief [(b) topographical characteristics], and relatively few disaster prevention facilities have been established in the area [(c) regional characteristics]. As a result, a strong linear relationship between the inundation depth and fatality ratio can be observed in some areas of the Sendai Plain [**Figure 4D**, such as Ishinomaki (Pearson's $R = 0.75$), Tagajo ($R = 0.85$), Sendai ($R = 0.75$), Natori ($R = 0.59$), and Watari ($R = 0.69$)], as shown in **Figure 4B**. Human fatality ratios in this region are likely controlled only by tsunami and personal characteristics, as shown in **Table 3** and Eq. 3.

$$\begin{aligned}\text{Human fatalities} \propto\ & \text{(a) Tsunami characteristics} \\ & +\text{(d) Personal characteristics}\end{aligned} \tag{3}$$

Factors That Affect Human Fatalities in the Urban Area of Ishinomaki City on the Sendai Plain

The urban area of Ishinomaki City comprises two main zones, including housing and factory zones, as shown in **Figures 4** and **5**. The tsunami evacuation ratio in the urban area of Ishinomaki City during the 2011 tsunami was uniformly quite low [(d) human characteristics] (Mikami, 2014). Hence, variations in the personal characteristics of the residents had little effect on variations in the human fatalities within this area, which were controlled mainly by the characteristics of the tsunami, as shown in Eq. 4 and **Table 3**. As a result, a strong correlation between the inundation depth and fatality ratio ($R = 0.85$ in **Figure 4D**) can be observed in **Figure 4C**.

$$\text{Human fatalities} \propto \text{(a) Tsunami characteristics} \tag{4}$$

Relationship between the Fatality Ratio and Building Damage

This section focuses on the fatality ratios and levels of building damage in the urban area of Ishinomaki City (**Figures 5** and **6**). **Figure 7A** shows a good correlation ($R = 0.75$) between the inundation depths and fatality ratios in the residential areas of the city. To compare this relationship with the level of building damage, the building damage ratio (P_D) is defined as shown in Eq. 5 based on the equation proposed by Hatori (1984).

$$\text{Building damage ratio (PD)(\%)} = \frac{\begin{array}{l}\text{no. of buildings washed} \\ \text{away and collapsed} + \\ \text{half of moderately} \\ \text{damaged buildings}\end{array}}{\text{all inundated buildings}} \times 100 \tag{5}$$

The results shown in **Figure 7B** reveal that the inundation depth exhibits a close correlation with the building damage ratio ($R = 0.89$). **Figure 7C** shows that the fatality ratio also exhibits a good correlation ($R = 0.75$) with the building damage ratio up to 0.9. However, some variability or weak correlation is observed when the building damage ratio is closer to 1.0. These findings

TABLE 3 | Summary of the dominant factors that affect human fatalities in each region.

Region	Factor			
	(a) Tsunami characteristics	(b) Topographical characteristics	(c) Regional characteristics	(d) Personal characteristics
Sanriku Coast	X	X	X	X
Sendai Plain	X			X
Ishinomaki urban area	X			

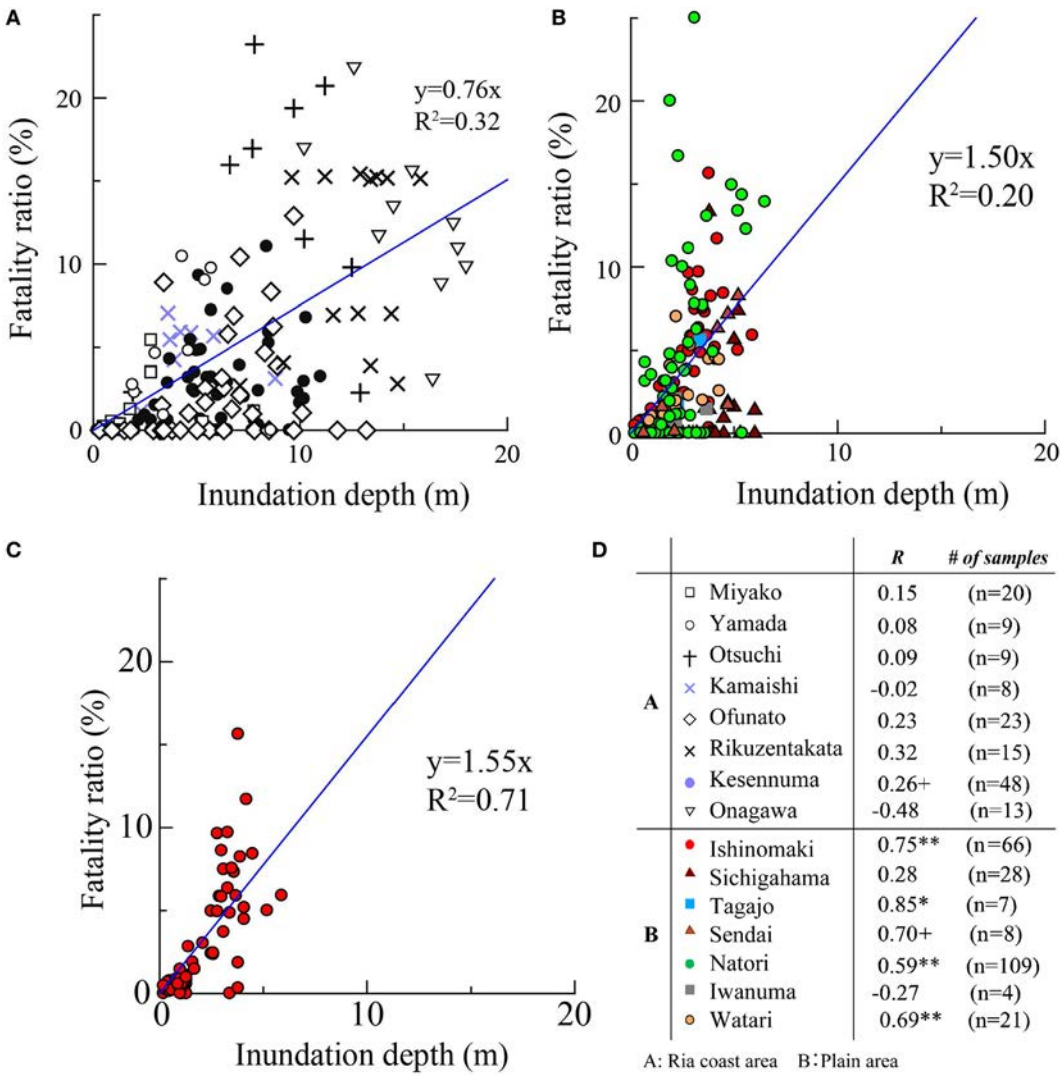

FIGURE 4 | Plots of fatality ratio vs. inundation depth for (A) the Sanriku Coast, (B) Sendai Plain, (C) the urban area of Ishinomaki City, and (D) the correlation coefficients in the form of Pearson's *R* for each location. Note that $^{**}p = 0.01$ and $^{+}p < 0.10$.

suggest that a large number of the human casualties in this event occurred in the victims' homes because of the low evacuation ratio. In other words, human fatalities and building damage likely occurred at the same time. This analysis is consistent with the survey results, which indicated that approximately 63% of the casualties in Ishinomaki occurred in the victims' homes. In addition, a study conducted by Goto (2015) found that no tsunami evacuation drills had been performed in the residential areas and that this scenario was responsible for the failure to evacuate at least 20% of the residents. By contrast, more extensive evacuation was observed in industrial areas (red circles in **Figure 7**), where far more tsunami information was available to the populations

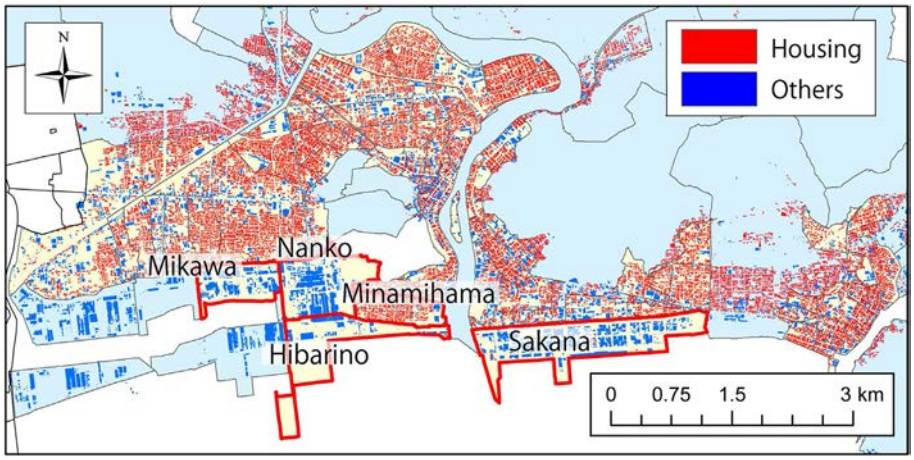

FIGURE 5 | **Spatial distribution of building types in the urban area of Ishinomaki City**.

FIGURE 6 | **Damage in Ishinomaki City: (A) photograph of an industrial area and (B) photograph of a residential area (photograph date: 15/4/2011)**.

of industrial workers. This suggests that tsunami warning and evacuation drills organized at the level of the workplace were effective.

Comparisons with Existing Empirical Equations for Human Fatality Estimation and Proposed New Equations

Several previous studies have been performed in Japan, which have yielded empirical equations for estimating fatality ratios. Miyano and Ro (1992) used the number of damaged buildings in the case of the 1944 Tonankai earthquake as a parameter for estimating the number of casualties. Shizuoka Prefecture (2001) adapted this previously developed equation by adding population data as an input parameter to address the case of the 1993 Okushiri tsunami. The Suppasri et al. (2012) in Japan used tsunami inundation depth and population data as input parameters for fatality estimation based on the same 1993 Okushiri tsunami.

Based on the findings from Sections "Factors That Affect Human Fatalities in the Urban Area of Ishinomaki City on the Sendai Plain" and "Relationship Between the Fatality Ratio and Building Damage," human fatalities in residential areas in Ishinomaki City, which is located in a plain area with few tsunami prevention facilities, low tsunami awareness, and limited evacuation plans, were strongly correlated with tsunami characteristics. In addition, many previously proposed models were relatively simple and used only tsunami-related parameters, namely, inundation depth and building damage. Therefore, we also develop empirical equations based on the improved fatality ratios in case of the 2011 tsunami. The exponential model and power model were selected to construct a single regression equation for calculating the fatality ratio using the inundation depth and building damage ratio. These models were selected because regression analysis can be performed based on the relationship between the fatality ratio, inundation depth, and building damage ratio, and a value of 0 is applicable when using these models.

In the present study, the inundation depths (H) and building damage ratios (P_D) in the case of the 2011 tsunami were considered as input parameters to estimate the fatality ratios via empirical equations. The data shown in **Figures 7A,B** were used as a basis for developing the equations for fatality ratio estimation shown in **Table 3**. Models (1) and (2) are equations in which the inundation depth is used as the input parameter ($FR = aH^b$), whereas models (3) and (4) use the building damage ratio $\left(FR=aP_D^b\right)$. Models (1) and (3) include data from industrial areas, whereas models (2) and (4) are based only on data from residential areas, as shown in **Figures 4** and **5**. The latter models can be used to estimate fatality ratios in areas where low evacuation rates are expected. Proposed equations for fatality ratio estimation are shown in **Table 4**. These formulas can be applied to areas where less evacuation or late evacuation behavior is expected.

Comparison with the 2004 Indian Ocean Tsunami

The fatality ratios of the historical tsunamis discussed in Section "Historical Tsunamis" were compiled based on tsunami run-up height rather than inundation depth. Therefore, a direct comparison with this study is not possible. However, a detailed study of the fatality ratios and inundation depths in the case of the 2004 Indian Ocean tsunami was performed by Koshimura et al. (2009).

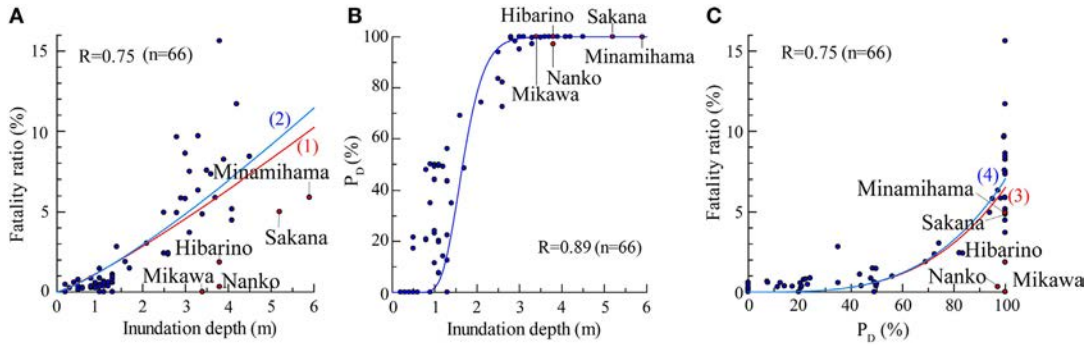

FIGURE 7 | Plots for the urban area of Ishinomaki City showing (A) fatality ratio vs. inundation depth, (B) building damage ratio vs. inundation depth, and (C) fatality ratio vs. building damage ratio. See **Figure 5** for geographic locations. (1) to (4) refers to models (1) to (4) as discussed in Section "Comparisons with Existing Empirical Equations for Human Fatality Estimation and Proposed New Equations."

TABLE 4 | Proposed equations for fatality ratio estimation.

Model number	**Model (1)**		**Model (2)**	
Model type	**FR = 1.28$H^{1.16}$**		**FR = 1.26$H^{1.23}$**	
Parameter	Coefficient	Standard error	Coefficient	Standard error
A	1.28***	0.33	1.26***	0.23
b	1.16***	0.20	1.23***	0.14
R^2	0.53		0.72	
Model number	**Model (3)**		**Model (4)**	
Model type	**FR = 6.53$P_D^{3.38}$**		**FR = 7.04$P_D^{3.45}$**	
Parameter	Coefficient	Standard error	Coefficient	Standard error
a	6.53***	0.43	7.04***	0.31
b	3.38***	1.01	3.45***	0.61
R^2	0.67		0.84	

*** $p < 0.001$.

These authors collected fatality ratios for each village in Banda Aceh, which was the largest area affected by this tsunami event. They reported that the potential tsunami casualties increased upwards from an inundation depth exceeding 2 m (fatality ratio = 10%) and that the maximum fatality ratio of 100% was reached for an inundation depth of 8 m.

By contrast, in the case of the 2011 Great East Japan tsunami analyzed in this study, the fatality ratio was approximately 3% at a 2 m inundation depth, and most fatality ratios for this event were below 20%. The fatality ratios in the case of the 2004 tsunami were much higher than those during the 2011 tsunami for the following reasons: (1) in case of the 2004 tsunami, a large number of weak buildings suffered damage from the earthquake; (2) the most recent event that occurred before the 2004 tsunami-like event was approximately 600 years prior (Jankaew et al., 2008; Monecke et al., 2008), resulting in less tsunami awareness due to a lack of experience; (3) no tsunami warning system or tsunami awareness education had been implemented in the Indian Ocean region before the 2004 tsunami; and (4) the existing small coastal defense structures in the Indian Ocean at the time of the 2004 event were intended only for shoreline protection or high-tide protection and not for protection against tsunamis.

Comparison to the 2007 Solomon Islands Tsunami

In the cases of the other studies discussed in Section "2004 Indian Ocean Tsunami, 2007 Solomon Islands Tsunami, and 2010 Chile Tsunami," the data are often incomplete, but partial comparisons are possible. In the 2007 Solomon Islands tsunami, although directly measured data on inundation depths are sparse, the relationship between inundation depth and fatality ratio can be inferred because the majority of the affected houses were stilt-type houses with floors 1 m to 2 m above ground level. Such houses are remarkably resistant to the effects of tsunamis that do not inundate their raised floors because the water flows freely past the cross-braced stilts [see, for example, Figure 3E of Fritz and Kalligeris (2008)], but they collapse at greater inundation depths when the force of the flow acts upon the walls of the upper part of the house. Thus, the destruction of all houses in many traditional communities affected by the 2007 Solomon Islands tsunami indicates inundation depths greater than the 1 m to 2 m range. Nevertheless, most of these communities reported 0% fatality ratios, while the community with the highest fatality ratio–of 3%–among affected traditional communities experienced inundation of no less than 5 m depth (Fritz and Kalligeris, 2008). We can therefore conclude that typical fatality ratios would therefore be much lower than 3% at a 2 m inundation depth in such communities and, therefore, even less than those observed at the same inundation depth in the 2011 Great East Japan tsunami.

CONCLUSION

First, this study reviewed the relationship between the maximum tsunami heights and fatality ratios of historical tsunamis in Japan. The data clearly reveal different trends, as extremely large tsunamis (associated with landslides or tsunami earthquakes) that occurred more than 100 years ago resulted in high fatality ratios. Experiences from these tsunamis appear to have reduced the fatality ratios in the subsequent generations, as is the case in South Pacific countries where damaging tsunamis occur with a

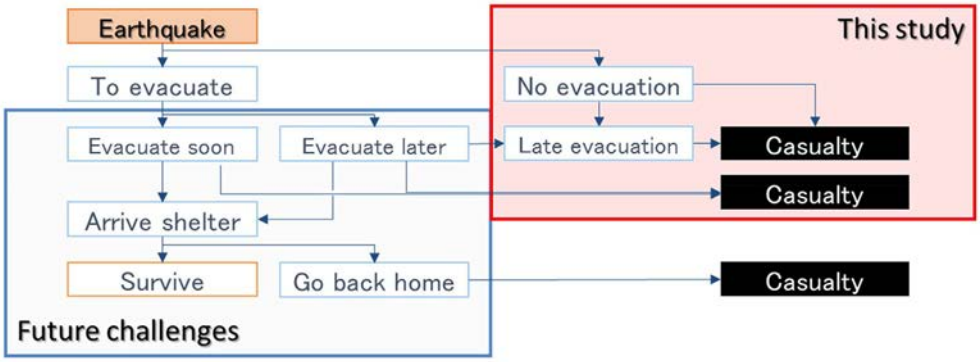

FIGURE 8 | **Flow chart of the causes of casualties in the case of an earthquake tsunami**.

high frequency of one every 50 years or less. As a result, traditional coastal communities in these places possess a high level of tsunami hazard awareness, the ability to self-warn based on a variety of warning signs, and knowledge of the necessity for rapid evacuation. However, a similar high-fatality scenario occurred recently in Japan (Okushiri, 1993) when a tsunami formed at an unexpected location and arrived very quickly.

Second, this study focused on the 2011 Great East Japan tsunami. The main limitations of previous studies were noted, namely, the scales of the areas used to calculate the fatality ratios relative to the areas of inundation. To address this shortcoming, the fatality and population data used in this study were carefully selected to ensure that the calculated fatality ratios had the same definition in all areas and to enable comparisons with other historical tsunamis. In this study, the factors that affect human fatalities were interpreted after careful investigation of the relationship between the maximum inundation depths and fatality ratios. The identified factors that affect human fatalities include tsunami characteristics, topographical characteristics, regional characteristics, and human characteristics. There were few disaster prevention facilities and a low evacuation ratio in the urban area of Ishinomaki City on the Sendai Plain because of the lack of historical large tsunamis in this area, which led to a strong relationship between the fatality ratios and building damage ratios. Empirical formulas were also proposed to estimate the fatality ratios based on the inundation depths and building damage ratios in the residential areas of Ishinomaki City. These formulas can be applied to areas where less evacuation or late evacuation behavior is expected.

Third, a comparison of the data from the 2011 tsunami (city area of Ishinomaki) and that from the 2004 Indian Ocean tsunami (Banda Aceh) reflects the effects of different regional characteristics and human characteristics on the human fatality rate, with a much lower fatality ratio at the same inundation depth in 2011 in Japan. A similar effect was observed for the variation in the fatality rates between different communities in the Solomon Islands 2007, Chile 2010, and other tsunamis.

We emphasize that analyses involving statistically significant correlations between characteristics and fatality rate must be performed with caution and based on various data sources, such as the information provided by survivor interviews and video recordings from tsunami disasters. As an example, we cite the correlation between pre-2011 political support for the governing LDP party and the fatality rate of the Tohoku 2011 tsunami identified by Aldrich and Sawada (2015), which they interpret as indicative that political support was rewarded by greater investment in tsunami defenses, local hazard awareness, and warning systems. However, survivor interviews (Ando et al., 2013) indicate that the net effect of the tsunami defenses may have been harmful, and decisions to evacuate were rarely influenced by locally generated official warnings but strongly associated with self-warning based on knowledge of previous events, as was observed during other tsunamis discussed above. Thus, the statistical correlation identified by Aldrich and Sawada may be associated with greater political support for the LDP in more stable and traditional communities, which are also characterized by more widespread and deeply ingrained knowledge of previous tsunamis, such as those of 1896 and 1933. Thus, correlation does not imply causation in this case.

In summary, this study has clarified the factors that affect human fatality ratios in the case of the 2011 tsunami in Japan and found that the urban area of Ishinomaki can serve as a good example of a case in which the residents decided not to evacuate, decided to evacuate but did so too late, and suffered fatalities during evacuation, as shown in **Figure 8**. Thus, the findings of this study can improve the understanding of evacuation scenarios that lead to human casualties and facilitate the estimation of human casualties associated with potential future tsunamis in similar areas.

ETHICS STATEMENT

Although the study analyzed and discussed about human casualty and analyzed fatality ratios, we have received a permission from the Reconstruction Support Survey Archive (http://fukkou.csis.u-tokyo.ac.jp/) for a usage of fatality data. These data are only officially provided to authorized institutions for academic purposes. We generalized the data and plotting so that individual data can not be identified in all explanations and illustrations. As stated above, we used the fatality data prepared by the archive.

The data are fatality ratio for each village where individual data cannot be identified.

AUTHOR CONTRIBUTIONS

AS wrote the whole paper, illustrations, and gave detailed discussions on the analysis and general comments. NH did the analysis and illustrations. FM gave detailed discussions on the analysis. FI and PL gave general comments. SD wrote additional parts of the paper and gave overall comments.

FUNDING

The authors would like to express our sincere gratitude to the reviewers for their valuable advice. This research was funded by the Reconstruction Agency of the Government of Japan, Tokio Marine & Nichido Fire Insurance Co., Ltd., Willis Research Network, and JSPS Grant-in-Aid for Young Scientists (B) "Applying developed fragility functions for the Global Tsunami Model (GTM)" (No. 16K16371), through IRIDeS, Tohoku University.

REFERENCES

Aldrich, D. P., and Sawada, Y. (2015). The physical and social determinants of mortality in the 3.11 tsunami. *Soc. Sci. Med.* 124, 66–75. doi:10.1016/j.socscimed.2014.11.025

Ando, M., Ishida, M., Hayashi, Y., Mizuki, C., Nishikawa, Y., and Tu, Y. (2013). Interviewing insights regarding the fatalities inflicted by the 2011 Great East Japan earthquake. *Nat. Hazards Earth Syst. Sci.* 13, 2173–2187. doi:10.5194/nhess-13-2173-2013

Day, S., and Fearnley, C. (2015). A classification of mitigation strategies for natural hazards: implications for the understanding of interactions between mitigation strategies. *Nat. Hazards* 79, 1219–1238. doi:10.1007/s11069-015-1899-z

Endoh, K., and Takahashi, S. (1995). "Numerically modelling personnel danger on a promenade breakwater due to overtopping waves," in *Proceedings of the XXIV International Conference on Coastal Engineering (ICCE)*, ed. B. L. Edge (Kobe, Japan: American Society of Civil Engineers), 1016–1029.

Fritz, H. M., and Kalligeris, N. (2008). Ancestral heritage saves tribes during 1 April 2007 Solomon Islands tsunami. *Geophys. Res. Lett.* 35, L01607. doi:10.1029/2007GL031654

Fritz, H. M., Petroff, C. M., Catalán, P. A., Cienfuegos, R., Winckler, P., Kalligeris, N., et al. (2011). Field survey of the 27 February 2010 Chile tsunami. *Pure Appl. Geophys.* 168, 1989–2010. doi:10.1007/s00024-011-0283-5

Goto, Y. (2015). Tsunami evacuation features of organizations and individuals in Kadonowaki and Minamihama of Ishinomaki. *Proc. Civ. Eng.* 71, 930–942; (in Japanese). doi:10.2208/jscejseee.71.I_930

Hatori, T. (1984). Damage probability of houses by tsunamis. *Bull. Earthq. Res. Inst.* 59, 433–439; (in Japanese).

Jaiswal, K. S., Wald, D. J., Earle, P. S., Porter, K. A., and Hearne, M. (2011). "Earthquake fatalities models within the USGS prompt assessment of global earthquakes for response (PAGER) system," in *Human Casualties in Earthquakes – Progress in Modelling and Mitigation*, eds R. Spence, E. So, and C. Scawthorn (Dordrecht: Springer), 83–94.

Jankaew, K., Atwater, B. F., Sawai, Y., Choowong, M., Charoentitirat, T., Martin, M. E., et al. (2008). Medieval forewarning of the 2004 Indian Ocean tsunami in Thailand. *Nature* 455, 1228–1231. doi:10.1038/nature07373

Kawata, Y. (1997). Prediction of loss of human lives due to catastrophic earthquake disaster. *Jpn. Soc. Nat. Disast. Sci.* 16, 3–13. Japanese.

Koshimura, S., Katada, T., Mofjeld, H., and Kawata, Y. (2006). A method for estimating casualties due to the tsunami inundation flow. *Nat. Hazards* 39, 265–274. doi:10.1007/s11069-006-0027-5

Koshimura, S., Oie, T., Yanagisawa, H., and Imamura, F. (2009). Developing fragility functions for tsunami damage estimation using numerical model and post-tsunami data from Banda Aceh, Indonesia. *Coast. Eng. J.* 51, 243–273. doi:10.1142/S0578563409002004

Marchand, M., Buurman, J., Pribadi, A., and Kurniawan, A. (2009). Damage and casualties modelling as part of a vulnerability assessment for tsunami hazards: a case study from Aceh, Indonesia. *J. Flood Risk Manag.* 2, 120–131. doi:10.1111/j.1753-318X.2009.01027.x

McAdoo, B. G., Fritz, H. M., Jackson, K. L., Kalligeris, N., Kruger, J., Bonte-Grapentin, M., et al. (2008). Solomon Islands tsunami, one year later. *EOS* 89, 169–170. doi:10.1029/2008EO180001

McAdoo, B. G., Moore, A., and Baumwoll, J. (2009). Indigenous knowledge and the near field population response during the 2007 Solomon Islands tsunami. *Nat. Hazards* 48, 73–82. doi:10.1007/s11069-008-9249-z

Mikami, T. (2014). The survey analysis about the victims by the tsunami under the Great East Japan earthquake – Yamada-cho and Ishinomaki city. *Proc. Civ. Eng.* 70, 908–915. Japanese. doi:10.2208/jscejseee.70.I_908

Miyano, M., and Ro, H. J. (1992). *Examination of Human Damage at the Time of the Earthquake Based on Historical Damage Survey Data*, Vol. 2. Report of Institute of Social Safety Science, 127–135. (in Japanese).

Miyazawa, K., Goto, K., and Imamura, F. (2012). "Re-evaluation of the 1771 Meiwa tsunami source model, southern Ryukyu Islands, Japan," in *Advances in Natural and Technological Hazards Research, Submarine Mass Movements and Their Consequences*, Vol. 31, eds Yamada Y., Kawamura K., Ikehara K., Ogawa Y., Urgeles R., Mosher D., et al. (Dordrecht: Springer), 497–506.

Monecke, K., Finger, W., Klarer, D., Kongko, W., McAdoo, B. G., Moore, A. L., et al. (2008). A 1,000-year sediment record of tsunami recurrence in northern Sumatra. *Nature* 455, 1232–1234. doi:10.1038/nature07374

Muhari, A., Imamura, F., Koshimura, S., and Post, J. (2011). Examination of three practical run-up models for assessing tsunami impact on highly populated areas. *Nat. Hazards Earth Syst. Sci.* 11, 3107–3123. doi:10.5194/nhess-11-3107-2011

Okal, E. A. (2015). The quest for wisdom: lessons from 17 tsunamis, 2004-2014. *Phil. Trans. R. Soc. A* 373, 20140370. doi:10.1098/rsta.2014.0370

Reconstruction Support Survey Archive. (2016). *Victims Situation*. Available at: http://fukkou.csis.u-tokyo.ac.jp/

Satake, K., Fujii, Y., Harada, T., and Namegaya, Y. (2013). Time and space distribution of coseismic slip of the 2011 Tohoku earthquake as inferred from tsunami waveform data. *Bull. Seismol. Soc. Am.* 103, 1473–1492. doi:10.1785/0120120122

Satake, K., and Tanioka, Y. (1999). Sources of tsunami and tsunamigenic earthquakes in subduction zones. *Pure Appl. Geophys.* 154, 467–483. doi:10.1007/s000240050240

Shizuoka Prefecture. (2001). *The 3rd Earthquake Damage Assumption Result*. Shizuoka, Japan, 171–175. (in Japanese).

Sieh, K. (2006). Sumatran megathrust earthquakes: from science to saving lives. *Philos. Trans. A Math. Phys. Eng. Sci.* 364, 1947–1963. doi:10.1098/rsta.2006.1807

Sugimoto, T., Murakami, H., Kozuki, Y., Nishikawa, K., and Shimada, T. (2003). A human damage prediction method for tsunami disasters incorporating evacuation activities. *Nat. Hazards* 29, 587–602. doi:10.1023/A:1024779724065

Suppasri, A., Imamura, F., and Koshimura, S. (2012). Tsunami hazard and casualty estimation in a coastal area that neighbors the Indian Ocean and South China Sea. *J. Earthquake and Tsunami* 6, 1250010. doi:10.1142/S1793431112500108

Suppasri, A., Koshimura, S., Imai, K., Mas, E., Gokon, H., Muhari, A., et al. (2012). Damage characteristic and field survey of the 2011 Great East Japan tsunami in Miyagi prefecture. *Coast. Eng. J.* 54, 1250008. doi:10.1142/S0578563412500088

Suppasri, A., Shuto, N., Imamura, F., Koshimura, S., Mas, E., and Yalciner, A. C. (2013). Lessons learned from the 2011 Great East Japan tsunami: performance of tsunami countermeasures, coastal buildings and tsunami evacuation in Japan. *Pure Appl. Geophys.* 170, 993–1018. doi:10.1007/s00024-012-0511-7

Tsuji, Y., Nishihata, T., Sato, T., and Sato, K. (2002). Inundation heights of the 1741 Oshima-Oshima volcanic eruption tsunami along the coast of Hokkaido. *Kaiyo Mon.* 28, 15–44; (in Japanese).

Ueda, R. (2012). "Multiple regression analyses of human damage due to tsunami in the 2011 Great East Japan earthquake – synthetic study on characteristics of

tsunami and social factors," in *Proceedings of Institute of Social Safety Science*, Vol. 18. (Tokyo: Institute of Social Safety Science), 443–450. (in Japanese).

Yamashita, F. (2008). *Tsunami and Disaster Prevention-Sanriku Tsunami*, Vol. 158. Tokyo: Kokon-Shoin Publishing. (in Japanese).

Yeh, H. (2010). Gender and age factor on tsunami casualties. *Nat. Hazard Rev.* 11, 29–34. doi:10.1061/(ASCE)1527-6988(2010)11:1(29)

Yeh, H. (2014). "Tsunami hazard and casualty estimation model," in *Tenth US National Conference on Earthquake Engineering* (Alaska: Frontiers of Earthquake Engineering Anchorage).

Yun, N. Y., and Hamada, M. (2015). Evacuation behaviour and fatality rate of residents during the 2011 Great East Japan earthquake and tsunami. *Earthq. Spectra* 31, 1237–1265. doi:10.1193/082013EQS234M

Conflict of Interest Statement: The authors declare that the research was conducted in the absence of any commercial or financial relationships that could be construed as a potential conflict of interest.

Copyright © 2016 Suppasri, Hasegawa, Makinoshima, Imamura, Latcharote and Day. This is an open-access article distributed under the terms of the Creative Commons Attribution License (CC BY). The use, distribution or reproduction in other forums is permitted, provided the original author(s) or licensor are credited and that the original publication in this journal is cited, in accordance with accepted academic practice. No use, distribution or reproduction is permitted which does not comply with these terms.

frontiers in Built Environment

ORIGINAL RESEARCH
published: 22 June 2015
doi: 10.3389/fbuil.2015.00008

The 2015 Gorkha Nepal earthquake: insights from earthquake damage survey

Katsuichiro Goda[1], Takashi Kiyota[2], Rama Mohan Pokhrel[2], Gabriele Chiaro[2], Toshihiko Katagiri[2], Keshab Sharma[3] and Sean Wilkinson[4]*

[1] Department of Civil Engineering, University of Bristol, Bristol, UK, [2] Institute of Industrial Science, University of Tokyo, Tokyo, Japan, [3] Department of Civil and Environmental Engineering, University of Alberta, Edmonton, AB, Canada, [4] School of Civil Engineering and Geosciences, Newcastle University, Newcastle upon Tyne, UK

The 2015 Gorkha Nepal earthquake caused tremendous damage and loss. To gain valuable lessons from this tragic event, an earthquake damage investigation team was dispatched to Nepal from 1 May 2015 to 7 May 2015. A unique aspect of the earthquake damage investigation is that first-hand earthquake damage data were obtained 6–11 days after the mainshock. To gain deeper understanding of the observed earthquake damage in Nepal, the paper reviews the seismotectonic setting and regional seismicity in Nepal and analyzes available aftershock data and ground motion data. The earthquake damage observations indicate that the majority of the damaged buildings were stone/brick masonry structures with no seismic detailing, whereas the most of RC buildings were undamaged. This indicates that adequate structural design is the key to reduce the earthquake risk in Nepal. To share the gathered damage data widely, the collected damage data (geo-tagged photos and observation comments) are organized using Google Earth and the kmz file is made publicly available.

Keywords: 2015 Nepal earthquake, earthquake damage survey, building damage, ground motion, aftershocks

OPEN ACCESS

Edited by:
Solomon Tesfamariam, The University of British Columbia, Canada

Reviewed by:
Vladimir Sokolov, Karlsruhe Institute of Technology, Germany
Takeshi Koike, Kyoto University, Japan

****Correspondence:***
Katsuichiro Goda, Department of Civil Engineering, University of Bristol, Queen's Building, University Walk, Bristol BS8 1TR, UK
katsu.goda@bristol.ac.uk

Specialty section:
This article was submitted to Earthquake Engineering, a section of the journal Frontiers in Built Environment

Received: *28 May 2015*
Accepted: *08 June 2015*
Published: *22 June 2015*

Citation:
Goda K, Kiyota T, Pokhrel RM, Chiaro G, Katagiri T, Sharma K and Wilkinson S (2015) The 2015 Gorkha Nepal earthquake: insights from earthquake damage survey. Front. Built Environ. 1:8. doi: 10.3389/fbuil.2015.00008

Introduction

An intense ground shaking struck Central Nepal on 25 April 2015 (local time 11:56 a.m.). The moment magnitude of the earthquake was M_w7.8 with its hypocenter located in the Gorkha region (about 80 km north–west of Kathmandu). The earthquake occurred at the subduction interface along the Himalayan arc between the Indian plate and the Eurasian plate (Avouac, 2003; Ader et al., 2012). The earthquake rupture propagated from west to east and from deep to shallow parts of the shallowly dipping fault plane [United States Geological Survey (USGS), (2015)], and consequently, strong shaking was experienced in Kathmandu and the surrounding municipalities. This was the largest event since 1934, M_w8.1 Bihar–Nepal earthquake (Ambraseys and Douglas, 2004; Bilham, 2004). The 2015 mainshock destroyed a large number of buildings and infrastructure in urban and rural areas, and triggered numerous landslides and rock/boulder falls in the mountain areas, blocking roads, and hampering rescue and recovery activities. Moreover, aftershock occurrence has been active since the mainshock; several major aftershocks (e.g., M_w6.7 and M_w7.3 earthquakes in the Kodari region, north–east of Kathmandu) caused additional damage to rural towns and villages in the northern part of Central Nepal. As of 26 May 2015, the earthquake damage statistics for Nepal from the 25 April 2015 mainshock stand at the total

number of 8,510 deaths and 199 missing[1]. In addition, the major aftershock that occurred on 12 May 2015 caused 163 deaths/missing. Center for Disaster Management and Risk Reduction Technology (CEDIM), (2015) reports that the total economic loss is in the order of 10 billion U.S. dollars, which is about a half of Nepal's gross domestic product. The 2015 earthquakes will have grave long-term socioeconomic impact on people and communities in Nepal [United Nations Office for the Coordination of Humanitarian Affairs (UN-OCHA), (2015)].

Earthquake field observations provide raw damage data of existing built environments and are useful for developing empirical correlation between ground motion intensity and damage severity for earthquake impact assessment of future events. To gain valuable lessons from this tragic event, an earthquake damage investigation team was jointly organized by the Japan Society of Civil Engineers and the Japan Geotechnical Society, and was dispatched to Nepal from 1 May 2015 to 7 May 2015. The survey trip was planned in such away that relatively large geographical areas that were affected by the earthquakes were covered to grasp spatial features of the damage in the earthquake-hit regions. A unique aspect of this damage investigation is that the data were collected at the early stage of disaster response and recovery (6–11 days after the mainshock), and thus first-hand earthquake damage observations were obtained before major repair work. The collected damage data, in the form of geo-tagged photos and some measurements (e.g., size of a landslide), are useful for other earthquake damage reconnaissance teams who visit Nepal several weeks after the mainshock, and serve as a starting point of longitudinal research of a recovery process from the earthquakes. To achieve this goal, damage photos that were taken during the survey trip are organized using Google Earth and are made publicly available; the kmz file is provided as supplementary resource of this paper. Viewers can download the photos directly and can use them for research and educational purposes; all photos are geo-tagged and are accompanied by brief comments.

This paper summarizes key findings of ground shaking damage in Nepal, and is organized as follows. To link building damage observations with available seismological data, seismotectonic setting of Nepal is reviewed, and earthquake rupture process and aftershock data, which are available from the U.S. Geological Survey (USGS), are analyzed to gain scientific insights into ground motions that were experienced during the mainshock and major aftershocks. It is important to note that strong motion observation networks in Nepal are not well developed and data are not publicly accessible. This means that the estimation of observed ground motions at building damage sites is highly uncertain. Currently, recorded time-history data of strong motion are only available at the KATNP station, which is located in the city center of Kathmandu. In this study, strong motion data at KATNP are analyzed and the results, in the form of elastic response spectra, are discussed by comparing with relevant ground motion prediction models [e.g., Kanno et al. (2006) and Boore and Atkinson (2008)] and with well-recorded strong motion data from the 2008 M_w7.9 Wenchuan China earthquake (Lu et al., 2010), seismological features of which are broadly similar to the 2015 Nepal earthquake. Furthermore, issues related to ground motion estimation for prompt earthquake impact assessment [e.g., Jaiswal and Wald (2010) and Center for Disaster Management and Risk Reduction Technology (CEDIM), (2015)] are discussed by examining how the way source-to-site distance measures, as in ground motion prediction equations, are evaluated affects the scenario shake map of a large subduction event within a fault rupture zone (note: size of the fault rupture zone can be in the order of a few hundred kilometers for M_w8.0+ earthquakes). Such investigations provide new insights for improvements in producing more reliable scenario shake maps and prompt earthquake impact assessments (Goda and Atkinson, 2014). Subsequently, building typology in Nepal is reviewed briefly, followed by earthquake damage observations in Kathmandu, Melamchi, Trishuli, and Baluwa. Finally, key lessons from the 2015 Nepal earthquake are summarized.

Regional Seismicity and Ground Motion

This section aims at providing with relevant seismological information for interpreting earthquake damage survey observations in Nepal (which are discussed in the following section). First, seismotectonic and seismological aspects of the on-going mainshock–aftershock sequence are reviewed by analyzing available earthquake catalog data and source rupture models of the mainshock. Strong ground motion recordings at KATNP are analyzed to estimate the observed ground motion intensity in Kathmandu. Subsequently, scenario shake maps are generated by considering different source-to-site distance measures to highlight the influence of finite-fault source representation for a large earthquake in applications to prompt earthquake impact assessment.

Seismotectonic Setting and Seismic Hazard in Nepal

Nepal is located along the active Main Himalayan Thrust arc, where the subducting Indian plate and the overriding Eurasian plate interact. This region accommodates approximately a half of the tectonic convergence between these two plates, i.e., about 20 mm/year (Avouac, 2003; Ader et al., 2012). The locked part of the subduction interface has a low-dip angle (about 10°) and is located at depths of 4–18 km (Bilham, 2004), and has potential to generate M_w8+ earthquakes (Gupta, 2006).

Historically, Nepal hosted several large earthquakes (Ambraseys and Douglas, 2004; Bilham, 2004). A map of Nepal and locations of major historical seismic events are shown in **Figure 1**. Western Nepal experienced a M_w8.2 event in 1505. This event occurred west of the rupture zone of the 2015 earthquake and accumulated strain in this seismic gap region has not been released since then; thus, there is high potential for future large earthquakes in the western region. In Eastern Nepal, two known major earthquakes occurred in 1833 and 1934. In particular, the 1934 M_w8.1 Bihar–Nepal earthquake was destructive and caused many fatalities (+10,000 deaths). The 2015 Gorkha–Kodari earthquakes have ruptured a fault section that overlaps with the fault rupture plane of the 1934 earthquake (see **Figure 1**). It is noted that the rupture planes of

[1]http://earthquake-report.com/

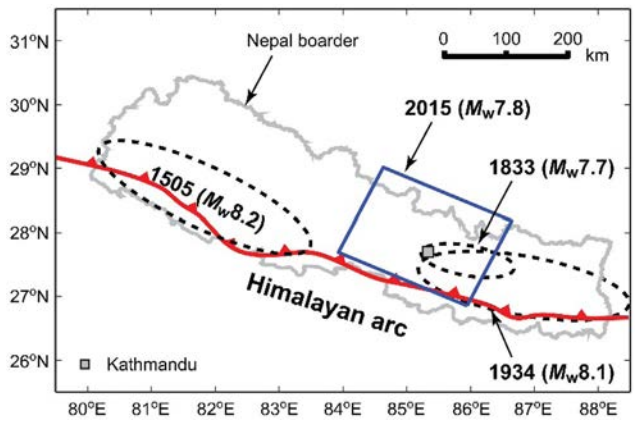

FIGURE 1 | Major historical earthquakes in Nepal along the Himalayan arc. The locations of three historical earthquakes (1505, 1833, and 1934) are approximate. For the M_w7.8 mainshock, the fault plane model by the USGS is shown.

the 1934 and 2015 earthquakes are directly beneath Kathmandu, although the locations of their hypocenters are east and west of Kathmandu, respectively.

Recently, several probabilistic seismic hazard studies have been conducted for Nepal by employing updated seismic source zone models based on improved earthquake catalogs and modern ground motion models [e.g., Nath and Thingbaijam (2012) and Ram and Wang (2013)]. The estimated peak ground acceleration (PGA) with 10% probability of exceedance in 50 years (i.e., return period of 475 years) in Western Nepal ranges between 0.5and 0.6 g, whereas that in Eastern Nepal ranges between 0.3 and 0.6 g. These hazard estimates are obtained for rock sites, therefore, when typical soil sites are considered (e.g., Kathmandu Valley), they need to be increased. An important observation is that the ground motion shaking in Kathmandu during the 2015 mainshock (which is discussed in detail in the following) was less than the PGA estimates with 10% probability of exceedance in 50 years, which may be considered as a basis for seismic design in Nepal.

Fault Rupture Model of the 25 April 2015 Mainshock

Several earthquake rupture models for the 2015 mainshock have been developed [e.g., United States Geological Survey (USGS) (2015); Yagi (2015)]. A common feature of the estimated slip distributions is that large slips occurred north and north–east of Kathmandu, and the rupture propagated from the hypocenter (north–west of Kathmandu) toward east as well as south (deeper to shallower depth). The slip distribution of the USGS model is illustrated in **Figure 2A**. The fault length and width of the rupture plane are 220 and 165 km, respectively, and its strike and dip are 295° and 10°, respectively. **Figure 3** overlays the route of the survey trip over the USGS source model to put visited locations (i.e., Melamchi, Trishuli, and Baluwa) into perspective with respect to the earthquake slip distribution. The USGS source model has its maximum slip of 3.11 m (north of Kathmandu). It is also interesting to observe that the estimated slip near the hypocenter is 1.29 m, which is about 40% of the maximum slip, and its distance from the maximum slip sub-fault (i.e., asperity) is about 70 km. By analyzing numerous earthquake rupture models statistically, Mai et al. (2005) found that the rupture often nucleates in the regions of low-to-moderate slip (sub-faults with slip <2/3 of the maximum slip) and close to the maximum slip sub-fault. The rupture nucleation of the 2015 mainshock (i.e., slip and location at the hypocenter) is in good agreement with these empirical rules suggested by Mai et al. (2005).

Aftershocks

In post-earthquake situations, one of the major concerns for evacuees and emergency response teams is the occurrence of major aftershocks, triggering secondary hazards. Generally, a larger earthquake is followed by more aftershocks, and returning to a background level of seismic activities takes longer. **Figure 2A** shows the spatial distribution of aftershocks that occurred before 25 May 2015 (30 days since the mainshock). The aftershock data are obtained from the USGS NEIC catalog[2]. Immediately after the mainshock, a moderate (M_w6.6) aftershock occurred near the hypocenter. On the other hand, the majority of aftershocks occurred in the Kodari region (north–east of Kathmandu); a notable event was the 12 May 2015 M_w7.3 aftershock, which caused additional damage and casualties. Comparison of the aftershock distribution with respect to the slip distribution of the mainshock indicates that the major aftershocks do not occur very near to the mainshock asperity (with large slip) but they occur in the surrounding areas of the mainshock asperity. This is because the spatial and temporal characteristics of aftershocks are the manifestation of internal crustal dynamics involving the redistribution of stress and displacement fields (Stern, 2002; Heuret et al., 2011).

To gain further insights into the aftershock occurrence process of the 2015 mainshock–aftershock sequence, statistical analysis of aftershock data is carried out by applying the Gutenberg–Richter law and the modified Omori law (Shcherbakov et al., 2005); the completeness magnitude is set to 4.5 for the analyses. The Gutenberg–Richter law describes the frequency–magnitude characteristics of an aftershock sequence, whereas the modified Omori law models a temporal decay of an aftershock occurrence rate. The fitting of the 2015 Nepal aftershock data to the Gutenberg–Richter relationship is satisfactory (**Figure 2B**); the estimated slope parameter (i.e., *b*-value) is −0.862. This slope is slightly gentler (i.e., more productive for larger aftershocks) than the typical *b*-value for global subduction earthquakes but within the expected range (Shcherbakov et al., 2013). **Figure 2C** shows that the modified Omori's law fits well with the aftershock data. The obtained parameters are typical for global subduction earthquakes (Shcherbakov et al., 2013). For example, the temporal decay parameter (i.e., *p* value, power parameter in the equation shown in **Figure 2C**) is 1.049, which is close to the global average of about 1.2 (by taking into account inherent variability of this parameter). The above results support the applicability of well-established empirical laws for characterizing the 2015 Nepal aftershock data. This is a useful confirmation from seismic risk management viewpoints because initial estimates of aftershock-related hazard can be obtained from

[2]http://earthquake.usgs.gov/earthquakes/search/

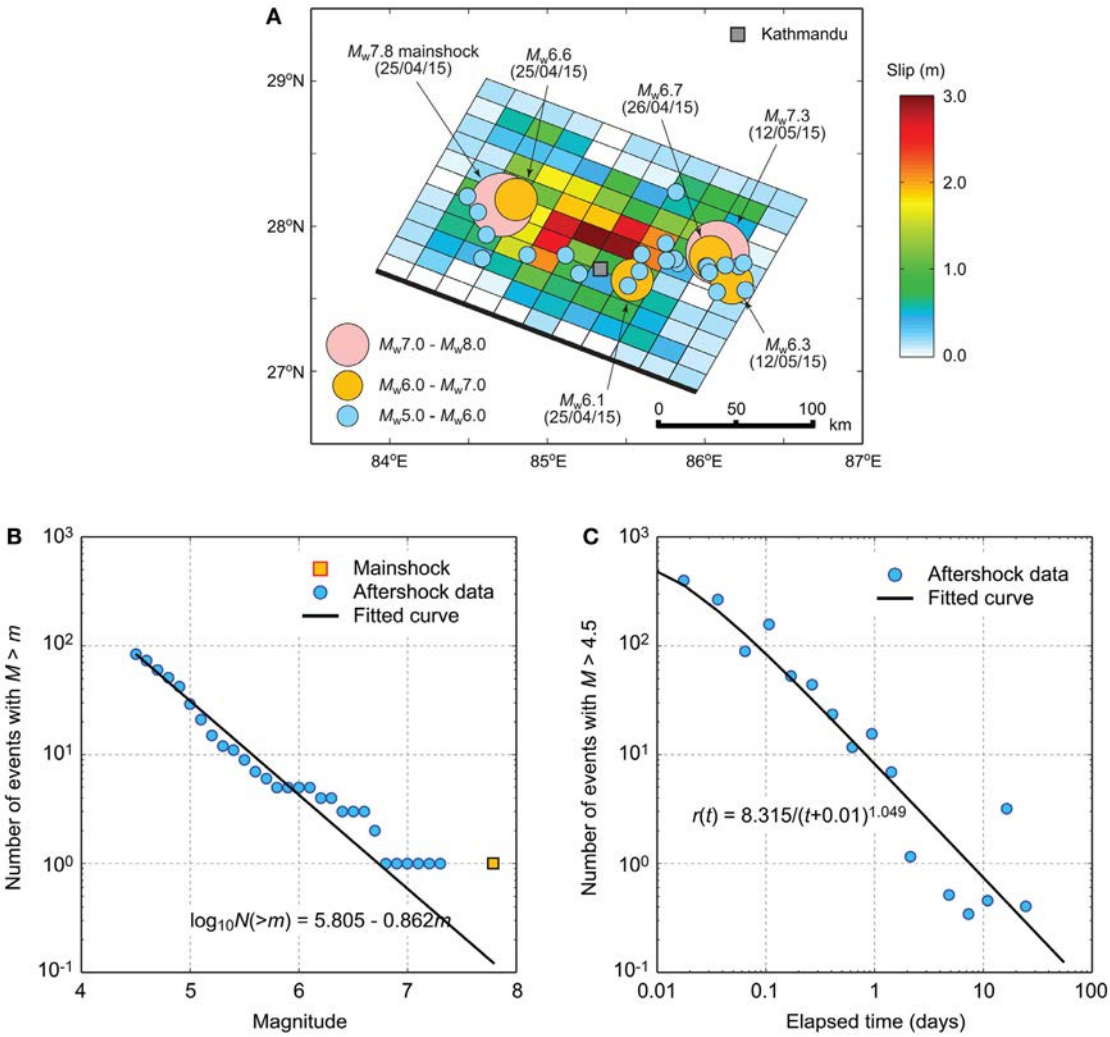

FIGURE 2 | **(A)** Aftershock distribution of the 2015 earthquake sequence; an earthquake source model by the USGS is shown. **(B)** Gutenberg–Richter relationship of the 2015 earthquake sequence. **(C)** Modified Omori law of the 2015 earthquake sequence.

the empirical aftershock models immediately after the mainshock (before real-time data are collected and analyzed).

Ground Motion in Kathmandu

The accelerograms recorded at KATNP are publicly available[3]. In light of poor strong motion network in Nepal, the recorded ground motion data at KATNP are invaluable and serve as a benchmark in estimating ground motion intensity at unobserved locations in Kathmandu. **Figure 4** shows the location of the KATNP station; the map also shows the locations of the earthquake damage survey sites in Kathmandu. The KATNP station is located near the historical district in the city center (e.g., Durbar Square), where severe damage and collapse of old historical buildings occurred.

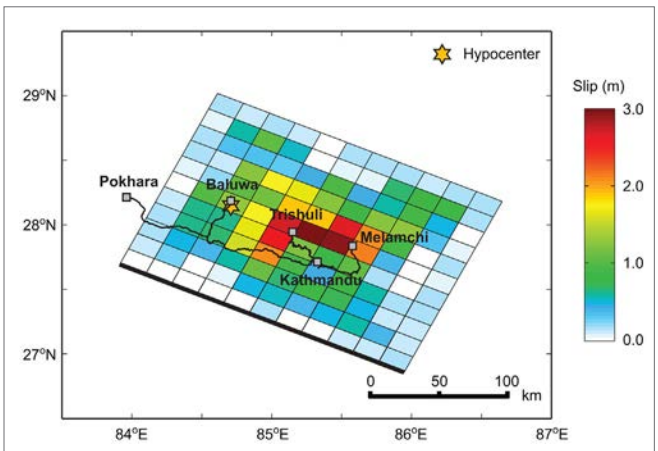

FIGURE 3 | **Earthquake damage survey locations**.

[3]http://www.strongmotioncenter.org/

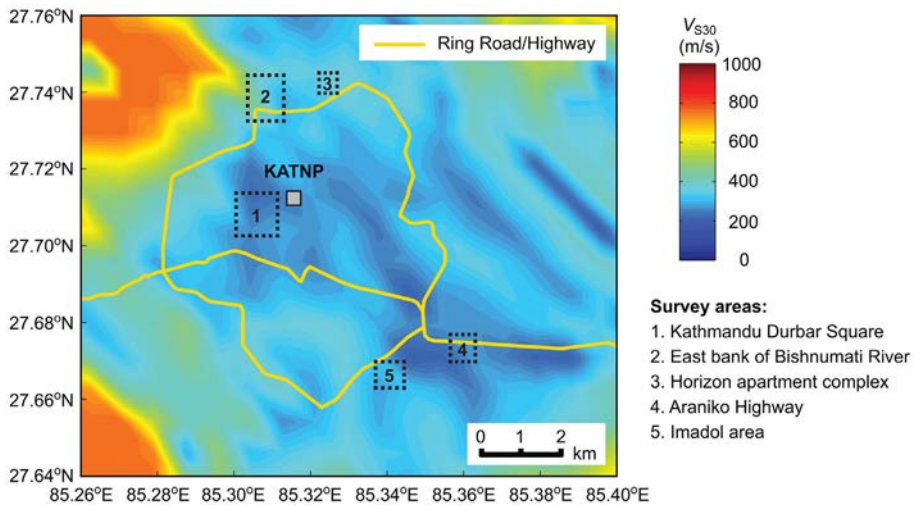

FIGURE 4 | **Location of the strong motion recording station KATNP and earthquake damage survey locations in Kathmandu**.

Prior to ground motion data analysis and estimation, it is important to review typical site conditions in Kathmandu, as they affect ground motion intensity significantly. Kathmandu is located in the Kathmandu Basin, where thick lacustrine and fluvio-lacustrine sediments are deposited (Sakai et al., 2002). The thickness of sediments (i.e., depth to bedrock) is in the range of 550–650 m. The setting of the Kathmandu Valley is similar to Mexico City (Paudyal et al., 2012), noting that during the 1985 Michoacán earthquake, long-period ground motions were significantly amplified in Mexico City due to soft lakebed deposits and caused catastrophic damage to mid-to-high-rise buildings. A seismic microzonation study in Kathmandu, conducted by Paudyal et al. (2012), indicates that the dominant periods of the ground at sites inside the Ring Road (see **Figure 4**) are between 1.0 and 2.0 s (i.e., high potential for resonating with long-period ground motions), and that the dominant period is correlated with the thickness of Pliocene and Quaternary deposits. The KATNP station is located within the long-dominant-period zone.

Another useful source of information in assessing site amplification potential of near-surface soil deposits in Kathmandu is the USGS global V_{S30} server (Wald and Allen, 2007)[4]. V_{S30} is the average shear-wave velocity in the uppermost 30 m and is often employed as a proxy site parameter in ground motion models [e.g., Kanno et al. (2006) and Boore and Atkinson (2008)]. Wald and Allen (2007) correlated V_{S30} data with topographic slope to derive the first-order estimate of the site amplification for two tectonic regimes, active and stable continental regions. The database is implemented to develop USGS ShakeMaps (Wald et al., 2005)[5], which are used for rapid earthquake impact assessment (Jaiswal and Wald, 2010)[6]. **Figure 4** shows the V_{S30} contour map in Kathmandu. The map indicates that the central part of Kathmandu has soft surface deposits (typically NEHRP site class D, V_{S30} between 180 and 360 m/s). The V_{S30} value at the KATNP station is 250 m/s. It is noteworthy that V_{S30} is applicable to near-surface site amplification only; amplification of long-period seismic waves due to a large-scale geological structure (e.g., basin) should be taken into account separately.

Figures 5A,B show recorded accelerograms (three components) at KATNP for the M_w7.8 mainshock and for the M_w7.3 aftershock, respectively (note: among other recorded aftershock ground motions at KATNP, the M_w7.3 aftershock records show the most significant effects). An inspection of the time-history data indicates that the PGA of the recorded ground motions is about 150–170 and 70–80 cm/s^2 for the M_w7.8 mainshock and the M_w7.3 aftershock, respectively. These are significantly smaller than the PGA estimates with 10% probability of exceedance in 50 years from the recent regional seismic hazard studies (Nath and Thingbaijam, 2012; Ram and Wang, 2013). It is also observed that long-period components are present in the M_w7.8 mainshock records (**Figure 5A**). To further investigate the extent of ground shaking at KATNP, 5%-damped response spectra of the recorded accelerograms for the M_w7.8 mainshock and the M_w7.3 aftershock are calculated and compared in **Figure 5C**. The results suggest that the amplitudes of response spectra for the mainshock are greater than those for the major aftershock (also applicable to other aftershocks). For the M_w7.8 mainshock, two large peaks of response spectra are present at vibration periods around 0.2–0.6 s (N–S component only) and around 4.0–6.0 s (both N–S and E–W components). The former is attributed to direct shaking due to near-source ruptures, whereas the latter is caused by the combination of rich long-period content of seismic waves at source (because of large moment magnitude) and site amplification due to the basin effects. Given the existing building stock in Kathmandu/Nepal (the majority of buildings are low-to-mid rise and thus are likely to have vibration periods <1.0 s; Chaulagain et al., 2015), the main causes of severe structural damage and collapse of buildings in

[4]http://earthquake.usgs.gov/hazards/apps/vs30/
[5]http://earthquake.usgs.gov/earthquakes/shakemap/
[6]http://earthquake.usgs.gov/earthquakes/pager/

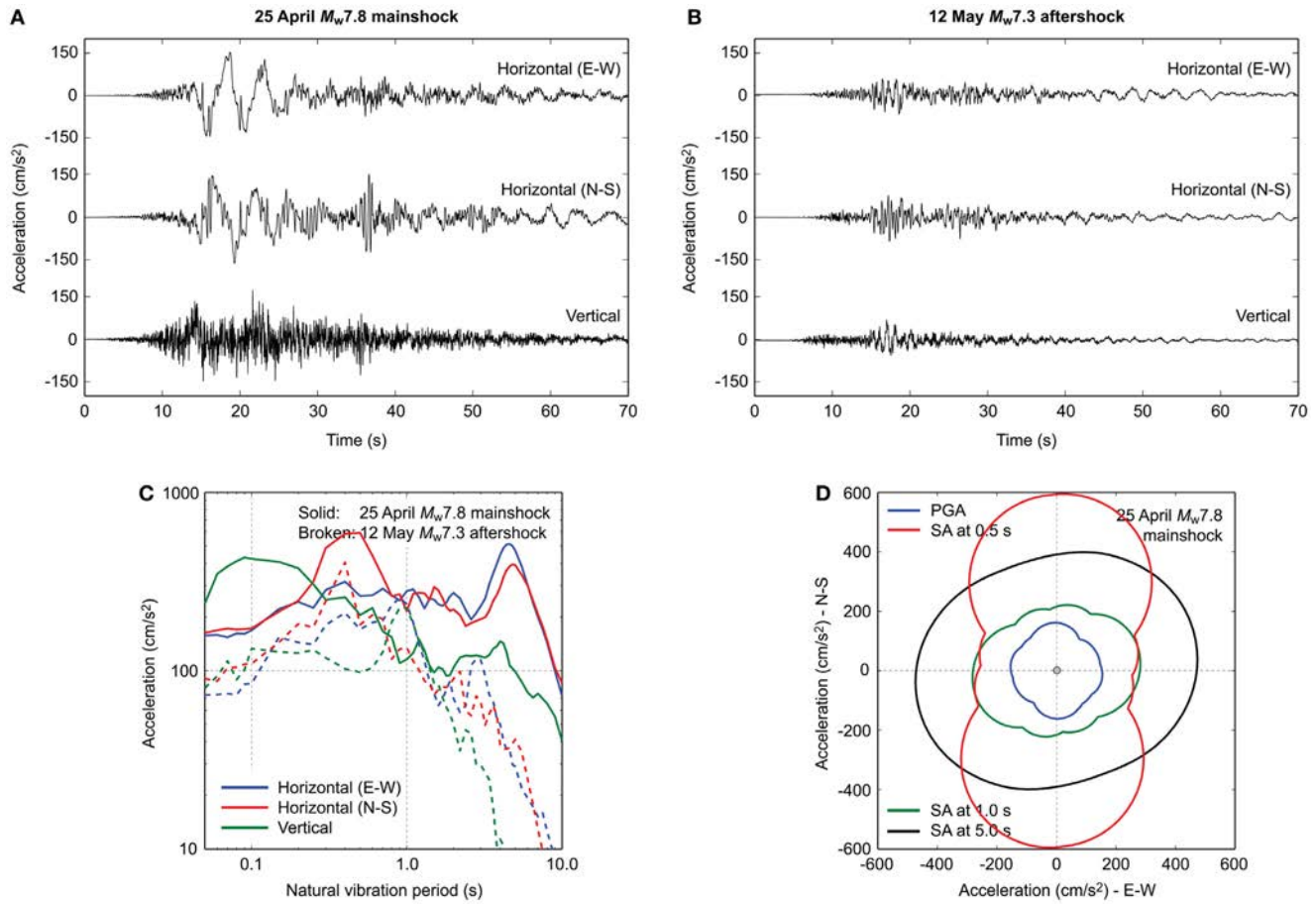

FIGURE 5 | **(A)** Recorded accelerograms at KATNP for the M_w7.8 mainshock. **(B)** Recorded accelerograms at KATNP for the M_w7.3 aftershock. **(C)** 5%-damped spectral accelerations (SA) of the recorded accelerograms at KATNP for the M_w7.8 mainshock and the M_w7.3 aftershock. **(D)** Polar plots of the PGA and spectral accelerations at 0.5, 1.0, and 5.0 s of the rotated accelerograms at KATNP for the M_w7.8 mainshock.

Kathmandu are due to the large peak in the short vibration period range. It is important to point out that buildings in Kathmandu were largely unaffected by the long-period ground motions in the Kathmandu Valley because of non-resonance. This was fortunate in the context of the current disaster. However, earthquake engineers should pay careful attention to long-period ground motions (Takewaki et al., 2011), when tall buildings are constructed in the central part of the Kathmandu Valley.

To further examine the orientation of ground motion parameters at KATNP for the M_w7.8 mainshock, PGA and 5%-damped spectral accelerations are computed by rotating accelerograms recorded at KATNP from 0° to 360° (Hong and Goda, 2007). The polar plots of PGA and spectral accelerations at 0.5, 1.0, and 5.0 s are shown in **Figure 5D**. The results are useful for understanding the orientation dependency of the peak seismic demand in the near-fault region (Huang et al., 2008). The results indicate that the spectral acceleration at 0.5 s (i.e., large response spectral peak in the short-vibration period range) is highly polarized; the ratio of the maximum-to-minimum response is about 2.5, while the degree of such polarization of the response spectra is much less pronounced at other vibration periods. Although it is beyond the scope of this study, a further insight can be gained by investigating the effects of the orientation of ground motion with regard to the structural axis of damaged versus non-damaged buildings near the KATNP station.

Comparison of Observed Ground Motion in Kathmandu with Ground Motion from the 2008 Wenchuan Earthquake and Predicted Ground Motion

Due to the limited availability of recorded ground motions in Central Nepal, ground motion estimation may need to rely on: (1) ground motion data from other seismic regions having broad similarity with the target region [e.g., Sharma et al. (2009)], (2) empirical ground motion prediction models [e.g., Nath and Thingbaijam (2011)], or (3) ground motion simulations [e.g., Harbindu et al. (2014)]. In this study, the first two options are explored to gain insights into actual ground motions for the M_w7.8 mainshock.

For Option 1, ground motion data from the 2008 M_w7.9 Wenchuan earthquake (Lu et al., 2010) are analyzed. This

earthquake is chosen because seismotectonic settings in Nepal and Tibet (i.e., southern and eastern sides of the Tibetan Plateau) are broadly similar and their earthquake magnitudes are comparable. The Wenchuan earthquake occurred along the Longmenshan fault Sichuan, China. The amplitude–distance plots of PGA and spectral accelerations at 0.5and 5.0 s are shown in **Figure 6**; only records at soft soil sites (V_{S30} <400 m/s) are considered. The rupture distance (R_{rup}, shortest distance from a site of interest to the fault rupture plane) for the Wenchuan data is calculated using the fault plane model by Ji (2008).

For Option 2, a ground motion model by Kanno et al. (2006) (hereafter Kanno06) is adopted. This prediction equation was developed by using ground motion records from Japanese earthquakes and from worldwide shallow crustal earthquakes (i.e., Next Generation Attenuation database). The Kanno06 equation is selected among other applicable models [e.g., Boore and Atkinson (2008), Sharma et al. (2009), and Harbindu et al. (2014)] for three reasons. The first reason is that the performance test of various ground motion models conducted by Nath and Thingbaijam (2011) indicates that the Kanno06 equation is superior to other candidate models in predicting PGA at rock sites in Northern India and Nepal. Second, the applicable moment magnitude range of the Kanno06 equation covers the moment magnitude of the 2015 Nepal earthquake; for instance, regional equations by Sharma et al. (2009) and Harbindu et al. (2014) are not applicable to M_w 8-class earthquakes. Third, the Kanno06 equation adopts R_{rup} as a representative distance measure, while the equation by Boore and Atkinson (2008) (hereafter BA08) adopts the Joyner–Boore distance (R_{jb}, shortest distance from a site of interest to the projected fault rupture plane on Earth's surface). The use of R_{jb} can be problematic because ground motion intensity for the locations above the fault rupture plane is evaluated using a uniform value of $R_{jb} = 0$ km (which results in significant bias of predicted ground motion intensity). This issue is revisited in the next subsection.

Figure 6 compares observed ground motions at KATNP (i.e., **Figure 5**) with the ground motion data from the M_w 7.9 Wenchuan earthquake as well as the Kanno06 model. The rupture distance for KATNP (=11.1 km) is calculated using the USGS finite-fault plane model (i.e., **Figure 2A**). For the Kanno06 model, 16th and 84th percentile curves are also shown to indicate a typical range of predicted ground motion variability. **Figure 6A** indicates that the observed PGA at KATNP is significantly smaller than the Wenchuan data in the similar distance range and the predicted PGA based on the Kanno06 equation (below the 16th percentile curve). The below-average trend of the observed ground motion intensity, in comparison with the Wenchuan data and the Kanno06 model, persists for spectral accelerations at vibration periods <2.0 s (**Figure 6B**). These comparisons indicate that the level of short-period ground motion near KATNP during the 2015 mainshock was smaller than expected ground motion levels based on empirical data/models for similar scenarios. On the other hand, **Figure 6C** shows an opposite trend: the long-period spectral acceleration at KATNP is significantly greater than the counterparts based on the Wenchuan data and the Kanno06 model. The large spectral acceleration in the long vibration period range is attributed to the basin effects. It is also interesting to note that the recent ground motion prediction model, such as Boore et al. (2014), can take into account the basin effects using a depth-to-bedrock parameter [note: in **Figure 6**, the equation by Boore et al. (2014) is not considered because it is based on R_{jb}]. Using the empirical model by Boore et al. (2014), the expected site amplification due to the basin effects is a factor of two for vibration periods longer than 2.0 s; the observed long-period spectral acceleration can be better explained. Therefore, it is important to adopt advanced ground motion models that can account for major systematic components (e.g., faulting mechanism and basin amplification) in predicting ground motion intensity for future earthquakes.

Scenario Shake Map

Rapid earthquake impact reports [e.g., Center for Disaster Management and Risk Reduction Technology (CEDIM), (2015)] are useful because emergency officers and international aiding agencies can appreciate the expected level of destruction due to an earthquake at the very early stage of a disaster. In producing rapid earthquake impact assessment, scenario shake maps are the essential input. In these applications, shake maps are generated by using a suitable ground motion model together with observed

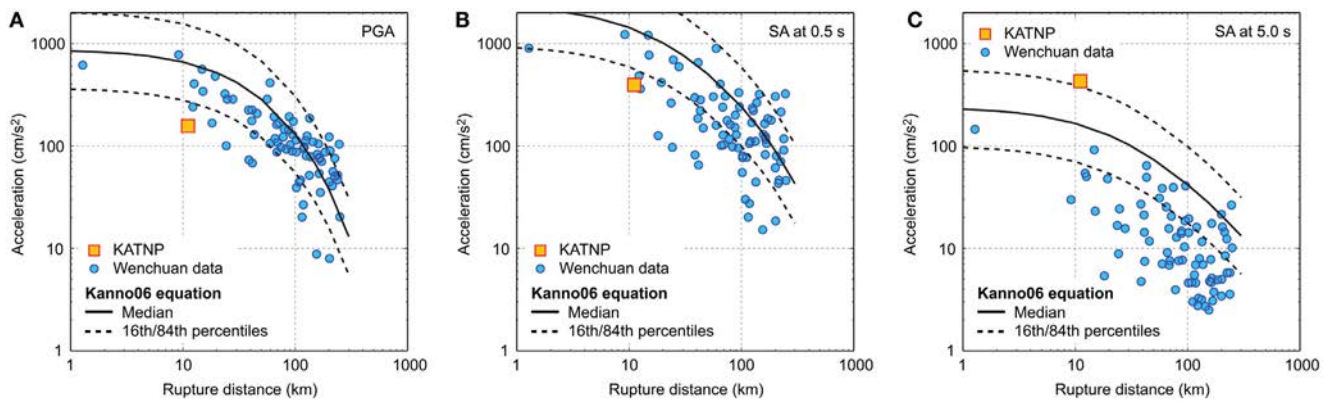

FIGURE 6 | Comparison of the observed PGA (A) and spectral accelerations [0.5 s in (B) and 5.0 s in (C)] at KATNP with the M_w 7.9 Wenchuan ground motion data and with the ground motion model by Kanno et al. (2006).

instrumental data and seismic intensity information (e.g., DYFI; Atkinson and Wald, 2007)[7]. In seismic regions with limited monitoring capability of strong motion, shake maps are more dependent on the accuracy of an adopted ground motion model as well as on initial estimates of the seismic event (e.g., moment magnitude). This is because there will not be many real-time observations to constrain the shake map predictions.

Modern ground motion models adopt extended-source-based distance measures, such as R_{rup} and R_{jb} (i.e., calculation of these distance measures requires a fault plane model). A simpler representation of an earthquake source is a point source model; in this case, hypocentral and epicentral distances, R_{hypo} and R_{epi}, are often used. When a slip distribution is available, another useful distance measure is the shortest distance to the asperity R_{asp} (Goda and Atkinson, 2014). For large subduction events having large fault plane dimensions, the calculated distance measures can vary significantly, depending on how a fault plane model is defined and which distance measure is adopted. For instance, for the M_w7.8 mainshock, distance measures at KATNP are evaluated as: R_{rup} = 11.1 km, R_{jb} = 0.1 km (numerical lower bound), R_{hypo} = 85.3 km, R_{epi} = 76.8 km, and R_{asp} = 29.4 km. The influence of distance measures is particularly significant for large magnitude events.

The above-mentioned problem has an important implication on shake map generation for a large earthquake. To demonstrate this for the M_w7.8 mainshock, four scenario PGA shake maps are developed by considering different distance measures and ground motion models. The results are shown in **Figure 7**. **Figures 7–C** are based on the Kanno06 model together with R_{rup}, R_{hypo}, and R_{asp}, respectively, whereas **Figure 7D** is based on the BA08 model with R_{jb}. For all shake maps, V_{S30} information at individual sites is taken into account. Strictly, R_{hypo} and R_{asp} should not be used in the Kanno06 model (as the distance measures and the model development process are incompatible); this is for illustration only. **Figure 7A** shows the predicted PGAs at sites above the fault plane are large (0.5–0.7 g) and predicted PGA values gradually decrease toward north (i.e., the fault plane becomes deeper). **Figures 7B,C** show different patterns from **Figure 7A** because the distance measures are essentially defined for point source but with different source locations (i.e., hypocenter versus asperity). The predicted PGA values in **Figures 7B,C** are less than those in **Figure 7A** and are in more agreement with observed ground motion intensity in Kathmandu. **Figure 7D** shows the most significant difference from the observed ground motion intensity in Kathmandu because for all sites above the fault plane, the distance measure is set to R_{jb} = 0.1 km. Indeed, the USGS ShakeMap is similar to **Figure 7D** in terms of amplitude and spatial pattern of the shake map. Importantly, bias in estimated ground motions propagates into rapid earthquake impact assessment. The key issue here is that the current ground motion model together with a finite-fault plane can result in biased predictions of overall earthquake impact (which may affect subsequent decisions for emergency response actions). From practical viewpoints, this issue needs to be resolved in the near future.

[7]http://earthquake.usgs.gov/earthquakes/dyfi/

Earthquake Damage Survey

This section presents main observations and findings from the earthquake damage survey in Nepal. The building typology in Nepal is briefly reviewed, and then, field observations in Kathmandu, Melamchi, Trishuli, and Baluwa are discussed. The regional map of the visited locations is shown in **Figure 3**, and the main survey locations in Kathmandu are indicated in **Figure 4**. The cases discussed in the following are selected to highlight main observations from the survey trip. Numerous photos are available through the Google Earth file as supplementary material to this paper.

Building Typology in Nepal

Buildings in Nepal are vulnerable to seismic actions. The majority of houses and buildings are not seismically designed and constructed, lacking ductile behavior. Due to poor seismic performance, many buildings were damaged/collapsed and these structural failures caused many fatalities during the 2015 earthquake sequences. This subsection briefly summarizes general characteristics of building typology in Nepal. More complete information (e.g., statistics of building characteristics) is available in Chaulagain et al. (2015). According to the 2011 National Population and Housing Census, the total number of individual households in Nepal is 5,423,297, while the population is 26,494,504. The census data indicate that mud-bonded brick/stone masonry buildings are the most common in all geographical regions of Nepal (44.2%), followed by wooden buildings (24.9%). In urban areas (e.g., Kathmandu Valley), buildings with cement-bounded brick/stone (17.6%) and cement concrete (9.9%) are popular.

In Nepal, many masonry buildings are constructed with walls made of sun-dried/fired bricks or stone with mud mortar, and the building frame is made of wood. These types of buildings generally have flexible floors and roof, and are prevalent in rural areas. The masonry materials are of low strength and thus are seismically vulnerable. Recently, with the advancement of the cement in Nepal, brick/stone buildings are constructed with cement mortar. The wooden buildings are popular near the forest areas in Nepal. In these buildings, wooden pillars are made out of tree trunks and walls are constructed with wooden planks or bamboo net cement/mud mortar plaster. The reinforced concrete (RC) building is a modern form of construction in Nepal, which began in late 1970s. The RC moment resisting frame assembly is comprised of cast-in-place concrete beams and columns with cast-in-place concrete slabs for floor and roof. Most of the conventional RC constructions are non-engineered (i.e., not structurally designed) and thus lack sufficient seismic resistance. Engineered RC buildings, which are relatively new, often adopt the Indian standard code with seismic provisions.

Survey Results in Kathmandu

Many historical buildings in the Kathmandu Durbar Square (in front of the Old Royal Palace of the former Kathmandu Kingdom and is a UNESCO World Heritage site) were devastated (area 1 in **Figure 4**). **Figure 8A** shows the collapse of the Basantapur Tower. The complete destruction in the Durbar Square was in sharp contrast with undamaged buildings surrounding the Durbar Square (**Figure 8B**; several wall cracks can be found on these buildings;

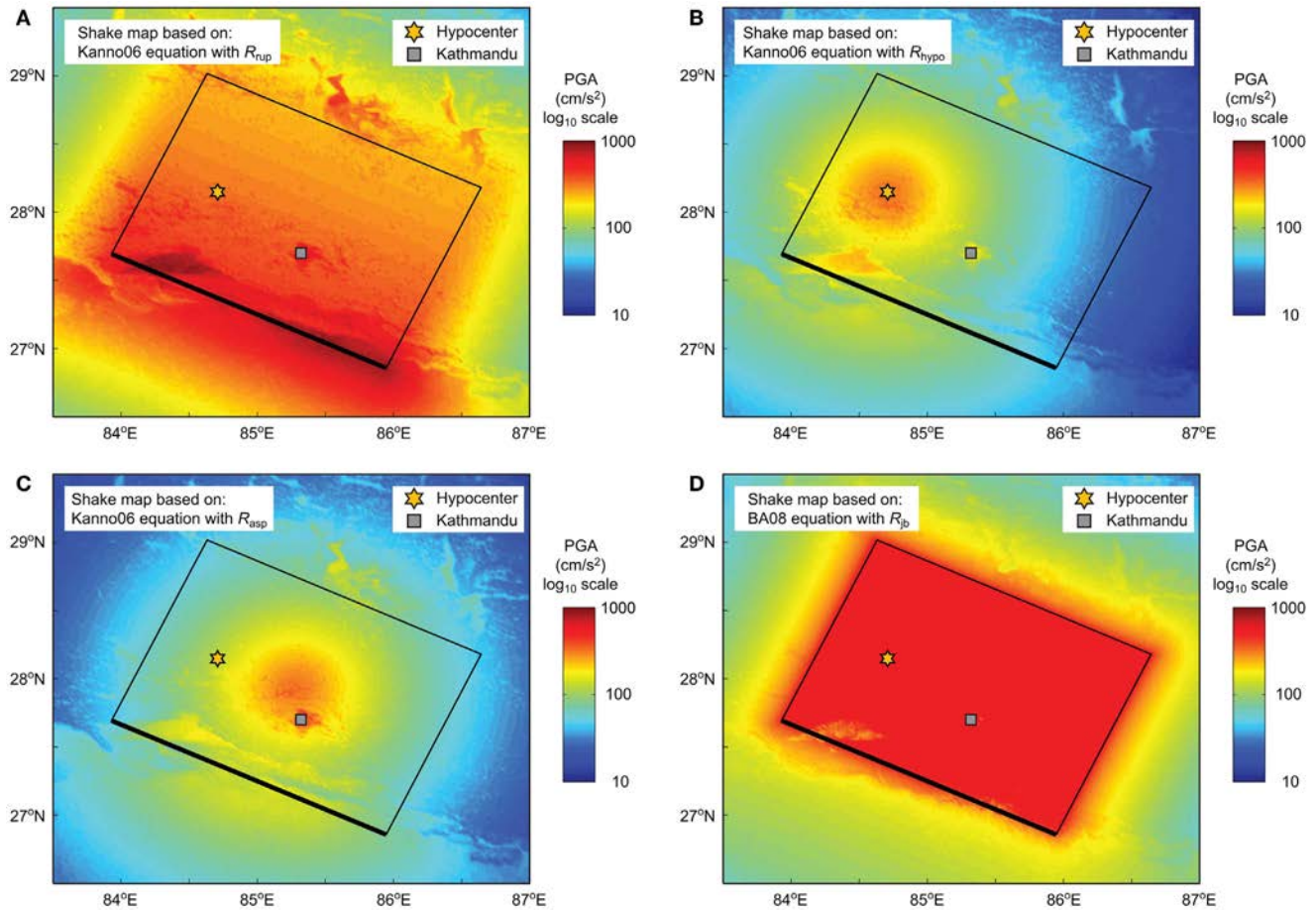

FIGURE 7 | **Comparison of scenario shake maps for the M_w7.8 mainshock using: (A) the Kanno06 equation with rupture distance (R_{rup}), (B) the Kanno06 equation with hypocentral distance (R_{hypo}), (C) the Kanno06 equation with distance closest to the asperity (R_{asp}), and (D) the BA08 equation with Joyner–Boore distance (R_{jb}).**

however, the majority of the masonry buildings are structurally stable). This indicates that the ground shaking experienced in this area (note: this is relatively close to the KATNP station; see **Figure 4**) was sufficient to cause the collapses of the old historical buildings but was not to cause severe damage to the surrounding buildings. This observation was confirmed by walking through the Indra Chowk area (market squares near the Old Palace), where many old masonry buildings (three to six stories) were densely constructed. Nevertheless, there were several buildings that collapsed completely and some search and rescue activities were undertaken (**Figures 8C,D**).

There were numerous building collapses in the north–west section of the Ring Road along the Bishnumati River (area 2 in **Figure 4**). According to the local geomorphological map, sites within about 300 m from the river are alluvial (Holocene) soil deposits, whereas sites farther east are Pleistocene soil deposits. Therefore, site amplification effects due to different soil conditions may be expected in this area. A walk-through survey was carried out to investigate the spatial distribution of collapsed and severely damaged buildings in this area. Out of 28 collapsed or severely damaged buildings, 19 buildings were in the alluvial deposit area (**Figure 9A**), whereas 9 buildings were in the Pleistocene deposit area but nearer to the boundary (**Figure 9B**). This qualitatively confirms the effects of local site conditions on the building damage and collapse.

In area 3, there was a 16-story high-rise apartment complex (Park View Horizon). The walls of this building suffered from many major cracks along its height (**Figure 9C**). Currently, the apartments are unfit for living and residents have evacuated. The causes of the major damage of the Horizon apartments (and similar high-rise buildings in Kathmandu) may be attributed to the long-period ground motions (**Figure 5**). In addition, local topological features may have contributed to extensive damage there (the complex is on a hill).

Along the Araniko Highway between Kathmandu and Bhaktapur (area 4 in **Figure 4**), a section of the highway (about 200 m in length) built upon embankments was damaged due to the ground settlement. The amount of settlements was about 0.5–2.0 m, depending on locations (**Figure 9D**). The central section of the highway was constructed using reinforced soil retaining wall and

FIGURE 8 | **Damage in Kathmandu (area 1 in Figure 4)**. **(A)** Collapse of the Basantapur Tower in the Kathmandu Durbar Square. **(B)** Undamaged buildings opposite of the Basantapur Tower in the Kathmandu Durbar Square. **(C)** Collapse of four 5- or 6-story old masonry buildings. **(D)** Collapse of a 4-story masonry building.

gravity-type retaining wall (2–3 m high and 100 m wide). The retaining walls were structurally intact and suffered from minor cracks and outward deformation only, whereas the natural slopes at both ends of the highway embankments experienced noticeable settlements (**Figure 9E**). Several buildings along the highway were tilted due to the settlements. A pedestrian footbridge crossing the highway suffered from the differential settlement of foundation, resulting in a gap of 45 cm between the bridge girder and the stair steps.

In area 5 (**Figure 4**), minor liquefaction, which was evidenced by sand boils and did not cause any structural damage, was observed in a small open land near a canal. In the surveyed area, a church was collapsed due to the ground shaking (**Figure 9F**). According to local residents, the church building was standing after the M_w7.8 mainshock but was collapsed due to the M_w6.7 aftershock on the following day. The extent of structural damage before the M_w6.7 aftershock is unknown. There were several houses that settled and tilted in this area. However, the degree of destruction in this area was minor.

Overall, earthquake damage in Kathmandu was not widespread but more localized. This may suggest that overall strong shaking experienced in Kathmandu was not extremely large. The areas that suffered from major destruction tend to have some local characteristics, such as soft soil conditions and structural deficiencies.

Survey Results in Melamchi

The survey was conducted along the road to Melamchi (about 30 km north–east of Kathmandu; **Figure 3**). Melamchi and the surrounding areas were close to the locations of major aftershocks (i.e., 26 April M_w6.7 aftershock and 12 May M_w7.3 aftershock; **Figures 2A** and **3**), and suffered from devastation due to these earthquakes. On the way to Melamchi, there were many small villages that suffered from earthquake damage. During interviews with local residents, they expressed serious concerns about incessant aftershocks and urgent need of repairs of the damaged houses before the arrival of rainy season. Proceeding north toward Melamchi, the occurrence of earthquake damage becomes more frequent.

Melamchi is a small town along the Indrawati River, and residents in the town have been involved with a major Melamchi Water Supply project[8], which diverts the river and channels its water to Kathmandu through tunnels. There were several factories along the road, which make water main pipes. Overall, the earthquake damage in Melamchi was severe, mostly affecting vulnerable masonry buildings, whereas the damage to RC buildings (4- to 5-story) was limited. For instance, the main

[8]http://www.melamchiwater.org/home/

FIGURE 9 | **Damage in Kathmandu (areas 2–5 in Figure 4)**. **(A)** Collapsed building along the Bishnumati River (alluvial soil deposit area; area 2 in **Figure 4**). **(B)** Collapsed building (soft story collapse) near the Bishnumati River (boundary between alluvial and Pleistocene soil deposit areas; area 2 in **Figure 4**). **(C)** Horizon apartment buildings (area 3 in **Figure 4**). **(D)** Settlement of the Araniko Highway (area 4 in **Figure 4**). **(E)** Damage to the Araniko Highway (area 4 in **Figure 4**). **(F)** Collapsed church in the Imadol area (area 5 in **Figure 4**).

street of Melamchi was not completely destroyed (**Figure 10A**); most buildings looked undamaged based on their appearances, although several buildings were collapsed. On the other hand, buildings along a side street were devastated by the earthquakes (**Figures 10B,C**). The majority of the damaged buildings were made of brick and stone. Along the road, several sections of the slope suffered from shallow landsides (**Figure 10D**), their debris blocked the road at one time but was removed. There was a steel truss bridge with RC deck for vehicle crossing; the bridge was not damaged (inspected from backside). It has been reported that further damage occurred in Melamchi due to the 12 May M_w7.3 aftershock. A further damage survey in Melamchi is required to investigate the effects of the aftershock with respect to the incurred damage prior to the aftershock (although it is beyond the scope of this study).

Survey Results in Trishuli

The survey was conducted along the road to Trishuli (about 30 km north–west of Kathmandu; **Figure 3**). One of the purposes of the trip was to investigate the earthquake damage near the Trishuli

FIGURE 10 | Damage in Melamchi (see Figure 3). **(A)** Main street in Melamchi. **(B)** Damaged stone masonry house. **(C)** Devastated street in Melamchi. **(D)** Shallow landslide along the main road.

hydroelectric station. Trishuli was closer to the hypocenter of the M_w7.8 mainshock, and thus severer damage, in comparison with Kathmandu, was expected. Along the way to Trishuli, earthquake damage in Ranipauwa (about 15 km north–west of Kathmandu) appeared relatively minor. Proceeding further north–west, earthquake damage to houses and landslides along the mountain slopes were observed more frequently. The rock fall, as secondary hazard, can be dangerous; a bus was hit by fallen boulder and several people were killed (**Figure 11A**). In Battar (about 25 km north–west of Kathmandu), a large number of brick/stone masonry buildings were collapsed (**Figure 11B**). The building materials of these damaged buildings were of poor quality; for example, two different types of the fragile bricks were used in one of the damaged houses (**Figure 11C**). According to local residents, many buildings were collapsed due to the 25 April M_w6.6 aftershock, which occurred 30 min after the mainshock.

In Trishuli, there was an earth fill dam for hydroelectric power generation. The main body of the dam was the excavated and compacted soil. The height of the dam was 12 m (upstream side) and 20 m (downstream side), and the crest width was about 4 m. Due to the earthquake, there were cracks at upstream side of the dam and fissures on the crest. Moreover, liquefaction (as evidenced by silt boils) and lateral spreading (**Figure 11D**) occurred inside of the dam reservoir due to the earthquake. The operation of the power generation had been suspended since the following day of the mainshock; at the time of the visit, no power was available in nearby villages. Overall, the earthquake damage to the Trishuli dam will not cause severe problems immediately. However, the extent of cracking along the dam axis may suggest a deterioration of the dam body, which may be accelerated into the dam failure by future earthquakes or penetration of rain water into the dam body through cracks. It is important to mention that in worst-case scenarios (note: this earthquake is not the extreme case in terms of ground shaking intensity), catastrophic dam failures could have been caused. As there are several major hydroelectric projects along the Trishuli River as well as in other major rivers in Nepal, ensuring dam safety against large earthquakes is important.

Survey Results in Baluwa

The survey team visited Baluwa (about 70 km north–west of Kathmandu; **Figure 3**) along the Daraudi River, which is close to the epicenter of the M_w7.8 mainshock. One of the aims for this visit was to investigate the earthquake damage very near to the epicenter. Along the Kathmandu–Pokhara highway (e.g., Abu Khaireni, a town located at an intersection between the main highway and the Daraudi link road; about 30 km from the epicenter), no major earthquake damage was observed. At distances of about 18 km from the epicenter, earthquake damage to houses was observed; proceeding further north toward Baluwa, the extent

FIGURE 11 | Damage in Trishuli (see Figure 3). **(A)** Destroyed bus due to boulder fall. **(B)** Damaged brick masonry house in Battar. **(C)** Different types of bricks used in the damaged masonry house in Battar. **(D)** Ground fissures in the Trishuli dam reservoir.

of earthquake damage to houses became severer. The first stone house that was collapsed due to the earthquakes was about 4.5 km from the epicenter. Similarly, many shallow landslides and rock falls were observed along the road to Baluwa (**Figure 12A**); the first middle-size landslide was observed at distances of about 15 km from the epicenter. At one location, the debris from a landslide blocked the road completely (**Figure 12B**; note: detour was possible). The spatial distribution of the collapsed houses and landslides was limited to the locations near the epicenter (within 10–15 km radius), and was in contrast with Melamchi and Trishuli (i.e., farther from the epicenter). This can be understood by referring to the slip distribution of the mainshock (**Figures 2A** and **3**).

A large slope failure was observed at the northern boundary of Baluwa (**Figure 12C**); the length and height of the slope failure were 300 and 100 m, respectively. The fallen boulders and debris blocked the road completely, disconnecting villages at the upstream of the Daraudi River (e.g., Barpak, 5 km north of Baluwa); people can reach these places on foot only. This hampered rescue and recovery activities by governments and international aid teams significantly, highlighting the importance of functional critical infrastructure during the natural disaster emergency. The houses in Baluwa were devastated by the earthquakes and many residents lived in tents (**Figure 12D**). Local residents mentioned that the number of fatalities in Baluwa was small because many of the residents were in the field for agricultural work at the time of the earthquake. Major concerns about the arrival of rainy season were expressed by the local residents.

Conclusion

The M_w7.8 subduction earthquake occurred along the Main Himalayan Thrust arc and triggered numerous major aftershocks. The earthquake damage was catastrophic, causing the fatalities of more than 8,500 and billions of dollars in economic loss. This paper presented important earthquake field observations in Nepal in the aftermath of the M_w7.8 mainshock. A unique aspect of the earthquake damage investigation is that the data were collected 6–11 days after the mainshock, and thus first-hand earthquake damage observations were obtained. To share the gathered damage data widely, geo-tagged photos with observation comments were organized using Google Earth and the kmz file was made publicly available. In the future, the updated version of the Google Earth file, containing more damage photos and measurements from follow-up investigations, will be available from http://www.gdm.iis.u-tokyo.ac.jp/index_e.html. Viewers can download the photos directly and can use them for research and educational purposes. To gain deeper understanding of the observed earthquake damage in Nepal, the seismotectonic setting and regional seismicity in Nepal were reviewed and available aftershock data and ground motion data were analyzed. In addition to ground motion data analysis, scenario shake maps were generated by trialing different combinations of applicable ground motion models and source-to-site distance measures to highlight the potential biases caused in estimated ground motion maps and prompt earthquake impact assessments for a large subduction earthquake.

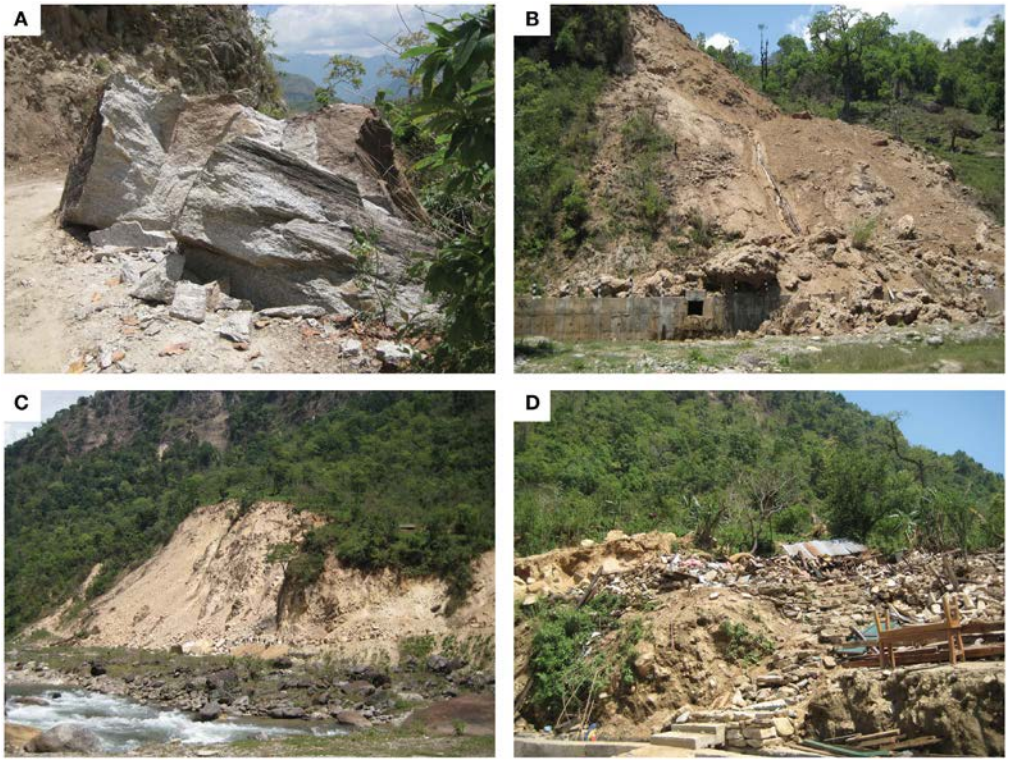

FIGURE 12 | **Damage in Baluwa (see Figure 3)**. **(A)** Fallen boulder. **(B)** Shallow landslide; debris blocked the road. **(C)** Large landslide (100 m high and 300 m wide); debris blocked the road and disconnected villages further north of Baluwa. **(D)** Devastated houses in Baluwa.

The main results from the earthquake damage surveys in Nepal are as follows:

1. In Kathmandu, earthquake damage to old historical buildings was severe, whereas damage to the surrounding buildings was limited. The damaged buildings were stone/brick masonry structures with wooden frames. The RC frame buildings performed well for this earthquake. This may indicate that ground motion intensity experienced in Kathmandu was not so intense, in comparison with those predicted from probabilistic seismic hazard studies for Nepal. Therefore, a caution is necessary related to future earthquakes in Nepal because the 2015 earthquake is not necessarily the worst-case scenario.
2. The Kathmandu Basin is deposited by thick soft sediments. This has led to the generation of long-period ground motions in the Kathmandu Valley. Although the majority of the existing buildings in Kathmandu were not directly affected by the long-period ground motions, such seismic waves can pose serious risks to high-rise buildings. Adequate earthquake engineering design considerations are essential for reducing potential seismic risk to these structures.
3. The building damage in Kathmandu was localized to specific areas. It appeared that the building collapse sites were affected by local soil characteristics and/or structural deficiencies. In this regard, microzonation studies provide valuable insights into earthquake damage occurrence.
4. Some buildings that were severely damaged by the mainshock were collapsed due to major aftershocks. The capability for aftershock forecasting, building evacuation procedure, building inspection and tagging, and building repairs and retrofitting (low-cost solutions) need to be improved to mitigate the earthquake damage potential.
5. In the mountain areas, numerous villages were devastated by the earthquake sequence and major landslides were triggered. On occasion, landslides blocked roads, disconnecting remote villages. The redundancy of the local transportation network in Nepal needs to be improved for enhancing the resilience of rural communities.

Acknowledgments

The authors thank Pradeep Pokhrel for his great assistance during the field survey. The financial support by the JSPS KAKENHI (15H02631) is greatly acknowledged. The work was also funded by the EPSRC grant (EP/I01778X/1) for the Earthquake Engineering Field Investigation Team (EEFIT).

Supplementary Material

The Supplementary Material for this article can be found online at http://journal.frontiersin.org/article/10.3389/fbuil.2015.00008

References

Ader, T., Avouac, J. P., Liu-Zeng, J., Lyon-Caen, H., Bollinger, L., Galetzka, J., et al. (2012). Convergence rate across the Nepal Himalaya and interseismic coupling on the Main Himalayan fault: implications for seismic hazard. *J. Geophys. Res.* 117, B04403. doi:10.1029/2011JB009071

Ambraseys, N. N., and Douglas, J. (2004). Magnitude calibration of north Indian earthquakes. *Geophys. J. Int.* 159, 165–206. doi:10.1111/j.1365-246X.2004.02323.x

Atkinson, G. M., and Wald, D. J. (2007). Did you feel it? intensity data: a surprisingly good measure of earthquake ground motion. *Seismol. Res. Lett.* 78, 362–368. doi:10.1785/gssrl.78.3.362

Avouac, J. P. (2003). Mountain building, erosion and the seismic cycle in the Nepal Himalaya. *Adv. Geophys.* 46, 1–80. doi:10.1016/S0065-2687(03)46001-9

Bilham, R. (2004). Earthquakes in India and the Himalaya: tectonics, geodesy and history. *Ann. Geophys.* 47, 839–858. doi:10.4401/ag-3338

Boore, D. M., and Atkinson, G. M. (2008). Ground motion prediction equations for the average horizontal component of PGA, PGV, and 5% damped PSA at spectral periods between 0.01 s and 10.0 s. *Earthquake Spectra* 24, 99–138. doi:10.1193/1.2830434

Boore, D. M., Stewart, J. P., Seyhan, E., and Atkinson, G. M. (2014). NGA-West2 equations for predicting PGA, PGV, and 5% damped PSA for shallow crustal earthquakes. *Earthquake Spectra* 30, 1057–1085. doi:10.1193/070113EQS184M

Center for Disaster Management and Risk Reduction Technology (CEDIM). (2015). *Nepal Earthquakes – Report #3*. Available at: https://www.cedim.de/english/index.php

Chaulagain, H., Rodrigues, H., Spacone, E., and Varum, H. (2015). Seismic response of current RC buildings in Kathmandu Valley. *Struct. Eng. Mech.* 53, 791–818. doi:10.12989/sem.2015.53.4.791

Goda, K., and Atkinson, G. M. (2014). Variation of source-to-site distance for megathrust subduction earthquakes: effects on ground motion prediction equations. *Earthquake Spectra* 30, 845–866. doi:10.1193/080512EQS254M

Gupta, I. D. (2006). Delineation of probable seismic sources in India and neighbourhood by a comparative analysis of seismotectonic characteristics of the region. *Soil Dynam. Earthquake Eng.* 26, 766–790. doi:10.1016/j.soildyn.2005.12.007

Harbindu, A., Gupta, S., and Sharma, M. L. (2014). Earthquake ground motion predictive equations for Garhwal Himalaya, India. *Soil Dynam. Earthquake Eng.* 66, 135–148. doi:10.1016/j.soildyn.2014.06.018

Heuret, A., Lallemand, S., Funiciello, F., Piromallo, C., and Faccenna, C. (2011). Physical characteristics of subduction interface type seismogenic zones revisited. *Geochem. Geophys. Geosyst.* 12, Q01004. doi:10.1029/2010GC003230

Hong, H. P., and Goda, K. (2007). Orientation-dependent ground-motion measure for seismic-hazard assessment. *Bull. Seismol. Soc. Am.* 97, 1525–1538. doi:10.1785/0120060194

Huang, Y. N., Whittaker, A. S., and Luco, N. (2008). Maximum spectral demands in the near-fault region. *Earthquake Spectra* 24, 319–341. doi:10.1193/1.2830435

Jaiswal, K. S., and Wald, D. J. (2010). An empirical model for global earthquake fatality estimation. *Earthquake Spectra* 26, 1017–1037. doi:10.1193/1.3480331

Ji, C. (2008). *Preliminary Result of the May 12, 2008 M_w 7.97 Sichuan Earthquake*. Available at: http://www.geol.ucsb.edu/faculty/ji/big_earthquakes/2008/05/12/ShiChuan.html

Kanno, T., Narita, A., Morikawa, N., Fujiwara, H., and Fukushima, Y. (2006). A new attenuation relation for strong ground motion in Japan based on recorded data. *Bull. Seismol. Soc. Am.* 96, 879–897. doi:10.1785/0120050138

Lu, M., Li, X. J., An, X. W., and Zhao, J. X. (2010). A comparison of recorded response spectra from the 2008 Wenchuan, China, earthquake with modern ground-motion prediction models. *Bull. Seismol. Soc. Am.* 100, 2357–2380. doi:10.1785/0120090303

Mai, P. M., Spudich, P., and Boatwright, J. (2005). Hypocenter locations in finite-source rupture models. *Bull. Seismol. Soc. Am.* 95, 965–980. doi:10.1785/0120040111

Nath, S. K., and Thingbaijam, K. K. S. (2011). Peak ground motion predictions in India: an appraisal for rock sites. *J. Seismol.* 15, 295–315. doi:10.1007/s10950-010-9224-5

Nath, S. K., and Thingbaijam, K. K. S. (2012). Probabilistic seismic hazard assessment of India. *Seismol. Res. Lett.* 83, 135–149. doi:10.1785/gssrl.83.1.135

Paudyal, Y. R., Bhandary, N. P., and Yatabe, R. (2012). Seismic microzonation of densely populated area of Kathmandu Valley of Nepal using microtremor observations. *J. Earthquake Eng.* 16, 1208–1229. doi:10.1080/13632469.2012.693242

Ram, T. D., and Wang, G. (2013). Probabilistic seismic hazard analysis in Nepal. *Earthquake Eng. Eng. Vib.* 12, 577–586. doi:10.1007/s11803-013-0191-z

Sakai, H., Fujii, R., and Kuwahara, Y. (2002). Changes in the depositional system of the Paleo-Kathmandu Lake caused by uplift of the Nepal Lesser Himalayas. *J. Asian Earth Sci.* 20, 267–276. doi:10.1016/S1367-9120(01)00046-3

Sharma, M. L., Douglas, J., Bungum, H., and Kotadia, J. (2009). Ground-motion prediction equations based on data from Himalayan and Zagros regions. *J. Earthquake Eng.* 13, 1191–1210. doi:10.1080/13632460902859151

Shcherbakov, R., Goda, K., Ivanian, A., and Atkinson, G. M. (2013). Aftershock statistics of major subduction earthquakes. *Bull. Seismol. Soc. Am.* 103, 3222–3234. doi:10.1785/0120120337

Shcherbakov, R., Turcotte, D. L., and Rundle, J. B. (2005). Aftershock statistics. *Pure Appl. Geophys.* 162, 1051–1076. doi:10.1007/s00024-004-2661-8

Stern, R. J. (2002). Subduction zones. *Rev. Geophys.* 40, 1012. doi:10.1029/2001RG000108

Takewaki, I., Murakami, S., Fujita, K., Yoshitomi, S., and Tsuji, M. (2011). The 2011 off the Pacific coast of Tohoku earthquake and response of high-rise buildings under long-period ground motions. *Soil Dynam. Earthquake Eng.* 31, 1511–1528. doi:10.1016/j.soildyn.2011.06.001

United Nations Office for the Coordination of Humanitarian Affairs (UN-OCHA). (2015). Available at: http://www.unocha.org/nepal

United States Geological Survey (USGS). (2015). Available at: http://earthquake.usgs.gov/earthquakes/eventpage/us20002926#scientific_finitefault

Wald, D. J., and Allen, T. I. (2007). Topographic slope as a proxy for seismic site conditions and amplification. *Bull. Seismol. Soc. Am.* 97, 1379–1395. doi:10.1785/0120060267

Wald, D. J., Worden, B. C., Quitoriano, V., and Pankow, K. L. (2005). *ShakeMap Manual: Technical Manual, User's Guide, and Software Guide*. Golden, CO: U.S. Geological Survey, 132.

Yagi, T. (2015). Available at: http://www.geol.tsukuba.ac.jp/~yagi-y/EQ/20150425/index.html

Conflict of Interest Statement: The authors declare that the research was conducted in the absence of any commercial or financial relationships that could be construed as a potential conflict of interest.

Copyright © 2015 Goda, Kiyota, Pokhrel, Chiaro, Katagiri, Sharma and Wilkinson. This is an open-access article distributed under the terms of the Creative Commons Attribution License (CC BY). The use, distribution or reproduction in other forums is permitted, provided the original author(s) or licensor are credited and that the original publication in this journal is cited, in accordance with accepted academic practice. No use, distribution or reproduction is permitted which does not comply with these terms.

frontiers in Built Environment

ORIGINAL RESEARCH
published: 18 November 2015
doi: 10.3389/fbuil.2015.00023

Ground Motion Characteristics of the 2015 Gorkha Earthquake, Survey of Damage to Stone Masonry Structures and Structural Field Tests

Rishi Ram Parajuli[1] and Junji Kiyono[2]*

[1] Department of Urban Management, Graduate School of Engineering, Kyoto University, Kyoto, Japan, [2] Graduate School of Global Environmental Studies, Kyoto University, Kyoto, Japan

On April 25, 2015, a M7.8 earthquake rattled central Nepal; ground motion recorded in Kantipath, Kathmandu, 76.86 km east of the epicenter suggested that the low-frequency component was dominant. We consider data from eight aftershocks following the Gorkha earthquake and analyze ground motion characteristics; we found that most of the ground motion records are dominated by low frequencies for events with a moment magnitude >6. The Gorkha earthquake devastated hundreds of thousands of structures. In the countryside, and especially in rural mountainous areas, most of the buildings that collapsed were stone masonry constructions. Detailed damage assessments of stone masonry buildings in Harmi Gorkha was done, with an epicentral distance of about 17 km. Structures were categorized as large, medium, and small depending on their plinth area size and number of stories. Most of the structures in the area were damaged; interestingly, all ridge-line structures were heavily damaged. Moreover, Schmidt hammer tests were undertaken to determine the compressive strength of stone masonry and brick masonry with mud mortar for normal buildings and historical monuments. The compressive strengths of stone masonry and brick masonry were found to be 12.38 and 18.75 MPa, respectively. Historical structures constructed with special bricks had a compressive strength of 29.50 MPa. Pullout tests were also conducted to determine the stone masonry-mud mortar bond strength. The cohesive strength of mud mortar and the coefficient of friction were determined.

Keywords: Gorkha earthquake, ground motion characteristics, damage survey, stone masonry, field test, Schmidt hammer test

OPEN ACCESS

Edited by:
Katsuichiro Goda, University of Bristol, UK

Reviewed by:
Siau Chen Chian, National University of Singapore, Singapore
Rama Mohan Pokhrel, University of Tokyo, Japan

****Correspondence:***
Rishi Ram Parajuli
parajuli.ram.27z@st.kyoto-u.ac.jp

Specialty section:
This article was submitted to Earthquake Engineering, a section of the journal Frontiers in Built Environment

Received: *21 August 2015*
Accepted: *04 November 2015*
Published: *18 November 2015*

Citation:
Parajuli RR and Kiyono J (2015) Ground Motion Characteristics of the 2015 Gorkha Earthquake, Survey of Damage to Stone Masonry Structures and Structural Field Tests. Front. Built Environ. 1:23. doi: 10.3389/fbuil.2015.00023

INTRODUCTION

Nepal lies in an active seismic zone in the Himalayan belt within the boundary between the Eurasian and Indian plates. Records of large earthquakes that have devastated Nepal, claiming a significant number of lives, have been kept for more than seven centuries. On June 7, AD 1255, a mega earthquake was the first ever documented earthquake in the region; it was likely to have had an intensity of MMI X and killed about one-third of the people in the current capital Kathmandu, including King Abhaya Malla of the Malla era [BECA World International (New Zealand) et al.,

1993]. Other major historical earthquakes occurred in 1408, destroying the Machhendra Nath temple in Patan, 1681 and 1810. Bilham (1995) stated that the major earthquake event of August 26, 1833 had a moment magnitude of 7.5–7.9 with a possible rupture length of 70 km and an epicenter located 50 km North or North-East of Kathmandu, and was preceded by two large foreshocks that took place 5 h and 15 min prior to the main shock. This alarmed people and caused them to stay outside their houses, thereby probably saving many lives. Another well-known devastating earthquake prior to the Gorkha earthquake was the Nepal–Bihar earthquake of 1934 with a Richter magnitude of 8.4. Bramha Smasher JBR stated in his book (Rana, 1935) that the 1934 mega-earthquake claimed 8,591 lives in total with 4,296 in Kathmandu valley, and destroyed 56,231 structures, including 492 temples and schools. A Richter magnitude 6.6 earthquake in August 1988 was another earthquake that devastated the eastern part of Nepal, having its epicenter in Udayapur. This earthquake claimed 721 lives in eastern Nepal, along with injuries to 6,213 people. A total of 14,965 dwellings were completely destroyed, most of which were constructed with mud-stone or clay brick masonry (Sato et al., 1989).

The Gorkha earthquake that struck on April 25 at 11:56 a.m. (NST) had an epicenter in Barpak, Gorkha. It ruptured to the east of the epicenter for a length of about 100 km at a strike angle of 295° (USGS, 2015). The size of this earthquake is 7.8 in moment magnitude and is 7.6 in local magnitude, as measured by Nepal's seismological center (NSC). The recent Gorkha earthquake claimed a total of 8,857 lives (as of August 8) (Government of Nepal, 2015). The greatest death toll was in the Sindhupalchok district, in the eastern part of Nepal, near to the estimated end point of the rupture. In this region, a total of 3,532 people lost their lives, whereas just 1,573 were seriously injured due to the quake. Most of the structures in this district are stone masonry buildings with mud mortar, reinforced with concrete frame structures exist only in few small towns (Central Bureau of Statistics, 2012). The district with the next highest death toll was the capital, Kathmandu, where 1,226 deaths were recorded, along with injuries to 7,952 people. Considering the three districts in the Kathmandu valley, the total death toll rises to 1,739, significantly more than that in Gorkha, the district where the epicenter was located, where the death toll was 449.

The death toll was affected by the timing of event, as it happened at noon when most of people in the hardest hit areas were out of their houses at work in the fields. Another factor that lowered the death toll and damage was the low-frequency dominant component of ground motion. The main shock of the earthquake had dominant frequencies of roughly 0.23, 0.23, and 0.27 Hz corresponding to the East-West (EW), North-South (NS), and Up-Down (UD) components recorded in Kathmandu. Recorded ground acceleration of the Gorkha earthquake in Kathmandu shows the peak value of <200 cm/s^2,where probabilistic seismic hazard analysis of Nepal suggested that PGA is around 100 cm/s^2 considering return period of 98 years and 450 cm/s^2 for return period of 475 years in soft soil areas (Parajuli et al., 2008). In this study, we analyze the characteristics of ground motions for nine earthquake events, including the "main shock." Ground motion data recorded by the USGS in Kathmandu (station code KATNP) have been downloaded from the strong motion archive (CESMD, 2015). Nepal has a total population of nearly 26.5 million, with about 17% of the people in urban areas and the rest in rural areas. Almost half of the population of Nepal lives in the relatively flat Terai region, with hilly areas retaining 43% of the population, and only 7% in the mountainous region. Building structure types used throughout Nepal are shown in **Figure 1**; most of the structures are of stone/brick masonry with mud mortar (SBMM); in the Terai region, stone/brick masonry with cement mortar (SBCM) is also common. Reinforced cement concrete (RCC) structures have only a small share, whereas wooden frame structures (WFS) are widely used in the Terai region. Structural types that cannot be characterized as above are specified as other (OTH), along with structures not specified (NS) during data collection.

The structures built to provide shelter for half the populations of the country in the hilly and mountainous region are mostly of stone masonry with mud mortar. Specifically, SBMM constructions account for 50% of buildings in hilly regions and 47% of buildings in mountainous regions. The use of SBMM for outer wall construction in rural areas is nearly 83%. In mountainous and hilly areas, 93 and 65% use SBMM for foundation, and 89 and 62% use SBMM for the outer walls, respectively. Outside the Kathmandu valley, with 19.63% of the fatalities, the death toll is much higher in mountainous and hilly areas, such as Sindhupalchok, Nuwakot, Dhading, Rasuwa, and Gorkha with 3,532, 1,109, 679, 660, and 449 deaths, respectively, and accounting for 73% of the total (Government of Nepal, 2015). A map of these five districts and the Kathmandu valley with locations of epicenter of the main shock and aftershocks are shown in **Figure 2**. The Gorkha earthquake most greatly affected areas with a greater share of SBMM constructions. Sindhupalchok district (92% of buildings), Nuwakot (93%), Dhading (87%), Rasuwa (90%), and Gorkha (88%) are all dominated by structures with such foundation. In those five districts, 90% of structures were built with mud mortar (Central Bureau of Statistics, 2012). In hilly areas, stone is commonly locally available, so more of the structures are built with it. Studying the damage patterns for such structures, and developing corresponding countermeasures for those, has to be in focus to increase the resiliency of such structures in rural areas.

Some damage surveys have been already conducted since the Gorkha earthquake. Goda et al. (2015) revealed that the damage scenario is not widespread, but localized in the Kathmandu valley. The damage assessments in the small towns of Melamchi, Trishuli, and Baluwa found that majority of stone and brick masonry buildings were severely damaged. We conducted a detailed damage survey in Harmi, a rural village in the Gorkha district, where all of the structures are made of stone masonry with mud mortar.

Local building materials in rural Nepal are spatially variable, even within a few kilometers. However, the general construction methods in rural Nepal consist of a foundation of stone masonry with mud mortar that rises up to a ridge supporting the outer walls. Timber columns and beams are commonly used to support

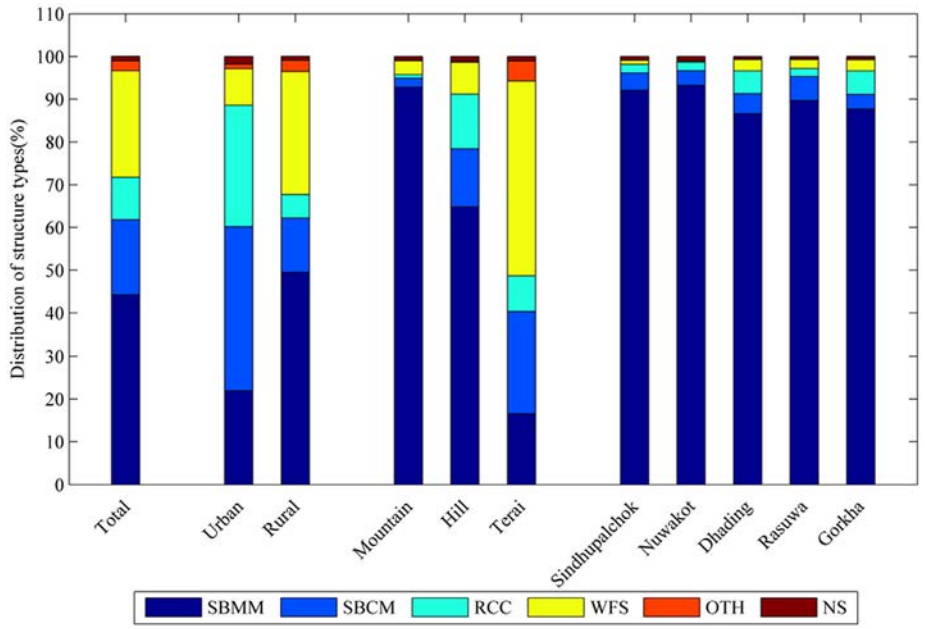

FIGURE 1 | Structure type distribution in Nepal and major affected districts (data source: CBS, Nepal).

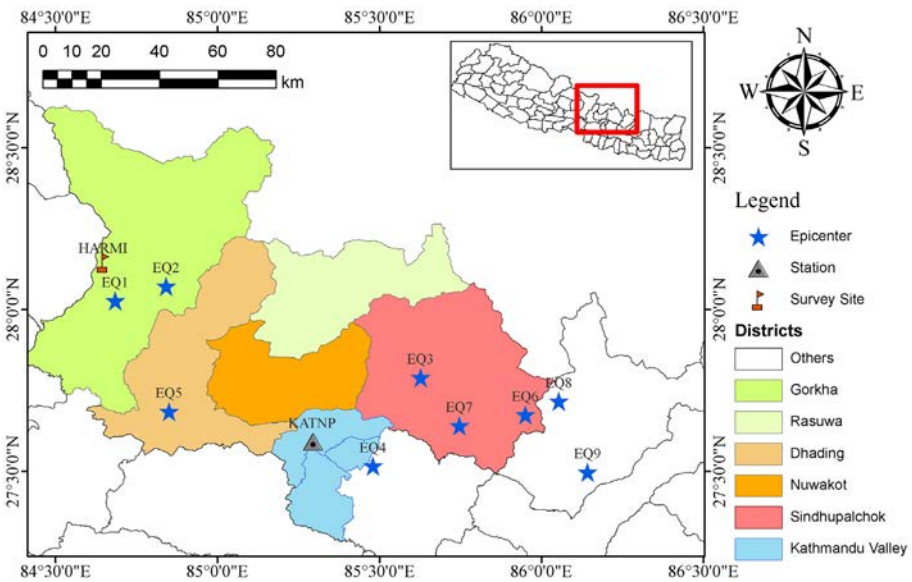

FIGURE 2 | Location of earthquake epicenters, damage survey location and major affected districts.

extended roofs and slabs as intermediate support. The material properties of such structures are not commonly studied, so we have undertaken field pullout tests to assess the strength of mortar. Similarly, Schmidt hammer tests have also been used for stone masonry structures and brick masonry structures, even though they are not well defined for use with stone masonry. In comparison to typical buildings in the region, historical monuments usually have special types of materials used in construction; mostly they consist of special brick masonry in three layers (inner, outer, and infill layers) with mud (Ranjitkar, 2000), and occasionally with lime-surkhi mortar. We have also tested the strength of such walls in the Gorkha palace using the Schmidt hammer.

GROUND MOTION CHARACTERISTICS

Nepal does not have a dense network of accelerometers; however, the USGS has established a station (KATNP) that records earthquakes in the capital, Kathmandu, and data from that station are analyzed in this paper. In total, nine independent datasets available from strongmotioncenter.org are analyzed and discussed here.

Table 1 presents detailed information regarding trigger dates and times, moment magnitudes, the locations of epicenters, and the epicentral distances from the recording station KATNP (27.7120°N, 85.3155°E). Earthquakes are numbered 1–9, with EQ1 representing the main shock, and EQ8 the major aftershock to the east of the fault plane. Earthquake events range from moment magnitude 5.2–7.8, with epicentral distances as far as 83.90 km and as near as 18.5 km.

The spatial distribution of the earthquakes extends to the east and west of the recording station, which help evaluate the effect of directivity of the seismic waves. **Figure 2** shows the location of the earthquakes relative to the recording station (KATNP) in Kathmandu and the damage survey site Harmi. Data are sampled at an interval of 0.005 s, and the length of recorded data varies for each event. For analysis, we have chosen a record length of 81.92 s (16,384 samples). This data selection of 2^{14} samples facilitates using fast Fourier transforms, which require a power of 2 for calculation. Records that are shorter than the required length were extended with null values for the remaining duration.

Ground motion, Fourier spectra and response spectra of the EW components of all earthquake events are shown in **Figure 3**, respectively, from left to right. All of the events are stacked into a single figure where base line accelerations for EQ1, EQ2, EQ3, EQ4, EQ5, E6, EQ7, EQ8, and EQ9 are 0, 300, 400, 500, 600, 700, 800, 900, and 1000 cm/s^2, respectively, as shown by dotted lines in the figure. The main shock of the Gorkha earthquake had an epicentral distance of 76.86 km NW from KATNP; maximum recorded accelerations were 155, 162, and 184 cm/s^2 for the EW, NS, and UD components, respectively. Fourier transforms to the frequency domain showed that all three components were dominated by low frequencies. **Figure 3** clearly shows that the dominant frequencies of large aftershocks (EQ2, EQ6, and EQ8) are low: even the small ones are in a higher range. In contrast to the Fourier spectra, spectral accelerations (**Figure 3**) show aftershock ground motions that are greater and in a higher frequency range, even though the main shock has a higher value over a lower range of frequencies (0.22 Hz).

Figure 4 shows the dominant frequencies of all earthquakes in all three directions. In four of the events [EQ1 (M7.8), EQ2 (M6.6) EQ6 (M6.7), and EQ8 (M7.3)], all of the components are dominated by low frequencies ≤1 Hz. Three of the events [EQ3 (M5.5), EQ4 (M5.3), and EQ5 (M5.2)] have dominant frequencies in all three components ≥1 Hz. EQ7 (M5.3) is low-frequency dominant in the EW and NS components, while the UD component had a slightly higher value of 1.26 Hz. The final event, EQ9 (M6.3), has variable frequency content, with peak Fourier amplitudes for the EW component at 0.28 Hz, the NS component at 2.43 Hz, and the UD component at 1.17 Hz.

The response of a structure to earthquake ground motion with a single degree of freedom is represented by response spectra for various natural frequency ranges for the structure. A damping ratio of 5% is assumed in the calculation of response spectra. **Figure 5** shows the tripartite plot of pseudo velocity spectra (centimeter per second) with axes for displacement (centimeter) and pseudo acceleration (square centimeter). Four earthquake events (EQ1, EQ2, EQ6, and EQ8) exceeded a velocity of 10 cm/s with peak values in range of 0.2–0.5 Hz. Despite EQ1, the main shock, other earthquake events had a small peak in the higher frequency range of 0.8–3 Hz but the main shock surges only at a lower frequency range with crossing value of 100 cm/s in range of 0.08–0.2 Hz. EQ9 also has the same trend as the other three stated above, but the value peaks at slightly <10 cm/s. Apart from EQ3, EQ7, and EQ8, the other events crossed the spectral acceleration value of 100 cm/s^2 in the range of 2.5–10 Hz; EQ4 and EQ5 have a peak value only in this range.

The response acceleration of the Gorkha earthquake (EQ1) has an almost flat shape in the range of 0.3–10 Hz. Maximum displacement during the main shock was nearly 300 cm for the structure with a frequency of nearly 0.25 Hz at a velocity of 380 cm/s and 500 cm/s^2 as acceleration. The phenomenon of such spectral parameters will be discussed briefly later in the discussion.

The characteristics of ground motion have an impact on damage scenarios all over the affected area. Low-rise masonry and reinforced concrete buildings in the Kathmandu valley have high natural frequency. Super high-rise, base isolated buildings could have suffered severe damage if they had been built in the affected area. The natural frequencies of various structures are shown in

TABLE 1 | Earthquake data.

SN	Description	Time (UTC)	Magnitude (M_w)	Location		Epicentral distance (km)
				Latitude	Longitude	
1	EQ1	25-04-015 06:11	7.8	28.1473	84.7079	76.86
2	EQ2	25-04-015 06:45	6.6	28.1927	84.8645	69.30
3	EQ3	25-04-015 06:56	5.5	27.9100	85.6501	33.00
4	EQ4	25-04-015 08:55	5.3	27.6364	85.5029	18.50
5	EQ5	25-04-015 23:16	5.2	27.8052	84.8744	43.60
6	EQ6	26-04-015 07:09	6.7	27.7945	85.9739	67.20
7	EQ7	26-04-015 16:26	5.3	27.7612	85.7704	44.80
8	EQ8	12-05-015 07:05	7.3	27.8368	86.0772	75.10
9	EQ9	12-05-015 07:36	6.3	27.6180	86.1659	83.90

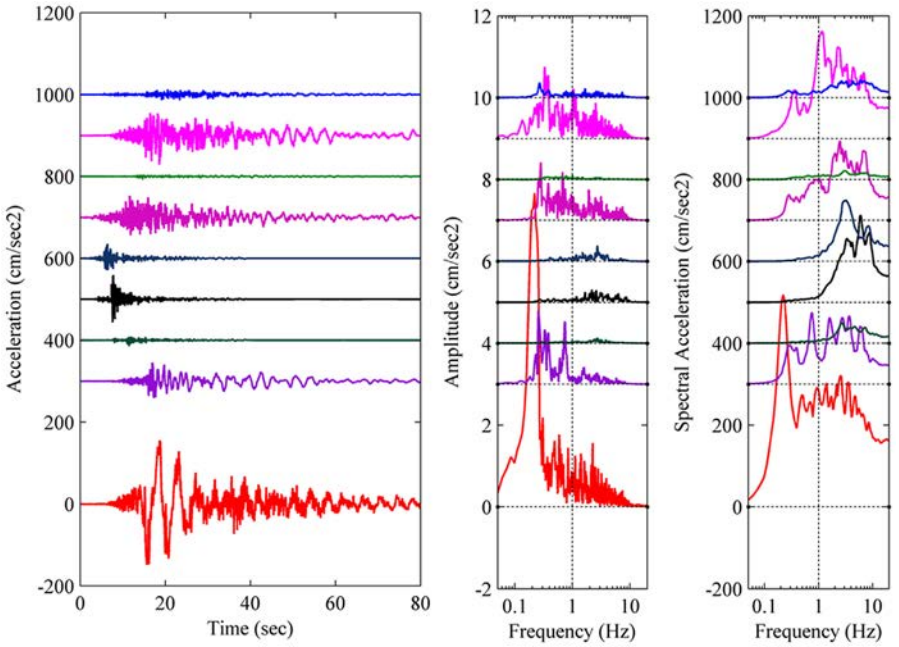

FIGURE 3 | Ground motions recorded in KATNP and corresponding Fourier and response spectra.

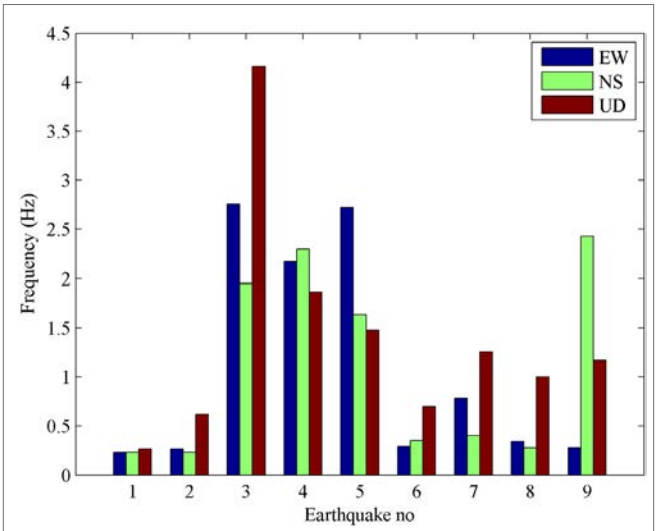

FIGURE 4 | Dominant frequencies in three components for all earthquakes.

Figure 6. Damage of any structure during earthquake directly relates to the strength itself and the amount of earthquake force that pushed it. Strength of the structures relies on materials used and the technique of construction. We found that in most affected areas, people live in stone masonry buildings with mud mortar, which is vulnerable for lateral loads. Even though earthquake ground motion records outside the Kathmandu valley are unavailable, we attempt to evaluate damage scenarios in rural areas. Most of the structures are two stories and some are three stories. The natural frequency of such structures is not so low to resonate with earthquake ground motion frequency.

DAMAGE SURVEY

Most settlements in the mountainous region of Nepal are in rural areas that are dominated by shelters constructed with stone masonry. Brick masonry structures and reinforced concrete structures are found in a few areas, mainly newly developed towns and areas accessible by road. The epicenter of the earthquake was in Barpak, Gorkha, which is a rural mountainous area where all of the structures are stone masonry with mud mortar with an exception of a few reinforced concrete buildings.

We chose a cluster of 149 structures in Harmi, Gorkha. The location is 165 km from Kathmandu by road. It is reached by following the Prithvi highway to the west up to Dumre, then along the Dumre–Beshisahar–Chame highway to Turture, and from there along the Turture–Palungtar road to Harmi. This area is about 17 km SW of the epicenter of the main shock. The topography of the area was selected as it starts from the ridge of a mountain, at an altitude of 1162 m extending down to 600 m at the bottom of a hill (**Figure 7**). We found that the damage scenario in these rural areas was localized with topography, so we plotted the locations of surveyed structures on a contour map of the area. To construct the contours, we used a free-source digital elevation model (Aster Gdem, 2009), with an accuracy of 30 m. Image tile "N28E084" was used as a base and the data were extracted for the study area. Contour lines were drawn at interval of 20 m. The north facing slope of the study area has a small local ridge at a level between 880 and 960 m. Another main ridge of that hill is found above 1160 m.

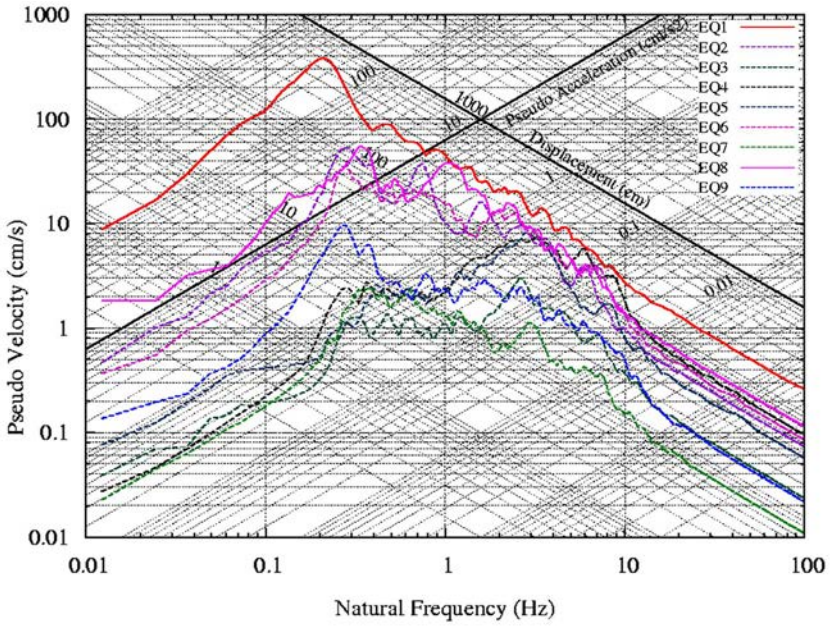

FIGURE 5 | Combined velocity, displacement, and acceleration response spectra of the earthquakes.

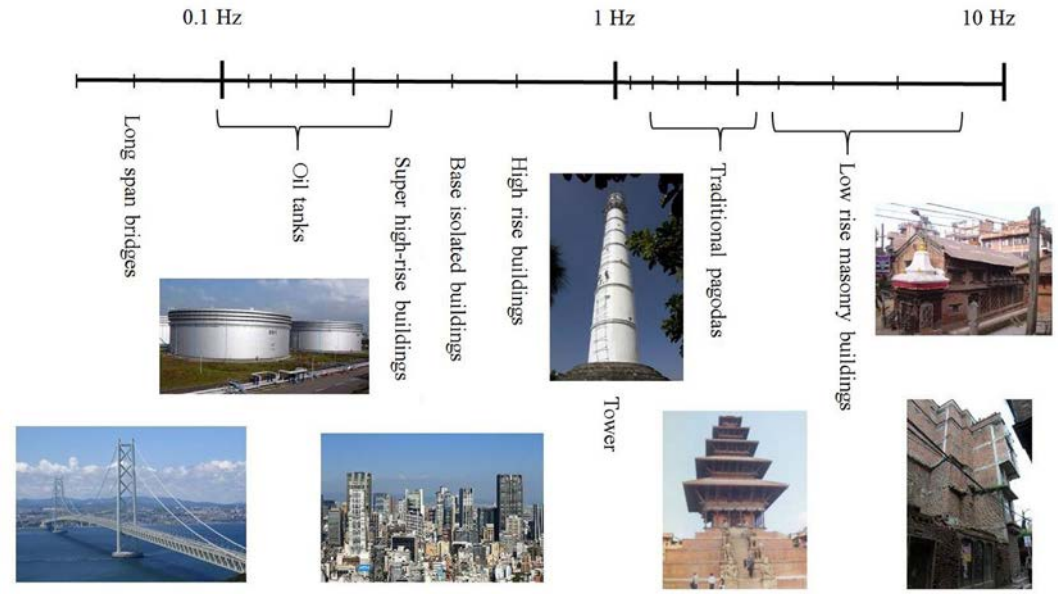

FIGURE 6 | Natural frequency of various structures.

The structures were categorized into three groups by size, where all of the structures are of stone masonry with mud mortar; a few of them have cement pointing on their outer faces. Large-sized structures (L) are of two to four stories and are larger in plinth area (around 75 m^2). Medium-sized structures (M) are single or double storied, having plinth area in the range of 45–75 m^2. The rest of the structures fall under the small (S) category. The damage grades used in the study lie in the range from 0 and 5, where 0 denotes no damage and 5 represents totally collapsed in all sides. A damage grade of 4 represents severely damaged structures where only cracked ground floor walls still stand, and the roof and upper floors have been brought down to the ground. Structures with severe damage but with building shape preserved, albeit with major cracks in the walls or partial

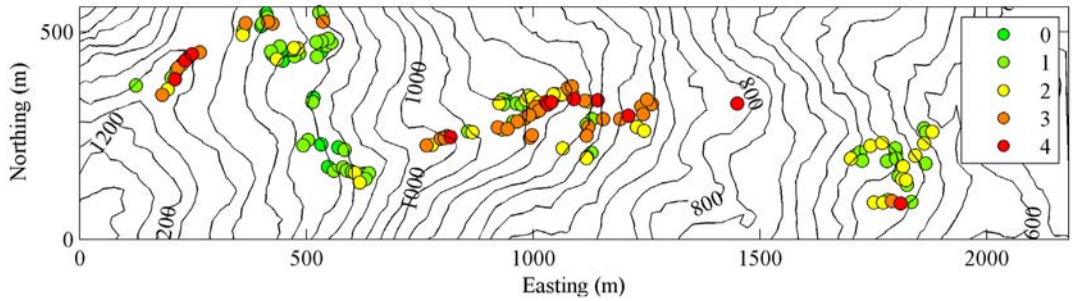

FIGURE 7 | Topographic map of the study area showing structural damage grade.

collapses, are categorized as grade 3. These structures are accessible with special precautions taken. Structures having a few major cracks in walls, but accessible even though they are not habitable without intensive maintenance work, fall under grade 2. The structural category for grade 1 corresponds to excessive minor cracks throughout the walls; these structures are habitable with little maintenance work. Intact structures with no damage or only a few minor cracks, which are habitable with little or no maintenance work required, are categorized in grade 0.

In the study cluster, there are 149 structures consisting of 58 large, 68 medium, and 23 small-sized buildings with 39, 46, and 15% of weightage, respectively. Damage grade and location were recorded using GPS at the site. **Figure 7** shows the damaged structures on a topographic map. Green colored dots represent grade 0 structures, whereas red dots represent the location of grade 4 structures (as we do not have any grade 5 structures). **Figure 8** shows the damage grade of structures with percentages of structures that include categories of structure sizes. We found that 8% of the structures had a damage grade of 0; 38% were in grade 1; and grade 2 and grade 3 structures were 24% each. The remaining 6% of the structures were damaged severely, at grade 4.

Here, we can see most of the structures fall under damage grades 1, 2, and 3, with less coming from grades 0 and 4. From the survey, we found that most of the buildings on ridge lines suffered heavy damage but those on side-slopes were not damaged as much. The study area comprises an area that includes a mountain ridge along with a local ridge line formed on the middle of the slope. Hence, we categorized the structures as ridge-line structures, those that are located on the ridge line. There are a total of 52 structures located on the ridge line, including the main and local ridge lines. Damage grade details of the structures on the ridge line are shown in **Figure 9**. There are no structures that fall under grade 0; in fact only 15% of the structures graded as 1 with 19% in grade 2. More than half of the structures, i.e., 52%, were grade 3 and the remaining 14% fell under grade 4. A small structure that was graded as 3 on the ridge line is shown in Image S1 in Supplementary Material.

The failure mechanisms of structures constructed with stone masonry with mud mortar are mainly seen in two categories. Delamination of the wall is the major failure mechanism and shear failure is secondary. The methods for constructing stone masonry with mud mortar are based around building two wall layers: an inner and an outer; however, this layered single wall

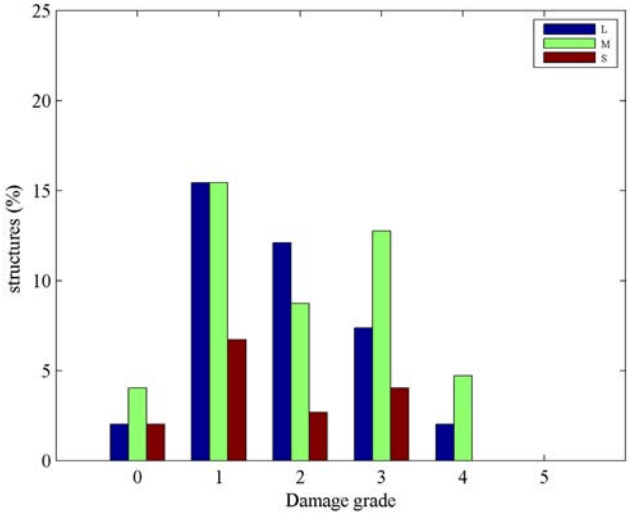

FIGURE 8 | Damage distribution for all structures.

can be a main cause for delamination. Bonding of the inner and outer walls does not exist, which causes the wall to act as two independent walls during an earthquake, thereby causing severe damage. There are many structures with vertical cracks appearing in association with the shear failure of the wall. Structures with horizontal bands of chiseled stone have a few cracks compared to those without the horizontal bans.

FIELD TEST

Pullout Test to Assess Bonding Strength of Mud Mortar

Materials used in local constructions are not of any specific standard. Most of the stone masonry structures in rural Nepal are constructed using local stone and mud. The properties of such materials are not well known. After the Bam earthquake in Iran, adobe and masonry structures were investigated to further characterize the bonding strength of mortar (Kiyono and Kalantari, 2004). We have done similar simple field tests here to determine material properties.

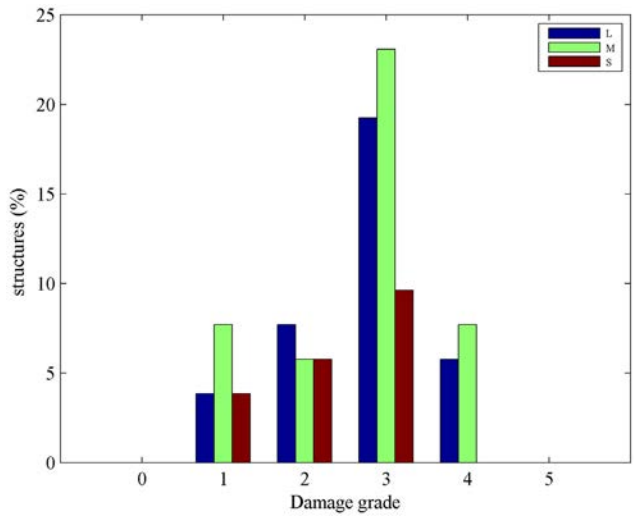

FIGURE 9 | Damage distribution for structures on ridge lines.

We conducted pullout tests in the field to determine the bonding strength of stone and mud mortar joints. Damaged buildings were chosen for sampling, selecting the most undisturbed sample from the remaining parts of a structure. Sample stone was carefully freed on three sides so that only the bottom remained bonded with mud mortar. A simple weighting gage and a rope to connect with sample and weighing gage were used in test. Weighing gage consisted of the spring type gage that shows the pulling force in kilogram, which can be adjusted in some range to make it 0. Weighing gage was tightened with a rope that bound the stone from the sides. We set the force applied during the stretching of rope to 0 from adjustable screw. Force was applied gradually to pull the stone out and the reading in the weighing gage (S) was recorded. After pulling out the stone, we measured the mortar joint area (A) that exactly bonded with the stone, ignoring voids at the joint surface. The weight of the sample stone (W) was also measured to facilitate the calculation of the normal stress acting on this surface.

Three samples were taken to calculate normal stress ($\sigma = W/A$) and shear stress ($\tau = S/A$) (shown in **Table 2**). Equation 1 shows the theoretical relationship of shear and normal stress with bonding stress (c) and coefficient of friction (μ), considering the equilibrium of forces in the horizontal direction.

$$\tau = c + \mu\sigma \quad (1)$$

In fitting the data from the test result, we found the value of cohesive strength (c) and coefficient of friction (μ) of stone masonry with mud mortar joints to be 0.001137 MPa, and 0.6, respectively.

Samples of the test are not enough to conclude the material strength; hence, we compare these values with the test results from the 2003 Iran Bam earthquake damage survey (Kiyono and Kalantari, 2004). Results of the test conducted in Iran and Nepal are shown in **Figure 10**. In Iran, tests were conducted for sun-dried and baked brick masonry structures, where the shear strengths of mortar bonding were estimated to be 0.0029 and 0.0097 MPa, respectively. The frictional coefficient for the joint was found to be 0.62 and 0.54, respectively, for sun dried and baked brick masonry. Test results from Nepal show that the frictional coefficient lies between the values of sun-dried and baked masonry structures in Iran, but shear bonding strength is much lower than that of both brick masonry structures.

Schmidt Hammer Test

A non-destructive test device, the Schmidt hammer, is often used to determine the surface hardness and penetration resistance of concrete or rock. Even though the device is designed for concrete structures, we have successfully used it for stone and brick masonry structures. To use a Schmidt hammer for stone and brick masonry structures, we must assume that the masonry components themselves stand as uniform blocks with mortar forming the matrix between hard elements. Rebounds of a hammer depend on the strength of the mortar too and, therefore, represent the overall strength of the masonry structure. There are some drawbacks in this assumption, but we anticipate that these measurements might be used as a reference for future studies. We conducted the test at several points on the surface of the structure, with a minimum distance between test points set to 30 mm. Conversion of rebound numbers to the probable strength of the structure is done using a chart based on the pressure resistance on a 15 cm cube of concrete, as provided by the manufacturer (Proceq, 2006). Categorically, we discuss three types of structures, i.e., stone masonry, brick masonry with mud mortar, and historical monument structure.

Stone Masonry with Mud Mortar

Stone masonry structures were tested at two sites in Harmi, Gorkha. One was a large structure constructed 38 years ago that had collapsed up to the first floor, but with intact ground floor walls (Image S3 in Supplementary Material). The other one was a small structure. In the large structure, we conducted the test at 26 points where we found large variations in rebound numbers. Some locations in joint areas could not show the data (i.e., they were below the lowest range value for hammer 10) and in some locations there were relatively large stone blocks that caused high rebound values and led to an overestimation of strength. Hence, we disregard data below the lower range and above rebound number 30; which corresponds to 26 MPa. A total of four data points from each of the lower and higher ranges were omitted and the remaining 18 data were taken into consideration to calculate the strength. Average rebound numbers range between 15 and 30 with an average of 21.47 and a standard deviation of 4.4. From the conversion chart, we found that the compressive strength of stone masonry is 12.0 MPa.

Similarly, we conducted the test on a small structure where a total of eight points were sampled. This structure was built only two and half years ago. In this structure, we did not find lower values, as there was a band of relatively large stone blocks. Ignoring two points having rebound number values >30, the remaining six data points had an average of 21.5 and a standard deviation of 5.12. Using the conversion chart, the probable strength of the stone masonry with mud mortar was found to be 12.75 MPa. From

TABLE 2 | Pullout test for bonding strength.

Sample no.	Weight (N)	Joint area (mm^2)	Normal stress σ (MPa)	Pullout force (N)	Shear stress τ (MPa)
1	129.49	24,000.00	0.0053955	107.91	0.00449625
2	103.01	28,000.00	0.00367875	85.35	0.00304811
3	56.90	19,500.00	0.00291785	60.82	0.00311908

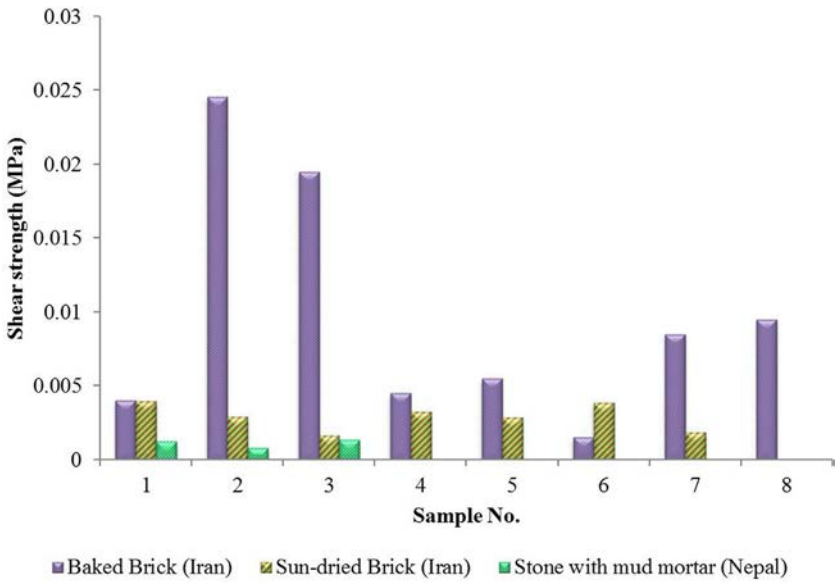

FIGURE 10 | Comparison of the shear strength of stone masonry with mud mortar joint in Nepal with shear strength of brick masonry wall joints in Bam, Iran.

these two tests of stone masonry with mud mortar structures, the probable compressive strength was determined to be 12.38 MPa, roughly the average of the sampled structures.

Brick Masonry with Mud Mortar

Brick masonry with mud mortar structures are common in newly developed towns and cities in Nepal. For testing, we chose a small two-story building that had some cracks in the walls due to the earthquake. This structure is located in Palungtar municipality, Gorkha. The load-bearing main wall of the structure had dimensions of 3750 mm × 5700 mm with a thickness of 350 mm and a height of 3900 mm. Four sampling points were selected in the short wall side of the structure, maintaining 35 mm for the edge distance. As the walls of the structure were cracked, we can make measurements in just four locations. Rebound numbers recorded in those points are 22, 27, 25, and 28. Hence, the average rebound value is 25.5 with a SD of 2.65, corresponding to a probable compressive strength of 18.75 MPa.

Historical Brick Masonry Structure with Mud Mortar

We chose the historical monument of the Gorkha durbar for structural testing (Image S4 in Supplementary Material). This structure was originally built in AD 1640 and was made of brick masonry and timber. This monument stands on a ridge of the same hill that hosts the Gorkha bazar on its southern slope. The structure experienced severe damage during the main earthquake at an epicentral distance of 27 km. The Gorkha durbar is a three-story building with a tile roof. We selected sampling points on the ground floor wall along two basal lines: one 380 mm from plinth level and another 350 mm above the first. Horizontal pitches of the sampling points were taken at 500 mm. A total of 42 blows were made on the wall, with the highest and lowest rebound numbers being 50 and 11, respectively. During the test we found, in some places, a brick element that was not intact and caused lower rebound values. Hence, we neglect such sampling points during the calculations. By not using two sampling points, we end up with 40 samples to evaluate the strength of the masonry wall in the historical structure. Rebound numbers ranged from 20 to 50, with an average of 32.4 and a SD of 6.92. From the conversion chart, the corresponding probable compressive strength of the wall is 29.5 MPa.

DISCUSSION

The earthquake ground motion observed during the Gorkha earthquake was dissimilar from previous earthquakes in the region. Many researchers expect that the triggering of such an earthquake would damage lots of structures in Kathmandu and claim tens of thousands of lives (Dixit et al., 2000; Wyss, 2005), which overestimates the actual toll by at least an order

of magnitude. One of the main reasons behind less damage is that the low-frequency ground motion reduced vulnerability in high-frequency structures. Most residential housing in the affected area does not have a natural frequency low enough to be in resonance with the ground motion recorded in Kathmandu.

The characteristics of ground motion alone, as recorded in KATNP, cannot adequately define the phenomena of such acceleration time history. The likelihood of amplification of the low-frequency component by soil strata is high, but is this the only reason for slow ground motions in Kathmandu? People who were surveyed in Gorkha concerning the shaking pattern and described the scene as buildings moving to and fro and trees behaving like swings. Considering these observations, we can argue that the source of the earthquake had an effective rupture mechanism that radiated low-frequency dominant ground motions. This was not only so for the main shock but also for the aftershocks, which had similar low-frequency component characteristics recorded at KATNP. This supports the evidence for low-frequency amplifying behavior in the soils of the Kathmandu basin. We should also consider the non-linearity of soil behavior; excitations with higher acceleration cause soil layers to act as filters for the high-frequency components while amplifying low frequencies with the resonance effect. Epicentral distance also has a key role in components of frequency range; events with spectra with higher frequencies correspond to nearer events, and those having low frequencies are generally distant events. Smaller events of less than moment magnitude 6 have higher frequency dominant acceleration, including the M6.3 event EQ9 aftershock on 12 May, which had high-frequency dominance. The dominant frequencies of all components for all earthquake events are shown in **Figure 11**, as related to epicentral distance and moment magnitude. These data recorded with high-frequency dominance focus the issues back on the characteristics of the source of earthquake mechanism not only in the local site condition that are responsible for the generation of ground motion events with different dominant frequencies.

In hilly areas, where most of the structures are built of stone masonry with mud mortar, damage along ridge lines is particularly notable. Structures located on slopes, with foundations lying over some layers of soil, generally had very low levels of damage even at short epicentral distances. The conventional thought of building safe houses on ridge lines, over hard rock foundations now becomes suspect. Local site effects of ground motion tended to amplify high-frequency components along ridge lines where bedrock is shallower. Previously, we showed a figure of a damage scenario in **Figure 9**. Now, considering the ratio of total structures to ridge structures, damage scenarios of higher grades are mostly concentrated along ridges. **Table 3** shows the percentage of structures damaged on a ridge line in the study area.

Large structures on ridge lines constituted 100% of the grade 4 damage. Damage at a grade 3 level also has a higher contribution from ridge-line structures. There are few structures having damage at grade 2 or even grade 1 level that exist due to special attention during construction. Horizontal bands of chiseled stone were used for a more esthetic appearance and also had external cement pointing on the walls.

During the 2011 Mw6.9 Nepal–Sikkim earthquake damage in stone masonry structures was reported widely, where delamination of walls is the major failure pattern (Shakya et al., 2013). They mentioned about the severe damages in Taplejung, Ilam, and Panchthar districts of Nepal, up to about 90 km (distance to Ilam bazar) as epicentral distance. We have similar topography in mountainous area so we can compare the scenario in eastern part (affected by the Nepal–Sikkim earthquake) and mid and western part (affected by the Gorkha earthquake). Spreading of damage due to Gorkha earthquake is not that high as compared to that of the smaller Nepal–Sikkim earthquake.

The pullout test conducted in damaged structures to find out the joint properties. Here, we compare the data with the test conducted in Iran after the Bam earthquake where the test was done similarly on the damaged structures. Shear strength of the joint from the test is very low that can be neglected for the modeling but frictional coefficient of mortar joint found significant.

The Schmidt hammer test for stone masonry with mud mortar was performed on walls of two, large and small structures having damage grade of 4 and 3, respectively. The wall itself in the area of hammer blow was intact (only with some minor cracks), which reflected on low bouncing values. We had neglected such values during the analysis; hence, we can generalize the result for all cases. The structure built up of brick masonry with mud mortar had some cracks in other sides but tested wall was intact during the time of test. The historical Gorkha durbar had also suffered from some damages on other sides but the front wall, where test was conducted had minor cracks with loosening of cladding bricks, which also appeared in result that we excluded for analysis. Hence, all the test results are not affected significantly by damage state of the structure.

Material properties for old masonry structures in Kathmandu studied previously (Parajuli et al., 2011) proposed the compressive strength of brick to be 11 MPa, where the same for mortar and wall are 1.6 and 1.8 MPa, respectively. Results from our tests in comparison with the previous study are almost ten times higher for wall strength. If we consider only the brick element, the resulting value from this test is almost 50% more than those experiments conducted previously. Brick quality for the experiment used in tested structures is different; hence, the results we obtained are able to take into account the compressive strength of stone and brick element itself rather than the integrated wall with mortar.

CONCLUSION

The ground motion characteristics of the Gorkha earthquake seem unique. The reasons for such characteristics require high priority research in the field of seismology. Source mechanisms, directivity, wave paths, and local site conditions should be investigated intensively. The western part of Nepal has a large seismic gap. Earthquakes with the same or even stronger shaking may occur in near future. The Gorkha earthquake had low-frequency ground motion with accelerations of <200 cm/s^2, but the velocity was relatively high which caused damage. One of the reasons behind the collapse of many historical structures, including Dharahara,

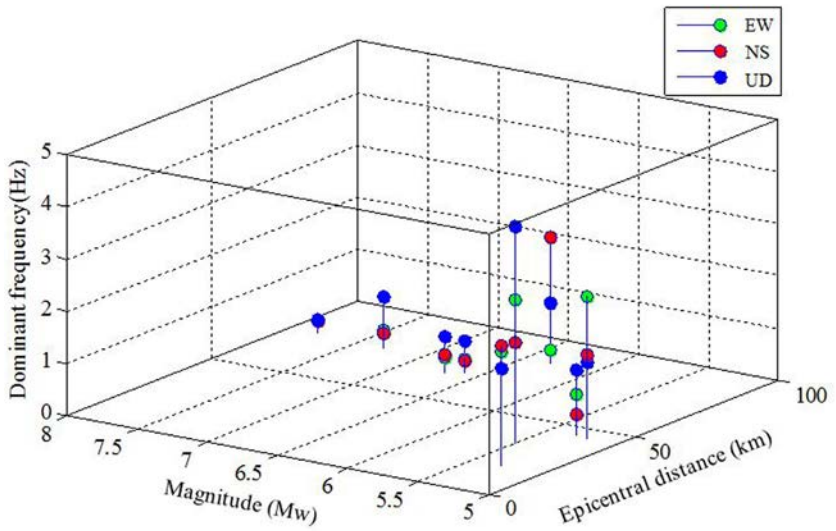

FIGURE 11 | Distribution of dominant frequencies for all earthquakes, all components over a given magnitude and epicentral distance.

TABLE 3 | Percentage of ridge-line structures damaged.

SN	Grade	Structure size		
		L (%)	M (%)	S (%)
1	0	0	0	0
2	1	9	17	20
3	2	22	23	75
4	3	91	63	83
5	4	100	57	NA
6	5	NA	NA	NA

a tower structure monument, in comparison with general buildings, is likely to be lower frequency dominant ground motion. We should consider the epicentral distance and rupture line during the interpretation of ground motion frequency components.

Rural areas in Nepal have a large stock of stone masonry structures used for shelter and other purposes. These need to be reinforced using locally available materials to make them more resilient. Ridge structures are at a higher risk of earthquake damage relative to structures on slopes. Local construction methods should be improved technically, by providing longitudinal and transverse bonding during construction.

The study of material properties used locally should be advanced in order to analyze the structural behaviors of various materials during an earthquake. Even though accuracy could not be assured for the Schmidt hammer tests (designed for reinforced concrete), we have shown test results that provide a probable strength for the stone/brick masonry structures. Stone used in masonry with mud mortar has a probable compressive strength of 12.38 MPa, where local bricks used in masonry with mud mortar have at strength of 18.75 MPa and bricks used in masonry with mud mortar for historical structures are at 29.5 MPa. Note that these results are based only on the surface hardness; masonry structures are not as homogeneous as concrete structures. Also the strength of the mortar is not well represented in such tests, even though loosening and degradation of mortar result in a drop in rebound number. Hence, these values should be used with caution. The bonding strength of stone masonry with mud mortar was investigated using a pullout test on site, which results in a cohesive strength of mud mortar of 0.001137 MPa, with a coefficient of friction of 0.6. Therefore, to study stone masonry with mud mortar, we can use mortar strength combined with the compressive strength of the stone.

ACKNOWLEDGMENTS

The authors thank Prof. Masakatsu Miyazima, Prof. Prem Nath Maskey, and Dr. Hari Ram Parajuli for providing insight and expertise. We are grateful to the inhabitants of Harmi, Gorkha for their kind support and cooperation during the damage survey in Nepal. We also show our gratitude to the USGS, http://www.strongmotioncenter.org/, for sharing data with us, and we thank the reviewers for their insight.

FUNDING

A part of the research was conducted under the support by JST J-RAPID program and JSPS KAKENHI Grant Number 26249067.

SUPPLEMENTARY MATERIAL

The Supplementary Material for this article can be found online at http://journal.frontiersin.org/article/10.3389/fbuil.2015.00023

IMAGE S1 | Small size structure failure with damage grade 3.

IMAGE S2 | Pullout test for bonding strength.

IMAGE S3 | Schmidt hammer test points (stone masonry).

IMAGE S4 | Schmidt hammer test on the Gorkha durbar.

REFERENCES

Aster Gdem. (2009). *Database – Aster Gdem*. Available at: http://gdem.ersdac.jspacesystems.or.jp/

BECA World International (New Zealand), SILT Consultants Pvt. Ltd. (Nepal), TAEC Consult Pvt. Ltd. (Nepal), Golder Associates (Canada), and Urban Regional Research (USA). (1993). *Seismic Hazard Mapping and Risk Assessment for Nepal*. UNDP/HMGN/UNCHS (Habitat) Subproject NEP/88/054/21.03.

Bilham, R. (1995). Location and magnitude of the 1833 Nepal earthquake and its relation to the rupture zones of contiguous great Himalayan earthquakes. *Curr. Sci.* 69, 155–187.

Central Bureau of Statistics. (2012). *National Population and Housing Census 2011 (National Report) Government of Nepal*. Vol. 01. Kathmandu: Government of Nepal.

CESMD. (2015). *Internet Data Reports for Earthquakes of 2015*. Available at: http://strongmotioncenter.org/

Dixit, A. M., Dwelley-Samant, L. R., Nakami, M., and Pradhanang, S. B. (2000). "The Kathmandu valley earthquake risk management project," in *12th World Conference on Earthquake Engineering*. (New Zealand: 12th WCEE held in Auckland), 1–8.

Goda, K., Kiyota, T., Pokhrel, R. M., Chiaro, G., Katagiri, T., Sharma, K., et al. (2015). The 2015 Gorkha Nepal earthquake: Insights from earthquake damage survey. *Front. Built Environ.* 1:8. doi:10.3389/fbuil.2015.00008

Government of Nepal. (2015). *Nepal Disaster Risk Reduction Portal*. Available at: http://drrportal.gov.np/

Kiyono, J., and Kalantari, A. (2004). Collapse mechanism of adobe and masonry structures during the 2003 Iran Bam earthquake. *Bull. Earthquake Res. Inst.* 79, 157–161.

Parajuli, H., Kiyono, J., Ono, Y., and Tsutsumiuchi, T. (2008). Design earthquake ground motions from probabilistic response spectra : case study of Nepal. *J. Jpn. Assoc. Earthquake Eng.* 8, 16–28. doi:10.5610/jaee.8.4_16

Parajuli, H. R., Kiyono, J., and Taniguchi, H. (2011). "Structural assessment of the Kathmandu world heritage buildings," in *Proceedings of the 31 St Conference on Earthquake Engineering* (Tokyo: JSCE), 1–5.

Proceq. (2006). *Proceq Concrete Test Hammer Manual*. Available at: http://www.proceq.com/fileadmin/documents/proceq/products/Concrete/Original_Schmidt/English/Proceq_Operating_Instructions_Original_Schmidt_E.pdf

Rana, B. S. J. R. (1935). *Great Nepal Earthquake 1934 (In Nepali)*. Kathmandu: Jorganesh Publishers.

Ranjitkar, R. (2000). *Seismic Strengthening of the Nepalese Pagoda*. Kathmandu: Kathmandu Valley Preservation Trust.

Sato, T., Fujiwara, T., Murakami, H. O., and Kubo, T. (1989). *Reconnaissance Report on the 21 August 1988 Earthquake in the Nepal-India Border Region*. Research Report on natural disasters. Japanese Group for the study of Natural Disaster science.

Shakya, K., Pant, D. R., Maharjan, M., Bhagat, S., Wijeyewickrema, A. C., and Maskey, P. N. (2013). Lessons learned from performance of buildings during the September 18, 2011 earthquake in Nepal. *Asian J. Civ. Eng.* 14, 719–733.

USGS. (2015). *M7.8 Nepal Earthquake of 25 April 2015*. Available at: http://earthquake.usgs.gov/earthquakes/eqarchives/poster/2015/NepalSummary.pdf

Wyss, M. (2005). Human losses expected in Himalayan earthquakes. *Nat. Hazards* 34, 305–314. doi:10.1007/s11069-004-2073-1

Conflict of Interest Statement: The authors declare that the research was conducted in the absence of any commercial or financial relationships that could be construed as a potential conflict of interest.

Copyright © 2015 Parajuli and Kiyono. This is an open-access article distributed under the terms of the Creative Commons Attribution License (CC BY). The use, distribution or reproduction in other forums is permitted, provided the original author(s) or licensor are credited and that the original publication in this journal is cited, in accordance with accepted academic practice. No use, distribution or reproduction is permitted which does not comply with these terms.

frontiers in Built Environment

ORIGINAL RESEARCH
published: 22 August 2016
doi: 10.3389/fbuil.2016.00019

The 2016 Kumamoto Earthquakes: Cascading Geological Hazards and Compounding Risks

Katsuichiro Goda[1], Grace Campbell[2], Laura Hulme[2], Bashar Ismael[3], Lin Ke[4], Rebekah Marsh[5], Peter Sammonds[6], Emily So[7], Yoshihiro Okumura[8], Nozar Kishi[9], Maki Koyama[10], Saki Yotsui[8], Junji Kiyono[8], Shuanglan Wu[8] and Sean Wilkinson[11]*

[1] Department of Civil Engineering, University of Bristol, Bristol, UK, [2] Arup, London, UK, [3] School of Mechanical, Aerospace and Civil Engineering, University of Manchester, Manchester, UK, [4] Willis Towers Watson, Tokyo, Japan, [5] Mott MacDonald, Singapore City, Singapore, [6] Institute for Risk and Disaster Reduction, University College London, London, UK, [7] Department of Architecture, University of Cambridge, Cambridge, UK, [8] Graduate School of Global Environmental Studies, Kyoto University, Kyoto, Japan, [9] Karen Clark & Company, Boston, MA, USA, [10] River Basin Research Center, Gifu University, Gifu, Japan, [11] School of Civil Engineering and Geosciences, Newcastle University, Newcastle, UK

OPEN ACCESS

Edited by:
Emilio Bilotta, University of Naples Federico II, Italy

Reviewed by:
Giovanni Lanzano, Istituto Nazionale di Geofisica e Vulcanologia, Italy
Domenico Lombardi, The University of Manchester, UK

***Correspondence:**
Katsuichiro Goda
katsu.goda@bristol.ac.uk

Specialty section:
This article was submitted to Earthquake Engineering, a section of the journal Frontiers in Built Environment

Received: *11 July 2016*
Accepted: *03 August 2016*
Published: *22 August 2016*

Citation:
Goda K, Campbell G, Hulme L, Ismael B, Ke L, Marsh R, Sammonds P, So E, Okumura Y, Kishi N, Koyama M, Yotsui S, Kiyono J, Wu S and Wilkinson S (2016) The 2016 Kumamoto Earthquakes: Cascading Geological Hazards and Compounding Risks. Front. Built Environ. 2:19. doi: 10.3389/fbuil.2016.00019

A sequence of two strike-slip earthquakes occurred on April 14 and 16, 2016 in the intraplate region of Kyushu Island, Japan, apart from subduction zones, and caused significant damage and disruption to the Kumamoto region. The analyses of regional seismic catalog and available strong motion recordings reveal striking characteristics of the events, such as migrating seismicity, earthquake surface rupture, and major fore-shock-mainshock earthquake sequences. To gain valuable lessons from the events, a UK Earthquake Engineering Field Investigation Team (EEFIT) was dispatched to Kumamoto, and earthquake damage surveys were conducted to relate observed earthquake characteristics to building and infrastructure damage caused by the earthquakes. The lessons learnt from the reconnaissance mission have important implications on current seismic design practice regarding the required seismic resistance of structures under multiple shocks and the seismic design of infrastructure subject to large ground deformation. The observations also highlight the consequences of cascading geological hazards on community resilience. To share the gathered damage data widely, geo-tagged photos are organized using Google Earth and the kmz file is made publicly available.

Keywords: 2016 Kumamoto earthquake, earthquake damage survey, surface rupture, ground deformation, ground motion, building damage, infrastructure damage

INTRODUCTION

A moderate-size earthquake struck the Kumamoto region of Kyushu Island, Japan on April 14, 2016 (21:26 p.m. local time). The Japan Meteorological Agency (JMA) registered a magnitude of M_J 6.5 (moment magnitude M_w 6.1). The fault rupture originated from the northern segment of the Hinagu fault. This earthquake caused intense shaking in the eastern part of Kumamoto Prefecture, and major earthquake damage was caused in Mashiki Town near the epicenter. Subsequently, on April 16, 2016 (1:25 a.m. local time), a larger M_J 7.3 earthquake (M_w 7.1) occurred along the Futagawa fault (NE of the Hinagu fault). This earthquake caused significantly greater damage in wider areas near the fault (e.g., Mashiki Town, Nishihara Village, and Minami Aso Village). The crustal deformation

due to the mainshock was observed as ground surface rupture at many locations along the Futagawa fault (Okumura, 2016). At several places, ground deformation up to 2 m was reported (Shirahama et al., 2016). The April 14 and 16, 2016 events were of right-lateral strike-slip type occurring at shallow depths, and their focal depths were 11 and 12 km, respectively. Although the two events were originated from close but different active faults, the Government of Japan referred to these events as foreshock and mainshock, respectively; this name convention will be followed in this paper. The JMA intensity of 7 (highest intensity in the JMA intensity scale) was recorded in Mashiki Town during both the foreshock and the mainshock (i.e., double shocks). Numerous buildings had collapsed due to the double shocks. The earthquake sequence also triggered several moderate earthquakes (and some damage) at remote locations, such as Yufu City and Kokonoe Town in Oita Prefecture (about 60 km NE of Mashiki Town). Moreover, an active aftershock sequence was observed in Kumamoto. The Kumamoto earthquakes differ from so-called megathrust subduction earthquakes, such as the 2011 Great East Japan earthquake (Fraser et al., 2013; Goda et al., 2013), and have occurred in the intraplate region, similarly to the 1995 Kobe earthquake.

The earthquakes caused significant tangible and intangible loss. As of July 1, 2016, the total number of fatalities was 69 (49 deaths were directly caused by building collapses and landslides and 20 deaths were due to indirect causes), while the total number of casualties was 1,747 (Fire and Disaster Management Agency, 2016). More than 180,000 people evacuated immediately after the mainshock. The total economic loss was estimated to be 24–46 billion US dollars (Cabinet Office of Government of Japan, 2016), while the insurance loss pay-out exceeded three billion US dollars (General Insurance Association of Japan, 2016). Due to the Kumamoto earthquake sequence, 8,050 houses were destroyed, whereas 24,147 buildings suffered major damage.[1] The majority of the collapsed buildings were timber houses with heavy rooves, which were constructed according to the pre-1981 seismic design provisions (Nakashima and Chusilp, 2003). Several cultural heritages (e.g., Kumamoto Castle and Aso Shrine) were also damaged severely due to the earthquakes. The earthquakes triggered numerous landslides in the mountainous areas of the Kumamoto region, and destroyed major infrastructure and facilities. In the plain areas of Kumamoto, several sections of Kyushu Expressway (bridges and road surface cracks) were damaged due to the earthquakes, resulting in major disruption of the regional traffic network. The operation of Kyushu Shinkansen was also interrupted after the mainshock caused one Shinkansen train (traveling at 80 km/h in the south of Kumamoto railway station when the mainshock struck) to derail. Along the Aso line, which connected Kumamoto City and Aso City, a local train was derailed, whereas its railway track was destroyed by the large landslide in the Tateno district of Minami Aso Village (which also blocked the national road Route 57).

The 2016 Kumamoto disasters were caused by multiple cascading geological hazards. The primary damage was due to the intense shaking and ground deformation of the foreshock-mainshock sequence (which occurred only 28 h apart). In the near-fault region, the effects of the ground deformation were remarkable; buildings and infrastructure that were directly above the fault rupture were damaged severely. The secondary damage was caused by landslides and other ground failures, including liquefaction, settlement, and lateral spreading along rivers and coastal areas. The earthquake damage was widespread over the rural areas of Kumamoto Prefecture. In particular, simultaneous damage/destruction to multiple key infrastructures, such as Aso bridge, Oogiribata bridge, Choyo bridge, and Tawarayama tunnel, disconnected main access routes (e.g., Route 57 and Road 28) between areas inside and outside Aso Caldera. As of June 2016, major detours were required to visit places inside Aso Caldera from the Kumamoto city center. In particular, this caused significant difficulty and stress to evacuees and recovery activities in Minami Aso Village, where devastating damage was observed.

This paper presents a summary of the rupture and ground motion characteristics of the 2016 Kumamoto earthquake sequence, and relates them to the observed earthquake damage during the sequence. The damage observations were made during the UK Earthquake Engineering Field Investigation Team (EEFIT) mission,[2] which was conducted between May 22, 2016 and May 26, 2016. To share the gathered damage data widely, geo-tagged photos are organized using Google Earth and the kmz file is made publicly available as supplementary information to this paper. The investigations highlight considerable earthquake shaking and deformation demand in the near-fault region, and provide useful insights for enhancing community resilience against major earthquake disasters. First, key features of the 2016 Kumamoto earthquake sequence are discussed by looking into geological conditions and active fault zones near the Futagawa and Hinagu faults. The spatiotemporal process of the foreshock–mainshock–aftershock sequence is characterized through observed seismic activities and seismological models, such as the Gutenberg–Richter relationship and the modified Omori's law. The available finite-fault model for the mainshock is used to estimate the ground deformation in the near-fault region. Second, ground motion characteristics of the foreshock and mainshock are studied in detail by analyzing ground motion records from the K-NET and KiK-net.[3] Especially, orientations of the deformation and intense ground shaking are compared with those of the damaged buildings in the near-fault region. Third, earthquake damage survey results and observations during the EEFIT mission are discussed to relate observed damage characteristics and patterns to recorded ground motions and ground deformation. Finally, aspects of the cascading geological hazards and their consequences on infrastructure and community resilience are discussed. Useful conclusions are drawn from the investigations to promote effective risk management of compounding earthquake disasters in the future.

[1] http://www.fdma.go.jp/bn/2016/

[2] https://www.istructe.org/resources-centre/technical-topic-areas/eefit

[3] http://www.kyoshin.bosai.go.jp/

2016 KUMAMOTO EARTHQUAKE SEQUENCE

Futagawa–Hinagu Faults

The Futagawa fault stretches from the outskirt of Aso Caldera to Uto Peninsula (Headquarters for Earthquake Research Promotion, 2016). Its orientation is ENE-WSW. The total length of the fault exceeds 64 km, consisting of three segments: Futagawa segment (circa 29 km), Uto segment (circa 20 km), and Uto Peninsula segment (circa 27 km). On the other hand, the Hinagu fault touches on the Futagawa fault in the north (near Mashiki Town) and extends to Yatsushiro Sea in the south (NE–SW orientation). The total length exceeds 80 km, consisting of three segments: Takano-Shirahata segment (circa 16 km), Hinagu segment (circa 40 km), and Yatsushiro Sea segment (circa 30 km). Both Futagawa and Takano-Shirahata segments are of right-lateral strike-slip type. Historically, there have been damaging earthquakes in the Kumamoto region. For instance, the M_w 6.3 1889 earthquake caused notable damage in Kumamoto City (20 deaths, 54 injuries, and 239 house collapses; Headquarters for Earthquake Research Promotion, 2016). However, the damage severity and earthquake impact of the 2016 sequence are far greater than these relatively recent damaging earthquakes in Kumamoto.

Figure 1A shows the Futagawa fault segment and the Hinagu (Takano-Shirahata) fault segment, based on the active fault database by the National Institute of Advanced Industrial Science and Technology (2016). In **Figure 1A**, epicentral locations of the April 14, 2016 foreshock and the April 16, 2016 mainshock are shown based on the unified JMA catalog, available from Hi-net.[4] In addition, locations of Kumamoto City, Mashiki Town, Nishihara Village, and Minami Aso Village are indicated with square symbols. The thin grey lines represent political boundaries of the municipalities in the Kumamoto region. **Figure 1B** shows an elevation map of the Kumamoto region based on the GDEM database.[5] The NE end of the Futagawa segment lies at the opening of the walls of Aso Caldera.

The most recent seismic hazard assessment by the Headquarters for Earthquake Research Promotion (2016) has taken into account rupture scenarios from the Futagawa and Hinagu faults. In the assessment, a scenario magnitude for the Futagawa segment is set to M_w 7.0 with occurrence probability of less than 1% in 30 years, noting that there is a possibility that all three segments of the Futagawa fault rupture simultaneously (in this case, the magnitude is estimated to be in the range of M_w 7.5–7.8). On the other hand, a scenario magnitude for the Hinagu (Takano-Shirahata) segment is considered to be M_w 6.8 with unknown occurrence probability. Similarly to the Futagawa fault, there is a possibility that all three segments of the Hinagu fault could rupture simultaneously, resulting in an M_w 7.7–8.0 earthquake. Moreover, because of the proximity of the Futagawa segment and the Takano-Shirahata segment, both faults might rupture simultaneously, potentially leading to an M_w 7.8–8.2 event. Importantly, during the 2016 Kumamoto earthquake sequence, numerous events occurred initially along the Takano-Shirahata segment (e.g., 14 April foreshock), and then along the Futagawa segment (e.g., 16 April mainshock).

The preceding hazard information (i.e., earthquake rupture potential of the Hinagu and Futagawa fault systems) has been utilized by the Headquarters for Earthquake Research Promotion in developing a wide range of probabilistic seismic hazard maps in Japan.[6] One type of seismic hazard maps display the probability of experiencing a certain shaking intensity in a 30-year period by

[4]http://www.hinet.bosai.go.jp/

[5]https://asterweb.jpl.nasa.gov/gdem.asp

[6]http://www.j-shis.bosai.go.jp/en/

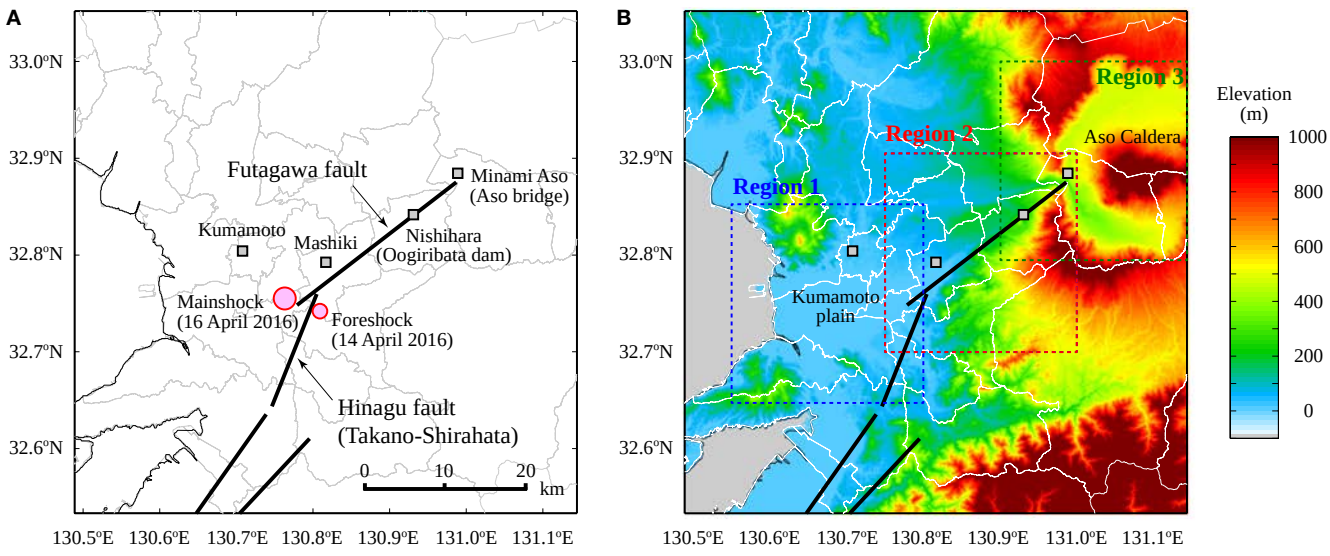

FIGURE 1 | **(A)** Locations of the Futagawa–Hinagu faults. **(B)** Elevation map of the Kumamoto region.

taking into account all possible seismic sources surrounding a site of interest. Another type is the scenario-based shaking map that is generated by the Green's function method using the characterized source model (Irikura and Miyake, 2011).

Seismic Activities

A prolific sequence of earthquakes was observed in the Kumamoto region, after the triggering foreshock event of April 14, 2016. **Figure 2A** shows the temporal variation of earthquakes having $M_J > 3$ over a period between April 13, 2016 and April 18, 2016, while **Figures 2B–F** show the spatial distribution of earthquakes occurring in different time periods. The earthquake data were based on the JMA catalog. The M_J 6.5 foreshock induced an active sequence of dependent events (including a M_J 6.4 event on April 15, 2016). From the spatial distribution of the events that occurred between the foreshock and the mainshock (**Figure 2D**), it can be observed that the triggered events by the foreshock were clustered along the Hinagu fault. Subsequently, the mainshock occurred on the southern tip of the Futagawa fault, and triggered an even more active subsequence of aftershocks (**Figures 2E,F**). The aftershock sequence was not only concentrated along the Futagawa–Hinagu faults but also in the Aso region (NE of the Futagawa fault). The migration of seismic activities over relatively wide spatial areas is a notable feature of the 2016 Kumamoto earthquake sequence.

Using the observed earthquake data in the Kumamoto region, statistical analysis of aftershocks is carried out by applying the Gutenberg–Richter law (i.e., frequency-magnitude characteristics of an aftershock sequence) and the modified Omori law (temporal decay of an aftershock occurrence rate; Guo and Ogata, 1997). It is considered that the JMA catalog is complete above M_J 3.5. In fitting these seismological models, the entire catalog is divided into two parts: events that occurred between the foreshock and the mainshock (72 earthquakes), and events that occurred after the mainshock (248 earthquakes). The results are shown in **Figure 3**. Due to the longer period and the larger triggering event, the number of events in the mainshock-aftershock sequence is greater than that of the foreshock-mainshock sequence. The b-value of the mainshock–aftershock sequence is steeper and has a value close to a typical b-value of 1.0 (Guo and Ogata, 1997). For the modified Omori law, the temporal decay parameter (p-value) for both datasets is estimated as 1.0, which is broadly consistent with the past studies of aftershock statistics (Guo and Ogata, 1997).

Finite-Fault Models and Estimated Ground Deformation

Finite-fault source models, which are determined through source inversion analysis, provide plausible images of earthquake rupture processes by achieving the consistency between observed data and geophysical model predictions (e.g., geodetic, teleseismic, and strong motion). After the Kumamoto foreshock and mainshock, several finite-fault models have been developed and were made available publicly. For example, the Geospatial Institute of Japan (GSI) (2016) developed finite-fault models for the Kumamoto foreshock and mainshock based on GEONET GPS observations. The finite-fault models for the foreshock and mainshock are shown in **Figure 4A**. The geometry is consistent with the fault strike by the National Institute of Advanced Industrial Science and Technology (**Figure 1A**). The estimated slip values for the foreshock and mainshock are 0.62 and 3.50 m, respectively (assumed to be uniform across the fault plane).

For the mainshock, at the Kumamoto GEONET station (32.8421°N, 130.7648°E), 0.75 m horizontal deformation in the ENE direction and 0.20 m downward deformation were recorded, while at the Choyo GEONET station (32.8707°N, 130.9962°E), 0.97 m horizontal deformation in the SW direction and 0.23 m upward deformation were recorded. These observations serve as important constraints in developing finite-fault models for the mainshock, indicating that the fault strike (approximately SW to WSW) should lie between the Kumamoto and Choyo stations.

Using the geometry and slip distribution of a finite-fault model, elastic deformation due to an earthquake can be calculated using Okada (1985) equations. The analytical formulae allow the estimation of NS, EW, and UD components of ground surface deformation. The results of the calculated elastic deformation profiles based on the GSI finite-fault model for the mainshock are shown in **Figures 4B–D**. The results at the GPS stations presented in **Table 1** and show good agreement, demonstrating that the GSI models are particularly useful for estimating permanent deformation at unmonitored locations due to the earthquake.

STRONG GROUND MOTION CHARACTERISTICS

In Japan, national strong motion networks, K-NET and KiK-net, were established after the 1995 Kobe earthquake, and currently more than 1,700 stations are operational. For the 2016 Kumamoto earthquakes, an extensive set of ground motion data is available. In this section, characteristics of observed ground motions in the Kumamoto region are investigated by focusing on: (i) strong motion characteristics in the near-fault region, (ii) regional ground motion characteristics and orientations of the major response axis with respect to the fault strike direction, (iii) comparison of observed ground motion recordings with an existing ground motion prediction equation (GMPE), and (iv) estimation of ground motion parameters at unobserved locations. For these purposes, available ground motion data for 20 seismic events that occurred in April 2016 ($M_J \geq 4.3$) are downloaded from the K-NET and KiK-net (in total, 6,177 records, including borehole recording data for the KiK-net; each record has three components), and are processed uniformly to compute acceleration and velocity waveforms as well as various ground motion parameters [peak ground acceleration (PGA) and 5%-damped spectral acceleration (SA)]. For the record processing, a standard procedure (e.g., tapering, zero-padding, and band-pass filtering) suggested by Boore (2005) is implemented.

Strong Motion Characteristics in the Near-fault Region

Ground motion data recorded at KMMH16 (Mashiki; 32.7967°N, 130.8199°E) are analyzed in detail, noting that the earthquake damage surveys were conducted near this station during the EEFIT mission. The KMMH16 station belongs to

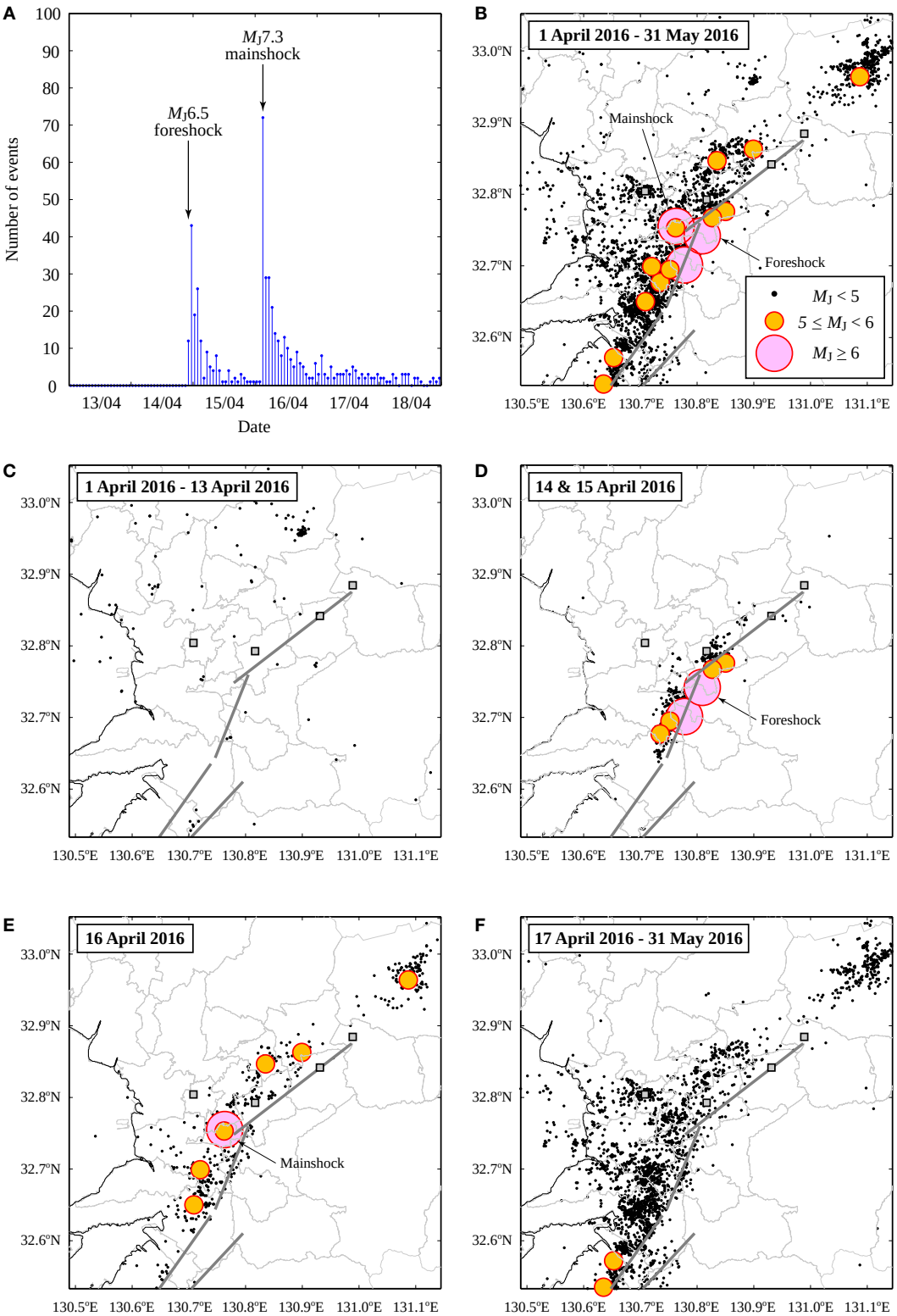

FIGURE 2 | **(A)** Number of earthquakes with $M_J > 3$ that occurred in the Kumamoto region during April 1, 2016 to May 31, 2016. Spatial distribution of earthquakes in the Kumamoto region: **(B)** April 1, 2016 to May 31, 2016, **(C)** April 1, 2016 to April 13, 2016, **(D)** April 14 and 15, 2016, **(E)** April 16, 2016, and **(F)** April 17, 2016 to May 31, 2016.

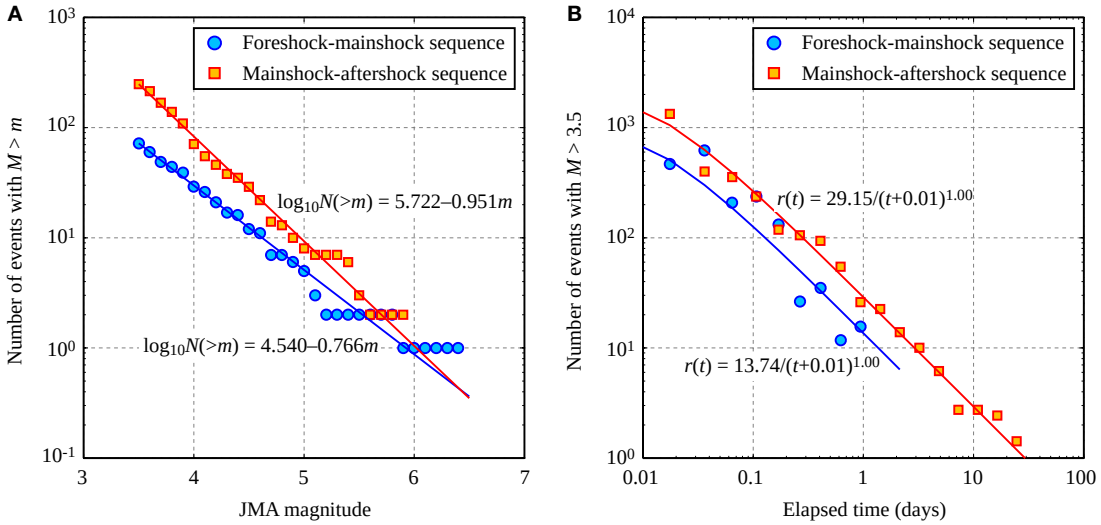

FIGURE 3 | Characteristics of foreshock-mainshock and mainshock-aftershock sequences: (A) Gutenberg–Richter models and (B) modified Omori models.

the KiK-net, and thus two sets of three component recordings at the ground surface and in borehole are available, enabling site amplification effects to be investigated. Another important aspect of the selected records is that KMMH16 is in the hanging wall region of the mainshock (i.e., within a projected fault plane on the ground surface), and thus intense ground shaking was observed during the mainshock. Moreover, at KMMH16, strong shaking due to the foreshock preceded the mainshock, resulting in double-shock ground motions (Kojima and Takewaki, 2016).

Figure 5 shows observed acceleration as well as velocity time-histories (three components) at KMMH16 for the foreshock and mainshock. The blue curves are for the ground surface recordings, whereas the red curves are for the borehole recordings. The significant amplification as well as different dominant frequency content of the ground motions can be observed by comparing the blue and red curves. Another notable observation is that for the velocity time-histories of the mainshock (i.e., **Figure 5D**), relatively large velocity waves are present at both ground surface and borehole (particularly for vertical motions). This indicates that site amplification for short-period components is significantly influenced by near-surface soil characteristics, while that for longer period components is more coherent at ground surface and borehole. The latter may also be attributed to the ground surface rupture near the Mashiki areas.

To examine the spectral content of the observed ground motions at KMMH16, 5%-damped response spectra for the foreshock and mainshock are calculated and shown in **Figure 6**. The results for the ground surface motions are presented with solid lines, while those for the borehole motions are shown with broken lines. The comparison of the response spectra indicates: (i) amplitudes of the response spectra are large, exceeding 1 g up to a period of about 1 s for the foreshock and about 2 s for the mainshock; (ii) generally site amplification is significant for all three components; (iii) horizontal motions are amplified in a period range between 0 s (i.e., PGA) and about 2–3 s, while vertical motions are significantly amplified at vibration periods less than 0.5 s.

At the KMMH16 station, relatively soft soil layers exist in the top 15 m (shear wave velocity less than 250 m/s), underlain by firm rock layers (**Figure 7A**). The borehole recording is installed at a depth of 255 m (ground surface is at 55 m altitude). Hence, major site amplification is anticipated between ground surface and borehole at this site because of high contrast of the shear wave velocities. The average shear wave velocity in the top 30 m of the soil (i.e., V_{s30}) is calculated as 280 m/s (i.e., NEHRP site class D). To investigate the site amplification at KMMH16 in detail, the borehole-to-surface ratios of Fourier amplitude spectra (Ghofrani et al., 2013) are computed for all 20 earthquakes that are analyzed as part of this study. The results are shown in **Figures 7B–D**; the borehole-to-surface spectral ratio curves are categorized into four groups, i.e., foreshock, events that occurred between the foreshock and the mainshock, mainshock, and events that occurred after the mainshock. The division of the datasets is intended for studying the temporal changes of the site response related to soil non-linearity during the Kumamoto foreshock–mainshock–aftershock sequence [e.g., Sawazaki et al. (2009) and Wu et al. (2009)]. The results indicate that the site amplification is period dependent; the horizontal ground motions are amplified significantly (by a factor of 5 or more) in the period range between 0.3 and 2.0 s, while the vertical ground motions are mainly amplified in the periods less than 0.5 s. For the horizontal components (**Figures 7B,C**), period shifts of the surface-to-borehole spectral ratios can be observed for the foreshock and mainshock in comparison with the majority of other smaller earthquakes

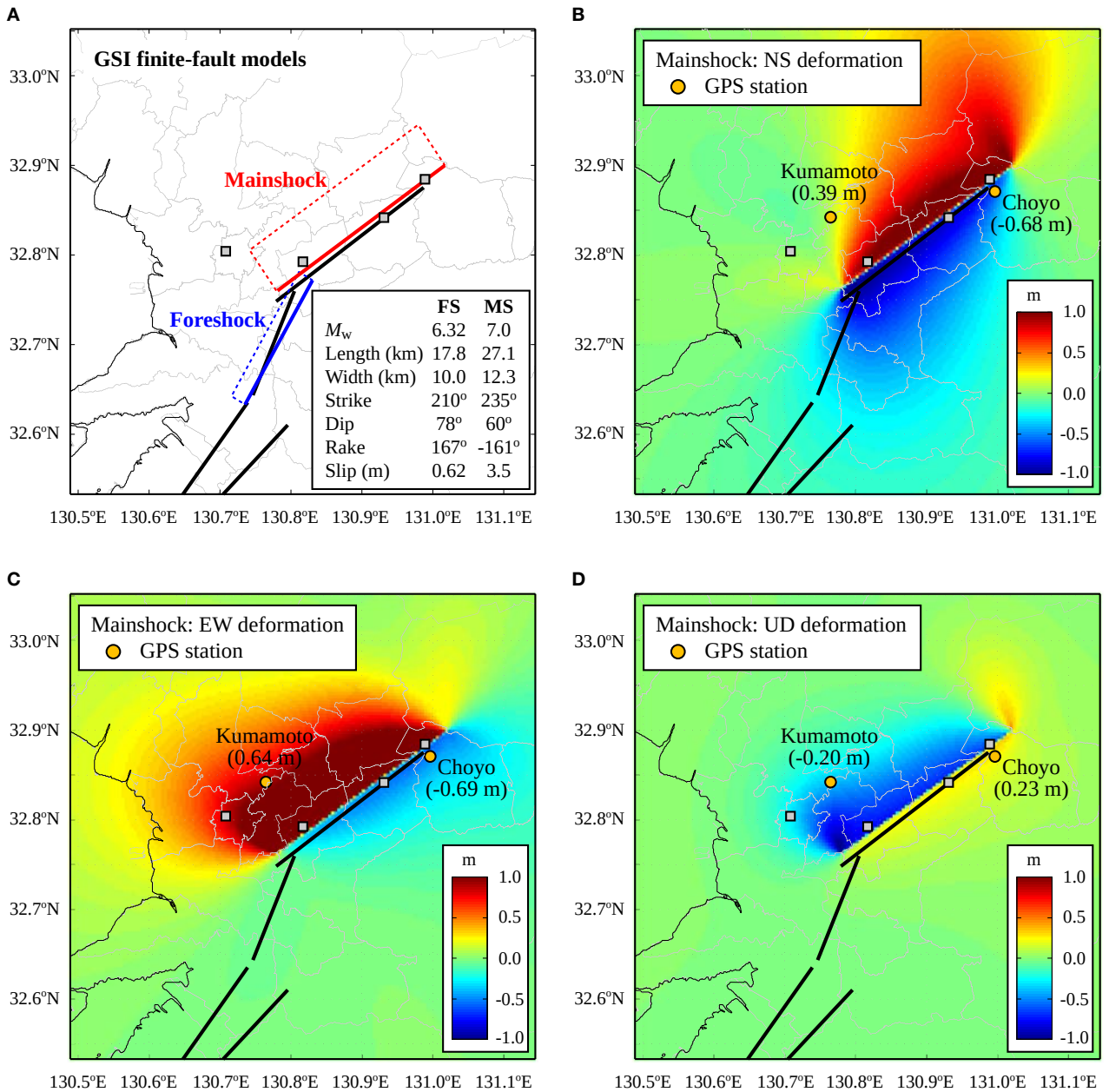

FIGURE 4 | **(A)** Finite-fault models by Geospatial Institute of Japan (GSI) (2016) for the foreshock and mainshock. Estimated elastic deformation profiles based on the GSI finite-fault model for the mainshock: **(B)** NS deformation, **(C)** EW deformation, and **(D)** UD deformation.

TABLE 1 | Comparison of the observed and estimated ground deformations at the Kumamoto and Choyo GPS stations for the mainshock.

GPS station	Observed deformations [NS, EW, UD (m)]	Estimated deformations [NS, EW, UD (m)]
Kumamoto	[0.39, 0.64, −0.20]	[0.0, 0.85, −0.30]
Choyo	[−0.68, −0.69, 0.23]	[−0.57, −0.50, 0.25]

(i.e., dominant peaks of the spectral ratios at 0.2–0.4 s are significantly reduced). For the vertical component (**Figure 7D**), very consistent site amplification is observed at periods less than 1.0 s, while the surface-to-borehole spectral ratios become more variable at longer periods. These observations are a strong argument for making more detailed investigations of the site amplification and the non-linear site response.

Regional Ground Motion Characteristics

It is interesting to investigate the amplitude and orientation of ground motion parameters with respect to the fault strike (Watson-Lamprey and Boore, 2007). For this purpose, the analyses of ground motion records are extended to other K-NET

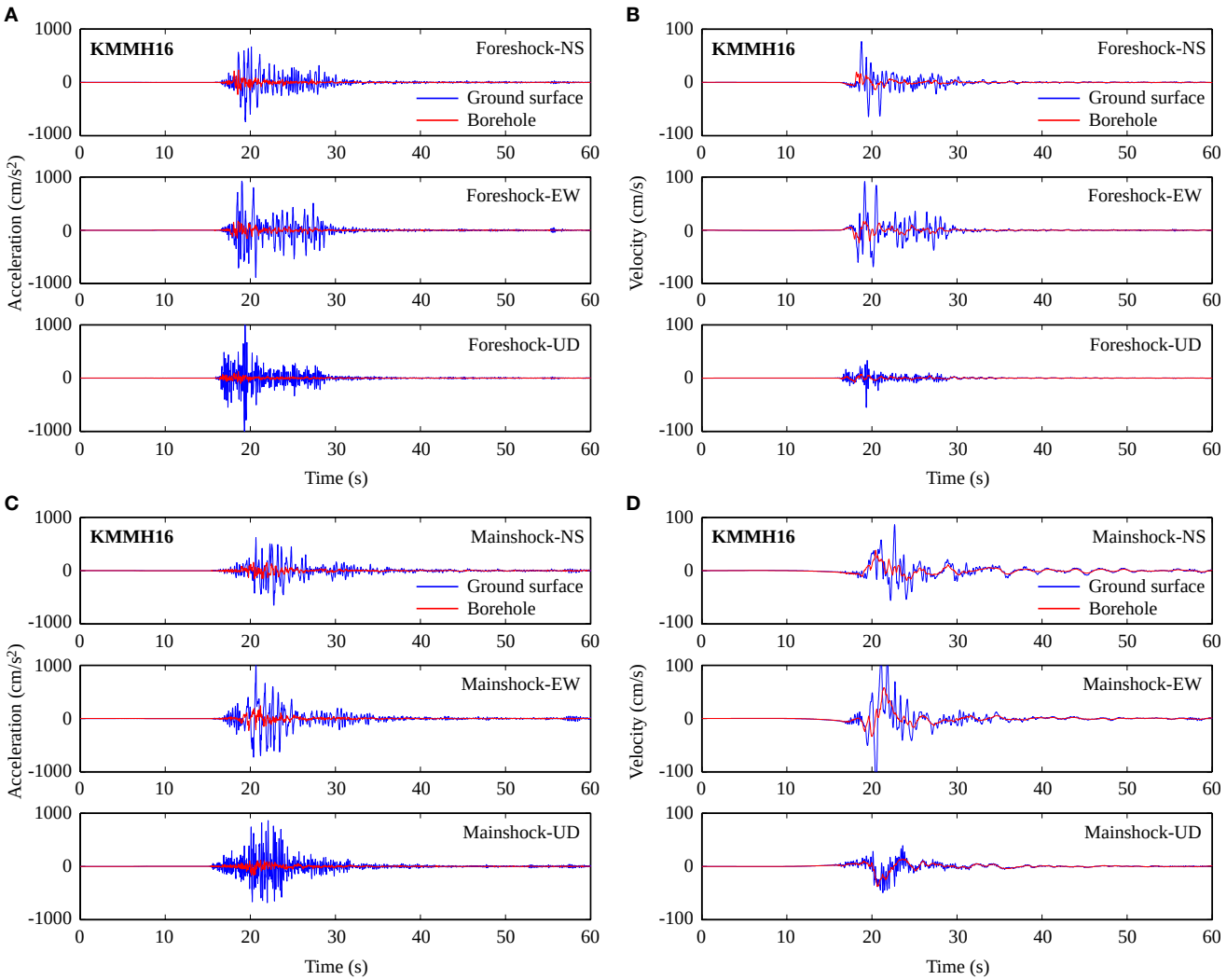

FIGURE 5 | **(A)** Acceleration time-histories for the foreshock at KMMH16. **(B)** Velocity time-histories for the foreshock at KMMH16. **(C)** Acceleration time-histories for the mainshock at KMMH16. **(D)** Velocity time-histories for the mainshock at KMMH16.

and KiK-net stations in the Kumamoto region, and for each station, two horizontal components on ground surface are rotated to a particular azimuth and then ground motion parameters are calculated using the rotated acceleration time-history. A rotation of ground motion records is carried out over 360° with 1° increment. The results can be plotted on a polar coordinate to examine the major and minor response axes of the ground motion records (Hong and Goda, 2007), in comparison with the fault orientation. The results for four ground motion parameters, i.e., PGA and SA at 0.3, 1.0, and 3.0 s, are shown in **Figure 8**; the response parameters in the EW and NS directions correspond to the responses due to un-rotated records. By focusing on the amplitudes of the responses (i.e., size of the response curve), **Figure 8** shows that intense ground motions due to the mainshock were observed over wide areas along the Futagawa and Hinagu faults. Large values of the ground motion parameters are particularly concentrated near KMMH16. Another notable feature of the results is the observation of intense ground shaking for SA at 3.0 s in the NE part of the map near KMM004 (**Figure 8D**).

Regarding the orientation of the major response axis of the observed ground motions, **Figure 8** shows that for PGA and SAs at 0.3 and 1.0 s, there is a clear dominant orientation of the ground motion parameters at KMMH16, KMM006, and KMM005, which is in parallel with the fault strike. Note that these stations are in the hanging wall region. Particularly for the short-period range, the trend of the major response orientation is consistent in the near-fault region. At longer vibration periods, the orientation of the major response axes at KMMH16 and KMM005 rotates to almost fault-normal direction, while that at KMM006 remains parallel with the fault strike. It is important to note that the major response directions at short-vibration periods for KMMH16 coincide with the directions of many collapsed houses in Mashiki Town. This indicates that in the near-fault region, effective countermeasures (e.g., bracing) can be implemented to mitigate shaking damage

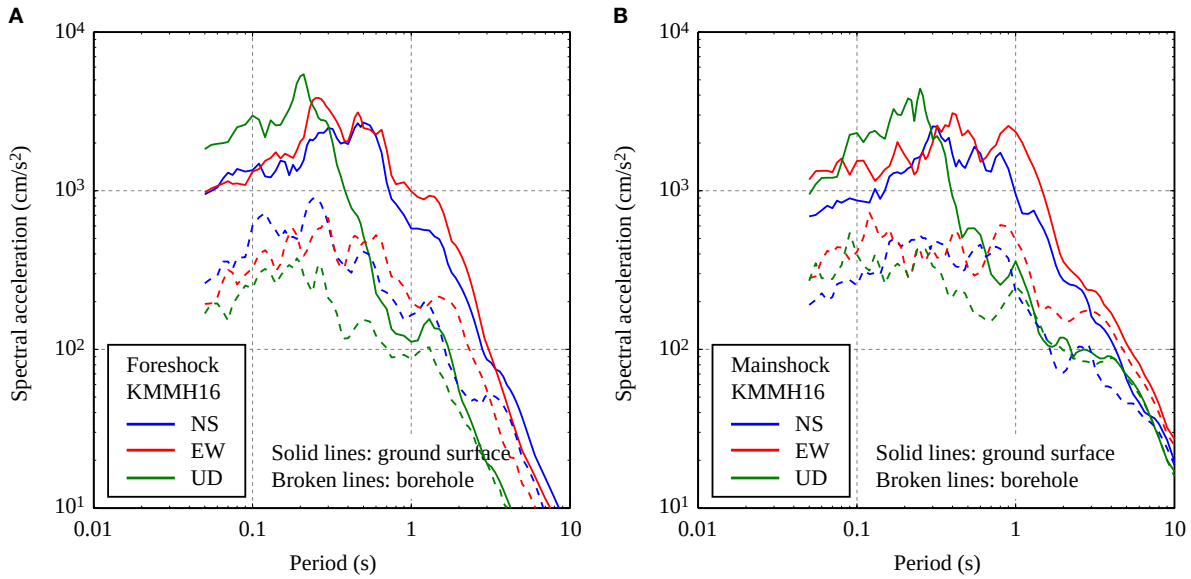

FIGURE 6 | **(A)** 5%-damped response spectra for the foreshock records at KMMH16. **(B)** 5%-damped response spectra for the mainshock records at KMMH16.

when the dominant direction of the ground shaking is known. Furthermore, outside the near-fault region, some consistent orientation effects can be observed. On the other hand, at KMM004, the fault-parallel component is dominant, particularly for SA at 3.0 s, noting that a large-amplitude velocity pulse is present in the EW component of the velocity time-history.

Comparison of Observed Ground Motions and Ground Motion Prediction Equations

It is important to compare the observed ground motions with existing empirical prediction models in the literature. Through such comparison, one can evaluate whether the ground motions from the Kumamoto earthquakes are unusual with respect to past events (note: such differences may arise due to various reasons, such as low/high stress drop and regional attenuation characteristics). In this study, a GMPE by Boore et al. (2014) is adopted. The Boore et al. model is developed using worldwide ground motion data for shallow crustal earthquakes (including ground motion data from Japanese earthquakes) and hence is well suited for such comparison. The moment magnitude for the mainshock is set to 7.1 according to F-net. The source-to-site distance for the Boore et al. model is based on the so-called Joyner-Boore distance; for the ground motion data from K-NET and KiK-net, this distance measure is evaluated using the GSI finite-fault plane geometry (**Figure 4A**). The Boore et al. model includes several adjustment parameters to refine the prediction, such as faulting mechanism and regional factor. In the comparison conducted herein, the strike-slip faulting mechanism and the regional factor for Japanese earthquakes are taken into account. For the comparison shown below, ground motion data that are recorded at sites with V_{s30} between 150 m/s and 500 m/s are considered (average V_{s30} is about 330 m/s). In applying the Boore et al. model, V_{s30} is set to 300 m/s. In the figures, to show the confidence interval of the Boore et al. model, curves that correspond to median plus/minus one SD are shown as broken lines, where the SD is the intra-event sigma as the predicted ground motions are compared with data from a single event.

Figure 9 compares observed ground motions with predicted mainshock ground motions, respectively, based on the Boore et al. model. The results for PGA and SAs at 0.3, 1.0, and 3.0 s are shown. The observed ground motions for the mainshock are generally consistent with the predicted values based on the Boore et al. model. In the distance range between 10 and 100 km, there are several observation data that exceed the median plus one sigma curve; these data are mainly located in the NE of the rupture zone (i.e., Yufu City and Kokonoe Town in Oita Prefecture). In these recorded accelerograms, the existence of a locally triggered event due to the mainshock was clearly observed; this increased the ground motion intensity at relatively remote locations. Overall, the recorded ground motion data for the mainshock of the Kuammoto sequence are in agreement with the Boore et al. prediction model (note: this conclusion is applicable to the majority of the earthquakes of the 2016 Kumamoto sequence).

Ground Motion Estimation at Unobserved Locations: Application to Kumamoto Port

The consistency of the observed ground motion data and the prediction model is useful for estimating ground motion parameters at unobserved locations where an estimate of experienced shaking intensity help understand the observed earthquake damage in the field. To improve the accuracy of ground motion estimation at unobserved locations, one can use both model predictions and observed ground motions nearby a site of interest by taking into account spatial correlation of ground motions (Goda and Hong, 2008; Bhattacharya and Goda, 2013). In this section, an application of the estimation

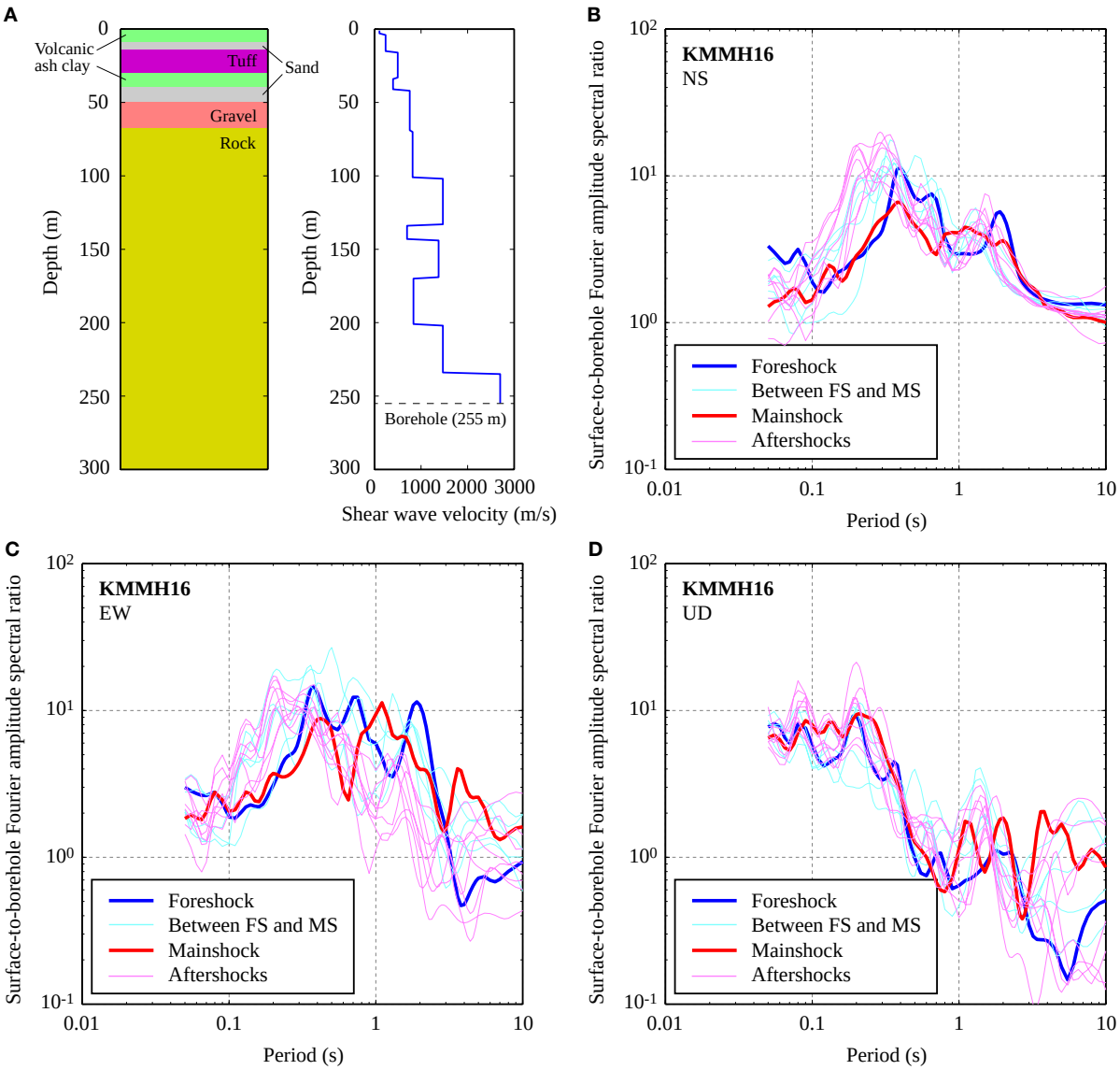

FIGURE 7 | **(A)** Borehole log and shear wave velocity profile at KMMH16. Surface-to-borehole ratios of Fourier amplitude spectra at KMMH16 for different earthquakes during the 2016 Kumamoto foreshock–mainshock–aftershock sequence: **(B)** NS components, **(C)** EW components, and **(D)** UD components.

method using a GMPE and spatial correlation model is demonstrated for Kumamoto port (32.7640°N, 130.5907°E), where liquefaction occurred during the Kumamoto mainshock but no actual recording of the ground motion was available. The nearest ground motion recording station is KMM008. The Joyner-Boore distance from the mainshock rupture plane to Kumamoto port is 15.0 km. The distance between Kumamoto port and KMM008 is 10.6 km.

For the estimation procedure outlined in Bhattacharya and Goda (2013), intra-event spatial correlation of ground motion residuals needs to be evaluated (Goda and Hong, 2008). The correlation model allows the interpolation of the observed ground motions at nearby recording stations to unobserved locations. The empirical spatial correlation curves for the Kumamoto mainshock ground motion data are shown in **Figure 10A**; each curve corresponds to a result for a ground motion parameter (e.g., PGA or SA at 0.3 s). The results show declining trends of the intra-event spatial correlation as a function of separation distance. The curves for different ground motion parameters vary. Overall, the spatial correlation coefficient of 0.5 is adopted as a representative value for the Kumamoto port and KMM008 (i.e., 10.6 km separation distance).

Using the observed response spectra at KMM008 (shown in **Figure 10B**), Boore et al. ground motion model, and spatial correlation coefficient (i.e., 0.5), response spectra at Kumamoto port are estimated. The average shear wave velocity at Kumamoto port is considered to be 200 m/s. The estimation results are shown in **Figure 10B**; both median and confidence

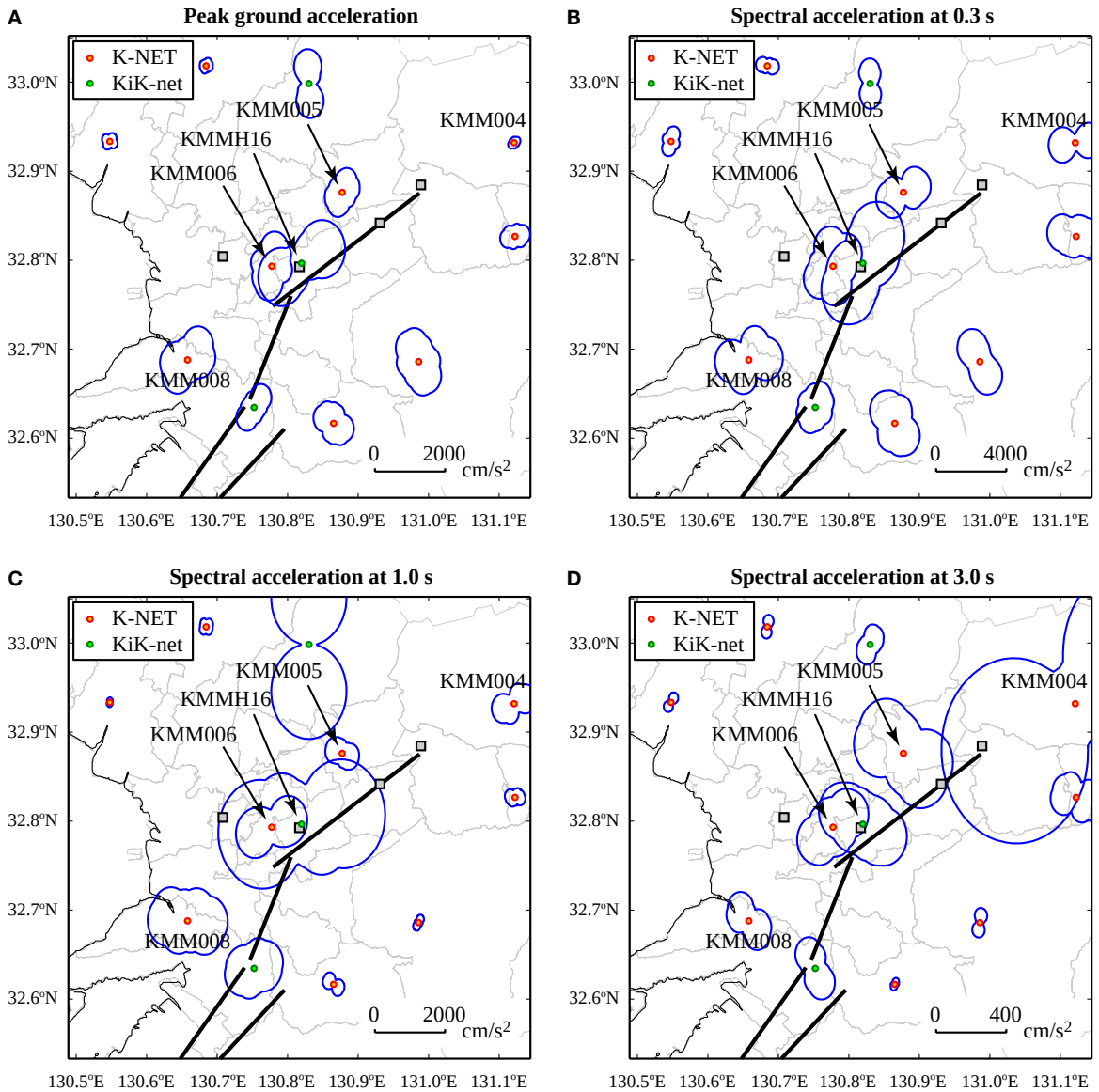

FIGURE 8 | **(A)** Acceleration time-histories for the mainshock at KMM006. **(B)** Velocity time-histories for the mainshock at KMM006. **(C)** Acceleration time-histories for the mainshock at KMM008. **(D)** Velocity time-histories for the mainshock at KMM008.

interval (16th and 84th percentiles) can be obtained through this method. For instance, the estimated PGA at Kumamoto port corresponds to a median of 0.48 g and a confidence interval ranges from 0.33 to 0.73 g (note: at KMM008, PGAs of 0.64 and 0.78 g were observed for the two horizontal components). The estimated PGA values are sufficiently large to trigger liquefaction for sandy soil layers (e.g., Idriss and Boulanger, 2008; Santucci de Magistris et al., 2013).

EARTHQUAKE DAMAGE SURVEYS

An earthquake damage investigation was conducted from May 22, 2016 to May 26, 2016. The main objective of the surveys was to assess the earthquake damage to buildings and infrastructure in relation to experienced fault rupture deformation and ground shaking. The surveyed sites include urban as well as rural areas of Kumamoto Prefecture. **Figure 11** shows three regions for the earthquake damage surveys; the locations of Regions 1, 2, and 3 are indicated in **Figure 1B**. Region 1 includes Kumamoto City and Uto City (i.e., urban areas in the Kumamoto plain); Region 2 includes Mashiki Town and Nishihara Village (i.e., rural areas outside of Aso Caldera), which are very close to the Futagawa fault and were shaken intensely during the mainshock; and Region 3 includes Minami Aso Village and Aso City, which are inside of Aso Caldera.

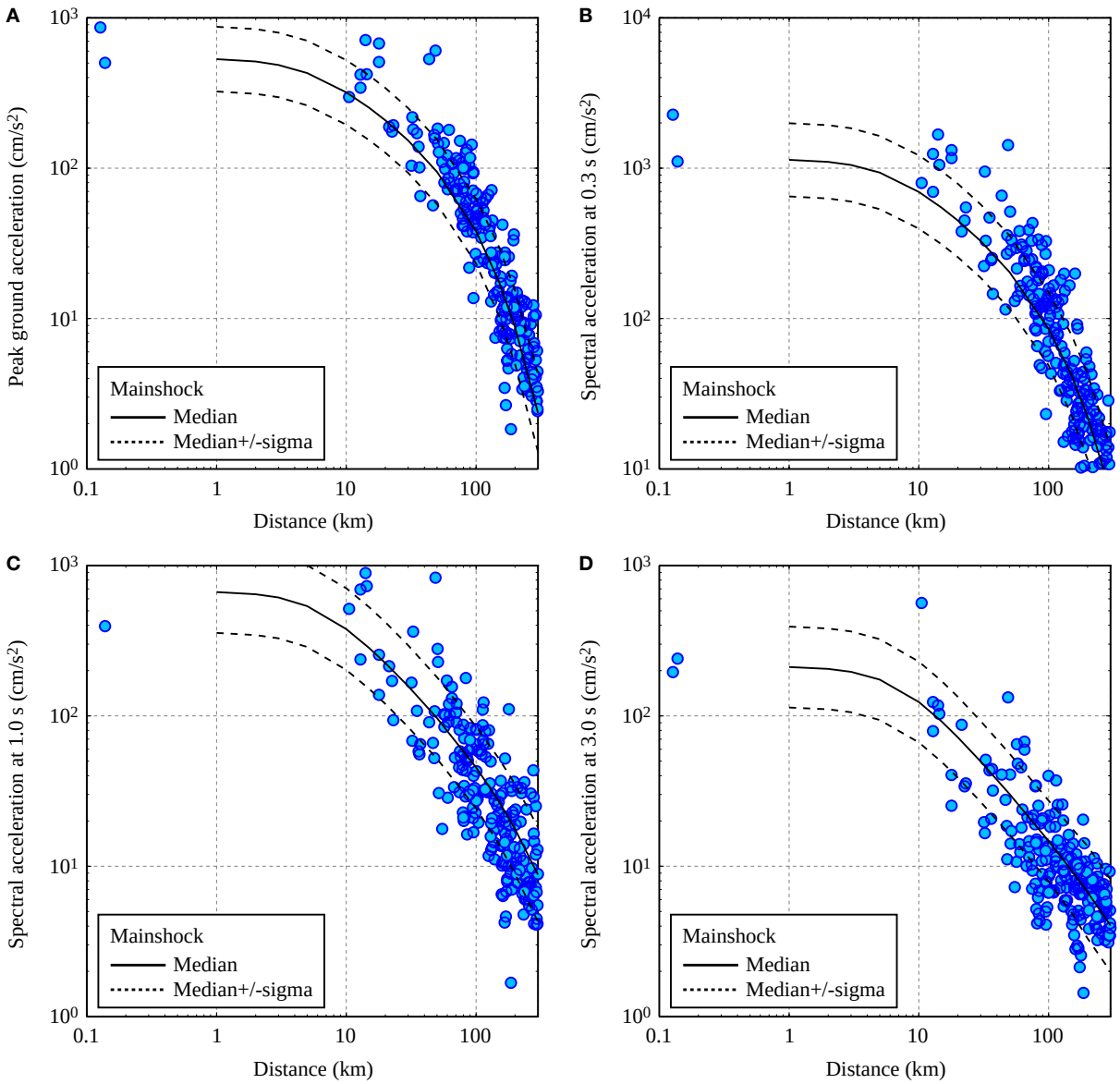

FIGURE 9 | Comparison of the observed ground motions with the prediction equation by Boore et al. (2014) for the mainshock: (A) peak ground acceleration, (B) spectral acceleration at 0.3 s, (C) spectral acceleration at 1.0 s, and (D) spectral acceleration at 3.0 s.

Damage in Kumamoto City and Uto City

A damage survey was conducted near Kumamoto Castle (i.e., downtown Kumamoto City; Location 1 in **Figure 11A**). A photo of Kumamoto Castle is shown in **Figure 12A**. The roof of the main castle (right-hand side) was damaged, and the wooden panels on the stone walls had collapsed. In fact, wooden panels as well as stone walls had collapsed at several places around the castle. At one location, the collapsed stone walls fell over a temple, destroying it. Along the moat of the castle, cracks were observed on the side walk and minor lateral spreading was observed (some buildings tilted toward the moat). During the walk-around survey in the downtown (near Kumamoto railway station and Kumamoto city office), damage to building cladding and external walls was observed (**Figure 12B**). Several high-rise buildings suffered earthquake damage, such as diagonal shear cracks that were visible from a distance. Although some old timber buildings suffered major damage and tilted (unrepairable damage), overall, major structural damage to modern buildings (timber/RC/steel) was neither major nor widespread, indicating that buildings in the city center performed well against the strong shaking experienced during the foreshock and mainshock.

Quick damage surveys were conducted near the KMM006 and KMM008 recording stations where actual recordings of

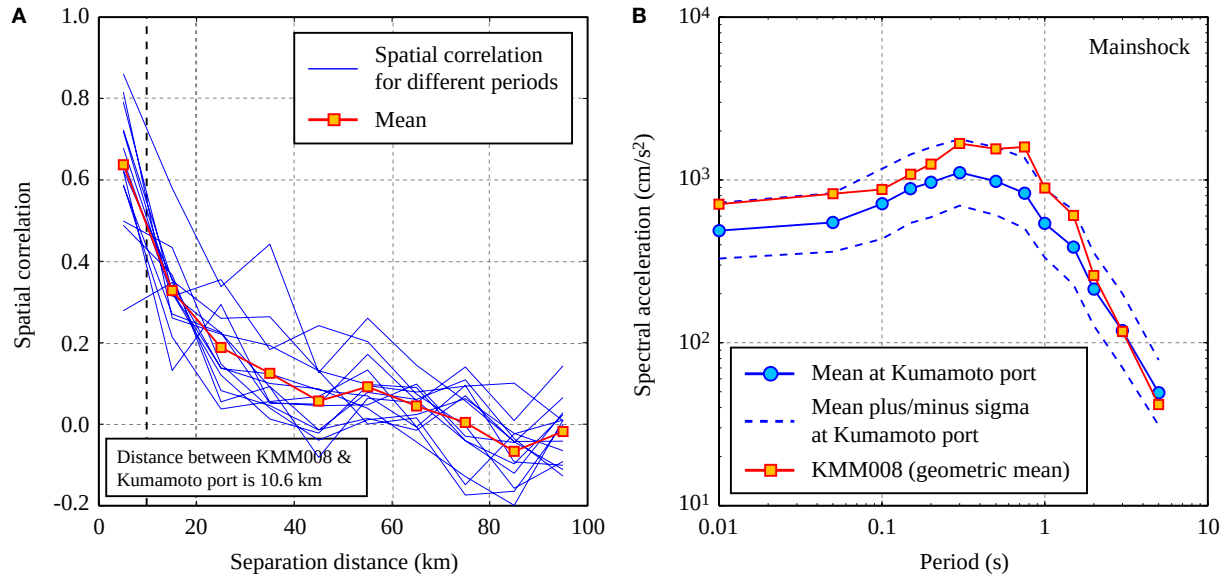

FIGURE 10 | **(A)** Spatial correlation of ground motion residuals for the mainshock. **(B)** Estimated response spectra at Kumamoto port based on the ground motion model by Boore et al. (2014) and the spatial correlation, conditioned on the observed ground motions at KMM008.

experienced ground motions were available. The KMM006 station was located in a residential area. The majority of houses in the neighborhood were two-story timber frames, and it appeared that they were constructed relatively recently. The buildings near KMM006 suffered slight damage only; the majority of the observed external damage was roof damage (**Figure 12C**). Near the KMM008 station (Location 2 in **Figure 11A**), no significant building damage was observed, except for the Uto city office, a 5-story reinforced concrete (RC) building (**Figure 12D**). The external RC frames of this city office suffered major damage, and the building was closed at the time of the survey. The third floor had partially collapsed, and window frames were distorted at the top two floors. Interestingly, the Uto city office was the only building in the area that was damaged significantly.

In the south of KMM006 (Location 3 in **Figure 11A**), a 9-story RC apartment was damaged (**Figure 12E**); many diagonal shear cracks were observed on walls at the lower three floors. Along Akitsu river (near Location 3 in **Figure 11A**), ground deformation and failures, including liquefaction, were reported. Moreover, a field investigation was conducted at Kumamoto port (Location 4 in **Figure 11A**). The port was constructed on a man-made island. Since the opening of Kumamoto port in 1993, the port has served as an important access route for people and goods. Some damage to port facilities was observed (e.g., overpass steel bridge at the ferry terminal). After the Kumamoto mainshock, sand boils were observed at the port as the sand used for reclamation was liquefiable (**Figure 12F**; note: borehole data at a site in the port island indicated a 3-m thick sand layer near the ground surface). The estimated ground motion at Kumamoto port, based on statistical analysis of observed ground motions at recording stations, indicates that the experienced PGA (typically 0.5 g) at Kumamoto port was sufficiently large to trigger liquefaction to landfilled sand layers.

Damage in Mashiki Town

Mashiki Town (location 5 in **Figure 11B**) was devastated by the 2016 Kumamoto earthquake sequence (both foreshock and mainshock). Numerous surface ruptures were observed in Mashiki Town (Shirahama et al., 2016). According to the seamless digital geological map of Japan[7], geological conditions near the Mashiki town office can be broadly categorized into two areas; geology of the northern part of Mashiki Town consists of deposits from pyroclastic flow of volcanic eruptions, while that of the southern part of Mashiki Town is formed by river terrace deposits.

Along Road 28, many buildings were severely damaged or had collapsed. The building shown in **Figure 13A** was a four-story steel building; the second floor had completely collapsed in a soft-story collapse mechanism. The majority of the buildings that had suffered a soft-story collapse had predominantly deformed/collapsed in the EW direction (more toward west), approximately parallel with Road 28 (e.g., **Figures 13A,B**). This coincides with the major response axes of the ground motion experienced in Mashiki Town (**Figure 8**). It has been reported that the effects due to the double-shock ground motions in Mashiki Town were significant. For example, a two-story steel building (**Figure 13B**) suffered minor-to-moderate damage due to the foreshock; however, it was destroyed by the subsequent mainshock. Several steel as well as RC buildings also suffered extensive damage. For instance, a RC-frame temple (**Figure 13C**) had collapsed due to the failures of beam-column joints (note: this building did not

[7]https://gbank.gsj.jp/seamless/index_en.html

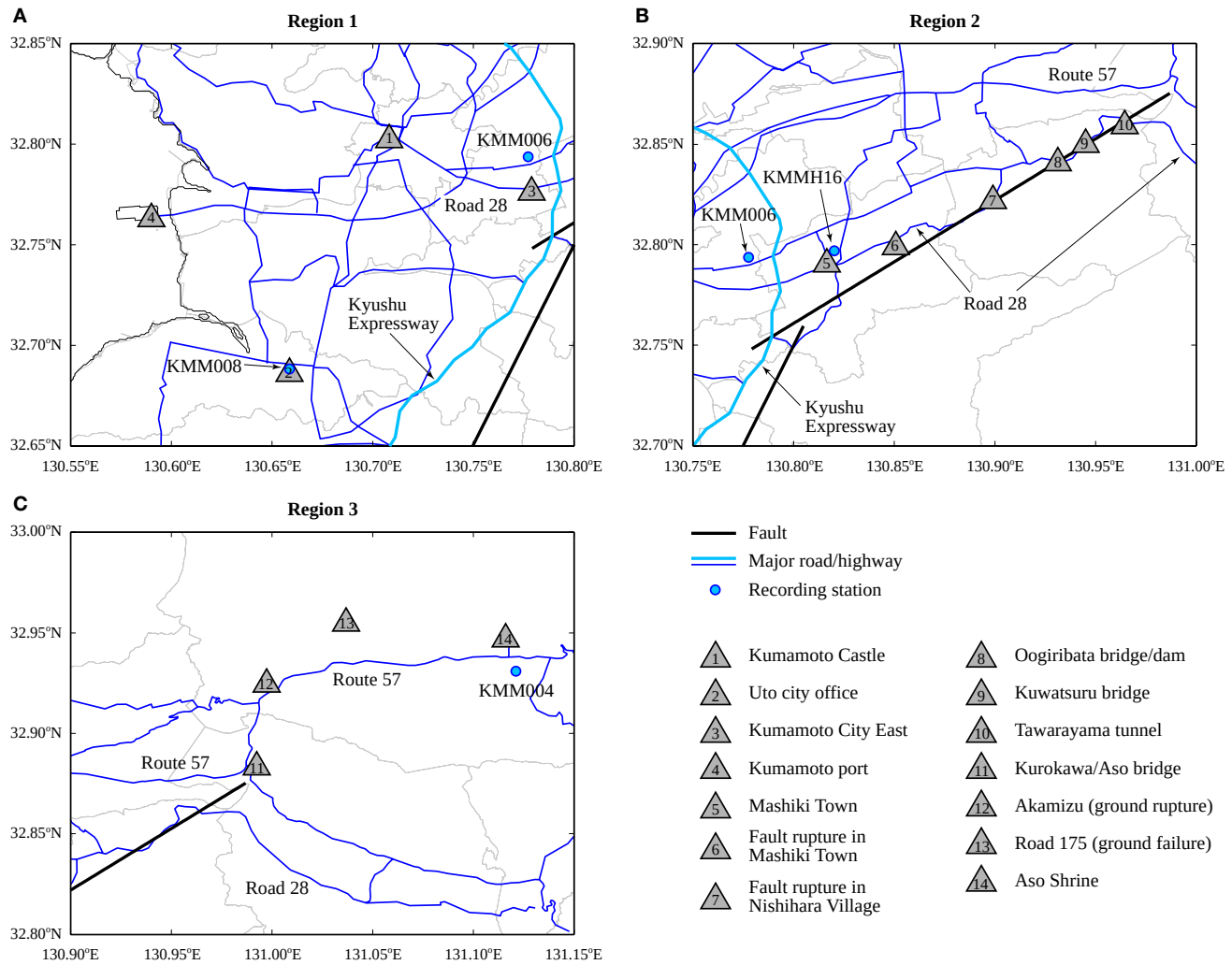

FIGURE 11 | **Locations of earthquake damage surveys: (A) region 1, (B) region 2, and (C) region 3**.

collapse after the foreshock but only suffered noticeable damage; it then collapsed due to the mainshock). Moreover, houses that were built on embankments suffered ground failures, and local soil conditions appear to be an important factor in the earthquake damage. For example, one row of six houses had collapsed partially due to foundation failures (**Figure 13D**). In the southern part of Mashiki Town (mainly agricultural areas along Kiyama river), uplifts of manholes were observed and settlements of the embankments along Kiyama river were seen (see also **Figure 15**), resulting in major gaps between the bridge deck and abutments. Typically, the bridge deck remained in its original position, while both sides of the embankments subsided by 0.4–0.5 m. RC piers of Daiichi Hatanaka bridge failed due to the ground deformation/failures (**Figure 13E**; Location 5 in **Figure 11B**; see also **Figure 15**). At the time of the survey, large sand bags (height of about 1 m) were placed along Kiyama river as temporary flood defenses. During the heavy rainfall on June 20 and 21, 2016 in Kumamoto, these temporary defenses were breached and Kiyama river and its surrounding areas were flooded. These are examples of the compounding disaster chain caused by the earthquakes and heavy rain.

The surface fault ruptures were observed in the paddy fields of Mashiki Town. **Figure 13F** shows the traces of the surface ruptures that appeared after the mainshock at Location 6 in **Figure 11B**. A clear misalignment of the ridge between paddy fields can be observed (circa 0.5–1.0 m, depending on the locations).

To understand the earthquake damage characteristics in Mashiki Town, a detailed damage survey was conducted near the Mashiki town office (note: JMA recording station was installed at the town office, which recorded the JMA intensity of 7 during the foreshock and mainshock). The surveyed areas were also close to the KMMH16 station. The surveys were carried out by two people to minimize the misassignment of the building damage grade. The survey was based on external visual inspections of buildings; building damage severity was assigned based on the

FIGURE 12 | **(A)** Damage to Kumamoto castle (location 1 in region 1). **(B)** Cladding damage to a building in the city center (location 1 in region 1). **(C)** Roof damage near KMM006. **(D)** Damage to the Uto city office (location 2 in region 1; near KMM008). **(E)** Damage to a high-rise residential building (location 3 in region 1). **(F)** Liquefaction site at Kumamoto port (location 4 in region 1).

earthquake damage grade categories that are similar to the EMS-98 guideline (Grünthal, 1998). Typically, five damage severities were considered: no damage, slight damage, moderate damage, heavy damage, and destruction. **Figure 14** shows examples of building damage classifications from the survey. During the survey, material type (wood, RC, steel, and unknown), story number, and use/occupancy class (residential, commercial, public, and etc.) were recorded in addition to the damage severity.

The results of the building damage survey in Mashiki Town are shown in **Figure 15**. In total, 277 buildings were inspected, consisting of 22 RC buildings, 15 steel buildings, 235 timber buildings, and 5 buildings with unknown material types. Out of 277 buildings, 47 buildings were undamaged, 63 buildings suffered slight damage, 50 buildings were heavily damaged, and 69 buildings were destroyed or are likely to be demolished due to unrepairable damage. Generally, newer timber houses as well as RC and steel buildings performed better than older timber houses. Houses in the south of the Mashiki town office were more severely damaged than those in the north, noting that the southern part of the surveyed areas was an older settlement. The differences of the damage extent in the northern and southern areas may also be attributed to geological conditions of the two areas (approximately, Road 28 is a boundary between the volcanic sediments and the river terrace deposits). Another important factor appeared to be the proximity to rivers (see **Figure 15**). Thus at the local scale, micro-zonation of soil types and geographical features may have been useful for evaluating seismic risk potential in this region *a priori*.

FIGURE 13 | **(A)** Collapsed steel building along Road 28 (location 5 in region 2). **(B)** Collapsed steel building along road 28 (location 5 in region 2). **(C)** Collapsed RC temple near the Mashiki town office (location 5 in region 2). **(D)** Building damage due to foundation failures (location 5 in region 2; near KMMH16). **(E)** Failures of RC piers of Daiichi Hatanaka bridge (location 5 in region 2). **(F)** Fault surface rupture (location 6 in region 2).

Damage in Nishihara Village

Nishihara Village is located outside of Aso Caldera and consists of a hilly/mountainous terrain. The eastern segment of the Futagawa fault traverses across Nishihara Village. EEFIT visited locations along the fault strike (**Figure 11B**), by following Road 28 (note: at several places Road 28 was blocked due to road failures and fallen objects). Along Road 28, many damaged/collapsed buildings (mainly timber houses) as well as landslides were observed. This section mainly focuses on infrastructure damage along Road 28 between Oogiribata bridge and Tawarayama tunnel. The Oogiribata-Tawarayama part of Road 28, an important access road to enter the Aso region, was not passable due to a series of bridge and road failures. It is noteworthy that the surveyed locations in Nishihara Village were very close to the Futagawa fault rupture zone, where large deformations and very intense ground shaking were observed. Therefore, it is likely that the causes of the observed infrastructure damage were due to the combined effects of the deformation and shaking.

A fault deformation and surface rupture in Nishihara Village were investigated at Location 7 in **Figure 11B**. The fault rupture cut across the ridge of a hill. At the surveyed location (a farmer's house and field), a vertical deformation up to 0.6 m was observed (**Figure 16A**). Buildings in the property suffered major damage or collapse; a timber structure (barn/storage) that was directly above

FIGURE 14 | Examples of damaged and collapsed timber buildings in Mashiki Town: (A) slight damage, (B) moderate damage, (C) heavy damage, and (D) collapse.

the fault rupture had collapsed, while the main house, a two-story timber building, was significantly damaged.

The major damage was observed near the Oogiribata reservoir (Location 8 in **Figure 11B**), which was essentially located directly above the Futagawa fault. The 23 m high earth-fill Oogiribata dam constructed in 1975 has been utilized for irrigation as well as fire-fighting purposes, and has played an important role in local communities. At the crest of Oogiribata dam, major surface rupture was observed (**Figure 16B**). The road pavements were destroyed due to compressional forces. The retaining walls of the spillway were damaged and were tilted significantly. Due to damage to the control gate for releasing water, a large volume of the stored water had leaked accidentally after the mainshock; no fatalities/casualties were reported to have been caused due to this damage.

In the same area, Oogiribata bridge, a curved 5-span steel girder bridge constructed in 2000, was damaged significantly. The bridge was constructed to bypass a valley, where a major landslide occurred along the slope; the slipped soils might have affected the bridge piers at their base. Large cracks and gaps were observed at both sides of the abutments/roads. At the upper side of the bridge, all five bridge supports, i.e., laminated rubber bearing, had sheared/ruptured completely (**Figure 16C**). Consequently, the bridge deck was dismantled and displaced by about 0.3–0.4 m toward the valley side of the slope (**Figure 16D**).

Along Road 28 to Tawarayama tunnel, which is about 2 km long and connects Nishihara Village and Minami Aso Village (i.e., outside and inside of Aso Caldera), major damage to bridges and roads was caused. For instance, Kuwatsuru bridge, a cable-stayed bridge constructed in 1997, was damaged severely due to significant settlements of bridge abutments, resulting in a gap of 0.3–0.4 m (**Figure 16E**). At Tawarayama bridge near the tunnel, similar abutment/ground failures were observed. In addition, several landslides/slope failures were observed along Road 28; some of them caused major damage to roads (**Figure 16F**). Tawarayama tunnel was also damaged due to the mainshock and was not passable at the time of the survey. Large cracks were observed on the concrete cover near the entrance of the tunnel (**Figure 16G**).

Damage in Minami Aso Village and Aso City

Minami Aso Village, which lies between Aso Mountains and Aso Caldera, was devastated by the Kumamoto mainshock. The earthquake damage in the Kurokawa district of Minami Aso Village (Location 11 in **Figure 11C**) was significant. Many timber buildings were destroyed (**Figure 17A**), and the surface ruptures were also observed. In the Kurokawa district, a detailed damage survey was carried out; the survey was led by the Kyoto

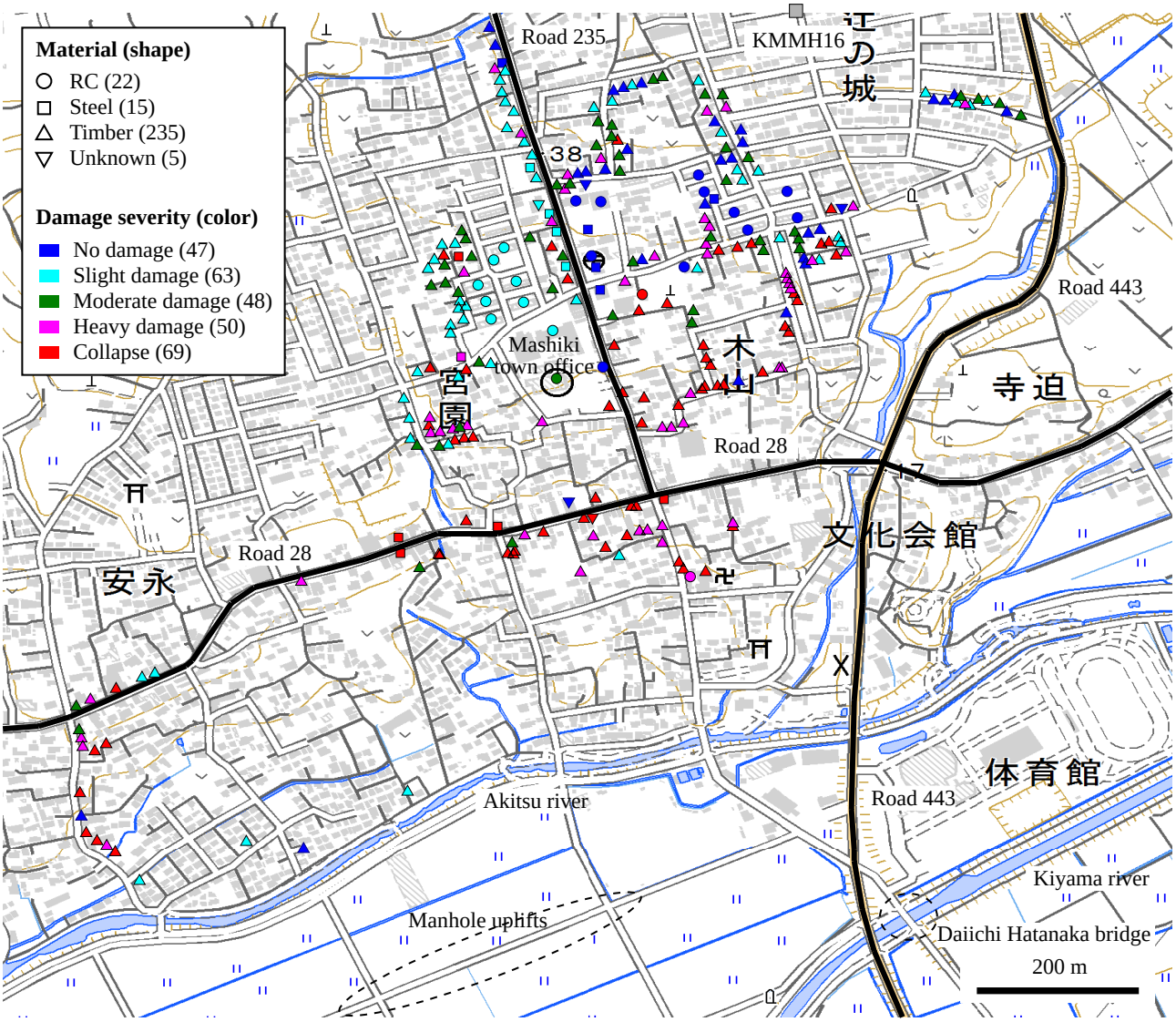

FIGURE 15 | **Damage survey results in Mashiki Town**. The base map was obtained from the Geospatial Institute of Japan.

University group. The results are presented in **Figure 18** (the format is similar to those shown in **Figure 15** for Mashiki Town). In total, 138 buildings were inspected; the majority of the surveyed structures were residential timber houses, while RC buildings were an elementary school and apartment buildings. **Figure 18** shows that more than a half of the timber houses had collapsed due to the mainshock. On the other hand, larger RC structures were not damaged. To examine the correlation between observed surface ruptures and building damage, videos taken from a UAV (unmanned aerial vehicle) that were provided by the GSI were analyzed. The identified surface ruptures in the Kurokawa district are indicated in **Figure 18**. It can be observed that some of the surface ruptures cut underneath buildings, which were destroyed.

One of the most significant events during the Kumamoto earthquake was the large-scale landslide in the Tateno district (**Figure 17B**; approximately, 700 m long and 200 m wide), which destroyed Route 57, which connected Kumamoto Prefecture and Oita Prefecture *via* Aso Caldera. The landslide caused the collapse of Aso bridge (Location 11 in **Figure 11C**). Aso bridge was a steel reversed Langer bridge constructed in 1970 crossing over Kurokawa river, and was a part of the regional road network, connecting the Tateno district and the Kurokawa district of Minami Aso Village (i.e., outside and inside of Aso Caldera). It is important to recognize that the Futagawa fault cut underneath of Aso bridge; henceforth, differential ground deformations at both sides of the bridge could have been significant (because of the strike-slip faulting and the locations are very near to the fault strike; see **Figure 4**). The collapse of Aso bridge may be due to the combined effects of the ground deformation and the landslide. More investigations are warranted regarding the exact cause of the bridge collapse.

FIGURE 16 | **(A)** Fault surface rupture in Mashiki Town (location 7 in region 2). **(B)** Fault surface rupture at the crest of Oogiribata dam (location 8 in region 2). **(C)** Shear fracture of bridge support underneath Oogiribata bridge (location 8 in region 2). **(D)** Damage to Oogiribata bridge (location 8 in region 2). **(E)** Damage to Kuwatsuru bridge (location 9 in region 2). **(F)** Road failure near Tawarayama tunnel (location 10 in region 2). **(G)** Cracks inside Tawarayama tunnel (location 10 in region 2).

Near Aso bridge, several other bridges that served as alternative access route between Minami Aso Village and Kumamoto downtown, were also damaged and made unpassable due to the mainshock. **Figure 17C** shows Choyo bridge, located in the Tateno district (downstream of Aso bridge along Kurokawa river); the abutment of the bridge had subsided significantly (even visible in **Figure 17C**).

Overall, simultaneous destruction of the access routes that connected areas inside and outside of Aso Caldera, i.e., Oogiribata-Tawarayama route (Road 28), Kumamoto-Oita route (Route 57), Tateno-Kurokawa route (Aso bridge), Tateno-Choyo route (Choyo bridge), caused significant disruptions and delays in rescue and evacuation operations immediately after the mainshock. At the time of the survey, major detours were necessary. This demonstrates the critical importance of the disaster recovery process in ensuring community resilience. The repairs and reconstructions of the key infrastructure in the near-fault region are important aspects of the overall seismic resilience and community resilience and need to be considered from a holistic perspective.

The earthquake damage surveys were also carried out in Aso City, NE of the fault rupture zone. Near the Akamizu railway station (Location 12 in **Figure 11C**), ground failures were observed in the paddy field (**Figure 17D**); about 0.7 m

FIGURE 17 | **(A)** Collapsed timber building in the Kurokawa district of Minami Aso Village (Location 11 in Region 3). **(B)** Route 57 blockage due to the landslide near Aso bridge (location 11 in Region 3). **(C)** Damage to Choyo bridge (location 11 in Region 3). **(D)** Ground cracks near the Akamizu railway station (location 12 in region 3). **(E)** Ground settlement over a timber house (location 13 in region 3). **(F)** Collapse of Aso Shrine (location 14 in region 3).

subsidence of the ground was observed. The direct cause of the subsidence is not yet known because the location is relatively distant from the fault rupture zone. Similar ground settlements were observed along Road 175 (Location 13 in **Figure 11C**). Subsidence of about 1.0–1.5 m was observed, depending on the locations. Houses directly above the ground cracks had been destroyed (**Figure 17E**), while houses on the subsided portion of the ground were intact (no viable damage externally). These ground failures were localized.

Earthquake Engineering Field Investigation Team also visited Aso Shrine (Location 14 in **Figure 11C**), which is designated as important cultural properties of the nation. The main structures of Aso Shrine had been destroyed by the mainshock (**Figure 17F**). On the other hand, in the surrounding areas of Aso Shrine, no obvious ground failures were observed. Because large long-period ground motions were recorded at the KMM004 station (**Figure 8**) and roof structures were heavy, the main cause of the collapse of Aso Shrine may be attributed to the shaking. Nonetheless, more investigations are warranted to understand the exact cause of the exceptionally large ground motions in these areas, which are remote from the fault rupture zone.

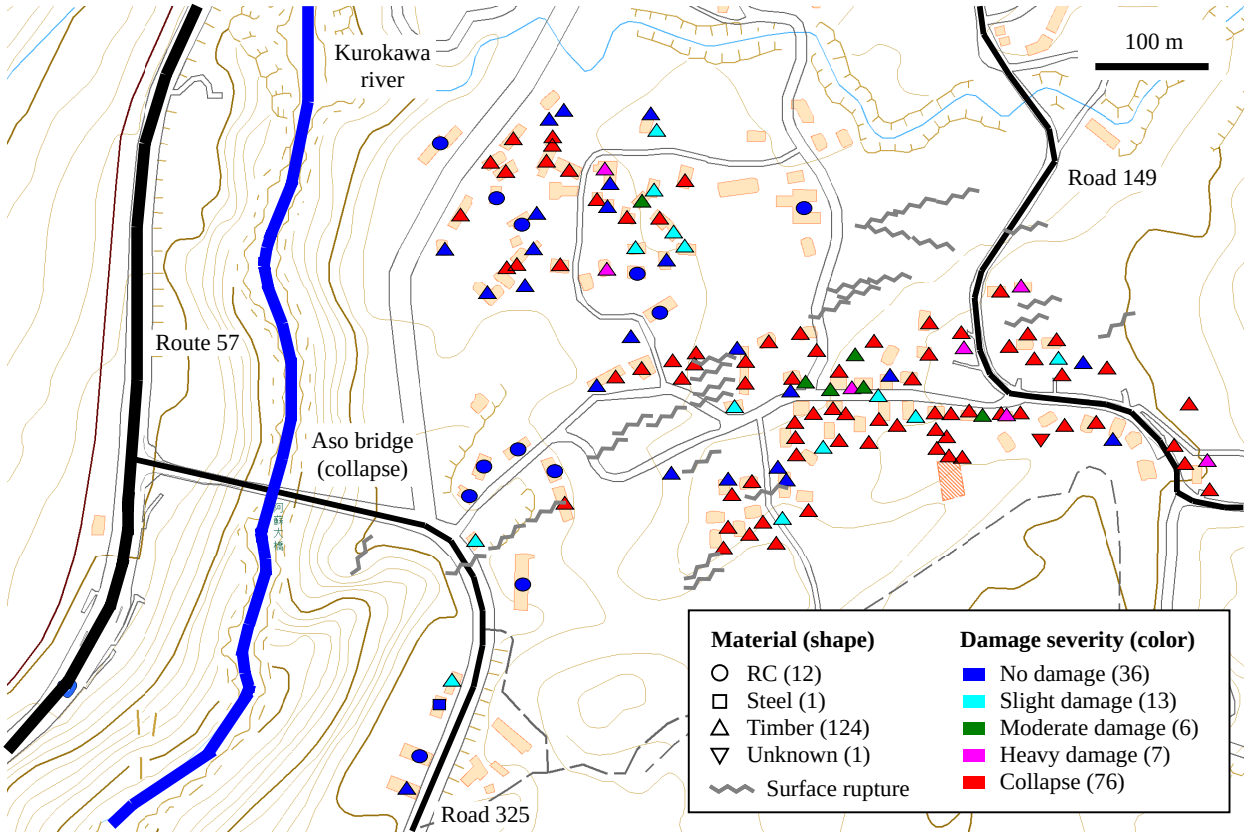

FIGURE 18 | Damage survey results in the Kurokawa district of Minami Aso village. The base map was obtained from the Geospatial Institute of Japan.

SUMMARY AND CONCLUSIONS

The 2016 Kumamoto earthquake sequence, consisting of an M_J 6.5 foreshock, an M_J 7.3 mainshock, and numerous aftershocks, caused significant damage to buildings and infrastructure in the intraplate region of Kyushu Island, Japan, apart from subduction zones. The earthquakes occurred along the Hinagu–Futagawa fault zones, which were considered to be capable of hosting M_w 7 earthquakes based on geological investigations but have not been particularly active in recent history. Consequently, the occurrence of the 2016 Kumamoto earthquakes was perceived as a surprise. The building stock in the Kumamoto region was not particularly resistant to intense ground shaking, resulting in the destruction and damage of more than 8,000 houses and 120,000 houses, respectively (as of 1 July 2016). Furthermore, significant effects due to large ground deformation were observed, and bridges and roads in the near-fault zone were damaged severely. On the other hand, during the earthquake sequence, numerous recordings of geophysical data, such as GPS measurements and strong motion time-histories, were obtained. These data are valuable in reconstructing the rupture processes of the earthquakes *via* rigorous inversion analysis. In addition, many field and remote sensing data (e.g., building damage surveys, fault rupture measurements, landslide occurrence, and ground deformation based on InSAR imagery) were collected and these are particularly useful for gaining deeper understanding of the main causes of the earthquake damage.

To learn key lessons from the observed damage and impact due to the Kumamoto earthquakes, a field investigation team was dispatched from the UK, and conducted earthquake damage reconnaissance surveys in Kumamoto. As part of the investigations, regional earthquake catalog data and strong motion data were analyzed. In particular, the ground deformation profiles were evaluated based on available finite-fault models for the Kumamoto earthquakes, and were compared with actual GPS measurements before and after the earthquakes. Detailed analyses of recorded ground motions in the near-fault zone (e.g., KMMH16) revealed striking features of the intense ground shaking, directivity of strong motion, and site amplification. The analyzed data were compared with an existing ground motion model for shallow crustal earthquakes. The earthquake damage surveys focused on locations near the fault rupture zone of the mainshock, i.e., Mashiki Town, Nishihara Village, and Minami Aso Village. Moreover, detailed damage surveys were conducted in Mashiki Town and Minami Aso Village to investigate the key contributing factors in the earthquake damage. The investigations of infrastructure damage in the near-fault zone showed significant impact due to substantial ground deformation.

The main results from the earthquake data analyses for the Kumamoto events are as follows:

1. Seismic activities of the 2016 Kumamoto sequence were distributed over a wide region, triggering numerous aftershocks. The migration of the earthquakes, originally from the Hinagu fault zone (i.e., foreshock) to the Futagawa fault zone (i.e., mainshock), was a notable feature of the sequence.
2. The recorded ground motions in the hanging wall region (e.g., KMMH16 in Mashiki Town) showed intense spectral acceleration amplitudes in the short-to-moderate vibration period range (exceeding 1 g) with significant site amplification due to soft sediments in the Kumamoto plain.
3. A clear directivity of ground motions in parallel with the fault strike was observed in the near-fault zone, which correlated well with the fallen directions of collapsed buildings in Mashiki Town.
4. The observed ground motion data were in agreement with an empirical ground motion model by Boore et al. (2014). Furthermore, typical decaying behavior for spatial correlation of the ground motion residuals was obtained as a function of inter-station distance. These results are useful for estimating ground motion parameters at unobserved locations. An application of the advanced ground motion estimation technique was demonstrated for a liquefaction site at Kumamoto port.

The main results from the earthquake damage surveys in the Kumamoto region are summarized as follows:

5. The earthquake damage in the Kumamoto downtown was relatively minor, despite the intense ground shaking experienced; however, major damage to Kumamoto Castle was caused. As locations become closer to the fault rupture zone, the occurrence of the structural damage become more frequent.
6. The building damage in Mashiki Town was extensive; numerous building collapses were observed. Influential factors of the earthquake damage occurrence include the construction material (timber versus steel/RC), construction age (old versus modern constructions), geological/geographical condition (e.g., proximity to rivers). In the near-fault region, the effects of ground deformation were also significant (e.g., settlement and slope failures). A detailed micro-zonation study would be useful for assessing the seismic risk potential of existing building stock.
7. More than 50% of the timber houses in the Kurokawa district of Minami Aso Village were destroyed by the mainshock; the causes of the building collapse were attributed to both strong ground shaking and surface ruptures.
8. The ground deformation and shaking in the near-fault zone affected various kinds of infrastructure, such as bridges, roads, and tunnels. During the mainshock, failures of the infrastructure occurred simultaneously at many locations, essentially disconnecting existing access routes between cities and towns inside Aso Caldera and those outside. Significant disruptions and delays in rescue and evacuation operations were caused due to destruction of the regional traffic network. The issues of maintaining the essential functionality of infrastructure are critical for communities that may be isolated after the major earthquake.

During and after the earthquakes, numerous incidents of compounded disasters were observed. For instance, a heavy rainfall in the Kumamoto region has led to occurrence of additional landslides, debris flows, and flooding. In the recovery process, viable solutions should be sought for by taking a holistic viewpoint of disaster resilience and sustainability of communities.

AUTHOR CONTRIBUTIONS

All authors contributed to the preparation of the submitted manuscript.

ACKNOWLEDGMENTS

The work is funded by the EPSRC grant (EP/I01778X/1) for the Earthquake Engineering Field Investigation Team (EEFIT). The financial supports for industrial members (GC, LH, LK, and RM) are provided by Arup, Mott MacDonald, and Willis. The first author is grateful to Dr. Takashi Kiyota, who generously shared his earthquake damage survey results immediately after the earthquake. The survey results by Dr. Kiyota can be found in http://www.gdm.iis.u-tokyo.ac.jp/index_e.html. The EEFIT members thank Prof Shinji Toda and Ms Zoe Mildon for sharing the information on the surface rupture locations. The JMA catalog was obtained from http://www.hinet.bosai.go.jp/, and ground motion data were obtained from http://www.kyoshin.bosai.go.jp/. The elevation data were obtained from https://asterweb.jpl.nasa.gov/gdem.asp.

SUPPLEMENTARY MATERIAL

The Supplementary Material for this article can be found online at http://journal.frontiersin.org/article/10.3389/fbuil.2016.00019

The collected earthquake damage data (i.e., geocoded pictures) of the 2016 Kumamoto EEFIT mission can be obtained from the supplementary information accompanying this paper (i.e., Google Earth kmz file).

REFERENCES

Bhattacharya, S., and Goda, K. (2013). Probabilistic buckling analysis of axially loaded piles in liquefiable soils. *Soil Dyn. Earthq. Eng.* 45, 13–24. doi:10.1016/j.soildyn.2012.10.004

Boore, D. M. (2005). On pads and filters: processing strong-motion data. *Bull. Seismol. Soc. Am.* 95, 745–750. doi:10.1785/0120040160

Boore, D. M., Stewart, J. P., Seyhan, E., and Atkinson, G. M. (2014). NGA-West 2 equations for predicting PGA, PGV, and 5%-damped PSA for shallow crustal earthquakes. *Earthq. Spectra* 30, 1057–1085. doi:10.1193/070113EQS184M

Cabinet Office of Government of Japan. (2016). *Estimated Economic Impact Due to the 2016 Kumamoto Earthquakes*. Available at: http://www5.cao.go.jp/keizai3/kumamotoshisan/kumamotoshisan20160523.pdf [accessed June 9, 2016].

Fire and Disaster Management Agency (2016). Available at http://www.fdma.go.jp/bn/2016/

Fraser, S., Pomonis, A., Raby, A., Goda, K., Chian, S. C., Macabuag, J., et al. (2013). Tsunami damage to coastal defences and buildings in the March 11th 2011 M_w9.0 Great East Japan earthquake and tsunami. *Bull. Earthq. Eng.* 11, 205–239. doi:10.1007/s10518-012-9348-9

General Insurance Association of Japan. (2016). *Key Figures Related to Insurance Claims Due to the 2016 Kumamoto Earthquake as of June 13, 2016*. Available at: http://www.sonpo.or.jp/en/news/2016/1606_03.html [accessed June 18, 2016].

Geospatial Institute of Japan (GSI). (2016). *The 2016 Kumamoto Earthquake*. Available at: http://www.gsi.go.jp/BOUSAI/H27-kumamoto-earthquake-index.html [accessed June 18, 2016].

Ghofrani, H., Atkinson, G. M., and Goda, K. (2013). Implications of the 2011 M9.0 Tohoku Japan earthquake for the treatment of site effects in large earthquakes. *Bull. Earthq. Eng.* 11, 171–203. doi:10.1007/s10518-012-9413-4

Goda, K., and Hong, H. P. (2008). Spatial correlation of peak ground motions and response spectra. *Bull. Seismol. Soc. Am.* 98, 354–365. doi:10.1785/0120070078

Goda, K., Pomonis, A., Chian, S. C., Offord, M., Saito, K., Sammonds, P., et al. (2013). Ground motion characteristics and shaking damage of the 11th March 2011 M_w9.0 Great East Japan earthquake. *Bull. Earthq. Eng.* 11, 141–170. doi:10.1007/s10518-012-9371-x

Grünthal, G. (1998). *European Macroseismic Scale 1998 (EMS-98)*. Luxembourg: Centre Européen de Géodynamique et de Séismologie, 99.

Guo, Z., and Ogata, Y. (1997). Statistical relations between the parameters of aftershocks in time, space, and magnitude. *J. Geophys. Res.* 102, 2857–2873. doi:10.1029/96JB02946

Headquarters for Earthquake Research Promotion. (2016). *Evaluation of the Futagawa and Hinagu Fault Zones*. Available at: http://www.jishin.go.jp/main/chousa/13feb_chi_kyushu/k_11.pdf [accessed May 15, 2016].

Hong, H. P., and Goda, K. (2007). Orientation-dependent ground motion measure for seismic hazard assessment. *Bull. Seismol. Soc. Am.* 97, 1525–1538. doi:10.1785/0120060194

Idriss, I. M., and Boulanger, R. W. (2008). *Soil Liquefaction During Earthquakes*. Oakland, CA: Earthquake Engineering Research Institute.

Irikura, K., and Miyake, H. (2011). Recipe for predicting strong ground motion from crustal earthquake scenarios. *Pure Appl. Geophys.* 164, 85–104. doi:10.1007/s00024-010-0150-9

Kojima, K., and Takewaki, I. (2016). A simple evaluation method of seismic resistance of residential house under two consecutive severe ground motions with intensity 7. *Front. Built Environ.* 2:15. doi:10.3389/fbuil.2016.00015

Nakashima, M., and Chusilp, P. (2003). A partial view of Japanese post-Kobe seismic design and construction practices. *Earthq. Eng. Eng. Seismol.* 4, 3–13.

National Institute of Advanced Industrial Science and Technology. (2016). *Active Fault Database of Japan*. Available at: https://gbank.gsj.jp/activefault/index_e_gmap.html [accessed June 7, 2016].

Okada, Y. (1985). Surface deformation due to shear and tensile faults in a half-space. *Bull. Seismol. Soc. Am.* 75, 1135–1154.

Okumura, K. (2016). *Earthquake Geology of the April 14 and 16, 2016 Kumamoto Earthquakes*. Available at: http://home.hiroshima-u.ac.jp/kojiok/kumamoto2016KOreport2.pdf [accessed May 15, 2016].

Santucci de Magistris, F., Lanzano, G., Forte, G., and Fabbrocino, G. (2013). A database for PGA threshold in liquefaction occurrence. *Soil Dyn. Earthq. Eng.* 54, 17–19. doi:10.1016/j.soildyn.2013.07.011

Sawazaki, K., Sato, H., Nakahara, H., and Nishimura, T. (2009). Time-lapse changes of seismic velocity in the shallow ground caused by strong ground motion shock of the 2000 Western-Tottori earthquake, Japan, as revealed from coda deconvolution analysis. *Bull. Seismol. Soc. Am.* 99, 352–366. doi:10.1785/0120080058

Shirahama, Y., Mori, H., Maruyama, T., and Yoshimi, M. (2016). *Geological Survey of Japan AIST Emergency Survey Report*. Available at: http://g-ever.org/updates/?p=334 [accessed June 7, 2016].

Watson-Lamprey, J., and Boore, D. M. (2007). Beyond $S_{aGMRotI}$: conversion to S_{aArb}, S_{aSN} and $S_{aMaxRot}$. *Bull. Seismol. Soc. Am.* 97, 1511–1524. doi:10.1785/0120070007

Wu, C., Peng, Z., and Assimaki, D. (2009). Temporal changes in site response associated with strong ground motion of 2004 M6.6 mid-Niigata earthquake sequences in Japan. *Bull. Seismol. Soc. Am.* 99, 3487–3495. doi:10.1785/0120090108

Conflict of Interest Statement: The authors declare that the research was conducted in the absence of any commercial or financial relationships that could be construed as a potential conflict of interest.

Copyright © 2016 Goda, Campbell, Hulme, Ismael, Ke, Marsh, Sammonds, So, Okumura, Kishi, Koyama, Yotsui, Kiyono, Wu and Wilkinson. This is an open-access article distributed under the terms of the Creative Commons Attribution License (CC BY). The use, distribution or reproduction in other forums is permitted, provided the original author(s) or licensor are credited and that the original publication in this journal is cited, in accordance with accepted academic practice. No use, distribution or reproduction is permitted which does not comply with these terms.

frontiers in Built Environment

ORIGINAL RESEARCH
published: 13 June 2017
doi: 10.3389/fbuil.2017.00030

Losses Associated with Secondary Effects in Earthquakes

James E. Daniell, Andreas M. Schaefer and Friedemann Wenzel*

Geophysical Institute, Center for Disaster Management and Risk Reduction Technology, Karlsruhe Institute of Technology, Karlsruhe, Germany

The number of earthquakes with high damage and high losses has been limited to around 100 events since 1900. Looking at historical losses from 1900 onward, we see that around 100 key earthquakes (or around 1% of damaging earthquakes) have caused around 93% of fatalities globally. What is indeed interesting about this statistic is that within these events, secondary effects have played a major role, causing around 40% of economic losses and fatalities as compared to shaking effects. Disaggregation of secondary effect economic losses and fatalities demonstrating the relative influence of historical losses from direct earthquake shaking in comparison to tsunami, fire, landslides, liquefaction, fault rupture, and other type losses is important if we are to understand the key causes post-earthquake. The trends and major event impacts of secondary effects are explored in terms of their historic impact as well as looking to improved ways to disaggregate them through two case studies of the Tohoku 2011 event for earthquake, tsunami, liquefaction, fire, and the nuclear impact; as well as the Chilean 1960 earthquake and tsunami event.

Keywords: tsunami, earthquake effects, socioeconomic losses, landslides, liquefaction, fatalities, economic losses, earthquake

OPEN ACCESS

Edited by:
Nobuhito Mori,
Kyoto University, Japan

Reviewed by:
Yoshio Kajitani,
Central Research Institute of Electric Power Industry, Japan
Kaiming Bi,
Curtin University, Australia

****Correspondence:***
James E. Daniell
j.e.daniell@gmail.com

Specialty section:
This article was submitted to Earthquake Engineering, a section of the journal Frontiers in Built Environment

Received: *06 February 2017*
Accepted: *04 May 2017*
Published: *13 June 2017*

Citation:
Daniell JE, Schaefer AM and Wenzel F (2017) Losses Associated with Secondary Effects in Earthquakes. Front. Built Environ. 3:30. doi: 10.3389/fbuil.2017.00030

INTRODUCTION

Disaggregation of secondary effect economic losses and fatalities demonstrating the relative influence of historical losses from direct earthquake shaking in comparison to tsunami, fire, landslides, liquefactions, fault rupture, and other type losses is important if we are to understand the key causes post-earthquake.

Existing studies have attempted to examine the key causes without putting dollar values to the losses, e.g., Bird and Bommer (2004) studied 50 earthquakes between 1980 and 2003 for all secondary effect types, Keefer (1984) and Rodrıguez et al. (1999) for landslide losses, and NGDC/NOAA (2010) for tsunami losses. Although most historical losses have been earthquake shaking related, the influence of the 2011 Tohoku earthquake has changed the historical percentages significantly for tsunami, just as the 1995 Kobe and 2011 Christchurch earthquakes have with regard to liquefaction. Liquefaction has occurred in many earthquakes but this is also difficult to disaggregate for older historical earthquakes. Fire in 1906 San Francisco and 1923 Great Kanto caused significant losses, but since then, important losses have also occurred in many earthquakes. Landslide losses in Haiyuan 1920, Ancash 1970, El Salvador 2001, Kashmir 2005, and Sichuan 2008 were dominant in the database, with many other incidents causing minor damages. Quite often for smaller events, landslides deliver a great amount of the clean-up cost, and indeed sectoral losses. Infrastructure, such as roads, is particularly vulnerable to landslides and secondary effects, often causing much of the damage (i.e., Kaikoura 2016).

This paper sets out to examine the percentage of socioeconomic losses of the secondary effects as compared to primary effects of earthquakes. It also sets out to examine the way in which secondary losses have been counted in past disasters by examining Tohoku 2011 and Chile 1960 in a fact-finding approach.

METHODOLOGY

The methodology to derive the losses due to secondary effects consists of a couple of steps:

(1) To define the different types of secondary effects
(2) To collect the data associated with the defined secondary effects types in past disasters.

Defining Secondary Effects

The primary effects of earthquakes are caused by the surface rupture along the fault and by the ground shaking *via* the earthquake energy release. The secondary effects are the effects that occur directly as a result of this earthquake shaking and energy release, i.e., the onset of a tsunami wave, or a landslide. Tertiary effects could include cascading effects such as the primary effect of an earthquake causing a secondary effect in the form of a tsunami which damages a nuclear power plant, and then a nuclear disaster develops. Another such tertiary effect is an epidemic or starvation due to the effects of the earthquake. The process of primary, secondary, and tertiary effects is shown in **Table 1**. It is very difficult to correctly differentiate between secondary and tertiary effects, and the whole sequence can sometimes simply be described as a cascading effect. The Tohoku earthquake of 2011 is a key example.

For the purposes of better defining the terms in this manuscript, the term "effects" refers to the changes to the earth's surface as a result of the earthquake (hazard-related); "losses" refer to the socioeconomic changes post-disaster be they deaths, or economic losses.

TABLE 1 | The process of primary, secondary, and tertiary effects of earthquakes.

Type of effect	Name	Key elements
Primary effects	Ground shaking	• Source effects (directivity, hanging/foot wall) • Path effects • Site effects (soil type, location)
Secondary effects	Tsunami	• Wave height • Size of fault rupture and proximity to coastline
	Landslide, slope failure	• Slope of the location • Soil typologies and stability of regolith • Geological map
	Liquefaction	• Sand/soil type (grain size) • Water table location (saturation)
	Changes in ground level	• Ground loading
	Fire	• Flammability Index and susceptible components
	Ground effects and surface breaks	• Surface effects, lateral spreading • Depth of hypocenter
	Flooding, dam breaks	• Location of shaking with respect to water bodies • Susceptible dams and potential earth locations
Tertiary effects	Epidemics	• Susceptibility of population and climate
	Socio-psychological	• Age, cultural and socioeconomic status
	Economical	• Economic status of the region
	Environmental	• Environmental susceptibility of the region

Collection of Data for Earthquake Fatalities and Economic Losses from Secondary Effects

There are many main sources of secondary effects due to earthquakes which have been collected in the literature of which will be explained *via* the individual parts of the definitions given above.

Landslides are induced by earthquakes where slopes lose stability as consequence of shaking, causing soil and rock masses to move downhill. This can be accentuated by rainfall and vegetation and mainly occurs in mountainous or steep sloping regions. Key factors are detailed in Khazai and Sitar (2004) examining the 1999 Chi-Chi earthquake. A study by Nadim et al. (2006) showed global landslide hotspots. In addition, a similar study has been undertaken as part of secondary effects analysis, using a combination of soil moisture indices and slopes for earthquakes worldwide to create a landslide hazard index. Godt et al. (2008) have developed a rapid loss estimation methodology for landslides worldwide as part of the PAGER project, using a PGA-slope relationship based on Newmark's method *via* the equations of Jibson (2007). Small-scale models to examine susceptibility to earthquake-triggered slope instability have been put forward by Jibson (2007) and Miles and Keefer (2009). In addition, great work during the COGEAR project was undertaken to examine historical landslide events and others even infer earthquake intensities (Beck, 2009). Parker (2013) continues to create relationships of the earthquake magnitude and ground motions vs. landslide density. A detailed study of earthquake-induced landslide losses has been undertaken by Bommer and Rodriguez (2002) and Keefer (1984, 2002) (**Table 2**).

TABLE 2 | The effect of larger landslide events since 1900.

Date and location	Magnitude of event	Fatalities due to landslides
1920 Haiyuan	Mw 8.3/8.6	136,700 deaths (50%)
1970 Ancash	Mw 7.9	26,700 deaths (40%)
2005 Kashmir	Mw 7.6	26,500 deaths (31%)
2008 Sichuan	Mw 7.9	26,500 deaths (30%)
1949 Khait	Mw 7.6	11,760 deaths (98%)
1976 Irian Jaya	Mw 7.1	5,520 deaths (92%)
1907 Karatag	Mw 7.2	4,900 deaths (35%)
1917 Daguan	Mw 7.3	1,800 deaths (96%)
1950 Assam, Chayu	Mw 8.6	1,450 deaths (30%)
1998 Badakhshan and Takhar Provinces	Mw 6.5	1,350 deaths (30%)

The largest death tolls in the last 117 years from landslides have come in the Chinese 1920 Haiyuan event, where many people

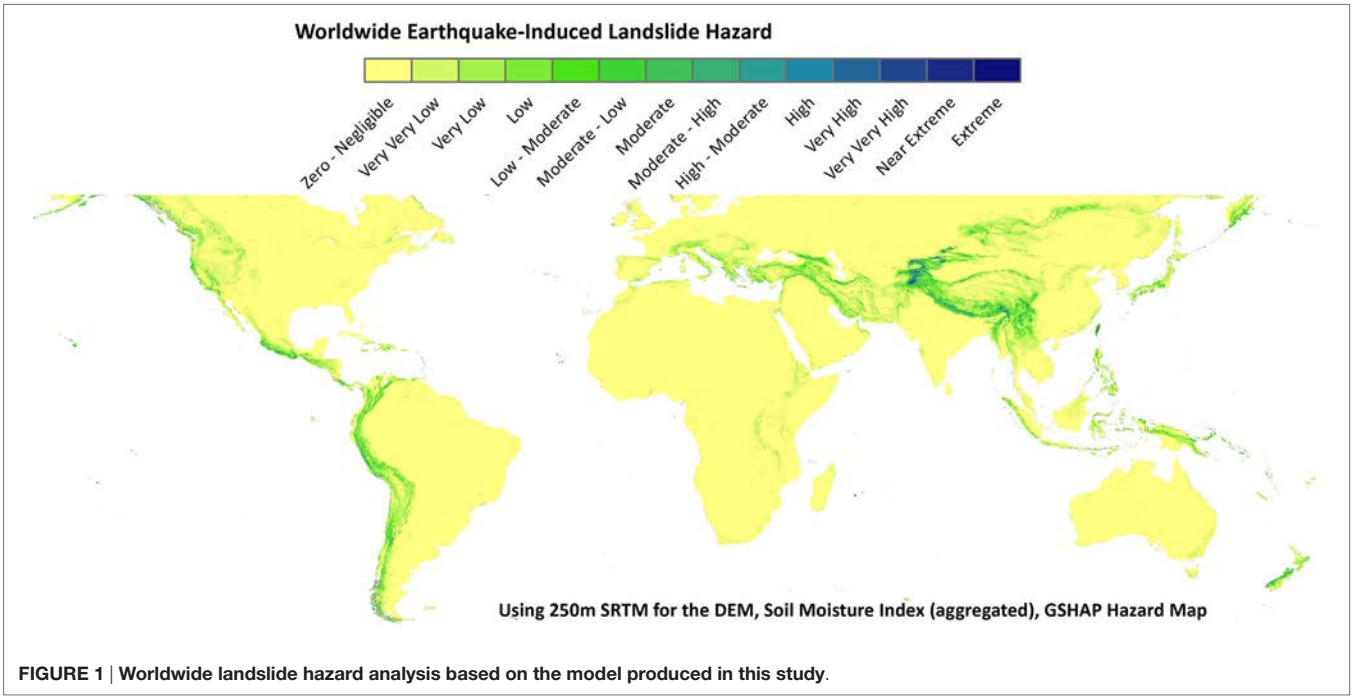

FIGURE 1 | Worldwide landslide hazard analysis based on the model produced in this study.

living in cave like buildings, and villages close to slopes, were buried with the M8.6 mainshock and resulting aftershocks *via* loess landslides.

In the study below, the slope was taken from global use of the SRTM250[1] dataset, the soil moisture index over a year from the global USDA, and the GSHAP map with historical landslides from earthquakes to calculate the landslide potential index. A landslide risk map can also be produced in conjunction with historical data and exposure. This, along with historical landslide losses, simply produces a flag system with the potential landslide susceptible areas. An example of a landslide analysis using a similar methodology is shown for Germany, Austria, and Switzerland and was calculated in Daniell et al. (2013) but with extension to estimated losses. **Figure 1** shows the worldwide landslide hazard analysis produced in this study.

We will refer to quake lakes and flooding in a subsequent paragraph.

Liquefaction occurs where saturated soil (usually not too fine-grained sand) layers are turned from solid to liquid, causing rapid failure. This generally only occurs in earthquakes with the shaking inducing a loss of shear strength. One of the first studies to calculate the potential for liquefaction was the study of Seed and Idriss (1971). Generally, the problem has been tackled *via* empirical methods, using soil properties [Standard Penetration Test (*via* blowcounts)] and water table level, in order to determine the liquefaction potential. For large-scale assessment, Vs,30 (average shear wave velocity in the first 30 m) has been used as a proxy to develop an equation for simplified liquefaction susceptibility (Dismuke and Mote, 2012). These can then be further classified into deterministic (Goh and Goh, 2007) and probabilistic (Cetin et al., 2002) approaches as well as into flow liquefaction and cyclic mobility (Kramer, 1996). For Japan, a good review of countermeasures stemming from some of the below locations has been made by Yasuda and Harada (2014). Currently, an expansion of the PAGER rapid loss system of the USGS is also considering liquefaction susceptibility following the work of Allstadt et al. (2017). Significant losses have not be seen for liquefaction globally in the form of fatalities, (except for loess liquefaction) however significant economic losses have been seen as shown in **Table 3**.

TABLE 3 | The effect of larger liquefaction events since 1900.

Date and location	Magnitude of event	Fatalities and/or economic losses
2010/2011 Christchurch Sequence	Mw 7.1, Mw 6.3, and subsequent aftershocks	No known fatalities, but 6,000+ buildings red zoned, and many other clean-up costs. Likely around $10bn+ associated with liquefaction losses
1964 Niigata	Mw 7.6	2 deaths, many collapses of multi-storey apartments
1995 Kobe	Mw 6.9	3 deaths, widespread damage
1999 Izmit	Mw 7.7	Extensive damage
1935 Taiwan; 2016 Taiwan	Multiple	16 deaths were believed to be associated in 1935; with liquefaction also believed to be a factor in the 2016 quake
1920 Haiyuan, 1989 Tajikistan, 2013 Diexi	Multiple	Loess liquefaction caused many fatalities (included above in landslide)

The 1989 Loma Prieta, 1964 Alaska, 1988 Bihar, 1990 Luzon, and 1905 Malatya also saw much liquefaction although these were associated mainly with minor economic losses. Loess liquefaction caused much damage in the 1920 Haiyuan earthquake among others and has been included in the landslide component.

Tsunamis occurs where fault movement from an offshore subduction earthquake causes a large volume of water to be displaced

[1] http://srtm.csi.cgiar.org/.

either directly by fault displacement of in consequence of a triggered large subsurface landslide or a combination of both effects. The long-wavelength distortion of the water surface, typically with amplitudes in the meter range, travels at about 800 km/h in open seas with little attenuation to large distances. Eventually, the water waves travel from deeper waters to shallow waters at the coastline, slowing the wave, increasing the amplitude, and resulting in large, destructive waves.

In recent years, the number of fatalities (**Table 4**) has been dominated by two large events, namely, the 2004 Indian Ocean earthquake and the 2011 Tohoku earthquake, both causing major losses due to tsunami effects. Using historical earthquakes, the tsunami risk can be evaluated qualitatively, given the advent of a new earthquake, by using the magnitude and historical earthquakes that have occurred in that location. Global Disaster Alert and Coordination System (2011) and various tsunami warning centers also provide potential runup heights post-earthquake based on analysis; hence, these results can be used to potentially map the inundated areas and by using population, capital stock, and gross domestic product estimates, work out the affected exposure. InaSAFE (2013) and TsuDAT (2013) are two software packages reviewed that can calculate the exposed metrics and the associated losses. An example of maximum tsunami water height runup from historical tsunamis is shown with much data derived from National Geophysical Data Center (USA) as seen below in **Figure 2** with the historical tsunami runups.

TABLE 4 | The effect of larger tsunami events since 1900.

Date and location	Magnitude of event	Fatalities and/or economic losses[a]
2004 Indian Ocean	Mw 9.1	168,000 (Indonesia), 35,300 (Sri Lanka), 15,800 (India), 8,200 (Thailand) (ca. 99%) deaths, and $10bn+ (event year)
2011 Tohoku	Mw 9.0	17,931 deaths (96% not including indirect) / $120bn + (event year)
1941 Andaman Islands	Mw 7.7	7,960 deaths (99.5%)
1976 Moro Gulf	Mw 8	6,229 deaths (88.0%)
1945 Makran	Mw 8	3,700 deaths (92.5%)
1933 Sanriku-oki	Mw 8.4	3,002 deaths (98.0%)
1998 Papua New Guinea	Mw 7	2,683 deaths (100.0%)
1908 Messina	Mw 7.24	2,578 deaths (3.0%)
1992 Flores	Mw 7.7	2,519 deaths (100.0%)
1952 Kamchatka	Mw 9.0	2,336 deaths (100.0%)

[a]*Median estimate from literature and analysis.*

As computation speeds have increased in the past few years, the ability to undertake probabilistic tsunami hazard modeling on a personal computer has become possible (Schaefer et al., 2015).

Fire is a result of earthquake shaking, influencing electricity, gas, or fire sources to ignite in and around infrastructure that is in the shaking area. In the past, this has been the greatest contributor to damage in many earthquakes, including 1906 San Francisco and 1923 Great Kanto (**Table 5**). At present, the influence of fire is still major in earthquakes; however, with better fire management practices in effect, and less buildings built of flammable materials, this is a reducing element in total loss statistics, with the recent Tohoku earthquake only having around 150 people dying due to fire. Many earthquakes in the US, Japan, and NZ have the chance for fires due to the wooden housing typologies often used. Scawthorn et al. (2005) details various case studies in his book as one of the better fire following earthquake references. In many countries in the world, wooden frames are used including

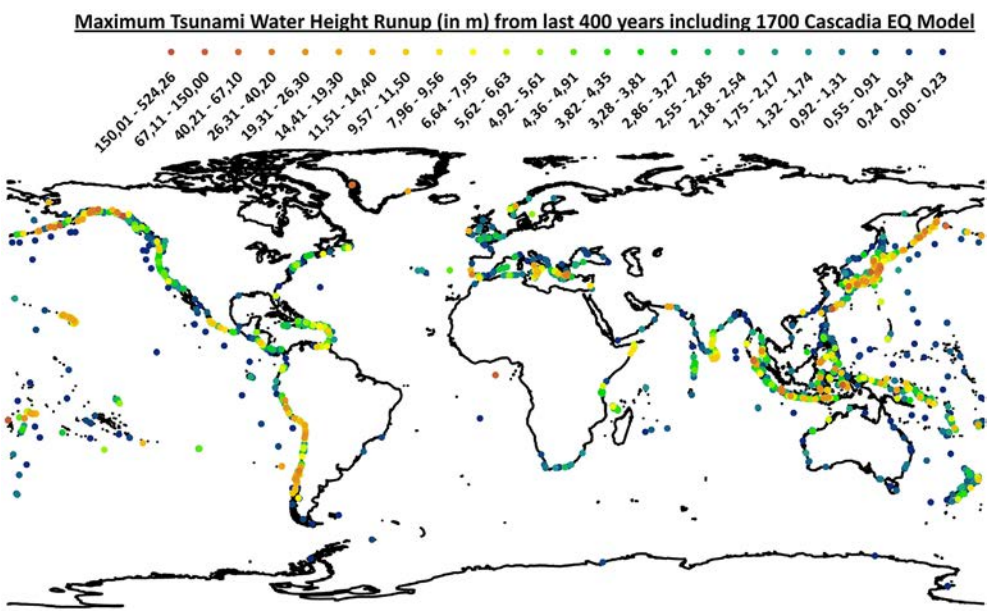

FIGURE 2 | Maximum tsunami water height runup (in meters) from the last 400 years from a combination of modeling and National Geophysical Data Center, including a 1700 Cascadia EQ Model.

California, Japan, New Zealand, and Australia as shown by the proportion of brown color (wooden stock) in **Figure 3** of each nation globally.

Flooding in terms of dam breaks and reservoir failures can cause major damage and also be a huge hazard to populations. Generally, large dams have been built to withstand earthquake forces, but the simple lateral shaking can sometimes cause massive failures of natural or man-made systems, such as seen in the 1933 Diexi earthquake (Shi-zhong, 2010) (**Table 6**). Landslides can also sometimes cause blockages to rivers, forming quake lakes which can then, if unstabilized, unleash huge flooding on settlements downstream. Although there have not been many instances, flow-on disasters such as a flood where an earthquake occurs simultaneously can have major cascading impacts. In **Figure 4**, 623 of the 6,862 dams are expected to have a shaking hazard of 0.3 g within 475 years (shown in orange and red). Of these, over half (333 out of 623) are over 45 years old, indicating the need for reassessment of these dams. Flooding also caused many fatalities in the 1949 Ambato/Pelileo earthquake in Ecuador. **Figure 4** depicts the earthquake hazard of 6,800+ dams and reservoirs worldwide.

Surface rupture is simply the visible displacement along the fault which causes surface cracks or surface slip to appear. This was seen visually in the 2008 Sichuan earthquake, where much damage was due to fault rupture. General laws have been that fault rupture occurs in earthquakes with a magnitude greater than 6. Surface fault rupture zones have not caused much damage historically, however, as the known fault zones are generally not built upon in locations such as the Western USA, and also the rupture surface is generally not very wide, thus minimizing the chance for damage. In the recent Kaikoura 2016 event, a 10-m displacement occurred through an existing house causing major damage but no fatalities.

Despite Hollywood film attempts to pitch fault rupture as a major cause of destruction in earthquakes, fault rupture has not recorded many observed fatalities.

TABLE 5 | The effect of larger fire events since 1900.

Date and location	Magnitude of event	Fatalities and/or economic losses[a]
1923 Great Kanto	Mw 7.9	92,190 deaths (87%); 2/3 of the damage ($40bn+ CPI adjusted); ca. $220bn HNDECI
1906 San Francisco	Mw 7.9	1,800 deaths (60%); ca. 5/6 of damage (ca. $10bn CPI adjusted); $50.6bn HNDECI
1995 Great Hanshin, Aawji, Kobe	Mw 6.9	570 deaths (9%)
1948 Fukui	Mw 7	513 deaths (10%)
1925 Dali	Ms 7	400 deaths (7%)
1906 Valparaiso	Mw 8.5	388 deaths (10%)

[a]*Median estimate from literature.*

AGGREGATED LOSSES DUE TO SECONDARY EFFECTS

A review of earthquake fatalities over time gives the first insight into the fatality risk of earthquakes. Using the CATDAT Damaging

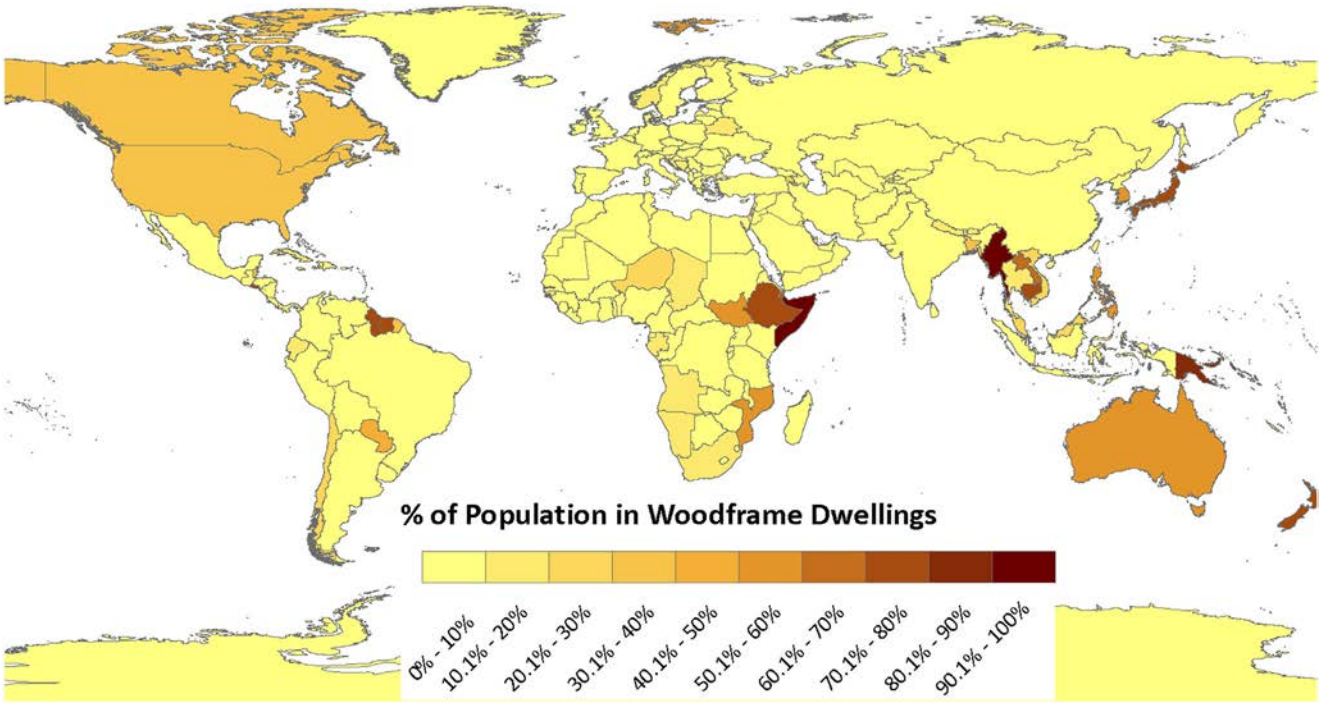

FIGURE 3 | The percentage of population in wood-frame buildings globally for each country as created as part of Daniell et al. (2011c).

Earthquakes Database (Daniell et al., 2011a) which contains ca. 16,000 damaging earthquake events through time, the earthquake fatalities are examined and trends built. For this paper, we focus on 1900 onward. The reader is instructed to examine Daniell et al. (2011a) and Slingsby et al. (2011) for details as to the structure and collection of the database.

Over the period from 2003 to 2016, the CATDAT Damaging Earthquakes Database has been collected from many sources globally. In-depth analysis has been undertaken to disaggregate fatalities from earthquakes into the different causes of the fatality, whether it be from direct structural collapse or secondary effects such as tsunami, landslide or otherwise from 1900 to 2016, and 9,900+ damaging earthquakes with economic losses since 1900. Earthquakes have caused over 2.3 million fatalities since 1900 in 2,233 fatal events, with many of these coming through large, infrequent events. In fact, since 1900, 59% of these fatalities have occurred in just 10 events. In fact, the top 100 events account for 93.25% of fatalities as seen in **Figure 5**.

A list of the top 10 fatal earthquakes since 1900 are included with the approximate breakdown of secondary and primary effects as well as an attempt as to the number of fatalities due to all engineered structures, showing the need for sensitive design for not only shaking but also for secondary effects in **Table 7**.

Many of these fatalities were as a result of secondary effects such as tsunami, fire, and landslide as can be seen in the above table. However, most were due to non-engineered collapse of masonry buildings (the % of engineered estimated structures is shown in the table of top 10 earthquakes). It has been found that over 57% of deaths have occurred in masonry buildings either by falling structural members, roof collapse, or falling debris. An additional 8.5% have died in concrete buildings and 3% in timber buildings. In total, approximately 71% of fatalities have occurred due to direct earthquake shaking and 29% to other earthquake secondary effects as shown in **Figure 6**. The database is a dynamic entity and continues to change as further reanalysis of past events takes place, including separating heart attack deaths and non-structural deaths.

A detailed study of all 9,920 damaging earthquakes from 1 January 1900 to 31 December 2016 has been undertaken by examining the original sources, descriptions, and expert opinion (where experts from various entities are asked as to their opinions post-disaster and their estimates weighted) where exact dollar amount losses with regard to disaggregation have been calculated. **Figure 7** shows results for direct losses and total economic losses from earthquakes. Approximately 70% of direct economic losses have come from direct earthquake effects, whereas 30% have occurred due to secondary effects of earthquakes. For total economic losses, taking into account the indirect losses, this percentage increases to 38%. This has many implications for our earthquake research. The focus on just shaking losses should be changed to one of holistic strategies for shaking and secondary effects losses.

Landslides can be seen to cause over 5% of economic losses, and this has only been low due to the relatively low populations living worldwide in mountainous areas exposed to earthquakes since 1900. China has experienced major losses through the 1920 Haiyuan and 2008 Sichuan earthquakes. 1949 Khait and 1970 Ancash were also major landslide-bearing earthquakes causing major economic losses to their respective countries. The 2011 Tohoku and 2004 Indian Ocean earthquakes have both brought about much of the economic losses due to tsunami in recent years; however, many tsunami-bearing earthquakes have caused much damage, such as 1960 Chile and 1964 Alaska with over 10% of

TABLE 6 | The effect of larger dam/blockage failures since 1900.

Date and location	Magnitude of event	Fatalities and/or economic losses
1933 Diexi	Mw 7.3	Ca. 4,700 deaths *via* collapsed dam
1949 Pelileo	Mw 6.8	Ca. 3,000 deaths *via* blocked channel
2008 Sichuan	Mw 7.9	Many quake lakes produced, mass evacuations

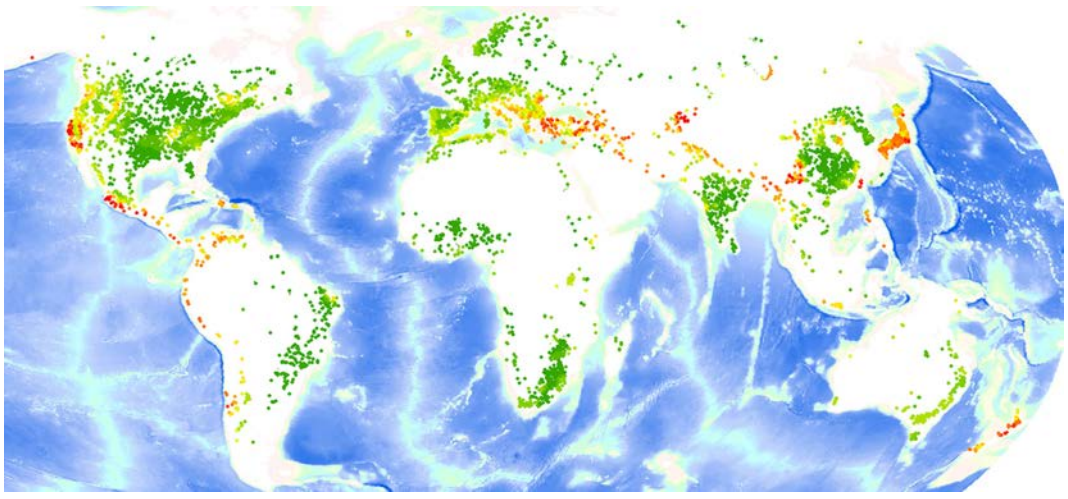

FIGURE 4 | The earthquake hazard of the 6,800+ dams and reservoirs worldwide from the GRanD database [in comparison to the GSHAP (10% exceedance in 50 years)].

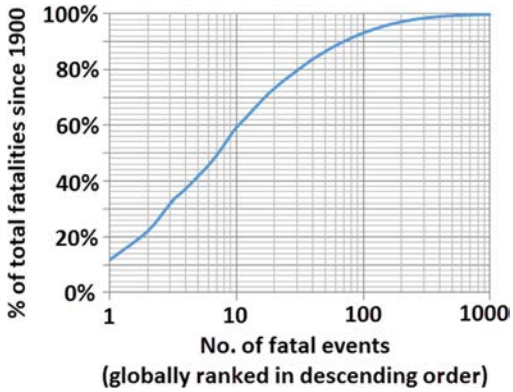

FIGURE 5 | No. of fatalities (cumulative) globally ranked in descending order from largest to smallest event.

TABLE 7 | The top 10 earthquakes in terms of fatalities.

Earthquake	Median	%Eng	Prim. (%)	Sec. (%)
1920 Haiyuan	273,400	<1	50.0	50.0
1976 Tangshan	242,400	20	100.0	0.0
2004 Ind. Ocean	228,100	<5	0.5	99.5
1923 Great Kanto	105,385	<5	10.5	89.5
1948 Aschgabat	100,000	50[a]	100.0	0.0
2008 Sichuan	88,300	<30	70.0	30.0
2005 Kashmir	87,400	<5	69.7	30.3
1908 Messina	86,000	<1	97.0	3.0
2010 Haiti	80,000	<10	100.0	0.0
1970 Ancash	66,800	<1	60.0	40.0
Total	1357,785	<10	817,533	540,252

[a]*Based on an early Soviet code.*

total losses due to tsunami, and additional NaTech losses *via* the power plant disaster in Tohoku.

CASE STUDIES

Two case studies are discussed to examine the disaggregation process, values, and uncertainties associated with the estimates of secondary effect losses.

Case Study 1: Tohoku Earthquake—Disaggregating the Fatalities

Within 50 separate articles produced after Tohoku (Daniell and Vervaeck, 2011), each spanning a few days, and associated situation reports in conjunction with http://earthquake-report.com, a detailed update of damage data, economic losses, and social impacts (homelessness, injuries, deaths) of the Fukushima disaster, including translations of the FDMA[2] reports, GIS data, and collated statistical data, was given to the public and many companies. Much work was also done to analyze the sectoral losses and to disaggregate the tsunami, earthquake, and power plant losses using information from each municipality to create non-coastal vs. coastal losses. In addition, historical Japanese damage ratio data and tsunami inundation maps were used to further disaggregate losses in the coastal municipalities and plot the 1.2 million buildings damaged.

The inundation map vs. the number of buildings in each municipality allowed the number of destroyed buildings to be

[2]http://www.fdma.go.jp/bn/higaihou/pdf/jishin/155.pdf.

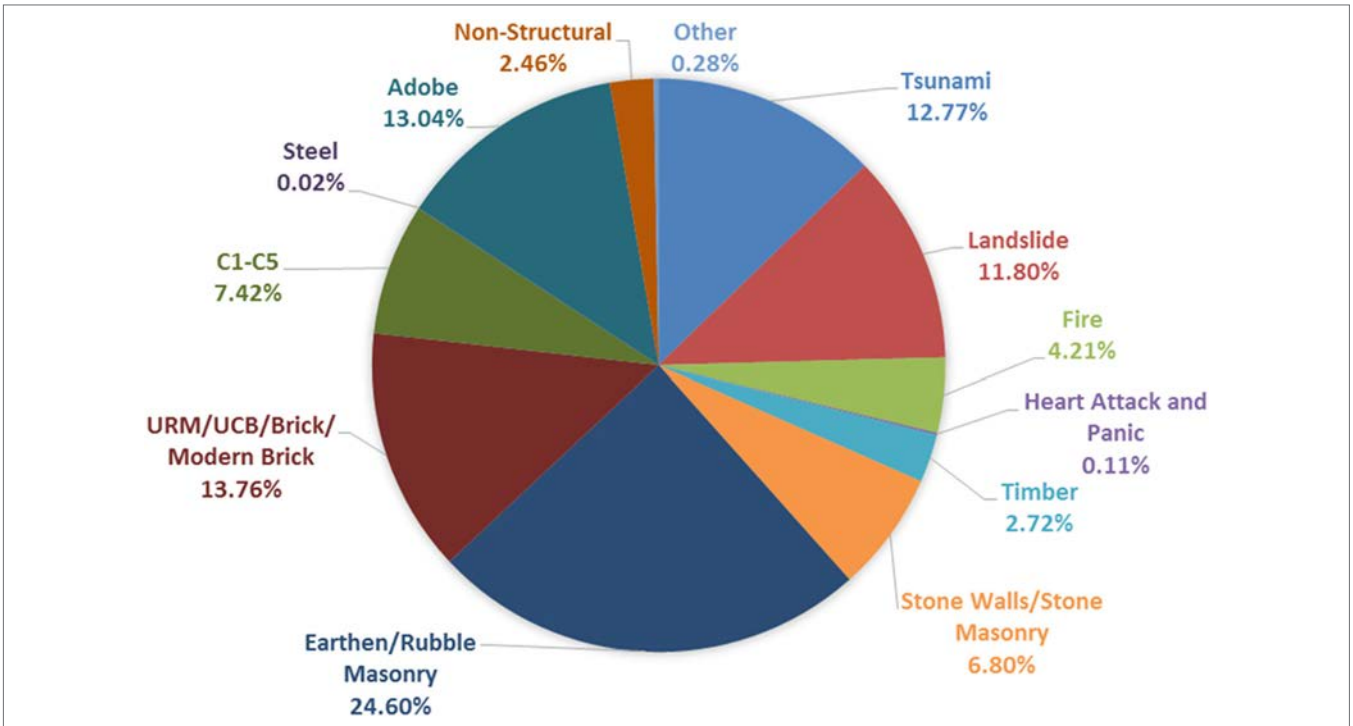

FIGURE 6 | The upper and lower bound death toll estimate of earthquakes in global literature compared to the median CATDAT death toll, current as of December 31, 2016.

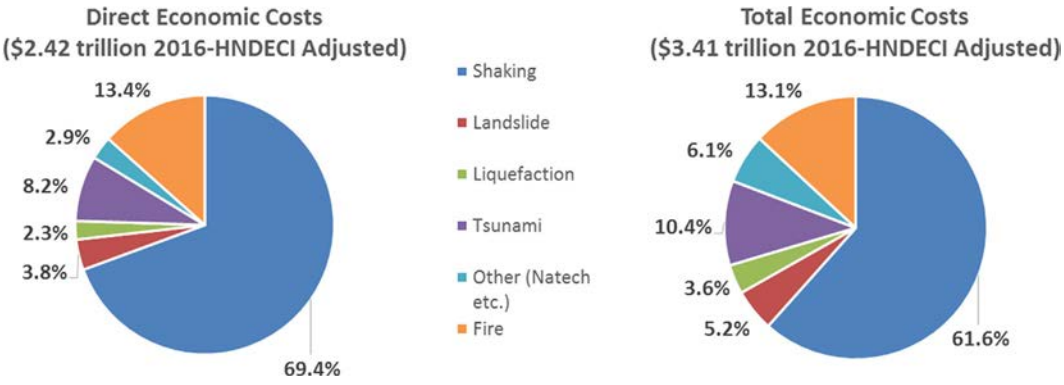

FIGURE 7 | Disaggregation of shaking and secondary effects economic costs from 9,920 earthquakes from 1900 to 2016—left: direct economic costs; right: total economic costs.

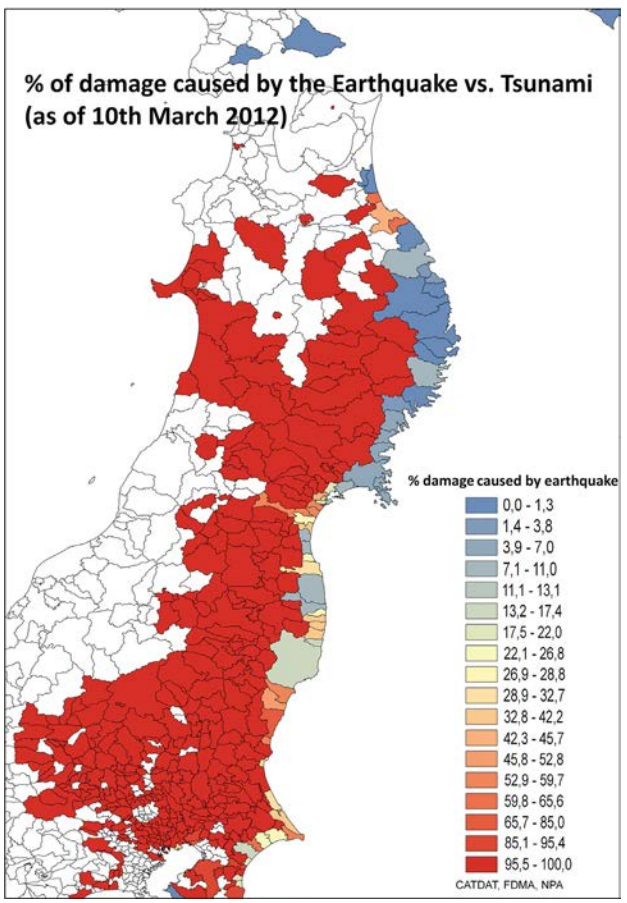

FIGURE 8 | The disaggregated earthquake versus tsunami damage in each municipality (dark red = 100% damage caused by earthquake, dark blue = 100% damage caused by tsunami, and yellow = 50% damage *via* earthquake, 50% *via* tsunami).

calculated, as shown in **Figure 8**, showing that the impact in Sendai itself was less than first expected *via* the tsunami but there was a higher percentage loss due to the earthquake (**Table 8**). The functions of were used to produce the damage functions that

TABLE 8 | Building damage statistics for the 2011 Tohoku EQ disaggregated for tsunami and earthquake.

Buildings	Destroyed	Partially destroyed	Partially damaged
Tsunami	98,697–112,402	78,294–158,636	31,225–95,254
Earthquake	13,721–28,147	113,277–194,367	705,198–771,616

were then utilized. The normalization of various parameters of historical earthquakes to 2011 conditions, using population and dwelling changes, vulnerability changes, and community wealth changes as per Daniell and Love (2010), were also checked.

An additional 35,466 buildings were in the towns and cities within the exclusion zone of the Fukushima I and II nuclear sites. The best estimate of damage to buildings from Daniell and Vervaeck (2011) and then Khazai et al. (2011) from each of the three events was the earthquake (49%), tsunami (39%), and nuclear disaster (12%). With total direct losses, this reduced to earthquake (44%), tsunami (38%), and nuclear disaster (18%).

There were around 30,000 shaking deaths in the CATDAT Damaging Earthquakes Database from 1900 to 2010 before the 2011 Tohoku Earthquake in Japan. Of these, most occurred in 1923 Great Kanto (11,000 shaking deaths), 1927 Tango (3,110), 1943 Tottori (1,325), 1945 Mikawa (2,306), 1948 Fukui (4,618), and 1995 Kobe (4,823).

The use of the seismic code index, other social vulnerability and building practice indicators, and other normalization strategies ensured that the casualty model was calibrated to today's conditions. It would be inaccurate to simply use casualties from a 1970 earthquake, as 80% of the Japanese building stock has been built since; thus, the Human Development Index shift in the fatality function calculates better the fatality change over time.

A comparison of results from various empirical Japanese casualty estimation models is shown in **Table 9** for the M9 earthquake, using a basis of 13,000–26,000 destroyed buildings and 74,000–126,000 half-destroyed buildings as a result of the earthquake. This is in comparison to the 92,000+ buildings destroyed and 78,000+ houses partially destroyed by the tsunami. MMI >7–7.5 townships were used for the regression methods of Ye and Okada (2001).

TABLE 9 | Casualty range loss estimates from selected casualty models for the 2011 Tohoku EQ for earthquake shaking deaths.

Casualty model	Lower	Median[a]	Upper
Kawasumi (1954)	2,187	3,410	5,567
Tokyo Metropolitan Government (1978)	1,716	2,334	3,132
Saitama Prefecture (1982)	35	39	43
Ohta et al. (1983)	210	288	409
Disaster Prevention Council and Tokyo Metropolitan Government (1985)	229	291	360
Ohta and Goto (1985)	95	120	156
Osaka Prefecture (1997)	781	1,098	1,601
Ikeda and Nakabayashi (1996)	729	1,026	1,496
Ye et al. (2001)	104	163	244
USGS PAGER v12—USGS (2011, 2013)	100	1,030	10,000
WAPMERR QLARM—World Agency of Planetary Monitoring and Earthquake Risk Reduction (2013)	0	Unk.	1,000
CATDAT EQLIPSE-Q—Daniell and Wenzel (2014)	291	673	1,340
CATDAT EQLIPSE-R—Daniell et al. (2011b)	133	420	781
Total shaking deaths from Japan	110	190–230	250

[a]*Median estimate equals 18,207 destroyed houses, 100,414 partially destroyed.*

It is still unknown how many victims have died directly due to the earthquake action. A total of 14,308 were reported in March 2012 to have drowned, 667 were crushed or died of internal injuries (mainly tsunami), and 145 perished *via* burns. It will never be known how many died due to the earthquake, as separated from the tsunami; however, the autopsies give us an indication that we can expect that about 1.0% of the 4.4% crushed were probably in earthquake collapsed houses.

In addition, we can assume a proportion of the remaining 2% that were unknown were also earthquake-related (a high value of 10% could be assumed). This would leave about 1.2% or about 158. When extrapolating for the final 3,000 deaths that were not stress or chronic disease related, then the total is approximately 220. This value corresponded quite well to the 137 non-tsunami impacted deaths that were recorded in the non-coastal areas when splitting the fatalities between coastal and non-coastal municipalities. Some of the non-coastal deaths, however, were due to heart attack, fire, or landslide. Thus, only around 110

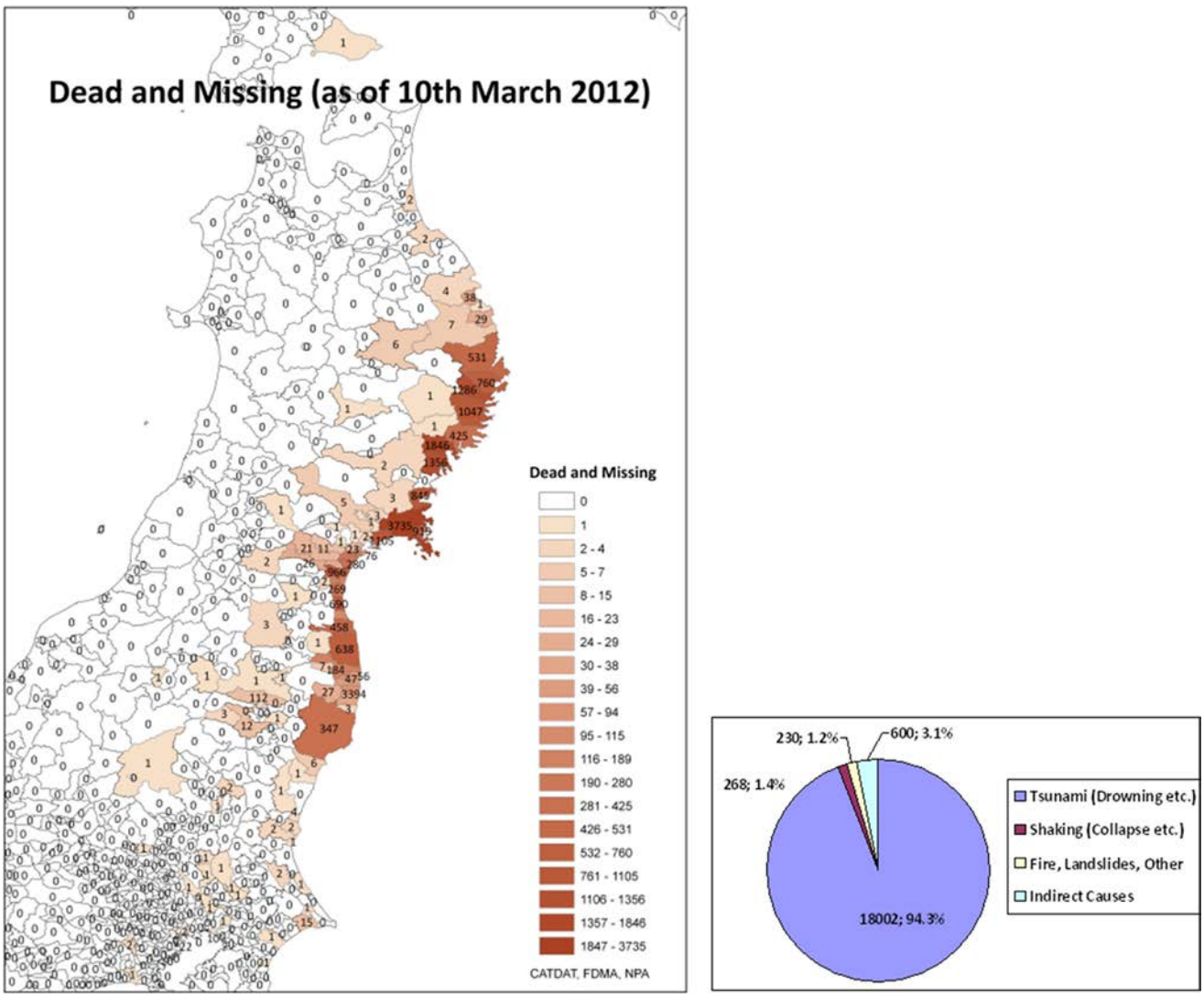

FIGURE 9 | Left: deaths in municipalities as collected from FDMA, National Police Agency Japan (NPA) (2011), and additional Japanese sources; right: the disaggregated deaths as of 11 March 2016 (5 years after). Of the 230 shaking deaths, only around 110 have been confirmed.

TABLE 10 | Casualty and economic loss information for the 1960 earthquake and tsunami event in Chile from various sources.

Source	Earthquake effects	Tsunami effects	Both
La Cruz del Sur, 28.05.1960 *via* Director-General of Police			962 dead, 1,410 missing
Flores (1960)	5,000 deaths		5,000 deaths
U.S. Coast and Geodetic Survey (1962)		231 deaths overseas	2,000 deaths in Chile, 231 deaths in other locations, $550m in Chile, $75m Hawaii, $50m Japan (1960)
Instituto Hidrografico de la Armada (1982)			2,000 deaths, $1,000m (1960)
Lander et al. (1993)		1,263 deaths, $75m	
Soloviev and Go (1975), translated 1984 through Iida et al. (1967)		1,000 deaths in Chile, 60 in Hawaii, 200 in Japan	1,000 deaths in Chile
MunichRe (1998) and Berz (1988)			3,000 deaths, $800–880m (1960)
Saint-Amand (1961)	500 deaths	1,000 deaths	1,500 deaths, $417m
Rothe (1969)			660 deaths and 717 missing (Tazieff, 1962), $550m (1960), 185 deaths (Japan), 61 deaths (Hawaii)
Lockridge (1985)		Chiloe Is. (200), Valdivia (130) as part of 1,000 in Chile	1,000 deaths (all of Chile), 61 deaths (Hawaii), 199 deaths (Japan)
Barrientos and Ward (1990)			$500–700m in Chile
EM-DAT	6,000 deaths, $550mn (1960)		
Lazo Hinrichs (2008)	$300b Pesos (houses) $50b CLP public and private buildings, $80b CLP agriculture and industry, $30b CLP transport, $20b CLP various		2,500 (Official)–5,000 deaths (Chile)

can be certain as due to shaking. It is likely that there are exact numbers available.

As of December 2016, the FDMA reported that 19,475 were killed and 2,587 were missing from the 11 March 2011 event with at least 3,440 deaths of these due to indirect causes. These values differ from the Fire Disaster Management Agency Japan (2011), given the inclusion of "additional related deaths" which have totaled around 2,400 as of 2013, and 600 at the time of the diagram in March 2012, as shown in **Figure 9**, slightly less than the percentage reported in the Kobe earthquake. With the removal of these, the total deaths from FDMA are also about 18,500. Around 110–220 deaths would be earthquake-collapse related. About 250 would be related to other causes such as fire, landslides, etc. Around 94% of deaths were tsunami related.

This means that the most reasonable estimates were derived from Ye et al. (2001). PAGER, QLARM, and this study (EQLIPSE-Q and R) all performed reasonably well, given the uncertainty of the number of shaking deaths 5 months after the event. The Tohoku earthquake in 2011 provided a situation where the size of the event was outside the expected values. Historical GMPEs and IPEs used for historical Japanese earthquakes were outside the magnitude range (Mw = 9.0). This made difficulties for the modeling of intensities and damage. The quality of data in terms of intensities and ground motion measurements made it possible to create loss estimates in the correct order of magnitude.

Case Study 2: 1960 Chile Tsunami

The 1960 Chile earthquake and tsunami sequence on 21 and 22 of May, 1960 caused shaking damage as well as tsunami and landslide effects. By far, the most devastating component was the shaking damage; however, the earthquake and tsunami are interesting for the fact of the range of uncertainties in the literature and the fact that the tsunami likely caused more fatalities than shaking.

The 1960 Chile earthquake caused somewhere between 1,600 and 3,500 deaths, with 1,655 or 2,000 or 2,500 the most accepted number. Of these, at least 1,000 deaths were tsunami-based, if not in the order of 1,500. The tsunami to earthquake death ratio was likely 2 to 1. The following shows the uncertainties within numbers in literature.

Estimates of up to 7,231 deaths exist in literature (**Table 10**), possibly being an error (EM-DAT) and as low as 490, with economic losses split in a ratio of $550mn for shaking vs. $50m for tsunami, with 6,000 deaths attributable to the earthquake, and 1,231 to tsunami originally. This has since been changed to just the earthquake shaking losses. Talley Jr. and Cloud (1962) gave an estimate of 2,000 deaths due to earthquake and 231 due to tsunami, whereas Saint-Amand (1961) gives 1,000 due to tsunami and 500 due to earthquake. Interestingly, Flores (1960) gives a value for the foreshock of 500 deaths on the 21st May and attributes then 5,000 deaths to the earthquake on the 22nd May. Preferred estimates for disasters are generally local, but even these differ from 500 to 5,700 deaths.

From the tsunami, these estimates from the entire Peru-Chile coastline ranged from 330 to 2,000 people with somewhere between 200 and 800 deaths on Isla Chiloe (which was the hardest hit location). The work of Mancilla and Mardones (2010) also mimics the uncertainty in numbers of deaths due to the tsunami and earthquake.

For exploratory reasons, the 1960 Chile tsunami, also called Valdivia tsunami has been selected. It occurred on the southern

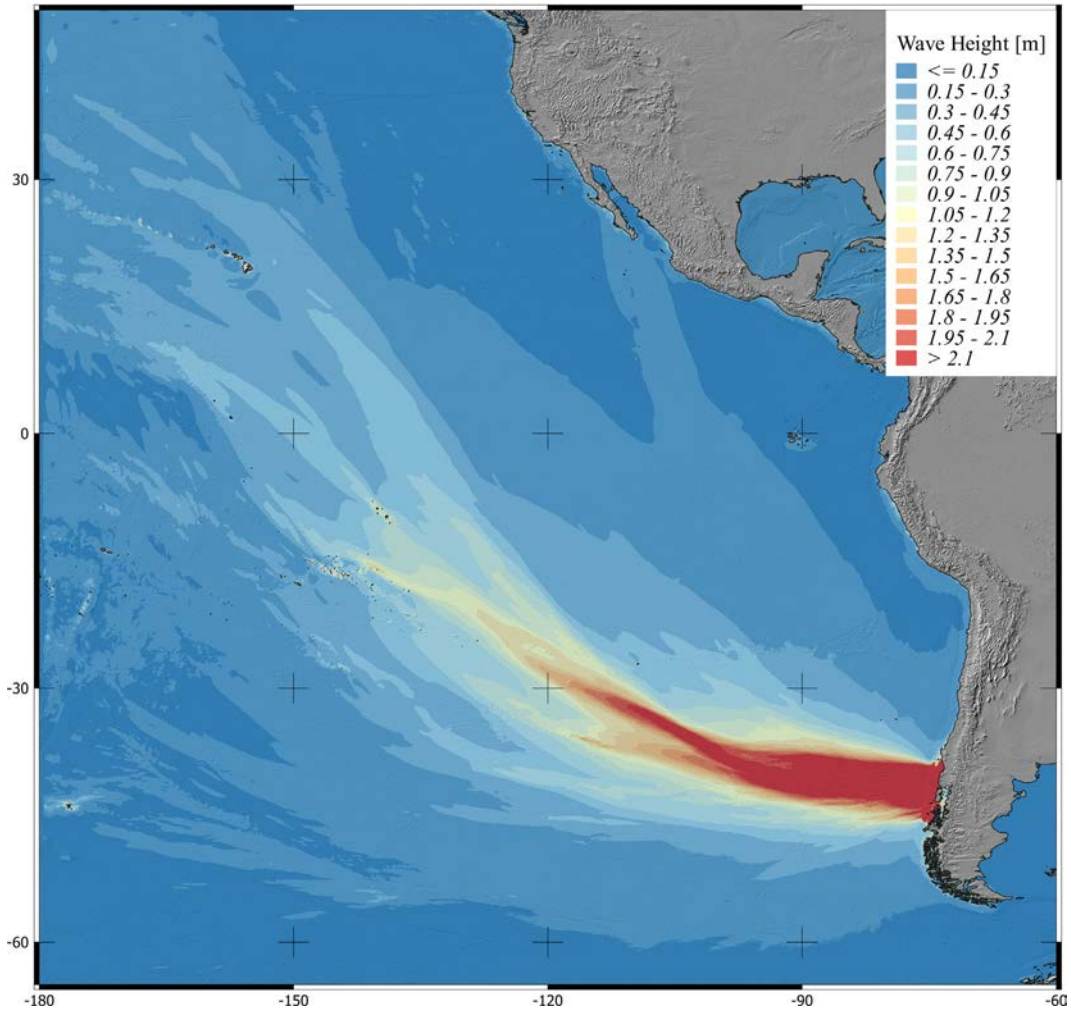

FIGURE 10 | The modeling of the reanalyzed 1960 tsunami event and the effects on Chile as well as Hawaii.

tip on of the most seismically active regions in the world, the Andean subduction zone of the Nazca plate offshore Chile (Schaefer et al., 2015). With a moment magnitude of about 9.5, it is the strongest earthquake ever recorded. Unfortunately, in 1960, the record of the tsunami is limited both for wave propagation and inundation; thus, reconstruction of this event is ambiguous.

For numerical modeling, the tsupy methodology of Schaefer and Wenzel (2017) is used. Here, the non-linear shallow water wave equations are used in a parallelized framework to compute propagation and inundation patterns on a moderate resolution. The tsunami source is modeled using a slip distribution considering the methodologies of Mai and Beroza (2002) and (Goda et al., 2014) representing the 3D distribution of movement along the fault plane of an earthquake rupture, which is afterward projected to a surface deformation using the equations of Okada (1985). It has been shown that the tsunami impact and inundation pattern along coastlines close to the epicenter is highly dependent on the slip distribution. Differences in inundation heights can reach well beyond a factor of two just by a variation of the slip distribution.

For this test case, the slip distribution of Fuji and Satake (2013) is considered, which has been resolved inversely from geodetic and observed tsunami data. As for recent event, inversely resolved distributions are not unique, e.g., for Japan where a tenfold of possible results could be considered. The tsunami is simulated numerically using two regular grids with resolutions of 1 km and 90 m as shown in **Figure 10**. The 1-km grid is used to calculate the long-distance travel of the tsunami, while the 90-m grid, which consists of the region between Concepcion and Valdivia, is used to compute the inundation. It is hoped that a reanalysis using this type of methodology, mimicking the historical observed tsunami inundations at various points; as well as adding the 1960 capital stock and building typologies at the time of the event may allow for better information on this event to be gained to better split the "estimated" secondary effect deaths and economic losses.

DISCUSSION AND CONCLUDING REMARKS

The role of secondary effects of earthquakes for damage and loss has been shown as highly relevant through history. Although somewhere between 60 and 75% of economic losses as well as deaths have been due to shaking effects, between 25 and 40% of these impacts have been due to secondary effects in the form of tsunamis, landslides, liquefaction, fire, and other less common types.

For fatalities, this study agrees well with the original work of Coburn and Spence (1992) that showed for 1,100 fatal earthquakes from 1900 to 1990 around 76% of fatalities were from shaking and 24% from secondary effects. Marano et al. (2010) in PAGER on 749 fatal earthquakes from September 1968 to June 2008 demonstrated that 25% of fatalities from earthquakes were due to secondary effects of earthquakes (tsunami, landslide, fire, liquefaction). A total of 913 fatal earthquakes were recorded in the CATDAT database in the same time period from 1968 to 2008. Both studies are much lower than the study of Bird and Bommer (2004) on 50 earthquakes from 1980 to 2003, showing that 90% of earthquake deaths are due to shaking. It should be noted that deaths due to volcanic effects have simply been removed from the earthquake records. The 2010 version of the CATDAT Damaging Volcanoes Database shows the various effects of volcano related earthquakes such as the 2002 eruption episode of Lake Kivu, and the 1914 Sakurajima earthquakes (Daniell, 2011).

It has been seen that there is much uncertainty in numbers post-disaster and depending on the source used there are many different opinions as to the influence of secondary effects in terms of the absolute numbers of their impact as seen by the number of sources in the Chile 1960 earthquake. In newer events, better reporting within countries with the advent of Desinventar[3] and formal loss collection mechanisms within governments, and thus the breakdown of secondary effects losses seen in the literature, has improved.

A few larger events such as Haiyuan 1920, Sumatra 2004, Great Kanto 1923, and Christchurch 2011 dominate the secondary effects seen since 1900; over 3,000 events of the almost 10,000 events have recorded secondary effects showing the additional importance of increased research in this field. As improved models for secondary effects of earthquakes continue to be created and better collection of loss statistics occur, the reanalysis of historic events should allow for scenario-based current and future effects of potential earthquake secondary effect cascading events to be analyzed, but also a potential check of the historical impacts. As more data sources become digitized, the historical event reanalysis is also being improved by better amalgamation of older reports on the events. The CATDAT database represents a step to disaggregate such events and continued collection of the data in the future will continue to improve the past disaster disaggregation of secondary effect losses.

[3] www.desinventar.org.

AUTHOR CONTRIBUTIONS

JD—the data analysis from CATDAT, studies into historical event losses, and secondary effect analysis. AS—tsunami analysis and general checking. FW—methodological changes, checks of analysis, editing and proofing diagrams and text, and secondary effect analysis. All authors have contributed to, read, modified, and approved the final manuscript.

ACKNOWLEDGMENTS

We acknowledge the support by Deutsche Forschungsgemeinschaft and Open Access Publishing Fund of Karlsruhe Institute of Technology.

REFERENCES

Allstadt, K., Hearne, M., Nowicki, M. A., Thompson, A., Wald, E. M., and Zhu, D. J. J. (2017). *Integrating Landslide and Liquefaction Hazard and Loss Estimates with Existing USGS Real-Time Earthquake Information Products, 16th World Conference on Earthquake Engineering*. Santiago, Chile.

Barrientos, S. E., and Ward, S. N. (1990). The 1960 Chile earthquake: inversion for slip distribution from surface deformation. *Geophys. J. Int.* 103, 589–598. doi:10.1111/j.1365-246X.1990.tb05673.x

Beck, C. (2009). Late quaternary lacustrine paleo-seismic archives in North-Western Alps: examples of earthquake-origin assessment of sedimentary disturbances. *Earth Sci. Rev.* 96, 327–344. doi:10.1016/j.earscirev.2009.07.005

Berz, G. (1988). List of major natural disasters, 1960–1987. *Nat. Hazards* 1, 97–99. doi:10.1007/BF00168223

Bird, J. F., and Bommer, J. J. (2004). Earthquake losses due to ground failure. *Eng. Geol.* 75, 147–179. doi:10.1016/j.enggeo.2004.05.006

Bommer, J. J., and Rodriguez, C. E. (2002). Earthquake-induced landslides in Central America. *Eng. Geol.* 63, 189–220. doi:10.1016/S0013-7952(01)00081-3

Cetin, K. O., Der Kiureghian, A., and Seed, R. B. (2002). Probabilistic models for the initiation of seismic soil liquefaction. *Struct. Saf.* 24, 67–82. doi:10.1016/S0167-4730(02)00036-X

Coburn, A. W., and Spence, R. J. S. (1992). *Earthquake Protection*. Wiley. Available at: http://books.google.de/books?id=8L83AQAAIAAJ

Daniell, J. E. (2011). *Damaging Volcanoes Database 2010 – The Year in Review: CEDIM Research Report 2011-02*. Available at: http://www.cedim.de/download/CATDAT_VOLC_Data_-_1st_Annual_Review_-_2010_-_James_Daniell_-_02.02.2011.pdf

Daniell, J. E., Khazai, B., Wenzel, F., and Vervaeck, A. (2011a). The CATDAT damaging earthquakes database. *Nat. Hazards Earth Syst. Sci.* 11, 2235–2251. doi:10.5194/nhess-11-2235-2011

Daniell, J. E., Vervaeck, A., and Wenzel, F. (2011b). "A timeline of the socio-economic effects of the 2011 Tohoku earthquake with emphasis on the development of a new worldwide rapid earthquake loss estimation procedure," in *Australian Earthquake Engineering Society 2011 Conference* (Barossa Valley, Australia).

Daniell, J. E., Wenzel, F., Khazai, B., and Vervaeck, A. (2011c). "A country-by-country building inventory and vulnerability index for earthquakes in comparison to historical CATDAT damaging earthquakes database losses," in *Australian Earthquake Engineering Society 2011 Conference* (Barossa Valley, Australia).

Daniell, J. E., and Love, D. (2010). "The socio-economic impact of historic Australian earthquakes," in *Australian Earthquake Engineering Society 2010 Conference* (Perth, WA), 8.

Daniell, J. E., Schäfer, A., Wenzel, F., and Khazai, B. (2013). "Worldwide Losses from earthquake induced secondary effects and their implications for D-A-CH and insurance (in German), beitragsnr. 138, 13," in *D-A-CH Tagung für*

Erdbebeningenieurwesen und Baudynamik (D-A-CH 2013), eds C. Adam, R. Heuer, W. Lenhardt, and C. Schranz (Wien, Österreich), 29–30.

Daniell, J. E., and Vervaeck, A. (2011). *The 2011 Tohoku Earthquake – CATDAT Situation Reports 1-52*. Available at: http://Earthquake-Report.com

Daniell, J. E., and Wenzel, F. (2014). "The production and implementation of socioeconomic fragility functions for use in rapid worldwide earthquake loss estimation," in *Paper No. 490, 15th ECEE European Conference of Earthquake Engineering* (Istanbul, Turkey).

Disaster Prevention Council, and Tokyo Metropolitan Government. (1985). *Report on Earthquake Damage Estimation in Tama District*. Tokyo, Japan: Disaster Prevention Council Report.

Dismuke, J. N., and Mote, T. I. (2012). "Approximate deaggregation method for determination of design earthquake magnitudes for Australia," in *Proceedings of the 15th World Conference of Earthquake Engineering* (Lisbon, Portugal).

Fire Disaster Management Agency Japan (FDMA). (2011). *2011 Tohoku Earthquake – Update of Damages – 1st-148th Version – 11th March 2011 to 9th September 2013 (in Japanese)*. Available at: http://www.fdma.go.jp/bn/2013/detail/691.html

Flores, R. A. (1960). "Engineering aspects of Chilean earthquakes of May 21 and 22, 1960," in *Proceedings of the 2nd World Conference of Earthquake Engineering* (Japan).

Fuji, Y., and Satake, K. (2013). Slip distribution and seismic moment of the 2010 and 1960 Chilean earthquakes inferred from Tsunami waveforms and coastal geodetic data. *Pure Appl. Geophys.* 170, 1493–1509. doi:10.1007/s00024-012-0524-2

Global Disaster Alert and Coordination System (GDACS). (2011). *GDACS Alert for the Tohoku Earthquake*. Available at: http://www.gdacs.org/report.aspx?eventtype=EQ&eventid=104706

Goda, K., Mai, P., Yasuda, T., and Mori, N. (2014). Sensitivity of tsunami wave profiles and inundation simulations to earthquake slip and fault geometry for the 2011 Tohoku earthquake. *Earth Planets Space* 66, 1–20.

Godt, J., Sener, B., Verdin, K., Wald, D. J., Earle, P. S., Harp, E., et al. (2008). "Rapid assessment of earthquake-induced landsliding," in *Proceedings of the First World Landslide Forum* (Tokyo, Japan: United Nations University).

Goh, A. T. C., and Goh, S. H. (2007). Support vector machines: their use in geotechnical engineering as illustrated using seismic liquefaction data. *Comput. Geotech.* 34, 410–421. doi:10.1016/j.compgeo.2007.06.001

Iida, K., Cox, D. C., and Pararas-Carayannis, G. (1967). *Preliminary Catalog of Tsunamis Occurring in the Pacific Ocean, HIG-67-10*. Honolulu, Hawaii: Hawaii Institute of Geophysics, University of Hawaii, 275.

Ikeda, T., and Nakabayashi, K. (1996). "Relevant analysis of human casualties and building damage of the earthquake disaster (in Japanese)," in *Social Safety Society Proceedings*. Shizuoka, Japan, 163–166.

InaSAFE. (2013). *InaSAFE Documentation – Release 1.2.0*. Available at: http://inasafe.org/

Instituto Hidrografico de la Armada. (1982). *Maremotos en la costa de Chile. Instituto Hidrografico de la Armada, IHA Pub 3016*. Valparaiso, Chile: Instituto Hidrografico de la Armada, 48.

Jibson, R. W. (2007). Regression models for estimating coseismic landslide displacement. *Eng. Geol.* 91, 209–218. doi:10.1016/j.enggeo.2007.01.013

Kawasumi, H. (1954). Intensity and magnitude of shallow earthquakes. *Publ. Du Bur. Cent. Séismol. Int. A Trav. Sci.* 19, 99–114.

Keefer, D. K. (1984). Landslides caused by earthquakes. *Geol. Soc. Am. Bull.* 95, 406–421. doi:10.1130/0016-7606(1984)95<406:LCBE>2.0.CO;2

Keefer, D. K. (2002). Investigating landslides caused by earthquakes – a historical review. *Surv. Geophys.* 23, 473–510. doi:10.1023/A:1021274710840

Khazai, B., Daniell, J. E., and Wenzel, F. (2011). The March 2011 Japan earthquake – analysis of losses, impacts, and implications for the understanding of risks posed by extreme events. *Technikfolgenabschätzung Theorie Prax.* 20, 22–33. Available at: http://www.tatup-journal.de/downloads/2011/tatup113_khua11a.pdf

Khazai, B., and Sitar, N. (2004). Evaluation of factors controlling earthquake-induced landslides caused by Chi-Chi earthquake and comparison with the Northridge and Loma Prieta events. *Eng. Geol.* 71, 79–95. doi:10.1016/S0013-7952(03)00127-3

Kramer, S. L. (1996). *Geotechnical Earthquake Engineering*. Upper Saddle River, NJ: Prentice Hall.

Lander, J. F., Lockridge, P. A., and Kozuch, M. J. (1993). *Tsunamis Affecting the West Coast of the United States, 1806–1992, KGRD no. 29, National Oceanic and Atmospheric Administration*. Boulder, CO: National Geophysical Data Center, 242.

Lazo Hinrichs, R. G. (2008). *Estudio de los Daños de los Terremotos del 21 y 22 de Mayo de 1960*. Masters thesis.

Lockridge, P. (1985). *Tsunamis in Peru-Chile*. Boulder, CO: National Geophysical Data Center (NOAA).

Mai, M., and Beroza, G. (2002). A spatial random field model to characterize complexity in earthquake slip. *J. Geophys. Res. Solid Earth* 107, ESE 10-1–ESE 10-21. doi:10.1029/2001JB000588

Mancilla, L., and Mardones, L. (2010). *El terremoto de 1960 en Castro, Imprenta Austral*. Chile: Imprenta Austral de Temaco.

Marano, K. D., Wald, D. J., and Allen, T. I. (2010). Global earthquake casualties due to secondary effects: a quantitative analysis for improving rapid loss analyses. *Nat. Hazards* 52, 319–328. doi:10.1007/s11069-009-9372-5

Miles, S. B., and Keefer, D. K. (2009). Evaluation of CAMEL – comprehensive areal model of earthquake induced landslides. *Eng. Geol.* 104, 1–15. doi:10.1016/j.enggeo.2008.08.004

MunichRe. (1998). *World Map of Natural Hazards*. Munich Reinsurance Company.

Nadim, F., Kjekstad, O., Peduzzi, P., Herold, C., and Jaedicke, C. (2006). Global landslide and avalanche hotspots. *Landslides* 3, 159–173. doi:10.1007/s10346-006-0036-1

National Police Agency Japan (NPA). (2011). *Damage Situation and Police Countermeasures Associated with 2011 Tohoku District – Off the Pacific Ocean Earthquake*. Available at: http://www.npa.go.jp/archive/keibi/biki/higaijokyo_e.pdf

NGDC/NOAA. (2010). *Significant Earthquakes Database & Significant Tsunami Database*. Available at: http://ngdc.noaa.gov

Ohta, H., and Goto, N. (1985). *Earthquake Loss Estimation Model: Vulnerability Analysis on a Household Level (in Japanese). Working Paper*. Tokyo, Japan: Scientific Foundation.

Ohta, Y., Goto, N., and Ohashi, H. (1983). An empirical construction of equations for estimating number of victims by earthquakes. *Zisin II* 36, 463–466. doi:10.4294/zisin1948.36.3_463

Okada, Y. (1985). Surface deformation due to shear and tensile faults in a half-space. *Bull. Seismol. Soc. Am.* 752, 1135–1154.

Osaka Prefecture. (1997). *Osaka Earthquake Damage Estimation: Survey Report (in Japanese)*. Osaka, Japan: Osaka Prefectural Government.

Parker, R. (2013). *Hillslope Memory and Spatial and Temporal Distributions of Earthquake-Induced Landslides*. Doctoral dissertation, Durham University.

Rodrıguez, C. E., Bommer, J. J., and Chandler, R. J. (1999). Earthquake-induced landslides: 1980–1997. *Soil Dyn. Earthquake Eng.* 18, 325–346.

Rothe, J. P. (1969). *The Seismicity of the Earth 1953-1965, United National Educational, Scientific, and Cultural Organization (UNESCO)*. Paris, France: UNESCO, 312.

Saint-Amand, P. (1961). *Los Terremotos de Mayo, Chile 1960*. China Lake, CA: Michelson Laboratories, US Naval Ordinance Test Station, 40. Technical Article 14, NOTS TP 2701.

Saitama Prefecture. (1982). *Earthquake Damage Estimation: Research Report (in Japanese)*. Japan: Saitama Government Report, Saitama Prefecture, 1–356.

Scawthorn, C., Eidinger, J. M., and Schiff, A. (eds) (2005). *Fire Following Earthquake*, Vol. 26. USA: American Society of Civil Engineers.

Schaefer, A., Daniell, J., and Wenzel, F. (2015). *M9 Returns – Towards a Pan-Pacific Tsunami Hazard Risk Model*. Sydney: Australian Earthquake Engineering Society.

Schäfer, A. M., and Wenzel, F. (2017). Tsupy: computational robustness in Tsunami hazard modelling. *Comput. Geosci.* 102, 148–57. doi:10.1016/j.cageo.2017.02.016

Seed, H. B., and Idriss, I. (1971). Simplified procedure for evaluating soil liquefaction potential. *J. Soil Mech. Found. Div.* 97, 1249–1273.

Shi-zhong, H. (2010). Newly collected report on the 1933 Diexi Earthquake published in Jialingjiang Daily. *Earthquake Res. Sichuan* 3, 7.

Slingsby, A., Daniell, J. E., Dykes, J., and Wood, J. (2011). "Sharing insights on the impact of natural disasters using Twitter," in *European Geosciences Union (EGU) (Ed.), Geophysical Research Abstracts*, Vol. 13 (Göttingen, Germany: Copernicus Publications), EGU2011–9171. Available at: https://www.researchgate.net/publication/258434425_Sharing_insights_on_the_impact_of_natural_disasters_using_Twitter

Soloviev, S. L., and Go, C. N. (1975). *A Catalogue of Tsunamis on the Eastern Shore of the Pacific Ocean [Dates Include 1513–1968]*. Moscow: Academy of Sciences of the USSR, Nauka Publishing House, 204. (Canadian Translation of Fisheries and Aquatic Sciences no. 5078, 1984).

Talley, H. C. Jr., and Cloud, W. K. (1962). *United States Earthquakes 1960*. US Department of Commerce & Coast and Geodetic Survey, U.S. Government Printing Office: Washington.

Tazieff, H. (1962). *Quand la terre tremble (When the Earth Shakes)*. Paris: Edition Fayard, 11–100.

Tokyo Metropolitan Government. (1978). *Report on Earthquake Damage Estimation in the Ward Districts of Tokyo: Disaster Prevention Council Report*. Tokyo, Japan.

TsuDAT. (2013). *Tsunami Data Access and Modelling Tool (TsuDAT)*. Available at: https://github.com/AIFDR/tsudat2

U.S. Coast and Geodetic Survey. (1962). *Earthquakes in the United States in 1960*. Technical Report.

U.S. Geological Survey (USGS). (2011, 2013). *PAGER – Prompt Assessment of Global Earthquakes for Response*. Available at: http://earthquake.usgs.gov/earthquakes/pager/

World Agency of Planetary Monitoring and Earthquake Risk Reduction. (2013). *QLARM*. Available at: http://www.wapmerr.org/qlarm.asp

Yasuda, S., and Harada, K. (2014). "Measures developed in Japan after the 1964 Niigata earthquake to counter the liquefaction of soil," in *10NCEE, Paper No. 1778, Frontiers of Earthquake Engineering,* July 21–25, 2014, Anchorage, Alaska.

Ye, Y., and Okada, N. (2001). "Improving management of urban earthquake disaster risks," in *Earthquake Engineering Frontiers in the New Millennium*, eds B. F. Spencer Jr. and Y. X. Hu (Netherlands: Swets and Zeitlinger), 113–118.

Conflict of Interest Statement: The authors declare that the research was conducted in the absence of any commercial or financial relationships that could be construed as a potential conflict of interest.

Copyright © 2017 Daniell, Schaefer and Wenzel. This is an open-access article distributed under the terms of the Creative Commons Attribution License (CC BY). The use, distribution or reproduction in other forums is permitted, provided the original author(s) or licensor are credited and that the original publication in this journal is cited, in accordance with accepted academic practice. No use, distribution or reproduction is permitted which does not comply with these terms.

frontiers in Built Environment

ORIGINAL RESEARCH
published: 02 June 2015
doi: 10.3389/fbuil.2015.00006

Empirical assessment of non-linear seismic demand of mainshock–aftershock ground-motion sequences for Japanese earthquakes

Katsuichiro Goda[1]*, *Friedemann Wenzel*[2] *and Raffaele De Risi*[1]

[1] Department of Civil Engineering, University of Bristol, Bristol, UK, [2] Geophysical Institute, Karlsruhe Institute of Technology, Karlsruhe, Germany

This study investigates the effects of earthquake types, magnitudes, and hysteretic behavior on the peak and residual ductility demands of inelastic single-degree-of-freedom systems and evaluates the effects of major aftershocks on the non-linear structural responses. An extensive dataset of real mainshock–aftershock sequences for Japanese earthquakes is developed. The constructed dataset is large, compared with previous datasets of similar kinds, and includes numerous sequences from the 2011 Tohoku earthquake, facilitating an investigation of spatial aspects of the aftershock effects. The empirical assessment of peak and residual ductility demands of numerous inelastic systems having different vibration periods, yield strengths, and hysteretic characteristics indicates that the increase in seismic demand measures due to aftershocks occurs rarely but can be significant. For a large mega-thrust subduction earthquake, a critical factor for major aftershock damage is the spatial occurrence process of aftershocks.

Keywords: peak ductility, residual ductility, Japanese earthquakes, mainshock and aftershocks, 2011 Tohoku earthquake

OPEN ACCESS

Edited by:
Nikos D. Lagaros, National Technical University of Athens, Greece

Reviewed by:
Carmine Galasso, University College London, UK
Bing Qu, California Polytechnic State University, USA

***Correspondence:**
Katsuichiro Goda, Queen's Building, University Walk, Bristol BS8 1TR, UK
katsu.goda@bristol.ac.uk

Specialty section:
This article was submitted to Earthquake Engineering, a section of the journal Frontiers in Built Environment

Received: *10 March 2015*
Accepted: *18 May 2015*
Published: *02 June 2015*

Citation:
Goda K, Wenzel F and De Risi R (2015) Empirical assessment of non-linear seismic demand of mainshock–aftershock ground-motion sequences for Japanese earthquakes. Front. Built Environ. 1:6. doi: 10.3389/fbuil.2015.00006

Introduction

Ground-motion records are the main source of uncertainty in predicting non-linear responses of structures subjected to earthquake loading. Key record features can be represented by amplitude, duration, frequency content, and their temporal evolution. They are influenced by physical environments and characteristics, such as earthquake type (crustal/interface/inslab), moment magnitude (M_w), faulting mechanism, stress drop, seismic wave propagation, and local site condition (Stein and Wysession, 2003). In the last decade, observation networks of strong motion around the world have been expanded significantly, and numerous recordings have been made available publicly, e.g., K-NET/KiK-net in Japan, TSMIP in Taiwan, GeoNet in New Zealand, and ITACA in Italy. These databases facilitate the development of new generations of empirical ground-motion prediction equations that are essential for probabilistic seismic hazard analysis (e.g., Morikawa and Fujiwara, 2013). Moreover, they are useful for developing inelastic seismic demand prediction models (e.g., Ruiz-García and Miranda, 2003; Vamvatsikos and Cornell, 2004; Federal Emergency Management Agency, 2005; Iervolino and Cornell, 2005). The integration of seismic hazard and ground-motion models with seismic vulnerability models results in a comprehensive performance-based earthquake

engineering (PBEE) framework that accounts for main sources of uncertainty related to seismic damage assessment and loss estimation (Cornell et al., 2002; Goulet et al., 2007).

Recent earthquake disasters highlight that a cluster of major aftershocks causes incremental damage to structures whose seismic capacities may have been reduced by a mainshock and poses significant risk to evacuees and residents in a post-disaster situation. For instance, the 2011 Christchurch aftershock sequence (notably the 22 February 2011 M_w6.2 event), initiated by the 2010 M_w7.0 Darfield event, caused extensive damage to buildings and infrastructure in downtown Christchurch (Smyrou et al., 2011). After the 2011 M_w9.0 Tohoku earthquake in Japan, numerous aftershocks as large as M_w7.9 were observed, and additional structural damage and disruption to utility services were caused by major aftershocks (Goda et al., 2013). In Indonesia, regional seismic activities have been heightened since the 2004 M_w9.3 Sumatra earthquake (Shcherbakov et al., 2013). Numerous moderate-to-large earthquakes occurred and caused major seismic damage to structures in Sumatra (e.g., 2005 M_w8.6 and 2007 M_w8.5 events). To evaluate seismic responses of different structures (i.e., steel, concrete, and wood-frame buildings) due to mainshock–aftershock (MS–AS) sequences, various models, such as single-degree-of-freedom (SDOF) and multi-degree-of-freedom systems with different hysteretic models, have been used (e.g., Li and Ellingwood, 2007; Moustafa and Takewaki, 2010; Goda, 2012; Ruiz-García, 2012; Zhai et al., 2013). The developed seismic demand models for MS–AS sequences can be incorporated into the PBEE framework to account for seismic damage and loss caused by aftershocks (Salami and Goda, 2014).

In Japan, national and regional strong-motion networks, K-NET/KiK-net[1] and SK-net[2], have been established aftermath the 1995 Kobe earthquake. The availability of strong-motion records in Japan has increased drastically and numerous invaluable data have been recorded. One of the events that are extremely well-recorded is the 2011 M_w9.0 Tohoku earthquake; more than 1000 high-quality recordings are available from these networks for ground motion and seismic vulnerability studies. Because numerous aftershocks were triggered by the 11 March 2011 mainshock, an extensive set of MS–AS sequence data can be developed. The new dataset for MS–AS sequences in Japan offers a new opportunity to compare the non-linear seismic demand potential due to different earthquake types (e.g., crustal versus interface events, which are often distinguished in seismic design codes). Moreover, for the 2011 Tohoku mainshock, the aftershock effects can be evaluated from not only temporal/sequential but also spatial viewpoints of the major aftershock occurrence, providing with valuable insights into the aftershock hazard processes.

The main objectives of this study are to investigate the non-linear seismic demand potential of inelastic SDOF systems due to real MS–AS sequences in Japan, and to establish an empirical benchmark for the non-linear seismic demand assessment for Japanese earthquakes. To draw generic conclusions, 112 inelastic SDOF systems having four intact vibration periods ($T = 0.2$, 0.5, 1.0, and 2.0 s), seven yield strengths, and four hysteretic characteristics (which are approximated by the Bouc–Wen model; Wen, 1976; Foliente, 1993; Goda and Atkinson, 2009), are considered. The yield strengths of the inelastic systems are expressed in terms of spectral acceleration, and their values are selected such that the considered yield capacities broadly represent those of typical building stock in Japan (Nagato and Kawase, 2004). As the non-linear response metrics, peak and residual ductility demands are focused upon. The latter parameter is relevant for PBEE-based seismic performance assessment where excessive residual displacements prohibit residents from reoccupation and result in demolishing non-collapse buildings (Ruiz-García and Miranda, 2006; Ramirez and Miranda, 2012). It is noted that the investigations carried out in this study (constant strength approach) differ from the constant R approach (where R is the strength reduction factor; Ruiz-García and Miranda, 2003), as carried out in the previous investigations (Goda and Atkinson, 2009; Goda, 2012). In the constant R approach, seismic excitation levels of ground-motion records are kept constant with respect to the yield strength of a structural system, whereas in the constant strength approach, the yield strength of a structural system is varied relative to a set of selected ground-motion records (Galasso et al., 2012). A novelty of this study is that an extensive dataset of as-recorded MS–AS sequences for Japanese earthquakes is compiled and employed for the non-linear seismic demand potential evaluation. The new dataset contains 531 MS–AS sequences from 20 mainshock events (note: each sequence consists of two horizontal components). The statistical analysis is performed to relate the non-linear seismic demand potential and aftershock effects to key seismological parameters. Among the 531 sequences, 304 sequences are from the 2011 Tohoku event. This facilitates a rigorous assessment of the aftershock effects with regard to the spatial distribution of major aftershocks. This paper is organized as follows. First, the construction of the real MS–AS sequence database based on the K-NET, KiK-net, and SK-net is explained, which is the main innovative feature of this study. Second, non-linear structural models with Bouc–Wen hysteresis are introduced, and non-linear structural responses due to the constructed real MS–AS sequence records for Japanese earthquakes are compared in terms of earthquake type, magnitude, and hysteretic behavior. Subsequently, the aftershock effects on the non-linear seismic demand are discussed by focusing upon the key seismological parameters for the increased ductility demands. Moreover, spatial aspect of the aftershock effects is evaluated for the 2011 Tohoku sequences.

Mainshock–Aftershock Sequence Records for Japanese Earthquakes

A new ground-motion database *2012 KKiKSK* is developed for the purpose of ground-motion prediction studies. It combines recordings from the K-NET, KiK-net, and SK-net up to the end of 2012. Records from different networks are first integrated by matching event information (occurrence time, location, earthquake size, etc.). Subsequently, duplicates and erroneous data (typically, SK-net recordings that contain spurious spikes, discontinuities, and base-line shift) are identified and removed from the database. A set of broad record selection criteria is then applied to determine records that are included in the database: (i) minimum Japan

[1]http://www.kyoshin.bosai.go.jp/
[2]http://www.sknet.eri.u-tokyo.ac.jp/

Meteorological Agency (JMA) magnitude M_{JMA} is 3.0; (ii) maximum focal depth is 500 km; (iii) maximum hypocentral distance is 1500 km; (iv) minimum horizontal peak ground acceleration (PGA) is 1.0 cm/s^2; and (v) at least 10 records are available for each seismic event (satisfying the preceding four conditions). This has led to a set of 555,750 records from 6261 earthquakes. Further checks are conducted to improve the quality of the database.

Subsequently, metadata, such as M_w, fault mechanism (normal/reverse/strike-slip), and earthquake type (crustal/inslab/interface), are assigned to seismic events with M_{JMA} greater than or equal to 5.5 individually by referring to the Harvard Centroid Moment Tensor (CMT) solutions[3] and the F-net CMT solutions[4]. In calculating representative source-to-site distances for moderate-to-large earthquakes, finite fault plane information for 57 events are gathered from the Geospatial Institute Authority of Japan webpages[5] and the EIC/NGY seismological notes by Kikuchi and Yamanaka[6,7]. Using the finite fault plane models, rupture distance (i.e., shortest distance from a site to a fault plane) is calculated. Note that the majority of significant earthquakes are associated with the finite fault plane models (exceptions include moderate-to-large events that occur off-shore regions). Site information for the K-NET and KiK-net is obtained from the NIED webpages (see text footnote 1); for the K-NET, relocation information is taken into account. For assigning site information to the SK-net sites, an approach adopted by Goda and Atkinson (2010) is implemented, which combines various kinds of site information, such as geomorphological classification, micro-tremor measurements, and borehole-logging. By reflecting the availability of site information, usability of record components is determined for the SK-net. In total, the usable record set contains 528,022 records from 6259 earthquakes. Individual components in the record set are processed uniformly (i.e., tapering, zero-padding, and band-pass filtering; Boore, 2005). Various elastic ground-motion parameters, such as PGA, peak ground velocity, and 5%-damped elastic response spectra at vibration periods ranging from 0.05 to 10.0 s, are computed using the processed record components.

The development of MS–AS record sequences based on the *2012 KKiKSK* database is carried out in two stages. In the first stage, the record database is downsized by eliminating weak ground motions. The record selection criteria that are applied are: (i) $M_w \geq 5.0$, (ii) focal depth is less than 150 km, (iii) average shear-wave velocity in the uppermost 30 m V_{S30} is between 100 and 1500 m/s, (iv) source-to-site distance is less than 300 km, and (v) average PGA of the two horizontal components (geometric mean) is greater than 75 cm/s^2 (such a criterion is typically applied in inelastic demand estimation studies; Ruiz-García and Miranda, 2003; Goda and Atkinson, 2009). The application of the above five criteria has resulted in 5000 records, consisting of 367 events.

In the second stage, a list of MS–AS sequences is developed using the reduced dataset of 5000 records. Initially, a candidate mainshock, or reference event, is identified as event having $M_w > 5.9$. For a given reference event, a time-space window is applied to identify possible candidate aftershock events; the length of the time window is set to 100 days before and after the date of occurrence of the reference event (note: for the 2011 Tohoku mainshock, the post-event time window is extended to 600 days), while the spatial window is circular in shape around the epicenter of the reference event and the radius is calculated by d (km) $= 0.02 \times 10^{0.5 \times \min(M_{w,ref}, 8.5)}$ (Kagan, 2002), where $M_{w,ref}$ is the moment magnitude of the reference event (i.e., initially $M_{w,ref}$ equals the magnitude of the candidate mainshock and is changed to magnitudes of reference events). In addition, the difference of focal depths of the reference event and a candidate aftershock is used to determine inclusion/exclusion of the candidate aftershock by considering a threshold of 30 km. The above search process is repeated for all events included in the identified MS–AS sequence; after the completion of the search process for the candidate mainshock, the reference event is changed to one of the identified aftershocks, and this process is continued until all candidate aftershocks are examined exhaustively. For instance, the process starts with a mainshock, and then when additional aftershock events are identified, they are included in the MS–AS sequence. The same screening process (i.e., space-time window) is applied to all events in the sequence (note: the size of the sequence usually grows and the radius of the spatial window varies). This process has led to the identification of 20 MS–AS sequences. Subsequently, for each sequence, eligible records are reorganized on a station basis, and time-history data for individual sequences are constructed by inserting 30 s of zeros between records. This has resulted in 531 MS–AS record sequences. In each sequence, an event with the largest magnitude is designated as *mainshock*, whereas an event with the second largest M_w is determined as *major aftershock*, consistent with the definitions adopted by Goda (2012). A summary of the mainshock characteristics of the identified 20 sequences is given in **Table 1**. The MS–AS sequences for the 2011 Tohoku earthquake comprise of about 57% of the database. This database is considered for record selection to be used in empirical assessment of inelastic seismic demand potential due to real MS–AS sequences.

Figure 1 shows the locations of mainshocks, magnitude–distance plots of mainshocks and major aftershocks, and histogram of V_{S30} for the sites included in the database. In the map (**Figure 1A**), the sequences are divided into four subsets: 2011 Tohoku event (304 sequences), 2003 Tokachi event (36 sequences), crustal events (122 sequences), and interface/inslab events (69 sequences, excluding those for the 2011 Tohoku and 2003 Tokachi events). The magnitudes for the 2011 Tohoku and 2003 Tokachi events are significantly greater than other events (**Table 1**), whereas the magnitudes for crustal events and interface/inslab events are broadly similar (in the range between M_w6 and M_w7) but their locations are different (i.e., on-shore versus off-shore, indicating different propagation paths). This classification is used for comparing the elastic and inelastic seismic demands of different earthquake types in the following. The magnitude–distance plots indicate that the magnitudes of

[3]http://www.globalcmt.org/
[4]http://www.fnet.bosai.go.jp/
[5]http://www.gsi.go.jp/bousai.html
[6]http://www.eri.u-tokyo.ac.jp/sanchu/Seismo_Note/
[7]http://www.seis.nagoya-u.ac.jp/sanchu/Seismo_Note/

TABLE 1 | Summary of the mainshock characteristics of the 20 mainshock–aftershock sequences.

Sequence ID	Date	Event type	Latitude	Longitude	Depth (km)	M_w	Number of sequences
1	1996/08/11	Crustal	38.920	140.630	10.0	5.92	1
2	1996/10/19	Inslab	31.803	131.998	22.0	6.70	4
3	1997/03/26	Crustal	31.986	130.365	10.0	6.10	11
4	2000/07/30	Crustal	33.965	139.397	10.0	6.45	1
5	2000/10/06	Crustal	35.278	133.345	10.0	6.65	3
6	2001/03/24	Inslab	34.123	132.705	50.0	6.80	3
7	2002/11/03	Inslab	38.896	142.138	39.0	6.40	1
8	2003/07/26	Crustal	38.405	141.170	6.0	6.04	10
9	2003/09/26	Interface	41.781	144.074	27.0	8.26	36
10	2004/04/04	Inslab	36.390	141.154	31.0	5.93	1
11	2004/09/05	Inslab	33.146	137.139	10.0	7.37	17
12	2004/10/23	Crustal	37.291	138.867	16.0	6.56	53
13	2004/11/29	Inslab	42.946	145.274	39.0	6.98	35
14	2005/03/20	Crustal	33.738	130.175	10.0	6.58	13
15	2007/03/25	Crustal	37.220	136.685	8.0	6.67	5
16	2007/07/16	Crustal	37.557	138.608	12.0	6.62	7
17	2008/06/14	Crustal	39.028	140.880	7.8	6.87	7
18	2010/03/14	Inslab	37.723	141.817	32.0	6.53	8
19	2011/03/11	Interface	38.103	142.860	24.4	9.08	304
20	2011/03/12	Crustal	36.985	138.597	9.3	6.30	11

A supplementary spreadsheet, which contains detailed record information of the mainshock–aftershock sequences, is provided as part of this paper.

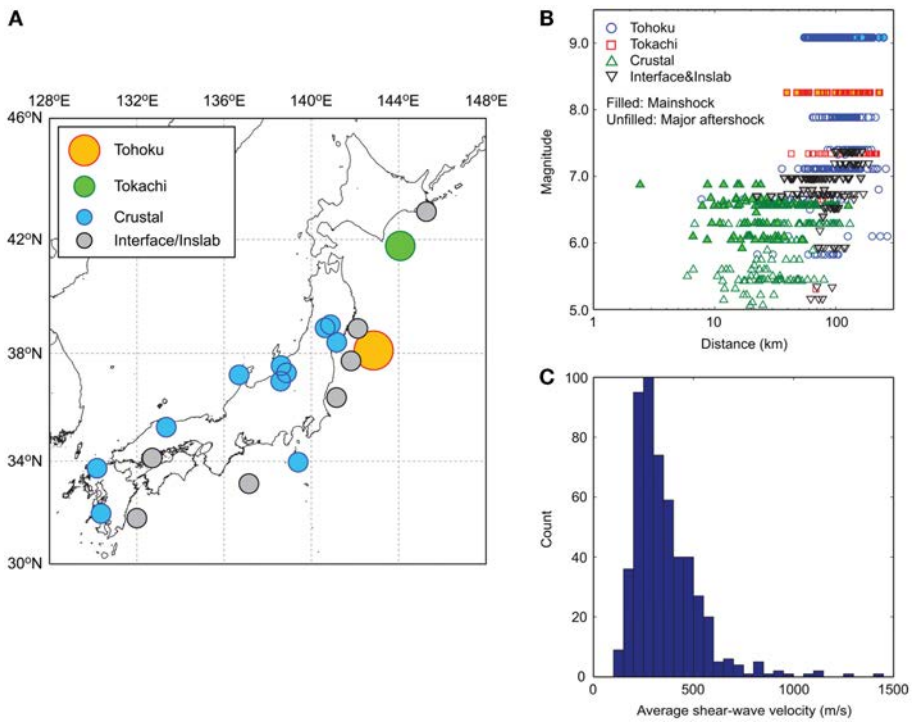

FIGURE 1 | Ground-motion data characteristics: (A) spatial distribution of mainshocks, (B) magnitude–distance plots of mainshocks and major aftershocks, and (C) histogram of average shear-wave velocity in the uppermost 30 m.

mainshocks are greater (by approximately one magnitude unit) than those of major aftershocks, which is expected and is broadly consistent with the empirical Bath's law (Shcherbakov et al., 2005). An implication of these differences is that frequency/spectral content of mainshock records and aftershock records differ significantly (on average). This is important when record scaling is implemented in seismic vulnerability assessment (e.g., incremental dynamic analysis; Goda, 2015). The histogram of V_{S30} indicates that the majority of sites included in the developed database are NEHRP site class C or D, and recordings at NEHRP site class A/B or E are rare.

Figure 2A compares the statistics (median, 16th percentile, and 84th percentile) of the 5%-damped response spectra that are calculated using the four datasets (i.e., Tohoku, Tokachi,

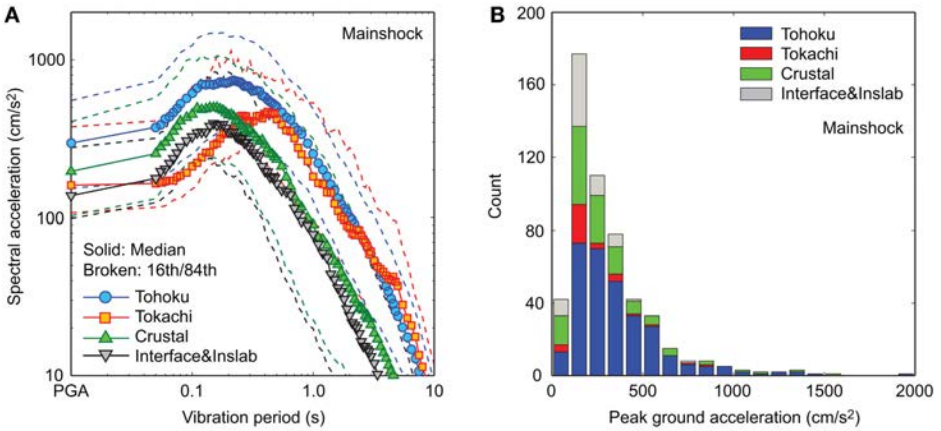

FIGURE 2 | (A) Median, 16th percentile, and 84th percentile of response spectra (mainshocks) and **(B)** histogram of average PGA (mainshocks).

Crustal, and Interface and Inslab). **Figure 2B** shows the histogram of PGA for the four datasets. Two key observations from **Figure 2A** are: (i) at short vibration periods ($T < 0.5$ s), response spectra for the Tohoku dataset are greater than the other three, whereas (ii) at moderate-to-long vibration periods ($T > 0.5$ s), response spectra for the Tohoku and Tokachi datasets are similar and are significantly greater than those for the Crustal and Interface and Inslab datasets. The seismic intensity parameters (for example, PGA as shown in **Figure 2B**) vary within the dataset significantly. Although the direct comparisons of the response spectra are not readily applicable due to different record features of these datasets (**Figure 1**), the former observation can be attributed to the complex source process of the 2011 Tohoku mainshock with high stress drop and low attenuation path (Goda et al., 2013). The latter can be explained by the differences of the earthquake magnitude (i.e., M_w8–9 versus M_w6–7; the source spectra tend to contain richer low-frequency content with increasing magnitude; Stein and Wysession, 2003). The important point is that the damage potential of ground-motion records can be associated with physical features of the source and path effects, and the developed database for MS–AS sequences is useful for investigating the effects of such features on the inelastic seismic demand statistically. This is the main focus of the subsequent sections.

Bouc–Wen Hysteretic Model

Hysteretic features of structures significantly affect the assessment of non-linear damage potential in a complex way and are important for inelastic seismic demand estimation. The Bouc–Wen model facilitates the flexible hysteresis representation, including degradation and pinching. In normalized displacement space, the equations of motion can be expressed as:

$$\ddot{\mu} + 2\xi\omega\dot{\mu} + \alpha\omega^2\mu + (1-\alpha)\omega^2\mu_z = -\ddot{u}_g(t)/u_y$$
$$\dot{\mu}_z = \frac{h(\mu_z,\varepsilon_n)}{1+\delta_\eta\varepsilon_n}[\dot{\mu} - (1+\delta_\nu\varepsilon_n)(\beta|\dot{\mu}||\mu_z|^{n-1}\mu_z + \gamma\dot{\mu}|\mu_z|^n)]$$

$$h(\mu_z,\varepsilon_n) = 1 - \zeta_s(1-e^{-p\varepsilon_n})\exp \times\left(-\left(\frac{\mu_z sgn(\dot{\mu}) - q/[(1+\delta_\nu\varepsilon_n)(\beta+\gamma)]^{1/n}}{(\lambda+\zeta_s[1-e^{-p\varepsilon_n}])(\psi+\delta_\psi\varepsilon_n)}\right)^2\right) \quad (1)$$
$$\dot{\varepsilon}_n = (1-\alpha)\dot{\mu}\mu_z$$

where μ and μ_z are the displacement and hysteretic displacement, respectively, normalized by the yield displacement capacity of an inelastic SDOF system u_y (i.e., $\mu = u/u_y$ and $\mu_z = z/u_y$, in which u and z are the displacement and hysteretic displacement, respectively); a dot represents the differential operation with respect to time; ξ is the damping ratio; ω is the natural vibration frequency (rad/s); $\ddot{u}_g(t)$ is the ground acceleration time-history; $h(\mu_z,\varepsilon_n)$ is the pinching function; ε_n is the normalized hysteresis energy; α, β, γ, and n are the shape parameters; δ_ν and δ_η are the degradation parameters; ζ_s, p, q, ψ, δ_ψ, and λ are the pinching parameters; and sgn(•) is the signum function. The main characteristics of the Bouc–Wen hysteretic systems are defined by the second relationship in Eq. 1, where non-linear restoring force is a function of the imaginary hysteretic displacement. More detailed explanations of the Bouc–Wen parameters can be found in Foliente (1993).

Inelastic seismic demand potential can be quantified using various damage measures. For the case of inelastic SDOF systems, choice of damage measures can be reduced to a few popular ones, such as peak ductility demand and residual ductility demand (Ruiz-García and Miranda, 2003, 2006). The peak ductility demand μ_{max} is defined as $\mu_{max} = \max(|\mu(t)|)$ for all t, while the residual ductility demand μ_{res} is defined as $\mu_{res} = \mu(t=\infty)$. For a given ground-motion record, μ_{max} can be evaluated for a combination of the natural vibration period T ($=2\pi/\omega$) and the yield displacement capacity u_y. For convenience, the yield displacement capacity of a system is specified in terms of spectral acceleration at yielding S_{ay}, rather than spectral displacement at yielding S_{dy} [i.e., $S_{ay} = S_{dy}(2\pi/T)^2$].

In total, 112 inelastic SDOF systems (combinations of four vibration periods, seven yield strengths, and four hysteresis models) are considered for assessing the non-linear seismic demand parameters (i.e., μ_{max} and μ_{res}) subjected to the 531 MS–AS sequences. The intact vibration periods are: $T = 0.2$, 0.5, 1.0,

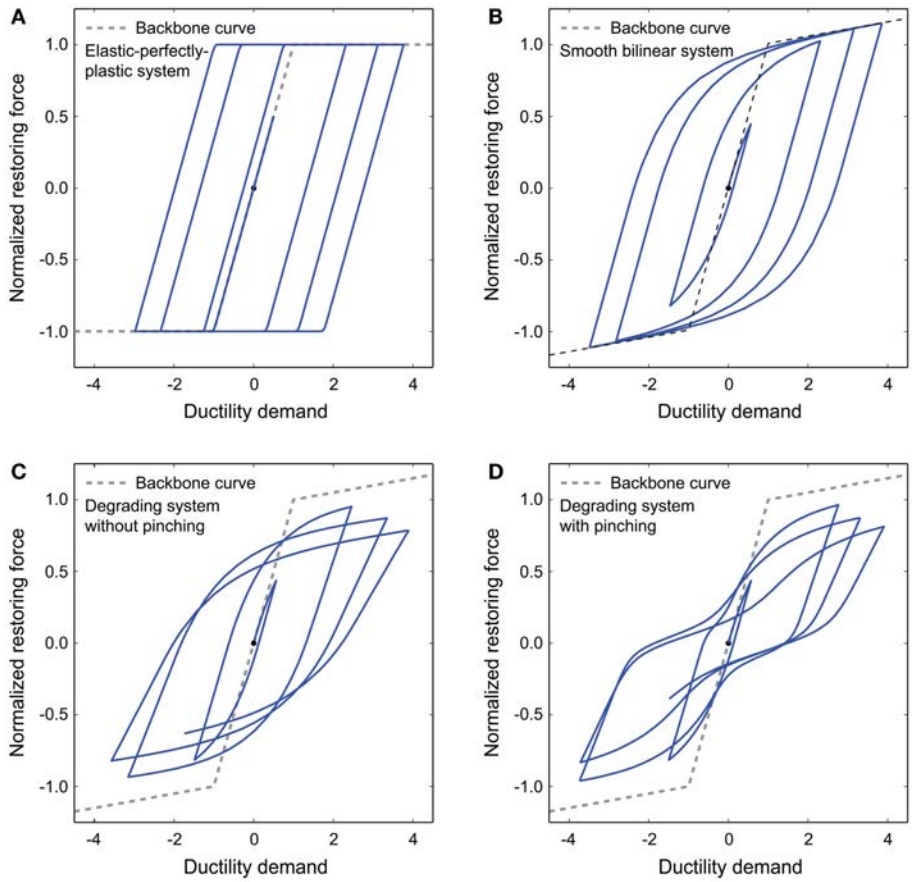

FIGURE 3 | Bouc–Wen hysteretic models: (A) elastic-perfectly plastic system, (B) smooth bilinear system, (C) degrading system, and (D) degrading system with pinching.

and 2.0 s (which cover a typical range for the first vibration mode dominated structures). The yield spectral acceleration levels are varied from 0.05 to 1.0 g: $S_{ay} = 0.05$, 0.1, 0.15, 0.2, 0.3, 0.5, and 1.0 g, which cover a range of existing structures broadly. For a given set of ground-motion records, systems with larger S_{ay} values are expected to behave linearly, while systems with smaller S_{ay} values tend to behave non-linearly. It is also instructive to compare the considered values of S_{ay} with the response spectra of the record data (**Figure 2A**). Four hysteretic models are considered: elastic-perfectly plastic (EPP) model ($\alpha = 0.0$, $\beta = \gamma = 0.5$, $n = 25$, $\delta_\nu = \delta_\eta = \zeta_s = 0.0$), smooth bilinear model ($\alpha = 0.05$, $\beta = \gamma = 0.5$, $n = 1$, $\delta_\nu = \delta_\eta = \zeta_s = 0.0$), degrading model without pinching ($\alpha = 0.05$, $\beta = \gamma = 0.5$, $n = 1$, $\delta_\nu = 0.1$, $\delta_\eta = 0.05$, $\zeta_s = 0.0$), and degrading model with pinching ($\alpha = 0.05$, $\beta = \gamma = 0.5$, $n = 1$, $\delta_\nu = 0.1$, $\delta_\eta = 0.05$, $\zeta_s = 0.9$, $p = 2.5$, $q = 0.15$, $\psi = 0.1$, $\delta_\psi = 0.005$, and $\lambda = 0.5$). **Figure 3** illustrates normalized displacement μ versus normalized restoring force $\alpha\mu + (1 - \alpha)\mu_z$, for the four Bouc–Wen hysteretic models.

Regarding the selected values of S_{ay} in this study, Nagato and Kawase (2004) estimated seismic capacities of reinforced concrete (RC), steel, and wooden structures using damage statistics from the 1995 Kobe earthquake. The methodology was to calibrate a yield base shear coefficient of an inelastic structural system (i.e., total shear force at base divided by total weight) such that the predicted damage statistics from the set of structural models approximately match actual damage statistics from the 1995 Kobe earthquake. Their results indicate: (i) for RC buildings (3-story to 12-story), natural vibration periods are around 0.3–0.8 s and average yield base shear coefficients are around 0.3–0.7 (depending on the number of stories; generally, low-rise structures have shorter vibration periods and greater base shear coefficients), (ii) for steel buildings (3-story to 5-story), natural vibration periods are around 0.5–0.9 s and average yield base shear coefficients are around 0.4–0.7, and (iii) for wooden buildings (2-story), natural vibration periods are about 0.3 s and average yield base shear coefficients are about 0.4–0.7. The drift ratios corresponding to the yield base shear coefficients are about 0.007–0.01, 0.005–0.008, and 0.01–0.015 for RC, steel, and wooden structures, respectively. It is noteworthy that the definition of the yield capacity point depends on the specifics of the adopted structural models; for instance, Nagato and Kawase (2004) used a trilinear force-deformation curve to characterize the hysteretic behavior. If a bilinear representation is considered, instead of the trilinear one, the yield point typically is located somewhere between the first and second yield points of the trilinear curve. Moreover, the calibrated structural models should be only regarded as representative, whereas actual structures have significant variability/uncertainty with regard to their yield (and ultimate) capacities;

according to Nagato and Kawase (2004), factors of 0.5 and 2.0 are possible. Based on the above information, it is thus possible to associate the inelastic SDOF systems that are considered in this study with typical buildings in Japan.

Non-Linear Seismic Demand Assessment

The main objectives of this section are: (i) to investigate the effects of earthquake types, magnitudes, and hysteretic behavior on the peak and residual ductility demands and (ii) to evaluate the effects of major aftershocks on the non-linear structural responses. In addition, spatial aspect of the aftershock effects is evaluated for the 2011 Tohoku sequences. In the following, MS–AS sequences having V_{S30} between 150 and 600 m/s (most prevalent site conditions in Japan) are focused upon (see **Figure 1C**); the total number of MS–AS sequences is 492. Initially, EPP models are used as base case and later other hysteretic models are considered (**Figure 3**). In the following, the discussion is focused upon structural systems having vibration periods of 0.2 and 1.0 s due to limitations of space. The results obtained for these two periods can be interpolated/extrapolated to structural systems with vibration periods of 0.5 and 2.0 s by taking into account input ground motion and structural characteristics. The detailed results for systems that are not presented in detail are available upon request.

Effects of Earthquake Types

First, subsets of the entire MS–AS database are focused upon to examine the similarity or dissimilarity of the non-linear seismic demand potential for different earthquake types. They are obtained by limiting sequences having the average PGA between 100 and 200 cm/s^2 (see **Figure 2B**). This criterion is selected such that homogenous datasets (to the extent possible) can be obtained for the Tohoku, Tokachi, Crustal, and Interface and Inslab events. The number of sequences is 69, 21, 38, and 36 for the Tohoku, Tokachi, Crustal, and Interface and Inslab subsets, respectively. These are considered as sufficient to obtain the statistics of the structural responses, noting that each sequence consists of two horizontal components. **Figure 4A** compares the median, 16th percentile, and 84th percentile of the response spectra for the four datasets. The result indicates that the response spectra for the Tohoku and Tokachi subsets are similar in terms of median and 16th/84th percentiles (i.e., red versus blue); the same can be observed for the Crustal and Interface and Inslab subsets (i.e., green versus black). On the other hand, the response spectra for the Tohoku and Tokachi subsets are significantly different from those for the Crustal and Interface and Inslab subsets (i.e., red/blue versus green/black). The main reason for the different elastic response spectra is the earthquake magnitude. It is noted that the differences of the response spectra in the short-period range for the Tohoku and Tokachi datasets that are observed in **Figure 2A** (by considering the entire database) disappear when more homogeneous datasets are considered.

Figure 5 shows the cumulative probability distributions of the peak and residual ductility demands of two EPP models with $T = 0.2$ s and $S_{ay} = 0.2\,g$ and with $T = 1.0$ s and $S_{ay} = 0.1\,g$ due to mainshock records only by considering the four subsets having the average PGA between 100 and 200 cm/s^2. The two systems are selected to illustrate the interesting results clearly and concisely (among many cases), and they correspond to structures with low seismic capacities among the existing building stock in Japan. The results shown in **Figure 5** indicate that both peak and residual ductility demands for the Tohoku and Tokachi subsets are greater than those for the Crustal and Interface and Inslab datasets. The differences of the non-linear structural responses are greater for $T = 1.0$ s and for residual ductility demands. The differences can be attributed to the response spectral characteristics of these subsets, shown in **Figure 4A**. Another attribute that has influence on residual ductility demand is the duration. The seismological source parameter that affects the spectral content and duration of ground motions is the earthquake magnitude.

To cover the parameter space of the calculated cases more widely, peak as well as residual ductility demand curves for EPP models ($T = 0.2$ and 1.0 s) with different yield spectral accelerations are compared in **Figure 6** by considering the four subsets. The peak ductility demand curves gradually decrease with increasing yield spectral acceleration (i.e., stronger systems), whereas the slopes of the residual ductility demand curves are steeper than those of the peak ductility demand curves. These

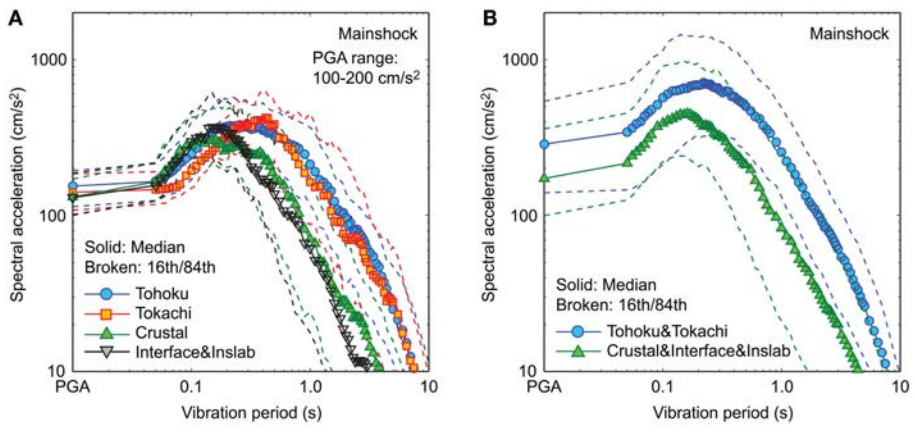

FIGURE 4 | Comparison of median, 16th percentile, and 84th percentile of response spectra (mainshocks): (A) Tohoku, Tokachi, Crustal, and Interface and Inslab datasets having average PGA between 100 and 200 cm/s^2 and (B) Tohoku and Tokachi and Crustal, Interface, and Inslab datasets.

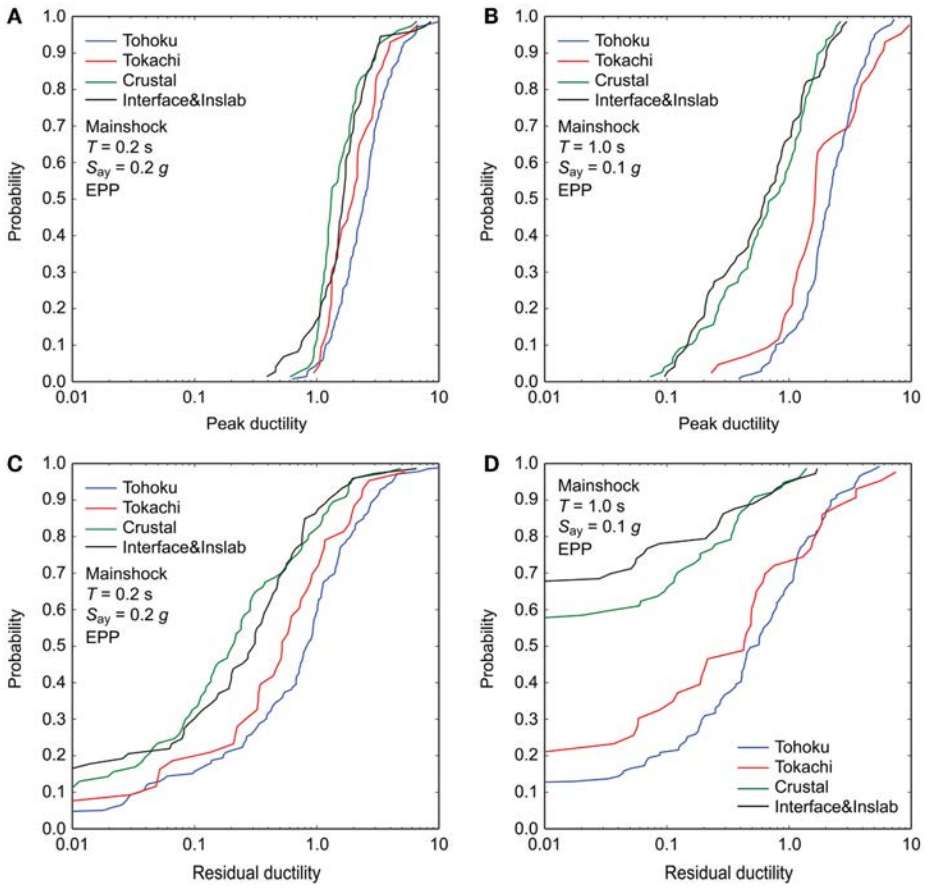

FIGURE 5 | Comparison of cumulative probability plots of ductility demands of EPP models due to mainshock records only by considering four subsets having average PGA between 100 and 200 cm/s^2: (A) peak ductility demand for $T = 0.2$ s and $S_{ay} = 0.2\,g$, (B) peak ductility demand for $T = 1.0$ s and $S_{ay} = 0.1\,g$, (C) residual ductility demand for $T = 0.2$ s and $S_{ay} = 0.2\,g$, and (D) residual ductility demand for $T = 1.0$ s and $S_{ay} = 0.1\,g$.

suggest that for the considered EPP models, seismic damage due to transient peak demands can occur for relatively moderate ground motions, whereas seismic damage due to permanent residual demands occurs when severe ground motions affect the structures. Importantly, the results confirm the similarity of peak and residual ductility demands for the Tohoku and Tokachi datasets and for the Crustal and Interface and Inslab datasets, and that the former is greater than the latter. The conclusions are applicable to different hysteretic models as well as subsets with different selection criteria.

Effects of Magnitudes and Hysteretic Behavior

Based on the above results, one of the controlling features of the ductility demands is the earthquake magnitude. To further investigate the key features that affect the non-linear seismic demand potential (i.e., hysteretic characteristics and major aftershocks), the entire MS–AS dataset is divided into two subsets according to the magnitude ranges: the Tohoku and Tokachi (T&T), or large-magnitude, dataset (319 sequences) and the Crustal, Interface, and Inslab (C&I&I), or moderate-magnitude, dataset (173 sequences). **Figure 4B** compares the median, 16th percentile, and 84th percentile of the response spectra for the two datasets. The response spectra for the large-magnitude dataset are greater than those for the moderate-magnitude dataset. The response spectral shape for the former dataset has richer long-period spectral content, in comparison with that for the latter dataset.

To inspect the results for specific systems, data points of peak/residual ductility demands and corresponding spectral acceleration values at the intact vibration periods are plotted in **Figure 7**. The considered systems are two EPP models with $T = 0.2$ s and $S_{ay} = 0.2\,g$ and with $T = 1.0$ s and $S_{ay} = 0.1\,g$ subjected to MS–AS sequences. In the figure, individual data points are displayed with small markers, whereas larger markers with a line show the median trend of the individual data. In the context of the PBEE methodology, ductility demands are the engineering demand parameters (EDP) and spectral accelerations are the intensity measures (IM). The results shown in **Figure 7** are the assessments of inelastic seismic demand (i.e., empirical IM–EDP relationships) based on cloud analysis (Jalayer and Cornell, 2009). Note that the main objective of this study is not the development of the (generic) inelastic seismic demand prediction models (e.g., constant R approach). Rather, it is focused upon identifying the key factors that result in different inelastic seismic demand predictions, and thus these parameters should be incorporated in developing such prediction models for specific structures.

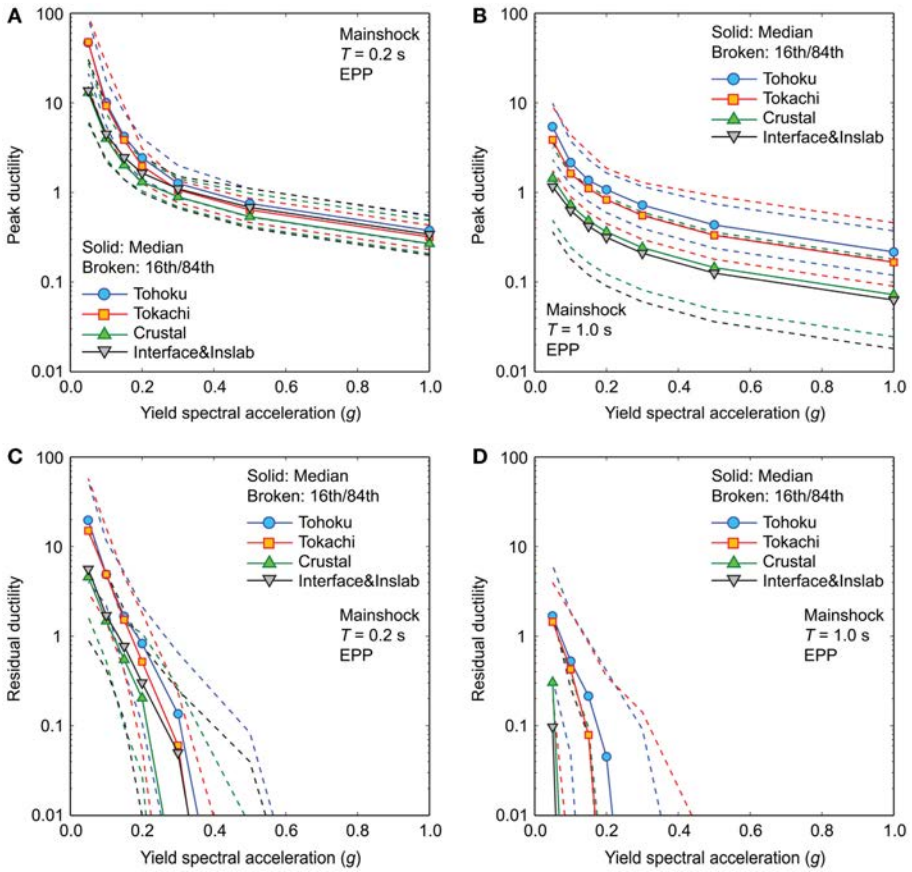

FIGURE 6 | Comparison of ductility demand curves for EPP models with different yield spectral accelerations due to mainshock records only by considering four subsets having average PGA between 100 and 200 cm/s^2: (A) peak ductility demand for $T = 0.2$ s, (B) peak ductility demand for $T = 1.0$ s, (C) residual ductility demand for $T = 0.2$ s, and (D) residual ductility demand for $T = 1.0$ s.

A notable trend of the results shown in **Figure 7** related to the magnitude ranges of the ground-motion data is that for $T = 0.2$ s (**Figures 7A,C**), the median ductility demand curves (both peak and residual) for the large-magnitude dataset are greater than those for the moderate-magnitude dataset. On the other hand, such differences are not observed for $T = 1.0$ s (**Figures 7B,D**). This may appear to be inconsistent with the results shown in **Figures 5** and **6**. The different trends are caused because in **Figure 7**, the base parameters for describing the seismic hazard intensity (i.e., IM) are the spectral accelerations at the intact vibration periods, while in **Figures 5** and **6**, the base IM parameter is the PGA (note: PGA is a popular parameter for record selection purposes). For the considered systems, spectral accelerations at the intact vibration period are more efficient than PGA (i.e., an IM–EDP relationship is characterized by smaller variability of the relationship; Luco and Cornell, 2007), and it is customary to adopt more efficient IMs in evaluating the values of EDP (however, full exploration of efficient IMs is beyond the scope of this study). More specifically, when the response spectra of the large-magnitude dataset and of the moderate-magnitude dataset are matched at $T = 0.2$ s (see **Figure 4B**), the former has the richer spectral content than the latter in the vibration period range greater than $T = 0.2$ s and when the structural systems go into the inelastic response domain, inelastic responses of the systems are strongly affected by ground motions in the vibration period range longer than the intact vibration period (Luco and Bazzurro, 2007). When the matching of response spectra is carried out at $T = 1.0$ s, the matched response spectra in the vibration period range longer than 1.0 s become similar (note: in this case, major differences appear in the vibration period range shorter than 1.0 s; however, the inelastic SDOF systems considered in this study are not sensitive to ground motions in this period range). Further to note, although no results are presented and discussed in this study, results for inelastic seismic demand estimation based on the constant R approach using the same MS–AS sequence datasets indicate that the magnitude effects on the ductility demands are significant for short-period structures.

Returning to the original focus of this study (i.e., empirical assessment of ductility demands), **Figure 8** compares peak ductility demand curves for EPP models subjected to MS–AS sequences with those for smooth bilinear models, degrading models, and degrading models with pinching (**Figure 3**). Both large- and moderate-magnitude datasets are considered. The intension of this figure is to present the effects of hysteretic characteristics of the inelastic SDOF systems on the peak ductility demands; it is not to compare the peak ductility demands for the two datasets (which

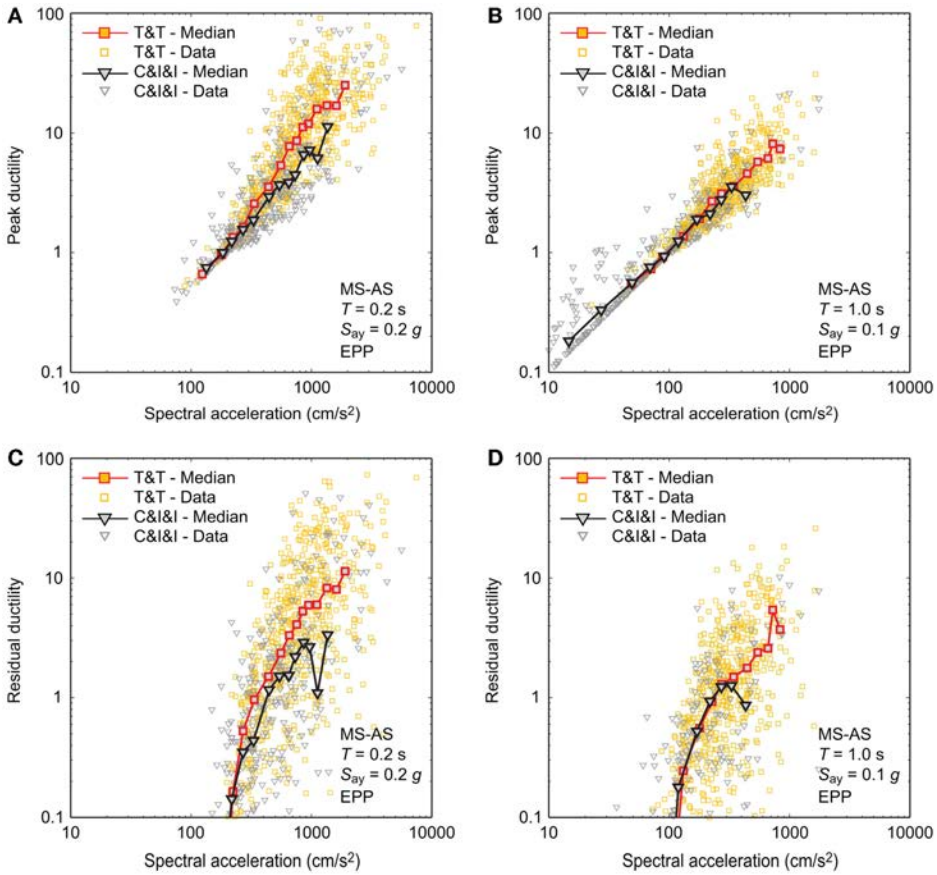

FIGURE 7 | Ductility demand – spectral acceleration curves for EPP models due to MS–AS sequences by considering the Tohoku and Tokachi (T&T) dataset and the Crustal, Interface, and Inslab (C&I&I) dataset: (A) peak ductility demand for $T = 0.2$ s and $S_{ay} = 0.2\,g$, (B) peak ductility demand for $T = 1.0$ s and $S_{ay} = 0.1\,g$, (C) residual ductility demand for $T = 0.2$ s and $S_{ay} = 0.2\,g$, and (D) residual ductility demand for $T = 1.0$ s and $S_{ay} = 0.1\,g$.

is not of interest because the seismic excitation levels are different). In these comparisons, EPP systems are used as reference and thus their results are shown in all figure panels.

Figures 8A,B suggest that the consideration of smooth bilinear systems (α and n are changed from EPP systems) leads to the decreased peak ductility demand, and that the extent of reduction of the peak ductility demand is greater for $T = 0.2$ s than for $T = 1.0$ s. The key factor for the decreased peak ductility demand is α (Ma et al., 2004). The consideration of degrading effects (**Figures 8C,D**) results in the increased peak ductility demand. The influence of degradation is more significant for $T = 0.2$ s than $T = 1.0$ s. For $T = 0.2$ s, the peak ductility demand curves for the degrading systems become greater than those for the EPP systems (i.e., overcoming the reduction due to the positive post-yield stiffness ratio), whereas for $T = 1.0$ s, the increase is minimal. The pinching behavior affects the structural systems having short vibration periods, whereas its effect on systems with long vibration periods is not significant (**Figures 8E,F**). For $T = 0.2$ s, the effect due to pinching behavior is particularly large, increasing the peak ductility demands in the low-to-moderate ranges significantly. It is noted that the effects of hysteretic behavior, as demonstrated above, depend on the vibration period as well as seismic excitation level. The above-mentioned observations are in agreement with Goda and Atkinson (2009).

The similar comparisons for the residual ductility demands for different hysteretic models are omitted for brevity. It is observed that when the hysteretic behavior is changed from EPP systems to other systems having positive post-yield stiffness ratios (i.e., $\alpha = 0.0$ versus $\alpha = 0.05$), the absolute values of the residual ductility demand decrease dramatically. For instance, the overall trends of the residual ductility demand curves for the EPP systems ($T = 0.2$ and 1.0 s) by considering the large-magnitude and moderate-magnitude datasets are similar to those shown in **Figure 6**. When the bilinear and degrading systems without/with pinching are considered, the absolute values of the residual ductility demand curves become significantly less (median as well as 84th percentile curves rarely exceed the ductility demand of 0.1, which is of no engineering significance). These results are in agreement with Ruiz-García and Miranda (2006).

Effects of Major Aftershocks

The effects of major aftershocks on the peak and residual ductility demands are evaluated by considering the large- and moderate-magnitude datasets. To inspect the impact of major aftershocks

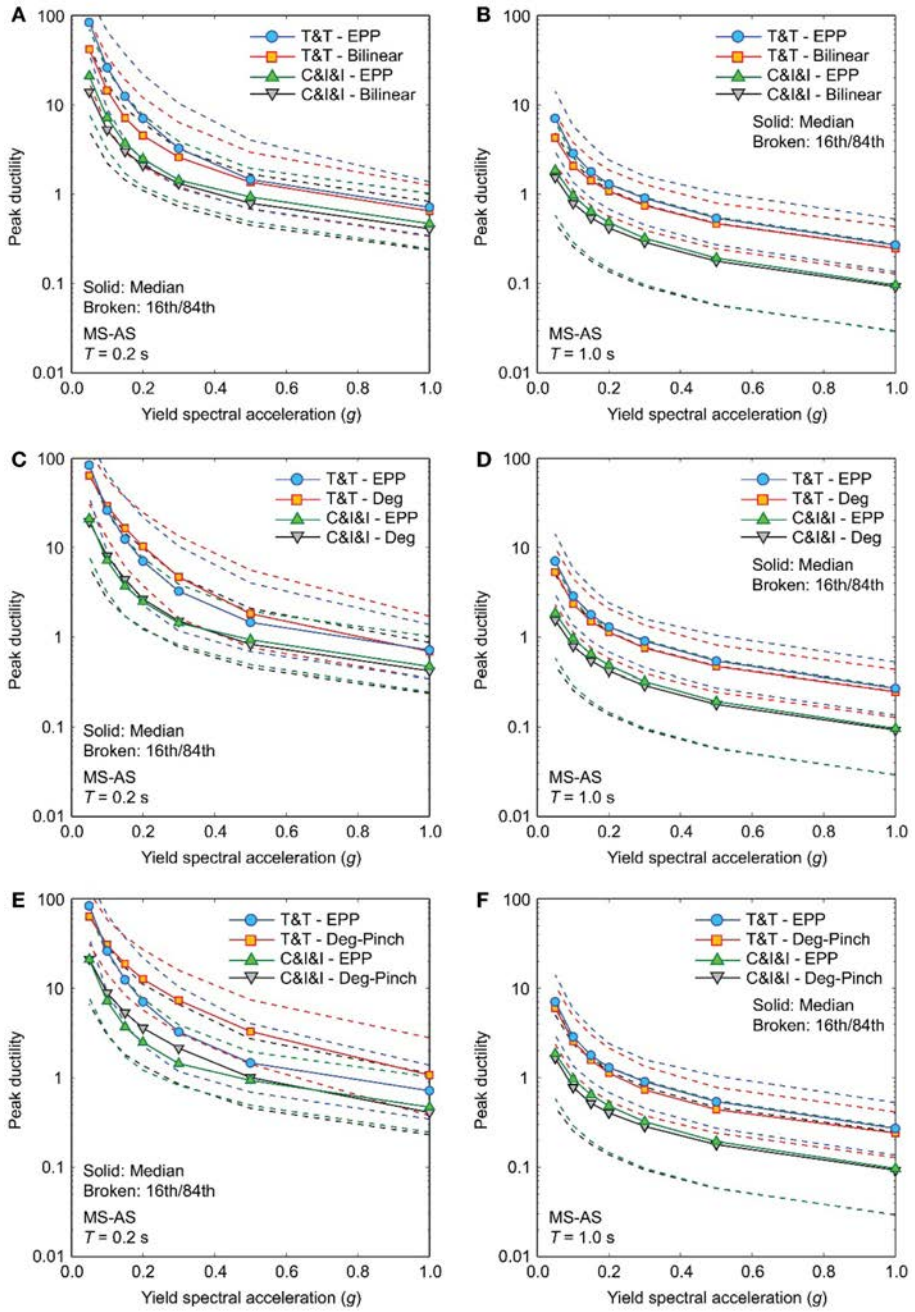

FIGURE 8 | Comparison of peak ductility demand curves for different hysteretic models with different yield spectral accelerations due to MS–AS sequences by considering the Tohoku and Tokachi (T&T) dataset and the Crustal, Interface, and Inslab (C&I&I) dataset: (A,B) bilinear models for $T = 0.2$ and 1.0 s, (C,D) degrading models for $T = 0.2$ and 1.0 s, and (E,F) degrading models with pinching for $T = 0.2$ and 1.0 s.

visually, median, 84th percentile, and 98th percentile of the MS–AS to mainshock ductility demand ratios (i.e., MS–AS to MS ratios) for EPP models ($T = 0.2$ and 1.0 s) are presented in **Figure 9**. Because the MS–AS to MS ratios can be extremely large when ductility demands for mainshock records only are small (this is particularly applicable to residual ductility demands) and such cases are of little engineering interests, the MS–AS to MS ratios are computed using peak/residual ductility demands due to mainshocks greater than 0.1. **Figure 9** shows that for the majority of the cases, the median ratios are 1 (both peak and residual), indicating that more than 50% of the cases, the major aftershocks do not increase the seismic demand levels caused by the mainshocks. However, in rare cases, the major aftershocks can increase the seismic damage extent significantly. The extent of the aftershock effects is greater for the moderate-magnitude dataset than for the large-magnitude dataset. For instance, the 98th percentile

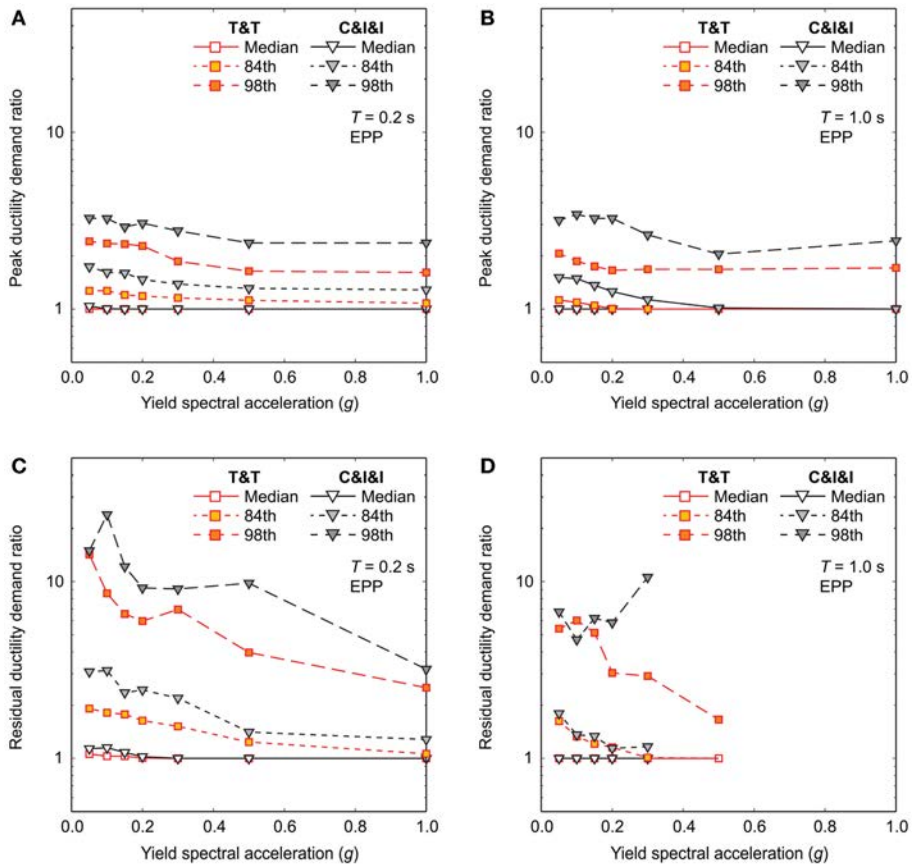

FIGURE 9 | Statistics of the MS–AS to mainshock ductility demand ratios for EPP models by considering the Tohoku and Tokachi (T&T) dataset and the Crustal, Interface, and Inslab (C&I&I) dataset: (A) peak ductility demand for $T = 0.2$ s, (B) peak ductility demand for $T = 1.0$ s, (C) residual ductility demand for $T = 0.2$ s, and (D) residual ductility demand for $T = 1.0$ s.

curves of the MS–AS to MS peak ductility demand ratios for the moderate- and large-magnitude datasets range around 2–3 and 1.5–2, respectively. The comparison of the results for the peak and residual ductility demands indicates that the MS–AS to MS ratios for the residual ductility demands are more sensitive than those for the peak ductility demands; these are partly attributed to the fact that for EPP systems the absolute values of the residual ductility demands are smaller than those of the peak ductility demands and the residual ductility demands tend to increase more rapidly with the yield spectral acceleration (**Figure 6**).

To further investigate the aftershock effects in terms of hysteretic behavior, **Figure 10** compares the 84th percentile and 98th percentile curves of the MS–AS to MS peak ductility demand ratios for different hysteretic models (note: 50th percentile curves are not shown as they are equal to 1 for most of the cases). Both large- and moderate-magnitude datasets are considered. Similarly to **Figure 8**, the results for EPP systems are used as reference. The consideration of bilinear systems with positive post-yield stiffness ratios results in slightly smaller MS–AS to MS peak ductility demand ratios (e.g., 84th percentile curves for $T = 0.2$ s), however, the overall impact is not significant (**Figures 10A,B**). The results for the degrading systems without/with pinching indicate that the MS–AS to MS peak ductility demand ratios for $T = 0.2$ s are slightly more influenced by hysteretic behavior than the ratios for $T = 1.0$ s (**Figures 10C–F**). Noticeable increases of the MS–AS to MS ratios are observed due to pinching behavior for $T = 0.2$ s (**Figure 10E**). Overall, it can be concluded that the effects of hysteretic characteristics on the MS–AS to MS peak ductility demand ratios are not particularly large. The similar results for the MS–AS to MS residual ductility demand ratios are omitted because the residual ductility demands for bilinear and degrading systems without/with pinching are small (the majority of the data are below the threshold of 0.1).

Finally, dependency of the MS–AS to MS ratios (both peak and residual) of EPP systems on various seismological parameters is investigated using the large- and moderate-magnitude datasets. The considered explanatory parameters are: mainshock peak/residual ductility demand, average shear-wave velocity (V_{S30}), mainshock magnitude, mainshock distance, aftershock magnitude, aftershock distance, mainshock PGA, mainshock spectral acceleration at the intact vibration period, aftershock PGA, and aftershock spectral acceleration at the intact vibration period. By visually inspecting the scatter plots of the MS–AS to MS ratios with respect to the examined parameters and by carrying out linear regression analysis (note: regression analyses are performed in log–log space, except for

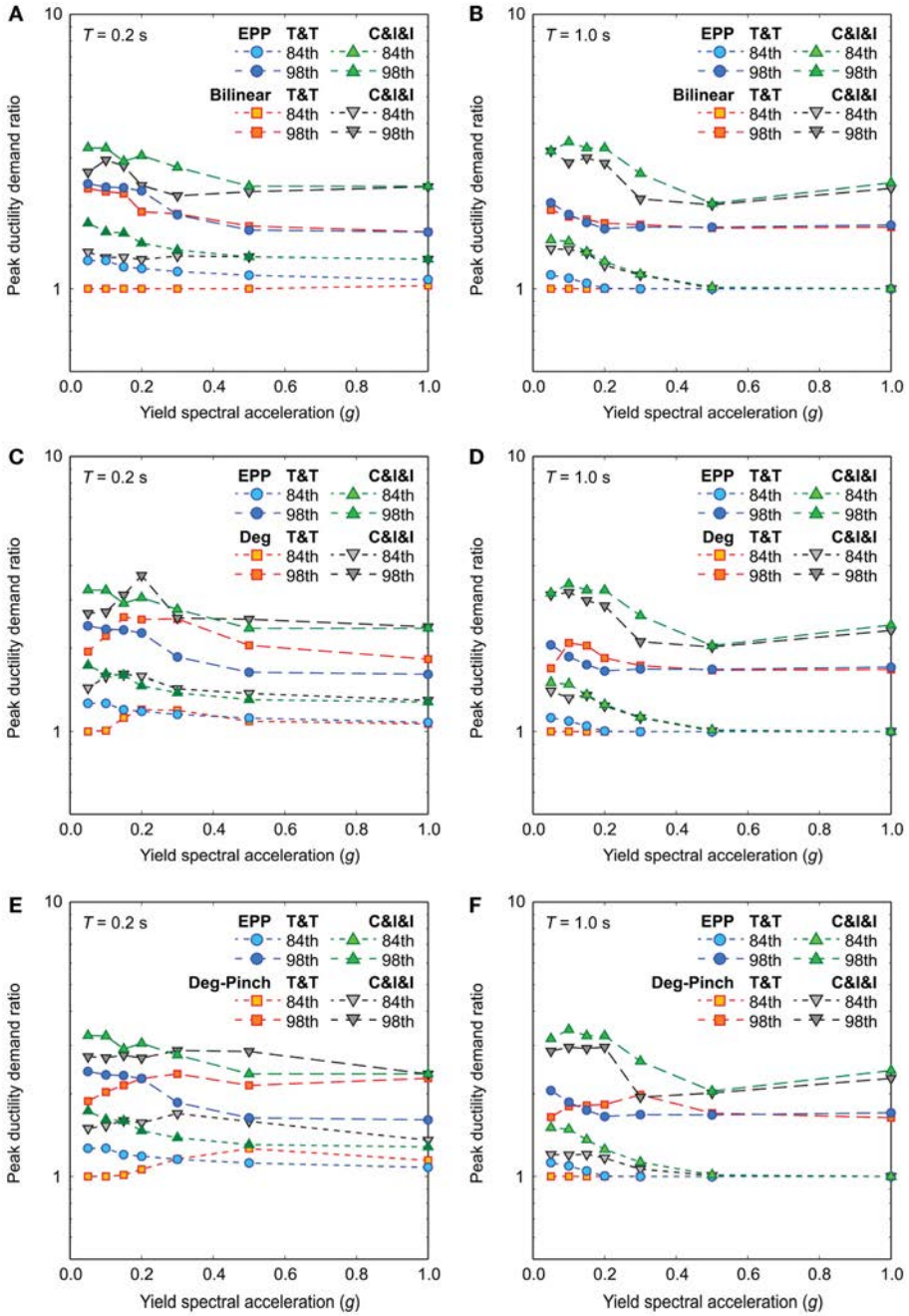

FIGURE 10 | Statistics of MS–AS to mainshock peak ductility demand ratios for different hysteretic models by considering the Tohoku and Tokachi (T&T) dataset and the Crustal, Interface, and Inslab (C&I&I) dataset: (A,B) bilinear models for $T = 0.2$ and 1.0 s, (C,D) degrading models for $T = 0.2$ and 1.0 s, and (E,F) degrading models with pinching for $T = 0.2$ and 1.0 s.

the mainshock/aftershock magnitude), their dependency is evaluated. The dependency between the MS–AS to MS ratios and the parameters is judged to be significant when the 95% confidence intervals of the slope coefficient do not include zero (i.e., confidence intervals are either both positive or both negative). The regression analysis results suggest that the MS–AS to MS peak ductility demand ratios clearly depend on aftershock PGA and spectral acceleration at the intact vibration period, while they are weakly dependent on the mainshock peak ductility demand. The former is simply interpreted that stronger aftershocks have greater potential to cause additional seismic damage, whereas the latter can be understood that relative effects due to major aftershocks become less critical when the mainshock causes large seismic damage to structures. Note that minor trends can be recognized for aftershock magnitude and distance; however, the trends are not consistent for the majority of cases and these parameters are

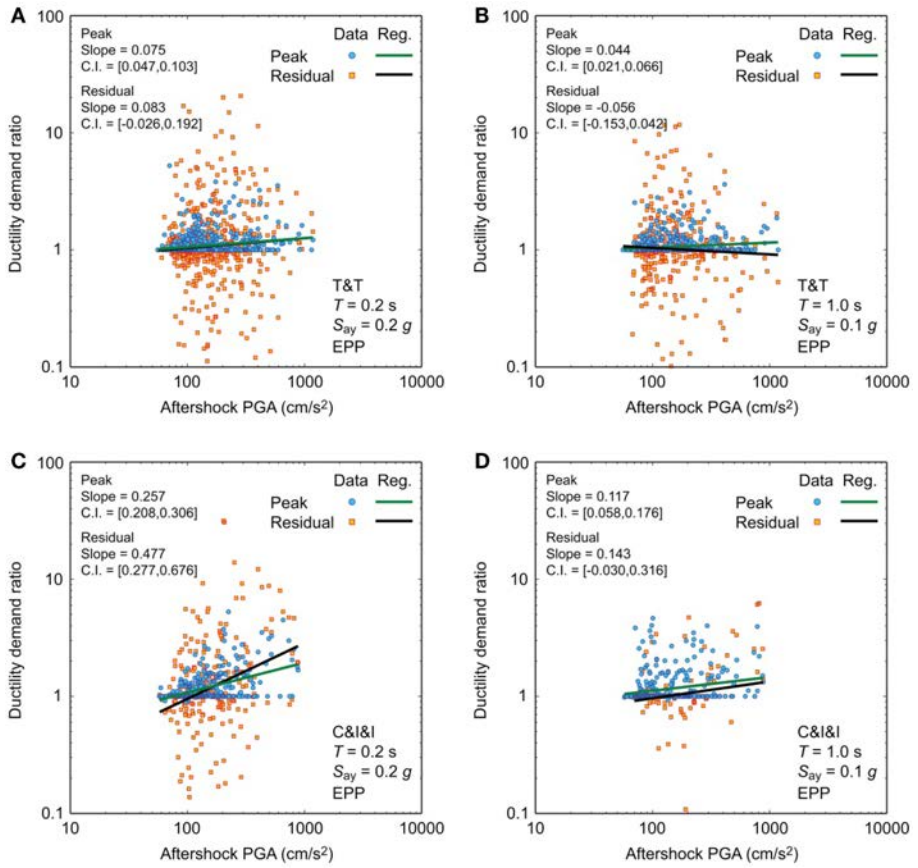

FIGURE 11 | Dependency of MS–AS to mainshock peak and residual ductility demand ratios for EPP systems by considering: (A) Tohoku and Tokachi (T&T) dataset for $T = 0.2$ s and $S_{ay} = 0.2\,g$, (B) Tohoku and Tokachi (T&T) dataset for $T = 1.0$ s and $S_{ay} = 0.1\,g$, (C) Crustal, Interface, and Inslab (C&I&I) dataset for $T = 0.2$ s and $S_{ay} = 0.2\,g$, and (D) Crustal, Interface, and Inslab (C&I&I) dataset for $T = 1.0$ s and $S_{ay} = 0.1\,g$.

regarded as secondary factors that affect aftershock PGA and spectral accelerations. On the other hand, the results for the MS–AS to MS residual ductility demand ratios are less clear because of large scatter of the data points. Therefore, it is concluded that the dependency between the MS–AS to MS residual ductility demand ratios and the aftershock elastic response parameters is too weak. To illustrate the above-mentioned observations, **Figure 11** presents the scatter plots of the MS–AS to MS ratio and the aftershock PGA for EPP systems with $T = 0.2$ s and $S_{ay} = 0.2\,g$ and with $T = 1.0$ s and $S_{ay} = 0.1\,g$ by considering the large- and moderate-magnitude datasets. In the figure panels, the regression lines as well as the slope value and its confidence intervals are included. For the peak ductility demands, clear positive trends are observed for $T = 0.2$ s, whereas such trends become weak for $T = 1.0$ s. Generally, aftershock spectral accelerations at the intact vibration period are more correlated with the MS–AS to MS ratios. **Figure 11** also shows that the scatter of the data points for the residual ductility demands is significantly greater than that for the peak ductility demands.

Spatial Distribution of Major Aftershocks for the 2011 Tohoku Sequence

Figure 12 shows the spatial distribution of the peak ductility demands, peak ductility demand ratios, residual ductility demands, and residual ductility demand ratios for two EPP systems with $T = 0.2$ s and $S_{ay} = 0.2\,g$ and with $T = 1.0$ s and $S_{ay} = 0.1\,g$. The intensity of the ductility demands and the ductility demand ratios are color-coded (see the captions in **Figure 12**); the ranges of the demand values and ratios are chosen to represent different seismic damage severities (e.g., peak ductility demand of 10 is considered to be major damage). In the figure panels for the peak/residual ductility demands (**Figures 12A,C,E,G**), strong-motion generation areas, which are characterized as areas with large slip velocities within a total rupture plane, are indicated. These areas are estimated by Kurahashi and Iikura (2013) via strong-motion source inversion of the 2011 Tohoku mainshock data. Whereas in the figure panels for the peak/residual ductility demand ratios (**Figures 12B,D,F,H**), locations of the major aftershocks for the 2011 Tohoku sequences are shown.

Inspection of the results for the peak ductility demands of EPP systems having $T = 0.2$ s and $S_{ay} = 0.2\,g$ (**Figure 12A**) indicates that the seismic damage potential due to the mainshock is high at sites around 38–39°N (Miyagi Prefecture) and at sites around 36–37°N (Fukushima and Ibaraki Prefectures). The sites in Miyagi Prefecture are affected by the two overlapping strong-motion generation areas (which resulted in noticeable multiple-shock features of the recorded ground motions), whereas the sites in Fukushima

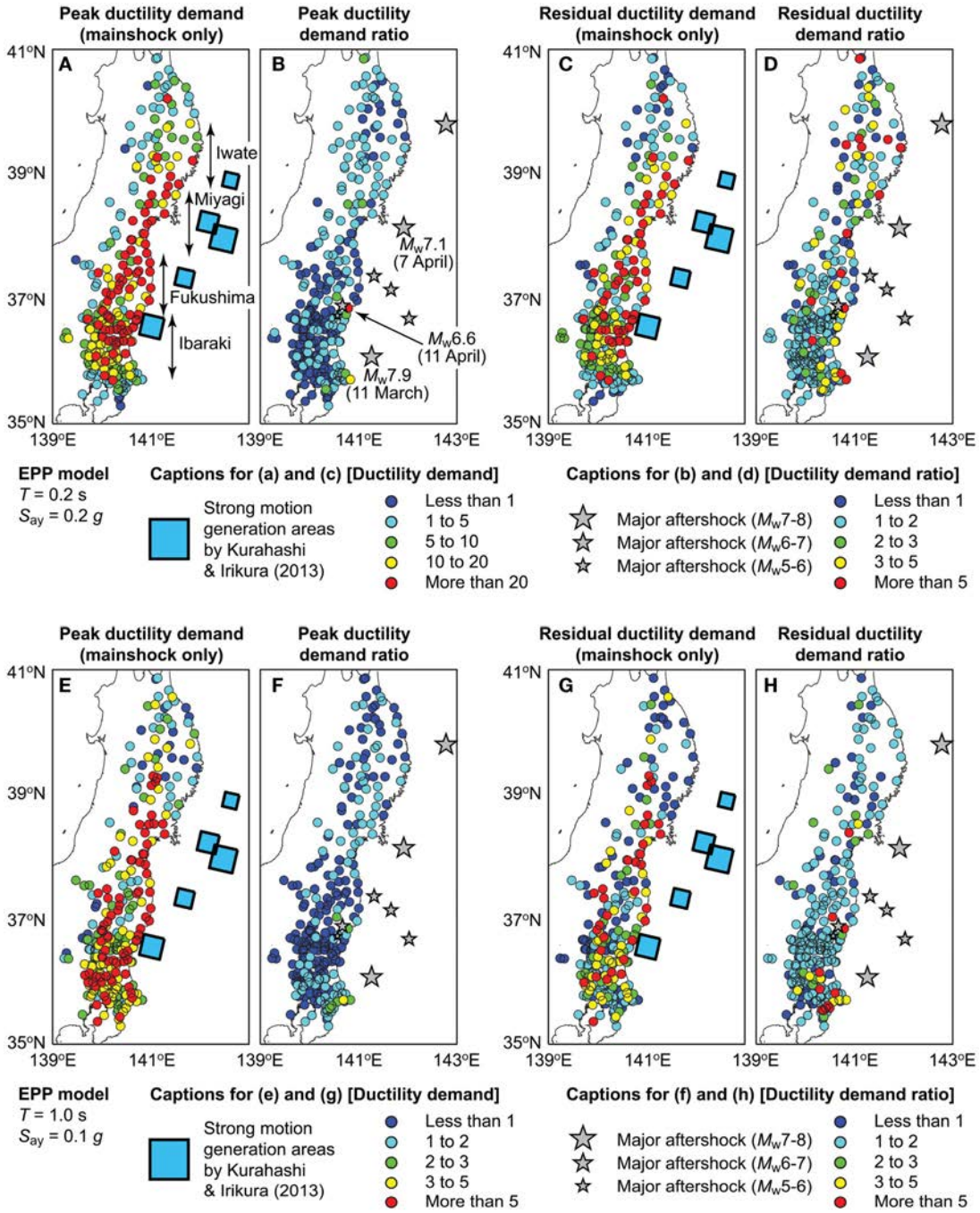

FIGURE 12 | Spatial distribution of ductility demands and ductility demand ratios by considering the Tohoku dataset: (A–D) peak ductility demand, peak ductility demand ratio, residual ductility demand, and residual ductility demand ratio for EPP systems ($T = 0.2$ s and $S_{ay} = 0.2\,g$), and (E–H) peak ductility demand, peak ductility demand ratio, residual ductility demand, and residual ductility demand ratio for EPP systems ($T = 1.0$ s and $S_{ay} = 0.1\,g$).

and Ibaraki Prefectures are influenced by the southernmost strong-motion generation area, which is located near the coastline. Furthermore, many of these structures are located along the coast, and therefore are likely to be subjected to the tsunami actions between mainshock and aftershock. Such actions may further degrade the structural behavior and make the buildings weaker, being unable to resist the next seismic excitation. Moreover, it can be observed from **Figure 12B** that the additional seismic damage occurs in the vicinity of major aftershocks. In particular, the M_w7.9 aftershock off Ibaraki Prefecture that occurred 30 min after the mainshock increases the peak ductility demands at sites in the southern part of Ibaraki Prefecture (green-to-yellow circles

in **Figure 12B**). The M_w7.1 aftershock that occurred on 7 April off Miyagi Prefecture causes small-to-moderate increase of the peak seismic demands in Miyagi Prefecture (light-blue-to-green circles in **Figure 12B**). Notably, the M_w6.6 aftershock that occurred on 11 April in the upper crust causes a major increase of the peak seismic demands at a nearby location (red circle in **Figure 12B**). The causal relationship between major aftershocks and increased seismic demands can be understood physically and intuitively; simply, when a major aftershock strikes near a site of interest, the seismic demand potential due to the aftershock becomes greater. The above explanations are applicable to the residual ductility demands (**Figures 12C,D**) as well as the results for the other EPP system (**Figures 12E–H**). The results shown in **Figure 12** are consistent with the results shown in **Figure 11**.

From seismic risk-management perspectives, critical situations arise when moderate-to-severe damage is caused by a mainshock and major aftershocks occur nearby, aggravating the conditions of the mainshock-damaged structures. The results shown in **Figure 12** highlight that the spatial occurrence process of aftershocks is important. This is a major source of uncertainty in ensuring the safe evacuation and deciding upon the reoccupation of buildings in a post-disaster environment. Moreover, by reflecting upon the observations made regarding **Figure 9** (i.e., aftershock effects for the moderate-magnitude dataset is greater than those for the large-magnitude dataset), the reason for less frequent occurrence of damaging aftershocks for mega-thrust subduction earthquakes may be attributed to the fact that mainshock seismic damage is caused at many locations over a larger geographical region but aftershock-triggered seismic damage is concentrated at more local areas. To study such aspects, spatial modeling of aftershock occurrence needs to be incorporated in generating artificial MS–AS sequences (Goda, 2012).

Conclusion

This study aimed at evaluating the peak and residual ductility demands of inelastic SDOF systems due to real MS–AS sequences from an empirical perspective. For this purpose, an extensive dataset of as-recorded MS–AS sequences for Japanese earthquakes was developed (containing 531 sequences; each with two horizontal components). The constructed dataset is large, compared with previous datasets of similar kinds, and thus more rigorous investigations regarding the non-linear seismic demand potential for MS–AS sequences can be carried out. To draw generic conclusions, numerous inelastic SDOF systems having different vibration periods, yield strengths, and hysteretic characteristics that are represented by the Bouc–Wen model, were considered. Such assessment is useful in two aspects. Firstly, it serves as a benchmark, when non-linear structural responses due to large mainshocks having different record characteristics and due to major aftershocks are evaluated using artificial MS–AS data. Back-to-back applications of (scaled) mainshock records as aftershocks often lead to overestimation of the aftershock seismic demand potential (Goda, 2015), and thus careful construction of artificial MS–AS sequences is important. Secondly, investigations of the relationships between seismic demands of inelastic SDOF systems and key seismological parameters of MS–AS sequences provide useful guidance as to which parameters should be taken into account in developing seismic demand prediction models for more realistic structural models. Moreover, the developed MS–AS sequence dataset facilitates the assessment of the aftershock effects in relation to the spatial distribution of major aftershocks. Numerical analysis was set up to investigate the above-mentioned problems.

Based on the analysis results, the following conclusions can be drawn:

1. One of the controlling factors for determining the severity of peak and residual ductility demands (for the same level of seismic excitation) is earthquake magnitude. For inelastic seismic demand estimation, earthquake magnitude or a surrogate measure, such as earthquake event type, may need to be included (depending on regional seismic hazard characteristics).
2. Hysteretic behavior of structural systems can have major influence on the estimation of the inelastic seismic demand. The consideration of the positive post-yield stiffness ratio, in comparison with zero post-yield stiffness ratio as in EPP systems, reduces peak and residual ductility demands (particularly significant impact on the residual ductility demand). Moreover, both degradation and pinching behavior have moderate effects on the peak ductility demand.
3. The aggravation of the inelastic seismic demand due to major aftershocks is not common, because the mainshock often causes severer damage to structures. However, in rare cases, major aftershocks can increase the seismic damage severity significantly. Moreover, hysteretic behavior does not affect the MS–AS to MS peak ductility demand ratios significantly. The key factors for damaging aftershocks are: the ground-motion intensity of major aftershocks and the severity of damage caused by the mainshock.
4. The causal relationship between major aftershocks and increased seismic demands can be understood physically; greater seismic demand potential results in greater seismic demand. For mega-thrust subduction events, such as the 2011 Tohoku earthquake, spatial occurrence process of aftershocks is critical, because the size of major aftershocks is significantly smaller than the mainshock and thus their impact are much more localized. Improved spatial modeling of major aftershocks needs to be incorporated in generating artificial MS–AS sequences for seismic vulnerability assessment.

Acknowledgments

Strong-motion data used in this study were obtained from the K-NET and KiK-net (http://www.kyoshin.bosai.go.jp/) and the SK-net (http://www.sknet.eri.u-tokyo.ac.jp/). KG is supported by the Alexander von Humboldt Fellowship for Experienced Researchers. RR is funded by the Engineering and Physical Sciences Research Council (EP/M001067/1).

Supplementary Material

The Supplementary Material for this article can be found online at http://journal.frontiersin.org/article/10.3389/fbuil.2015.00006/abstract

References

Boore, D. M. (2005). On pads and filters: processing strong-motion data. *Bull. Seismol. Soc. Am.* 95, 745–750. doi:10.1785/0120040160

Cornell, C. A., Jalayer, F., Hamburger, R. O., and Foutch, D. A. (2002). Probabilistic basis for 2000 SAC Federal Emergency Management Agency steel moment frame guidelines. *J. Struct. Eng.* 128, 526–533. doi:10.1061/(ASCE)0733-9445(2002)128:4(526)

Federal Emergency Management Agency. (2005). *Improvement of Nonlinear Static Seismic Analysis Procedures*. Washington, DC: Federal Emergency Management Agency.

Foliente, G. C. (1993). *Stochastic Dynamic Response of Wood Structural Systems*. Ph.D. dissertation, Virginia Polytechnic Institute and State University, Blacksburg, VA.

Galasso, C., Zarain, F., Iervolino, I., and Graves, R. W. (2012). Validation of ground motion simulations for historical events using SDOF systems. *Bull. Seismol. Soc. Am.* 102, 2727–2740. doi:10.1785/0120120018

Goda, K. (2012). Nonlinear response potential of mainshock-aftershock sequences from Japanese earthquakes. *Bull. Seismol. Soc. Am.* 102, 2139–2156. doi:10.1785/0120110329

Goda, K. (2015). Record selection for aftershock incremental dynamic analysis. *Earthquake Eng. Struct. Dyn.* 44, 1157–1162. doi:10.1002/eqe.2513

Goda, K., and Atkinson, G. M. (2009). Seismic demand estimation of inelastic SDOF systems for earthquakes in Japan. *Bull. Seismol. Soc. Am.* 99, 3284–3299. doi:10.1785/0120090107

Goda, K., and Atkinson, G. M. (2010). Intraevent spatial correlation of ground-motion parameters using SK-net data. *Bull. Seismol. Soc. Am.* 100, 3055–3067. doi:10.1785/0120100031

Goda, K., Pomonis, A., Chian, S. C., Offord, M., Saito, K., Sammonds, P., et al. (2013). Ground motion characteristics and shaking damage of the 11th March 2011 M_w9.0 Great East Japan earthquake. *Bull. Earthquake Eng.* 11, 141–170. doi:10.1007/s10518-012-9371-x

Goulet, C. A., Haselton, C. B., Mitrani-Reiser, J., Beck, J. L., Deierlein, G. G., Porter, K. A., et al. (2007). Evaluation of the seismic performance of a code-conforming reinforced-concrete frame building – from seismic hazard to collapse safety and economic losses. *Earthquake Eng. Struct. Dyn.* 36, 1973–1997. doi:10.1002/eqe.694

Iervolino, I., and Cornell, C. A. (2005). Record selection for nonlinear seismic analysis of structures. *Earthquake Spectra* 21, 685–713. doi:10.1193/1.1990199

Jalayer, F., and Cornell, C. A. (2009). Alternative nonlinear demand estimation methods for probability-based seismic assessments. *Earthquake Eng. Struct. Dyn.* 38, 951–972. doi:10.1002/eqe.876

Kagan, Y. Y. (2002). Aftershock zone scaling. *Bull. Seismol. Soc. Am.* 92, 641–655. doi:10.1785/0120010172

Kurahashi, S., and Iikura, K. (2013). Short-period source model of the 2011 M_w 9.0 off the Pacific coast of Tohoku earthquake. *Bull. Seismol. Soc. Am.* 103, 1373–1393. doi:10.1785/0120120157

Li, Q., and Ellingwood, B. R. (2007). Performance evaluation and damage assessment of steel frame buildings under main shock-aftershock earthquake sequences. *Earthquake Eng. Struct. Dyn.* 36, 405–427. doi:10.1002/eqe.667

Luco, N., and Bazzurro, P. (2007). Does amplitude scaling of ground motion records result in biased nonlinear structural drift responses? *Earthquake Eng. Struct. Dyn.* 36, 1813–1835. doi:10.1002/eqe.695

Luco, N., and Cornell, C. A. (2007). Structure-specific scalar intensity measures for near-source and ordinary earthquake ground motions. *Earthquake Spectra* 23, 357–392. doi:10.1193/1.2723158

Ma, F., Zhang, H., Bockstedte, A., Foliente, G. C., and Paevere, P. (2004). Parameter analysis of the differential model of hysteresis. *ASME J. Appl. Mech.* 71, 342–349. doi:10.1115/1.1668082

Morikawa, N., and Fujiwara, H. (2013). A new ground motion prediction equation for Japan applicable up to M9 mega-earthquake. *J. Disaster Res.* 8, 878–888.

Moustafa, A., and Takewaki, I. (2010). Modeling critical ground-motion sequences for inelastic structures. *J. Adv. Struct. Eng.* 13, 665–680. doi:10.1260/1369-4332.13.4.665

Nagato, K., and Kawase, H. (2004). Damage evaluation models of reinforced concrete buildings based on the damage statistics and simulated strong motions during the 1995 Hyogo-ken Nanbu earthquake. *Earthquake Eng. Struct. Dyn.* 33, 755–774. doi:10.1002/eqe.376

Ramirez, C. M., and Miranda, E. (2012). Significance of residual drifts in building earthquake loss estimation. *Earthquake Eng. Struct. Dyn.* 41, 1477–1493. doi:10.1002/eqe.2217

Ruiz-García, J. (2012). Mainshock-aftershock ground motion features and their influence in building's seismic response. *J. Earthquake Eng.* 16, 719–737. doi:10.1080/13632469.2012.663154

Ruiz-García, J., and Miranda, E. (2003). Inelastic displacement ratios for evaluation of existing structures. *Earthquake Eng. Struct. Dyn.* 32, 1237–1258. doi:10.1002/eqe.271

Ruiz-García, J., and Miranda, E. (2006). Evaluation of residual drift demands in regular multi-storey frames for performance-based seismic assessment. *Earthquake Eng. Struct. Dyn.* 35, 1609–1629. doi:10.1002/eqe.593

Salami, M. R., and Goda, K. (2014). Seismic loss estimation of residential wood-frame buildings in southwestern British Columbia considering mainshock-aftershock sequences. *J. Perform. Constr. Facil.* 28, A4014002. doi:10.1061/(ASCE)CF.1943-5509.0000514

Shcherbakov, R., Goda, K., Ivanian, A., and Atkinson, G. M. (2013). Aftershock statistics of major subduction earthquakes. *Bull. Seismol. Soc. Am.* 103, 3222–3234. doi:10.1785/0120120337

Shcherbakov, R., Turcotte, D. L., and Rundle, J. B. (2005). Aftershock statistics. *Pure Appl. Geophys.* 162, 1051–1076. doi:10.1007/s00024-004-2661-8

Smyrou, E., Tasiopoulou, P., Bal, IE., Gazetas, G., and Vintzileou, E. (2011). Ground motions versus geotechnical and structural damage in the February 2011 Christchurch earthquake. *Seismol. Res. Lett.* 82, 882–892. doi:10.1785/gssrl.82.6.882

Stein, S., and Wysession, M. (2003). *An Introduction to Seismology, Earthquakes, and Earth Structure*. Hoboken, NJ: Wiley-Blackwell.

Vamvatsikos, D., and Cornell, C. A. (2004). Applied incremental dynamic analysis. *Earthquake Spectra* 20, 523–553. doi:10.1193/1.1737737

Wen, Y. K. (1976). Method for random vibration of hysteretic systems. *J. Eng. Mech.* 102, 249–263.

Zhai, C. H., Wen, W. P., Chen, Z. Q., Li, S., and Xie, L. L. (2013). Damage spectra for the mainshock-aftershock sequence-type ground motions. *Soil Dyn. Earthquake Eng.* 45, 1–12. doi:10.1016/j.soildyn.2012.10.001

Conflict of Interest Statement: The authors declare that the research was conducted in the absence of any commercial or financial relationships that could be construed as a potential conflict of interest.

Copyright © 2015 Goda, Wenzel and De Risi. This is an open-access article distributed under the terms of the Creative Commons Attribution License (CC BY). The use, distribution or reproduction in other forums is permitted, provided the original author(s) or licensor are credited and that the original publication in this journal is cited, in accordance with accepted academic practice. No use, distribution or reproduction is permitted which does not comply with these terms.

frontiers in Built Environment

ORIGINAL RESEARCH
published: 29 September 2017
doi: 10.3389/fbuil.2017.00055

Overview of Ground-Motion Issues for Cascadia Megathrust Events: Simulation of Ground-Motions and Earthquake Site Response

Hadi Ghofrani, Gail M. Atkinson and Sheri Molnar*

Department of Earth Sciences, Western University, London, ON, Canada

Ground motions for earthquakes of **M**7.5 to 9.0 on the Cascadia subduction interface are simulated based on a stochastic finite-fault model and used to estimate average response spectra for reference firm soil conditions. The simulations are first validated by modeling the wealth of ground-motion data from the 2011 **M**9.0 Tohoku earthquake of Japan. Adjustments to the calibrated model are then made to consider average source, attenuation and site parameters for the Cascadia region. This includes an evaluation of the likely variability in stress drop for large interface earthquakes and an assessment of regional attenuation and site effects. We perform best-estimate simulations for a preferred set of input parameters. Typical results suggest mean values of 5%-damped pseudoacceleration in the range from about 100 to 200 cm/s^2, at frequencies from 1 to 4 Hz, for firm-ground conditions in Vancouver. Uncertainty in most-likely value of the parameter representing stress drop causes variability in simulated response spectra of about ±50%. Uncertainties in the attenuation model produce even larger variability in response spectral amplitudes—a factor of about two at a closest distance to the rupture plane (*Rcd*) of 100 km, becoming even larger at greater distances. It is thus important to establish the regional attenuation model for ground-motion simulations and to bound the source properties controlling radiation of ground motion. We calculate theoretical one-dimensional spectral amplification estimates for four selected Fraser River Delta sites to show how the presence of softer sediments in the region may alter the predicted ground motions. The amplification functions are largely consistent with observed spectral amplification at Fraser River delta sites, suggesting amplification by factors of 2.5–5 at the peak frequency of the site; we note that deep sites in the delta have a low peak frequency, ~0.3 Hz. This work will aid in seismic hazard assessment and mitigation efforts in the active Cascadia region of southwestern BC. An important consideration is that the uncertainties are large and present a dominant unknown when assessing seismic risk. We find that variability in the expected motions exceeds a factor of two even on rock-like sites, with uncertainty in site response further increasing this factor. Such large uncertainties pose a major challenge in preparing for the potential consequences of the next megathrust event in Cascadia.

Keywords: cascadia megathrust earthquake, simulation of ground motions, earthquake site response, seismic hazard assessment, ground-motion prediction equations for large interface earthquakes

OPEN ACCESS

Edited by:
Solomon Tesfamariam, University of British Columbia, Canada

Reviewed by:
Vladimir Sokolov, Saudi Geological Survey, Saudi Arabia
Alin Radu, University of Bristol, United Kingdom

****Correspondence:***
Hadi Ghofrani
hghofra@uwo.ca

Specialty section:
This article was submitted to Earthquake Engineering, a section of the journal Frontiers in Built Environment

Received: *22 June 2017*
Accepted: *12 September 2017*
Published: *29 September 2017*

Citation:
Ghofrani H, Atkinson GM and Molnar S (2017) Overview of Ground-Motion Issues for Cascadia Megathrust Events: Simulation of Ground-Motions and Earthquake Site Response. Front. Built Environ. 3:55. doi: 10.3389/fbuil.2017.00055

INTRODUCTION

Megathrust interplate earthquakes in a subduction zone cause catastrophic damage and loss to modern society. The 2004 **M**9.1 Indian Ocean (Sumatra-Andaman) earthquake, the 2010 **M**8.8 Maule, Chile, earthquake, and the 2011 **M**9.0 Tohoku earthquake are recent examples of such tragic events. Ground motions due to megathrust earthquakes may cause widespread collapse of buildings and infrastructure and disrupt essential lifeline services (Goda and Tesfamariam, 2017). To mitigate seismic risk due to subduction earthquakes, it is important to take into account the effects due to both ground shaking and tsunami (Geist, 2005; De Risi and Goda, 2016; Goda et al., 2016).

The Cascadia subduction zone is one of the major subduction regions around the world, extending from Vancouver Island to Northern California (Hyndman and Wang, 1995; Flück et al., 1997; Hyndman et al., 2003; Wang et al., 2003). The zone spans more than 1,000 km in the North-South direction, whereas its width varies depending on the latitude (about 100–200 km). The tsunami observations in Japan and tsunami modeling by Satake et al. (2003) indicate that the most recent Cascadia event occurred in 1,700 and its moment magnitude is estimated as **M**9.0 (**M**8.7 to **M**9.2). Paleoseismic investigations of marine sediments/turbidites on/off the coast indicate that the mean recurrence period of the Cascadia subduction event ranges from 500 to 600 years (typically around 530 years) with large variability (Adams, 1990; Atwater et al., 2004; Mazzotti and Adams, 2004; Goldfinger et al., 2008, 2012). Preparation for the next megathrust Cascadia subduction event is critical. Risk mitigation measures include design and retrofitting of buildings and infrastructure, including coastal defense structures, and development of emergency management protocols. These measures require realistic estimates of the potential effects of such events.

This study focuses on estimation of ground motions from a Cascadia megathrust event and their uncertainty, using a stochastic finite fault algorithm known as EXSIM (Motazedian and Atkinson, 2005; Atkinson et al., 2009; Boore, 2009). EXSIM uses a simple representation of seismic source and path effects to simulate ground motion time-histories. The fault rupture of a large earthquake is modeled as a collection of smaller point sources. By summing the effects of individual ruptures with appropriate time delays at the observation point, overall ground motion at a site of interest, resulting from the entire fault plane, can be generated. The simulated time-histories are the fundamental input to advanced earthquake engineering applications (e.g., seismic design, non-linear dynamic analysis, and seismic loss estimation).

Previous simulations of Cascadia ground motions based on a stochastic finite-fault model were performed by Gregor et al. (2002) and Atkinson and Macias (2009). In this study, we calibrate model components of the Cascadia-EXSIM model by using the 2011 **M**9.0 Tohoku ground motion data, because this is the best-recorded megathrust event of comparable size. We first ensure the model can reproduce overall characteristics of the 2011 Tohoku ground motions including amplitudes, duration and attenuation of the mainshock and aftershocks. For the information on the Tohoku event, we reference a number or sources. Goda et al. (2012) provides an overview of the motions. The source rupture process, involving multiple asperities, was described by Kurahashi and Irikura (2011) and Irikura and Kurahashi (2012) among others. Site effects were investigated by Ghofrani et al. (2012). Previous simulations of the Tohoku event using EXSIM are described by Ghofrani et al. (2013).

The calibrated Tohoku-EXSIM model can be adjusted for the Cascadia subduction events by accounting for regional differences of attenuation of ground shaking and site effects. Selection of attenuation parameters for EXSIM is guided by regional ground motion studies for southwestern British Columbia by Atkinson (2005) and Babaie Mahani and Atkinson (2013). Site amplification factors for sites in the greater Vancouver area, including the Fraser River Delta, are derived using regional shear-wave velocity data and geological information (Britton et al., 1995; Hunter et al., 1998; Cassidy and Rogers, 2004). Using the developed shear-wave profiles for the selected sites, we calculate theoretical one-dimensional (1D) spectral amplification estimates using Thomson-Haskell's approach (Thomson, 1950; Haskell, 1953) for selected Fraser River Delta sites to show how the presence of softer sediments in the region may alter the predicted ground motions, relative to those for reference firm soil conditions (site class B/C or V_{s30} of 760 m/s). This will provide an overview level of ground motions in the region and their uncertainty, that can be further refined in the future.

The simulations are used to calculate ground-motion parameters [5%-damped pseudospectral acceleration (PSA)] for developing regional ground-motion prediction equations (GMPEs) for Cascadia interface events. We compare these to other GMPEs (Gregor et al., 2002; Atkinson and Boore, 2003; Zhao et al., 2006; Somerville et al., 2008; Atkinson and Macias, 2009; Ghofrani and Atkinson, 2013; Abrahamson et al., 2016) and draw conclusions on further required studies.

STOCHASTIC FINITE-FAULT MODELING: EXSIM

The stochastic finite-fault method of Motazedian and Atkinson (2005) (i.e., EXSIM) subdivides an earthquake fault plane into a grid of subsources, and assigns a stochastic point source to each of them (i.e., a stochastic Green's function). Each subsource is activated once, with an appropriate delay time based on rupture propagation from the hypocenter to the subsource. In this study, stochastic finite-fault modeling is implemented by incorporating modifications suggested by Boore (2009) [see also Atkinson et al. (2009)]. The modifications improved the performance of EXSIM in several ways: (i) scaling of high-frequency motions are based on the integral of squared acceleration spectrum, rather than velocity spectrum; (ii) there is no truncation of subsource time-history data, which avoids bias in long-period motions introduced by filtering (Boore, 2005a); and (iii) the performance in the low-frequency range is improved.

For each subsource, a stochastic point source waveform with an underlying Brune ω^2-source spectrum (Brune, 1970, 1971) is generated; the model spectrum for a point source is derived by multiplication of source, path, and site spectra in the frequency domain (Boore, 1983, 2003). Following Brune (1970), the far-field

displacement spectrum of a finite source is flat (proportional to M_0) at low frequencies while at frequencies above the corner frequency (f_c) it decays as ω^{-2}; by contrast, the acceleration spectrum is flat at high frequencies, and decays as ω^{-2} at frequencies below the corner frequency. The acceleration spectrum of a point source can be given by (Boore, 1983, 2003):

$$Y(M_0, R, f) = A(M_0, f)\, P(R, f) G(f), \tag{1}$$

where $A(M_0, f)$, $P(R, f)$, and $G(f)$ represent the source, path, and site spectra, respectively; M_0 is the seismic moment in dyne-cm; R is hypocentral distance; and f is frequency.

The source spectrum is based on the Brune model (Brune, 1970), and its Fourier acceleration spectrum is calculated as (Boore, 1983, 2003):

$$A(M_0, f) = \frac{R^{\theta\phi} VF}{4\pi\rho_s\beta_s^3} M_0 R^{-1} (2\pi f)^2 \Big/ \left[1 + (f/f_c)^2\right], \tag{2}$$

where $R^{\theta\phi}$ is the average radiation pattern over a sphere and equals 0.55; F is the free surface amplification and equals 2.0; V is the partition of energy into two horizontal components and equals 0.71; ρ_s is the density (gm/cm^3); β_s is the shear-wave velocity (in km/s); f_c is the corner frequency and is given by $f_c = 4.9 \times 10^6 \beta_s (\Delta\sigma/M_0)^{1/3}$, in which $\Delta\sigma$ is the stress drop in bars. The path effect $P(R, f)$, including both geometrical spreading and anelastic attenuation, needs to be specified by an appropriate regional model. The site effect $G(f)$ includes the site amplification factor and the near-surface high-frequency diminution effects, typically modeled by the kappa parameter (Anderson and Hough, 1984).

The normalized and delayed subsource contributions are summed in the time domain as:

$$A(t) = \sum_{i=1}^{N} H_i \times A_i(t + \Delta t_i + T_i), \tag{3}$$

where $A(t)$ is the total seismic signal at site, H_i is the normalization factor for the ith subsource that aims to conserve energy, $A_i(t)$ is the signal of the ith subsource activation, N is the total number of subsources, Δt_i is the fracture initiation and wave propagation delay time of the subsource, and T_i is a fraction of rise time entered for further randomization. For each subsource, seismic moment M_{0i}, corner frequency f_{ci}, and normalization factor H_i need to be specified. The moment of a subsource is derived from the total moment and the slip distribution:

$$M_{0i} = \frac{M_0 \times s_i}{\sum_{i=1}^{N} s_i}, \tag{4}$$

where s_i is the slip of the ith subsource. EXSIM determines the corner frequency of newly activated elements based on a dynamic corner frequency concept (Motazedian and Atkinson, 2005), in which the frequency content of the radiated seismic waves shifts to lower frequencies as the rupture area grows. This process continues until the active rupture surface reaches a predefined limiting fraction of the fault area; after this fraction is reached, the corner frequency of newly activated subsources remains constant. Mathematically, the corner frequency of a subsource is given by:

$$f_{ci} = 4.9 \times 10^6 \beta_s \left(\frac{\Delta\sigma}{\min\left[N_R/N, F_{\text{pulse}}\right] \times M_0} \right)^{1/3}, \tag{5}$$

where N_R is the total number of active subsources at the time of the ith subsource activation, and F_{pulse} is the maximum fraction of the fault area for active rupture.

The normalization factor H_i is given by:

$$H_i = \frac{M_0}{M_{0i}} \sqrt{\sum_j \left(\frac{f_0^2 f_j^2}{f_0^2 + f_j^2} \right)^2 \Big/ N \sum_j \left(\frac{f_{0i}^2 f_j^2}{f_{0i}^2 + f_j^2} \right)^2}, \tag{6}$$

where f_0 is the corner frequency of the entire fault, f_j is the jth frequency ordinate, and f_{0i} is the corner frequency of the ith subsoruce. The high-frequency energy radiated from all subsources is assumed to be equal, with the sum being constrained by the total high-frequency energy of the earthquake, as implied by its Fourier spectral acceleration amplitude level at high frequencies.

The use of the dynamic corner frequency allows subsources to generate a range of low-frequency to high-frequency spectra, such that the final waveform of the simulation will contain sufficient low-frequency energy even if a very small subsource size is chosen. The scaling of the source spectrum based on the normalization factor forces the method to generate a constant amount of energy, no matter how many subsources are contributed in the summation. In other words, the use of the dynamic corner frequency and the normalization factor based on the squared acceleration spectrum make the spectral shape and spectral level of the resultant accelerograms relatively independent of subsource size.

CALIBRATION OF EXSIM FOR THE TOHOKU EARTHQUAKE

The source characteristics of a megathrust subduction earthquake are complex and have significant impact on generated ground motions. Such complex features were highlighted during the 2011 Tohoku earthquake in Japan by observations of multiple phases of seismic wave arrivals due to local asperities, referred to as strong-motion generation areas (SMGAs) (Kurahashi and Irikura, 2011; Goda et al., 2012). Another important aspect of the Tohoku event was its remarkable site effects, leading to significant site amplification at high frequency (with little soil non-linearity), as pointed out by Ghofrani et al. (2012). From a ground-motion modeling viewpoint, the Tohoku earthquake provides an excellent and unique opportunity for detailed calibration and validation of simulation methods, due to the hundreds of high-quality ground motion records from the K-NET and KiK-net arrays. No other **M**9.0 events have a comparable wealth of data.

Finite-fault ground-motion modeling of the 2011 Tohoku earthquake, using EXSIM, was carried out by Ghofrani et al. (2013), providing a useful calibration exercise. Notable features of the analysis included: (i) regional attenuation models for fore-arc and back-arc sites were taken into account (Ghofrani and Atkinson, 2011); (ii) detailed investigations of site effects were

incorporated by analyzing borehole and surface motions at the KiK-net sites (Ghofrani et al., 2012); and (iii) source characteristics (e.g., stress drop and rupture geometry) were modeled through both single-rupture and multiple-rupture approaches. The single-rupture model uses a rectangular fault plane, determined by source inversion analysis, using teleseismic and GPS data (Geospatial Information Authority of Japan, 2011; Shao et al., 2011). In EXSIM, an average stress drop is assigned to all subsources, while the slip distribution may be uniform, random, or specified for individual subsources. This provides limited flexibility in matching key features of strong ground motion from a megathrust earthquake at various locations. The study of Ghofrani et al. (2013) extended EXSIM to allow for multiple-rupture scenarios which can account for local SMGAs, which are distributed over the background fault plane. This is accomplished by triggering multiple EXSIM simulations that incorporate local features of the rupture, thus allowing different stress drops and moment magnitudes to be assigned to individual asperities. The generated seismic waves from different asperities are modified in the frequency domain using matching filters (to avoid double-counting of low-frequency content) and are summed up in the time domain with appropriate delays. This approach was used to implement the SMGA model of Kurahashi and Irikura (2011) suggested five SMGAs in their model of the Tohoku source, achieving reasonable agreement between real data and simulated ground motions based on the empirical Green's function (EGF) method of Kamae et al. (1998). The difference between the EGF method and the multiple-rupture EXSIM method is that the EGF method uses carefully chosen events (either aftershocks or previous smaller events in the same region) to represent path effects, whereas EXSIM adopts a stochastic point source representation in modeling earthquake rupture and seismic wave propagation from individual subsources. **Figure 1** shows the locations of the five SMGAs with respect to the fault plane and also selected times-series from stations located parallel to the strike of the event to depict the complexities of waveforms and multiple phase arrivals. The detailed descriptions of the multiple-rupture EXSIM method can be found in Ghofrani et al. (2013).

Table 1 summarizes input parameters of the Tohoku-EXSIM simulations (Ghofrani et al., 2013). The geometrical parameters of the background fault plane (fault length L, fault width W, strike ϕ, dip δ, and depth to the top of the fault plane H_{top}) are adopted from GSI (2011), whereas the geometrical parameters of five SMGAs as well as their source parameters (i.e., moment magnitude and stress drop) are adopted from Kurahashi and Irikura (2011). The path and site parameters, such as kappa, attenuation models, duration, and site amplification factors (both crustal and near-surface) are obtained from empirical investigations (Ghofrani and Atkinson, 2011; Ghofrani et al., 2012). We consider both single-rupture and multiple-rupture models, assuming a random slip distribution (within a fault plane) for both cases (see Ghofrani et al. (2013) for more results). It is noteworthy than the stress parameters for the single-rupture and multiple-rupture models, and corner frequencies of the matching

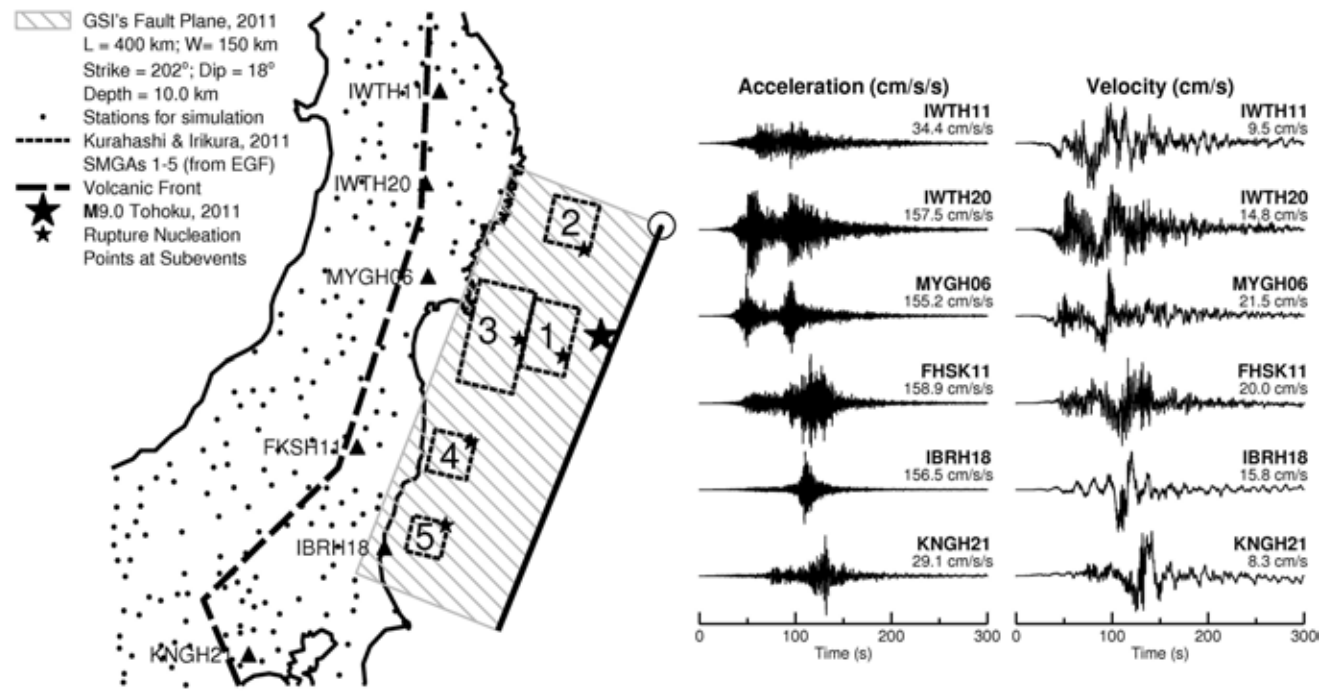

FIGURE 1 | Map showing Tohoku fault plane and stations used for the EXSIM simulations (black dots) at closest distance from the fault plane (Rcd) ranging from 41 to 420 km. Graphical representation of the background fault plane for the mainshock, adopted from GSI (2001) finite-fault model, hatched rectangle. Hypocenter of the mainshock, large star close to the trench. Five asperities from empirical Green's function (EGF) simulations (Kurahashi and Irikura, 2011), dashed rectangles; the star in each strong-motion generation area (SMGA) shows the nucleation point in each asperity. Details of the source model are given in **Table 1**. Observed time histories of ground motion (acceleration and velocity) at selected stations (triangles on the map). Numbers at the end of traces are the peak ground accelerations and velocities, respectively.

TABLE 1 | Input parameters of Tohoku-EXSIM simulations (Ghofrani et al., 2013).

Model components	Single-rupture model (random)	Multiple-rupture model (SMGA)
Rupture plane	$L = 400$ km $W = 150$ km $\phi = 202$ $\delta = 18$ $H_{top} = 10$ km 20×10 subsources	One background plane (same as the single-rupture model) and five SMGAs; see Kurahashi and Irikura (2011) SMGA1: $L = 62.4$ km; $W = 41.6$ km; $H_{top} = 28.03$ km; 6×4 subsources SMGA2: $L = 41.6$ km; $W = 41.6$ km; $\phi = 193$; $\delta = 10$; $H_{top} = 28.53$ km; 4×4 subsources SMGA3: $L = 93.6$ km; $W = 52.0$ km; $H_{top} = 35.43$ km; 9×5 subsources SMGA4: $L = 38.5$ km; $W = 38.5$ km; $H_{top} = 39.53$ km; 5×5 subsources SMGA5: $L = 33.6$ km; $W = 33.6$ km; $H_{top} = 40.73$ km; 7×7 subsources $\phi = 193$ and $\delta = 10$ for all SMGAs
Moment magnitude	9.0	8.92, 8.21, 7.87, 8.39, 7.69, 7.70
Stress drop	150 bar	35, 413, 236, 295, 164, and 260 bar
Delay time	N/A	15.64, 66.42, 68.41, 109.71, and 118.17 s for SMGA 1–5, respectively, with respect to the initiation of the background rupture
Matching filter	N/A	0.224, 0.246, 0.200, 0.256, and 0.274 Hz for SMGA 1–5, respectively. No filtering for the background plane
Kappa	0.03 s	
Geometrical spreading	Body wave geometrical spreading (−1.0) for all distance ranges	
Anelastic attenuation	Q factor models for forearc and backarc regions, developed by Ghofrani and Atkinson (2011), are used	
Slip distribution	Random (within a fault plane)	
Duration	$T_0 + 0.1208R_{hypo}$, where T_0 is the source duration	
Site amplification factor	Generic crustal amplification factors are used for borehole stations (Ghofrani et al., 2012). In addition, when surface motions are generated, site/station-specific surface-to-borehole ratios (as function of frequency) are included as local site amplification factors	

filter for the multiple-rupture model have been calibrated against real records by minimizing the overall bias of model prediction (Ghofrani et al., 2013).

Figure 2 compares the performance of EXSIM in predicting response spectra and acceleration time series at two representative stations, for the two considered source-rupture models. Single-rupture models with random and prescribed slips tend to over-predict the observed PSA at low frequencies and require a relatively high stress parameter, of ∼150 bar (15 MPa), to match the high frequencies. By contrast, the multiple-rupture model (background fault + five SMGAs) produces an excellent match of the observed and simulated PSA over all frequency ranges for most of the selected stations. The multiple-rupture model also provides much more realistic time series; the required stress parameter for the background fault is 35 bar (3.5 MPa) to match the spectra at high frequencies. Detailed validation results in terms of peak linear and non-linear structural responses at different KiK-net stations can be found in Goda et al. (2015). The validation based on non-linear structural responses ensures that the simulated time-histories from the multiple-rupture SFF method can be substituted for real strong motion records in non-linear dynamic analysis and therefore are useful for evaluating the seismic performance of structures.

We use the simulations for Tohoku as a starting point for a **M**9.0 event in Cascadia, recognizing that the multiple-rupture model may be less appropriate for this application due to the lack of knowledge concerning the details of future events along the Cascadia subduction interface. For the single-rupture model, the value assumed for the stress parameter is important to the generated high-frequency ground motion content. It is difficult to make definitive comparisons of stress parameter between this and other studies, as the stress parameter is model dependent (Atkinson et al., 2009) and is intertwined with attenuation and site parameters. Atkinson and Macias (2009) report average values of ∼170 bar for Chilean and Japanese earthquakes, with a value of 120 bar for the 2008 Tokachi-Oki mainshock. For the 2011 Tohoku event, the value is ∼150 bar for the single-rupture model.

MODEL PARAMETERS FOR CASCADIA INTERFACE SIMULATIONS

The main simulation parameters include the fault rupture model, the geometrical spreading and anelastic attenuation model, and the site response model. In this study, we generate ground motion for a reference site condition and use time-domain non-linear modeling to determine the site response from the bedrock to the surface. In the following, we discuss the input model parameters for the simulations.

FAULT RUPTURE MODEL

The Cascadia subduction zone stretches over more than 1,000 km from Vancouver Island to northern California, along the plate boundary between the oceanic Juan de Fuca and Gorda plates and

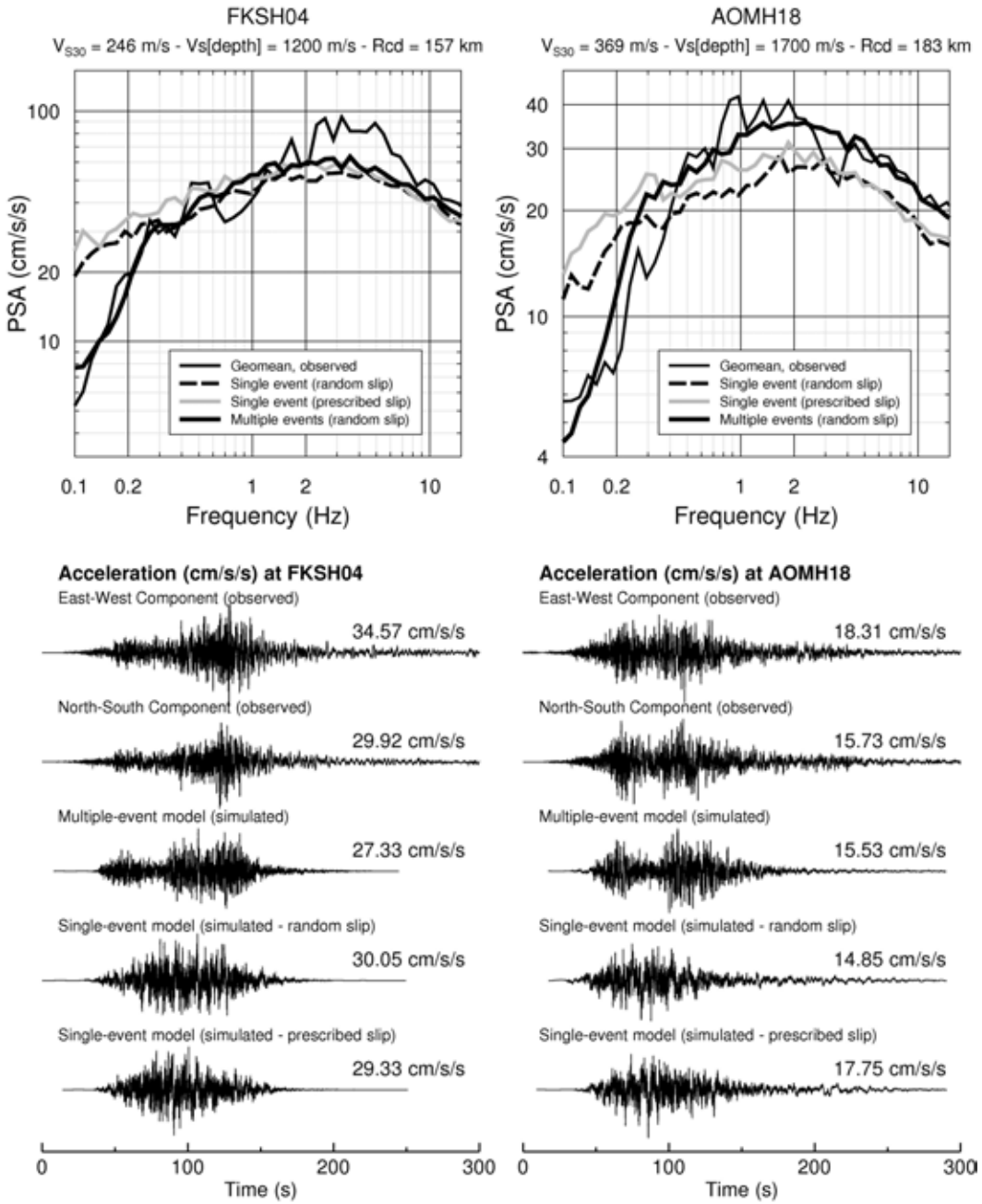

FIGURE 2 | Comparison of observed (borehole) and simulated pseudospectral acceleration (PSA) for two selected stations. Simulated PSAs are the average of 30 trials for each case (single-rupture models with random and prescribed slip, and multiple-rupture model). Depths of borehole installation for FKSH04 and AOMH18 are 268 and 100 m, respectively.

the continental North American plate. The geodetic convergence rate is typically about 35–40 mm/year (Flück et al., 1997; Wang et al., 2003). Along the down-dip direction, the interface gradually becomes steeper. This subduction zone hosts megathrust **M**9.0 events, as indicated by various sources of evidence including tsunami, liquefaction, and paleoseismic investigations (Adams, 1990; Satake et al., 2003; Atwater et al., 2004; Goldfinger et al., 2012). The subduction zone is considered to be "locked" at the shallow plate interface, which is constrained by the geothermal conditions of crustal rocks (150–350°C; Hyndman and Wang, 1995; Flück et al., 1997). To the landward side of the locked zone there is a "transition" zone, where the temperature is estimated between 350 and 450°C. The combined area of the locked and transition zones is often taken as the seismogenic rupture plane. The uncertainty in defining the down-dip limit of the rupture area affects seismic hazard and risk assessment, as it determines the proximity of the rupture to the centers of populations (e.g., Vancouver and Victoria).

Several fault plane models have been proposed for the Cascadia subduction zone, including the 2008 USGS model (Frankel and Petersen, 2008a,b) and the 2012 GSC model (Adams et al., 2012; Rogers et al., 2015), as shown in **Figure 3**. These models are rather similar, with the main difference that will be important being how close the rupture area comes to cities on-land. The USGS model was adopted in the 2008 USGS National Seismic Hazard Maps, while the 2012 GSC model was adopted in the 2015 National Building Code of Canada hazard maps. The geometry of the fault plane is mainly based on 3D dislocation models by Flück et al. (1997) and Wang et al. (2003), which were updated by McCrory et al. (2006), to incorporate information from new seismic reflection/refraction studies.

In the Cascadia-EXSIM model, a complex rupture surface is represented by a rectangular plane, such as the thick dotted lines shown in **Figure 4**. In order to simulate a curved rupture plane, portions of the rectangle can be assigned zero slip. The slip model illustrated in **Figure 4** considers the combined area of the locked and transition zones off the State of Washington (latitude between 46.5 and 48.5°). For subsources beyond the down-dip limit of the transition boundary, a negligible relative slip value is assigned, resulting in near-zero slip and energy. (Note: in EXSIM, the length, width, strike, dip, moment magnitude, stress drop, fault plane discretization, and relative slip distribution are specified, from which absolute values of the slip distribution are computed internally.)

EXSIM can account for the heterogeneity of slip distribution over the fault plane by assigning spatially varying relative slip weights. A random slip distribution can be specified (as in **Figure 4**), which is equivalent to randomizing the stress drop on the fault plane (Assatourians and Atkinson, 2007). As noted in the previous section, source inversion studies of the 2011 Tohoku earthquake (Kurahashi and Irikura, 2011; Irikura and Kurahashi, 2012) indicated that observed high-frequency ground motion features of that event could be modeled by adopting the concept of strong-motion-generation-areas (SMGA; Miyake et al., 2003). Because the primary focus of this study is to assess the strong ground motion intensity at Canadian major cities, such as Vancouver and Victoria, where the details of the slip distribution for future events are unknown, we assumed a single-rupture model

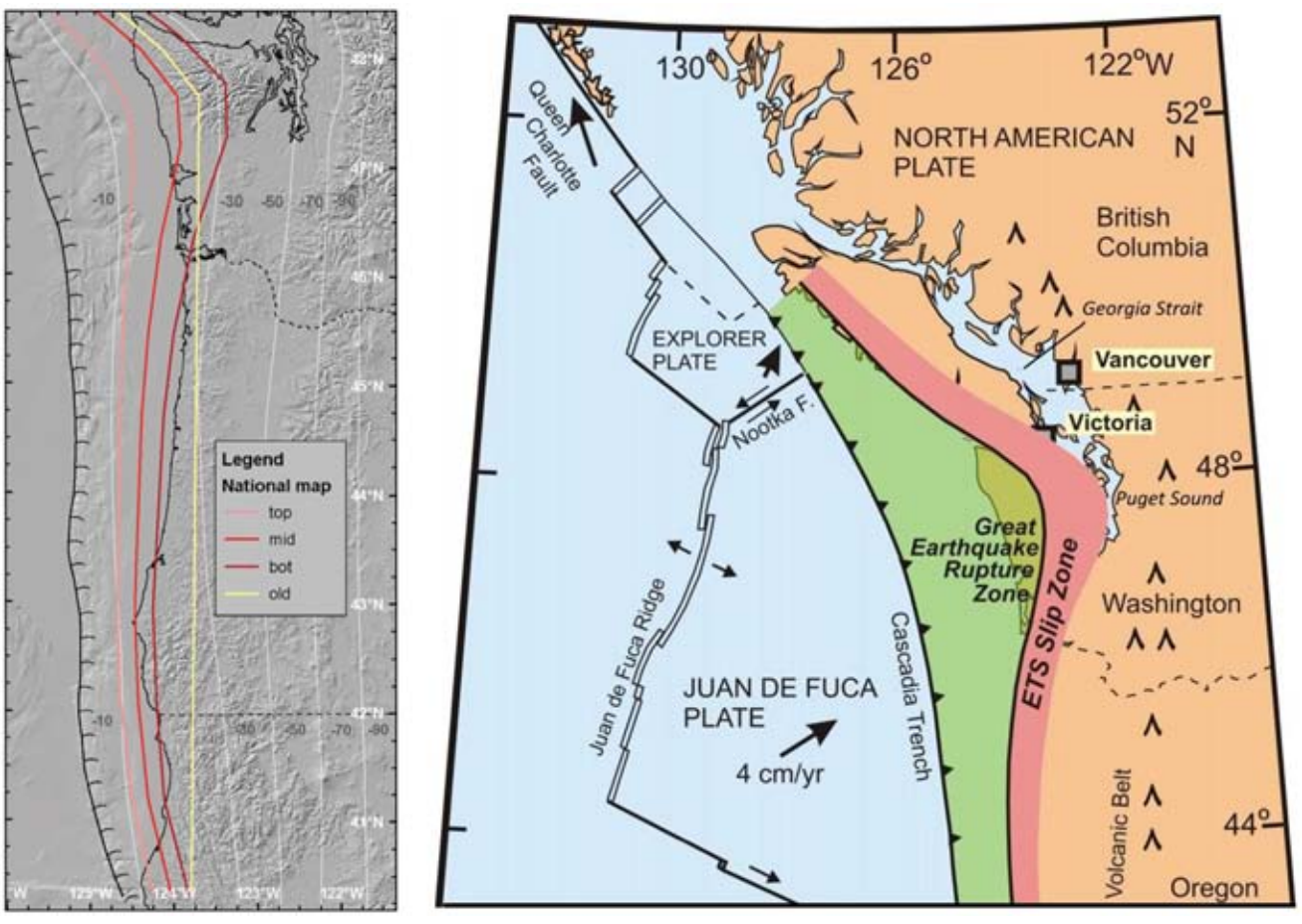

FIGURE 3 | Fault plane geometry of the 2008 USGS model (Frankel and Petersen, 2008a,b) and the 2012–2015 GSC model (Adams et al., 2012; Rogers et al., 2015). (Left) Map of the Cascadia megathrust, showing (as colored lines) the eastern edge of earthquake rupture zones. The light gray lines indicate the subduction interface from McCrory et al. (2004). (Right) Expected rupture zone of great megathrust earthquakes (in green) that is currently stuck and accumulating strain. The pink area is the approximate region of stick-slip behavior called Episodic Tremor and Slip (ETS).

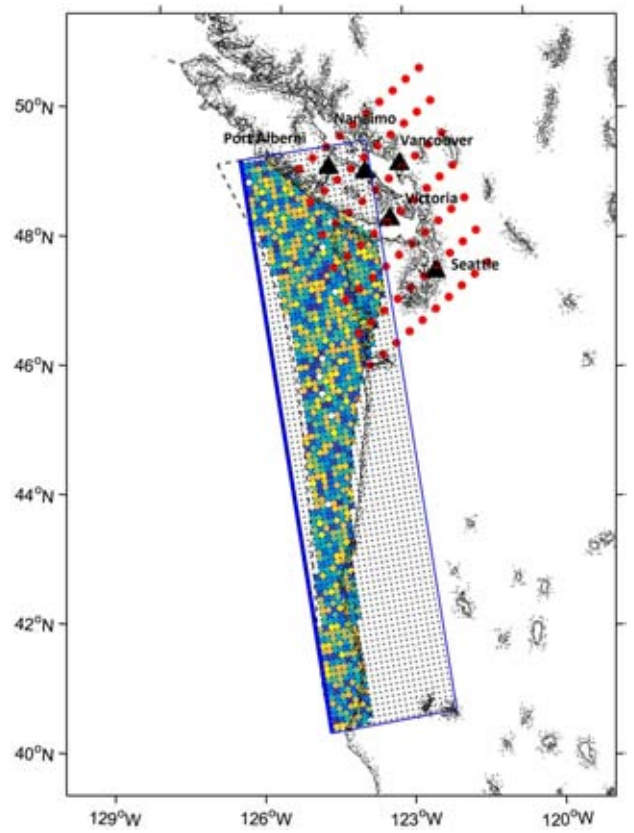

FIGURE 4 | Locations of observation sites (red circles) and slip distributions for the random model (colorful circles distributed on the subducting interface). Black triangles show the location of major cities. Subsources within the fault boundary (dashed black polygon) have randomly generated relative slip inputs, while those outside the boundary but inside the overall fault plane (blue rectangle) are assigned near-zero values.

with an average stress parameter of 100 bar, and a random slip distribution. The actual stress and slip distribution for future events is a source of significant uncertainty.

PATH PARAMETERS

In stochastic simulations, geometrical spreading and anelastic attenuation control the decay of simulated ground motion amplitudes over distance. In the path model used by Atkinson and Macias (2009) for Cascadia ground motion modeling, the geometrical spreading function is characterized by a bilinear model with a transition point at 40 km with slopes of −1.0 and −0.5 before and after the transition point. The anelastic attenuation is governed by the regional Quality factor (an inverse measure of anelasticity), given as $Q_S = 180f^{0.45}$. These parameters were adopted from large California crustal events (Atkinson and Silva, 2000). Investigations by Babaie Mahani and Atkinson (2013) show that moderate crustal earthquakes in the Pacific Northwest and south-western BC can be fitted with a bilinear attenuation model characterized by a transition point at 70 km with slopes of −1.24 and −0.5 before and after the transition point, with $Q_S = 244f^{0.6}$. The actual attenuation rates for sources on the subduction interface are not known due to the lack of empirical data from such events in Cascadia, and thus the assumed path parameters are a significant source of uncertainty.

TABLE 2 | Input parameters for Cascadia-EXSIM simulations (**M**9.0).

Model parameters	Representative value
Fault plane	GCS fault model (Rogers et al., 2015)
Fault dimension	1,000 km × 220 km
Subfault dimension	10 km × 10 km
Fault geometry	Strike = 350° | Dip = 7.5° | Depth-of-Top = 5 km
Stress parameter	100 bar
Hypocenter location	Random
Number of simulations *per* site	5
Slip distribution	Random
Pulsing percentage with dynamic corner frequency	50
Shear-wave velocity (β_s)	3.7 km/s
Density (ρ_s)	2.8 g/cm^3
Rupture propagation velocity	$0.8\beta_s$
Crustal model	California B/C site amplification
Duration model	Boore and Thompson, 2014
Geometrical spreading	$b^{-1.3}$ for $R \leq 50$ km and $b^{-0.5}$ for $R > 50$ km
Q-model	California Q-model (YA15)
Kappa (κ)	0.025 s

Considering the similarity of empirical path models among regions, we adopted the generic model developed by Yenier and Atkinson (2015), which is applicable in both western and eastern North America with a change in only the Q_S model. For this model, the geometric spreading term is $R^{-1.3}$ to 50 km, and $R^{-0.5}$ at greater distances, where R is an effective distance measure. In the Yenier and Atkinson model, an equivalent point-source concept is used, in which the effective distance measure accommodates near-distance saturation due to finite fault effects. In EXSIM, by contrast, finite-fault effects are inherently included due to the model geometry. We thus assume that the geometric spreading is applied from each subsource, and R becomes the distance from a subsource to the observation point. The anelastic function for western North America is given by $Q_S = \max(100, 170.3f^{0.45})$ (Yenier and Atkinson, 2015); this Q_S model is very similar to other western North American models discussed in the foregoing.

Near-surface path effects are modeled by a diminution function, $D(f)$, that implements the kappa filter (κ) proposed by Anderson and Hough (1984):

$$D(f) = \exp(-\pi\kappa f), \tag{7}$$

where κ determines the steepness of high-frequency decay of the Fourier acceleration spectrum. Typical values of κ are around 0.005–0.04 s, depending on site conditions; harder site profiles are associated with smaller κ values. For example, Atkinson (1996) suggested that $\kappa = 0.011$ for hard rock sites in British Columbia (site class A). For generic rock sites (site class C), Boore and Joyner (1997) suggested $\kappa = 0.035$. Atkinson and Macias (2009) used $\kappa = 0.03$ for a site in the Fraser River Delta (site class C) and $\kappa = 0.02$ for sites in Seattle and Victoria (site class B/C boundary). Ghofrani et al. (2012) suggested that $\kappa = 0.04$ is suitable for reference rock sites (site class B/C boundary) for Japanese stations. Thus typical κ values for western Canada may range between 0.01 and 0.04 (Atkinson, 1996; Atkinson and Macias, 2009), depending on site conditions.

Table 2 summarizes the input parameters used for EXSIM simulations for the Cascadia megathrust event. To show the effect of event size on the ground motions, we considered both an **M**9.0 rupture and a smaller rupture of **M**7.5. The **M**7.5 scenario event is chosen to occur at the eastern edge of the expected rupture zone, to represent an event with a smaller magnitude but at closer distance to the major cities in comparison to a **M**9.0 megathrust event. We note that the **M**7.5 event could be conceptualized as an asperity within the larger rupture plane of an **M**9.0 event. For the **M**7.5 scenario, we considered a rupture plane with a dimension of 81 km × 57 km (Strasser et al., 2010), strike = 310°, and depth-of-top ∼25 km. The fault plane is divided into 27 × 19 subfaults (3 km × 3 km). The Slip distribution is assumed to be random; the hypocenter is located at the center of the fault.

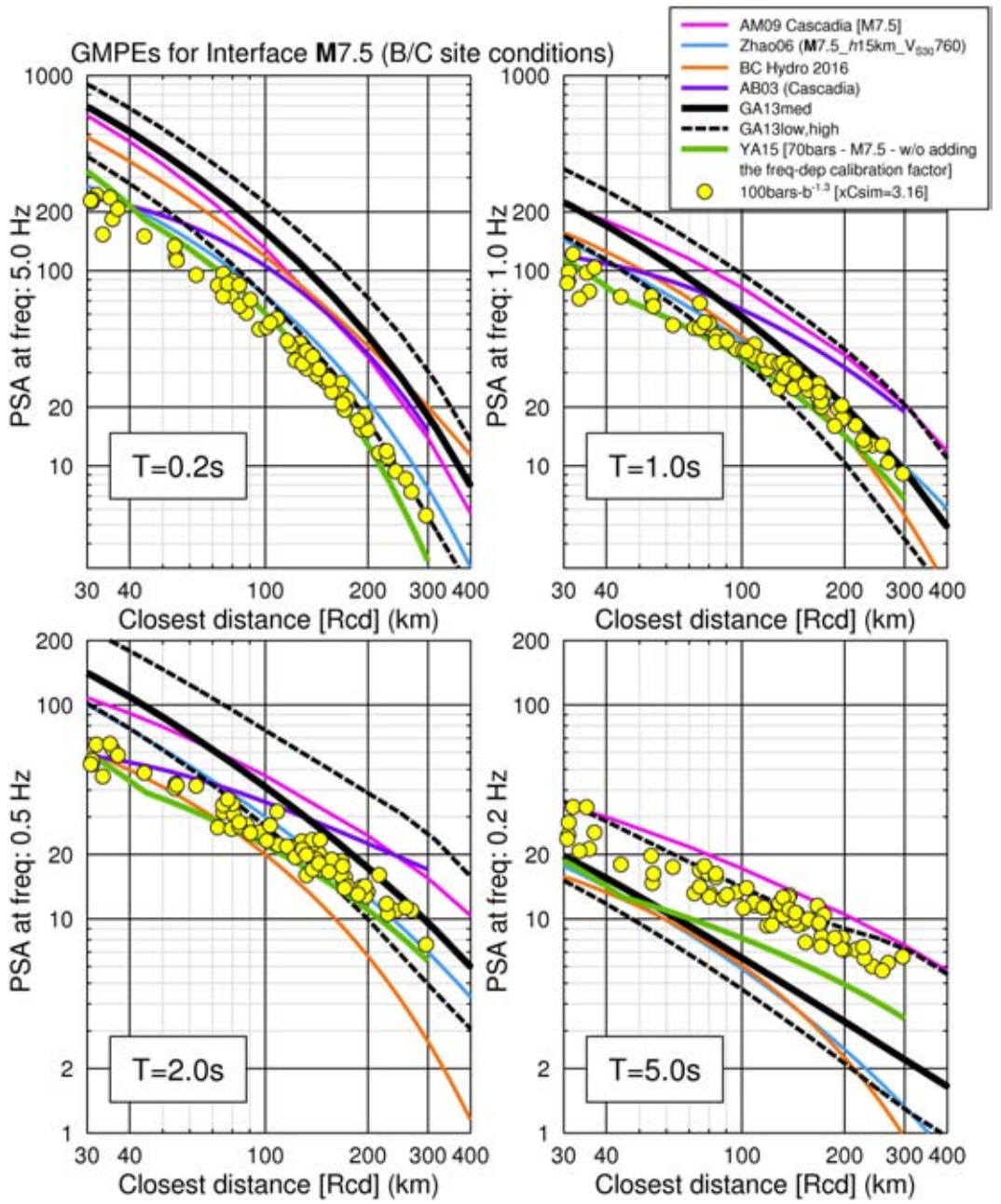

FIGURE 5 | EXSIM-simulated motions for stress parameter of 100 bar (yellow circles) and interface ground-motion prediction equations (GMPEs) for an **M**7.5 interface event. The interface GMPEs are shown as magenta (AM09), cyan (Zhao06), orange (BC Hydro 2016), purple (AB03), and black (GA13) curves. YA15 point-source model (70 bar) is shown as a solid green line. Japan to Cascadia site factor corrections have been applied to both Zhao et al. (2006) and Ghofrani and Atkinson (2013) models to account for the deeper soil profiles in Cascadia compared to Japan, for the same value of V_{s30} (see Ghofrani et al., 2012 for details). The models reflect forearc attenuation conditions.

RESULTS

Figure 5 plots the response spectral amplitudes of simulated ground motions versus distance from the EXSIM simulations for the **M**7.5 scenario, in comparison to the predictions of several interface GMPEs. All GMPEs are plotted for B/C site conditions, for a typical Cascadia soil profile (see Ghofrani and Atkinson, 2013 for details). For this exercise, we considered the GMPEs of Gregor et al., 2002; Atkinson and Boore, 2003 (AB03); Zhao et al., 2006 (Zhao06); Atkinson and Macias, 2009 (AM09); Ghofrani and Atkinson, 2013 (GA13); Somerville et al., 2008; and Abrahamson et al., 2016 (BC Hydro 2016). We also plotted for reference the generic GMPE of Yenier and Atkinson (2015) (hereinafter referred to as YA15) which is a regionally adjustable model developed based on equivalent point-source simulations. Although this is not a subduction GMPE, it is based on a similar stochastic model, using an equivalent point source rather than a finite fault. Additionally, it has the feature of an adjustable stress drop, which provides a useful aid in interpretation of the simulated motions. In order to make the Yenier and Atkinson point-source simulations comparable to the finite-fault simulations with EXSIM, we did not add the frequency-dependent calibration constant that Yenier and Atkinson use to match the simulations to empirical data in California. Instead, we used the generic simulation calibration factor (Csim = 3.16) described in Yenier and Atkinson (2015) which levels the simulations and observations, when using the geometric spreading term of $R^{-1.3}$. This same factor was applied to the EXSIM simulations. The plotted stress for the Yenier and Atkinson GMPE, 70 bar, was selected to approximately match the EXSIM amplitude levels at short periods. (Note: the corresponding value from Yenier and Atkinson for California is 100 bar.) A noteworthy feature of **Figure 5** is the wide spread of predictions among the GMPEs. The EXSIM predictions for an event of **M**7.5 are similar to the Yenier and Atkinson equivalent point-source model for crustal events in California at most periods—but at long periods EXSIM predicts higher motions, due to the different ways that finite-fault effects are modeled in the two algorithms.

Figure 6 provides insight into the frequency content of the ground motions and its dependence on the stress parameter used in the simulations. In this figure, the predicted average response spectrum of ground motions from the **M**7.5 scenario event is shown at a distance of 30 km from the rupture plane. As explained earlier in the text, this scenario event is chosen to occur at the eastern edge of the expected rupture zone, to represent an event with a smaller magnitude but at closer distance to the major cities in comparison to a **M**9.0 megathrust event. If a future megathrust event in Cascadia results in a complex source rupture process, the **M**7.5 event could be considered as an asperity within the larger

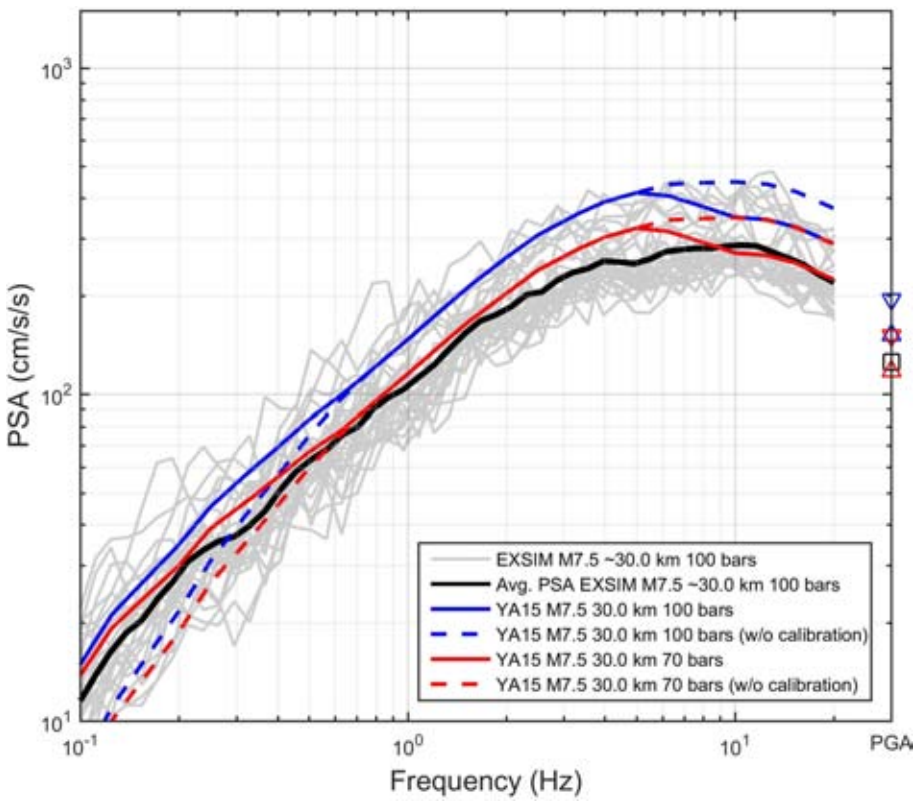

FIGURE 6 | Magnitude scaling at Rcd = 30 km for an **M**7.5 event. Black line is the mean of pseudospectral acceleration (PSA) for all stations at Rcd ∼30 km (shown with gray lines). Solid Blue and red curves are YA15 model for stress parameter of 100 and 70 bar (frequency-dependent calibration factor is included), respectively. Dashed blue and red lines represent YA15 without considering the calibration factor. Black square is the mean of simulated PGA for all stations at Rcd ∼30 km, up and down blue triangle symbols are PGA based on YA15 models for stress parameter of 100 and 70 bar, respectively, and up and down red triangle symbols are PGA based on YA15 models without considering the calibration factor.

rupture plane of an **M**9.0 event. To place the simulated response spectrum trend in context, we plotted the YA15 equivalent-point-source GMPE model in **Figure 6** for reference. As shown in this figure, we need a stress parameter of ∼70 bar in the context of the YA15 model to match the EXSIM-simulated spectrum. This implies that crustal events in active tectonic regions (e.g., California) would tend to produce larger ground motions at high frequencies, reflecting a higher value of the stress parameter, in comparison to interface events. As explained in Yenier and Atkinson (2015), an empirical frequency-dependent calibration factor can be used to reconcile the predictions of the YA15 equivalent point-source model with observed amplitudes in a target region; the calibration factor accounts in a crude way for the overall effects of factors that are missing or misfit in simulations (e.g., discrepancies between the assumed and true values of crustal properties, near-distance attenuation effects, regional site amplification, κ_0,

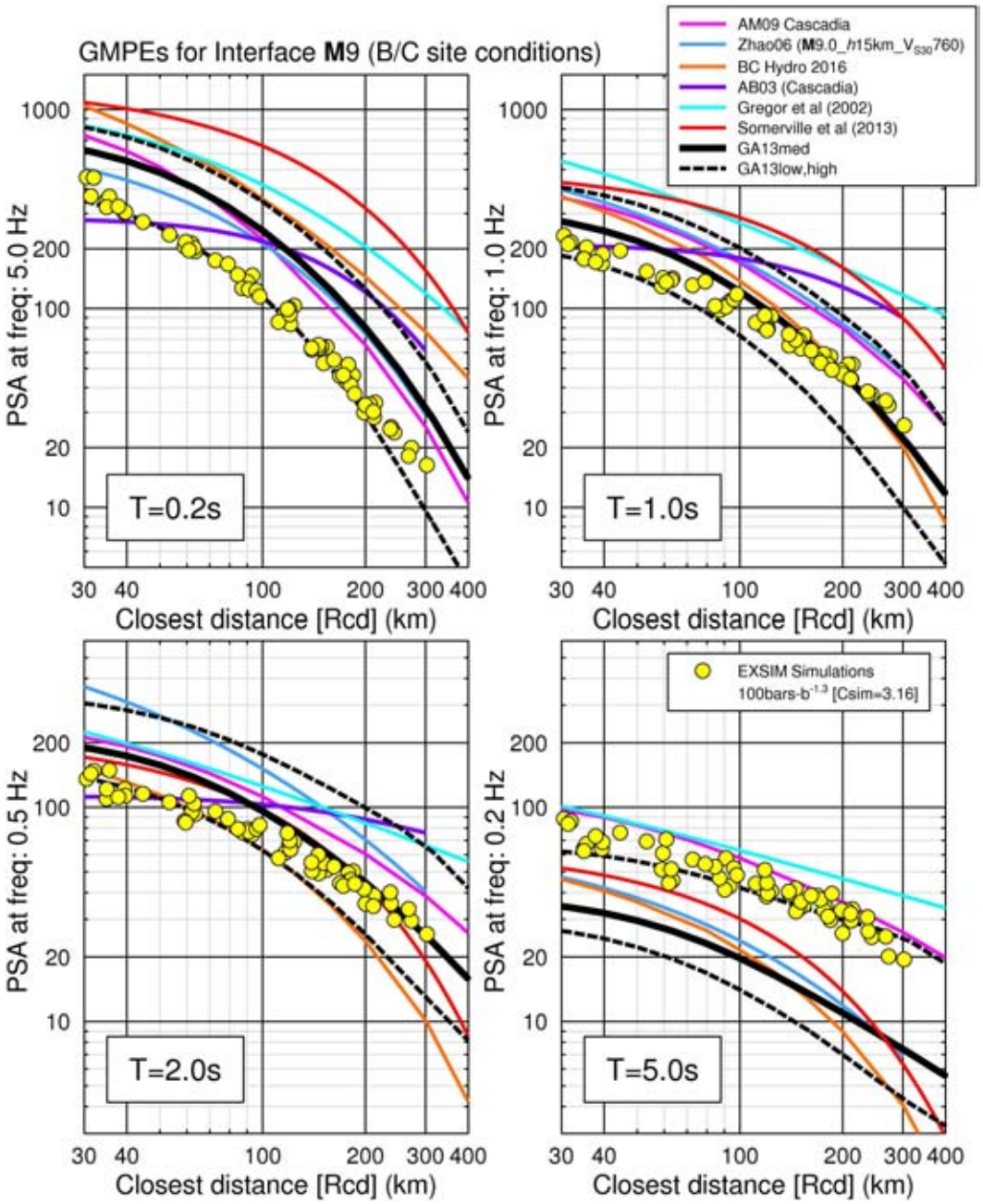

FIGURE 7 | EXSIM-simulated motions (yellow circles) and interface ground-motion prediction equations (GMPEs) for an **M**9.0 interface event. The interface GMPEs are shown as magenta (AM09), blue (Zhao06), orange (BC Hydro 2016), purple (AB03), cyan (Gregor et al., 2002), red (Somerville et al., 2013), and black (GA13) curves. Japan to Cascadia site factor corrections have been applied to both Zhao et al. (2006) and Ghofrani and Atkinson (2013) models to account for the deeper soil profiles in Cascadia compared to Japan, for the same value of V_{s30} (see Ghofrani et al., 2012 for details). The models reflect forearc attenuation conditions.

and path duration). To explore the impact of these effects in the simulated ground-motions, we plotted the YA15 model with and without the empirical calibration factor that Yenier and Atkinson used to match their equivalent point-source simulations to the California ground-motion database. This figure suggests that the EXSIM simulations tend to produce lower ground motions for large events than do the corresponding equivalent point-source simulations of Yenier and Atkinson (2015). This likely occurs because the point source simulations concentrate the source radiation at a single point (placed at an equivalent distance), while finite-fault simulations spread it over a larger fault plane. The consequent differences in the way that attenuation from the source is handled means that the values of the stress parameter do not carry the same meaning for equivalent point source and finite fault simulations for large events (see Atkinson et al., 2009). This discrepancy will become more pronounced as magnitude grows. This points to the importance of calibration of simulation algorithms with empirical data to ensure realistic parameter values.

Figure 7 plots the amplitudes of simulated ground motions versus distance from the EXSIM simulations for the **M**9.0 scenario, in comparison to the predictions of several interface GMPEs. All GMPEs are plotted for B/C site conditions, for a typical Cascadia soil profile. The plotted stress for the Yenier and Atkinson GMPE, 40 bar, was selected to approximately match the EXSIM amplitude levels at short periods. A noteworthy feature of **Figure 7** is the wide spread of predictions among the GMPEs (i.e., large epistemic uncertainty). The EXSIM simulations plot near the low end of the GMPEs at short periods, and near the high end of the GMPEs at long periods. This likely reflects the tuning of empirical GMPEs to match the motions from the Tohoku event—the only **M**9.0 event in the database. The Tohoku event was rich in short periods and deficient in long periods relative to what was expected based on other subduction earthquakes and ground-motion models (see discussion in Ghofrani and Atkinson, 2013). It has been suggested that the Tohoku event might be better considered as a composite of several events of $\mathbf{M} < 9.0$ (Geospatial Information Authority of Japan, 2011; Maercklin et al., 2012).

Figure 8 provides insight into the frequency content of the ground motions and its dependence on the stress parameter used in the simulations. In this figure, the predicted average spectrum of ground motions from the **M**9.0 scenario event is shown at a distance of 30 km from the rupture plane. To appreciate the level of simulated ground-motions, we plotted the YA15 GMPE model in **Figure 8** for reference. As show in this figure, we need a stress parameter of ∼40 bar to match the YA15 model to the simulated spectrum, although we note that use of the YA15 model for **M**9.0 represents an extrapolation that should not be accorded much significance.

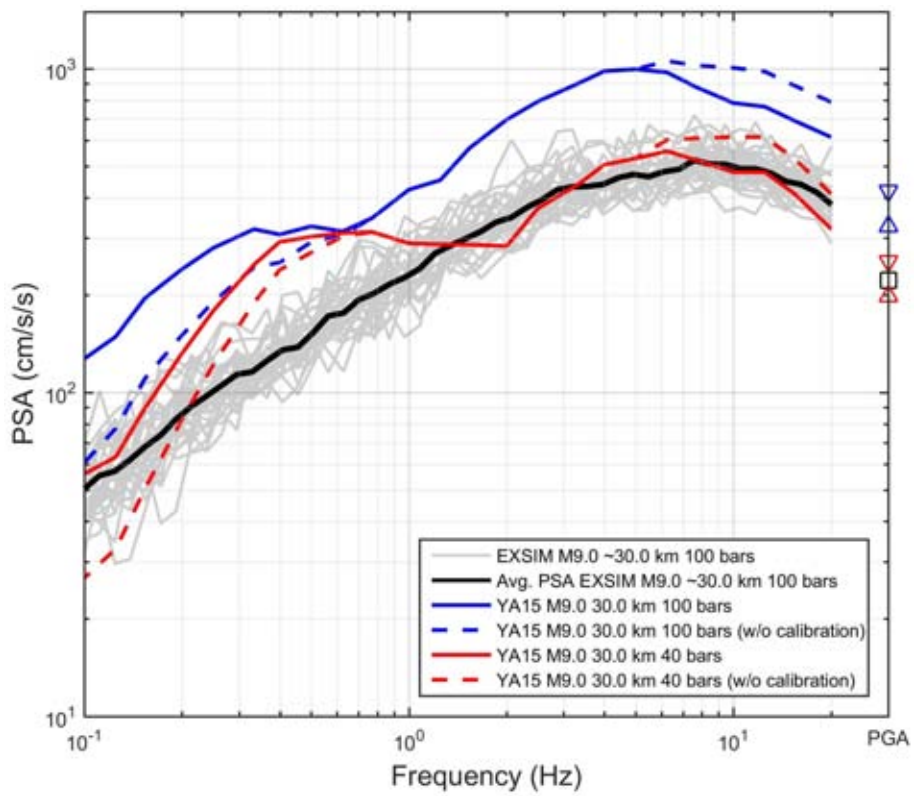

FIGURE 8 | Alternative estimates of response spectra at Rcd = 30 km for an **M**9.0 event. Black line is the mean of pseudospectral acceleration (PSA) for all stations at Rcd ∼30 km (shown with gray lines). Solid Blue and red curves are YA15 model for stress parameter of 100 and 40 bar, respectively. Dashed blue and red lines represent YA15 without considering the calibration factor. Note that YA15 is an extrapolation for **M**9.0. Black square is the mean of simulated PGA for all stations at Rcd ∼30 km, up and down blue triangle symbols are PGA based on YA15 models for stress parameter of 100 and 40 bar, respectively, and up and down red triangle symbols are PGA based on YA15 models without considering the calibration factor.

EFFECTS OF PARAMETER UNCERTAINTIES

Stress Parameter

One of the key uncertainties in the source parameters that control ground-motion amplitudes in EXSIM is the subevent stress parameter. In **Figure 9**, we show the sensitivity of results to this stress parameter, by comparing amplitudes for values of 30 and 150 bar—these are the estimates of the lower and upper limits on the stress-drop parameter based on interface events around the world, within the context of the EXSIM model, as determined by Atkinson and Macias (2009). The comparison is for a **M**9.0 scenario; the effect is similar for other magnitudes. **Figure 9** suggests that uncertainty in ground-motion spectral amplitudes for Cascadia events due to uncertainty in the appropriate stress parameter value is about ±50%; this uncertainty is partly epistemic (we do not know the median stress parameter value) and partly aleatory (the stress parameter for individual events will vary about the median).

Regional Attenuation and Crustal Velocity Model

A key uncertainty in the path model is the geometric spreading model. Uncertainties in the path model can produce even larger uncertainties in response spectral amplitudes in comparison to uncertainties in source parameters. For example, a geometric spreading of $R^{-1.0}$ results in an amplitude decay of 1.0 log10 units over the rupture distance interval from 10 to 100 km, while a spreading of $R^{-1.3}$ would result in an amplitude decay of 1.3 log10 units over the same distance interval; thus there would be a difference of a factor of two (e.g., 0.3 log units) in predicted amplitude for sites at 100 km. The path parameters in simulation models such as EXSIM should be calibrated using regional data—but such data are lacking for megathrust events in Cascadia, necessitating assumptions regarding the geometric spreading parameters based on observations in other regions. The resulting uncertainty is about a factor of 2 at 100 km and would become even larger at greater distances.

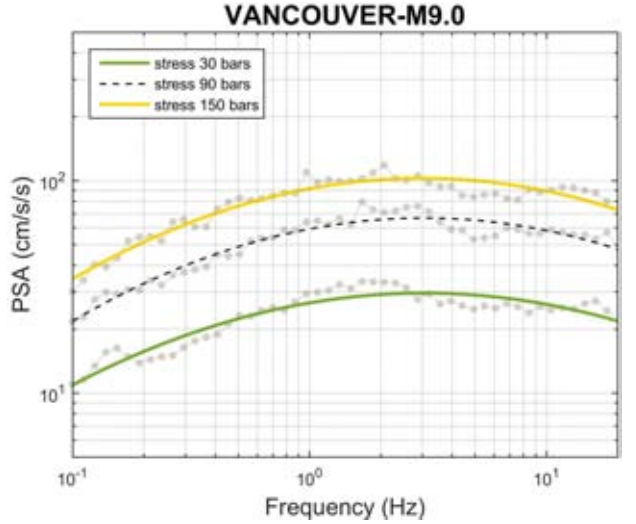

FIGURE 9 | Uncertainty in response spectra for **M**9.0 at Vancouver due to stress parameter uncertainty. Light black dashed line is the average (over numerous simulations) PSA for $\Delta\sigma = 90$ bar; green and orange solid lines are average PSA for $\Delta\sigma = 30$ bar and $\Delta\sigma = 150$ bar, respectively. Light gray dots are the average PSA values of 30 runs for the given stress parameters. The relative effect of stress parameter at Victoria is very similar.

SITE RESPONSE OF FRASER RIVER DELTA SEDIMENTS

The near-surface soil profile has significant influence on ground motions, altering both amplitude and frequency content of seismic waves. These effects are often investigated through site response analysis. Various methods, ranging from linear site response analysis (either frequency- or time-domain) to non-linear site response analysis, are available. The results from such analyses can be employed to develop site amplification factors, which are modeled as a function of soil parameters, such as average shear-wave velocity near the ground surface and fundamental site period. Development of generic site amplification factors is motivated by several practical considerations, which may include a lack of detailed soil information or the additional effort required to perform site response analysis. Moreover, the use of generic site amplification functions based on proxy indicators is inevitable for regional-scale seismic hazard and risk assessments and aids in the implementation of site response analysis in seismic hazard and risk analysis (e.g., Bazzurro and Cornell, 2004; Choi and Stewart, 2005; Cadet et al., 2012; Ghofrani et al., 2012).

Our synthetic ground motions of a scenario **M**9.0 Cascadia subduction earthquake are calculated here for a reference firm soil condition (site class B/C or V_{s30} of 760 m/s). This condition may be a fair approximation in Vancouver, which is located on overconsolidated Pleistocene glacial tills. However, the thick unconsolidated Holocene sediments of the Fraser River delta, south of Vancouver, are softer and tend to amplify earthquake shaking. They are also susceptible to liquefaction when saturated and cohesionless sand is present. As a simple demonstration of the potential amplification effects, we calculate theoretical 1D spectral amplification estimates for four selected Fraser River Delta sites.

SHEAR-WAVE VELOCITY PROFILES IN FRASER RIVER DELTA

The subsurface geology in southern Vancouver is comprised of three main geological units, from base to top: (i) Tertiary sedimentary rocks (bedrock), (ii) Pleistocene glacial/inter-glacial deposits, and (iii) Holocene sediments of the Fraser River (Britton et al., 1995; Hunter et al., 1998; Cassidy and Rogers, 2004). Tertiary rocks typically have a shear-wave velocity (V_s) of 1.5 km/s or greater (i.e., site class A). Pleistocene glacial till deposits are exposed on the ground surface at many locations in Vancouver and have V_s of ∼0.5 km/s (i.e., site class C) with significant variability (Cassidy and Rogers, 2004). Holocene Fraser River delta silts and sands have low V_s of about 0.1–0.2 km/s (i.e., site class D/E). The thickness of these geological units varies spatially. Holocene sediments can reach a depth of 0.3 km, whereas the

surface of Tertiary bedrock varies from 0 to 0.8 km [average depth is about 0.5 km; Britton et al. (1995)].

The locations of four selected sites in the Fraser River Delta are reported in **Table 3** and their V_s depth profiles are shown in **Figure 10**. The depth to Pleistocene material varies between 100 and 300 m among the sites, whereas depth of Tertiary bedrock is relatively consistent at ∼550 m.

THE QUARTER WAVELENGTH (QWL) METHOD

One of the simplest approaches for characterizing site amplification is based on the combined use of the QWL method and the kappa filter (Boore and Joyner, 1997; Boore, 2003). The overall effect of the site amplification $G(f)$ is expressed as:

$$G(f) = S(f)D(f), \tag{8}$$

TABLE 3 | The location of the four sites in the Fraser River Delta.

Site code	Lat. (°)	Long. (°)	V_{s30} (m/s)	Average V_s for entire profile (m/s)	Site class (NEHRP)
FD94-4	49.018	−123.162	143	440	E
FD87-1	49.052	−123.067	241	496	D
FD96-1	49.162	−123.137	188	446	D
SFU90-2	49.038	−123.051	170	462	E

where $S(f)$ is the amplification factor for wave propagation from source to ground surface and $D(f)$ is the diminution function that accounts for path-independent loss of energy. $S(f)$ is characterized by shear-wave velocity (β) and density (ρ) profiles over depth and is given by:

$$S(f) = \sqrt{\frac{\rho_s \beta_s}{\bar{\rho}\bar{\beta}}}, \tag{9}$$

where β_s and ρ_s are the shear-wave velocity and density near the source, and $\bar{\beta}$ and $\bar{\rho}$ are the shear-wave velocity and density averaged over a depth up to z, where z is taken as the depth corresponding to a quarter-wavelength: $z = (1/4)\beta(z(f))/f$. Note that by taking the depth corresponding to a quarter-wavelength, z becomes a function of frequency; this is considered to be the influential depth for the site amplification factor at a specific frequency (see **Figure 9** in Boore and Joyner (1997)). $\bar{\beta}$ and $\bar{\rho}$ are defined as:

$$\bar{\beta} = \frac{1}{z(f)} \int_0^{Z(f)} \beta(z) dz, \tag{10}$$

and

$$\bar{\rho} = z(f) \left[\int_0^{z(f)} \frac{1}{\rho(z)} dz \right]^{-1}, \tag{11}$$

respectively. The advantage of this method is its basis in simple fundamental physics, as represented by the square root of the impedance ratio. This method captures the smooth tendency of the site amplification over frequency (ignoring local

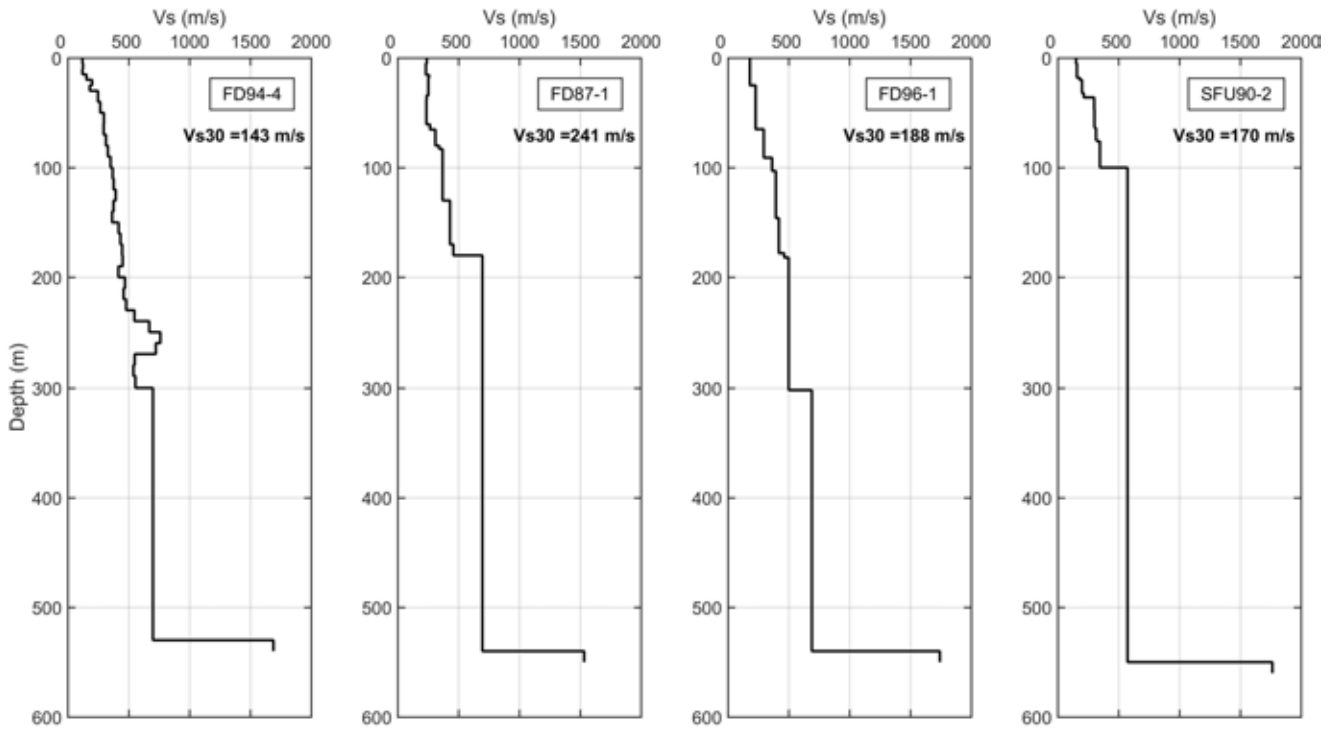

FIGURE 10 | Shear-wave velocity profiles of the four selected sites. In the Fraser Delta, there is a pervasive layer of Pleistocene deposits that overlies the Tertiary bedrock; the Pleistocene layer has a stable V_s gradient from 400 to 1,000 m/s, while the Tertiary bedrock has an average V_s of 1,500 m/s (Hunter, 1995; Hunter et al., 1997).

features due to resonance), its use in stochastic simulation as the overall frequency-dependent site amplification factor is adequate.

For the diminution function $D(f)$, a popular choice that reflects a wealth of empirical data is the kappa (κ) filter (Anderson and Hough, 1984), which is given by Eq. 7.

Here, we are referencing the zero-distance kappa intercept [often denoted $\kappa(0)$], which reflects the near-surface component of high-frequency spectral decay after regional anelastic path effects have been removed.

THEORETICAL TRANSFER FUNCTIONS

A slightly more sophisticated way to compute the theoretical site response is to calculate the 1D transfer function of horizontally stratified constant-slowness layers over an elastic bedrock, for a vertically propagating shear-wave (SH), using Thomson-Haskell's approach (Thomson, 1950; Haskell, 1953). For this calculation, we use the Nrattle program (C. Mueller, US Geological Survey with modification by R. Herrmann) included in the Boore (2005b) ground motion simulation program SMSIM. The input data for Nrattle are the layered velocity model, specifying the thickness, density, β, and seismic attenuation (Q_S) factor for each layer. The other input parameters are the shear-wave velocity and density of the half-space, incident angle, and the depth with respect to which the transfer function is calculated. We set the half-space equal to the β and ρ of the deepest measured layer. The Nrattle solution is exactly equivalent to the solution computed by the equivalent-linear site response program SHAKE for linear modulus reduction and damping curves (Schnabel et al., 1972).

EVALUATION OF SITE AMPLIFICATION FACTORS

To conduct site amplification analysis, suitable values for shear-wave velocity, density, and damping of the near-surface materials are needed. For the four velocity profiles considered, we set β_s to the value for Tertiary bedrock at the ~550-m base of all profiles (**Figure 10**). The angle of incidence is set to 0. The density profile over depth is calculated based on a relationship suggested by Hunter et al. (1998): $\rho(z) = \min[1.770 + 0.414\beta(z), 2.8]$. Nrattle mimics the effect of diminution at high frequencies using Quality

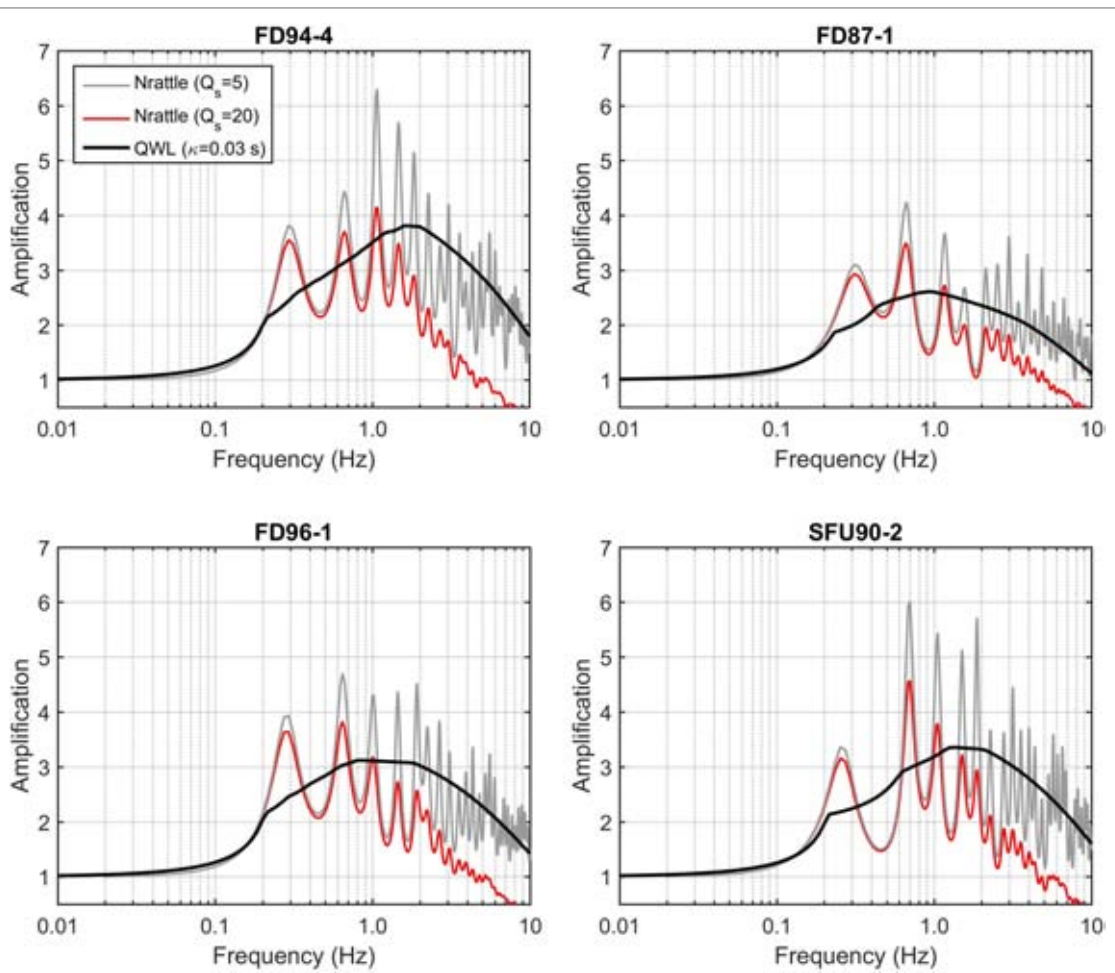

FIGURE 11 | Transfer (i.e., linear amplification) functions of four select Fraser River Delta sites. The gray and red curves are the theoretical site response computed using Nrattle with $Q_S = 5$ and $Q_S = 20$, respectively. The black curve is the amplification factor based on the quarter-wavelength method using kappa of 0.03 s.

factor or damping for each layer, rather than the kappa filter. At 0 epicentral distance, the seismic attenuation parameter kappa, κ, is related to the average near-surface shear wave velocity quality factor, $\overline{Q_S}$, as:

$$\kappa = H \Big/ \left(\overline{Q_S} \beta_{Savg} \right), \tag{12}$$

where H is the total thickness of the crust over which the energy loss occurs and β_{Savg} is the average shear wave velocity over H. It is important to note that a κ value of 0.03 s, which we used in our simulations, includes the total damping in the upper portion of the crust. By contrast, when considering the amplification effects of near-surface soils, the corresponding value of κ is that attributed to attenuation in the very shallow crust directly beneath the site (Hough and Anderson, 1988). Silva and Darragh (1995) suggest that these effects extend from the surface down to several hundred meters and possibly as deep as 1–2 km. In this study, we use a $\overline{Q_S}$ of 20 (Molnar et al., 2013) for calculating the damping effects of these near-surface materials. For comparison, we note that a value of $Q_S = 5$ used within Nrattle would be equivalent to $\kappa = 0.03$ s within the quarter-wavelength framework. This is shown in **Figure 11**, in which the amplifications for the four sites are plotted. Note that the near-surface materials provide significant high-frequency attenuation for the assumed value of $\overline{Q_S}$.

The peak frequency (f_0) of the transfer function for the four sites is relatively stable at ∼0.3 Hz, because the depth to the largest impedance contrast is consistent, at ∼550 m. Amplification is a factor of 4 (elastic) or 3 (with attenuation) at f_0. The theoretical 1D linear amplification functions in **Figure 11** are largely consistent with observed spectral amplification at Fraser River delta sites. For example, Molnar et al. (2013) report peak amplifications near 0.3 Hz of 2.5 and 5, from earthquake and microtremor recordings, respectively. Caution must be exercised when site amplification factors for soft soils are used to assess ground motions due to the **M**9.0 Cascadia events because local soil features may not be captured by these amplification factors and expected non-linear deamplification site effects are not taken into account.

We calculated site amplification factors for selected sites as a function of frequency for Vancouver's Fraser Delta. For other neighboring locations such as Victoria and Seattle, amplifications should be constructed separately, as studies suggest there are significant differences in shallow crustal structure. For example, a thinner layer of accreted sediments lies beneath Victoria in comparison to that beneath the Fraser Delta or Seattle (Ellis et al., 1983; McMechan and Spence, 1983; Graindorge et al., 2003; Ramachandran et al., 2006). Moreover, we have not modeled 3D basis effects that complicate observed amplifications.

CONCLUSION

Ground motions for earthquakes of **M**7.5–9.0 on the Cascadia subduction interface were simulated based on a stochastic finite-fault model and used to estimate average response spectra for firm-site conditions near the city of Vancouver. An important attribute of the simulations is that the methodology was first validated by reproducing the wealth of ground-motion data from the 2011 **M**9.0 Tohoku-Oki earthquake sequence of Japan. Adjustments to the calibrated model were then made to consider average source, attenuation, and site parameters for the Cascadia region, and to model the effects of parameter uncertainty. The simulations provide estimates of response spectra for firm-site conditions (B/C boundary in top of the Pleistocene in Vancouver); these motions could be input at the base of a soil layer to consider other site conditions, which may amplify the motions.

We have considered the major uncertainties in source, path and site effects. We conclude that uncertainty in stress parameter causes uncertainty in simulated response spectra of about ±50%. Uncertainties in the attenuation model produce even larger uncertainties in response spectral amplitudes—a factor of about two at 100 km, becoming even larger at greater distances. Uncertainty in site response further increases the total uncertainty. Moreover, the number of simulations and parameter combinations considered here may not be statistically sufficient for capturing extreme values that could result from the full range of potential model parameters; an exhaustive study of uncertainties was beyond the scope of this article.

We conclude that the large uncertainties in potential ground motions, due to uncertainties in regional source and attenuation parameters, are a dominant consideration when assessing seismic risk from Cascadia megathrust events. This also suggests that combining data from regions with different source and attenuation characteristics into a global subduction zone database for development of global empirical GMPEs may not be a sound practice. Future studies should aim to improve the regional attenuation model for Cascadia events and gain more information on the potential range of source parameters.

AUTHOR CONTRIBUTIONS

HG led the drafting of the text, conducted the simulation and ground motion analyses, and prepared most of the figures. GA participated equally in guiding methodology and direction/drafting of the article. SM provided key information and insights on site characteristics in BC and assisted in site response analyses.

ACKNOWLEDGMENTS

This work is funded by the Natural Sciences and Engineering Research Council of Canada. We are grateful to our colleague, Dr. Katsuchiro Goda, the PI of the project CRUST: Cascading Risk and Uncertainty assessment of earthquake Shaking & Tsunami, for his kind support and encouragement over the course of this project. The authors would like to thank the editor, Dr. Solomon Tesfamariam, and the reviewers, Dr. Vladimir Sokolov and Dr. Alin Radu for their constructive comments, which helped us to improve the manuscript.

REFERENCES

Abrahamson, N., Gregor, N., and Addo, K. (2016). BC hydro ground motion prediction equations for subduction earthquakes. *Earthquake Spectra* 32, 23–44. doi:10.1193/051712EQS188MR

Adams, J. (1990). Paleoseismicity of the Cascadia subduction zone: evidence from turbidites off the Oregon-Washington margin. *Tectonics* 9, 569–583. doi:10.1029/TC009i004p00569

Adams, J., Halchuk, S., and Rogers, G. (2012). *Cascadia Interface Subduction Source Model*. Vancouver, Canada: Internal Draft Prepared for the Canadian National Committee on Earthquake Engineering (CANCEE).

Anderson, J., and Hough, S. (1984). A model for the shape of the Fourier amplitude spectrum of acceleration at high frequencies. *Bull. Seismol. Soc. Am.* 74, 1969–1993.

Assatourians, K., and Atkinson, M. (2007). Modeling variable-stress distribution with the stochastic finite-fault technique. *Bull. Seismol. Soc. Am.* 97, 1935–1949. doi:10.1785/0120060203

Atkinson, G. M. (1996). The high-frequency shape of the source spectrum for earthquakes in eastern and western Canada. *Bull. Seismol. Soc. Am.* 86, 1067–1112.

Atkinson, G. M. (2005). Ground motions for earthquakes in southwestern British Columbia and Northwestern Washington: crustal, in-slab, and offshore events. *Bull. Seismol. Soc. Am.* 95, 1027–1044. doi:10.1785/0120040182

Atkinson, G. M., Assatourians, K., Boore, D. M., Campbell, K. W., and Motazedian, D. (2009). A guide to differences between stochastic point-source and stochastic finite-fault simulations. *Bull. Seismol. Soc. Am.* 99, 3192–3201. doi:10.1785/0120090058

Atkinson, G. M., and Boore, D. M. (2003). Empirical ground-motion relations for subduction zone earthquakes and their application to Cascadia and other regions. *Bull. Seismol. Soc. Am.* 93, 1703–1729. doi:10.1785/0120020156

Atkinson, G. M., and Macias, M. (2009). Predicted ground motions for great interface earthquakes in the Cascadia subduction zone. *Bull. Seismol. Soc. Am.* 99, 1552–1578. doi:10.1785/0120080147

Atkinson, G. M., and Silva, W. (2000). Stochastic modeling of California ground motions. *Bull. Seismol. Soc. Am.* 90, 255–274. doi:10.1785/0119990064

Atwater, B. F., Tuttle, M. P., Schweig, E. S., Rubin, C. M., Yamaguchi, D. K., and Hemphill-Haley, E. (2004). "Earthquake recurrence inferred from paleoseismology," in *The Quaternary Period in the United States: Developments in Quaternary Science 1*, eds A. R. Gillespie, S. C. Porter, and B. F. Atwater (Amsterdam, New York: Elsevier), 331–350.

Babaie Mahani, A., and Atkinson, G. (2013). Regional differences in ground-motion amplitudes of small-to-moderate earthquakes across North America. *Bull. Seismol. Soc. Am.* 103, 2604–2620. doi:10.1785/0120120350

Bazzurro, P., and Cornell, A. C. (2004). Nonlinear soil-site effects in probabilistic seismic-hazard analysis. *Bull. Seismol. Soc. Am.* 94, 2110–2123. doi:10.1785/0120030216

Boore, D. M. (1983). Stochastic simulation of high-frequency ground motions based on seismological models of the radiated spectra. *Bull. Seismol. Soc. Am.* 73, 1865–1894.

Boore, D. M. (2003). Simulation of ground motion using the stochastic method. *Pure Appl. Geophys.* 160, 635–676. doi:10.1007/PL00012553

Boore, D. M. (2005a). On pads and filters. *Bull. Seismol. Soc. Am.* 95, 745–750. doi:10.1785/0120040160

Boore, D. M. (2005b). *SMSIM – FORTRAN Programs for Simulating Ground Motions from Earthquakes (Ver. 2.3)*. Available at: http://w.daveboore.com/software_online.html

Boore, D. M. (2009). Comparing stochastic point-source and finite-source ground-motion simulations: SMSIM and EXSIM. *Bull. Seismol. Soc. Am.* 99, 3202–3216. doi:10.1785/0120090056

Boore, D. M., and Joyner, W. B. (1997). Site amplifications for generic rock sites. *Bull. Seismol. Soc. Am.* 87, 327–341.

Boore, D. M., and Thompson, E. M. (2014). Path durations for use in the stochastic-method simulation of ground motions. *Bull. Seismol. Soc. Am.* 104, 2541–2552. doi:10.1785/0120140058

Britton, J., Harris, J., Hunter, J. A., and Luternauer, J. (1995). *The Bedrock Surface Beneath the Fraser River Delta in British Columbia Based on Seismic Measurements. Current Research 1995-E*. Geological Survey of Canada, 83–89.

Brune, J. N. (1970). Tectonic stress and the spectra of seismic shear waves from earthquakes. *J. Geophys. Res.* 75, 4997–5009. doi:10.1029/JB075i026p04997

Brune, J. N. (1971). Correction. *J. Geophys. Res.* 76, 5002.

Cadet, H., Bard, P. Y., Duval, A. M., and Bertrand, E. (2012). Site effect assessment using KiK-net data: part 2 – site amplification prediction equations based on f0 and Vsz. *Bull. Earthquake Eng.* 10, 451–489. doi:10.1007/s10518-011-9324-9

Cassidy, J. F., and Rogers, G. C. (2004). "Variation in ground shaking on the Fraser River Delta (Greater Vancouver, Canada) from analysis of moderate earthquakes," in *Proceedings of the 13th World Conference on Earthquake Engineering* (Vancouver, Canada), 1010.

Choi, Y., and Stewart, J. P. (2005). Nonlinear site amplification as function of 30 m shear wave velocity. *Earthquake Spectra* 21, 1–30. doi:10.1193/1.1856535

De Risi, R., and Goda, K. (2016). Probabilistic earthquake-tsunami multihazard analysis: application to the Tohoku region, Japan. *Front. Built Environ.* 2:25. doi:10.3389/fbuil.2016.00025

Ellis, R. M., Spence, G. D., Clowes, R. M., Waldron, D. A., and Jones, I. F. (1983). The Vancouver island seismic project: a co-crust onshore-offshore study of a convergent margin. *Can. J. Earth Sci.* 20, 719–741. doi:10.1139/e83-065

Flück, P., Hyndman, R. D., and Wang, K. (1997). Three-dimensional dislocation model for great earthquakes of the Cascadia subduction zone. *J. Geophys. Res.* 102, 20539–20550. doi:10.1029/97JB01642

Frankel, A. D., and Petersen, M. D. (2008a). "Cascadia subduction zone," in *The Uniform California Earthquake Rupture Forecast, Version 2* (Renton: US Geological Survey).

Frankel, A. D., and Petersen, M. D. (2008b). *Cascadia Subduction Zone (Appendix L)*. Open File Report 2007-1437L. Golden, Colorado: U.S. Geological Survey.

Geist, E. L. (2005). "Local tsunami hazards in the Pacific Northwest from Cascadia subduction zone earthquakes," in *Earthquake Hazards of the Pacific Northwest Coast and Marine Regions*, ed. R. Kayen (U.S. Department of the Interior, U.S. Geological Survey, Professional Paper), 1661–B.

Geospatial Information Authority of Japan. (2011). *Crustal Deformation and Fault Model Obtained from GEONET Data Analysis*. Available at: http://www.gsi.go.jp/cais/topic110422-index-e.html

Ghofrani, H., and Atkinson, G. (2011). Forearc versus backarc attenuation of earthquake ground motion. *Bull. Seismol. Soc. Am.* 101, 3032–3045. doi:10.1785/0120110067

Ghofrani, H., and Atkinson, G. M. (2013). Ground-motion prediction equations for interface earthquakes of M7 to M9 based on empirical data from Japan. *Bull. Earthquake Eng.* 12, 549–571. doi:10.1007/s10518-013-9533-5

Ghofrani, H., Atkinson, G. M., and Goda, K. (2012). Implications of the 2011 M9.0 Tohoku Japan earthquake for the treatment of site effects in large earthquakes. *Bull. Earthquake Eng.* 11, 171–203. doi:10.1007/s10518-012-9413-4

Ghofrani, H., Atkinson, G. M., Goda, K., and Assatourians, K. (2013). Stochastic finite-fault simulations of the 11th March Tohoku, Japan. *Earthquake Bull. Seismol. Soc. Am.* 103, 1307–1320. doi:10.1785/0120120228

Goda, K., Petrone, C., De Risi, R., and Rossetto, T. (2016). Stochastic coupled simulation of strong motion and tsunami for the 2011 Tohoku, Japan earthquake. *Stoch. Environ. Res. Risk Assess.* 1–19. doi:10.1007/s00477-016-1352-1

Goda, K., Pomonis, A., Chian, S. C., Offord, M., Saito, K., Sammonds, P., et al. (2012). Ground motion characteristics and shaking damage of the 11th March 2011 Mw9.0 Great East Japan earthquake. *Bull. Earthquake Eng.* 11, 141–170. doi:10.1007/s10518-012-9371-x

Goda, K., and Tesfamariam, S. (2017). Seismic risk management of existing reinforced concrete buildings in the Cascadia subduction zone. *Nat. Hazards Rev.* 18, B4015003. doi:10.1061/(ASCE)NH.1527-6996.0000206

Goda, K., Wenzel, F., and De Risi, R. (2015). Empirical assessment of nonlinear seismic demand of mainshock-aftershock ground motion sequences for Japanese earthquakes. *Front. Built Environ.* 1:6. doi:10.3389/fbuil.2015.00006

Goldfinger, C., Grijalva, K., Bürgmann, R., Morey, A. E., Johnson, J. E., Nelson, C. H., et al. (2008). Late Holocene rupture of the Northern San Andreas fault and possible stress linkage to the Cascadia subduction zone. *Bull. Seismol. Soc. Am.* 98, 861–889. doi:10.1785/0120060411

Goldfinger, C., Nelson, C. H., Morey, A. E., Johnson, J. E., Patton, J., Karabanov, E., et al. (2012). *Turbidite Event History – Methods and Implications for Holocene Paleoseismicity of the Cascadia Subduction Zone*. U.S. Geological Survey Professional Paper 1661-F, 170.

Graindorge, D., Spence, G., Charvis, P., Collot, J. Y., Hyndman, R., and Tréhu, A. M. (2003). Crustal structure beneath the strait of Juan de Fuca and southern Vancouver island from seismic and gravity analysis. *J. Geophys. Res.* 108, 2484. doi:10.1029/2002JB001823

Gregor, N. J., Silva, W. J., Wong, I. G., and Youngs, R. R. (2002). Ground-motion attenuation relationships for Cascadia subduction zone megathrust earthquakes. *Bull. Seismol. Soc. Am.* 92, 1923–1932. doi:10.1785/0120000260

Haskell, N. A. (1953). The dispersion of surface waves on multilayered media. *Bull. Seismol. Soc. Am.* 72, 17–34.

Hough, S. E., and Anderson, J. G. (1988). High-frequency spectra observed at Anza, California: implications for Q structure. *Bull. Seismol. Soc. Am.* 78, 692–707.

Hunter, J. (1995). *Shear Wave Velocities of Holocene Sediments, Fraser River Delta, British Columbia*. Current Research 1995-A, Geological Survey of Canada, 29–32.

Hunter, J., Harris, J., and Britton J. (1997). *Compressional and Shear Wave Interval Velocity Data for Quaternary Sediments in the Fraser River Delta from Multichannel Seismic Reflection Surveys*. Geological Survey of Canada Open-File Report 97-3325.

Hunter, J. A., Burns, R., Good, R., and Pelletier, C. (1998). *A Compilation of Shear Wave Velocities and Borehole Geophysics Logs in Unconsolidated Sediments of the Fraser River Delta*. Open-File Report 3622. Geological Survey of Canada.

Hyndman, R. D., Mazzotti, S., Weichert, D., and Rogers, G. C. (2003). Frequency of large crustal earthquakes in Puget Sound-southern Georgia Strait predicted from geodetic and geological deformation rates. *J. Geophys. Res.* 108, 2033. doi:10.1029/2001JB001710

Hyndman, R. D., and Wang, K. (1995). The rupture zone of Cascadia great earthquakes from current deformation and the thermal regime. *J. Geophys. Res.* 100, 22133–22154. doi:10.1029/95JB01970

Irikura, K., and Kurahashi, S. (2012). "High acceleration motions generated from the 2011 Pacific coast off Tohoku, Japan earthquake," in *Proc. 15th World Conf. Earthquake Eng* (Lisbon, Portugal).

Kamae, K., Irikura, K., and Pitarka, A. (1998). A technique for simulating strong ground motion using hybrid Green's function. *Bull. Seismol. Soc. Am.* 88, 357–367.

Kurahashi, S., and Irikura, K. (2011). Source model for generating strong ground motions during the 2011 off the Pacific coast of Tohoku earthquake. *Earth Planets Space* 63, 571–576. doi:10.5047/eps.2011.06.044

Maercklin, N., Festa, G., Colombelli, S., and Zollo, A. (2012). Twin ruptures grew to build up the giant 2011 Tohoku, Japan, earthquake. *Sci. Rep.* 2, 709. doi:10.1038/srep00709

Mazzotti, S., and Adams, J. (2004). Variability of near-term probability for the next great earthquake on the Cascadia subduction zone. *Bull. Seismol. Soc. Am.* 94, 1954–1959. doi:10.1785/012004032

McCrory, P. A., Blair, J. L., Oppenheimer, D. H., and Walter, S. R. (2004). *Depth to the Juan de Fuca Slab Beneath the Cascadia Subduction Margin-A 3-D Model for Sorting Earthquakes*. U.S. Geol. Surv. Data Series, 91, 1.2.

McCrory, P. A., Blair, J. L., Oppenheimer, D. H., and Walter, S. R. (2006). *Depth to the Juan de Fuca Slab Beneath the Cascadia Subduction Margin – a 3-D Model for Sorting Earthquakes*. Menlo Park, California: U.S. Geological Survey Data Series 91.

McMechan, G. A., and Spence, G. (1983). P-wave velocity structure of the Earth's crust beneath Vancouver island. *Can. J. Earth Sci.* 20, 742–752. doi:10.1139/e83-066

Miyake, H., Iwata, T., and Irikura, K. (2003). Source characterization for broadband ground-motion simulation, kinematic heterogeneous source model and strong motion generation area. *Bull. Seismol. Soc. Am.* 93, 2531–2545. doi:10.1785/0120020183

Molnar, S., Cassidy, J. F., and Dosso, S. E. (2013). Uncertainty of linear earthquake site amplification via Bayesian inversion of surface seismic data. *Geophysics* 78, WB37–WB48. doi:10.1190/geo2012-0345.1

Motazedian, D., and Atkinson, G. M. (2005). Stochastic finite-fault modeling based on a dynamic corner frequency. *Bull. Seismol. Soc. Am.* 95, 995–1010. doi:10.1785/0120030207

Ramachandran, K., Hyndman, R. D., and Brocher, T. M. (2006). Regional P-wave velocity structure of the northern Cascadia subduction zone. *J. Geophys. Res.* 111, B12301. doi:10.1029/2005JB004108

Rogers, G., Halchuk, S., Adams, J., and Allen, T. (2015). *5th Generation (2015) Seismic Hazard Model for Southwest British Columbia, 11th Canadian Conference on Earthquake Engineering*. Victoria: 21–24.

Satake, K., Wang, K., and Atwater, B. F. (2003). Fault slip and seismic moment of the 1700 Cascadia earthquake inferred from Japanese tsunami descriptions. *J. Geophys. Res.* 108, 2535. doi:10.1029/2003JB002521

Schnabel, P. B., Lysmer, J., and Seed, H. B. (1972). *SHAKE: A Computer Program for Earthquake Response Analysis of Horizontally Layered Sites*. Technical Report Rept. EERC 72-12. Berkeley: Earthquake Engineering Research Center, University of California.

Shao, G., Li, X., Ji, C., and Maeda, T. (2011). Focal mechanism and slip history of the 2011 Mw9.1 off the Pacific coast of Tohoku earthquake, constrained with teleseismic body and surface waves. *Earth Planets Space* 63, 559–564. doi:10.5047/eps.2011.06.028

Silva, W. J., and Darragh, R. B. (1995). *Engineering Characterization of Strong Ground Motion Recorded at Rock Sites*. Draft Final Report Submitted to Electric Power Res. Inst., EPRI RP 2556-48.

Somerville, P., Skarlatoudis, A., and Li, W. (2013). *Ground Motions and Tsunamis from Large Cascadia Subduction Earthquakes Based on the 2011 Tohoku, Japan Earthquake*. U.S. Geol. Surv. Final Report. 81.

Somerville, P., Graves, R., and Collins, N. (2008). *Ground Motions from Large Cascadia Subduction Earthquakes*. U.S. Geol. Surv. Final Rept. Award Number 06HQGR0160.

Strasser, F. O., Arango, M. C., and Bommer, J. J. (2010). Scaling of the source dimensions of interface and intraslab subduction-zone earthquakes with moment magnitude. *Seismol. Res. Lett.* 81, 941–950. doi:10.1785/gssrl.81.6.941

Thomson, W. T. (1950). Transmission of elastic waves through a stratified solid. *J. Appl. Phys.* 21, 89–93. doi:10.1063/1.1699629

Wang, K., Wells, R., Mazzotti, S., Hyndman, R. D., and Sagiya, T. (2003). A revised dislocation model of interseismic deformation of the Cascadia subduction zone. *J. Geophys. Res.* 108, 2026. doi:10.1029/2001JB001227

Yenier, E., and Atkinson, G. M. (2015). Regionally adjustable generic ground-motion prediction equation based on equivalent point-source simulations: application to central and Eastern North America. *Bull. Seismol. Soc. Am.* 105, 1989–2009. doi:10.1785/0120140332

Zhao, J. X., Zhang, J., Asano, A., Ohno, Y., Oouchi, T., Takahashi, T., et al. (2006). Attenuation relations of strong ground motion in Japan using site classification based on predominant period. *Bull. Seismol. Soc. Am.* 96, 898–913. doi:10.1785/0120050122

Conflict of Interest Statement: The authors declare that the research was conducted in the absence of any commercial or financial relationships that could be construed as a potential conflict of interest.

Copyright © 2017 Ghofrani, Atkinson and Molnar. This is an open-access article distributed under the terms of the Creative Commons Attribution License (CC BY). The use, distribution or reproduction in other forums is permitted, provided the original author(s) or licensor are credited and that the original publication in this journal is cited, in accordance with accepted academic practice. No use, distribution or reproduction is permitted which does not comply with these terms.

frontiers in Built Environment

ORIGINAL RESEARCH
published: 07 October 2015
doi: 10.3389/fbuil.2015.00018

Seismic performance evaluation framework considering maximum and residual inter-story drift ratios: application to non-code conforming reinforced concrete buildings in Victoria, BC, Canada

Solomon Tesfamariam[1]* *and Katsuichiro Goda*[2]

[1] School of Engineering, The University of British Columbia, Kelowna, BC, Canada, [2] Department of Civil Engineering, University of Bristol, Bristol, UK

OPEN ACCESS

Edited by:
Panagiotis Mergos,
City University London, UK

Reviewed by:
Mohammad Mehdi Kashani,
University of Bristol, UK
Sameh Samir F. Mehanny,
Cairo University, Egypt
Anaxagoras Elenas,
Democritus University of Thrace, Greece

***Correspondence:**
Solomon Tesfamariam,
The University of British Columbia,
EME 4253 – 1137 Alumni Avenue,
Kelowna, BC V1V 1V7, Canada
solomon.tesfamariam@ubc.ca

Specialty section:
This article was submitted to Earthquake Engineering, a section of the journal Frontiers in Built Environment

Received: 12 August 2015
Accepted: 17 September 2015
Published: 07 October 2015

Citation:
Tesfamariam S and Goda K (2015) Seismic performance evaluation framework considering maximum and residual inter-story drift ratios: application to non-code conforming reinforced concrete buildings in Victoria, BC, Canada. Front. Built Environ. 1:18. doi: 10.3389/fbuil.2015.00018

This paper presents a seismic performance evaluation framework using two engineering demand parameters, i.e., maximum and residual inter-story drift ratios, and with consideration of mainshock–aftershock (MSAS) earthquake sequences. The evaluation is undertaken within a performance-based earthquake engineering framework in which seismic demand limits are defined with respect to the earthquake return period. A set of 2-, 4-, 8-, and 12-story non-ductile reinforced concrete (RC) buildings, located in Victoria, BC, Canada, is considered as a case study. Using 50 mainshock and MSAS earthquake records (2 horizontal components per record), incremental dynamic analysis is performed, and the joint probability distribution of maximum and residual inter-story drift ratios is modeled using a novel copula technique. The results are assessed both for collapse and non-collapse limit states. From the results, it can be shown that the collapse assessment of 4- to 12-story buildings is not sensitive to the consideration of MSAS seismic input, whereas for the 2-story building, a 13% difference in the median collapse capacity is caused by the MSAS. For unconditional probability of unsatisfactory seismic performance, which accounts for both collapse and non-collapse limit states, the life safety performance objective is achieved, but it fails to satisfy the collapse prevention performance objective. The results highlight the need for the consideration of seismic retrofitting for the non-ductile RC structures.

Keywords: seismic performance, maximum inter-story drift, residual inter-story drift, non-code conforming reinforced concrete building, mainshock–aftershock earthquake

Introduction

Motivation

The eastern and western provinces of Canada are subject to moderate to large magnitude earthquakes. As a result, Canadian buildings are prone to earthquake-induced damage (Bruneau and Lamontagne, 1994; Ventura et al., 2005). Since 1900, several destructive earthquakes have been reported (**Table 1**; **Figure 1**), including the 1918 and 1946 earthquakes in Vancouver Island and the 1949, 1965, and 2001 (Nisqually) deep earthquakes in Washington, DC, USA. The recurrence

of the Cascadia subduction earthquakes (magnitudes of 8–9) can affect a vast region of the Pacific coast from Vancouver Island to Washington/Oregon (Hyndman and Rogers, 2010). For large interface events, intense long-period ground motions having long duration are anticipated. To assess seismic performance of structures and infrastructure more accurately, a novel seismic performance evaluation framework that accounts for probabilistic characteristics of multivariate engineering demand parameters caused by major earthquake ground motions as well as their aftershock ground motions is proposed. The developed methodology is applied to a set of non-ductile reinforced concrete (RC) structures that are located in Victoria, British Columbia (BC), Canada. In the framework, regional seismicity in southwestern BC is fully taken into account in defining seismic performance levels and in evaluating the nonlinear structural responses via rigorous ground motion record selection.

Through lessons learned from performance of buildings during previous earthquakes and research over the last three decades, Canadian seismic design provisions have evolved (Mitchell et al., 2010). The first attempt for seismic hazard quantification in Japan and North America followed the 1923 Kanto (Tokyo) earthquake and the 1933 Long Beach (California) earthquake (Atkinson, 2004; Otani, 2004). Subsequently, the first edition of the National Building Code of Canada (NBCC) was published in 1941 (NRCC, 1941) and adopted provisions for seismic design based on the 1935 Uniform Building Code (UBC) in an appendix. Initially, the earthquake hazard quantification was introduced through seismic coefficients. Later, the provisions were incorporated into the main text of the 1953 NBCC and Canadian seismic zoning map was introduced. However, the seismic zones were introduced on a qualitative evaluation of hazard (Atkinson, 2004). The 1965 NBCC adopted the first seismic modification factor, as the construction factor, in the calculation of the minimum seismic base shear (NRCC, 1965). In late 1960s, the probabilistic quantification of seismic hazard has gained popularity. In 1970, the seismic code was changed to include the structural flexibility factor in addition to the construction factor (NRCC, 1970). To date, although the state of knowledge has improved, the same methods are still used in modern design codes; for engineering design purposes, these hazard factors in the newer code have been calibrated to a previous version (Atkinson, 2004). In the 1985, 1990, and 1995 NBCC, zonal velocity ratios (which have only four categories) are used to define seismic design loads at building locations, whereas since the 2005 NBCC, uniform hazard spectrum (UHS) is introduced to provide more site-specific seismic hazard values for calculating seismic design loads for buildings.

In BC, seismic provisions of the NBCC were not adopted by municipalities until 1973 (Ventura et al., 2005). Therefore, most of the pre-1970 buildings constructed in BC may have limited seismic capacity against severe earthquake forces (Onur et al., 2005). The cause–effect relationships of earthquake-induced damage on buildings designed without seismic capacity methods are summarized in **Table 2**. Most of these older buildings are currently operational and are required to be further assessed and upgraded to improve life safety (LS) and to mitigate potential economic consequences due to seismic damage.

In Canada, different building vulnerability assessment techniques have been proposed with different levels of complexity, ranging from a simple scoring to more detailed methods of non-linear structural analyses. The Institute for Research in Construction (IRC) of the National Research Council has developed a national seismic screening manual for buildings and different performance modifiers are taken into consideration (Rainer, 1992; Foo and Davenport, 2003). The methodology of the IRC manual follows the 1988 FEMA-154 screening guidelines (ATC, 2002). This seismic screening manual computes the seismic priority index (SPI), which is obtained as a summation of two indices, structural index (SI) and non-structural index (NSI). Saatcioglu et al. (2013) have updated the manual in accordance with the 2005 NBCC. Ventura et al. (2005) has developed building classification and fragility curves for southwestern BC to estimate the probability of damage at a given seismic intensity. The method

TABLE 1 | Damaging earthquakes in eastern and western Canada.

Damaging earthquakes in western Canada	Damaging earthquakes in eastern Canada
1949 M8.1 Queen Charlotte Islands earthquake	1988 M5.9 Saguenay earthquake
1946 M7.3 Vancouver Island earthquake	1944 M5.6 Cornwall-Massena earthquake
1918 M7.0 Vancouver Island earthquake	1935 M6.2 Timiskaming earthquake
1872 M7.4 North Cascades earthquake	1929 M7.2 Grand Banks earthquake
1700 M9.0 Cascadia earthquake	1925 M6.2 Charlevoix-Kamouraska earthquake

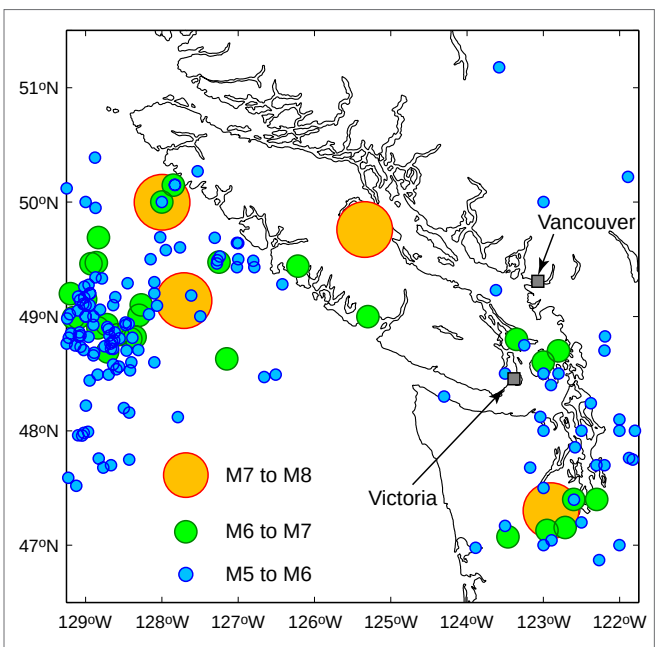

FIGURE 1 | Regional seismicity in southwestern British Columbia, Canada.

TABLE 2 | Cause–effect relationships for buildings designed without seismic capacity methods (Liel and Deierlein, 2008; Tesfamariam and Saatcioglu, 2008).

Cause	Effect
Inadequate anchorage of longitudinal reinforcement	• Yield strength of the reinforcement not being developed during the cyclic loading caused by earthquakes • Lap splices may fail if placed in potential plastic hinge regions
Inadequate anchorage of transverse reinforcement	• Transverse reinforcement will not be effective if not properly anchored and/or of insufficient quantity • 90° end hooks are inadequate for perimeter hoops, since spalling of cover concrete will result in loss of anchorage; end hooks should be bent through at least 135°
Inadequate quantities of transverse reinforcement	• Failure in shear

TABLE 3 | Vision 2000 recommended seismic performance objectives for buildings (SEAOC, 1995).

Earthquake design level (probability of exceedance)	Performance limit states			
	Immediate occupancy (IO)	Damage control (DC)	Life safety (LS)	Collapse prevention (CP)
Frequent (50% PE in 30 years)	■	×	×	×
Occasional (50% PE in 50 years)	♦	■	×	×
Rare (10% PE in 50 years)	◊	?	■	×
Very rare (2% PE in 50 years)		◊	?	■

■ *Basic objective – proposed NBCC normal importance.*
♦ *Essential service objective – proposed NBCC high importance.*
◊ *Safety critical objective – not proposed NBCC category.*
× *Unacceptable performance for new construction.*
The color shades are provided to group the performance limit states.

was used for regional damage estimation and is not intended for individual buildings.

Performance-Based Seismic Evaluation of Buildings

Cornell and Krawinkler (2000) proposed a rational means of integrating the probabilistic performance-based earthquake engineering for seismic design and risk assessment. The analytical procedure probabilistically integrates seismic hazard analysis, structural analysis, damage assessment, and loss estimation. Performance-based design philosophy is adopted in the 2005 Canadian seismic design code (DeVall, 2003) following Structural Engineers Association of California (SEACO) Vision 2000 (SEAOC, 1995). The maximum inter-story drift ratio (MaxISDR) is used in Canadian and most building codes as the only performance metric. Relationships between different earthquake return periods and acceptable performance limit states in terms of MaxISDR are shown in **Table 3**. It can be highlighted that for frequent [50% probability of exceedance (PE) in 30 years], occasional (50% PE in 50 years), rare (10% PE in 50 years), and very rare (2% PE in 50 years) earthquake levels, the corresponding design performance limit states are immediate occupancy (IO), damage control (DC), LS, and collapse prevention (CP), respectively. Descriptions of the limit states are summarized in **Table 4**. In the Canadian code, the limit states for IO, DC, LS, and CP, in terms of MaxISDR are 0.2, 0.4, 1, and 2.5%, respectively. These limit state values are lower than values suggested in FEMA P-58-1 (2012). In this paper, limit state values similar to FEMA P-58-1 (2012) will be used.

Consideration of Maximum and Residual Drift Ratios in Seismic Risk Assessment of Structures

The seismic performance of a structure is often evaluated through MaxISDR. Recent post-earthquake functionality assessment of structures has highlighted that residual inter-story drift ratio (ResISDR) is an important factor in the post-earthquake safety of a building and economic feasibility of repair and reconstruction (Kawashima et al., 1998; Ruiz-García and Miranda, 2006; Ramirez and Miranda, 2009; FEMA P-58-1, 2012). MacRae and Kawashima (1997) and Kawashima et al. (1998) implemented the first time risk assessment of bridges based on residual drift. **Table 4** summarizes the limits of MaxISDR and ResISDR for IO, DC, LS, and CP based on FEMA 356 (2000) and FEMA P-58-1 (2012). The ResISDR limits for CP are expressed in terms of the design shear force V_{design} normalized by the building weight W to consider cases where P-delta might be dominant at smaller drift ratios.

Christopoulos et al. (2003) and Pampanin et al. (2003) studied the effect of residual drift on single-degree-of-freedom (SDOF) and multi-degree-of-freedom (MDOF) systems, respectively. Christopoulos et al. (2003) proposed an assessment criterion as a weighted sum of structural and non-structural residual drifts. Pampanin et al. (2003) further extended this formulation into a MDOF system and proposed a seismic performance evaluation framework based on a MaxISDR–ResISDR matrix. In the absence of extensive data and information, in FEMA P-58-1 (2012), a simple relation between MaxISDR and ResISDR was provided for the four limit states. Erochko et al. (2011) have proposed a mechanistic equation to estimate residual drifts as a function of expected peak drift and elastic recoverable drift. For post-earthquake risk assessment of buildings, the residual drift can be easily measured, and as a result, the maximum drift is typically estimated as a function of residual drift (Hatzigeorgiou and Beskos, 2009; Erochko et al., 2011; Hatzigeorgiou et al., 2011; Christidis et al., 2013). Reported equations that relate MaxISDR and ResISDR are summarized in **Table 5**.

In the seismic performance assessment, the values for MaxISDR and ResISDR are subject to significant uncertainty and are dependent on each other. Uma et al. (2010) extended the performance-based seismic assessment framework by Pampanin et al. (2003) by taking into account the joint occurrence of MaxISDR and ResISDR of a SDOF system (modeled by a bivariate lognormal probability function). On the other hand, Goda and Tesfamariam (2015) have shown that MaxISDR and ResISDR of a MDOF system are statistically dependent, and that their marginal distributions can be represented by the Frechet and generalized

TABLE 4 | Limit states for maximum and residual inter-story drift ratios (FEMA 356, 2000; FEMA P-58-1, 2012).

Damage state	Description	Maximum inter-story drift ratio (MaxISDR) (%)	Residual inter-story drift ratio (ResISDR)
Immediate occupancy (IO)	No structural realignment is necessary for structural stability; however, the building may require adjustment and repairs to non-structural and mechanical components that are sensitive to the building alignments (e.g., elevator rails, curtain walls, and doors)	0.4	0.2% (equal to the maximum out-of-plumb tolerance typically permitted in new construction)
Damage control (DC)	Realignment of structural frame and related structural repairs required to maintain permissible drift limits for non-structural and mechanical components and to limit degradation in structural stability (i.e., collapse safety)	0.9	0.5%
Life safety (LS)	Major structural realignment is required to restore margin of safety for lateral stability; however, the required realignment and repair of the structure may not be economically and practically feasible (i.e., the structure might be at total economic loss)	2.5	1%
Collapse prevention (CP)	Residual drift is sufficiently large that the structure is in danger of collapse from earthquake aftershocks (note: this performance point might be considered as equivalent to collapse but with greater uncertainty)	4.5	• High ductility systems 4% $<0.5V_{design}/W$ • Moderate ductility systems 2% $<0.5V_{design}/W$ • Limited ductility systems 1% $<0.5V_{design}/W$

TABLE 5 | Equations to relate residual and maximum inter-story drift ratios.

Reference	Description	Comments
MacRae and Kawashima (1997)	$d_r = \begin{cases} d_l & \text{for } H_{yb} \le 0 \le H_{yt} \\ d_L = d_y\left(\frac{1-r}{r}\right) & \text{for } r > 0 \text{ and either } H_{yb} \ge 0 \text{ or } H_{yt} \le 0 \end{cases}$	d_r = maximum residual drift; d_l = displacement where the elastic response line at the end of the analysis crosses the zero force line; d_L = displacement where the post-elastic line intersects the zero force line; d_y = yield displacement; r = bilinear factor = k_2/k_1; k_1 = initial elastic stiffness; k_2 = second post-yielding stiffness; H_{yt} = yield force at the top of the line; H_{yb} = yield force at the bottom of the line Structure type: bilinear SDOF systems
Kawashima et al. (1998)	$d_r = \begin{cases} (\mu-1)(1-r)d_y & \text{for } r(\mu-1) < 1 \\ [(1-r)/r]d_y & \text{for } r(\mu-1) \ge 1 \end{cases}$	d_r = maximum residual drift; μ = ductility factor; d_y = yield displacement; r = bilinear factor = k_2/k_1; k_1 = initial elastic stiffness; k_2 = second post-yielding stiffness Structure type: bilinear SDOF systems
Christopoulos et al. (2003)	$\text{RDDI} = \begin{cases} \phi \times \text{RDDI}_S + \chi \times \text{RDDI}_{NS} & \text{for RDDI}_s < 1 \\ 1 & \text{for RDDI}_s = 1 \end{cases}$	RDDI = residual deformation damage index [0, 1]; RDDI_S = residual deformation structural damage index [0, 1]; RDDI_{NS} = residual deformation non-structural damage index [1]; φ and χ = relative importance factors for structural failure and non-structural failure, respectively Structure type: hysteretic SDOF systems
Hatzigeorgiou et al. (2011)	$d_m = (a_1 T + a_2 d_r + a_3 d_r^2 + a_4 T d_r) \times (1 + a_5 r + a_6 r^2)$	d_m = maximum drift; T = period (in seconds); d_r = maximum residual drift; $a_{1 \ldots 6}$ = regression coefficients Structure type: Bilinear SDOF systems
Erochko et al. (2011)	$d_r = d - d_e$	d_r = maximum residual drift; d = drift; d_e = elastic recoverable drift = yield shear/elastic stiffness of a typical story Structure type: steel building; MDOF with 2 and 12 stories in height; special momentresisting frames and buckling-restrained braced frames
FEMA P-58-1 (2012)	$d_r = \begin{cases} 0 & \text{for } d \le d_y \\ d_r = 0.3(d - 3d_y) & \text{for } d_y < d < 4d_y \\ d_r = d - 3d_y & \text{for } d \ge 4d_y \end{cases}$	d_r = maximum residual drift; d = drift; d_y = yield drift Structure type: MODF systems
Christidis et al. (2013)	$\lvert d_m \rvert = (a_1 + a_2 \ln(N) + a_3 \lvert d_r \rvert) \times (1 + a_4 r)$	d_m = maximum drift; N = number of story; d_r = maximum residual drift; r = bilinear factor = k_2/k_1; k_1 = initial elastic stiffness; k_2 = second post-yielding stiffness; $a_{1 \ldots 4}$ = regression coefficients Structure type: steel building; MDOF with 3, 6, 9, 12, 15 and 20 stories in height; moment resisting steel frames and concentrically Xbraced steel frames

Pareto distributions, respectively, whereas their dependence can be characterized by different copulas (e.g., normal, *t*, Gumbel, Frank, Clayton, and asymmetrical Gumbel). Tesfamariam and Goda (2015) further developed the copula-based multivariate seismic demand model and applied it to seismic loss assessment of a non-code conforming RC building with consideration of mainshock–aftershock (MSAS) earthquake records.

Mainshock–Aftershock Earthquakes on RC Buildings

The 2011 M_w6.3 Christchurch earthquake in New Zealand (Elwood, 2013; Leite et al., 2013) and the 2011 M_w9.0 Tohoku earthquake in Japan (Goda et al., 2013, 2015) have highlighted vulnerability of buildings subject to MSAS earthquake sequences. There are an increasing number of studies on vulnerability assessment of RC buildings subject to MSAS sequences. Ryu et al. (2011) presented a methodology for developing fragilities for mainshock-damaged SDOF buildings by performing incremental dynamic analysis (IDA, Vamvatsikos and Cornell, 2002) with aftershock ground motions. The aftershock fragilities are computed conditional on the damage caused by the mainshock (MS) earthquake. Their analyses showed that the effect of aftershocks is not significant. Hatzigeorgiou and Liolios (2010) quantified vulnerability of non-code and code conforming RC frames with prevalent irregularity. The MSAS sequences were obtained from actual MSAS records and 40 artificial seismic sequences. They concluded that aftershocks have significant impact on drift demand of the non-code conforming and irregular buildings. Tesfamariam et al. (2015) investigated MSAS earthquakes on non-code conforming RC frames with vertical irregularity. A set of 50 MSAS earthquake sequences was selected for Vancouver with consideration of regional seismic hazard. For the irregular structures, the MSAS sequences caused higher drift values than MS records only. Tesfamariam and Goda (2015) investigated the effect of MSAS earthquake sequences on a 4-story non-code conforming RC building. Their results showed that the MSAS earthquake had no marked effect on collapse and loss assessment of the RC building. This study, with the consideration of seismicity in Victoria, BC, extends the 4-story RC building investigated in Tesfamariam and Goda (2015) to 2-, 8-, and 12-story RC buildings. The building vulnerability assessment is further undertaken for collapse and non-collapse damage limit states.

Research Objective and Methodology

The objective of this paper is to carry out probabilistic building vulnerability assessment with consideration of regional probabilistic seismic hazard. The novel aspects of the proposed building vulnerability assessment are as follows:

i. Consideration of non-code conforming RC buildings having different story numbers, i.e., 2-, 4-, 8-, and 12-story, extending the work by Tesfamariam and Goda (2015) for the 4-story RC building;
ii. Consideration of three earthquake sources, i.e., crustal, inslab, and interface to reflect regional seismicity of southwestern BC in record selection (i.e., subduction environments and extensive ground motion datasets for the 2011 Tohoku earthquake records, which can be regarded as closest proxy for the Cascadia subduction events);
iii. Consideration of MSAS sequences as seismic excitation;
iv. Multivariate seismic demand modeling, MaxISDR and ResISDR, for seismic performance evaluation; and
v. Consideration of collapse and non-collapse limit states in the form of a bivariate seismic performance matrix.

Figure 2 illustrates a methodology for probabilistic building vulnerability assessment. It consists of five basic steps:

- Step 1: finite-element (FE) models of the 2-, 4-, 8-, and 12-story RC buildings are prepared to consider non-linear behavior of structural components and assembly. Modal analysis is performed to identify the three dominant fundamental periods (T_1, T_2, and T_3).
- Step 2: a suite of ground motions which corresponds to a target seismic hazard level is selected on the basis of T_1 by reflecting detailed characteristics of regional seismic hazard. Multiple conditional mean spectra (CMS) for different earthquake types are employed as target response spectra (Baker, 2011; Goda and Atkinson, 2011). Each ground motion consists of a MS record and a MSAS sequence.
- Step 3: a set of RC frames are analyzed through IDA to collapse limit states for the suite of MS records and MSAS sequences, and the performance parameters MaxISDR and ResISDR are recorded for each motion. The collapse fragilities are evaluated using the IDA results.
- Step 4: from non-collapsed results, marginal probability distributions of MaxISDR and ResISDR are derived, and corresponding dependency is characterized using copulas.
- Step 5: the performance matrix (**Table 3**) and limit states (**Table 4**) are used to carry out seismic performance evaluation. From the seismic performance evaluation, the probability unsatisfactory seismic performance with regard to the specified limit state criteria is derived for the MS and MSAS earthquake records.

Salient features of the key components of the framework are explained in the following.

Structural Model

Tesfamariam and Goda (2015) studied the effect of MSAS earthquake records on the loss assessment of a 4-story non-code conforming RC space frame structure. This study extends this investigation to archetypical structures with different story numbers reported in Liel and Deierlein (2008). The archetype structures are: 2-, 4-, 8-, and 12-story non-code conforming RC buildings; the structures were designed as a space frame, and all columns and beams were part of the lateral resisting system. The buildings were designed according to the 1967 UBC seismic provisions (ICBO, 1967). Beam and column elements have the same amount of over-strength; each element is 15% stronger than the code-minimum design level. The design is governed by strength and stiffness requirements, as the 1967 UBC had few requirements for special seismic design or ductile detailing.

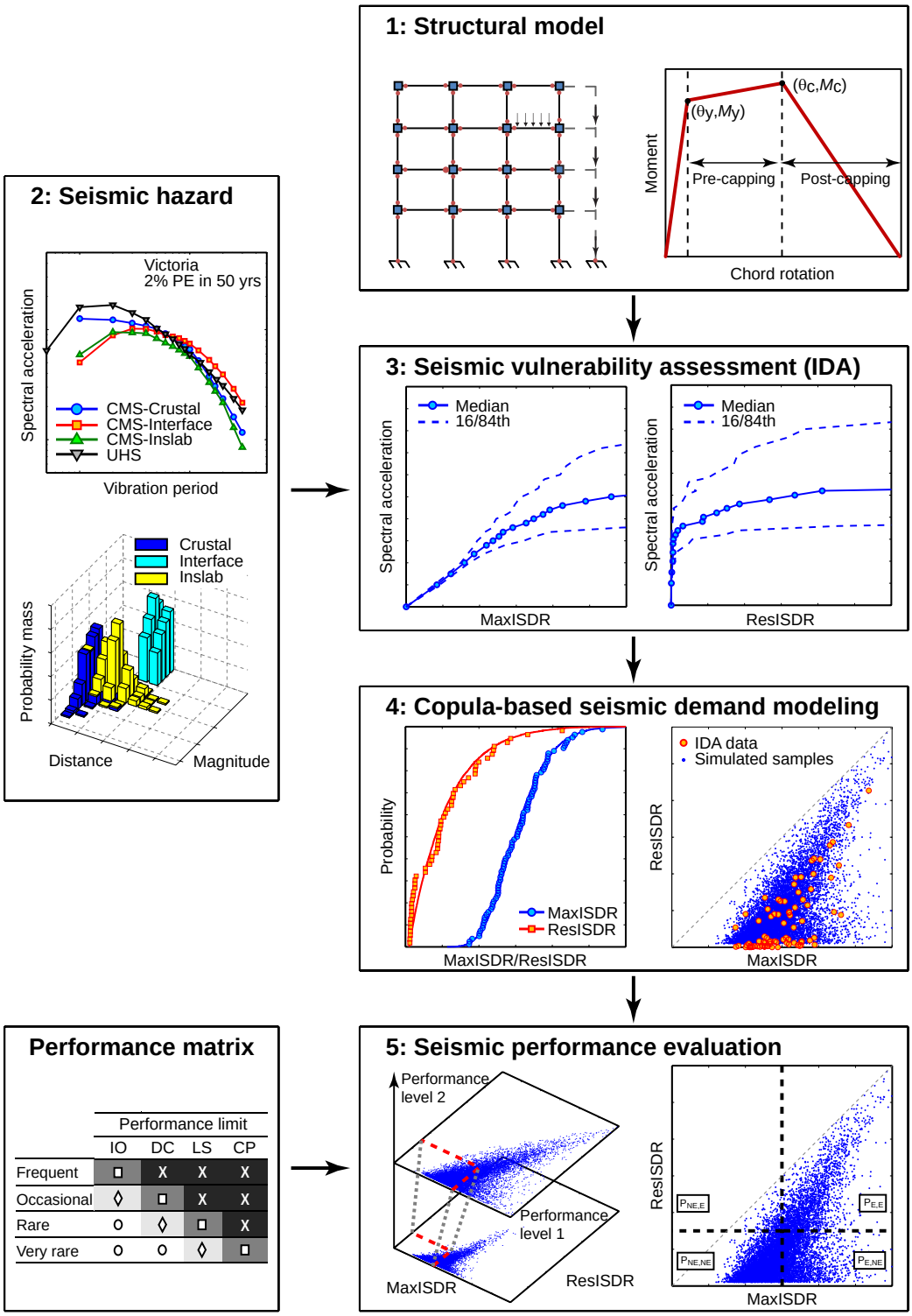

FIGURE 2 | Probabilistic seismic vulnerability assessment framework.

Finite-element modeling of structures can be achieved using a fiber or lumped plasticity model. In the fiber model, the element cross section is discretized and corresponding non-linear material properties of the core concrete, cover concrete, and reinforcing bars are assigned. On the other hand, in the lumped plasticity model, non-linearity of the beam-column element is introduced at the two ends (hinges), which are connected by an elastic element. Advantages and disadvantages of each approach

are summarized in **Table 6**. Haselton et al. (2008) indicated that the lumped plasticity model, equipped with adequate hysteretic models for plastic hinges, can simulate global collapse behavior well (note: they observed that the fiber model may be numerically unstable when the responses become highly non-linear).

Figure 3A shows a schematic of the 4-story building. It has a floor area of 38.1 m (125 ft) by 53.3 m (175 ft); columns are spaced at 7.6 m (25 ft), and story heights are 4.6 m (15 ft) and 4.0 m (13 ft) at the ground floor and higher floor levels, respectively. The non-ductile RC models used in this paper are developed by Liel and Deierlein (2008). The models are based on a lumped plasticity approach in Open system for earthquake engineering simulation (OpenSees, McKenna et al., 2000). The lumped plasticity element models used to simulate plastic hinges in beam-column elements (**Figure 3B**) utilize a tri-linear non-linear spring model that is developed by Ibarra et al. (2005) and implemented in OpenSees by Altoontash (2004). **Figure 3B** shows the tri-linear backbone curve, coupled with the associated hysteretic rules, which is used to model the structures to post-peak response and near-collapse response. The post-peak response enables modeling of the strain hardening behavior associated with concrete crushing, rebar buckling and fracture, and bond failure (Haselton et al., 2008; Liel and Deierlein, 2008). Liel and Deierlein (2008) and Haselton et al. (2008) reported that the Ibarra et al. model was calibrated with data from 255 RC column test results. Details of the calibration process and building details are provided in Liel and Deierlein (2008) and Haselton et al. (2008); for brevity, they are not repeated here. P-Δ effects are modeled using a leaning column. The vibration periods for the first three modes for the 2-, 4-, 8-, and 12-story buildings are summarized in **Table 7**.

TABLE 6 | Advantages and disadvantages of fiber and lumped plasticity models (Haselton et al., 2008).

Fiber model	Lumped plasticity model
Ability to consider shear flexibility by modeling shear DOF in the sections	Not able to capture shear flexibility
Used where cracking and tension-stiffening behavior governs	Used for collapse prediction
Inability to capture deterioration of the steel reinforcing bars due to rebar buckling and low-cycle fatigue	Captures deterioration of steel rebar due to buckling and low-cycle fatigue
Not able to capture strength and stiffness deterioration	Well captures strength and stiffness deterioration to assess global collapse

Seismic Hazard for Victoria and Ground Motion Selection

Victoria is the provincial capital of BC and is located at the southern tip of Vancouver Island (**Figure 1**). Due to its geographical location, Victoria is affected by three types of earthquakes. The first type of the influential events is an earthquake at shallow depth in the crust; historically, the 1918 and 1946 earthquakes fall under this category. The other two types of the influential earthquakes are related to the movements of the Juan de Fuca Plate, Explorer Plate, Gorda Plate, and North American Plate in the Cascadia subduction zone. In the subducting slab, deep earthquakes occur (e.g., 2001 Nisqually earthquake), while at the plate interfaces, mega-thrust subduction earthquakes, as larger as M_w9.0, occur (e.g., 1700 Cascadia earthquake, Hyndman and Rogers, 2010). It is important to recognize that the three types of dominant earthquakes in southwestern BC have distinct characteristics in terms of recurrence interval, earthquake magnitude, location, and depth and thus should be treated differently.

The key features of the critical earthquake scenarios for a given location can be evaluated quantitatively via probabilistic seismic hazard analysis. Atkinson and Goda (2011) conducted seismic hazard studies for southwestern BC, by incorporating recent advancements in seismology. Typical outputs from probabilistic seismic hazard analysis, which are essential for seismic performance assessment of buildings and infrastructure, are the UHS and seismic deaggregation. Currently, the UHS at 2% PE in

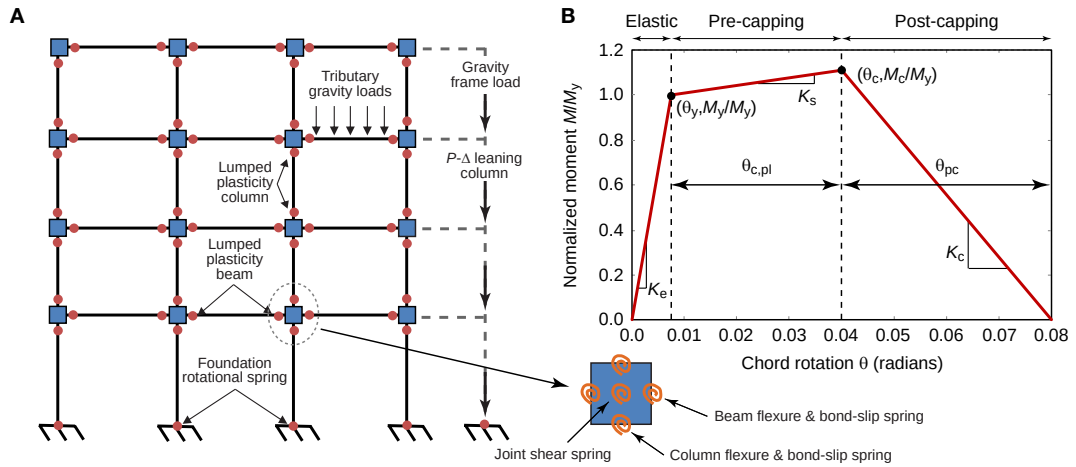

FIGURE 3 | (A) Non-linear finite-element model of a 4-story non-ductile RC frame, and **(B)** backbone curve for beam-column elements.

50 years (equivalent to the return period of 2500 years) is adopted as the basis for seismic design provisions for new construction in Canada. The seismic deaggregation identifies critical earthquake scenarios (for instance, in terms of magnitude, distance, and earthquake type) for a selected probability level. **Figure 4A** shows UHS for Victoria at 10, 5, and 2% PE in 50 years, where the site condition is set to site class C, which is represented by the average shear-wave velocity in the upper 30 m between 360 and 760 m/s. The three probability levels are relevant for assessing the seismic performance of structures in Canada. **Figure 5** shows the seismic deaggregation results for $T = 1.0$ and 2.0 s for 10, 5, and 2% PE in 50 years; the selected vibration periods correspond to the adopted seismic intensity measure (IM) for the 2-story building and the 4-, 8-, and 12-story buildings, respectively (**Table 7**). In **Figure 5**, relative contributions due to crustal, mega-thrust (Cascadia) interface, and deep inslab earthquakes are indicated. The seismic deaggregation results suggest that relative contributions due to the Cascadia subduction earthquakes increase with the probability level and the seismic hazard values for longer vibration periods are affected more significantly by the large subduction events. The variable characteristics of the dominant scenarios are important for seismic performance evaluations and thus should be taken into account in selecting ground motion records for non-linear dynamic analyses of structural models.

Careful record selection is of critical importance to produce unbiased estimates of seismic vulnerability. In particular, when record scaling is implemented to reach high seismic excitation levels, record selection needs to account for the spectral shape effects (Luco and Bazzurro, 2007). One practical method that is widely adopted for mitigating the record scaling bias is the CMS method (Baker, 2011). In the CMS-based record selection, the target response spectrum is modified based on dominant earthquake scenarios and relevant ground motion prediction equations at a selected performance level. Typically, the base target response spectrum for record selection is a UHS and is further modified based on the mean scenarios obtained from seismic deaggregation; several tens of ground motion records that match the modified target response spectrum (i.e., CMS) are selected as input motion. However, for the seismic environments in southwestern BC, it may be too simplistic to use a single target response spectrum for a given probability level because three dominant earthquakes with different characteristics are present (**Figure 5**). For this reason, in this study, the multiple CMS-based record selection method by Goda and Atkinson (2011) is adopted, which defines three different target spectra considering the different earthquake characteristics and ground motion prediction models for these earthquake types. Examples of the CMS for crustal, interface, and inslab earthquakes are shown in **Figures 4B,C**; **Figure 4B** is for the 2-story building, whereas **Figure 4C** is for the 4-, 8-, and 12-story buildings. It is noted that the CMS for the interface events have richer spectral content with respect to other two earthquake types because of larger earthquake magnitudes and longer propagation paths.

TABLE 7 | First three fundamental periods of 2-, 4-, 8-, and 12-story buildings.

Building story	Design ID	Period(s)		
		Mode-1	Mode-2	Mode-3
2	3001	1.10	0.20	0.03
4	3004	1.92	0.55	0.27
8	3016	2.23	0.80	0.41
12	3026	2.35	0.85	0.47

Another important aspect for record selection is to prepare a suitable ground motion dataset for the seismic environments of interest. For southwestern BC, the base ground motion dataset should contain records from large mega-thrust subduction events. Moreover, the record database should contain as-recorded MSAS sequence records. To achieve these requirements, a new composite database of real MSAS sequences is compiled by combining the database that was constructed based on the Next Generation Attenuation database (Goda and Taylor, 2012) and the new database for Japanese earthquakes from the K-NET, KiK-nt, and SK-net (Goda et al., 2015). It is noteworthy that the new Japanese database includes records from the 2011 Tohoku earthquake, which may be considered as appropriate surrogate for the Cascadia subduction events. The composite dataset consists of 606 real MSAS sequence records; 75 sequences are from the NGA database and 531 sequences are from the Japanese database (each sequence has two horizontal components). This database is the largest dataset for as-recorded MSAS sequences and is sufficient to select a suitable set of record sequences by taking into account various requirements, such as earthquake type, magnitude, distance, and site class.

Incremental Dynamic Analysis

Incremental dynamic analysis implements a series of non-linear dynamic analyses by scaling a set of input ground motions based on an adopted IM, and develops prediction equations of engineering demand parameters (EDP, e.g., MaxISDR and ResISDR) at different IM levels. The IM is the spectral acceleration at the fundamental period of a structure. For the different building story numbers, the maximum scaling required in IDA can vary. For the 2-story building, the spectral acceleration at 1.0 s is selected as IM (**Table 7**) and the scaling range in IDA is varied from 0.05 to 1.4 *g*. For the 4-, 8-, and 12-story buildings, the spectral acceleration at 2.0 s (i.e., IM) ranges from 0.05 to 0.7 *g*. In general, numerical instability is encountered when the inter-story drift ratio of the frames exceeds 0.10. The first occurrence of such large deformation responses is treated as "*collapse*" (Vamvatsikos and Cornell, 2002). In characterizing the inelastic demand, non-linear responses that are in "collapse" and "non-collapse" states are distinguished. The collapse results are modeled by collapse fragility curves (see Collapse Fragility Assessment), whereas the non-collapse results are represented by multivariate seismic demand models (see Coupla-Based Seismic Demand Modeling). Eventually, the overall performance of the building is assessed by integrating collapse results and non-collapse results in the Section "Seismic Performance Evaluation."

Incremental dynamic analysis is carried out for the 2-, 4-, 8-, and 12-story RC frames using the set of 50 MS records as well

as a set of 50 MSAS sequences, which are selected based on the multiple CMS-based procedures. The IDA results for both MS records and MSAS sequences (i.e., EDP-IM plot) are shown in **Figures 6** and **7**; **Figure 6** is for MaxISDR, whereas **Figure 7** is for ResISDR. To present the uncertainty of the IDA results, 16th–84th percentile curves (corresponding to mean ± 1 SD), are included in the figures. The overall characteristics of the IDA curves for MaxISDR and ResISDR are different; the former increases gradually with the seismic intensity level, whereas the latter increases rapidly when the seismic intensity level reaches in the range of 0.2–0.3 *g* for the 2-story building and 0.15–0.20 *g* for the 4-, 8-, and 12-story buildings; similar observations are also noted in FEMA P-58-1 (2012). It is noteworthy that the uncertainty of ResISDR is much greater than that of MaxISDR,

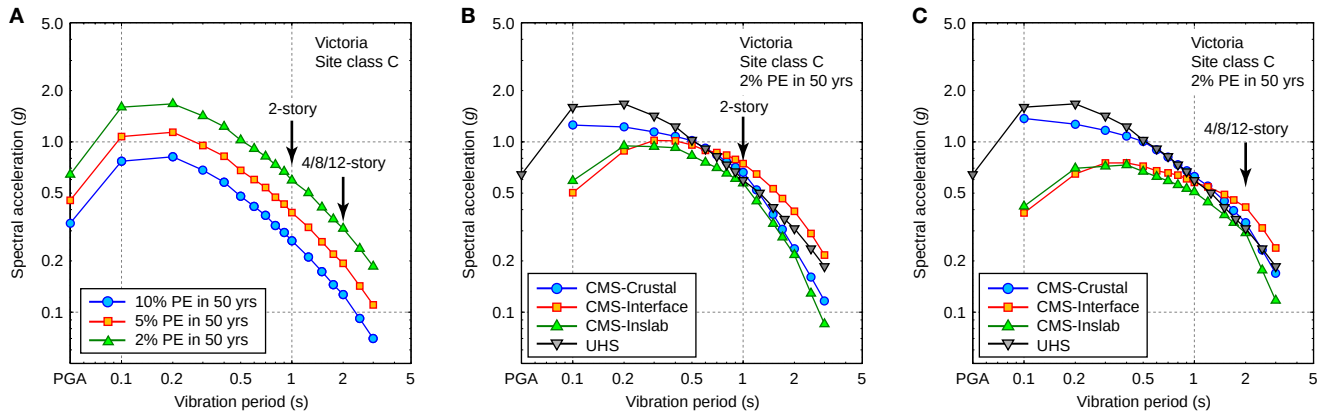

FIGURE 4 | (A) Uniform hazard spectra, **(B)** conditional mean spectra for the anchor vibration period of 1.0 s (for the 2-story RC frame), and **(C)** conditional mean spectra for the anchor vibration period of 2.0 s (for the 4-, 8-, and 12-story RC frames).

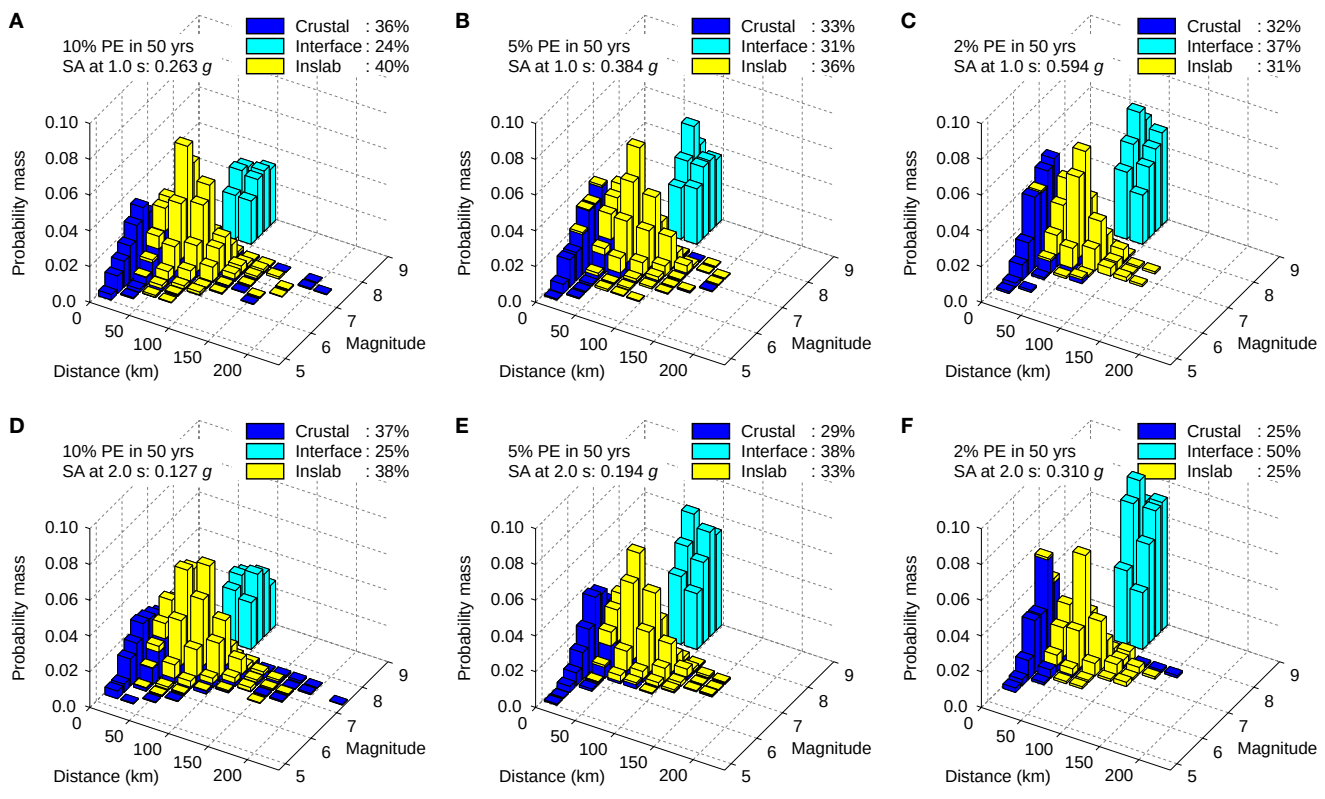

FIGURE 5 | Seismic deaggregation results for Victoria: (A–C) *T* = 1.0 s for 10, 5, and 2% probability of exceedance in 50 years, and (D–F) *T* = 2.0 s for 10, 5, and 2% probability of exceedance in 50 years.

as noted by Ruiz-García and Miranda (2006). To appreciate the differences of the IDA curves for the buildings with different story numbers, the 50th, 16th, and 84th percentile curves for the 4-, 8-, and 12-story buildings are overlaid together in **Figure 8**, noting that the same IM is adopted for these buildings (thus the IDA results can be compared directly). The results shown in **Figure 8** indicate that for a given seismic excitation level, both MaxISDR and ResISDR decrease with the story number; therefore, for the considered non-ductile RC frames, the 4-story building is more vulnerable than the other taller buildings.

Moreover, from the EDP-IM plots, it can be observed that the impact of aftershock records is significant for the 2-story building (**Figures 7A** and **8A**), whereas such marked effects diminish with increase in story number (**Figures 7B–D–8B–D**). One of the main reasons for the pronounced influence of aftershock records on MaxISDR and ResISDR for the 2-story building is related to its fundamental period (≈1.0 s; **Table 7**) and the dominant spectral content of the aftershock records; generally, aftershock records have richer spectral content in the short vibration period range (Goda et al., 2015). For all cases, the impact of MSAS earthquake sequence is more significant for ResISDR as compared with MaxISDR. For instance, for the 4-story building (**Figures 7B** and **8B**), in terms of median, the consideration of MSAS sequences leads to 5–10% increase for MaxISDR and up to 100% increase for ResISDR with respect to the results for MS records.

Collapse Fragility Assessment

The collapse fragility can be represented by a lognormal cumulative distribution function (CDF):

$$P_C = \Phi\left(\frac{\ln(x/\theta)}{\beta}\right) \quad (1)$$

where P_C is the probability that a ground motion with IM = x will cause the structure to collapse, $\Phi(\bullet)$ is the standard normal CDF, θ is the median of the fragility function (the IM level with 50% probability of collapse), and β is the SD of lnIM (sometimes referred to as the dispersion parameter). **Figure 9** shows the collapse fragility results (raw data and fitted lognormal curve) for MS records and MSAS sequences. The estimated values of θ and β are also provided in the figure. The impact of aftershocks is pronounced for the 2-story building, where the median collapse capacity θ is reduced by 13% (i.e., the curve is shifted toward

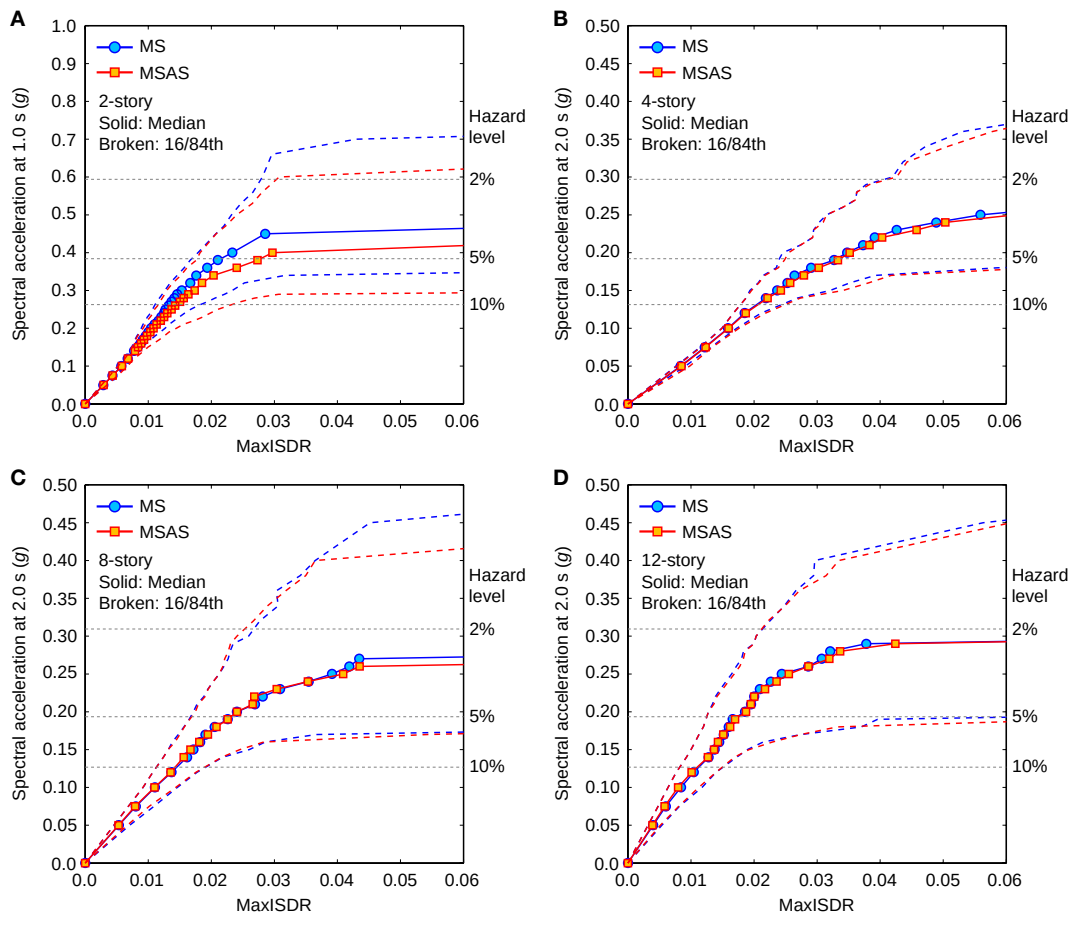

FIGURE 6 | Incremental dynamic analysis results for MaxISDR by considering MS records and MSAS sequence records: (A) 2-story, (B) 4-story, (C) 8-story, and (D) 12-story.

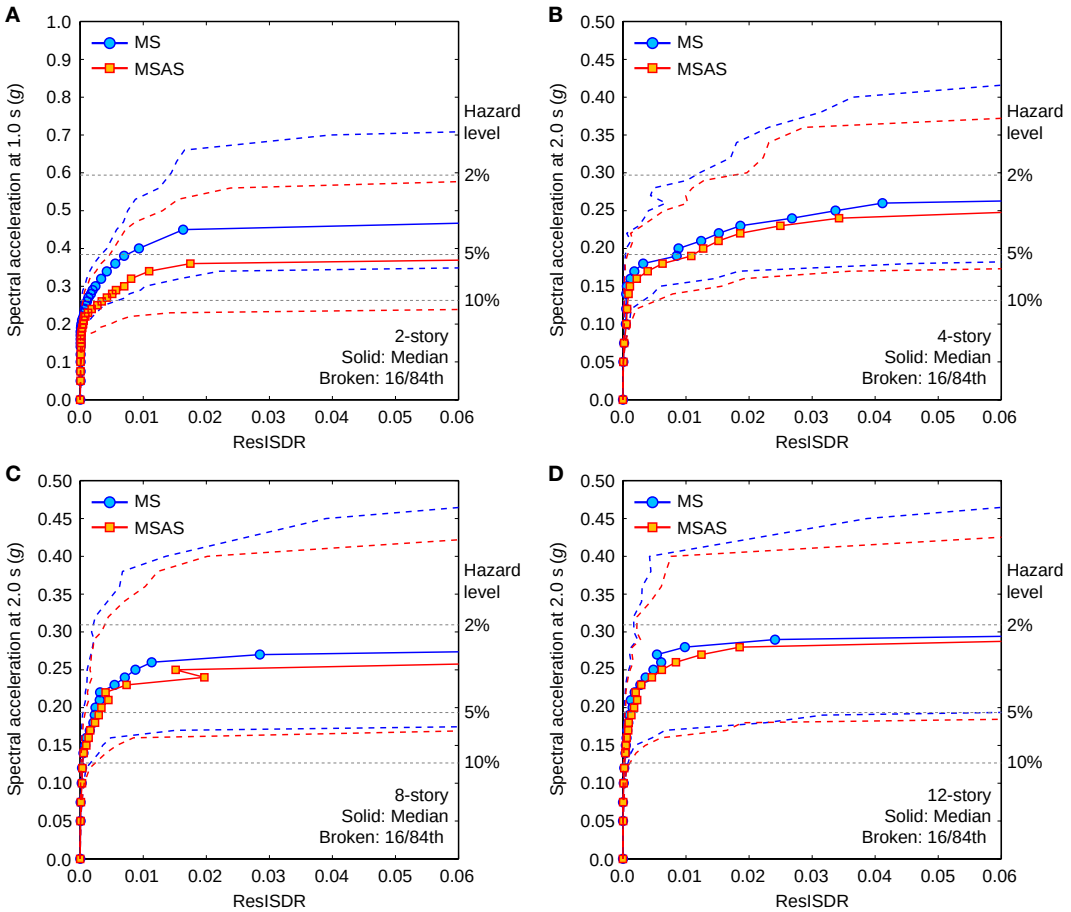

FIGURE 7 | Incremental dynamic analysis results for ResISDR by considering MS records and MSAS sequence records: (A) 2-story, (B) 4-story, (C) 8-story, and (D) 12-story.

left). On the other hand, the collapse fragility curves of the 4-, 8-, and 12-story buildings show no or slight differences. These results are consistent with the IDA curves shown in **Figure 6**. Furthermore, in **Figure 10**, the collapse fragility results for the 4-, 8-, and 12-story buildings are superimposed. The comparison shown in **Figure 10** indicates that the median collapse capacity θ as well as the dispersion β increases with the story number; the differences of the collapsed fragility curves are more pronounced at the greater seismic excitation levels.

Coupla-Based Seismic Demand Modeling

MaxISDR and ResISDR are statistically dependent (Goda and Tesfamariam, 2015) and thus this should be taken into account when these EDPs are characterized. For the seismic demand modeling, first, marginal probability distributions of MaxISDR and ResISDR should be developed, and second, corresponding dependence needs to be characterized. The probabilistic modeling of MaxISDR and ResISDR is performed at individual IM levels using non-collapse MaxISDR and ResISDR data (note: the number of available data points for seismic demand modeling decreases with the IM level because more data fall into collapse states; **Figure 9**).

Figure 11A shows the scatter plot for the 4-story building by considering MS records at 5% PE in 50 years level. In the figure, marginal distributions of MaxISDR and ResISDR are plotted along the horizontal axis and vertical axis, respectively. Note that ResISDR has a heavy right tail. Goda and Tesfamariam (2015) considered six probability distributions, i.e., lognormal, Gumbel, Frechet, Weibull, gamma, and generalized Pareto, for marginal probability distribution modeling of MaxISDR and ResISDR. For MS records and MSAS sequences, Goda and Tesfamariam (2015) showed that the Frechet distribution (Eq. 2) and generalized Pareto distribution (Eq. 3) are suitable for MaxISDR and ResISDR, respectively. The probability density functions of the Frechet and the generalized Pareto models are given by:

$$f(x)=\frac{\xi}{\sigma}\left(\frac{x-\mu}{\sigma}\right)^{-1-\xi}\exp\left[-\left(\frac{x-\mu}{\sigma}\right)^{-\xi}\right] \tag{2}$$

and,

$$f(x)=\frac{1}{\sigma}\left(1+\xi\frac{x-\mu}{\sigma}\right)^{-(1/\xi+1)} \tag{3}$$

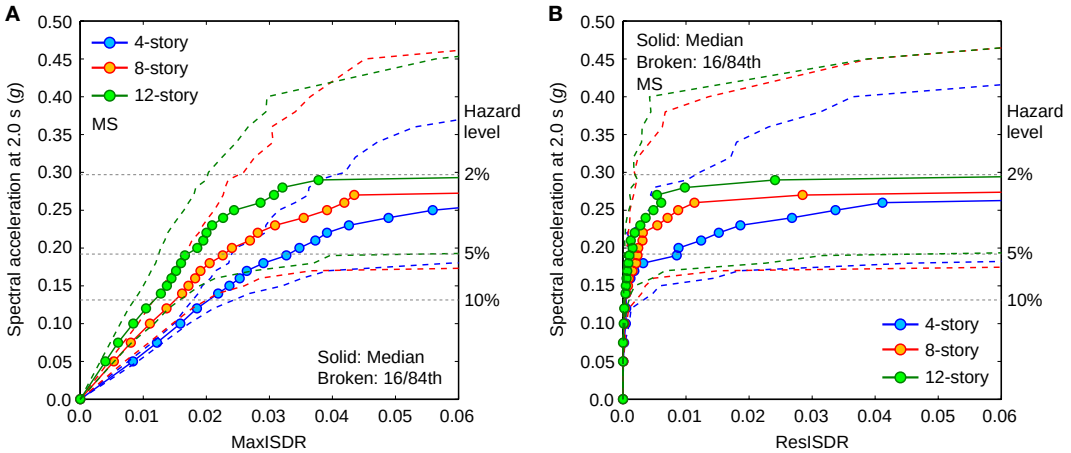

FIGURE 8 | Comparison of incremental dynamic analysis results for the 4-, 8-, and 12-story RC frames by considering MS records: (A) MaxISDR and (B) ResISDR.

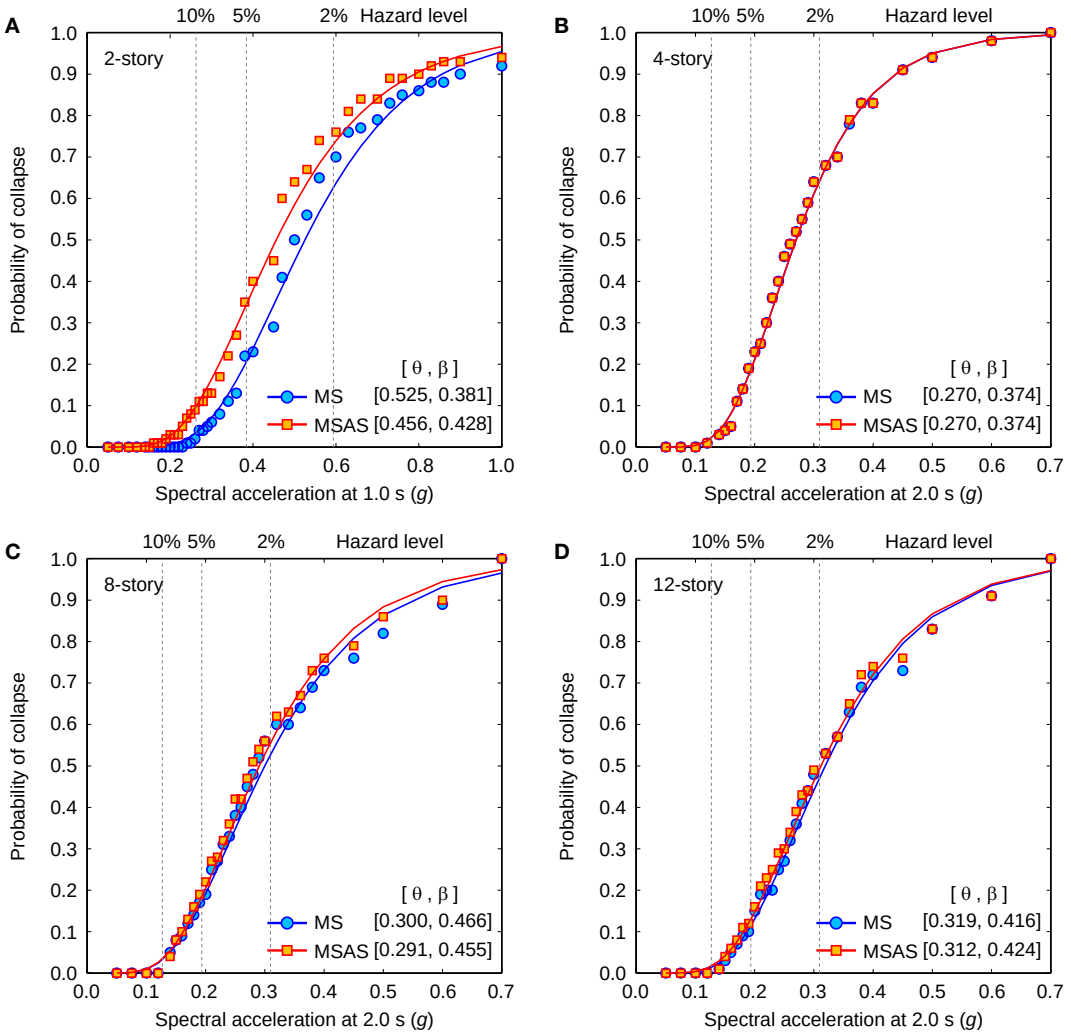

FIGURE 9 | Collapse fragility results by considering MS records and MSAS sequence records: (A) 2-story, (B) 4-story, (C) 8-story, and (D) 12-story.

where μ is the location parameter, and σ is the scale parameter, and ξ is the shape parameter. These marginal distributions are non-normal (in particular, ResISDR); in such cases, conventional multivariate normal (or lognormal) distribution modeling is not ideal, and a more elaborate approach is necessary.

The dependence of MaxISDR and ResISDR can be characterized by using elliptical copulas, such as normal and *t*, and Archimedean copulas, such as Gumbel, Frank, and Clayton (McNeil et al., 2005). The asymmetric Archimedean copula is a mixture of one of the Archimedean copulas and the independence copula; this copula class is useful in modeling data that exhibit uneven distribution of the data points along the upper-left-lower-right diagonal line in the transformed space. In the context of joint probability distribution modeling of MaxISDR and ResISDR, the uneven distribution of the data is related to the physical relationship between MaxISDR and ResISDR (i.e., MaxISDR ≥ ResISDR; Goda and Tesfamariam, 2015). To model the observed dependence of MaxISDR and ResISDR (e.g., scatter plot shown in **Figure 11A**), parametric copula functions are fitted to empirical copula samples using the maximum likelihood method (McNeil et al., 2005). The copula fitting of MaxISDR and ResISDR at various IM levels suggests that overall, the Gumbel (or asymmetrical Gumbel) copula (Eq. 4) is suitable for the majority of the cases examined in this study.

$$C_\delta(u_1,u_2)=\exp\left(-[(-\ln u_1)^\delta+(-\ln u_2)^\delta]^{1/\delta}\right),\delta>1 \qquad (4)$$

where u_1 and u_2 are the uniform random variables, and δ is the model parameter.

The developed statistical seismic demand models of MaxISDR and ResISDR can be used for seismic performance evaluation of structures. For instance, considering the fitted dependence function for the 4-story building at 5% PE in 50 years, numerous copula samples are first generated; their marginal distributions are uniformly distributed with the specified dependence characteristics. Using the simulated copula samples and the fitted marginal distribution models for MaxISDR and ResISDR, pairs of MaxISDR and ResISDR samples can be obtained using the inverse transformation method. The results of 5,000,000 simulations are presented in **Figure 11B**. Indeed, similar figures can be generated for different building story numbers as well as seismic hazard levels, and can be used in the seismic performance evaluation.

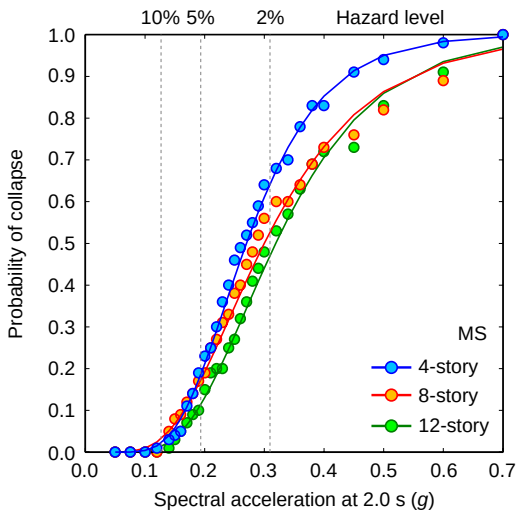

FIGURE 10 | Comparison of collapse fragility results for the 4-, 8-, and 12-story RC frames by considering MS records.

Seismic Performance Evaluation

The collapse fragility curves and the joint probability model of non-collapse inelastic seismic demands outlined in the previous sections can now be used to carry out performance-based

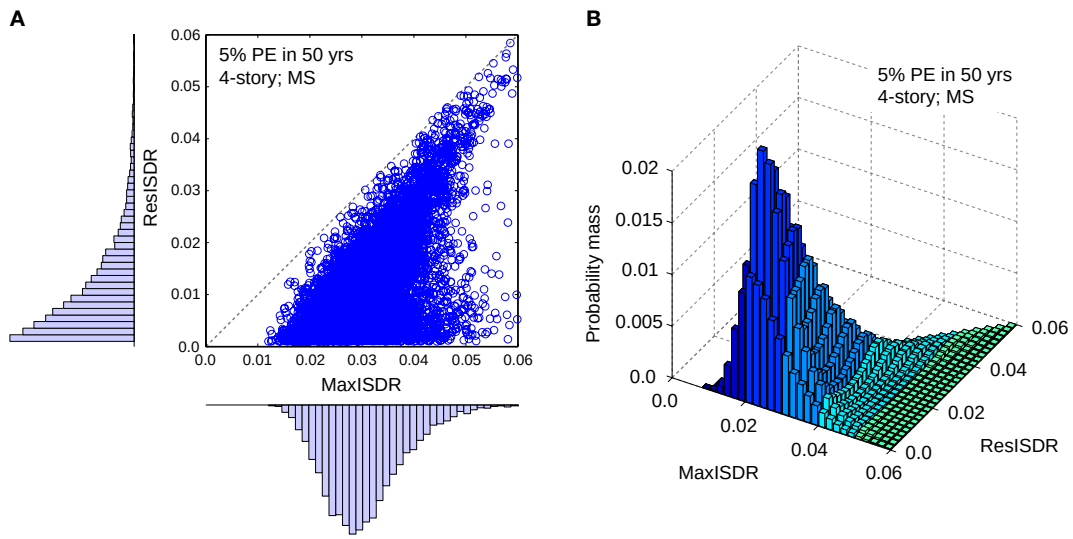

FIGURE 11 | (A) Scatter plot and corresponding marginal probability distributions of MaxISDR and ResISDR and **(B)** joint distribution of MaxISDR and ResISDR for the 4-story building at 5% probability of exceedance in 50 years.

evaluation of a building with the limit states provided in **Tables 3** and **4**. For example, for the NBCC normal importance buildings (*basic objective*), the acceptable limit states are LS and CP for 10 and 2% PE in 50 years, respectively. For the NBCC high importance buildings (*essential service objective*), the required limit states are more stringent and correspond to DC and LS for the same performance levels. For these cases, the corresponding values of [MaxISDR, ResISDR] are as follows (**Table 4**):

- *Basic objective:* LS = [2.5, 1.0%] for 10% PE in 50 years and CP = [4.5, 1.0%] for 2% PE in 50 years;
- *Essential service objective:* LS = [0.9, 0.5%] for 10% PE in 50 years and CP = [2.5, 1.0%] for 2% in 50 years.

For the structural models that are considered in this study (which should meet the *basic objective*), IO and DC are not applicable to evaluate their seismic performances based on bivariate structural responses. This is because the structures, when subjected to expected ground motions at IO and DC hazard levels, are essentially linear-elastic and residual responses are very small (near zero). In other words, the seismic hazard levels corresponding to 50% PE in 30 or 50 years are mainly related to the serviceability limit state and are too low to cause significant non-linear responses. As our focus in this paper is upon the non-linear responses, LS and CP are mainly concerned and an intermediate seismic performance level between LS and CP, i.e., 5% PE in 50 years (corresponding to the return period of 1000 years), is introduced.

To illustrate the proposed seismic performance evaluation method, three performance levels, i.e., 10, 5, and 2% PE in 50 years, are considered with the limit states of [MaxISDR, ResISDR] = [2.0, 1.0%], [3.0, 1.5%], and [5.0, 2.0%], respectively. These demand levels are similar to those presented in **Table 4**. **Figure 12A** shows the scatter plots of MaxISDR and ResISDR (for non-collapse cases) at the three performance levels, noting that the collapse cases are dealt with collapse fragility curves (**Figure 9**). The corresponding limit states are indicated with red broken lines. By connecting the limit state thresholds at different performance levels (gray broken lines) and plotting the seismic demands in bivariate space (blue dots), the evolution of the seismic performance evaluation of the structure can be visualized, facilitating the better understanding of the seismic performance of the structure at multiple seismic excitation levels.

The overall performance of the building is assessed through unconditional probability of unsatisfactory seismic performance (P_{NS}) (i.e., overall measure at a seismic performance level). The steps followed to compute P_{NS} are outlined below, with the results shown in **Figure 12B** as an example. **Figure 12B** illustrates the calculations of the probabilities of exceedance and non-exceedance of the specified limit state thresholds for the 5% PE in 50 years performance level for non-collapse cases. First, from **Figure 12B**, four probabilities of exceedance and non-exceedance can be derived:

- the lower-left quadrant corresponds to the probability of joint non-exceedance of the MaxISDR and ResISDR limits, $P_{NE,NE}$ (=0.494),
- the lower-right quadrant corresponds to the probability of exceedance of the MaxISDR limit and non-exceedance of the ResISDR limit, $P_{E,NE}$ (=0.271),
- the upper-left quadrant corresponds to the probability of non-exceedance of the MaxISDR limit and exceedance of the ResISDR limit, $P_{NE,E}$ (=0.025), and
- the upper-right quadrant corresponds to the probability of joint exceedance of the MaxISDR and ResISDR limits, $P_{E,E}$ (=0.210).

The four probabilities are useful for assessing the causes of unsatisfactory seismic performance for non-collapse cases. A large value of $P_{E,NE}$ tends to indicate that the unsatisfactory seismic performance is due to MaxISDR, whereas a large value of $P_{NE,E}$ suggests that the structure may need to be demolished after the earthquake. It is noteworthy that $P_{NE,NE}$, $P_{E,NE}$, $P_{NE,E}$, and $P_{E,E}$ are conditional probabilities upon non-collapse cases. Second, the collapse probability P_C and the non-collapse probability P_{NC}, i.e., $P_{NC} = (1 - P_C)$, need to be evaluated for the given seismic intensity level using the corresponding collapse fragility curve (**Figure 9**). Finally, once the different probability values are obtained as outlined above, the value of P_{NS} can be calculated by:

$$\begin{aligned} P_{NS} &= P_C + P_{NC} \times (P_{NE,E} + P_{E,NE} + P_{E,E}) \\ &= P_C + P_{NC} \times (1 - P_{NE,NE}) \end{aligned} \quad (5)$$

Figure 13 shows 4 by 3 panels (i.e., four buildings and three performance levels) of the bivariate MaxISDR–ResISDR data/performance limits for MS records; four conditional probabilities of exceedance and non-exceedance as well as collapse/non-collapse probabilities are indicated in the figure, whereas **Figure 14** shows the same set of results for MSAS sequences. To facilitate the comparison of the calculated probabilities for different cases, values of $P_{NE,NE}$, $P_{E,NE}$, $P_{NE,E}$, $P_{E,E}$, P_C, P_{NC}, and P_{NS} are summarized in **Tables 8** and **9** for MS records and MSAS sequences, respectively.

Figures 13 and **14** show that MaxISDR and ResISDR become severer with the increase in the seismic performance level; this can be inspected from the scatter of the data points as well as the increase of the collapse probability. The 2- and 4-story buildings are more vulnerable, in comparison with the 8- and 12-story buildings. The collapse probabilities for the 2-story building are generally greater than those for the 4-story building; however, for the non-collapse cases, MaxISDR and ResISDR data are more widely distributed and consequently, conditional probabilities of unsatisfactory seismic performance (e.g., $P_{E,NE}$, $P_{NE,E}$, and $P_{E,E}$) for the 4-story building are greater than those for the 2-story building. Overall, unconditional probabilities of unsatisfactory seismic performance for the 4-story building are greater than others (P_{NS} in **Tables 8** and **9**). Note that the causes of unsatisfactory seismic performance vary depending on building story numbers and performance levels for the non-collapse cases. For example, for the 2-story building, unsatisfactory performance is mainly due to large residual seismic demands; in this case, the damaged building may be demolished. On the other hand, for the 4-story building (e.g., 5% PE in 50 years), the unsatisfactory performance is mainly due to excessive peak transient seismic demands. These

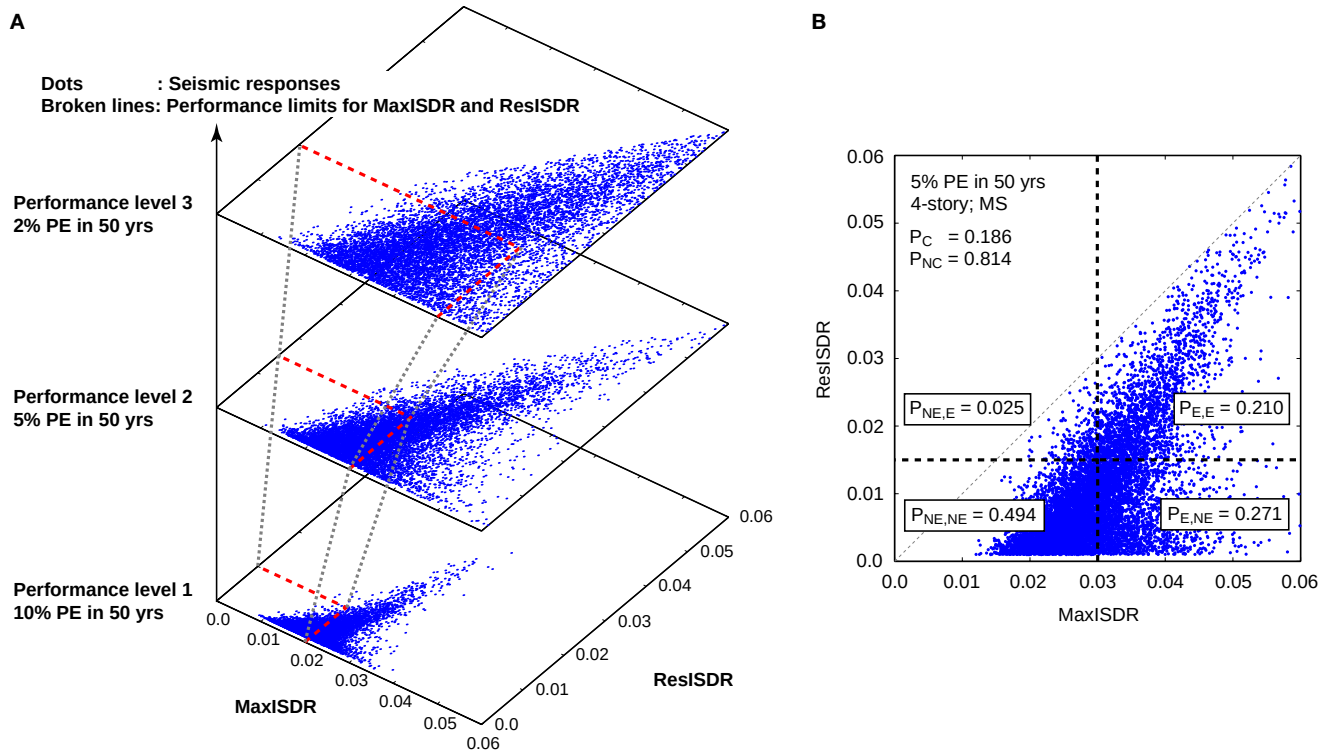

FIGURE 12 | (A) Scatter plots of MaxISDR and ResISDR at the three performance levels (10, 5, and 2% PE in 50 years) and **(B)** probabilities of exceedance and non-exceedance of the limit state demand levels.

results indicate that different counter measures may need to be implemented for different buildings as their damage mechanisms may be different.

The comparison of the results shown in **Figures 13** and **14** as well as **Tables 8** and **9** suggests that the observations made for MS records are generally applicable to MSAS sequences. However, additional seismic demands due to major aftershocks have noticeable influence on both MaxISDR and ResISDR for the 2-story building (**Figures 6A** and **9A**). Consequently, counter measures against aftershock risks should be specific to building types (i.e., dynamic structural characteristics and susceptible failure mode).

Importantly, the calculated values of PNS listed in **Tables 8** and **9** indicate that for all four non-ductile buildings, their seismic capacities may be judged as satisfactory (because PNS is relatively low) at the LS performance level (i.e., return periods of 500–1000 years), whereas they fail to meet the CP performance level required by the current standards suggested by FEMA P-58-1 (2012). Therefore, for this class of non-ductile RC buildings, seismic retrofitting should be implemented to improve the seismic performance.

Discussion and Conclusion

The primary objective of the building design code was LS. In developed countries, this has been met through improved seismic design provisions. Seismic vulnerability of existing buildings remains to be a major concern because of the use of older design codes and/or poor construction practices at the time of design and construction. Most of these older buildings are currently operational and are required to be further assessed and upgraded to improve potential economic consequences due to seismic damage. An accurate assessment of potential impact of future destructive earthquakes is essential for effective disaster risk reduction. Probabilistic seismic risk analysis entails comprehensive understanding of ground shaking information, such as fault rupture process, wave propagation, and site effects, as well as vulnerability of structures, such as structural damage accumulation, seismic loss generation, and societal/economic impact (Cornell and Krawinkler, 2000). Through probabilistic calculus, it evaluates the potential damage and loss that a certain group of structures is likely to experience due to various seismic events (Tesfamariam and Goda, 2015).

The current state of the art for seismic performance assessment of buildings in North America is FEMA P-58-1 (2012). It has been developed based on generic ground motions that are applicable to the seismicity of California, which might not be compatible with the seismicity in Canada. Furthermore, the damage observed from the MSAS sequence of the 2011 M_w6.3 Christchurch earthquake in New Zealand has highlighted the need for further study on the collapse risk of RC buildings in Canada (Elwood, 2013). The rigorous probabilistic seismic performance evaluation method can be used to aid in an informed decision-making by comparing performance metrics of alternative seismic risk mitigation measures quantitatively. Accurate representation

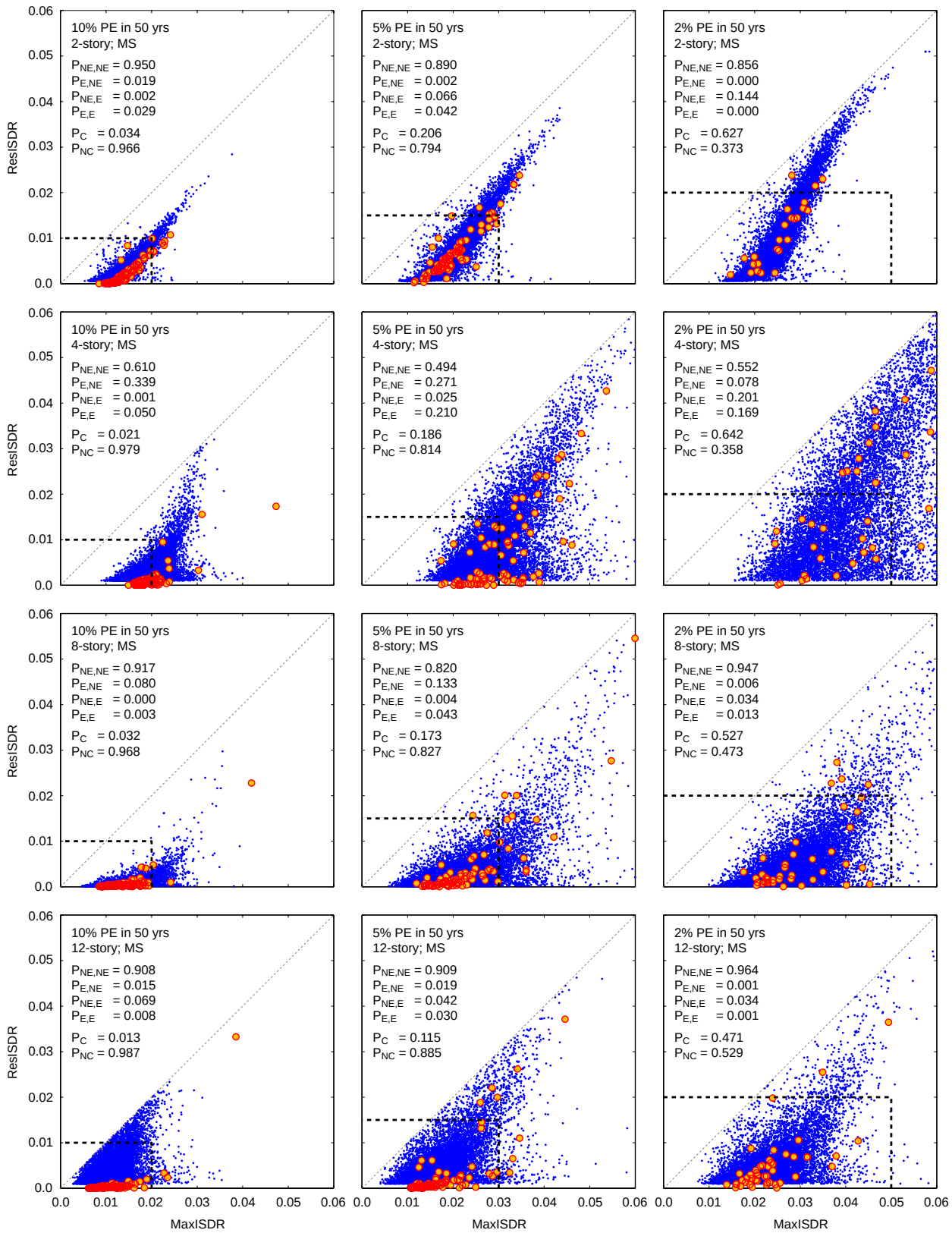

FIGURE 13 | Mainshock earthquake record – probabilities of exceedance and non-exceedance of the 2-, 4-, 8-, and 12-story building (rows) and 10, 5, and 2% PE in 50 years hazard levels (columns). Red circles are the IDA results.

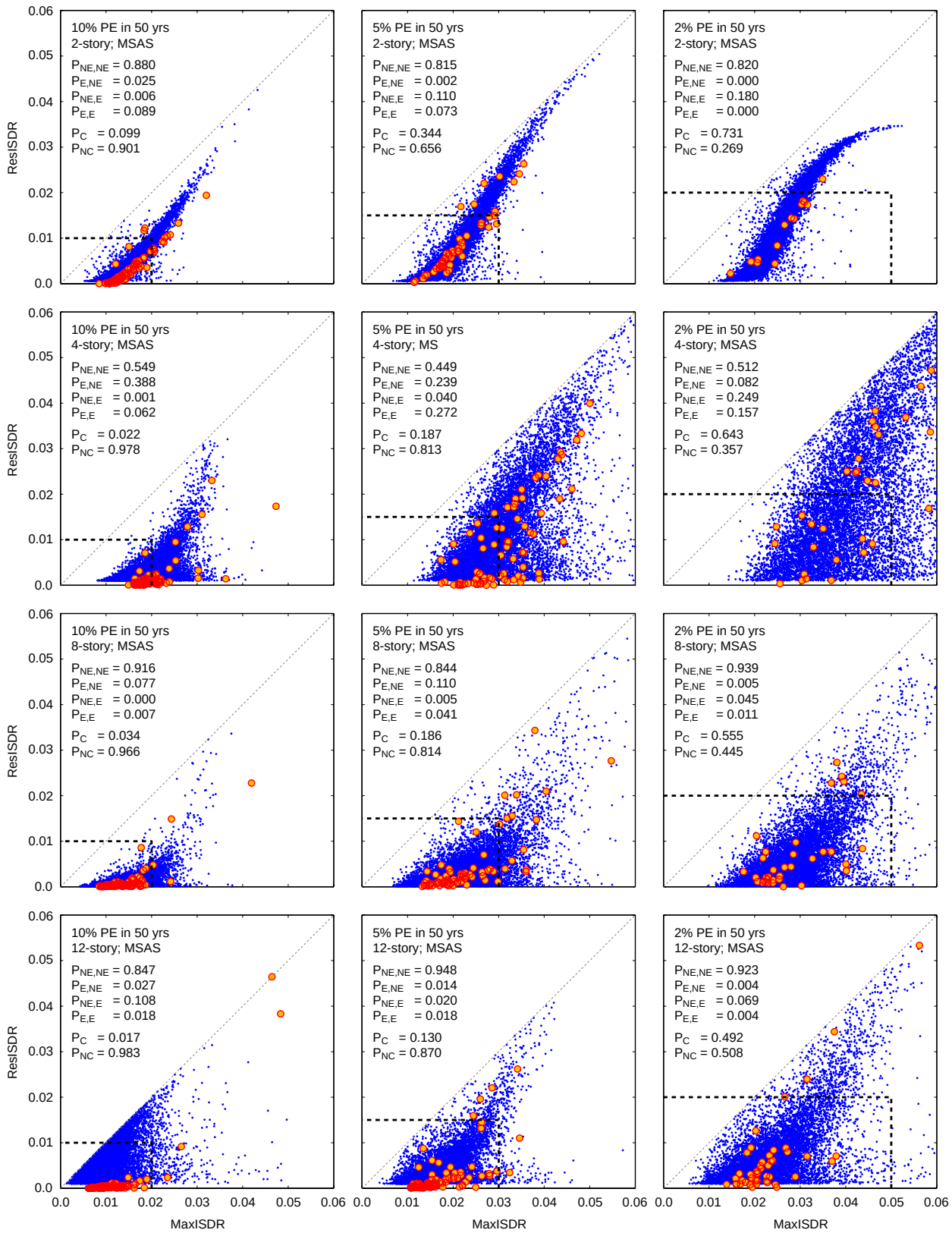

FIGURE 14 | Mainshock–aftershock earthquake sequence records – probabilities of exceedance and non-exceedance of the 2-, 4-, 8-, and 12-story building (rows) and 10, 5, and 2% PE in 50 years hazard levels (columns). Red circles are the IDA results.

TABLE 8 | Collapse and non-collapse probabilities and probabilities of exceedance and non-exceedance of the different limit states for MS records.

Building story	Probability of exceedance in 50 years (%)	Probabilities of exceedance and non-exceedance of the different limit states				Non-collapse probability	Collapse probability	$P_{NS} = P_C + P_{NC} \times (1 - P_{NE,NE})$
		$P_{NE,NE}$	$P_{E,NE}$	$P_{E,E}$	$P_{NE,E}$	P_{NC}	P_C	
2	10	0.950	0.019	0.029	0.002	0.966	0.034	0.082
	5	0.890	0.002	0.042	0.066	0.794	0.206	0.293
	2	0.856	0.000	0.000	0.144	0.373	0.627	0.681
4	10	0.610	0.339	0.050	0.001	0.979	0.021	0.403
	5	0.494	0.271	0.210	0.025	0.814	0.186	0.598
	2	0.552	0.078	0.169	0.201	0.358	0.642	0.802
8	10	0.917	0.080	0.003	0.000	0.968	0.032	0.112
	5	0.820	0.133	0.043	0.004	0.827	0.173	0.322
	2	0.947	0.006	0.013	0.034	0.473	0.527	0.552
12	10	0.908	0.015	0.008	0.069	0.987	0.013	0.104
	5	0.909	0.019	0.030	0.042	0.885	0.115	0.196
	2	0.964	0.001	0.001	0.034	0.529	0.471	0.490

TABLE 9 | Collapse and non-collapse probabilities and probabilities of exceedance and non-exceedance of the different limit states for MSAS sequence records.

Building story	Probability of exceedance in 50 years (%)	Probabilities of exceedance and non-exceedance of the different limit states				Non-collapse probability	Collapse probability	$P_{NS} = P_C + P_{NC} \times (1 - P_{NE,NE})$
		$P_{NE,NE}$	$P_{E,NE}$	$P_{E,E}$	$P_{NE,E}$	P_{NC}	P_C	
2	10	0.880	0.025	0.089	0.006	0.901	0.099	0.207
	5	0.815	0.002	0.073	0.110	0.656	0.344	0.465
	2	0.820	0.000	0.000	0.180	0.269	0.731	0.779
4	10	0.549	0.388	0.062	0.001	0.978	0.022	0.463
	5	0.449	0.239	0.272	0.040	0.813	0.187	0.635
	2	0.512	0.082	0.157	0.249	0.357	0.643	0.817
8	10	0.916	0.077	0.007	0.000	0.966	0.034	0.115
	5	0.844	0.110	0.041	0.005	0.814	0.186	0.313
	2	0.939	0.005	0.011	0.045	0.445	0.555	0.582
12	10	0.847	0.027	0.018	0.108	0.983	0.017	0.167
	5	0.948	0.014	0.018	0.020	0.870	0.130	0.175
	2	0.923	0.004	0.004	0.069	0.508	0.492	0.531

of different limit states, robust ground motion selection, and multivariate inelastic seismic demands are vitally important in the assessment. In this paper, a robust seismic evaluation tool, within the performance-based earthquake engineering framework, is developed. Two EDPs, MaxISDR and ResISDR, are used to determine the severity of seismic damage and consequences. The joint probability distribution and dependency are modeled using the advanced copula technique. Following SEAOC (1995) and FEMA P-58-1 (2012), the two EDPs reaching different performance limit states are defined. Moreover, the aftershock ground motions are incorporated with the conventional seismic performance evaluation methodology, and furnished a better representation of the prevalent risk. The proposed evaluation tool can indeed be used for existing structures or design of new buildings.

The proposed framework was applied to 2-, 4-, 8-, and 12-story non-ductile RC buildings located in Victoria, BC, Canada. Considering regional seismicity in southwestern BC (i.e., shallow crustal earthquakes, off-shore mega-thrust interface earthquakes from the Cascadia subduction zone, and deep inslab earthquakes), 50 MS records and 50 MSAS sequence records were selected. Subsequently, IDA was performed and the computed MaxISDR and ResISDR data were used for developing collapse fragility curves and for developing probabilistic inelastic seismic demand models using copulas.

The general conclusions related to the aftershock effects are as follows:

- The MSAS sequence earthquake has significant influence on the 2-story building, where the median collapse capacity is reduced by 13%.
- The MSAS sequence records for the 4-, 8-, and 12-story buildings showed no marked differences in the collapse fragility. This partly may be ascribed to the considered model limitation. The collapse limit states as modeled in this paper are associated with flexure. The model does not consider shear failure, and gravity load collapse.
- The MSAS sequence records, however, have shown marked differences in the non-collapse limit states.

The unconditional probability of unsatisfactory seismic performance P_{NS} integrates the collapse and non-collapse limit states and thus can be used as an overall seismic performance measure

of structures. The general conclusions related to the P_{NS} results for the four non-ductile RC frames are as follows:

- With increasing hazard levels (10, 5, and 2% PE in 50 years), the corresponding P_{NS} is increasing.
- Seismic capacities at the LS performance level (i.e., return periods of 500–1000 years) are judged to be satisfactory (i.e., P_{NS} is relatively low).
- Seismic capacities at the CP performance level (i.e., return period of 2500 years) may not be satisfactory (i.e., P_{NS} is high). This highlights the need for undertaking seismic retrofitting to improve the seismic performance.

Finally, the proposed performance-based seismic screening criteria and methods can be used for Canadian buildings. The methodology can be extended to different building types and seismicity (e.g., Eastern Canada). The consideration of MSAS sequences as seismic input was found to be important for the seismic risk assessment of low- to mid-rise buildings, and further investigations are warranted in the future. Furthermore, the aftershock effects should also be integrated in the design of Canadian buildings.

Acknowledgments

Ground motion data for Japanese earthquakes and worldwide crustal earthquakes were obtained from the K-NET/KiK-net/SK-net databases at http://www.kyoshin.bosai.go.jp/ and http://www.sknet.eri.u-tokyo.ac.jp/, and the PEER-NGA database at http://peer.berkeley.edu/nga/index.html, respectively. This work was supported by the Natural Science Engineering Research Council Canada (RGPIN-2014-05013) to the first author and the Engineering and Physical Sciences Research Council (EP/M001067/1) to the second author.

References

Altoontash, A. (2004). *Simulation and Damage Models for Performance Assessment of Reinforced Concrete Beam-Column Joints*. Doctoral Dissertation, Stanford University, Stanford, CA.

ATC. (2002). *Rapid Visual Screening of Buildings for Potential Seismic Hazard: A Handbook*, 2nd Edn. Washington, DC: Applied Technology Council.

Atkinson, G. M. (2004). "An overview of developments in seismic hazard analysis," in *13th World Conference on Earthquake Engineering* Vancouver, BC, Paper No. 5001.

Atkinson, G. M., and Goda, K. (2011). Effects of seismicity models and new ground motion prediction equations on seismic hazard assessment for four Canadian cities. *Bull. Seismol. Soc. Am.* 101, 176–189. doi:10.1785/0120100093

Baker, J. W. (2011). The conditional mean spectrum: a tool for ground motion selection. *J. Struct. Eng.* 137, 322–331. doi:10.1061/(ASCE)ST.1943-541X.0000215

Bruneau, M., and Lamontagne, M. (1994). Damage from 20th century earthquakes in Eastern Canada and seismic vulnerability of unreinforced masonry buildings. *Can. J. Civil Eng.* 21, 643–662. doi:10.1139/l94-065

Christidis, A. A., Dimitroudi, E. G., Hatzigeorgiou, G. D., and Beskos, D. E. (2013). Maximum seismic displacements evaluation of steel frames from their post-earthquake residual deformation. *Bull. Earthq. Eng.* 11, 2233–2248. doi:10.1007/s10518-013-9490-z

Christopoulos, C., Pampanin, S., and Priestley, M. J. N. (2003). Performance-based seismic response of frame structures including residual deformations – part I: single-degree-of-freedom system. *J. Earthq. Eng.* 7, 97–118. doi:10.1080/13632460309350443

Cornell, C. A., and Krawinkler, H. (2000). *Progress and Challenges in Seismic Performance Assessment*. PEER Center News 3. Available at: http://peer.berkeley.edu/news/2000spring/performance.html

DeVall, R. H. (2003). Background information for some of the proposed earthquake design provisions for the 2005 edition of the National Building Code of Canada. *Can. J. Civil Eng.* 30, 279–286. doi:10.1139/l02-048

Elwood, K. J. (2013). Performance of concrete buildings in the 22 February 2011 Christchurch earthquake and implications for Canadian codes. *Can. J. Civil Eng.* 40, 759–776. doi:10.1139/cjce-2011-0564

Erochko, J., Christopoulos, C., Tremblay, R., and Choi, H. (2011). Residual drift response of SMRFs and BRB frames in steel buildings designed according to ASCE 7-05. *J. Struct. Eng.* 137, 589–599. doi:10.1061/(ASCE)ST.1943-541X.0000296

FEMA 356. (2000). *Prestandard and Commentary for the Seismic Rehabilitation of Buildings*. Washington, DC: Federal Emergency Management Agency.

FEMA P-58-1. (2012). *Seismic Performance Assessment of Buildings Volume 1 – Methodology*. Washington, DC: Federal Emergency Management Agency.

Foo, S., and Davenport, A. (2003). Seismic hazard mitigation for buildings. *Nat. Hazards (Dordr.)* 28, 517–535. doi:10.1023/A:1022950629065

Goda, K., and Atkinson, G. M. (2011). Seismic performance of wood-frame houses in South-Western British Columbia. *Earthq. Eng. Struct. Dyn.* 40, 903–924. doi:10.1002/eqe.1068

Goda, K., Pomonis, A., Chian, S. C., Offord, M., Saito, K., Sammonds, P., et al. (2013). Ground motion characteristics and shaking damage of the 11th March 2011 M_w9.0 Great East Japan earthquake. *Bull. Earthq. Eng.* 11, 141–170. doi:10.1007/s10518-012-9371-x

Goda, K., and Taylor, C. A. (2012). Effects of aftershocks on peak ductility demand due to strong ground motion records from shallow crustal earthquakes. *Earthq. Eng. Struct. Dyn.* 41, 2311–2330. doi:10.1002/eqe.2188

Goda, K., and Tesfamariam, S. (2015). Multi-variate seismic demand modelling using Copulas: application to non-ductile reinforced concrete frame in Victoria, Canada. *Struct. Saf.* 56, 39–51. doi:10.1016/j.strusafe.2015.05.004

Goda, K., Wenzel, F., and De Risi, R. (2015). Empirical assessment of nonlinear seismic demand of mainshock-aftershock ground motion sequences for Japanese earthquakes. *Front. Built Environ.* 1:6. doi:10.3389/fbuil.2015.00006

Haselton, C. B., Liel, A. B., Lange, S. T., and Deierlein, G. G. (2008). *Beam-Column Element Model Calibrated for Predicting Flexural Response Leading to Global Collapse of RC Frame Buildings*. PEER Report 2007/03. Berkeley, CA: PEER Center, University of California, Berkeley.

Hatzigeorgiou, G. D., and Beskos, D. E. (2009). Inelastic displacement ratios for SDOF structures subjected to repeated earthquakes. *Eng. Struct.* 31, 2744–2755. doi:10.1016/j.engstruct.2009.07.002

Hatzigeorgiou, G. D., and Liolios, A. A. (2010). Nonlinear behaviour of RC frames under repeated strong ground motions. *Soil Dyn. Earthq. Eng.* 30, 1010–1025. doi:10.1016/j.soildyn.2010.04.013

Hatzigeorgiou, G. D., Papagiannopoulos, G. A., and Beskos, D. E. (2011). Evaluation of maximum seismic displacements of SDOF systems from their residual deformation. *Eng. Struct.* 33, 3422–3431. doi:10.1016/j.engstruct.2011.07.006

Hyndman, R. D., and Rogers, G. C. (2010). Great earthquakes on Canada's west coast: a review. *Can. J. Earth Sci.* 47, 801–820. doi:10.1139/E10-011

Ibarra, L. F., Medina, R. A., and Krawinkler, H. (2005). Hysteretic models that incorporate strength and stiffness deterioration. *Earthq. Eng. Struct. Dyn.* 34, 1489–1511. doi:10.1002/eqe.495

ICBO. (1967). *Uniform Building Code*. Pasadena, CA: International Conference of Building Officials.

Kawashima, K., MacRae, G. A., Hoshikuma, J., and Nagaya, K. (1998). Residual displacement response spectrum. *J. Struct. Eng.* 124, 523–530. doi:10.1061/(ASCE)0733-9445(1998)124:5(523)

Leite, J., Lourenco, P. B., and Ingham, J. M. (2013). Statistical assessment of damage to churches affected by the 2010-2011 Canterbury (New Zealand) earthquake sequence. *J. Earthq. Eng.* 17, 73–97. doi:10.1080/13632469.2012.713562

Liel, A. B., and Deierlein, G. G. (2008). *Assessing the Collapse Risk of California's Existing Reinforced Concrete Frame Structures: Metrics for Seismic Safety Decisions*. Technical Report No. 166. Stanford, CA: John A. Blume Center Earthquake Engineering Center.

Luco, N., and Bazzurro, P. (2007). Does amplitude scaling of ground motion records result in biased nonlinear structural drift responses? *Earthq. Eng. Struct. Dyn.* 36, 1813–1835. doi:10.1002/eqe.695

MacRae, G. A., and Kawashima, K. (1997). Post-earthquake residual displacements of bilinear oscillators. *Earthq. Eng. Struct. Dyn.* 26, 701–716. doi:10.1002/(SICI)1096-9845(199707)26:7<701::AID-EQE671>3.3.CO;2-9

McKenna, F., Fenves, G. L., and Scott, M. H. (2000). *Open System for Earthquake Engineering Simulation*. Berkeley, CA: University of California Berkeley.

McNeil, A. J., Frey, R., and Embrechts, P. (2005). *Quantitative Risk Management: Concepts, Techniques and Tools*. Princeton, NJ: Princeton University Press.

Mitchell, D., Paultre, P., Tinawi, R., Saatciouglu, M., Tremlay, R., Elwood, K., et al. (2010). Evolution of seismic design provisions in the National Building Code of Canada. *Can. J. Civil Eng.* 37, 1157–1170. doi:10.1139/L10-054

NRCC. (1941). *National Building Code of Canada. Associate Committee on the National Building Code*. Ottawa, ON: National Research Council of Canada.

NRCC. (1965). *National Building Code of Canada. Associate Committee on the National Building Code*. Ottawa, ON: National Research Council of Canada.

NRCC. (1970). *National Building Code of Canada. Associate Committee on the National Building Code*. Ottawa, ON: National Research Council of Canada.

Onur, T., Ventura, C. E., and Finn, W. D. L. (2005). Regional seismic risk in British Columbia – damage and loss distribution in Victoria and Vancouver. *Can. J. Civil Eng.* 32, 361–371. doi:10.1139/l04-098

Otani, S. (2004). Earthquake resistant design of reinforced concrete buildings past and future. *J. Adv. Concr. Technol.* 2, 3–24. doi:10.3151/jact.2.3

Pampanin, S., Christopoulos, C., and Priestley, M. J. N. (2003). Performance-based seismic response of frame structures including residual deformations – part II: multi-degree-of-freedom systems. *J. Earthq. Eng.* 7, 119–147. doi:10.1080/13632460309350444

Rainer, J. H. (1992). *Manual for Screening of Buildings for Seismic Investigation*. Institute for Research in Construction. Ottawa: National Research Council of Canada.

Ramirez, C. M., and Miranda, E. (2009). *Building-Specific Loss Estimation Methods & Tools for Simplified Performance-Based Earthquake Engineering*. Technical Report No. 171. Stanford, CA: John A. Blume Center Earthquake Engineering Center.

Ruiz-García, J., and Miranda, E. (2006). Evaluation of residual drift demands in regular multi-storey frames for performance-based seismic assessment. *Earthq. Eng. Struct. Dyn.* 35, 1609–1629. doi:10.1002/eqe.593

Ryu, H., Luco, N., Uma, S. R., and Liel, A. B. (2011). "Developing fragilities for mainshock-damaged structures through incremental dynamic analysis," in *Proceedings, Ninth Pacific Conference on Earthquake Engineering, Building an Earthquake-Resilient Society*, Auckland.

Saatcioglu, M., Shooshtari, M., and Foo, S. (2013). Seismic screening of buildings based on the 2010 National Building Code of Canada. *Can. J. Civil Eng.* 40, 483–498. doi:10.1139/cjce-2012-0055

SEAOC. (1995). *Vision 2000: Performance-Based Seismic Engineering of Buildings*. Sacramento, CA: Structural Engineers Association of California.

Tesfamariam, S., and Goda, K. (2015). Loss estimation for non-ductile reinforced concrete building in Victoria, British Columbia, Canada: effects of mega-thrust M_w9-class subduction earthquakes and aftershocks. *Earthq. Eng. Struct. Dyn.* 44, 2303–2320. doi:10.1002/eqe.2585

Tesfamariam, S., Goda, K., and Mondal, G. (2015). Seismic vulnerability of RC frame with unreinforced masonry infill due to mainshock-aftershock earthquake sequences. *Earthq. Spectra* 31, 1427–1449. doi:10.1193/042313EQS111M

Tesfamariam, S., and Saatcioglu, M. (2008). Risk-based seismic evaluation of reinforced concrete buildings. *Earthq. Spectra* 24, 795–821. doi:10.1193/1.2952767

Uma, S. R., Pampanin, S., and Christopoulos, C. (2010). Development of probabilistic framework for performance-based seismic assessment of structures considering residual deformations. *J. Earthq. Eng.* 14, 1092–1111. doi:10.1080/13632460903556509

Vamvatsikos, D., and Cornell, C. A. (2002). Incremental dynamic analysis. *Earthq. Eng. Struct. Dyn.* 31, 491–514. doi:10.1002/eqe.141

Ventura, C. E., Finn, W. D. L., Onur, T., Blanquera, A., and Rezai, M. (2005). Regional seismic risk in British Columbia – classification of buildings and development of damage probability functions. *Can. J. Civil Eng.* 32, 372–387. doi:10.1139/l04-099

Conflict of Interest Statement: The authors declare that the research was conducted in the absence of any commercial or financial relationships that could be construed as a potential conflict of interest.

Copyright © 2015 Tesfamariam and Goda. This is an open-access article distributed under the terms of the Creative Commons Attribution License (CC BY). The use, distribution or reproduction in other forums is permitted, provided the original author(s) or licensor are credited and that the original publication in this journal is cited, in accordance with accepted academic practice. No use, distribution or reproduction is permitted which does not comply with these terms.

frontiers in Built Environment

ORIGINAL RESEARCH
published: 30 May 2017
doi: 10.3389/fbuil.2017.00029

Energy-Based Seismic Risk Evaluation of Tall Reinforced Concrete Building in Vancouver, BC, Canada, under M_w9 Megathrust Subduction Earthquakes and Aftershocks

Solomon Tesfamariam[1]* *and Katsuichiro Goda*[2]

[1] School of Engineering, The University of British Columbia, Kelowna, BC, Canada, [2] Department of Civil Engineering, University of Bristol, Bristol, UK

This article presents a seismic performance evaluation framework for reinforced concrete (RC) buildings, comprising shear walls and gravity frames. The evaluation is undertaken within a performance-based earthquake engineering framework by considering regional seismicity and site-specific ground motion selection. Different engineering demand parameters (EDPs), i.e., maximum interstory drift ratio (MaxISDR) and energy-based damage index, are considered as performance indicators. Various prediction models of EDPs are developed by considering four ground motion intensity measures (IMs), i.e., spectral acceleration at the fundamental period, Arias intensity, cumulative absolute velocity (CAV), and significant duration of ground motion. For this study, a 15-story RC building, located in Vancouver, BC, Canada, is considered as a case study. By using 50 mainshock and 50 mainshock–aftershock (MS-AS) earthquake records (2 horizontal components per record and bidirectional loading), non-linear dynamic analyses are performed. Subsequently, the calculated MaxISDRs and damage indices are correlated with suitable IMs using cloud analysis, and the most *efficient* IM-EDP prediction models are selected by comparing standard deviations (SDs) of the regression errors. The MaxISDR of the shear walls is less than 1% for the mainshock and MS-AS records. The energy-based damage index shows sensitivity to delineate impact of earthquake types and aftershocks. The CAV is showed to be the most efficient IM for the energy-based damage index.

Keywords: seismic performance, energy-based damage index, gravity frame, shear wall, reinforced concrete building, mainshock–aftershock earthquake

OPEN ACCESS

Edited by:
Oren Lavan,
Technion – Israel Institute of Technology, Israel

Reviewed by:
Marie-José Nollet,
École de technologie supérieure, Canada
Rita Bento,
Universidade de Lisboa, Portugal

***Correspondence:**
Solomon Tesfamariam
solomon.tesfamariam@ubc.ca

Specialty section:
This article was submitted to Earthquake Engineering, a section of the journal Frontiers in Built Environment

Received: *07 March 2017*
Accepted: *28 April 2017*
Published: *30 May 2017*

Citation:
Tesfamariam S and Goda K (2017) Energy-Based Seismic Risk Evaluation of Tall Reinforced Concrete Building in Vancouver, BC, Canada, under M_w9 Megathrust Subduction Earthquakes and Aftershocks. Front. Built Environ. 3:29. doi: 10.3389/fbuil.2017.00029

INTRODUCTION

Motivation

Seismic performance of reinforced concrete (RC) shear wall systems designed with Canadian design codes has been investigated by various researchers (e.g., Tremblay et al., 2001; Adebar et al., 2010; Boivin and Paultre, 2010, 2012; Luu et al., 2014). For RC core buildings designed with the CSA standard A23.3-04, Boivin and Paultre (2010) showed that the RC core performs

satisfactorily for flexural demand, while potential deficiency under significant shear demand may be a concern. Koduru and Haukaas (2010) studied the seismic performance and economic loss of a 15-story RC building constructed in 1988 and located in Vancouver, BC, Canada. Their study was comprehensive, covering from regional seismic hazard, seismic vulnerability assessment, and economic impact estimation. Nevertheless, important improvements can be made with regard to use of ground motion records that are applicable to megathrust interface records from the Cascadia subduction zone, noting that the records used by Koduru and Haukaas (2010) were calibrated based on shallow crustal records. On the other hand, adopting PEER's performance-based earthquake engineering (PBEE) framework (Cornell and Krawinkler, 2000), Yang et al. (2012) carried out a seismic loss assessment for a 42-story RC dual-system building, i.e., a centrally located core wall building with perimeter special moment-resisting frames. With a design earthquake intensity level, the maximum interstory drift ratio (MaxISDR) calculated was less than 2%.

In older Canadian codes, shear wall buildings are the primary seismic force resisting systems, and detailing of gravity frames are often neglected (Adebar et al., 2010). The poor detailing associated with the gravity frames can be (Tesfamariam and Saatcioglu, 2008) inadequate lap splice length, lap splice located in a potential plastic hinge zone, poor detailing of transverse reinforcement anchorage, welded detailing, and lack of support to longitudinal bars. Gravity frames, however, located in the plastic hinge zone of the shear wall can experience excessive deformation and, if not detailed properly, can sustain severe damage (Adebar et al., 2010). This type of damage, for example, was reported in the 27 February 2010 Maule Chile earthquake (Naeim et al., 2011) and the 22 February 2011 Christchurch earthquake (Stirrat et al., 2014). Furthermore, older buildings in Canada lack consideration of large interface events in seismic design procedures. (Note: the potential risk due to the Cascadia subduction earthquakes was only recognized in late 1990s.) The problem is further compounded with the prevalence of mainshock–aftershock (MS-AS) earthquake sequences.

The structural analysis, using an appropriate structural model for the calculation of engineering demand parameter (EDP) and collapse capacity/probability, is an essential component of the seismic vulnerability evaluation. To assess the probability of attaining a specific structural response level conditioned on seismic excitation, incremental dynamic analysis (Vamvatsikos and Cornell, 2002) and cloud and stripe analyses (Jalayer et al., 2007) can be used. Different damage indices are used as a surrogate measure for EDP*s* that are categorized as follows (Williams and Sexsmith, 1995): (a) non-cumulative, (b) deformation-based cumulative, (c) energy-based cumulative, and (d) combined (non-cumulative and energy-based) indices. The most common approach to relate seismic demands to structural performance limits (i.e., capacity) is based on non-cumulative drift-based EDP, such as MaxISDR and residual interstory drift ratio. For RC shear wall buildings, however, the drift-based damage indicator may show satisfactory seismic resistance performance while underestimating overall damage in the plastic region due to cyclic loading. In this article, the cumulative energy-based damage index proposed by Mehanny and Deierlein (2000), which takes into account both peak amplitude and duration of non-linear responses of structural members in quantifying the structural damage, will be used. Alternatively, other damage indices that were proposed in the literature (e.g., Park and Ang, 1985; DiPasquale and Cakmak, 1989; Reinhorn and Valles, 1995) can be adopted.

Objectives

This article presents a seismic vulnerability evaluation of a 15-story RC shear wall structure located in Vancouver, BC, Canada. The RC shear wall building includes gravity frames, which are more vulnerable to low-amplitude repeated ground motions and is modeled in OpenSees finite element software by accounting for the non-linearity in the model. The shear walls for the tall building act as a cantilever beam, and the plastic hinge is formed at the base (assumed to be the first four stories), whereas the gravity columns within this plastic region are modeled with non-linear material elements. The seismic risk assessment that is carried out in this study accounts for:

- Consideration of MS-AS earthquake records and earthquake types, i.e., shallow crustal earthquakes, deep inslab earthquakes, and megathrust Cascadia subduction earthquakes, by selecting applicable records for subduction environments from extensive MS-AS ground motion data sets (Goda and Taylor, 2012; Goda et al., 2015), including the 2011 Tohoku earthquake records that can be regarded as closest proxy for the Cascadia subduction events.
- Energy-based damage indices, which are computed from the hysteretic responses of the structural model. In this article, Mehanny–Deierlein damage index (Mehanny and Deierlein, 2000) is considered, which captures the responses from long-duration earthquakes. The damage indices for different structural elements are primarily integrated based on a combination rule suggested by Bracci et al. (1989).
- Impact of different intensity measures (IMs) on *efficiency*. The cumulative absolute velocity (CAV) is identified as the most efficient IM for characterizing the damage index, and subsequently seismic demand prediction models are developed using CAV. Finally, convoluting the seismic demand model with the seismic hazard of Vancouver, seismic risk is computed quantitatively.

PBEE FOR SEISMIC VULNERABILITY ASSESSMENT

Disaster risk reduction against future earthquakes requires decision support tools for cost-effective risk mitigation options. For seismic risk assessment and design, a PBEE methodology, originally advocated by Cornell and Krawinkler (2000) and later extended by various researchers (e.g., Goulet et al., 2007), can be adopted. In PBEE, the mean annual rate of exceedance of earthquake impact expressed in terms of damage measures (DM) and $\nu(\mathrm{DM})$, is quantified, involving seismic hazard, structural, and damage analyses. Mathematically, $\nu(\mathrm{DM})$ can be expressed as:

$$\nu(\mathrm{DM}) = \iiint G(\mathrm{DM}|\mathrm{EDP})\,dG(\mathrm{EDP}|\mathrm{IM})\,|d\lambda(\mathrm{IM})|, \qquad (1)$$

where λ(IM) is the mean annual rate that a certain level of IM is exceeded, $G(\text{EDP}|\text{IM})$ is the complementary cumulative distribution function of EDP given IM, and $G(\text{DM}|\text{EDP})$ is the complementary cumulative distribution function that can be characterized through damage analysis by relating EDP to the physical extent of structural damage, represented by DM. The accuracy of the earthquake impact assessment depends on the available data and the choices of the relevant models and parameters.

Hazard Consideration and IMs

In western BC, Canada, three dominant earthquake sources are present: crustal, inslab, and interface events (Hyndman and Rogers, 2010). The latter two types are originated from the Cascadia subduction zone (**Figure 1A**), where the oceanic Juan de Fuca Plate sinks beneath the continental North American Plate. When the stored strain along the fault is released, a megathrust subduction earthquake, similar to the 2010 Maule Chile and 2011 Tohoku Japan earthquakes, can happen. The structural damage potential and consequences due to these three earthquake types can be significantly different because of their ground motion characteristics, depending on buildings and infrastructure of interest. Generally, in comparison with crustal and inslab earthquakes, large interface ground motions, originated from the Cascadia subduction zone, have much longer duration (**Figure 1B**). The spectral content of the ground motion records for three earthquake types can differ significantly due to different earthquake source characteristics in terms of magnitude and distance (**Figure 1C**). For instance, the effects of long-duration ground motions on tall buildings have been highlighted for the 2011 Tohoku earthquake (Takewaki et al., 2011).

The three earthquake types have different input characteristics. Thus, besides selecting appropriate EDPs, selecting the corresponding IM is important in the overall risk assessment. As such, consideration of spectral acceleration at the fundamental period $S_a(T_1)$, which is most commonly adopted in modern seismic hazard and risk studies, may not be the most suitable indicator of the energy input from the ground motion. In this article, Arias intensity (AI; Arias, 1970), CAV (Electrical Power Research Institute , EPRI), and significant duration of ground motion ($D_{5-95\%}$, Trifunac and Brady, 1975) are considered, and their correlations with structural damage are quantified. The definitions of AI and CAV are given as follows:

$$\text{AI} = \frac{\pi}{2g}\int_0 [a(t)]^2 \text{dt} \tag{2}$$

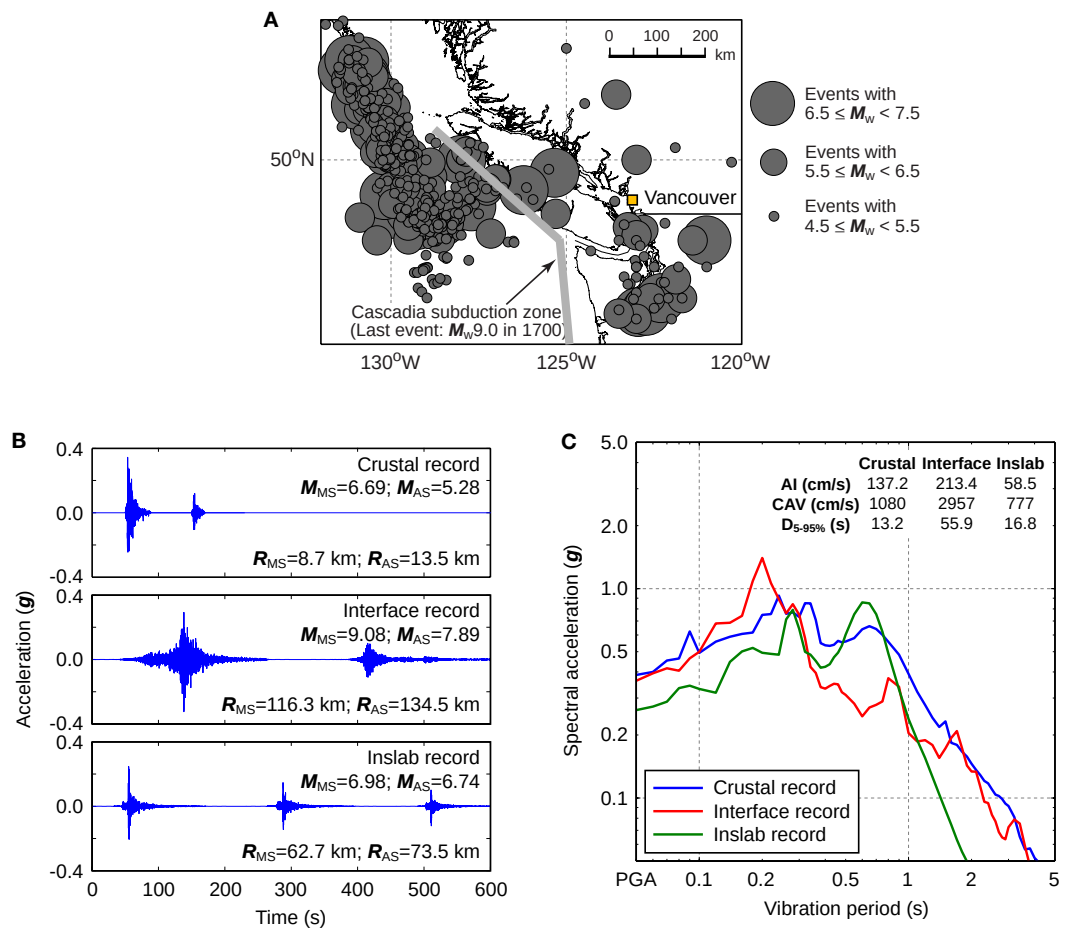

FIGURE 1 | (A) Regional seismicity in southwestern British Columbia, Canada. **(B)** Sample ground motion records for crustal, interface, and inslab events. **(C)** Five percent damped response spectra of the sample ground motion records [single horizontal component shown in panel **(B)**] for crustal, interface, and inslab events.

and

$$\mathrm{CAV} = \int_0^{\infty} |a(t)| \mathrm{dt}, \tag{3}$$

where $a(t)$ is the accelerogram. $D_{5-95\%}$ is defined as duration between times the AI of a ground motion record reaches 5 and 95% of its final value.

Energy-Based Damage Index

Energy-based damage indices are cumulative and are computed with consideration of hysteretic response (Gosain et al., 1977; Park and Ang, 1985; Kraetzig et al., 1989; Mehanny and Deierlein, 2000; see **Table 1**). Gosain et al. (1977) formulated a model to describe damage by using energy absorption normalized by yield force and displacement. Park and Ang (1985) proposed a widely used damage index D_{PA} as a linear combination of deformation and absorbed energy under cyclic loading. The weighing factor used for the energy term in D_{PA} is calibrated through experimental work. Kraetzig et al. (1989) developed an energy-based damage index D_K that accounts for the energy dissipated in primary half cycles (PHCs) and follower half cycles (FHCs) for positive and negative parts of the response. Mehanny and Deierlein (2000) extended the Kraetzig et al.'s damage index by introducing weights on the PHCs and FHCs and the positive and negative damage indices and associated it with extent of physical damage. In this article, following Koduru and Haukaas (2010), the Mehanny–Deierlein damage index D_{MD} is used. The limit states for D_{MD} are shown in **Table 2**.

To define relationships between different earthquake return periods and acceptable performance limit states, seismic performance matrices are often adopted (**Table 3**). It is highlighted that for frequent [50% probability of exceedance (PE) in 30 years], occasional (50% PE in 50 years), rare (10% PE in 50 years), and very rare (2% PE in 50 years) earthquake design levels, the corresponding design performance limit states are immediate occupancy (IO), life safety (LS), and collapse prevention (CP), respectively. For the energy-based earthquake damage evaluation, limit states indicated in **Table 3** can be used with the corresponding definitions of the damage index (**Table 2**).

SEISMIC PERFORMANCE EVALUATION

Structural Model

The reference structure considered in this study is a 15-story RC building constructed in 1988 and located in Vancouver, BC, Canada (Ventura et al., 2001; Koduru and Haukaas, 2010). The primary lateral load-resistant element of the building is shear walls (**Figure 2**). The building is fairly regular in plan, with minor

TABLE 2 | Limit states for the Mehanny–Deierlein damage index.

Damage level	Performance level
$D_{\mathrm{MD}} < 0.3$	Immediate occupancy
$0.3 \le D_{\mathrm{MD}} < 0.6$	Life safety
$0.6 \le D_{\mathrm{MD}} < 0.95$	Near collapse
$D_{\mathrm{MD}} \ge 0.95$	Collapse

TABLE 1 | Energy-based and combined damage indices.

Reference	Equations	Comments
Gosain et al. (1977)	$D_e = \sum_i \frac{F_i \delta_i}{F_y \delta_y}, \quad F_i/F_y \ge 0.75$	D_e = energy-related damage index; F_i = force in ith cycle; δ_i = displacement in ith cycle; F_y = yield force; and δ_y = yield displacement Hysteresis loops that drop below 75% of the yielding value after reaching the yielding value were negligible for the remaining capacity of the member
Park and Ang (1985)	$D_{\mathrm{PA}} = \frac{\Delta_m}{\Delta_u} + \frac{\beta_{\mathrm{PA}}}{F_{ey}\Delta_u} \int \mathrm{dE}$	D_{PA} = Park–Ang damage index; Δ_m = maximum deformation during the loading; Δ_u = ultimate deformation under monotonic loading determined experimentally; β_{PA} = calibration parameter; F_{ey} = (equivalent) yield force; and $\int \mathrm{dE}$ = total incremental hysteretic energy
Kraetzig et al. (1989)	$D_K = D_K^+ + D_K^- - D_K^+ D_K^-$, where $D_K^+ = \frac{\sum E^+_{\mathrm{PHC},i} + \sum E^+_{\mathrm{FHC},i}}{E_f^+ + \sum E^+_{\mathrm{FHC},i}}$ (positive deformation) $D_K^- = \frac{\sum E^-_{\mathrm{PHC},i} + \sum E^-_{\mathrm{FHC},i}}{E_f^- + \sum E^-_{\mathrm{FHC},i}}$ (negative deformation)	D_K = Kraetzig damage index; D_K^+, D_K^- = Kraetzig damage index for positive and negative parts of the response, respectively; $E^+_{\mathrm{PHC},i}, E^-_{\mathrm{PHC},i}$ = dissipated energy for primary half cycle (PHC); $E^+_{\mathrm{FHC},i}, E^-_{\mathrm{FHC},i}$ = dissipated energy for follower half cycle (FHC); E_f^+, E_f^- = energy from a monotonic test to failure
Mehanny and Deierlein (2000)	$D_{\mathrm{MD}} = \sqrt[\gamma]{\left(D^+_{\mathrm{MD}}\right)^{\gamma} + \left(D^-_{\mathrm{MD}}\right)^{\gamma}}$, where $D^+_{\mathrm{MD}} = \frac{\left(\sum_{i=1}^{N^+} E^+_{\mathrm{PHC},i}\right)^{\alpha} + \left(\sum_{i=1}^{n^+} E^+_{\mathrm{FHC},i}\right)^{\beta}}{\left(E_f^+\right)^{\alpha} + \left(\sum_{i=1}^{n^+} E^+_{\mathrm{FHC},i}\right)^{\beta}}$ (positive deformation) $D^-_{\mathrm{MD}} = \frac{\left(\sum_{i=1}^{N^-} E^-_{\mathrm{PHC},i}\right)^{\alpha} + \left(\sum_{i=1}^{n^-} E^-_{\mathrm{FHC},i}\right)^{\beta}}{\left(E_f^-\right)^{\alpha} + \left(\sum_{i=1}^{n^-} E^-_{\mathrm{FHC},i}\right)^{\beta}}$ (negative deformation)	D_{MD} = Mehanny–Deierlein damage index; $D^+_{\mathrm{MD}}, D^-_{\mathrm{MD}}$ = Mehanny–Deierlein damage index for positive and negative parts of the response, respectively; N^+, n^+ = number of PHC and FHC, respectively, for positive part of the response; N^-, n^- = number of PHC and FHC, respectively, for negative part of the response; α, β, and γ = calibration parameters

setbacks at the fourth and fourteenth story levels (**Figure 2A**). The mixed-use building has commercial occupancy at the first floor and residential occupancy at the remaining floors. The shear walls in the staircase and elevator shafts are concentrated at the central core and form the main lateral load-resisting system (**Figure 2B**).

The first story height varies from 2.7 to 4.7 m, and subsequent stories are 2.7 m. Mass and stiffness of the building are used as a base model, and further simplifications are considered in developing a numerical model (Koduru, 2008). For example, four levels of underground parking below grade were not considered in the model, and the foundation was considered to be fixed at base. The numerical model for this building was developed by Koduru and Haukaas (2010) in OpenSees (McKenna et al., 2000). Finite element modeling of the structure was implemented using a fiber element, where the element cross-sections are discretized, and corresponding non-linear material properties of the core concrete, cover concrete, and reinforcing bars were assigned. The structural model consists of three components, i.e., gravity support columns, shear walls, and header beams. The modeling assumptions made by Koduru (2008) are outlined as follows:

- The effect of the RC flat plate slab is accounted for by means of the "rigid diaphragm" option in OpenSees.
- The gravity support columns, header beams, and shear walls are modeled as beam-column elements.
- The shear walls are designed to yield and form plastic hinges between the first and fourth stories. In the plastic region, the shear walls (first to fourth stories) and gravity columns (first to third stories) are modeled with fiber-discretized sections by accounting for bending moments and axial forces interaction.
- From the 4th to 10th story, the shear walls and gravity columns are modeled with non-linear elements. A hysteretic material model includes the force–deformation curve from section analysis and a stiffness degradation factor of 0.05. The shear force–deformation model is separately included in the section models of all non-linear elements. The upper stories, from the 10th to 15th, are modeled as elastic elements.
- The header beams, which connect the shear walls, are modeled as non-linear elements with a hysteretic model for the moment–curvature relationship.

Modal analysis is carried out; the first three modal vibration periods and corresponding damping ratios are obtained as follows. The first mode corresponds to the sway motion in the short structural axis direction; its vibration period and damping ratio are 0.9 s and 3.0%, respectively. The second mode is related to the torsional motion, and its vibration period and damping ratio are 0.84 s and 3.0%, respectively. The third mode is the sway mode in the long structural axis direction, and the corresponding vibration period and damping ratio are 0.25 s and 5.7%, respectively. The calculated vibration periods are in agreement with the measured vibration periods of the building by Ventura et al. (2001), i.e., first mode (0.81 s, short structural axis), second mode (0.79 s, torsional), and third mode (0.69 s, long structural axis).

TABLE 3 | Vision 2000 recommended seismic performance objectives for buildings (SEAOC, 1995).

Earthquake design level [probability of exceedance (PE)]	Performance limit states			
	Immediate occupancy	Damage control	Life safety	Collapse prevention
Frequent (50% PE in 30 years)	■	×	×	×
Occasional (50% PE in 50 years)	♦	■	×	×
Rare (10% PE in 50 years)	◇	♦	■	×
Very rare (2% PE in 50 years)		◇	♦	■

■, *basic objective—proposed National Building Code of Canada (NBCC) normal importance;* ♦, *essential service objective—proposed NBCC high importance;* ◇, *safety critical objective—not proposed NBCC category;* ×, *unacceptable performance for new construction.*

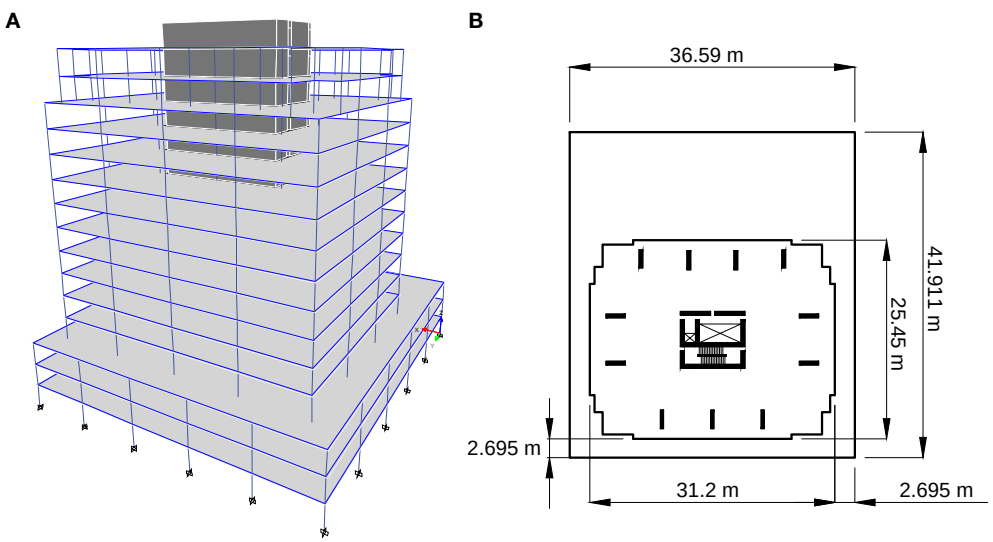

FIGURE 2 | (A) Schematic view of the Heritage Court Tower building. **(B)** Schematic of a typical floor plan.

These dynamic characteristics are important for selecting ground motion records for use in non-linear dynamic analyses.

Seismic Hazard for Vancouver and Ground Motion Selection

The development of seismic damage prediction models requires a series of non-linear dynamic analyses of a structural model subjected to a set of ground motion records, which reflect the regional seismic hazard of interest. In this article, record selection based on multiple conditional mean spectra (CMS) for different earthquake types is carried out by following the same procedures described in the studies by Tesfamariam et al. (2015) and Tesfamariam and Goda (2015). The target CMS are developed for crustal, interface, and inslab earthquakes, based on full probabilistic seismic hazard analysis (PSHA) results by Atkinson and Goda (2011). The site of interest is Vancouver, and its surface soil is classified as site class C (average top 30 m shear-wave velocity ranges from 360 to 760 m/s). **Figures 3A,B** show the uniform hazard spectrum and seismic disaggregation result, respectively, at the return period of 2,500 years. The seismic disaggregation is based on spectral acceleration at 0.9 s (i.e., same as the fundamental vibration period of the building model). To develop CMS for different earthquake types, mean record characteristics for individual earthquake types are obtained from the PSHA results. Three CMS are included in **Figure 3A**, illustrating different spectral characteristics for the three earthquake types. For the considered case (i.e., Vancouver, site class C, vibration period of 0.9 s, and return period of 2,500 years), crustal, interface, and inslab events contribute equally to the overall seismic hazard.

To select a set of suitable ground motion records that match with the constructed CMS, an extended data set of real MS-AS sequences is used, which was developed by combing the worldwide (NGA) database (Goda and Taylor, 2012) with the Japanese (K-KiK-SK) database (Goda et al., 2015). The number of available MS-AS sequences is 606; among them, there are 197 crustal earthquakes, 340 interface earthquakes, and 69 inslab earthquakes. The interface events are from the M_w8.3 2003 Tokachi-oki earthquake and the M_w9.0 2011 Tohoku earthquake (which have similar event characteristics as the expected Cascadia subduction earthquake).

A set of ground motion records is selected by comparing response spectra of candidate records with the target spectra (i.e., CMS). The total number of records is set to 50. (Note: each record has two horizontal components.) The contributions from the 3 earthquake types are equal; as a result, 17, 17, and 16 records are selected for the crustal, interface, and inslab earthquakes, respectively. Response spectral matching is conducted in a least squares sense by considering the geometric mean of the response spectra of two horizontal components. (Note: spectral matching is performed for mainshock records of MS-AS sequences.) The vibration period range for spectral matching is from 0.1 to 2.0 s, which is inclusive of major vibration periods of the tall building model. **Figures 3C–E** show the statistics of the response spectra of the selected ground motion records (i.e., median as well as 16th and 84th percentile curves). For comparison, **Figures 3C–E** include the target CMS as well as the CMS $\pm$ 1 conditional standard deviation (SD) (Jayaram et al., 2011). The response spectra of the selected records and the target CMS are similar for the crustal and interface records; for inslab records, the selected records contain richer short-period spectral content than the target spectra. Given the availability of ground motion records and the dataset size of ground motion records (i.e., 16–17 for each earthquake type), matching of the candidate response spectra with the target is judged as adequate. **Figure 3F** shows the response spectra of the unscaled mainshock ground motions that are selected based on the preceding method. It is noted that the mean spectral acceleration at 0.9 s of the 50 records is about 0.36 *g*, which corresponds to the return period of 1,300 years, while 8 of 50 records exceed the spectral acceleration at 0.9 s that corresponds to the return period of 2,500 years (i.e., 0.5 *g*).

Figure 4A shows the magnitude–distance distribution of the selected earthquake records; in the figure, record characteristics for mainshocks and major aftershocks (i.e., events having the second largest magnitude within individual sequences) are included. Finally, **Figures 4B,C** compare the $D_{5-95\%}$-AI plot and the $D_{5-95\%}$-CAV plot for different earthquake types (mainshocks only). **Figures 4B,C** indicate that the interface records are associated with longer duration and larger CAV values than the crustal and inslab records.

The selected ground motion records are used for seismic performance assessment of the tall building in Vancouver. The records reflect regional seismic hazard and dominant record characteristics. In particular, consideration of the 2011 Tohoku records is relevant to the seismic performance assessment in Vancouver because of the anticipated macro-level similarity between the 2011 Tohoku earthquake and possible Cascadia events. The relative contributions from the crustal, interface, and inslab events are equal (for the considered scenario), and thus, these records can also be used for evaluating the effects of ground motion records having different record characteristics (i.e., spectral content and duration) on non-linear seismic demand and earthquake damage potential. The records can be employed in cloud analysis to develop probabilistic seismic demand models. For this purpose, target spectral acceleration levels need to be defined.

Dynamic Analysis and Cloud Analysis

The structural analysis is carried for the 50 MS and 50 MS-AS earthquake records discussed in the previous section. The simulations are carried out using unscaled ground motions in bidirectional horizontal excitations of the 3D model (shown in **Figure 2A**). Various structural responses are stored for postprocessing, including time history data for interstory drift ratios and floor accelerations at all 16 stories, and Mehanny–Deierlein damage indices in the plastic hinge zone. The bidirectional interstory drift ratios were combined through geometric mean, and the corresponding drift values are used in the subsequent analysis. **Figure 5** illustrates calculated time histories of structural responses subjected to the three crustal/interface/inslab ground motion records, which are the same as those shown in **Figure 1B**. **Figure 5A** shows results for the interstory drift ratio at the ninth story, while **Figure 5B** shows results for the Mehanny–Deierlein damage index for gravity column at the third story. The results of the third-story column is selected because the damage index of this structural element is in the middle of all other structural elements of the gravity frame system and is thus suitable to show

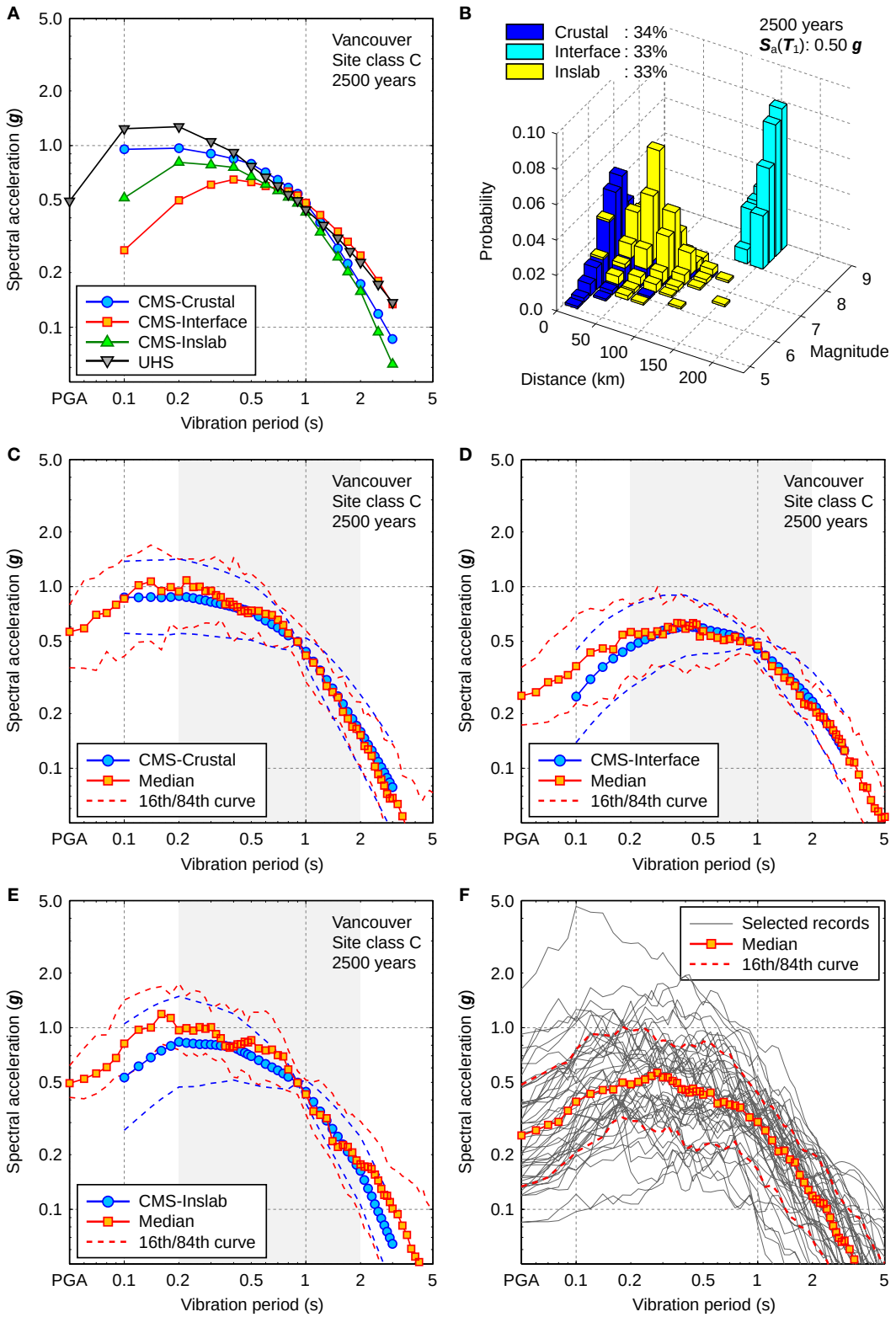

FIGURE 3 | (A) Uniform hazard spectrum and conditional mean spectra for crustal, interface, and inslab events in Vancouver (site class C; return period of 2,500 years). **(B)** Seismic disaggregation for spectral acceleration at 0.9 s in Vancouver (site class C; return period of 2,500 years). Comparison of response spectra of the selected (mainshock) ground motion records (50th/16th/84th curve) and conditional mean spectra (mean and mean ± 1 SD): **(C)** crustal earthquakes, **(D)** interface earthquakes, and **(E)** inslab earthquakes. **(F)** Geometric mean response spectra of the selected mainshock ground motions.

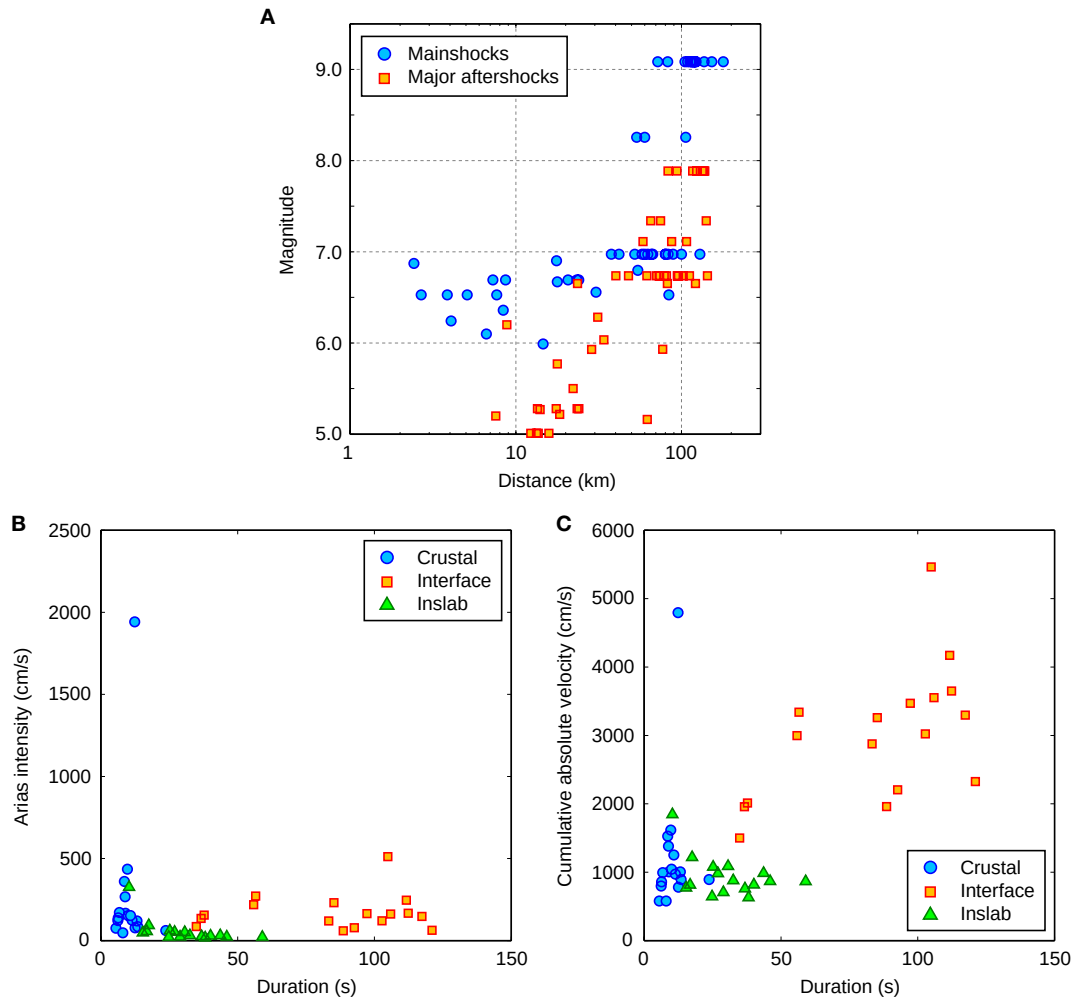

FIGURE 4 | (A) Magnitude–distance distribution of mainshocks and major aftershocks of the selected ground motion sequences. **(B)** Duration–Arias intensity distribution of the selected mainshock ground motion records. **(C)** Duration–cumulative absolute velocity distribution of the selected mainshock ground motion records.

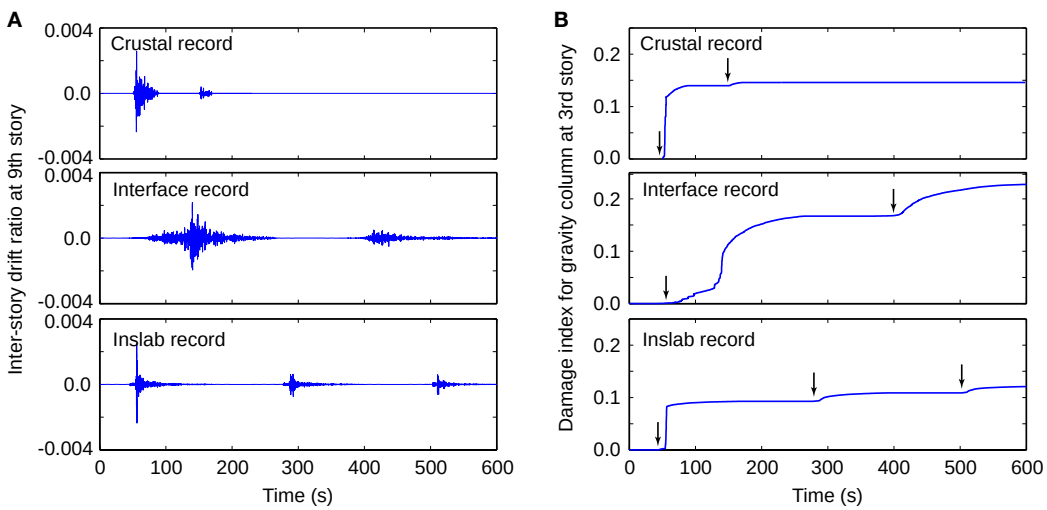

FIGURE 5 | Sample time histories of structural responses subjected to three ground motion records (crustal, interface, and inslab; same records shown in Figures 1B): (A) interstory drift ratio at the ninth story and (B) damage index for gravity column at the third story.

the average trends. It can be inspected from **Figure 5A** that under the three input records, the structure behaves elastically as the MaxISDR is only 0.3–0.4%, and there is no significant residual drift after the earthquake sequences. On the other hand, accumulation of cumulative seismic demands to the structure can be observed in **Figure 5B**; in particular, a major aftershock following the interface mainshock record (middle panel in **Figure 5B**) shows noticeable increase of the damage index. The maximum values of D_{MD} for the gravity column are still less than 0.3 for the three records; therefore, the structural damage to this element is considered to be negligible for these cases (see **Table 2**).

Figures 6A,B show storywise profiles of interstory drift ratios (left) and relationships between MaxISDR and spectral acceleration (right), $S_a(T_1)$-MaxISDR, for MS and MS-AS records, respectively. The results are obtained from the cloud analysis, and the responses due to different earthquake types are color coded in the figures. For both MS and MS-AS records, MaxISDR is less than 1% (minimal damage) and tends to take the largest values at the 8th to 10th stories. This is a result of higher mode effects on the response of the structure. The drift is minimal in the plastic hinge zone (the first four stories), as a combined effect of the shear walls and gravity columns. The $S_a(T_1)$-MaxISDR plots display that MaxISDR is well correlated with $S_a(T_1)$. In the figure panels, fitted prediction models, having a form of $\log_{10}\text{EDP} = a + b\log_{10}\text{IM}$, where a and b are the regression coefficients, are also included. As a quantitative measure of *efficiency* (Luco and Cornell, 2007),

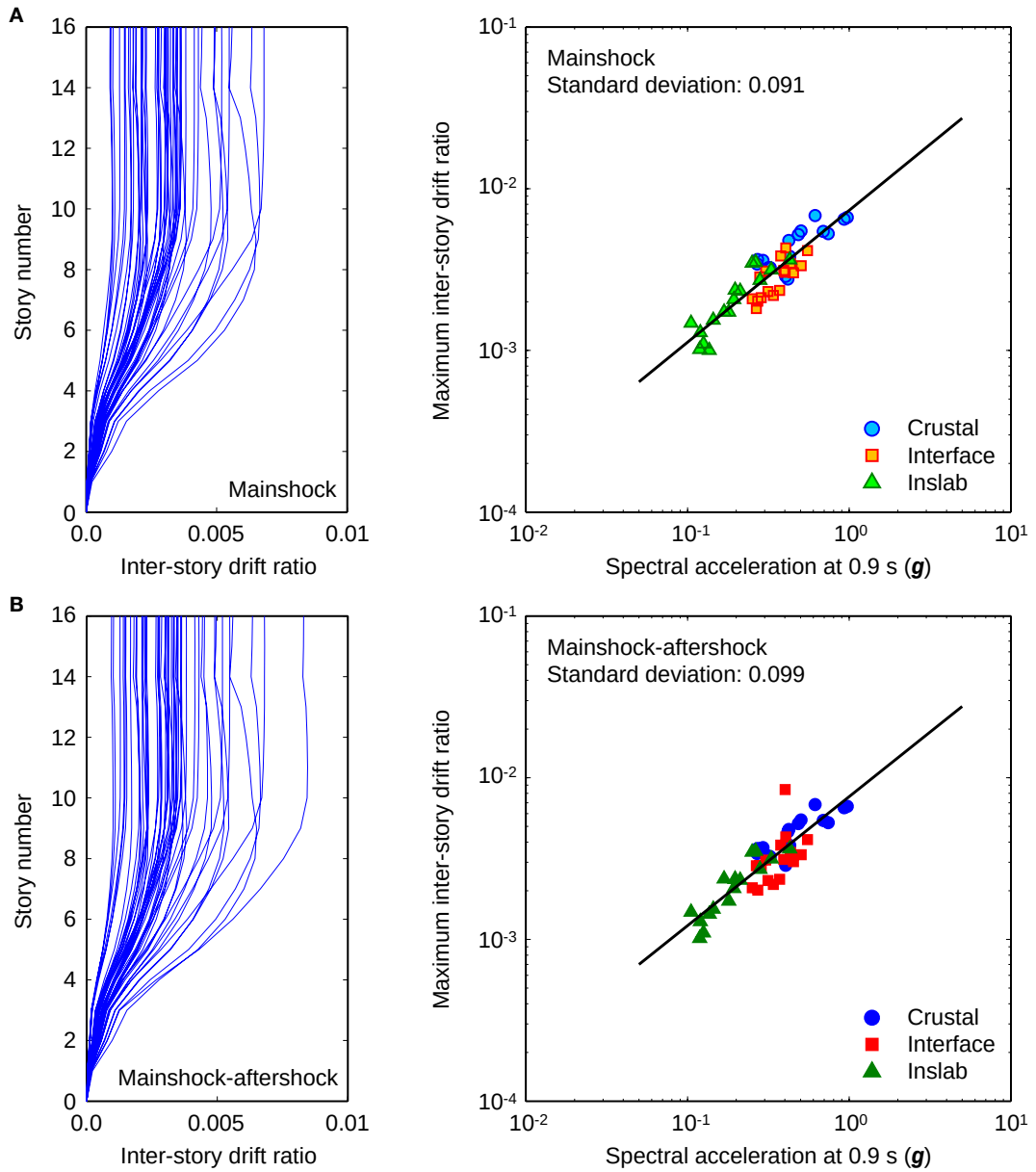

FIGURE 6 | Peak drift demands from cloud analysis displaying storywise profiles of interstory drift ratios and maximum interstory drift ratio and spectral acceleration relationships: (A) MS records and (B) mainshock–aftershock records.

SD of the regression residuals is indicated in the figure panels. It is noteworthy that although detailed results are not shown, similar regression analyses were performed for different IM variables, such as spectral accelerations at different vibration periods, AI, CAV, and $D_{5-95\%}$. It was found that for MaxISDR, $S_a(T_1)$ is the most efficient; this conclusion may be due to the elastic responses of the shear wall core under the ground motion records considered.

Overall, the results shown in **Figure 6** indicate the effects of aftershocks are not significant in terms of interstory drift. It is noteworthy that the average increase due to major aftershocks is about 8%. However, this increase is mainly caused by only 6 sequences of 50; the majority of the aftershocks do not increase the overall interstory drift. This observation is in agreement with Goda and Taylor (2012) and Goda et al. (2015). Under the considered ground motions, the shear wall core structure remains to be mainly in the linear elastic range, and this indeed reiterates that the shear walls RC cores are not vulnerable (e.g., Yang et al., 2012). For this reason, the subsequent investigations focus upon the seismic damage evaluation of the plastic zone, gravity columns (first to third stories), header beams (second to fourth stories), and shear walls (first to fourth stories) based on the energy-based damage index; see **Figure 2**. This focus is justified because the members in the plastic zone area are susceptible to severe damage due to cyclic loading (Koduru and Haukaas, 2010).

Efficient IM for Energy-Based Damage Index

Effectiveness of each IM on the estimation of EDPs is assessed using the concept of *efficiency*. An efficient IM results in relatively small variability of EDP given IM (Luco and Cornell, 2007). This property can be quantified by the SD of the regression residuals of predicted EDP values for a given IM. In this section, the Mehanny–Deierlein damage indices D_{MD} for the structural elements in the plastic zone are considered as EDP. More specifically, in total, 10 damage indices are focused upon; 3 are for the gravity columns (first/second/third story denoted as D_{MD}-C_1, D_{MD}-C_2, and D_{MD}-C_3, respectively), 3 are for the header beams (second/third/fourth story denoted as D_{MD}-HB_2, D_{MD}-HB_3, and D_{MD}-HB_4, respectively), and 4 are for the shear walls (first/second/third/fourth story denoted as D_{MD}-SW_1, D_{MD}-SW_2, D_{MD}-SW_3, and D_{MD}-SW_4, respectively). On the other hand, four IMs are considered to identify the efficient IM parameters: $S_a(T_1)$, AI, CAV, and $D_{5-95\%}$.

To compute efficiency of each IM, the log-linear model, i.e., $\log_{10}\text{EDP} = a + b\log_{10}\text{IM}$, is fitted using a least squares method. **Table 4** summarizes the logarithmic SD of the regression residuals for all combinations of EDP and IM for both MS records and MS-AS records. To show the results graphically, scatter plots of the damage index (D_{MD}-C_3) versus four IMs for MS-AS records are presented in **Figures 7A–D**. The results shown in **Table 4** and **Figure 7** indicate that the SDs of the residuals are smallest for CAV, followed by AI, $S_a(T_1)$, and $D_{5-95\%}$. The results are consistent for all EDPs and for MS/MS-AS records. It can be concluded that CAV is the most efficient IM for D_{MD}. Moreover, the results shown in **Figures 7A–D** suggest that interface records tend to result in greater damage index values in comparison with crustal and inslab records. This is because interface records are long-duration ground motions (**Figure 4C**), and thus, their cumulative damage potential is higher than other short-duration ground motions. The consideration of D_{MD} as EDP facilitates the incorporation of cumulative damage modes into the seismic performance evaluation.

TABLE 4 | Efficiency measure (i.e., logarithmic SD of regression residuals) for different intensity measures and engineering demand parameters (EDPs).

EDP	Mainshock				Mainshock–aftershock			
	$S_a(T_1)$	Arias intensity (AI)	Cumulative absolute velocity (CAV)	$D_{5-95\%}$	$S_a(T_1)$	AI	CAV	$D_{5-95\%}$
D_{MD}-C_1	0.201	0.190	0.147	0.281	0.245	0.231	0.128	0.243
D_{MD}-C_2	0.184	0.185	0.156	0.271	0.235	0.229	0.145	0.245
D_{MD}-C_3	0.186	0.182	0.161	0.282	0.234	0.226	0.143	0.253
D_{MD}-HB_2	0.225	0.141	0.123	0.304	0.256	0.199	0.105	0.261
D_{MD}-HB_3	0.245	0.186	0.100	0.299	0.275	0.235	0.099	0.249
D_{MD}-HB_4	0.250	0.194	0.096	0.299	0.280	0.242	0.101	0.249
D_{MD}-SW_1	0.217	0.191	0.137	0.289	0.259	0.237	0.123	0.250
D_{MD}-SW_2	0.202	0.182	0.137	0.281	0.249	0.230	0.122	0.246
D_{MD}-SW_3	0.215	0.198	0.142	0.284	0.261	0.246	0.134	0.249
D_{MD}-SW_4	0.247	0.219	0.110	0.277	0.275	0.255	0.122	0.226

Figure 7E compares the scatter plots of CAV and D_{MD}-C_3 for MS and MS-AS records, respectively. The results clearly show that the effects of major aftershocks for D_{MD}-C_3 are significant, resulting in increased earthquake damage. Based on the two fitted curves, the average increase of D_{MD} can be quantified as 54%, which is in sharp contrast with the increase of MaxISDR shown in **Figure 6**. It is important to emphasize the differences of the aftershock effects on D_{MD}-C_3 and MaxISDR. For D_{MD}-C_3, the effects due to major aftershocks are noticeable for the majority of the cases, rather than a small fraction of the cases (which was applicable to MaxISDR). To demonstrate this clearly, a histogram of the ratios of D_{MD}-C_3 between MS-AS records and MS records is shown in **Figure 7F**. The results highlight the widespread influence of the major aftershocks on the damage index.

Combined Damage Index

The abovementioned results clearly indicate that the CAV is the efficient IM for all D_{MD}, and the effects of earthquake types (long-duration interface events versus other earthquake types) and aftershocks have major influence on the earthquake damage evaluation. To perform probabilistic seismic risk analysis of the system in the plastic zone of the tall building, a combined measure of earthquake damage needs to be defined. It is noteworthy that the damage index computed for each component of the system represents local damage.

By assigning relative importance or weight to each local damage index, a global damage index can be computed. Park et al. (1987) proposed a story damage index D_{story} as:

$$D_{story} = \frac{\sum D_i E_i}{\sum E_i}, \tag{4}$$

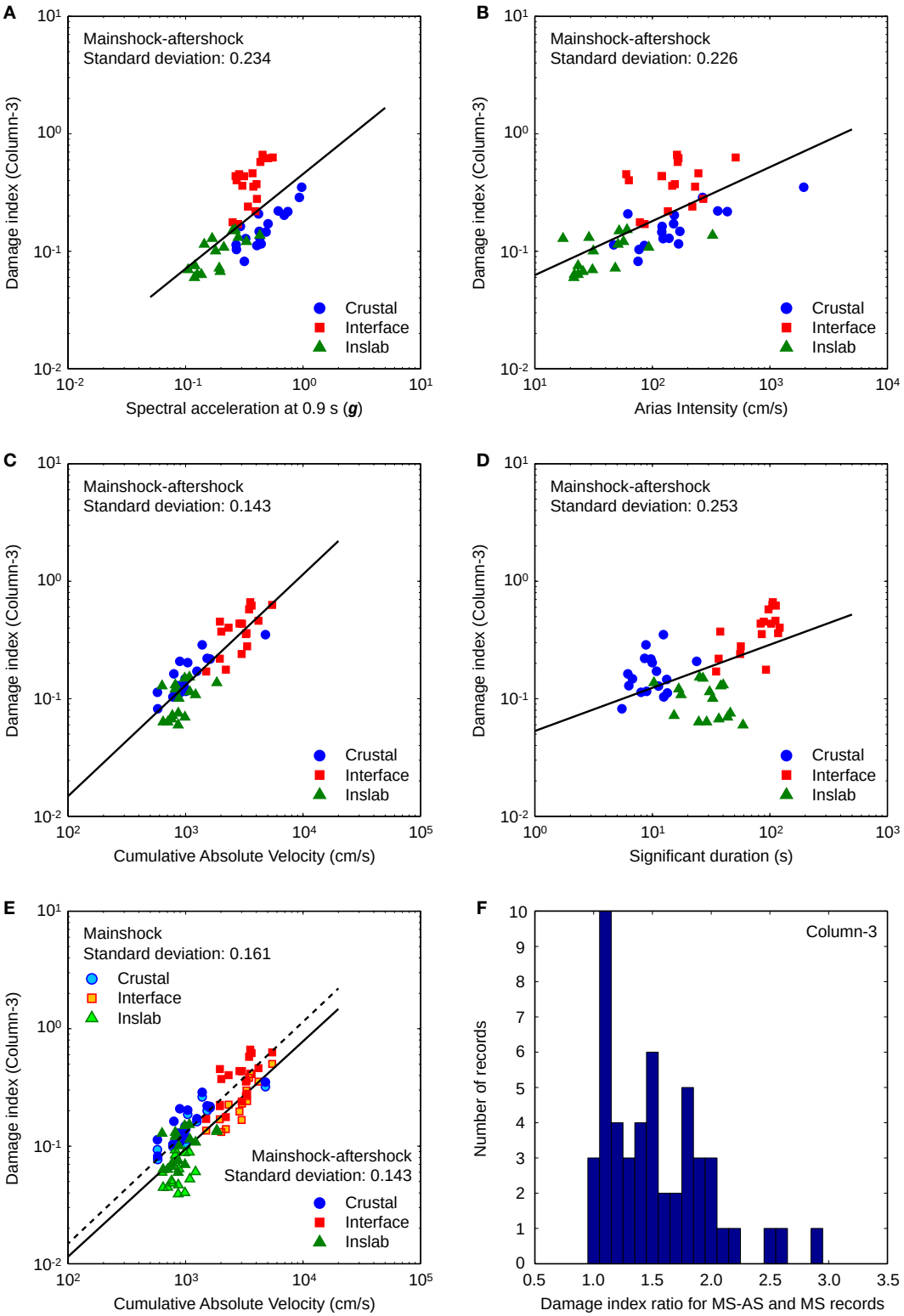

FIGURE 7 | Scatter plots of damage index (D_{MD}-C_3) versus four intensity measures by considering mainshock–aftershock (MS-AS) records: (A) spectral acceleration at 0.9 s, (B) Arias intensity, (C) cumulative absolute velocity, and (D) significant duration. (E) Scatter plot of damage index (D_{MD}-C_3) versus cumulative absolute velocity by considering MS records and MS-AS records. **(F)** Histogram of the damage index ratios (D_{MD}-C_3) between MS-AS records and MS records.

where D_i is the local damage index at location i and E_i is the corresponding energy absorbed at location i. The energy dissipated, however, is also incorporated in the damage computation. This index can potentially misrepresent the overall damage state (Williams and Sexsmith, 1995). A more general combination rule for computing a global damage index was proposed by Bracci et al. (1989). They proposed weighing each local damage index by importance weight w_i, and corresponding D_{story} is computed as follows:

$$D_{\text{story}} = \frac{\sum w_i D_i^{(c+1)}}{\sum w_i D_i^{c}}. \tag{5}$$

Parameter c is used to give higher importance to the most severely damaged elements. Bracci et al. (1989) suggested $c = 1$ and an equal weight to structural elements within the same story level. The global damage index is computed for each structural element, i.e., gravity columns, header beams, shear walls, within the plastic region. For simplicity, in this article, in assigning the weight, the number of structural elements at each floor is taken into consideration. For example, at the first and fourth stories, where only two types of structural members are considered, an equal weight of 0.5 can be assigned to each. On the other hand, for the second and third stories, three structural member types are present, and the weight can be assigned as 1/3. Furthermore, the damage index computed for each floor level is extended for the global damage index over the first four stories of the plastic regions, by assigning an equal weight (=0.25) to each floor.

Alternatively, more uniform weighting schemes may be considered. For instance, $c = 0$ in Eq. 5 corresponds to the arithmetic mean. Another popular choice for a uniform combination rule is the geometric mean of all contributing elements. In the following, these combination rules, in addition to Eq. 5 with $c = 1$, as proposed by Bracci et al. (1989), will be considered as a part of epistemic uncertainty associated with the structural damage assessment.

Figure 8A compares the 10 local damage indices of the gravity frame system for MS records with the combined damage index based on Eq. 5 with $c = 1$. It can be observed that the coupling beam at the second story shows the lowest damage index. The shear walls and gravity columns show higher damage indices, whereas the fourth story shear walls exhibit the highest damage potential. **Figure 8B** compares three combined damage indices in the plastic hinge zone for MS records, i.e., the Bracci et al. combination rule (Eq. 5 with $c = 1$), arithmetic mean, and geometric mean. The consideration of the Bracci et al. combination rule leads to higher values of the combined damage index because more weight is given to severe damage cases. The average ratios of the arithmetic mean and the geometric mean with respect to the Bracci et al. case are 0.67 and 0.52, respectively. This comparison illustrates the importance of the combination rule for defining the global damage index based on multiple local damage indices.

Based on the combined damage index for the gravity frame system (Bracci et al.'s combination rule with Eq. 5 and $c = 1$), prediction models of $D_{\text{MD},C}$ in terms of CAV are developed as:

$$\log_{10} D_{\text{MD},C} = -3.877 + 1.055 \log_{10} \text{CAV} \tag{6}$$

for MS records, and

$$\log_{10} D_{\text{MD},C} = -3.538 + 1.002 \log_{10} \text{CAV} \tag{7}$$

for MS-AS records. The SDs of the regression residuals $\beta_{\text{D'CAV}}$ for Eqs 6 and 7 are 0.121 and 0.121, respectively. This is considered as the base case in the subsequent analyses.

As mentioned above, the combination rule of different local damage indices into a global damage index is an influential source of uncertainty. To investigate the effects of this uncertainty on seismic risk assessment, more uniform combination rules, such as arithmetic mean and geometric mean, can also be considered. By redefining the combined damage index $D_{\text{MD},C}$ as arithmetic mean of the 10 local damage indices, seismic demand perdition models for $D_{\text{MD},C}$ can be obtained as:

$$\log_{10} D_{\text{MD},C} = -4.052 + 1.055 \log_{10} \text{CAV} \tag{8}$$

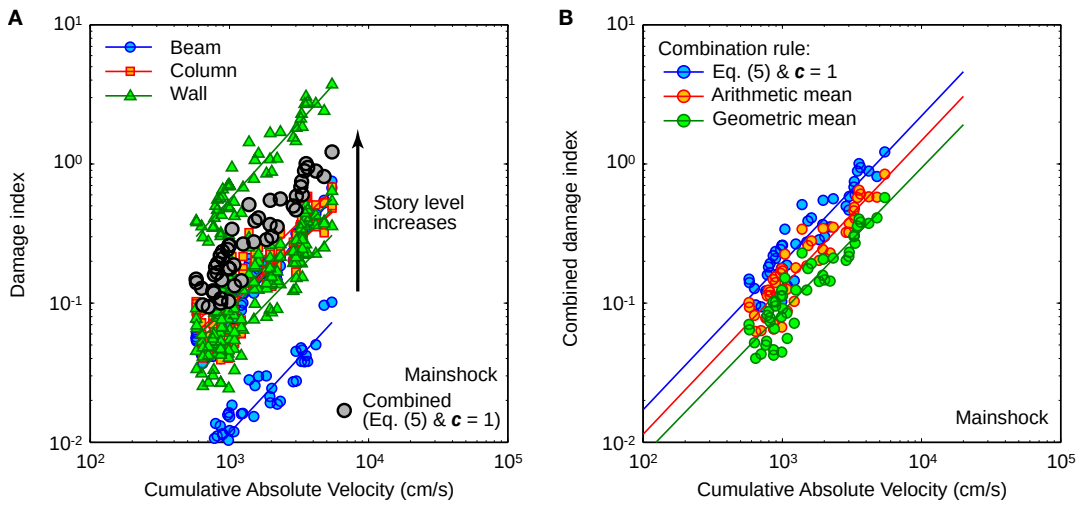

FIGURE 8 | (A) Comparison of local damage indices with the combined damage index in the plastic hinge zone for MS records. **(B)** Comparison of three combined damage indices in the plastic hinge zone for MS records.

for MS records, and

$$\log_{10} D_{MD,C} = -3.741 + 1.011 \log_{10} CAV \quad (9)$$

for MS-AS records. The SDs for Eqs 8 and 9 are 0.120 and 0.115, respectively. Moreover, by adopting the geometric mean combination rule, seismic demand prediction models for $D_{MD,C}$ can be obtained as:

$$\log_{10} D_{MD,C} = -4.159 + 1.032 \log_{10} CAV \quad (10)$$

for MS records, and

$$\log_{10} D_{MD,C} = -3.911 + 1.008 \log_{10} CAV \quad (11)$$

for MS-AS records. The SDs for Eqs 10 and 11 are 0.123 and 0.110, respectively.

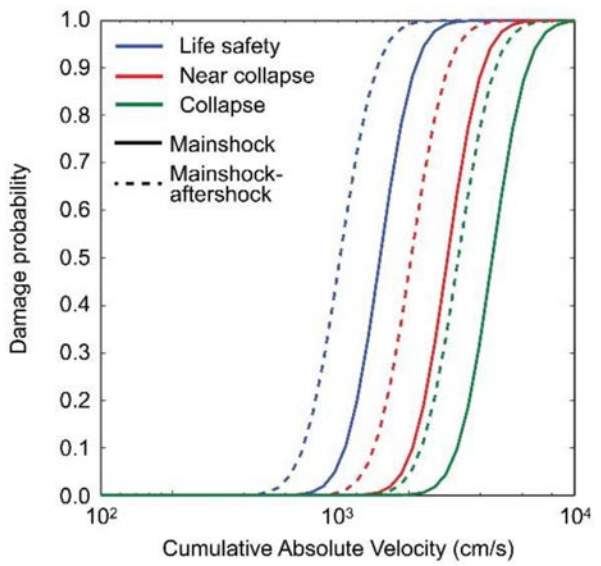

FIGURE 9 | CAV-$D_{MD,C}$ fragility models for MS and mainshock–aftershock records based on the damage index thresholds listed in Tables 2 and 3. $D_{MD,C}$ is calculated based on Eq. 5 with $c = 1$.

Fragility Curves for Energy-Based Damage Index

The developed CAV-$D_{MD,C}$ models (e.g., Eqs 6 and 7) can be used to derive fragility curves. The distribution of seismic demand about its median is often assumed to follow a two-parameter lognormal probability distribution. After estimating dispersion $\beta_{D'CAV}$ of the demand about its median, the fragility, i.e., probability that $D_{MD} > D_{MD,C}$ at a given CAV, can be computed as:

$$P(D_{MD} > C_{MD,C} | CAV = cav) = 1 - \Phi\left(\frac{\ln(\hat{C}_{MD,C}) - \ln(a \cdot cav^b)}{\beta_{D|CAV}}\right), \quad (12)$$

where $\hat{C}$ is the median structural capacity associated with the limit state. By taking the damage limit states shown in **Tables 2** and **3** and the combination rule for the global damage index based on Eq. 5 with $c = 1$ (i.e., Eqs 6 and 7), three fragility curves are developed for the LS threshold (i.e., $D_{MD,C} = 0.30$), near collapse (NC) threshold (i.e., $D_{MD,C} = 0.60$), and collapse (C) threshold (i.e., $D_{MD,C} = 0.95$). The fragility curves derived using Eq. 12 for MS records and MS-AS records are compared in **Figure 9**. The comparison of the fragility curves indicates that the effects of major aftershocks can be significant.

It is noteworthy that Eq. 12 accounts for statistical uncertainty associated with seismic demand predictions only. On the other hand, there are other important uncertain elements in assessing seismic fragility, such as aleatory uncertainty of capacity C and epistemic modeling uncertainty, denoted by β_C and β_M, respectively (Ellingwood et al., 2007). To include these effects in evaluating the seismic fragility, the SD $\beta_{D|CAV}$ in Eq. 12 can be replaced by:

$$\beta = \sqrt{\beta_{D|CAV}^2 + \beta_C^2 + \beta_M^2}. \quad (13)$$

β_M is assumed to be 0.20, by considering that the modeling process yields an estimate of building frame response that, with 90% confidence, is within ±30% of the actual value (Ellingwood et al.,

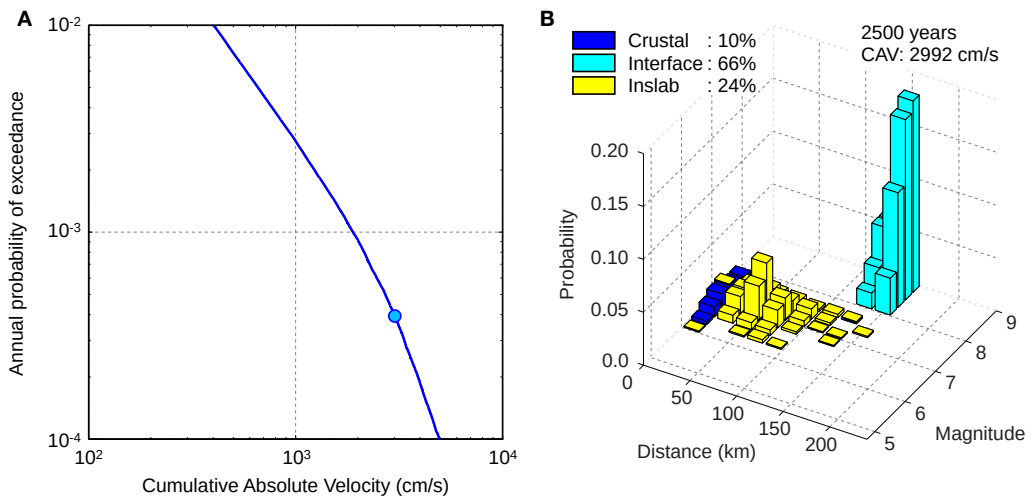

FIGURE 10 | Cumulative absolute velocity-based seismic hazard results: (A) seismic hazard curve and (B) seismic hazard disaggregation.

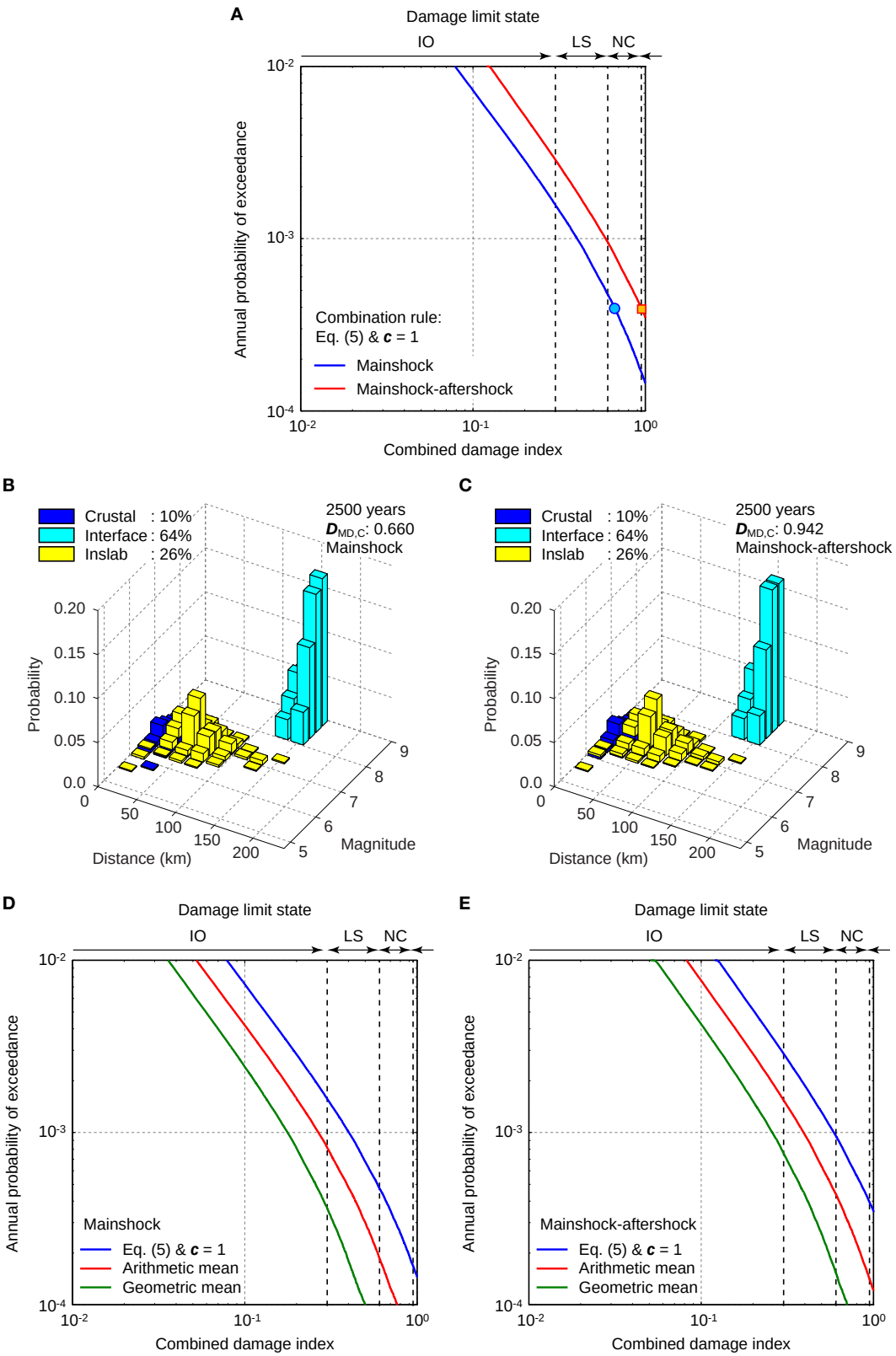

FIGURE 11 | Damage index-based seismic risk results: (A) seismic risk curves for MS and mainshock–aftershock (MS-AS) records, (B) seismic risk disaggregation for MS records, and (C) seismic risk disaggregation for MS-AS records. Comparison of seismic risk curves based on three different combination rules for defining the combined damage index: **(D)** MS records and **(E)** MS-AS records.

2007). β_C is assumed to be 0.25 for IO and LS, following Celik and Ellingwood (2009). For CP, however, β_C can be considered to be 0.17 for the four-story gravity frame and 0.13 for the shear walls. Note that the mentioned values of β_M and β_C are obtained from the literature and are applicable to structural models that were considered therein. Therefore, caution should be exercised before adopting these recommended values of logarithmic SDs.

Probabilistic Seismic Risk Analysis

It is important to assess the seismic performance of the gravity frame system of the tall RC building by taking into account uncertainties associated with regional seismic hazards, ground motions, and seismic vulnerability. The PBEE-based risk analysis methodology, as formulated in Eq. 1, is suitable for such assessments. In carrying out such risk assessments for the tall building in Vancouver, the regional seismic hazard model by Atkinson and Goda (2011) can be used as a starting point. Changes to the ground motion models are necessary because the adopted IM for the gravity frame system is CAV, instead of $S_a(T_1)$. In this study, two ground motion models for CAV are considered. A model by Campbell and Bozorgnia (2012) is applicable to crustal earthquakes because this model was developed by using strong motion data from worldwide crustal earthquakes compiled in the PEER-NGA database. For the interface and inslab earthquakes, a model by Foulser-Piggott and Goda (2015) can be used because it was developed based on the extensive strong motion database of Japanese earthquakes, including the 2011 Tohoku data. For the seismic vulnerability assessment, the CAV-$D_{MD,C}$ models for MS records and MS-AS records developed in the study (see Eqs 6 and 7) are adopted. The numerical evaluation of Eq. 1 is conducted using Monte Carlo simulations. More specifically, a synthetic earthquake catalog of regional seismicity having five million years is generated from the regional seismicity model of Atkinson and Goda (2011). For a given seismic event in the catalog, a value of CAV is simulated by taking into account earthquake types (i.e., crustal, interface, and inslab). Subsequently, a value of $D_{MD,C}$ is sampled from the developed prediction models (i.e., Eqs 6–11). This is repeated for all seismic events in the catalog. In the CAV-based seismic hazard analysis, the average shear-wave velocity in the uppermost 30 m is set to 555 m/s (i.e., site class C). Once all values of CAV and $D_{MD,C}$ are evaluated, annual maximum hazard and risk values can be extracted to develop a seismic hazard curve (i.e., exceedance probability curve) for CAV [i.e., λ(IM) in Eq. 1] as well as a seismic risk curve for $D_{MD,C}$ [i.e., ν(DM) in Eq. 1]. In addition to the hazard and risk curves, seismic disaggregation plots can be obtained through the postprocessing of the results.

Figure 10 depicts the CAV-based seismic hazard results (i.e., hazard curve and corresponding disaggregation) at the return period of 2,500 years. The seismic hazard curve shown in **Figure 10A** indicates that the CAV values at the return periods of 500 and 2,500 years correspond to 1,230 and 2990 cm/s, respectively. The disaggregation plot at the 2,500-year return period level highlights significant contribution from the interface events (i.e., events having magnitudes greater than 8.0). The increase is in sharp contrast with the counterpart for $S_a(T_1)$, shown in **Figure 3B**. This is because long-duration characteristics of the interface events result in greater values of CAV.

Figure 11 shows the $D_{MD,C}$-based seismic risk results. Two risk curves for MS records and MS-AS records are presented in **Figure 11A**, whereas the seismic risk disaggregation plots for MS records and MS-AS records at the 2,500-year return period are shown in **Figure 11B** and **Figure 11C**, respectively. The seismic demand prediction models used for obtaining the results shown in **Figures 11A–C** are Eqs 6 and 7. To relate the estimated damage potential to the limit states, four ranges of the damage limit states for D_{MD} (i.e., **Tables 2** and **3**) are indicated along the upper boundary of the figure panel. The results shown in **Figures 11A–C** indicate that the influence of major aftershocks on the damage potential is significant, increasing the damage index values by approximately 40% for a given probability level. When the mainshock effects only are considered, the return periods that correspond to incipient of LS and NC damage states (i.e., $D_{MD,C} = 0.3$ and 0.6, respectively) are 650 years and 2050 years. These return period levels are decreased to 350 years and 1,050 years (i.e., greater risks) when the aftershock effects are taken into account in addition to those due to the mainshocks. Comparison of the disaggregation plots for CAV and $D_{MD,C}$ suggests that they are very similar; these are because the differences of the earthquake types effectively capture the long-duration effects, as shown in **Figure 7C**.

Finally, the effects of the combination rule for defining the global damage index on seismic risk assessment are investigated. For this purpose, seismic risk assessments are carried out by considering three sets of seismic demand prediction models of $D_{MD,C}$, i.e., Eqs 6 and 7 versus Eqs 8 and 9 versus Eqs 10 and 11. The results are shown in **Figures 11D,E**. The base case (i.e., Eqs 6 and 7) leads to greater damage index values, in comparison with the two other cases (i.e., arithmetic mean and geometric mean) because more weights are given to severely damaged structural elements. The differences of the seismic risk curves for the three cases are significant, highlighting the importance of capturing this uncertainty in seismic risk assessments.

CONCLUSION

Seismic performance of an RC shear wall system designed with Canadian design codes has shown acceptable performance in terms of drift limits. Recent damaging earthquakes have highlighted that MS-AS earthquake records are important factors in the overall risk assessment. Furthermore, gravity columns, which are not seismically detailed and thus have exhibited severe damage, can potentially lead to localized collapse. However, drift-based limit states showed little sensitivity to MS-AS earthquake records and impact of earthquake types. In this article, an energy-based damage index is considered to capture the effects of long-duration earthquake ground motions. It is important to assess the seismic performance of the gravity frame system of the tall RC building by taking into account uncertainties associated with regional seismic hazards, ground motions, and seismic vulnerability. The PBEE-based risk analysis methodology is suitable for such assessments. Thus, in this article, seismic performance of the 15-story RC shear wall building located in Vancouver, BC, Canada, was investigated. For the seismicity of Vancouver, BC, Canada, scope of the study and conclusions are summarized below.

- Three earthquake types, i.e., shallow crustal earthquakes, deep inslab earthquakes, and megathrust Cascadia subduction earthquakes, were considered. The three earthquake types have different frequency content and duration, and their impact on the seismic performance were evaluated.
- Drift-based and energy-based damage indices were considered as EDPs. The MaxISDR for both MS and MS-AS earthquake records was less than 1%. This indeed is within the IO limit state and could give a false sense of security that the building is safe. For the plastic zone located at the base of the building, the energy-based damage index is computed. The Mehanny–Deierlein damage index D_{MD} is considered, which captures the responses from long-duration earthquakes. Earthquake types (long-duration interface events versus other earthquake types) and aftershocks have major influence on the earthquake damage evaluation in terms of D_{MD}. As expected, the energy-based damage index has indeed shown to perform well in capturing the long-duration earthquake types.
- For D_{MD}, four IMs, i.e., $S_{\mathrm{a}}(T_1)$, AI, CAV, and $\mathrm{D}_{5-95\%}$, were considered, and their *efficiency* was measured through residuals of the fitted prediction equations. From the calculated efficiency values, it was clearly shown that CAV is the most efficient IM for all D_{MD}. Thus, CAV is used in the subsequent risk analysis.
- Seismic demand prediction models as well as fragility curves were developed based on the combined damage index. Both prediction models and fragility curves clearly showed the impact of major aftershocks on the vulnerability of the building.
- Convoluting the prediction model for the energy-based damage index with the seismic hazard of Vancouver, seismic risk was computed. The influence of major aftershocks on the damage potential was significant, increasing the damage index values by approximately 40% for a given probability level.
- The combination rule for defining a global damage index based on local damage indicators has major influence on seismic risk assessments. This kind of epistemic uncertainty should be taken into account.

AUTHOR CONTRIBUTIONS

Both authors have contributed in this paper. ST performed the modeling, analysis, and computed the energy-based damage index. KG contributed in the ground motion selection, efficiency measure computation, and risk analysis.

ACKNOWLEDGMENTS

Ground motion data for Japanese earthquakes and worldwide crustal earthquakes were obtained from the K-NET/KiK-net/SK-net databases at http://www.kyoshin.bosai.go.jp/ and http://www.sknet.eri.u-tokyo.ac.jp/, and the PEER-NGA database at http://peer.berkeley.edu/nga/index.html, respectively. This work was supported by the Natural Science Engineering Research Council Canada (RGPIN-2014-05013) to the first author and the Engineering and Physical Sciences Research Council (EP/M001067/1) to the second author. Part of this research was undertaken when the first author was a Benjamin Meaker visiting professor at the University of Bristol and the financial support is acknowledged.

REFERENCES

Adebar, P., Bazargani, P., Mutrie, J., and Mitchell, D. (2010). Safety of gravity-load columns in shear wall buildings designed to Canadian standard CSA A23.3. *Can. J. Civil Eng.* 37, 1451–1461. doi:10.1139/L10-075

Arias, A. (1970). "A measure of earthquake intensity," in *Seismic Design for Nuclear Power Plants*, ed. R. J. Hansen (Cambridge, MA: MIT Press), 438–483.

Atkinson, G. M., and Goda, K. (2011). Effects of seismicity models and new ground motion prediction equations on seismic hazard assessment for four Canadian cities. *Bull. Seismol. Soc. Am.* 101, 176–189. doi:10.1785/0120100093

Boivin, Y., and Paultre, P. (2010). Seismic performance of a 12-storey ductile concrete shear wall system designed according to the 2005 National building code of Canada and the 2004 Canadian Standard Association standard A23.3. *Can. J. Civil Eng.* 37, 1–16. doi:10.1139/L09-115

Boivin, Y., and Paultre, P. (2012). Seismic force demand on ductile reinforced concrete shear walls subjected to western North American ground motions: part 1—parametric study. *Can. J. Civil Eng.* 39, 723–737. doi:10.1139/l2012-044

Bracci, J. M., Reinhorn, A. M., Mander, J. B., and Kunnath, S. K. (1989). *Deterministic Model for Seismic Damage Evaluation of RC Structures*. Technical Report NCEER-89-0033. Buffalo, NY: National Center for Earthquake Engineering Research, State University of New York.

Campbell, K. W., and Bozorgnia, Y. (2012). A comparison of ground motion prediction equations for Arias intensity and cumulative absolute velocity developed using a consistent database and functional form. *Earthq. Spectra* 28, 931–941. doi:10.1193/1.4000067

Celik, O. C., and Ellingwood, B. R. (2009). Seismic risk assessment of gravity load designed reinforced concrete frames subjected to Mid-America ground motions. *J. Struct. Eng.* 135, 414–424. doi:10.1061/(ASCE)0733-9445(2009)135:4(414)

Cornell, C. A., and Krawinkler, H. (2000). "Progress and challenges in seismic performance assessment," in *PEER Center News 3*. Available at: http://peer.berkeley.edu/news/2000spring/performance.html

DiPasquale, E., and Cakmak, A. S. (1989). *On the Relation between Local and Global Damage Indexes*. Report No. NCEER-89-0034. Buffalo: National Center for Earthquake Engineering Research, State University of New York at Buffalo.

Electrical Power Research Institute (EPRI). (1988). *A Criterion for Determining Exceedance of the Operating Basis Earthquake*. Report No. EPRI NP-5930. Palo Alto, CA.

Ellingwood, B. R., Celik, O. C., and Kinali, K. (2007). Fragility assessment of building structural systems in Mid America. *Earthq. Eng. Struct. Dyn.* 36, 1935–1952. doi:10.1002/eqe.693

Foulser-Piggott, R., and Goda, K. (2015). Ground-Motion Prediction Models for Arias Intensity and cumulative absolute velocity for Japanese earthquakes considering single-station sigma and within-event spatial correlation. *Bull. Seismol. Soc. Am.* 105, 1903–1918. doi:10.1785/0120140316

Goda, K., and Taylor, C. A. (2012). Effects of aftershocks on peak ductility demand due to strong ground motion records from shallow crustal earthquakes. *Earthq. Eng. Struct. Dyn.* 41, 2311–2330. doi:10.1002/eqe.2188

Goda, K., Wenzel, F., and De Risi, R. (2015). Empirical assessment of nonlinear seismic demand of mainshock-aftershock ground motion sequences for Japanese earthquakes. *Front. Built Environ.* 1:6. doi:10.3389/fbuil.2015.00006

Gosain, N. K., Brown, R. H., and Jirsa, J. O. (1977). Shear requirements for load reversals on RC members. *J. Struct. Eng.* 103, 1461–1476.

Goulet, C. A., Haselton, C. B., Mitrani-Reiser, J., Beck, J. L., Deierlein, G. G., Porter, K. A., et al. (2007). Evaluation of the seismic performance of a code-conforming reinforced-concrete frame building – from seismic hazard to collapse safety and economic losses. *Earthq. Eng. Struct. Dyn.* 36, 1973–1997. doi:10.1002/eqe.694

Hyndman, R. D., and Rogers, G. C. (2010). Great earthquakes on Canada's west coast: a review. *Can. J. Earth Sci.* 47, 801–820. doi:10.1139/E10-011

Jalayer, F., Franchin, P., and Pinto, P. E. (2007). A scalar decision variable for seismic reliability analysis of RC frames. *Earthq. Eng. Struct. Dyn.* 36, 2050–2079. doi:10.1002/eqe.704

Jayaram, N., Lin, T., and Baker, J. W. (2011). A computationally efficient ground-motion selection algorithm for matching a target response spectrum mean and variance. *Earthq. Spectra* 27, 797–815. doi:10.1193/1.3608002

Koduru, S. D., and Haukaas, T. (2010). Probabilistic seismic loss assessment of a Vancouver high-rise building. *J. Struct. Eng.* 136, 235–245. doi:10.1061/(ASCE)ST.1943-541X.0000099

Koduru, S. M. (2008). *Performance-Based Earthquake Engineering with the First-Order Reliability Method*. Ph.D. thesis, The University of British Columbia, Vancouver.

Kraetzig, W., Meyer, I., and Meskouris, K. (1989). "Damage evolution in reinforced concrete members under cyclic loading," in *Proc. of* 5th International Conference on Structural Safety and Reliability (ICOSSAR 89) (San Francisco, CA), 795–802.

Luco, N., and Cornell, C. A. (2007). Structure-specific scalar intensity measures for near-source and ordinary earthquake ground motions. *Earthq. Spectra* 23, 357–392. doi:10.1193/1.2723158

Luu, H., Léger, P., and Tremblay, R. (2014). Seismic demand of moderately ductile reinforced concrete shear walls subjected to high-frequency ground motions. *Can. J. Civil Eng.* 41, 125–135. doi:10.1139/cjce-2013-0073

McKenna, F., Fenves, G. L., and Scott, M. H. (2000). *Open System for Earthquake Engineering Simulation*. Berkeley, CA: University of California. Available at: http://opensees.berkeley.edu

Mehanny, S. S., and Deierlein, G. G. (2000). *Modeling of Assessment of Seismic Performance of Composite Frames with Reinforced Concrete Columns and Steel Beams*. California: The John A. Blume Earthquake Engineering Center, Stanford University. Report No 135.

Naeim, F., Lew, M., Carpenter, L. D., Youssef, N. F., Rojas, F., Saragoni, G. R., et al. (2011). Performance of tall buildings in Santiago, Chile during the 27 February 2010 offshore Maule, Chile earthquake. *Struct. Des. Tall Spec. Build.* 20, 1–16. doi:10.1002/tal.675

Park, Y. J., and Ang, A. H.-S. (1985). Mechanistic seismic damage model for reinforced concrete. *J. Struct. Eng.* 111, 722–739. doi:10.1061/(ASCE)0733-9445(1985)111:4(722)

Park, Y. J., Ang, A. H.-S., and Wen, Y. K. (1987). Damage-limiting aseismic design of buildings. *Earthq. Spectra* 3, 1–26. doi:10.1193/1.1585416

Reinhorn, A. M., and Valles, R. E. (1995). *Damage Evaluation in Inelastic Response of Structures: A Deterministic Approach*. Report No. NCEER-95. Buffalo: National Center for Earthquake Engineering Research, State University of New York at Buffalo.

SEAOC. (1995). *Vision 2000: Performance-Based Seismic Engineering of Buildings*. Sacramento, CA: Structural Engineers Association of California.

Stirrat, A. T., Gebreyohaness, A. S., Jury, R. D., and Kam, W. Y. (2014). "Seismic performance assessment of non-ductile columns," in *2014 NZSEE Conf.: New Zealand Society of Earthquake Engineering NZSEE* (Auckland, New Zealand).

Takewaki, I., Murakami, S., Fujita, K., Yoshitomi, S., and Tsuji, M. (2011). The 2011 off the Pacific coast of Tohoku earthquake and response of high-rise buildings under long-period ground motions. *Soil Dyn. Earthq. Eng.* 31, 1511–1528. doi:10.1016/j.soildyn.2011.06.001

Tesfamariam, S., and Goda, K. (2015). Seismic performance evaluation framework considering maximum and residual inter-story drift ratios: application to non-code conforming reinforced concrete buildings in Victoria, BC, Canada. *Front. Built Environ.* 1:18. doi:10.3389/fbuil.2015.00018

Tesfamariam, S., Goda, K., and Mondal, G. (2015). Seismic vulnerability of RC frame with unreinforced masonry infill due to mainshock-aftershock earthquake sequences. *Earthq. Spectra* 31, 1427–1449. doi:10.1193/042313EQS111M

Tesfamariam, S., and Saatcioglu, M. (2008). Risk-based seismic evaluation of reinforced concrete buildings. *Earthq. Spectra* 24, 795–821. doi:10.1193/1.2952767

Tremblay, R., Léger, P., and Tu, J. (2001). Inelastic seismic response of concrete shear walls considering P-delta effects. *Can. J. Civil Eng.* 28, 640–655. doi:10.1139/cjce-28-4-640

Trifunac, M. B., and Brady, A. G. (1975). A study on the duration of strong earthquake ground motion. *Bull. Seismol. Soc. Am.* 65, 581–626.

Vamvatsikos, D., and Cornell, C. A. (2002). Incremental dynamic analysis. *Earthq. Eng. Struct. Dyn.* 31, 491–514. doi:10.1002/eqe.141

Ventura, C. E., Brincker, R., Dascotte, E., and Andersen, P. (2001). "FEM updating of the heritage court building structure," in *Proc. of Conference on Structural Dynamics* (IMAC-XIX) (Orlando, FA), 324–330.

Williams, M. S., and Sexsmith, R. G. (1995). Seismic damage indices for concrete structures: a state-of-the-art review. *Earthq. Spectra* 11, 319–349. doi:10.1193/1.1585817

Yang, T. Y., Moehle, J. P., Bozorgnia, Y., Zareian, F., and Wallace, J. W. (2012). Performance assessment of tall concrete core-wall building designed using two alternative approaches. *Earthq. Eng. Struct. Dyn.* 41, 1515–1531. doi:10.1002/eqe.2219

Conflict of Interest Statement: The authors declare that the research was conducted in the absence of any commercial or financial relationships that could be construed as a potential conflict of interest.

Copyright © 2017 Tesfamariam and Goda. This is an open-access article distributed under the terms of the Creative Commons Attribution License (CC BY). The use, distribution or reproduction in other forums is permitted, provided the original author(s) or licensor are credited and that the original publication in this journal is cited, in accordance with accepted academic practice. No use, distribution or reproduction is permitted which does not comply with these terms.

frontiers in Built Environment

ORIGINAL RESEARCH
published: 24 October 2017
doi: 10.3389/fbuil.2017.00061

Estimation of Seismic Loss for a Portfolio of Buildings under Bidirectional Horizontal Ground Motions due to a Scenario Cascadia Event

Taojun Liu[1,2]* *and Hanping Hong*[3]

[1]Department of Civil, Environmental and Architectural Engineering, University of Colorado Boulder, Boulder, CO, United States, [2]United States Geological Survey, Golden, CO, United States, [3]Department of Civil and Environmental Engineering, University of Western Ontario, London, ON, Canada

Earthquake ground motions induced by a scenario event are spatially (partially) correlated and (partially) coherent. Simulated ground motion records can be used to carry out nonlinear inelastic time history analysis for a portfolio of buildings to estimate the seismic loss, which is advantageous as there is no need to develop and apply empirical ground motion prediction equations and the ductility demand rules, or to search the scenario-compatible recorded records at selected sites that may not exist. Further, if the structures being considered are sensitive to the orientation of the excitation, multiple-component ground motion records are needed. For the simulation of such ground motion records, previous studies have shown that correlation and coherency between any pair of ground motion components need to be incorporated. In this study, the seismic loss of a portfolio of hypothetical buildings in downtown Vancouver under bidirectional horizontal ground motions due to a scenario Cascadia event is estimated by using simulated bidirectional ground motion records that include realistic correlation and coherency characteristics. The hysteretic behaviors of the buildings are described by bidirectional Bouc–Wen model. The results show that the use of unidirectional ground motions and single-degree-of-freedom system structural model may underestimate the aggregated seismic loss.

Keywords: seismic risk, ground motion simulation, bidirectional excitation, 2-degree-of-freedom hysteretic model, Cascadia earthquake

OPEN ACCESS

Edited by:
Katsuichiro Goda,
University of Bristol, United Kingdom

Reviewed by:
Shinichi Matsushima,
Kyoto University, Japan
Alkis Daskaloudis,
Mott MacDonald, United Kingdom

***Correspondence:**
Taojun Liu
liutaojun@hotmail.com

Specialty section:
This article was submitted to Earthquake Engineering, a section of the journal Frontiers in Built Environment

Received: *07 June 2017*
Accepted: *02 October 2017*
Published: *24 October 2017*

Citation:
Liu T and Hong H (2017) Estimation of Seismic Loss for a Portfolio of Buildings under Bidirectional Horizontal Ground Motions due to a Scenario Cascadia Event. Front. Built Environ. 3:61. doi: 10.3389/fbuil.2017.00061

INTRODUCTION

Seismic loss estimation for a portfolio of buildings under scenario events generally requires three sets of information. The first one is the scenario event and its associated multiple component ground motions at the spatially distributed sites of the buildings. The second set is associated with non-linear inelastic dynamic characteristics of the buildings and their responses or degree of damage under seismic excitations. The third set contains the damage loss functions for different structure types and degree of damage. For simplicity, seismic loss estimation for a portfolio of buildings is often carried out by using the ground motion measures such as the peak ground acceleration (PGA) and spectral acceleration (SA) for random orientation. The structural responses and damage are then represented using predetermined fragility curves based on experience, expert opinion, or numerical analysis and experimental investigation [HAZUS-Earthquake,

Federal Emergency Management Agency (FEMA) and the National Institute of Building Sciences (NIBS), 2003; Whitman et al., 1997]. The seismic risk of a portfolio of buildings is then estimated by incorporating the (uncertainty in the) ground motion measures of the scenario event, the fragility curves, and the damage cost functions. Therefore, significant computing task in this approach, in terms of structural responses, is to establish the fragility curves for generic structures of different structural types. Instead of using fragility curves, Goda and Hong (2008a,b) considered that each building can be approximated as a non-linear inelastic single-degree-of-freedom (SDOF) system, and the spatially distributed buildings are subjected to spatially correlated ground motion measures. To assess the degree of damage, use of the ductility demand rules for bilinear systems developed based on selected ground motions (Hong and Hong, 2007) were considered. It was shown that the consideration of realistic spatial correlation is crucial in assessing the tail of the probability distribution of seismic loss of a portfolio of buildings. The approach avoids the need for predetermining the fragility curve of the degree of damage conditioned on the ground motion measure such as SA, and approximately takes into account dynamic and inelastic characteristics of each of the buildings. However, the ductility demand rules could be affected by records from different earthquake types (Hong et al., 2010).

To avoid the need to develop empirical ductility demand rules for structures having different hysterical behavior and different ground motion characteristics, Liu and Hong (2015a) considered that the structural responses and damage levels can be estimated directly through the time history analysis under spatially correlated and coherent ground motion excitations. Their study, again, showed the importance of considering realistic spatial correlation in assessing the tail of the probability distribution of seismic loss of a portfolio of buildings. The approach of using time history analysis is also advantageous as there is no need to develop and apply empirical ground motion prediction equations. Furthermore, the use of the simulated ground motion records avoids the search for the scenario compatible actual records at the considered building sites that are unlikely to be available in the existing database of ground motion records.

For the simulation of the ground motion records, both the spatial correlation (Goda and Hong, 2008a; Jayaram and Baker, 2009; Liu et al., 2012) and spatial coherency (Abrahamson et al., 1991; Zerva, 2009) need to be taken into account. The coherency between two ground motion record components can be estimated from the power spectral density functions of the records; it represents the correlation between the random phase variations. The spatial correlation is used to measure the correlation of ground motion measures such as the PGA or SA at two sites. Furthermore, seismic events cause multidirectional ground motions. Methodology for the simulation of ground motion records that considers both spatial correlation and coherency for multidirectional excitations at multiple sites was presented in Hong and Liu (2014), Liu and Hong (2015a,b) based on stochastic simulations (e.g., point source model and finite-fault model) (Motazedian and Atkinson, 2005; Atkinson et al., 2009). These methods apply partially (and directional-dependent) coherent white noises generated using spectral representation method as the input for stochastic simulation techniques and incorporates spatially correlated Fourier amplitude spectra (FAS).

It must be emphasized that although multidirectional synthetic ground motion record components at multiple sites can be simulated, the estimation of seismic loss by considering multidirectional excitations for a portfolio of buildings for a scenario event has not been investigated. This can be important as the seismic response of buildings could be sensitive to multidirectional excitations (Clough and Penzien, 2003; Zerva, 2009), and a building could be modeled approximately by using a non-linear inelastic 2-degree-of-freedom (2DOF) system in lieu of a SDOF system, where each degree of freedom is associated with one of the two orthogonal horizontal directions. The hysteretic behavior of the 2DOF system could be modeled by the Bouc–Wen model (Wen, 1976; Lee and Hong, 2010), which can be used to reproduce sophisticated inelastic behavior of structural components/systems under cyclic loadings.

The main objectives of this study are to provide an overall framework to estimate seismic loss of a group of buildings under multidirectional excitations, and to investigate the effect of bidirectional ground motions on the aggregate seismic loss of buildings for a scenario event. The tasks include (a) simulating ground motion record components in two horizontal orthogonal directions at multiple sites for a scenario event such as that from the Cascadia subduction zone considering spatial (and directional) correlation and coherency models derived from historical records; (b) applying the simulated records in estimating seismic responses, and aggregate losses of a portfolio of buildings for the scenario event. In the following, first, the framework to estimate the aggregate seismic loss for a portfolio of buildings under multidirectional ground motions is described. The overall framework is then illustrated by a numerical example focused on the estimation of the seismic loss of a portfolio of buildings located in downtown Vancouver under a scenario Cascadia event, though we expect the conclusions of this study are independent of the study area.

FRAMEWORK FOR ESTIMATING SEISMIC LOSS OF A PORTFOLIO OF BUILDINGS CONSIDERING BIDIRECTIONAL HORIZONTAL GROUND MOTIONS

In this section, the proposed framework to estimate the aggregate seismic loss of a group of buildings is presented. The procedure consists of three major components: the simulation of ground motion records (or field); the approximation of structural modeling and nonlinear inelastic analysis, and the estimation and characterization of aggregate seismic loss using the damage cost functions. For the simulation of ground motion records, approach and empirical correlation and coherency models among ground motion components given in the literature (Hong and Liu, 2014; Liu and Hong, 2015b) are considered, except that the reference FAS and time modulation function of the records are defined using the stochastic finite-fault method (Atkinson et al., 2009). For efficiency, the bidirectional Bouc–Wen model is used to calculate the non-linear inelastic response of the 2DOF system and the

damage factor; the aggregated seismic loss for the portfolio of buildings is estimated by adopting cost functions in the literature.

Simulation of Bidirectional Ground Motion Records at Multiple Sites

For the simulation of ground motion record components in two horizontal orthogonal directions at multiple sites, it is considered that the reference FAS and the time modulating functions for a random horizontal component can be defined based on the finite-fault model (Motazedian and Atkinson, 2005; Atkinson et al., 2009). As the two horizontal orthogonal ground motion components at a site are considered to be random with respect to the source-to-site orientation, both the reference FAS and the time modulating function for one direction that is perpendicular to the other orientation is considered to be the identical.

To obtain the reference FAS and time modulating function at the j-th site, simulation by using the finite-fault model is carried out n_G times for a considered scenario event with moment magnitude $\mathbf{M}$. For each simulated record component, the FAS is evaluated and the time window profile (i.e., time modulating function) is estimated using the Hilbert transform. The reference FAS denoted as $y_j(\mathbf{M}, R_j, f)$, and the time modulating function are then calculated by averaging over n_G simulations, where f is the frequency in Hz and R_j is the distance from the j-th site to finite-fault source (i.e., closest distance to the fault plane). Based on the obtained reference $y_j(\mathbf{M}, R_j, f)$, and the time modulating function, the simulation of the ground motion record components in two horizontal orthogonal directions are carried out as illustrated in **Figure 1** and outlined below (Hong and Liu, 2014):

(a) Generate two band-limited noises with 0 mean and unit variance at each considered site that are compatible with a specified target spatial coherency;
(b) Apply the corresponding time modulating function to the sampled noises at each site;
(c) Calculate and normalize the FAS of each time-modulated time series of the noises by its square-root of the mean squared amplitude spectrum;
(d) Multiply the normalized spectrum by its corresponding reference FAS and by the sampled spatial correlated scaling factor; and,
(e) Apply the inverse Fourier transform to the spectra obtained in step (d) to compute the acceleration ground motion time history.

The target coherency functions needed in Step (a) by considering the j-th and k-th sites is denoted by $\bar{\gamma}_{pq,jk}(\Delta, f)$, where j, $k = 1, \ldots, n_R$ represents the sites, p, $q = 1$ or 2 represents the first

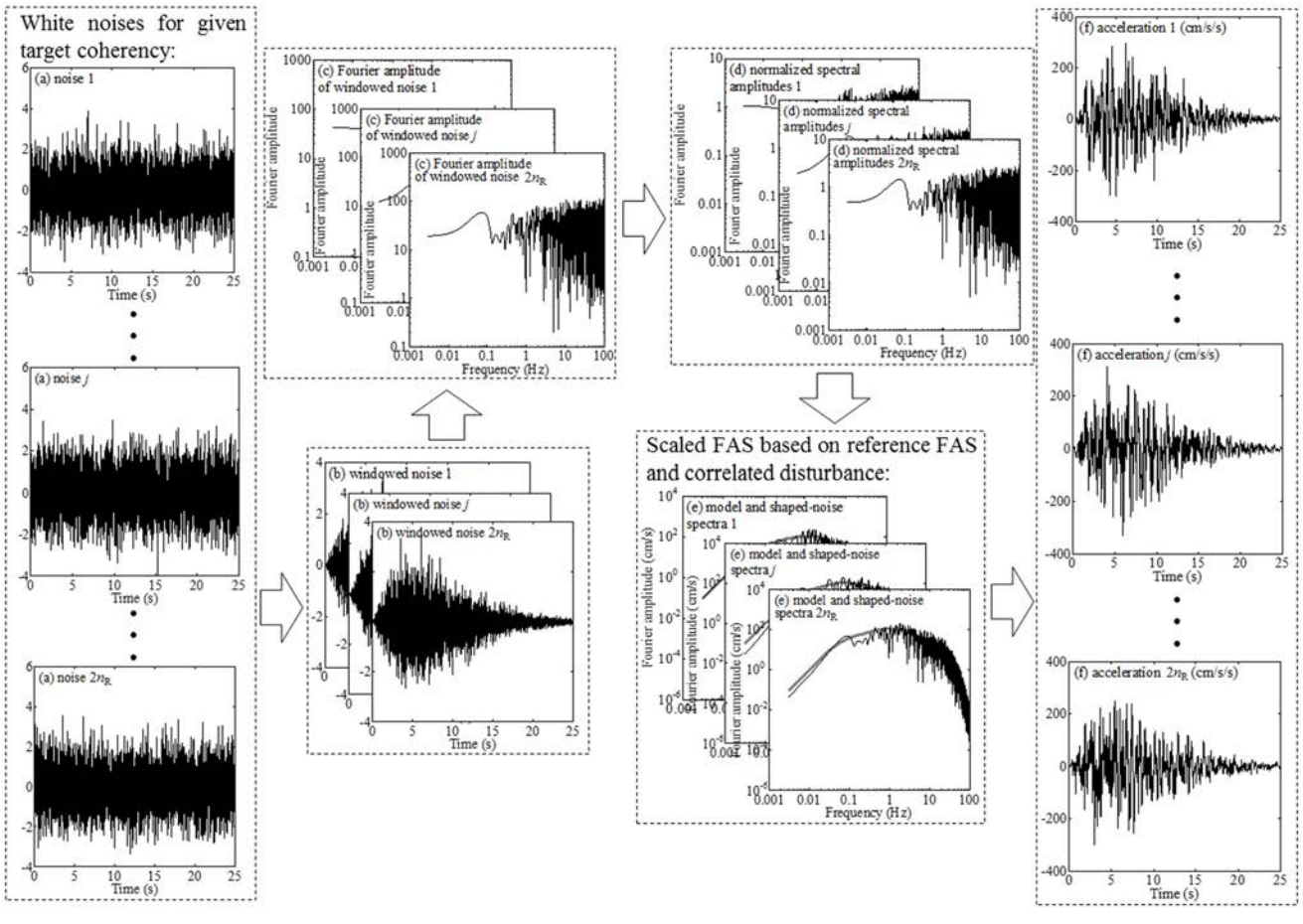

FIGURE 1 | Illustration of simulating spatially correlated and coherent record using the extended finite-fault model.

and second horizontal ground motion component (for a common coordinate system) and Δ (kilometers) is the distance between the j-th and k-th sites. By taking into account the symmetry and the fact that $\bar{\gamma}_{\mathrm{pp,jj}}(0,f) = 1$ by definition, there are six remaining coherency functions need to be considered: $\bar{\gamma}_{12,\mathrm{jj}}(0,f)$, $\bar{\gamma}_{11,\mathrm{jk}}(\Delta,f)$, $\bar{\gamma}_{12,\mathrm{jk}}(\Delta,f)$, $\bar{\gamma}_{21,\mathrm{jk}}(\Delta,f)$, $\bar{\gamma}_{22,\mathrm{jk}}(\Delta,f)$, and $\bar{\gamma}_{12,\mathrm{kk}}(0,f)$. The coherency function for two ground motion components along the same orientation (i.e., $\bar{\gamma}_{11,\mathrm{jk}}(\Delta,f)$ or $\bar{\gamma}_{22,\mathrm{jk}}(\Delta,f)$), can be expressed as (Harichandran and VanMarcke, 1986),

$$\bar{\gamma}_{\mathrm{pp,jk}}(\Delta,f) = \left|\bar{\gamma}_{\mathrm{pp,jk}}(\Delta,f)\right| \exp(-i2\pi f\Delta_P/v_{\mathrm{ap}}), \text{ for } j \neq k \quad (1)$$

where Δ_P is the projection of the separation distance Δ in the direction of wave propagation; v_{ap} (kilometer per second) represents the apparent velocity; $2\pi f\Delta_P/v_{\mathrm{ap}}$ represents phase angle of the wave passage effect (Der Kiureghian, 1996); the lagged coherency $\left|\bar{\gamma}_{\mathrm{pp,jk}}(\Delta,f)\right|$ is given by (Harichandran and VanMarcke, 1986),

$$\left|\bar{\gamma}_{\mathrm{pp,jk}}(\Delta,f)\right| = A\exp\left(-\frac{2000\Delta}{\alpha_0\theta(f)}(1-A+\alpha_0 A)\right) + (1-A)\exp\left(-\frac{2000\Delta}{\theta(f)}(1-A+\alpha_0 A)\right), \quad (2)$$

in which $\theta(f) = k\left(1+(f/f_0)^B\right)^{-1/2}$, and A, α_0, k, f_0, and B are model parameters.

According to Hong and Liu (2014) and Liu and Hong (2015b), the lagged coherency for two horizontal orthogonal components can be considered to be independent of Δ, and can be approximated by

$$\left|\bar{\gamma}_{\mathrm{pq,jk}}(\Delta,f)\right| = c_0 - c_1 f, \text{ for } p \neq q \quad (3)$$

where c_0 and c_1 are model parameters. A set of typical parameters for the model shown in Eqs 1–3 are listed in **Table 1**. Note that these parameters are developed based on data from Taiwan. However, previous studies did not show dependency on geographical locations (Harichandran and VanMarcke, 1986; Hong and Liu, 2014; Liu and Hong, 2015a). Furthermore, to the authors knowledge, there is no literature discussed the impact of different geological and seismic settings on (spatial) coherency.

The generation of band-limited noises for given $\bar{\gamma}_{\mathrm{pq,jk}}(\Delta,f)$ can be carried out by applying the spectral representation method (Shinozuka and Jan, 1972) and using Eigen decomposition (Shinozuka et al., 1990) or square root decomposition.

Using the sampled time series of the noises, the analyses for Steps (b) and (c) are straight forward. To incorporate the spatial correlation structure of the FAS for two horizontal orthogonal directions, it is considered that the FAS of the p-th direction at the j-th site equals $r_{\mathrm{Ap},j} \times y_j(\mathbf{M}, R_j, f)$, where $r_{\mathrm{Ap},j}$ ($p = 1, 2$) denotes the correlated random (scaling) disturbance of $y_j(\mathbf{M}, R_j, f)$. Similar to the case of the spatial coherency, the (intraevent) correlation coefficient between $\ln(r_{\mathrm{Ap},j})$ and $\ln(r_{\mathrm{Aq},k})$ for j and $k = 1,\ldots, n_R$, p and $q = 1$ or 2, denoted as $\rho_{\mathrm{mn,jk}}(\Delta)$ is defined by six elements. The results of statistical analysis (Liu and Hong, 2013; Hong and Liu, 2014) suggested that $\ln(r_{\mathrm{Ap},j})$ could be modeled as a normal variate with the SD equals 0.523 and $\rho_{\mathrm{mm,jk}}(\Delta)$ can be modeled using,

$$\rho_{\mathrm{mm,jk}}(\Delta) = \exp\left(-a_1\Delta^{b_1}\right), \quad (4)$$

for the record components along the same direction and

$$\rho_{\mathrm{mn,jk}}(\Delta) = r_0\exp\left(-a_2\Delta^{b_2}\right), \quad (5)$$

for the record components along the orthogonal direction, where a_1, b_2, r_0, a_2, and b_2 are model parameters. Typical values of r_0, a_2, and b_2 are listed in **Table 1**. The suggested values shown in **Table 1** are developed based on records obtained from stations with separation greater than 100 m, which are considered to be adequate for the present study, although parameters for a closely separation (i.e., $\Delta < 100$ m) can be found in Liu and Hong (2015b).

Samples of $r_{\mathrm{Ap},j}$ can be simulated based on the above specified probabilistic model and the values of $r_{\mathrm{Ap},j} \times y_j(\mathbf{M}, R_j, f)$ (i.e., reference FAS) can be calculated. Using the obtained reference FAS for the p-th direction at the j-th site, scaling of the FAS is carried out in Step (d), and the application of inverse Fourier transformation in Step (e) results in a set of record components for a considered scenario event. Multiple simulation cycles for the same scenario events can be carried out by repeating Steps (a)–(e).

TABLE 1 | Typical model parameters for spatial correlation and coherency models based on Hong and Liu (2014).

Model parameter	Parameter value and notes
Lagged coherency model	$[A, \alpha_0, k, f_0, B] = [0.46, 6.6\times10^{-4}, 5\times10^{7}, 3.5, 5.7]$ and $v_{\mathrm{ap}} = 2.5$ km/s for Eqs 1 and 2, $[c_0, c_1] = [0.61, 4.8\times10^{-3}]$ for Eq. 3
Correlation model	$[a_1, b_1] = [0.17, 0.5]$ for Eq. 4 $[r_0, a_2, b_2] = [0.8, 0.036, 0.88]$ for Eq. 5, $\ln(r_{\mathrm{Ap},j})$ is a normal variate with zero mean and SD of 0.523

Scenario Earthquake

It must be noted that although the selection of a scenario event is not a trivial task, it can be carried out based on seismic hazard deaggregation for a specified probability of exceedance (Bazzurro and Cornell, 1999; Hong and Goda, 2006). It can also be assigned based on engineering judgment and emergency preparedness planning requirements. Alternatively, it can be identified based on geological and seismological investigation of seismic source zones if results of such investigation are available. In this study, a scenario earthquake event described in Atkinson and Macias (2009) was adopted. The scenario is an interface event with a moment magnitude **M**8.5 and a rupture plane of 380 km × 90 km, placed symmetrically about a perpendicular line from the Juan de Fuca trench to the city of Vancouver. The top corner of the fault plane is placed at [47.1°N, 124.5°W], and 10 km deep from the sea level. The strike and dip angle are equal to 310° and 10°, respectively. A map showing the surface projection of the rupture plane is produced in Figure 9 in Atkinson and Macias (2009). The parameters used in the finite-fault model for this event and the site amplification factors are shown in **Tables 1** and **2** in Liu and Hong (2015a). These model parameters differ from those used by Atkinson and Macias (2009) because a newer version of the program for the finite-fault model that included several changes (Atkinson et al., 2009; Boore, 2009) was employed.

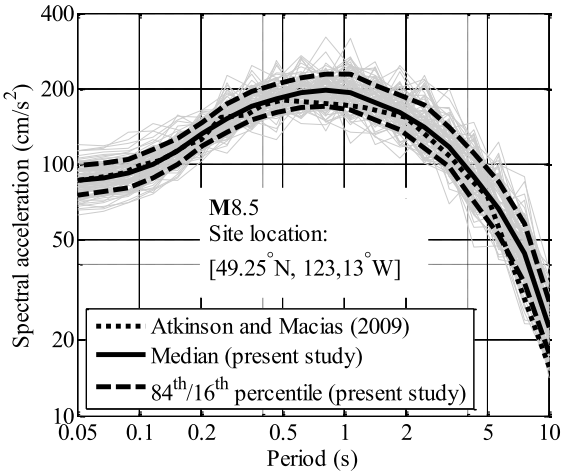

FIGURE 2 | Comparison of the average response spectrum given by Atkinson and Macias (2009) and finite-fault simulations using parameters shown in **Tables 1** and **2**.

The local site condition in downtown Vancouver is considered to be site class C according to NEHRP (National Earthquake Hazards Reduction Program) (Cassidy and Rogers, 2004), where V_{S30} (average shear wave velocity for the top 30 m soil) ranges between 360 and 760 m/s (NRCC, 2005). Therefore, it is assumed that $V_{S30} = 414$ m/s is adequate for sites located in downtown Vancouver, which is consistent with the amplification parameters considered in Liu and Hong (2015a).

Figure 2 shows the comparison between response spectra based on 100 simulation cycles of the simulation in this study with that estimated by Atkinson and Macias (2009) for (49.25°N, 123.13°W). The median spectrum for the 100 simulation cycles and the spectra corresponding to 84th and 16th percentile are also included in **Figure 2** to illustrate the dispersion due to simulation. The comparison indicates an adequate match that justifies the simulation method at a single site.

Non-Linear Inelastic 2DOF Systems As Proxy to Buildings and Damage Index

If a building is approximated by a non-linear inelastic SDOF system with Bouc–Wen hysteretic model under unidirectional excitations as was done in Liu and Hong (2015a), the governing equation is expressed in the following using the normalized displacement:

$$\begin{aligned}
&\ddot{\mu}_x + 2\xi_x\omega_{nx}\dot{\mu}_x + \alpha\omega_{nx}^2\mu_x + (1-\alpha)\omega_{nx}^2\mu_{zx} = -\ddot{u}_{gx}(t)/\Delta_{Yx}\\
&\dot{\mu}_{zx} = \frac{1}{1+\delta_\eta\varepsilon_{nx}}\left[\dot{\mu}_x - (1+\delta_v\varepsilon_{nx})\,\mu_{zx}I_x\right]\\
&\varepsilon_{nx} = (1-\alpha)\int_0^T \dot{\mu}_x\mu_{zx}dt,
\end{aligned} \tag{6}$$

where $I_x = \left|\dot{\mu}_x\right|\left|\mu_{zx}\right|^{n-1}(\beta + \gamma\,\mathrm{sgn}(\dot{\mu}_x\mu_{zx}))$, μ and μ_z are the displacement and hysteretic displacement normalized by the yield displacement capacity of the inelastic SDOF system, Δ_Y (i.e., $\mu = u/\Delta_Y$ and $\mu_z = z/\Delta_Y$, in which u and z are the displacement and hysteretic displacement of the SDOF system, respectively); $\omega_n = (k/m)^{0.5}$ is the natural vibration frequency, in which k and m are the stiffness and mass of the system; $\ddot{u}_g(t)$ is the ground acceleration time history; ε_n is the normalized dissipated energy through hysteresis; α, β, γ, and n are shape parameters in which $\beta + \gamma = 1$, α controls the post-yield stiffness, and n controls the smoothness of the transition from linear elastic to non-linear inelastic responses; δ_η and δ_v are stiffness and strength degradation parameters, respectively. The defined symbols with additional subscript x are used to denote that they represent the quantities associated with X-axis; and an overdot on a variable denotes its temporal derivative.

The yield displacement Δ_Y of the non-linear inelastic model could be approximately related to the seismic design requirements (NRCC, 2005), where the minimum required design base shear force V_d is given by $V_d = C_s W$, W is the total weight of the structure and C_s is the design base shear coefficient given in **Table 2** for different building types. It can be shown that Δ_Y is

$$\Delta_Y = R_N C_S W/k \tag{7}$$

where R_N is the coefficient taking into account that the actual yield strength of a designed structure is greater than V_d. μ_R and R_N are considered to be lognormally distributed with mean values shown in **Table 2** and coefficient of variation (cov) of 0.3 and 0.15 (Ellingwood et al., 1980; Ibarra, 2003), respectively. μ_R and R_N are assumed to be independent for each building.

As mentioned in the Section "Introduction," the use of the non-linear inelastic 2DOF system to represent a building is more realistic than the use of SDOF system, especially if bidirectional horizontal ground motions are considered. In such a case, the governing equation in terms of normalized displacements can be represented by Park et al. (1986), Yeh and Wen (1990), Lee and Hong (2010):

$$\begin{aligned}
&\ddot{\mu}_x + 2\xi_x\omega_{nx}\dot{\mu}_x + \alpha\omega_{nx}^2\mu_x + (1-\alpha)\omega_{nx}^2\mu_{zx} = -\ddot{u}_{gx}/\Delta_{Yx}\\
&\ddot{\mu}_y + 2\xi_y\omega_{ny}\dot{\mu}_y + \alpha\omega_{nx}^2\mu_x + (1-\alpha)\omega_{ny}^2\mu_{zy} = -\ddot{u}_{gy}/\Delta_{Yy}\\
&\dot{\mu}_{zx} = \frac{1}{1+\delta_\eta\varepsilon_n}\left[\dot{\mu}_x - (1+\delta_v\varepsilon_n)\,\mu_{zx}I\right]\\
&\dot{\mu}_{zy} = \frac{1}{1+\delta_\eta\varepsilon_n}\left[\dot{\mu}_y - (1+\delta_v\varepsilon_n)\,\mu_{zy}I\right]\\
&\varepsilon_n = (1-\alpha)\int_0^t \left(\mu_{zx}\dot{\mu}_x + \mu_{zy}\dot{\mu}_y\right)\left(\left|\cos^n\theta\right| + \left|\sin^n\theta\right|\right)^{2/n}dt
\end{aligned} \tag{8}$$

where $I = \left|\dot{\mu}_x\right|\left|\mu_{zx}\right|^{n-1}[\beta + \gamma\,\mathrm{sgn}(\dot{\mu}_x\mu_{zx})] + \left|\dot{\mu}_y\right|\left|\mu_{zy}\right|^{n-1}[\beta + \gamma\,\mathrm{sgn}(\dot{\mu}_y\mu_{zy})]$, $\theta = \tan^{-1}(\mu_y/\mu_x)$, and the symbols defined previously but with an additional subscript y instead of x represents the quantities associated with the Y-axis. The solution of Eq. 8 can be used to evaluate the "normalized" displacement at time t,

$$\mu_D(t) = \left(\left|\mu_x(t)\right|^n + \left|\mu_y(t)\right|^n\right)^{1/n} \tag{9}$$

At the incipient yield, $\max(\mu_D(t))$ equals to 1.0; $\max(\mu_D(t))$ represents the peak ductility demand if it is greater than 1.0. By considering that the ductility capacity equals μ_{cap}, collapse occurs

TABLE 2 | Damage cost information (Goda and Hong, 2008b) and considered portfolio of buildings for downtown Vancouver.

I_{BT}[a]	$L_{BL}(1)$, $L_{CO}(1)$, $L_{BI}(1)$ (CAD/ft^2)	β_{BL}, β_{CO}, β_{BI}	#B, #S, Size[b] (m)	Mean T_n (s)	Mean R_N	Mean μ_R	Target C_S[c]
1	87.6, 21.9, 19.9	0.75, 0.68, 0.57	4, 2, 10 × 12	0.4	2	6	0.12
2	87.6, 21.9, 19.9	0.75, 0.68, 0.57	4, 1, 8 × 12	0.4	2	6	0.12
3	111.4, 27.9, 26.3	0.81, 0.68, 0.62	8, 2, 15 × 30	0.4	2	6	0.12
4	47.8, 26.5, 23.9	0.81, 0.68, 0.43	6, 2, 15 × 30	0.4	2	6	0.12
5	111.4, 27.9, 26.3	0.69, 0.58, 0.53	1, 5, 18 × 36	0.7	2.25	4	0.1
6	103.5, 51.7, 163.9	0.70, 0.58, 0.57	1, 5, 18 × 36	0.7	2.25	4	0.1
7	111.4, 27.9, 26.3	0.69, 0.59, 0.53	1, 13, 18 × 36	1.4	2.25	3	0.075
8	103.5, 51.7, 163.9	0.70, 0.59, 0.57	1, 13, 18 × 36	1.4	2.25	3	0.075
9	111.4, 27.9, 26.3	0.76, 0.64, 0.58	3, 2, 15 × 30	0.4	2.5	6	0.12
10	47.8, 26.5, 23.9	0.75, 0.64, 0.41	5, 2, 15 × 30	0.4	2.5	6	0.12
11	111.4, 27.9, 26.3	0.75, 0.64, 0.58	9, 5, 18 × 36	0.6	2.5	5	0.12
12	103.5, 51.7, 163.9	0.77, 0.64, 0.62	13, 5, 18 × 36	0.6	2.5	5	0.12
13	111.4, 27.9, 26.3	0.76, 0.64, 0.58	6, 15, 18 × 36	1.65	3	3	0.05
14	103.5, 51.7, 163.9	0.77, 0.64, 0.62	13, 15, 18 × 36	1.65	3	3	0.05
15	111.4, 27.9, 26.3	0.81, 0.69, 0.62	2, 2, 15 × 30	0.35	2	5	0.08
16	47.8, 26.5, 23.9	0.81, 0.69, 0.43	17, 2, 15 × 30	0.35	2	5	0.08
17	111.4, 27.9, 26.3	0.81, 0.69, 0.63	2, 3, 20 × 40	0.5	2	3.3	0.08
18	61.0, 33.4, 19.5	0.80, 0.69, 0.49	4, 3, 20 × 40	0.5	2	3.3	0.08

[a] *I_{BT} is the building index. Building index is related to the structural and occupancy types defined in HAZUS-Earthquake [Federal Emergency Management Agency (FEMA) and the National Institute of Building Sciences (NIBS), 2003] (1 = W1-RES1, 2 = W1-RES1, 3 = W2-RES3, 4 = W2-COM1, 5 = S4M-RES3, 6 = S4M-COM4, 7 = S4H-RES3, 8 = S4H-COM4, 9 = C2L-RES3, 10 = C2L-COM1, 11 = C2M-RES3, 12 = C2M-COM4, 13 = C2H-RES3, 14 = C2H-COM4, 15 = URMLR-RES3, 16 = URMLR-COM1, 17 = URMMR-RES3, 18 = URMMR-COM2).*

[b] *#B = the number of buildings and #S = number of stories.*

[c] *The target C_S is used to represent the seismic design level for existing buildings.*

if $\max(\mu_D(t))$ is greater than μ_{cap}. Based on these consideration, for simplicity and being similar to the case of nonlinear inelastic SDOF system (Goda and Hong, 2008b), a damage factor is defined by using,

$$\delta_{DF} = \max(\min(\delta_{Shift}, 1), 0) \tag{10}$$

where $\delta_{Shift} = \left[\max\left(\left(|\mu_x|^n + |\mu_y|^n\right)^{1/n}\right) - 1\right] \Big/ \left[\mu_{cap} - 1\right]$. If δ_{DF} equals 0, it implies the responses is within elastic range (or at most at incipient yield). Collapse is observed if $\delta_{DF} = 1.0$, and partial damage occurs for δ_{DF} within (0, 1).

Aggregate Seismic Loss for a Portfolio of Buildings

One of the most difficult and important task in estimating seismic loss is to establish the damage cost function in terms of the damage level (e.g., in terms of damage factor defined in the previous section). This can be carried out if sufficient damage survey data from historical earthquakes are available. However, as the data are always scarce, the damage cost function is often established based on structural component testing results and expert opinion or judgment. A significant set of cost functions is available in HAZUS [Federal Emergency Management Agency (FEMA) and the National Institute of Building Sciences (NIBS), 2003]. These functions for several structural types and in terms of Canadian dollars are given in Goda and Hong (2008b). More specifically, it is considered that seismic losses associated with a building are categorized into three types: building-related loss $L_{BL}(\delta)$, contents-related loss $L_{CO}(\delta)$, and business-interruption related loss $L_{BI}(\delta)$, where $\delta = \delta_{DF}$. These damage-loss functions can be expressed as,

$$L_{BL}(\delta) = \delta^{\beta_{BL}} L_{BL}(1), L_{CO}(\delta) = \delta^{\beta_{CO}} L_{CO}(1), \text{ and}$$
$$L_{BI}(\delta) = \delta^{\beta_{BI}} L_{BL}(1) \tag{11}$$

where the values of losses for the complete damage $L_{BL}(1)$, $L_{CO}(1)$, and $L_{BI}(1)$, as well as the model parameters β^{BL}, β^{CO}, and β^{BI} are shown in **Table 2** for each building type. By using the damage-loss functions, the aggregate seismic loss L for n_R buildings subjected to the scenario earthquake is calculated using:

$$L = \sum_{j=1}^{n_R} \left(L_{BL}(\delta_j) + L_{CO}(\delta_j) + L_{BI}(\delta_j)\right) \tag{12}$$

where δ_j denotes the damage factor δ_{DF} for the j-th building. The maximum possible aggregate loss, L_{max}, equals that calculated from Eq. 12 for $\delta_j = 1$.

NUMERICAL EXAMPLE APPLICATION IN SEISMIC LOSS ESTIMATION

In this section, an example application of the framework shown in the previous section is presented for a scenario seismic event and a portfolio of buildings. For the numerical analysis, the scenario seismic event of moment magnitude **M**8.5 elaborated previously is considered. The selection of hypothetical portfolio of 100 buildings as well as the analysis results are discussed in the following. Comparison of the aggregate seismic loss of the portfolio of buildings obtained under bidirectional excitations are compared with that obtained by considering unidirectional excitation.

Considered Portfolio of 100 Buildings

A portfolio of 100 hypothetical buildings located in downtown Vancouver is considered for the numerical example. The sites of the buildings are randomly selected over a square area of 2.5 km by 2.5 km centered at (49.2°N, 123.2°W), which contains 4,000

property lots, each with an area of 25 m × 50 m. The selected locations are illustrated in **Figure 3**. Similar to Liu and Hong (2015a), the set of 100 buildings consists of 18 building types shown in **Table 2**. The buildings are of different structural types and occupancies (40 residential buildings and 60 commercial buildings). They are sampled based on the statistical information describing the existing building stocks in downtown Vancouver (Munich Reinsurance Company of Canada, 1992; Onur, 2001). As explained previously, the ductility capacity μ_{cap} is considered to be lognormally distributed with cov of 0.3. The mean of the ductility capacity for different building types are shown in **Table 2**. However, unlike the case in Liu and Hong (2015a), in this study, the capacities of a building in two orthogonal horizontal orientations (i.e., along X-axis and Y-axis) rather than in a single orientation are considered. The yield displacements Δ_{Yx} and Δ_{Yx} of each building are defined according to Eq. 7, which can be written as $\Delta_Y = R_N C_S g T_n^2/(2\pi)^2$ with T_n denote the natural vibration period. For each structure, T_n in two orthogonal directions are considered to be independent identically uniformly distributed with mean shown in **Table 2** and lower and upper bounds equal to minus and plus 10% of the mean value. This is to represent the fact that the T_n along two horizontal orthogonal direction may differ. R_N is considered to be independently lognormally distributed with mean shown in **Table 2**, and cov equal to 0.15 as discussed previously. Only a single set of structural characteristics of the buildings are sampled and considered in the following numerical analysis.

Illustration of Simulated Ground Motion Components, Calculated Structural Responses, and Damage Cost

For the 100 building sites marked on **Figure 3**, samples of simulated time histories for two building sites obtained by applying the procedure outlined in the previous section are presented in **Figure 4**. Note that since the adequacy of the adopted simulation procedure for ground motion records to match the target spatial correlation and coherency and FAS are already discussed extensively elsewhere (Hong and Liu, 2014; Liu and Hong, 2015a), they are not repeated in here. By applying these time histories to the buildings modeled as nonlinear inelastic 2DOF systems, the responses from the time history analysis is shown in **Figure 5** in terms of the normalized displacements μ_x, μ_y, and μ_D. The peak values for the normalized displacement and their corresponding time are also shown in the figure. The figure illustrates that the occurrence of peak demand along different component could

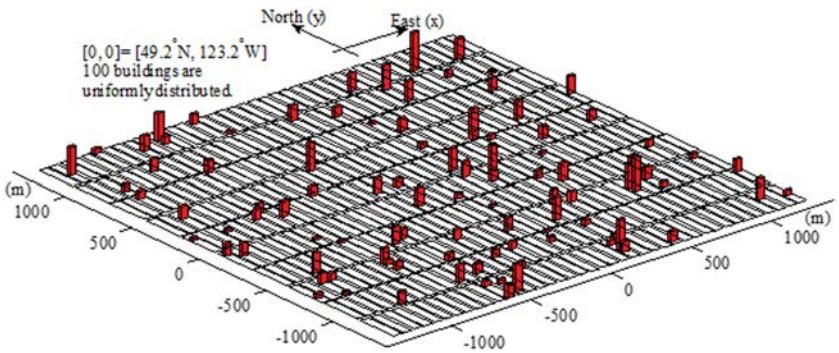

FIGURE 3 | Sites for the portfolio of 100 hypothetical buildings.

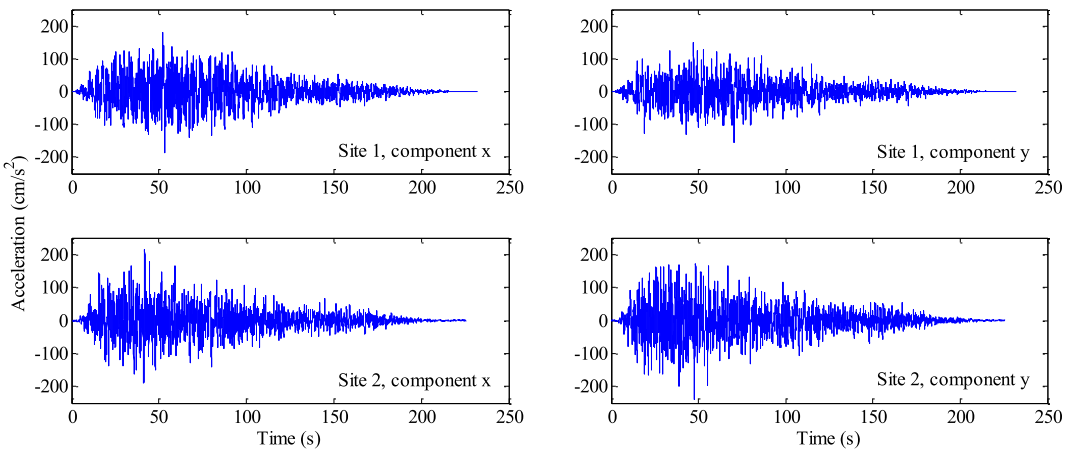

FIGURE 4 | Illustration of simulated spatially correlated and coherent records for two selected sites.

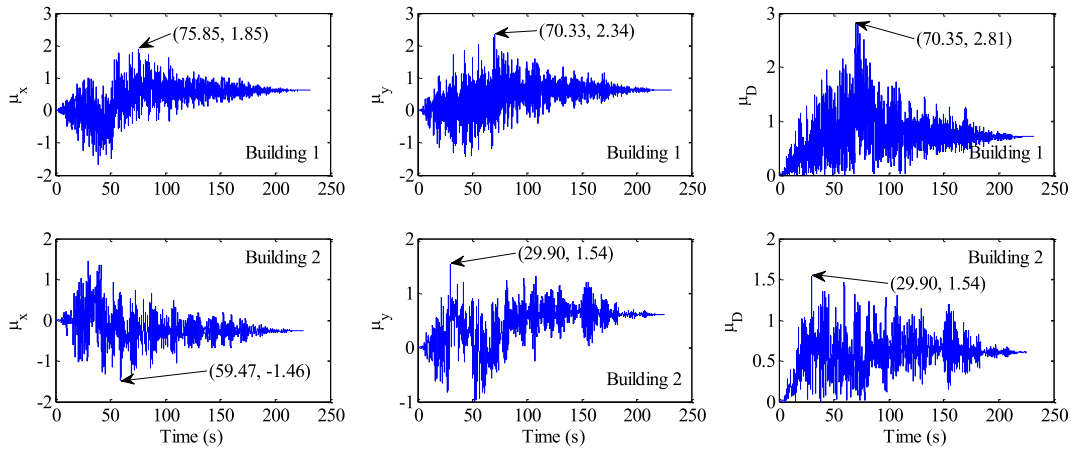

FIGURE 5 | Nonlinear inelastic response of the buildings modeled as 2-degree-of-freedom systems, in terms of normalized displacement response μ_x, μ_y, and μ_D, under the bidirectional ground motions shown in **Figure 4**. The peak normalized displacement and its corresponding time is also shown.

differ. The total displacement demand μ_D is greater than a single component.

Based on the non-linear inelastic response, the damage factor of the 2DOF system can be evaluated using Eq. 10. For the two examples given in **Figure 5**, Building 1 is a 2-story wood frame residential building ($T_{nx} = 0.366$ s; $T_{ny} = 0.432$ s); Building 2 is a 15-story reinforced concrete commercial building ($T_{nx} = 1.664$ s; $T_{ny} = 1.552$ s). The calculated damage factor, $\delta_{DF} = 0.0475$ for Building 1 and $\delta_{DF} = 0.554$ for Building 2.

Estimation of the Aggregate Loss

The numerical calculation carried out in the previous section is repeated for all 100 considered building. Using the calculated damage cost for each of the 100 buildings, $L_{BL}(\delta)$, $L_{CO}(\delta)$, and $L_{BI}(\delta)$, and summing them up according to Eq. 10, the value of the aggregate loss of the portfolio of buildings L is obtained. This obtained value represents a sample of the aggregate loss for the considered scenario seismic event because of the uncertainty in the ground motions even for the same scenario event. By repeating the above analysis 100 times for the same set of buildings, samples of L are obtained and shown in **Figure 6**.

The figure shows that the aggregated seismic loss for the 2DOF system is generally following a straight line on the Gumbel probability paper, with median equal to 0.26.

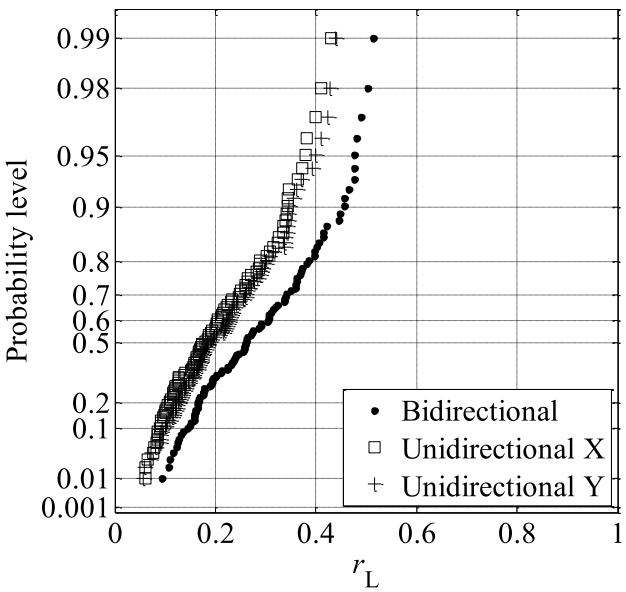

FIGURE 6 | Aggregated seismic loss for the 100 buildings under the scenario earthquake plotted on Gumbel probability paper.

Effect of Approximating Building As SDOF Systems versus 2DOF Systems

Now, reconsider the ground motions and the structures shown in **Figure 3** but only considering the excitations along the X-axis and the buildings modeled as SDOF with the structural properties along the X-axis as well. The calculated responses, the damage factors, and the damage cost for the two buildings are shown in **Figure 7**. Comparison of the results with those shown in **Figure 5** indicate that the profile of the response time history of a SDOF system is generally similar with that of a 2DOF system along the same direction. However, the maximum response could differ significantly because of the consideration of interactions between the two orthogonal directions.

By repeating the analysis for the building modeled as SDOF systems and subjected to the same set of excitations along the X-axis used in 2DOF system case, samples of L are obtained and also presented in **Figure 6**. The results follow Gumbel distribution well with a median value of 0.18. Similar analysis is also carried out for Y-axis; the results are also plotted in **Figure 6**.

Comparison of the results for SDOF systems under unidirectional excitations versus 2DOF systems subjected to bidirectional excitations indicate that the simplification of using unidirectional excitations and SDOF models can underestimate the aggregated seismic loss in a scenario earthquake event. Such underestimation is somewhat more significant at upper tail where the probability of exceedance is small. This observation emphasizes that the importance of using properly simulated bidirectional ground

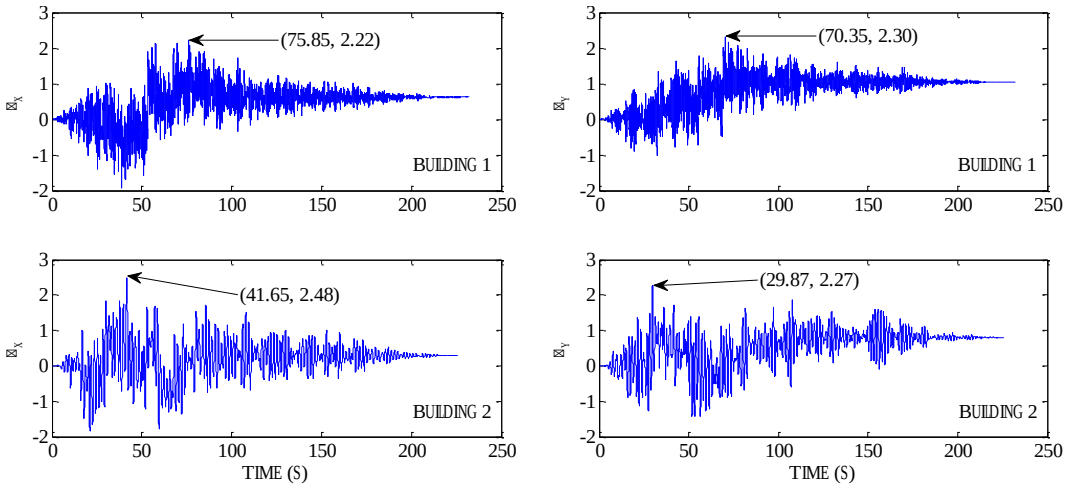

FIGURE 7 | Non-linear inelastic response of the buildings modeled as single-degree-of-freedom systems, in terms of normalized displacement response μ_x and μ_y, under the unidirectional ground motions shown in **Figure 4**. The peak normalized displacement and its corresponding time is also shown.

motion excitations and realistic 2DOF structural models in the seismic risk assessment of structures that are sensitive to the orientation of the excitations.

CONCLUSION

In this study, we first simulate bidirectional spatially (partially) correlated and (partially) coherent ground motion records for a scenario Cascadia earthquake using a simulation procedure based on stochastic finite-fault model. The seismic loss of a portfolio of hypothetical buildings in downtown Vancouver under the simulated bidirectional horizontal ground motions is then estimated. Each building is modeled as a 2DOF system with different dynamic characteristics in two orthogonal horizontal directions. The hysteretic behaviors of the 2DOF systems are described by bidirectional Bouc–Wen model. The results indicate that if unidirectional ground motions and SDOF structural models are considered, the aggregated seismic loss could be underestimated, emphasizing the importance of using realistic bidirectional ground motions that includes spatial coherency and correlation structure and modeling buildings as 2DOF systems with different characteristics in two horizontal directions. If the computation power is not limited, the framework presented in this study can be expanded to investigate the effect of tri-directional ground motions and more complicated structural models.

AUTHOR CONTRIBUTIONS

TL carried out the analysis and wrote the manuscript. HH oversaw the project and revised the manuscript.

FUNDING

The financial support received from the Natural Sciences and Engineering Research Council of Canada and the University of Western Ontario is gratefully acknowledged.

REFERENCES

Abrahamson, N. A., Schneider, J. F., and Stepp, J. C. (1991). Spatial coherency of shear waves from the Lotung, Taiwan large-scale seismic test. *Struct. Saf.* 10, 145–162. doi:10.1016/0167-4730(91)90011-W

Atkinson, G. M., Assatourians, K., Boore, D. M., Campbell, K., and Motazedian, D. (2009). A guide to differences between stochastic point-source and stochastic finite-fault simulations. *Bull. Seism. Soc. Am.* 99, 3192–3201. doi:10.1785/0120090058

Atkinson, G. M., and Macias, M. (2009). Predicted ground motions for great interface earthquakes in the Cascadia subduction zone. *Bull. Seism. Soc. Am.* 99, 1552–1578. doi:10.1785/0120080147

Bazzurro, P., and Cornell, C. A. (1999). Disaggregation of seismic hazard. *Bull. Seism. Soc. Am.* 89, 501–520.

Boore, D. M. (2009). Comparing stochastic point-source and finite-source ground-motion simulations: SMSIM and EXSIM. *Bull. Seism. Soc. Am.* 99, 3202–3216. doi:10.1785/0120090056

Cassidy, J. F., and Rogers, G. C. (2004). "Variation in ground shaking on the Fraser River delta (Greater Vancouver, Canada) from analysis of moderate earthquakes," in *Proceedings, 13th World Conference on Earthquake Engineering* (Vancouver, Canada). Paper No. 1010.

Clough, R. W., and Penzien, J. (2003). *Dynamics of Structures*. Berkeley, CA: Computers & Structures, Inc.

Der Kiureghian, A. (1996). A coherency model for spatially varying ground motions. *Earthq. Eng. Struct. Dynam.* 25, 99–111. doi:10.1002/(SICI)1096-9845(199601)25:1<99::AID-EQE540>3.0.CO;2-C

Ellingwood, B. R., Galambos, T. V., MacGregor, J. G., and Cornell, C. A. (1980). *Development of a Probability Based Load Criterion for American National Standard A58*. Washington, DC: National Bureau of Standards. National Bureau of Standards Special Publication No. 577.

Federal Emergency Management Agency (FEMA) and the National Institute of Building Sciences (NIBS). (2003). *HAZUS-Earthquake: Technical Manual*. Washington, DC: FEMA and NIBS.

Goda, K., and Hong, H. P. (2008a). Spatial correlation of peak ground motions and response spectra. *Bull. Seism. Soc. Am.* 98, 354–365. doi:10.1785/0120070078

Goda, K., and Hong, H. P. (2008b). Estimation of seismic loss for spatially distributed buildings. *Earthq. Spectra* 24, 889–910. doi:10.1193/1.2983654

Harichandran, R. S., and VanMarcke, E. H. (1986). Stochastic variation of earthquake ground motion in space and time. *J. Eng. Mech.* 112, 154–174. doi:10.1061/(ASCE)0733-9399(1986)112:2(154)

Hong, H. P., Garcia-Soto, A. D., and Gomez, R. (2010). Impact of different earthquake types on the statistics of ductility demand. *J. Struct. Eng.* 136, 770–780. doi:10.1061/(ASCE)ST.1943-541X.0000177

Hong, H. P., and Goda, K. (2006). A comparison of seismic hazard and risk deaggregation. *Bull. Seism. Soc. Am.* 96, 2021–2039. doi:10.1785/0120050238

Hong, H. P., and Hong, P. (2007). Assessment of ductility demand and reliability of bilinear single-degree-of-freedom systems under earthquake loading. *Can. J. Civil Eng.* 34, 1606–1615. doi:10.1139/L07-077

Hong, H. P., and Liu, T. J. (2014). Assessment of coherency for bi-directional horizontal ground motions and its application for simulating multiple-station bidirectional ground motions. *Bull. Seism. Soc. Am.* 104, 2491–2502. doi:10.1785/0120130241

Ibarra, L. F. (2003). *Global Collapses of Frame Structures under Seismic Excitations*. Ph.D. thesis, Stanford University, Stanford, CA.

Jayaram, N., and Baker, J. W. (2009). Correlation model for spatially distributed ground-motion intensities. *Earthq. Eng. Struct. Dynam.* 38, 1687–1708. doi:10.1002/eqe.922

Lee, C. S., and Hong, H. P. (2010). Statistics of inelastic responses of hysteretic systems under bidirectional seismic excitations. *Eng. Struct.* 32, 2074–2086. doi:10.1016/j.engstruct.2010.03.008

Liu, T. J., Atkinson, G. M., Hong, H. P., and Assatourians, K. (2012). Intraevent spatial correlation characteristics of stochastic finite – fault simulations. *Bull. Seism. Soc. Am.* 102, 1740–1747. doi:10.1785/0120110266

Liu, T. J., and Hong, H. P. (2013). Simulation of multiple-station ground motions using stochastic point-source method with spatial coherency and correlation characteristics. *Bull. Seism. Soc. Am.* 103, 1912–1921. doi:10.1785/0120120203

Liu, T. J., and Hong, H. P. (2015a). Application of spatially correlated and coherent records of scenario event to estimate seismic loss of a portfolio of buildings. *Earthq. Spectra* 31, 2047–2068. doi:10.1193/060513EQS143M

Liu, T. J., and Hong, H. P. (2015b). Simulation of horizontal ground motions with spatial coherency in two orthogonal horizontal directions. *J. Earthq. Eng.* 19, 752–769. doi:10.1080/13632469.2014.999175

Motazedian, D., and Atkinson, G. M. (2005). Stochastic finite-fault modeling based on a dynamic corner frequency. *Bull. Seism. Soc. Am.* 95, 995–1010. doi:10.1785/0120030207

Munich Reinsurance Company of Canada. (1992). *A Study of the Economic Impact of a Severe Earthquake in the Lower Mainland of British Columbia*. Vancouver, Canada: Munich Reinsurance Company of Canada.

NRCC. (2005). *National Building Code of Canada 2005*. Ottawa, Canada: NRCC.

Onur, T. (2001). *Seismic Risk Assessment in Southwestern British Columbia*. Ph.D. thesis, University of British Columbia, Vancouver, Canada.

Park, Y. J., Wen, Y. K., and Ang, A. (1986). Random vibration of hysteretic systems under bi-directional ground motions. *Earthq. Eng. Struct. Dyn.* 14, 543–557. doi:10.1002/eqe.4290140405

Shinozuka, M., and Jan, C. M. (1972). Digital simulation of random processes and its applications. *J. Sound. Vib.* 25, 111–128. doi:10.1016/0022-460X(72)90600-1

Shinozuka, M., Yun, C. B., and Seya, H. (1990). Stochastic methods in wind engineering. *J. Wind Eng. Indus. Aerodyn.* 36, 829–843. doi:10.1016/0167-6105(90)90080-V

Wen, Y. K. (1976). Method for random vibration of hysteretic systems. *J. Eng. Mech. Div.* 102, 249–263.

Whitman, R. V., Anagnos, T., Kircher, C. A., Lagorio, H. J., Lawson, R. S., and Schneider, P. (1997). Development of a national earthquake loss estimation methodology. *Earthq. Spectra* 13, 643–661. doi:10.1193/1.1585973

Yeh, C. H., and Wen, Y. K. (1990). Modeling of nonstationary ground motion and analysis of inelastic structural response. *Struct. Saf.* 8, 281–298. doi:10.1016/0167-4730(90)90046-R

Zerva, A. (2009). *Spatial Variation of Seismic Ground Motions: Modeling and Engineering Applications*. Boca Raton, FL: CRC Press, Taylor & Francis Group.

Conflict of Interest Statement: The authors declare that the research was conducted in the absence of any commercial or financial relationships that could be construed as a potential conflict of interest.

Copyright © 2017 Liu and Hong. This is an open-access article distributed under the terms of the Creative Commons Attribution License (CC BY). The use, distribution or reproduction in other forums is permitted, provided the original author(s) or licensor are credited and that the original publication in this journal is cited, in accordance with accepted academic practice. No use, distribution or reproduction is permitted which does not comply with these terms.

frontiers in Built Environment

ORIGINAL RESEARCH
published: 23 December 2016
doi: 10.3389/fbuil.2016.00033

Tsunami Hazard Analysis of Future Megathrust Sumatra Earthquakes in Padang, Indonesia Using Stochastic Tsunami Simulation

Ario Muhammad[1,2], Katsuichiro Goda[1] and Nicholas Alexander[1]*

[1] Department of Civil Engineering, University of Bristol, Bristol, UK, [2] Department of Civil Engineering, University of Narotama, Surabaya, Indonesia

OPEN ACCESS

Edited by:
Nikos D. Lagaros, National Technical University of Athens, Greece

Reviewed by:
Filippos Vallianatos, Technological Educational Institute of Crete, Greece
David De Leon, Universidad Autónoma del Estado de México (UAEM), Mexico

****Correspondence:***
Ario Muhammad
ario.muhammad@bristol.ac.uk

Specialty section:
This article was submitted to Earthquake Engineering, a section of the journal Frontiers in Built Environment

Received: *21 September 2016*
Accepted: *07 December 2016*
Published: *23 December 2016*

Citation:
Muhammad A, Goda K and Alexander N (2016) Tsunami Hazard Analysis of Future Megathrust Sumatra Earthquakes in Padang, Indonesia Using Stochastic Tsunami Simulation. Front. Built Environ. 2:33. doi: 10.3389/fbuil.2016.00033

This study assesses the tsunami hazard potential in Padang, Indonesia probabilistically using a novel stochastic tsunami simulation method. The stochastic tsunami simulation is conducted by generating multiple earthquake source models for a given earthquake scenario, which are used as input to run Monte Carlo tsunami simulation. Multiple earthquake source models for three magnitude scenarios, i.e., M_w 8.5, M_w 8.75, and M_w 9.0, are generated using new scaling relationships of earthquake source parameters developed from an extensive set of 226 finite-fault models. In the stochastic tsunami simulation, the effect of incorporating and neglecting the prediction errors of earthquake source parameters is investigated. In total, 600 source models are generated to assess the uncertainty of tsunami wave characteristics and maximum tsunami wave height profiles along coastal line of Padang. The results highlight the influence of the uncertainty of the scaling relationships on tsunami simulation results and provide a greater range of tsunamigenic scenarios produced from the stochastic tsunami simulation. Additionally, the results show that for the future major earthquakes in the Sunda megathrust, the maximum tsunami wave height in Padang areas can reach 20 m and, therefore, significant damage and loss may be anticipated in this region.

Keywords: stochastic tsunami simulation, earthquake source modeling, uncertainty and sensitivity of tsunami hazard, Sunda megathrust, West Sumatra

INTRODUCTION

Located among three major plates, namely the Indian-Australian, the Pacific, and the Eurasian, Indonesia archipelago is one of the most seismically active regions in the world. In the last 20 years (1994–2014), 528 earthquakes occurred in Indonesia, i.e., about 26 earthquakes per year (United States Geological Survey (USGS), 2015). Sumatra Island is the most seismically active region since it is located at the interface between the Indian-Australian and Eurasian Plates. Two major seismic sources are the 1,900-km long Sumatran fault located along the center of Sumatra Island and the Sunda megathrust zone traversing more than 2,000 km along the western coast of Sumatra

(Sieh and Natawidjaja, 2000). In the past two decades, several large earthquakes occurred along the Sunda megathrust including the Aceh-Andaman earthquake in December 2004 (M_w 9.15), the Nias earthquake in March 2005 (M_w 8.6), two earthquakes of Bengkulu in September 2007 (M_w 8.4 and 7.9), the Mentawai tsunamigenic earthquake in October 2010 (M_w 7.7), and the Indian Ocean earthquake in April 2012 (M_w 8.6). Two of the most devastating earthquake events among those were the 2004 Aceh-Andaman earthquake triggering large tsunamis along the coastal line of Sumatra, Thailand, Sri Lanka, and India with the casualties of more than 250,000 people and the 2005 Nias earthquake which killed 2,000 people (Hsu et al., 2006; Banerjee et al., 2007).

The 2004 Aceh-Andaman earthquake was caused by the 1,600-km long rupture of the Sunda megathrust starting from North of Simeulue Island to North of Andaman Islands (Meltzner et al., 2006). This failure led to another 400 km rupture of the megathrust fault in the southern part of Simeulue Island (see **Figure 1**) causing the M_w 8.6 2005 Nias earthquake (Briggs et al., 2006). A paleotsunami study based on a 1,000-year long record of tsunami deposits in North-West of Sumatra suggests that the occurrence interval of tsunamigenic earthquakes (M_w 9.15) from the Sumatra-Andaman region is about 600 years (Monecke et al., 2008). Although the devastating tsunami event might not occur in the next few centuries in the Sumatra-Andaman segment, the ruptures of the megathrust fault have increased the failure probability of the Mentawai segment of the Sunda megathrust areas (see **Figure 1**) which is located in South of the fault rupture areas of the 2004 and 2005 events (Nalbant et al., 2005; Chlieh et al., 2008; Sieh et al., 2008; Collings et al., 2012, 2013). The past seismicity in the Mentawai segment indicates that there were two major tsunamigenic events occurred in 1797 and 1833 (M_w ~8.8) that

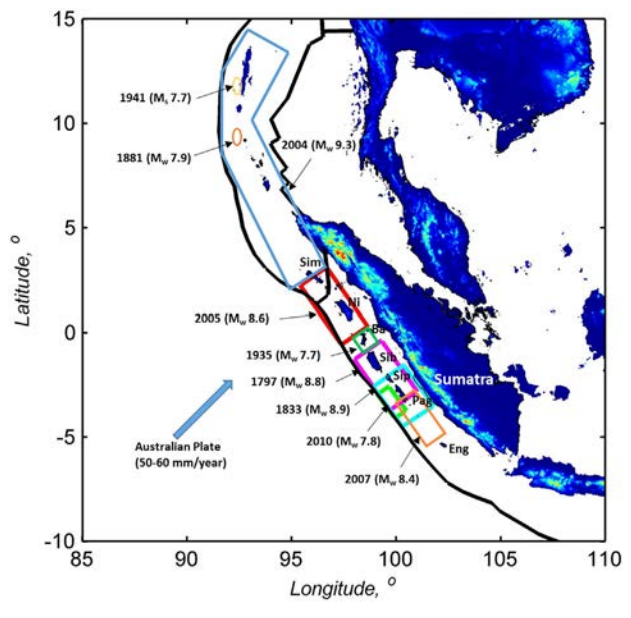

FIGURE 1 | Historical recent seismic activities in the Sumatra areas (Sim: Simeulue, Ni: Nias, Ba: Batu Islands, Sib: Sibereut, Sip: Sipora, Pag: Pagai Islands, and Eng: Enggano).

affected the coastal areas of Padang and Bengkulu. Geodetic and paleogeodetic studies indicate that the slip deficit accumulated in the Mentawai segment has already exceeded the slip occurred during the 1797 and 1833 earthquakes (Collings et al., 2013). A large earthquake in 2007 (M_w 8.4) that ruptured the Sunda megathrust near the 1833 rupture area was significantly smaller than the accumulated slip since the twin events of the 1797 and 1833 earthquakes (McCloskey et al., 2005; Nalbant et al., 2005). Hence, the possibility of earthquake and tsunami hazards in West of Sumatra from the Mentawai segment which has a recurrence interval of 200 years according to paleoseismological studies remains large (Sieh et al., 2008). In addition, the slip deficit is sufficient to generate a M_w 8.8–9.0 earthquake (Zachariasen et al., 1999; Sieh et al., 2008).

Several earthquake source models have been developed with respect to the unruptured Mentawai segment (Borrero et al., 2006; Aydan, 2008; Griffin et al., 2016) and have been implemented to assess the earthquake and tsunami potential in several highly populated areas along the western coast of Sumatra, i.e., Padang, Painan, Bengkulu, and Pariaman (Borrero et al., 2006; McCloskey et al., 2008; Muhari et al., 2010, 2011). A wide range of rupture scenarios is essential for evaluating the earthquake and tsunami risk potential in coastal areas to capture worst (extreme) cases for emergency response preparedness and risk mitigation actions. However, except for the investigations by McCloskey et al. (2008) and Griffin et al. (2016), those studies implemented uniform slip models that oversimplify the earthquake source characteristics and considered a limited number of scenarios for future tsunamigenic events. On the other hand, McCloskey et al. (2008) considered the uncertainty of slip distribution by implementing the heterogeneous spatial distribution of slips based on a methodology proposed by Mai and Beroza (2002) and produced more than 100 scenarios to assess the tsunami hazards along the western coast of Sumatra. However, the events evaluated by Mai and Beroza (2002) were crustal earthquakes of magnitudes up to 8 and were not tsunamigenic. Recently, the Mai–Beroza method has been extended to apply to M_w 9.0 megathrust subduction earthquakes by adopting inverted source models from the 2011 Tohoku, Japan earthquake (Goda et al., 2014, 2015). Griffin et al. (2016) generated heterogeneous earthquake slips to assess tsunami hazard in Mentawai Islands based on the random slip modeling proposed by Gallovič and Brokešová (2004). Up to 15 million random slip models were generated using existing scaling relationships that were based on only seven subduction earthquake events in Sumatra and eventually 1,000 tsunami simulations from those slip models were further performed to assess the tsunami hazard in Mentawai Islands.

Moreover, those previous investigations for the Mentawai-Sunda subduction zone adopted the global empirical scaling relationships [e.g., Mai and Beroza (2002), Gallovič and Brokešová (2004), and Aydan (2008)] to generate only either deterministic fault geometry parameters (width and length) or slip distribution parameters without considering the uncertainty and relationships among earthquake source parameters. Recently, new probabilistic scaling relationships of fault geometry, slip statistics, and spatial slip heterogeneity parameters have been developed by Goda et al. (2016) using numerous inversion models (226 models) from the

SRCMOD database (Mai and Thingbaijam, 2014) and can be used for tsunami hazard analysis. In those previous studies, the evaluation of regional earthquake source parameters from the finite-fault models of the past Sunda subduction earthquakes with respect to the global empirical relationships is also neglected. Hence, it is highly desirable to generate multiple earthquake source models by taking into account all relevant source parameters that are consistent with the regional source characteristics of the future tsunamigenic earthquakes in the Mentawai-Sunda zone.

Additionally, within the area of the Mentawai segment, Padang is one of the most anticipated areas to be affected by the tsunami compared to the other areas in the western coast of Sumatra. With the total population of 850,000 people, the social and economic impacts due to the future tsunamigenic earthquakes are high. The investigations considering multiple earthquake scenarios by McCloskey et al. (2008) and Griffin et al. (2016) only estimated the maximum tsunami height along the western coast of Sumatra and assessed the tsunami hazard in Mentawai Islands but excluded a rigorous evaluation in Padang areas. Moreover, the past tsunami hazard assessment studies in several important cities along the western coast of Sumatra, i.e., Padang, Painan, and Bengkulu, were performed using deterministic earthquake scenario approaches only (Borrero et al., 2006; Li et al., 2012). Therefore, it is important to apply the stochastic tsunami simulation method to assess the tsunami hazard in Padang probabilistically due to the future megathrust earthquakes in the Mentawai segment of the Sunda subduction zone.

The main objectives of this study are (1) to develop stochastic earthquake slip models for the future tsunamigenic earthquakes in the Mentawai segment of the Sunda subduction zone, (2) to evaluate the impact of stochastic earthquake slip on tsunami simulation results in terms of tsunami wave profiles and maximum tsunami height along the coastal line of Padang by considering the uncertainty and dependency of the earthquake source parameters, and (3) to assess the tsunami hazard in Padang using a wide range of earthquake scenarios generated from the novel stochastic tsunami simulation method. Extensive tsunami simulation for the future tsunamigenic earthquakes is conducted by developing a large number of stochastic earthquake slip models for different magnitude ranges. Three magnitudes, i.e., M_w 8.5, M_w 8.75, and M_w 9.0, are selected to develop stochastic source models. The earthquake source parameters from the finite-fault models of the past Sunda subduction earthquakes are first calculated and then compared with the global scaling relationships developed by Goda et al. (2016) to validate the applicability of the global models to the Sunda subduction zone. The verified scaling relationships are further used to generate the earthquake source models for tsunami simulation. Uncertainty and dependency of the earthquake source parameters are taken into account in producing earthquake source models stochastically which have not been implemented in the past studies of the tsunami hazard analysis in West of Sumatra. In total, 600 synthetic earthquake slip models are generated to obtain multiple realizations of maximum tsunami wave heights at various locations in Padang areas. For validation purposes, the simulated tsunami wave profiles for the M_w 9.0 scenario are used to compare with the results by Muhari et al. (2010) because they used M_w 8.92 to define their earthquake source scenario. The tsunami hazard analysis in Padang areas are further performed by evaluating the tsunami wave height profiles and the maximum tsunami wave height along the coastal line of Padang.

In this study, the tsunamigenic earthquake potential of the Mentawai segment in the Sunda subduction zone is first discussed. The earthquake source parameters from the finite-fault models of the past Sunda subduction are further evaluated to determine the applicability of the global scaling relationships for the Mentawai-Sunda subduction zone. A summary of the stochastic tsunami simulation used in this study is then presented, and the stochastic source models for the Mentawai-Sunda megathrust are further developed. Subsequently, the main tsunami simulation results using different earthquake source models in Padang areas are discussed. To demonstrate the tsunami simulation results in comparison to the previous work, the results for the M_w 9.0 scenario are presented first. The tsunami simulation results for the other scenarios are then discussed to evaluate the tsunami hazard potential in Padang areas. Finally, the key conclusions of this work are drawn.

TSUNAMI POTENTIAL OF THE MENTAWAWI-SUNDA MEGATHRUST ZONE

Extensive paleogeodetic, geodetic, and numerical modeling studies suggest that the potential of megathrust tsunamigenic earthquakes in the Mentawai segment of the Sunda subduction zone is high (Natawidjaja et al., 2006; McCloskey et al., 2008; Collings et al., 2012, 2013). The past seismicity in the Mentawai segment indicates that the most destructive historical event in this segment occurred in 1833. The shaking was reported from Bengkulu to Pariaman and near Pagai Islands. Tsunamis were observed along the western coast of Sumatra extending from Pariaman to Bengkulu due to this event. Bengkulu and Indrapura areas were greatly affected by the 1833 tsunamigenic event. The tsunami heights reaching 3–4 m were recorded near Padang. Another historical earthquake event occurred in 1797 produced a destructive tsunami at Padang and nearby. The shaking was the strongest in living memory in Padang, and the tsunami flow depth in Padang was about 5 m (Natawidjaja et al., 2006).

Rupture scenarios of the 1797 and 1833 earthquakes were developed based on the seismotectonic features, geodetic, and paleogeodetic measurements (see **Figure 2**). The seismotectonic study by Newcomb and McCan (1987) concluded that the rupture of the 1833 earthquake extended ~300 km from near Enggano Island in South to Batu Islands in North with the earthquake size of M_w 8.7–8.8. A paleogeodetic study by Natawidjaja et al. (2006) based on the measurements of the coral microatoll uplift confirmed that the uplift between 1 and 3 m occurred over a 170-km long stretch of the Sumatran outer arc ridge. Elastic dislocation modeling of those uplift data yielded the slip prediction of 9–18 m between 2°S and 5°S. The 220-km long rupture extension from the southern part of the uplift was defined as the south-eastern boundary of the 1833 fault rupture. In addition, the north-western limit of the rupture was likely to be at

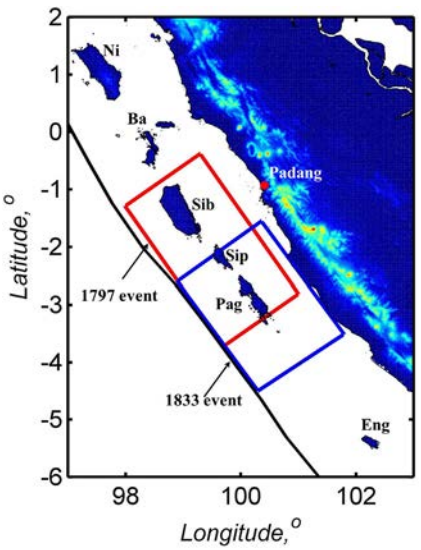

FIGURE 2 | Geometry of earthquake source models of the 1797 and 1833 events (Ni: Nias, Ba: Batu Islands, Sib: Sibereut, Sip: Siora, Pag: Pagai Islands, and Eng: Enggano).

2°S; the end point may be extended as much as 160 km farther North-West with much smaller amounts of slip. The North-West extension of 160 km beyond the rupture of the 1833 event was likely to stop at 0.5°S. The earthquake size was predicted in the range of M_w 8.7–8.9. On the other hand, the records of coral and microatoll uplift due to the 1797 earthquake showed that the 1797 event preceded the 1833 giant earthquake by 37 years. The south-eastern limit of the rupture was at about 3.2°S since the south-eastern limit of the uplift due to the 1797 event was on South Pagai Island. The slip was estimated to be in the range of 4–8 m with the depth from 34 to 50 km. In addition, the magnitude of the earthquake was estimated to be in the range of M_w 8.5–8.7 (Natawidjaja et al., 2006).

A recent significant earthquake occurred in the Mentawai segment was the M_w 8.4 12 September 2007 Bengkulu earthquake. Twelve hours later, a subsequent fault rupture produced another major earthquake of M_w 7.9. The geodetic and paleogeodetic modeling suggested that the rupture areas of these two events extended from North of Sipora Island at ~2°S to South of Pagai Islands at ~5°S. The maximum slip from this event is only a half of the maximum slip from the 1833 earthquake. Moreover, the total seismic moment released from the two earthquakes of Bengkulu in 2007 was significantly smaller than the 1833 rupture and the accumulated moment deficit since the last rupture in the Mentawai segment. Therefore, the potential for large tsunamigenic events in the Mentawai segment remains high (Konca et al., 2008). In addition, a 700-year sea-level change recorded in the corals of the Mentawai segment implies that the recurrence time of the major earthquakes, i.e., the sequence of the 1797 and 1833 earthquakes, is ~200 years (Sieh et al., 2008). At least two of the three ancient sequences began with events that were smaller than the main events and in this context, the 2007 earthquakes may be considered to be only the beginning of an episode of the rupture of the Sunda megathrust in the Mentawai segment (Sieh et al., 2008). The failure of the Mentawai segment may significantly affect the western coast of Sumatra specifically in Padang areas. With the plain topographic features and high population density in urban areas, Padang will face significant economic and social losses due to the future tsunamigenic event in the Mentawai segment of the Sunda subduction zone.

EARTHQUAKE SOURCE PARAMETERS FOR SUMATRA EARTHQUAKES

This study implements the stochastic tsunami simulation to assess the tsunami hazard in Padang areas. To run the stochastic tsunami simulation, earthquake source models need to be generated stochastically. Predicting the earthquake source parameters, i.e., the geometry of the fault, slip statistics, and spatial slip distribution parameters, are needed to generate earthquake source models. In order to generate the earthquake source parameters, the fault length (L), fault width (W), mean slip (D_a), maximum slip (D_m), Box–Cox parameter (λ), correlation length along strike direction (A_x), correlation length along dip direction (A_z), and Hurst number (H) of 19 finite-fault models of the past Sunda subduction earthquakes are calculated. The width, length, strike, and dip angles define the geometry of the fault plane, while the mean slip, maximum slip, and Box–Cox parameter characterize the slip statistics values. In addition, the correlation lengths and Hurst number are used to model the spatial heterogeneity of the slip values. Subsequently, the calculated earthquake source parameters of the past Sunda subduction earthquake are evaluated against the global scaling relationships developed by Goda et al. (2016). The global scaling relationships developed by Goda et al. (2016) will be adopted only if the calculated earthquake source parameters from the 19 finite-fault models of the Sunda subduction earthquakes are consistent with these global relationships. Otherwise, the global scaling relationship should be adjusted to account for the regional differences of the source parameters based on the finite-fault models of the past Sunda subduction earthquakes. Calculations of the earthquake source parameters of the finite-fault models from the past Sunda subduction earthquakes are based on the effective dimension analysis (Mai and Beroza, 2000), Box–Cox analysis, and spectral analysis (Mai and Beroza, 2002; Goda et al., 2014). The effective dimension analysis is carried out to calculate the width, length, mean slip, and maximum slip, while the Box–Cox analysis is used to characterize the probability distribution of the slip values. In addition, the spectral analysis is conducted to define the correlation lengths along dip and strike and the Hurst number. **Figure 3** illustrates the procedures of earthquake source parameter estimation using the Konca et al. (2007) model from the 2007 Bengkulu earthquake event.

First, the effective dimension analysis is carried out. The motivation to analyze the effective dimensions of the finite-fault models is because some of the finite-fault models have insignificant portions of slip located along the edges. The use of these

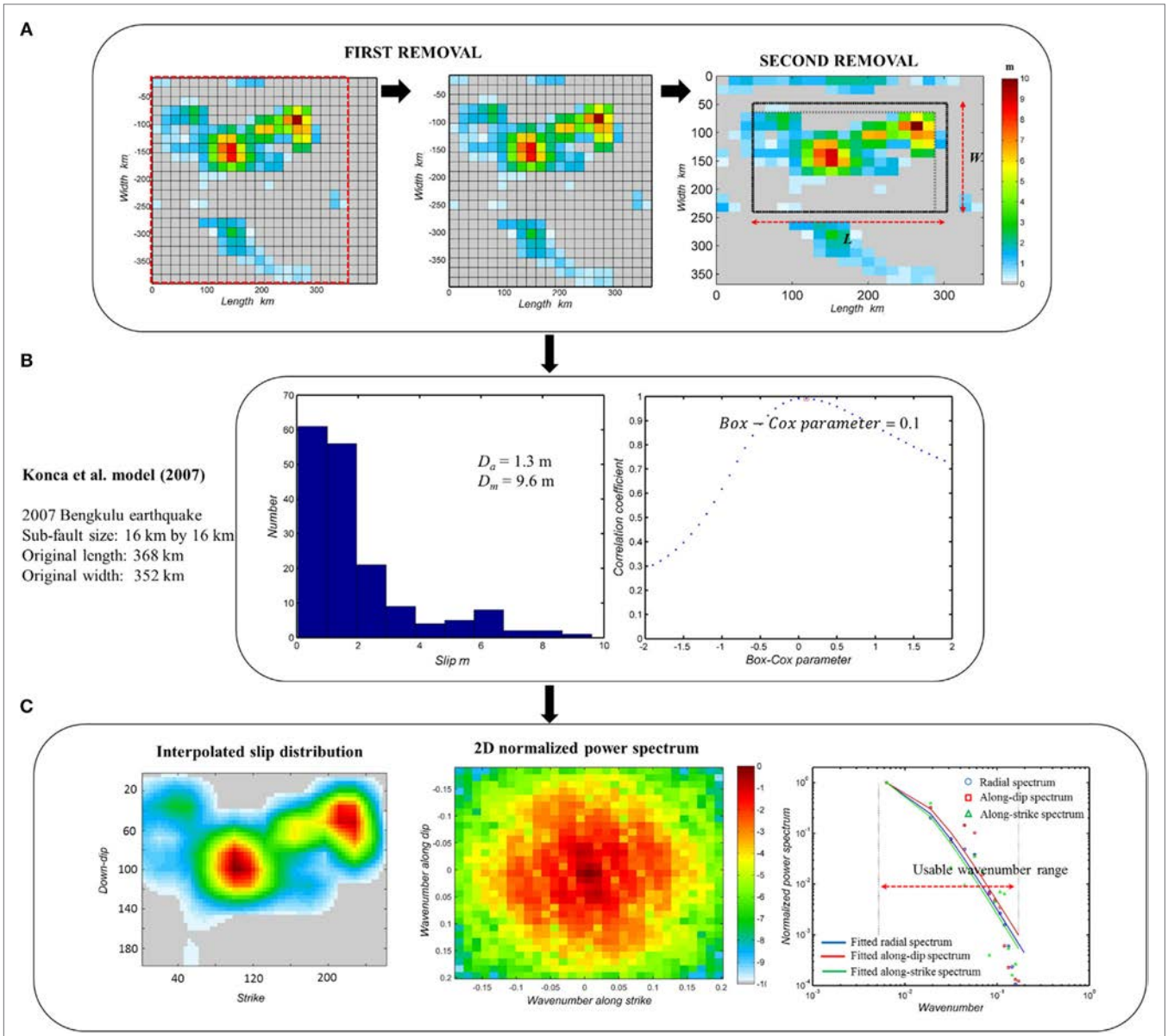

FIGURE 3 | **Procedures for source parameter estimation**. **(A)** Effective dimension analysis. **(B)** Box–Cox analysis. **(C)** Spectral analysis.

insignificant portions may lead to overestimation of the rupture area and hence, it should be excluded from the source models. The insignificant portions of earthquake slip are removed in two steps. The first step is to simply trim the slip distribution when rows/columns having zero slip exist along the edges of the slip distribution. As shown in **Figure 3A**, three rows having zero slips are removed to produce a trimmed slip distribution. The second step is to determine the effective width and length by calculating the auto-correlation dimensions as defined by Mai and Beroza (2000). These dimensions, i.e., effective width and length, are then defined as W and L, respectively. Using the results from effective dimension analysis, the slip statistics parameters, D_a and D_m, are calculated. The mean slip may be changed from the original mean slip due to the effective dimension analysis.

Second, using the effective dimension, the Box–Cox analysis is conducted to characterize the probability distribution of slip values within the fault plane by identifying the best power parameter (λ) to transform a non-normal random variable (X) to a normal random variable (Y) as presented in Eq. 1.

$$Y = \frac{X^{\lambda} - 1}{\lambda} (\lambda \# 0) \tag{1}$$

The Box–Cox parameters corresponds to the lognormal transformation if the $\lambda = 0$. The best power parameter (Box–Cox parameter) can be determined by calculating the linear

correlation coefficient of the standard normal variable and the transformed variable of the slip values (after standardization). The Box–Cox parameter (λ) is then obtained based on the value that achieves the maximum linear correlation coefficient (see **Figure 3B**).

Third, Fourier spectral analysis is carried out to calculate spatial heterogeneity parameters of the slip, i.e., A_x, A_z, and H. The Hurst number is used to characterize spectral decay as a function of wavenumber. Before carrying out spectral analysis, a cell-based grid of the finite-fault models is converted to a grid-based slip distribution and then the slip is interpolated using a selected grid spacing which is not smaller than one-fifth of the original grid resolution (left panel of **Figure 3C**). The interpolated grid-based slip distribution is then tapered using a Hanning window to control the edges of the rupture plane so that no significant slips occur along the rupture plane edges. Two-dimensional Fast Fourier Transform is calculated to obtain the 2D normalized power spectrum (middle panel of **Figure 3C**). The applicable wavenumber range for the spectral analysis is then defined by considering the original grid resolution and the characteristic size of the fault plane (right panel of **Figure 3C**). The circular average of the normalized wavenumber spectra is calculated, and the fractal dimension D_f is defined based on the least squares fitting. The Hurst number is then calculated after converting from the fractal dimension (i.e., $H = 3 - D_f$). Finally, A_z and A_x are obtained by minimizing the norm between the along-dip/along-strike wavenumber spectrum and the analytical von Kármán model (Mai and Beroza, 2002) calculated using Eq. 2 by varying the correlation length along-dip/along-strike.

$$P(k) \propto \frac{A_z A_x}{\left(1 + k^2\right)^{H+1}} \tag{2}$$

where $P(k)$ is the power spectrum of von Kármán model and k is the wavenumber defined as, $k = \left(A_z^{\,2} k_z^{\,2} + A_x^{\,2} k_x^{\,2}\right)^{0.5}$ (Goda et al., 2016).

The results of estimated source parameters for the nineteen source models are shown in **Table 1** and **Figure 4**. Fourteen from the 19 source models shown by model number 1–14 in **Table 1** are part of the 226 models used in Goda et al. (2015). In **Figure 4**, scaling relationships for tsunamigenic earthquakes by Goda et al. (2016) are also included. These equations are summarized in **Table 2**, noting that they are indeed probabilistic prediction models that allow characterizing the prediction errors. In the equations, epsilon terms represent the prediction errors of the equations, and furthermore, their correlation coefficients are given in **Table 3**. The results shown in **Figure 4** indicate that the estimated source parameters are in agreement with the scaling relationships; for most cases, the estimated parameters fall within the 16th to 84th percentile confidence interval of the prediction equations. Therefore, the use of the scaling relationships by Goda et al. (2016) for generating stochastic source models for the future tsunamigenic earthquakes in the Mentawai segment of the Sunda subduction zone can be justified. In **Figure 4**, the source parameters for the model 19 by Muhari et al. (2010) are shown with the red circle (see also **Table 1**). This model is used as a benchmark to be compared with stochastic tsunami simulation results in Padang areas.

STOCHASTIC TSUNAMI SIMULATION

The stochastic tsunami simulation can be conducted by generating multiple source models for a given earthquake scenario and by performing tsunami forward modeling iteratively. **Figure 5** presents a computational flowchart of the stochastic tsunami simulation. In the following, detailed procedures of

TABLE 1 | Summary of earthquake source parameters for the 19 finite-fault models of the Sumatra subduction earthquakes.

No	Date	M_w	W (km)	L (km)	Strike (°)	Dip (°)	Mean slip (m)	Maximum slip (m)	Box–Cox parameter	Correlation length along dip (km)	Correlation length along strike (km)	Hurst number	References
Model 1	26/12/2004	8.89	180	450	320	11	6.77	19.82	0.5	54.00	121.50	0.99	Ji (2005a)
Model 2	28/03/2005	8.68	220	340	326	8	3.14	12.50	0.4	64.60	98.80	0.99	Shao and Ji (2005)
Model 3	28/03/2005	8.5	192	304	325	10	2.13	15.20	0.0	58.24	99.84	0.83	Konca et al. (2007)
Model 4	28/03/2005	8.7	192	380	325	15	3.34	13.75	0.5	60.00	108.00	0.99	Ji (2005b)
Model 5	12/09/2007	7.9	90	225	319	19	0.68	3.89	0.3	31.30	84.51	0.99	Ji and Zeng (2007)
Model 6	12/09/2007	7.9	110	192	323	15	0.69	6.00	0.0	28.80	36.00	0.99	Konca et al. (2008)
Model 7	12/09/2007	7.9	100	168	319	19	0.83	7.40	−0.2	38.40	52.80	0.99	Sladen and Konca (2007)
Model 8	12/09/2007	8.5	225	300	328	9	1.55	5.44	0.1	64.00	80.00	0.99	Gusman et al. (2010)
Model 9	12/09/2007	8.4	159.5	460	323	12	1.08	3.61	0.7	56.00	100.80	0.99	Ji (2007)
Model 10	12/09/2007	8.4	192	256	324	15	1.30	9.60	0.1	44.00	68.00	0.46	Konca et al. (2008)
Model 11	20/02/2008	7.4	155	110	296	7.55	0.14	1.00	0.0	54.40	27.20	0.29	Hayes and Ji (2008)
Model 12	20/02/2008	7.4	112	152	302	7	0.15	1.08	−0.2	24.32	25.84	0.99	Sladen (2008)
Model 13	06/04/2010	7.8	144	144	313	12.04	0.43	3.17	−0.2	40.80	31.20	0.67	Hayes (2010a)
Model 14	09/05/2010	7.2	54	72	305	17.52	0.35	1.13	0.4	15.30	17.10	0.99	Hayes (2010b)
Model 15	25/10/2010	7.7	140	195	325	11.62	0.28	1.20	0.1	33.75	45.00	0.99	Hayes (2010c)
Model 16	25/10/2010	7.7	120	210	326	9.75	1.35	6.10	0.8	52.50	115.50	0.66	Satake et al. (2013)
Model 17	25/10/2010	7.7	72.5	180	324	7.5	4.10	23.41	0.2	25.20	41.40	0.99	Yue et al. (2014)
Model 18	25/10/2010	7.8	140	225	325	11.62	2.10	9.63	0.4	36.00	60.75	0.99	Newman et al. (2011)
Model 19	Future event	8.92	240	520	325	13.00	7.48	14.90	0.9	83.20	140.40	0.99	Muhari et al. (2010)

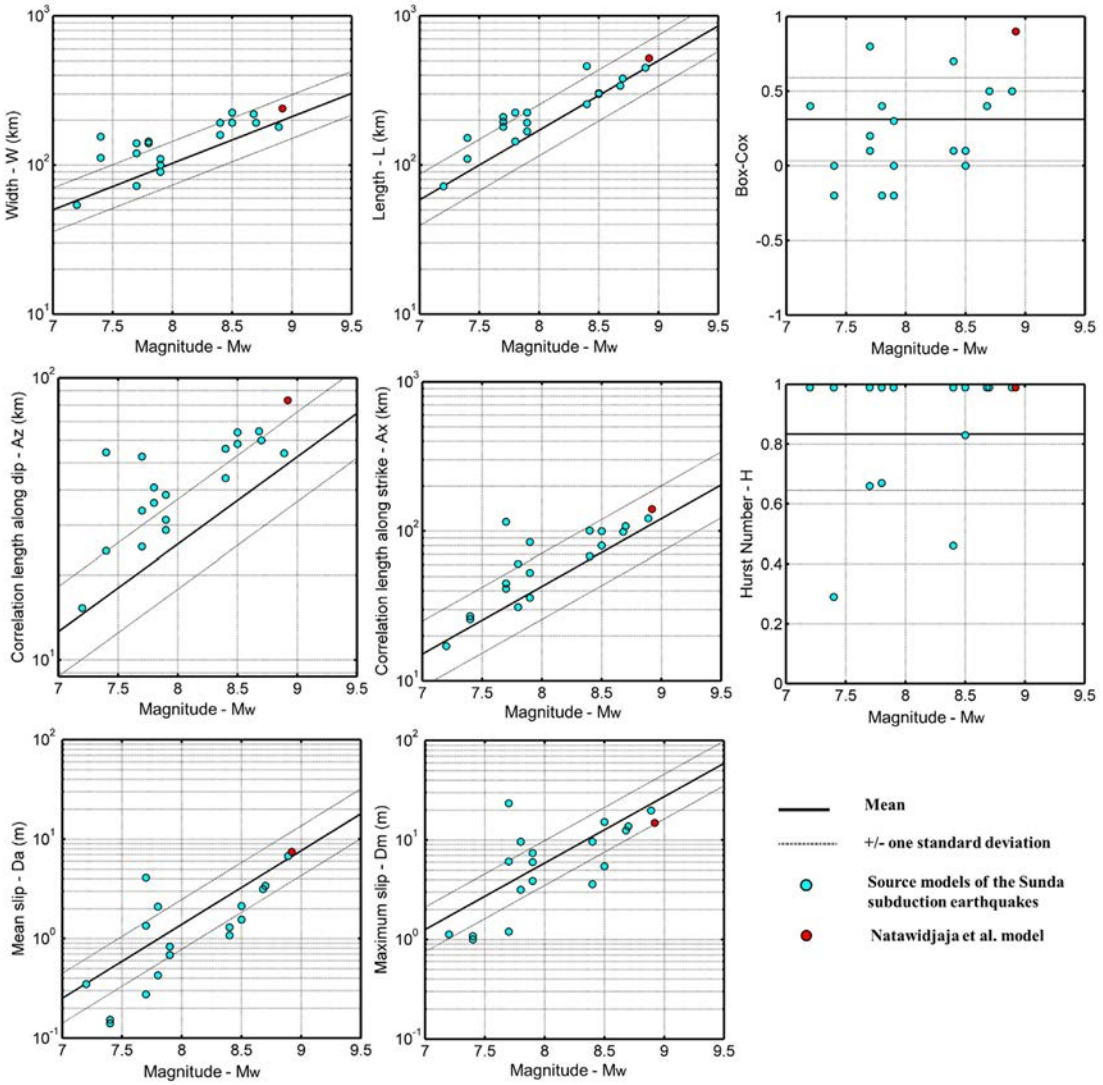

FIGURE 4 | Comparison of the estimated source parameters for the 19 finite-fault models of the Sunda subduction earthquakes with the corresponding scaling relationships.

TABLE 2 | Scaling relationships of the earthquake source parameters (Goda et al., 2016).

Parameter	Prediction models
W	$\log_{10}W = -0.4877 + 0.3125M_w + 0.1464\epsilon_W$
L	$\log_{10}L = -1.5021 + 0.4669M_w + 0.1717\epsilon_L$
D_a	$\log_{10} D_a = -5.7933 + 0.7420M_w + 0.2502\varepsilon_{D_a}$
D_m	$\log_{10} D_m = -4.5761 + 0.6681M_w + 0.2249\varepsilon_{D_m}$
A_z	$\log_{10} A_z = -1.0644 + 0.3093M_w + 0.1592\varepsilon_{A_z}$
A_x	$\log_{10} A_x = -1.9844 + 0.4520M_w + 0.2204\varepsilon_{A_x}$
Box–Cox power	A normal variable with mean = 0.312 and SD = 0.278
Hurst number	A value of 0.99 with probability of 0.43 and a normal variable with mean = 0.714 and SD = 0.172 with probability of 0.57

The prediction error terms of the scaling relationships are represented by epsilons, which are the standard normal variables (i.e., zero mean and unit SD).

TABLE 3 | Linear correlation coefficients of regression residuals of the scaling relationships for the six earthquake source parameters.

Variables	ε_W	ε_L	ε_{D_a}	ε_{D_m}	ε_{A_z}	ε_{A_x}
ε_W	1	0.139	−0.68	−0.545	0.826	0.035
ε_L	0.139	1	−0.595	−0.516	0.249	0.734
ε_{D_a}	−0.68	−0.595	1	0.835	−0.62	−0.374
ε_{D_m}	−0.545	−0.516	0.835	1	−0.564	−0.337
ε_{A_z}	0.826	0.249	−0.62	−0.564	1	0.288
ε_{A_x}	0.035	0.734	−0.374	−0.337	0.288	1

Note that the Box–Cox parameter and the Hurst number are considered to be independent.

the stochastic tsunami simulation for the future tsunamigenic earthquake in the Mentawai segment of the Sunda subduction zone are explained.

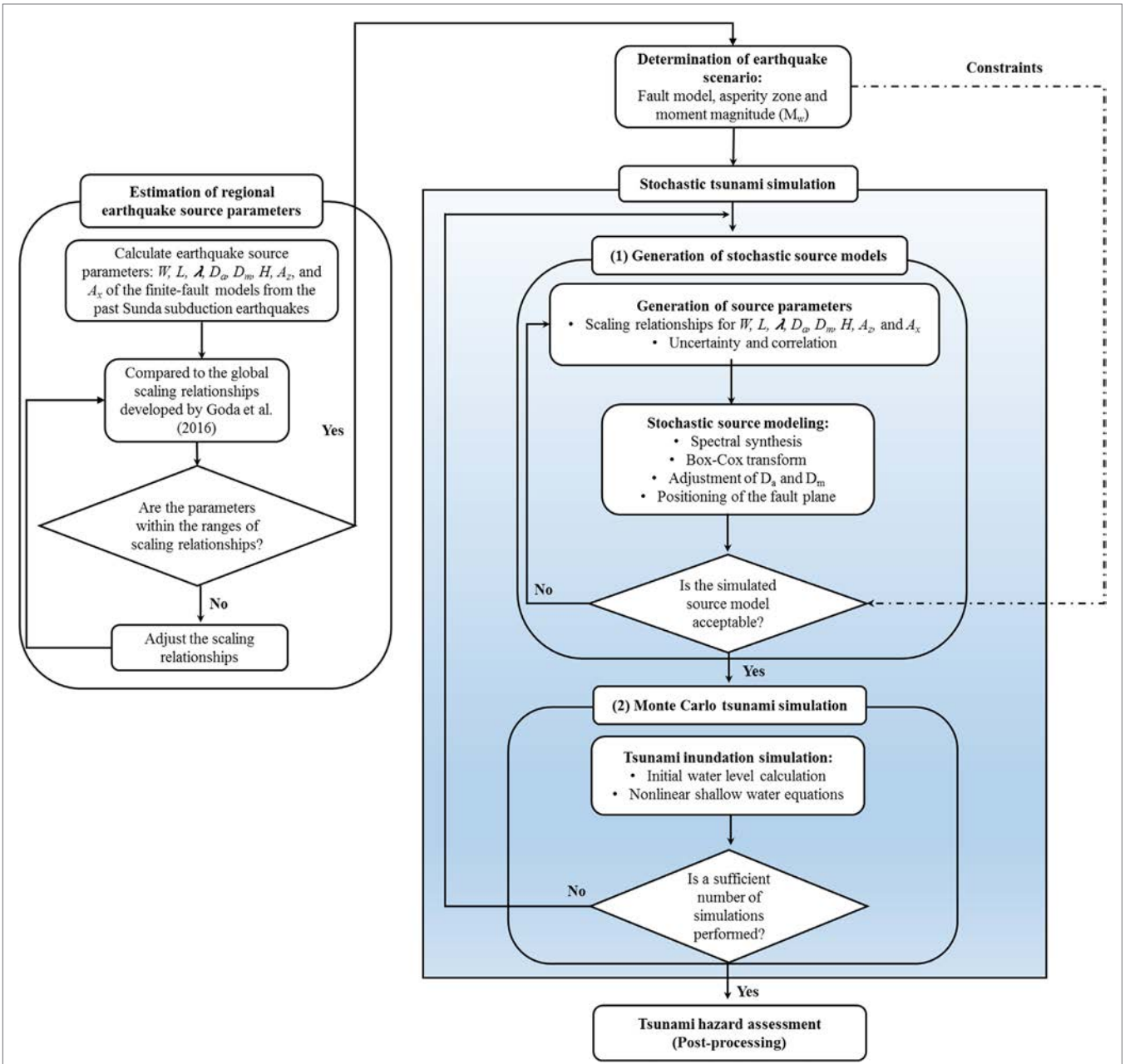

FIGURE 5 | **Flowchart of stochastic tsunami simulation**.

Earthquake Scenarios and Fault Zone Model

Before running the stochastic tsunami simulation, earthquake scenarios (e.g., magnitude and source zone) need to be selected and a suitable fault rupture zone model (e.g., geometry and asperity zone) needs to be defined. The fault plane is used to model the source zone of the earthquake, while within the fault plane the so-called asperity zone is set up. When generating stochastic earthquake source models, the source zone of the earthquake is needed to define the area of earthquake source and the asperity zone is essential as the concentration region for certain amount of slip. In addition, the selected magnitude should be determined based on the purpose of the analysis. Since this work aims at assessing the tsunami hazards in Padang due to megathrust earthquakes from the Mentawai segment of the Sunda subduction zone, three magnitudes are considered: M_w 8.5, M_w 8.75, and M_w 9.0.

First, a possible source zone of the future tsunamigenic earthquakes in the Mentawai segment is defined based on source models for the past Sunda subduction earthquakes. The 19 source models of the past Sunda subduction earthquakes are

used to determine the rupture areas for the future megathrust tsunamigenic earthquakes in the Mentawai segment (**Table 1**). The strike and dip angles of these models are typically in the range of 296° to 326° and 7° to 19°, respectively. A generic fault model covers the region of the Mentawai segment starting from North of Batu Islands to South of Enggano Island. The length and width of the Mentawai source zone are 920 and 250 km, respectively. The top-edge of the fault plane is located at a depth of 3 km. This depth is consistent with the past Mentawai finite-fault models developed for the 2010 Mentawai tsunamigenic earthquakes and the twin events of the 1797 and 1833 tsunamigenic Mentawai earthquakes which have the top-edge depth between 2 and 5 km (Newman et al., 2011; Satake et al., 2013; Philibosian et al., 2014; Yue et al., 2014). The fault plane has a constant strike angle of 325°. On the other hand, dip angles are varied depending on the depth. The dip angles for the depth from 3 to 10 km, from 10 to 17 km, from 17 to 29 km, and below 29 km are 8°, 10°, 12°, and 16°, respectively. These values are comparable to the slab models for the Sunda subduction zone produced by the USGS (Hayes et al., 2009, 2012). For stochastic source modeling and Monte

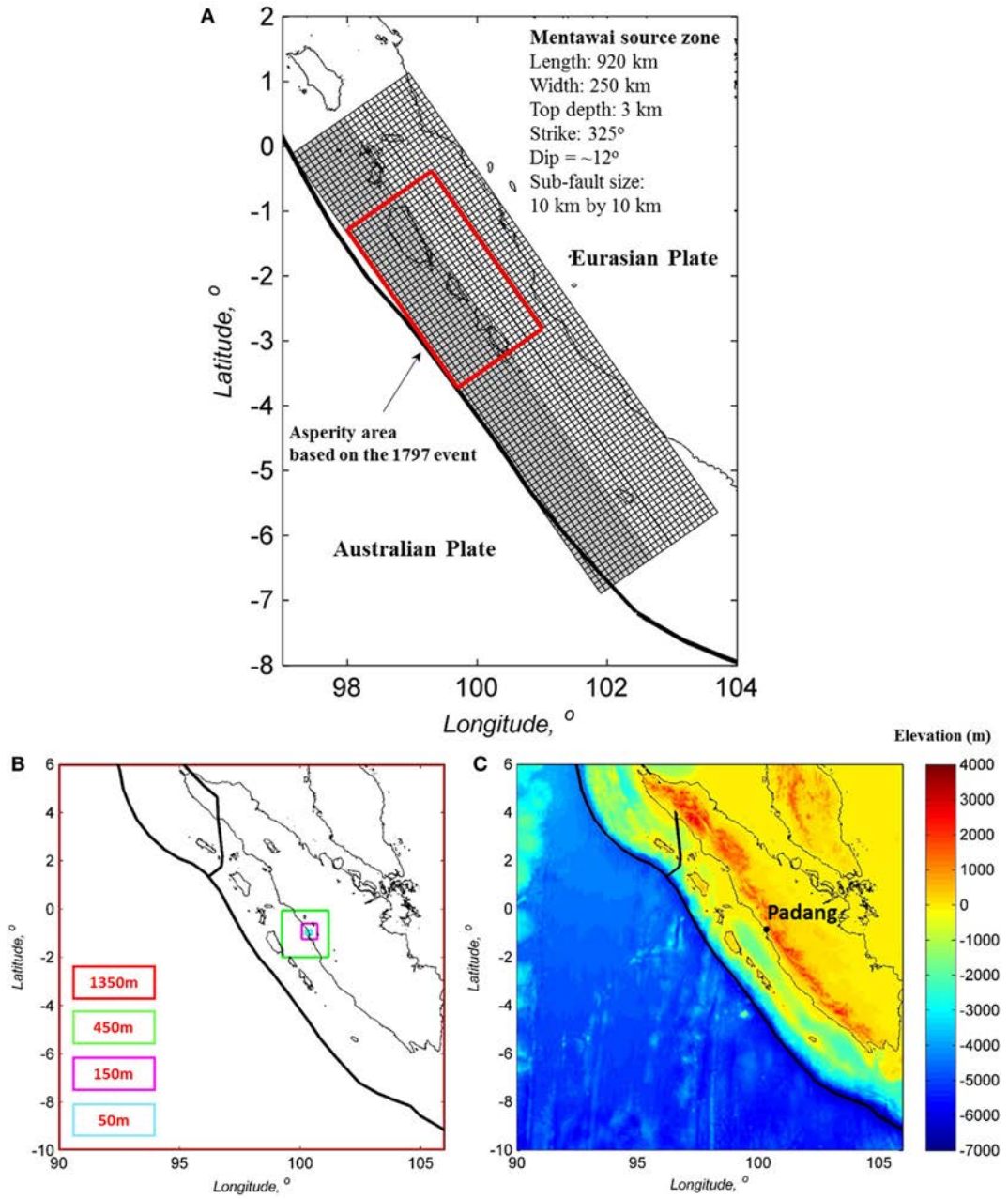

FIGURE 6 | **(A)** Tsunami source zone. **(B)** Nested grid system for tsunami simulation in Padang. **(C)** GEBCO2014 bathymetry for the Sumatra region.

Carlo simulation, the Mentawai source zone is discretized into 10 km by 10 km sub-faults. In stochastic source modeling, slip values that are consistent with considered spatial slip distribution features are generated.

Second, an asperity zone is set up within the fault plane of the source zone along with the required slip concentration range. The seismological knowledge of earthquake rupture in the target region must be reflected in the asperity zone. Basically, the asperity zone serves as crude constraints of the generated source model regarding the spatial distribution of earthquake slip within the fault plane. In generating the stochastic source models, a certain amount of slip must be concentrated within the target region. Generally, the determination of asperities of the future tsunamigenic earthquake in the Mentawai segment of the Sunda subduction zone is complex and involves large uncertainty (McCloskey et al., 2008; Philibosian et al., 2014). The interseismic coupling and coseismic slip modeling based on the paleogeodetic study confirm that the asperities in the Mentawai segment must be multiple. A future megathrust earthquake in the Mentawai segment may rupture similar to the scenarios of either the 1797 event or the 1833 event. This assumption is based on the paleogeodetic study that finds the potential of giant earthquakes is high in the Mentawai segment as the source earthquake region for the 1797 and 1833 events (Chlieh et al., 2008; Sieh et al., 2008). The asperity areas of the 1797 event are closer to Padang in comparison with those of the 1833 event (Philibosian et al., 2014). In addition, effects of the 1797 event in Padang in terms of ground shaking and flow depth were greater than the 1833 event. Therefore, the asperity zone of the future megathrust earthquake for tsunami hazard assessment in Padang is assumed to follow the asperity areas of the 1797 event (see **Figure 6A**).

Stochastic Tsunami Simulation

Essentially, the stochastic tsunami simulation involves two main calculations, i.e., generation of stochastic source models and Monte Carlo tsunami simulation (**Figure 5**). First, earthquake source parameters, i.e., W, L, D_a, D_m, λ, A_z, A_x, and H, are generated using the prediction models (**Tables 2** and **3**). The uncertainty and correlation associated with the prediction models are taken into account in sampling the values of the earthquake source parameters from the multivariate normal distribution. To control the consistency of the generated earthquake source

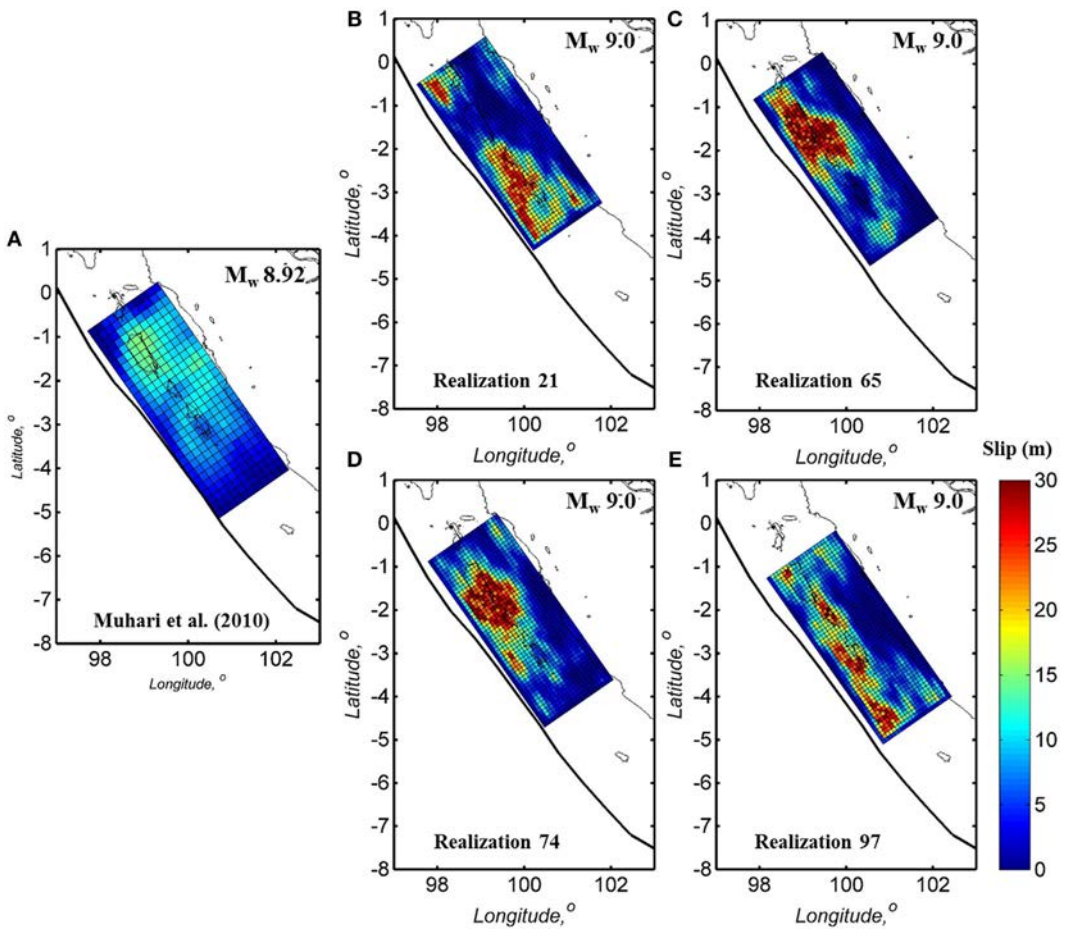

FIGURE 7 | **(A)** Muhari et al. source model. **(B–E)** Stochastic source models for the future tsunamigenic earthquake scenario without considering the uncertainty of the scaling relationships.

parameters, the simulated seismic moment ($M_o = \mu WLD_a$, where μ is the rock rigidity which is set to 40 GPa) is compared with the target seismic moment defined by the scenario magnitude. The combination of W, L, and D_a are calculated iteratively until the seismic moment criterion is satisfied (note: a tolerance of ±0.05 magnitude units is permitted).

Subsequently, a random slip field is generated using a Fourier integral method (Pardo-Iguzquiza and Chica-Olmo, 1993). The synthesized slip distribution is converted *via* Box–Cox transformation to achieve slip distribution with realistic positive skewness (Goda et al., 2014). To achieve the target mean slip D_a and to avoid very large slip values exceeding the target maximum slip D_m, the transformed slip distribution is further adjusted. Next, the synthesized fault plane position is randomly located within the source region. The final synthesized earthquake slip model should be consistent with the seismotectonic features of the target region. For this purpose, two criteria for acceptance of the candidate slip model are implemented, i.e., the asperity area ratio of the candidate slip distribution is within the range of 0.2 and 0.3 and the simulated earthquake slip is more concentrated in the considered asperity region with the percentage range of 50–80%. Multiple slip distributions are generated iteratively until an acceptable source model is obtained which has all the expected features.

Once a realistic stochastic source model is generated, the initial water surface elevation is calculated using Okada (1985) and Tanioka and Satake (1996) formulae which consider the deformation due to both vertical and horizontal displacements of seafloor. Tsunami wave propagation is then evaluated by solving non-linear shallow water equations with run-up (Goto et al., 1997). The effects of surface roughness on tsunami flows are modeled through the Manning's bottom friction formula with a uniform roughness coefficient of 0.025 $m^{-1/3}s$. The fault rupture is assumed to occur instantaneously, while the duration of the simulation is set to 2 h and the time step for the simulation is 0.5 s, which satisfies the C.F.L. criterion for the bathymetry and elevation data for the Mentawi region.

For tsunami forward modeling, digital elevation model (DEM) and bathymetry data are needed. For the western coast of Sumatra, the bathymetry and elevation data are constructed from the publicly available data, i.e., GEBCO2014 (http://www.gebco.net/data_and_products/gridded_bathymetry_data/) and GDEM2 (https://asterweb.jpl.nasa.gov/gdem.asp). The nested grid systems of bathymetry and DEM having four resolutions are developed to assess the tsunami hazard in Padang due to the future tsunamigenic earthquakes in the Mentawai segment. The crudest grid is 1,350 m, while the finest grid is 50 m. To connect grid systems with different resolutions, two grids having different grid resolutions by a factor of 3 are considered. Therefore, the nested grid resolutions to carry out tsunami simulation in Padang are 1,350, 450, 150, and 50 m (**Figure 6B**). The 1,350 m region covers the entire region of West Sumatra.

The GEBCO2014 dataset is adopted for bathymetry data with the resolution of 30 arc-sec (~900 m). The bathymetry plot of the Sumatra region from GEBCO2014 is presented in **Figure 6C**. For DEM, the GDEM2 dataset having the resolution of 1 arc-sec (~30 m) is used. In this study, bathymetry data with a 50-m resolution are adopted to run the tsunami simulation in the shallow water and land regions. To develop such bathymetry datasets, GEBCO2014, GDEM2, and SRTM Water Body Data (SWBD), are merged by considering the resolution of 1 arc-sec (same as GDEM2). The merging of the datasets is conducted by simply substituting NaN (Not a Number) values (i.e., ocean areas) in GDEM2 with the GEBCO2014 data at the same coordinate, while all land elevations from the GEBCO2014 data are neglected. In addition, the coastal line data from SWBD are defined as "zero" in the merged dataset. Subsequently, linear interpolation is performed to produce a 1 arc-sec of the merged data. The merged and interpolated data are used to produce a 50 m resolution dataset along the coastal line of Padang areas. The use of the linear interpolation scheme is deemed as appropriate over other more complex schemes, such as spline interpolation, because at the near coastal line areas (where drastic changes of the spatial density of the data points are inevitable), complex interpolation methods may over-interpolate the topographical features.

Finally, the above simulation procedure is run iteratively until a sufficient number of acceptable source models are generated and their tsunami inundation heights at locations of interest are evaluated. The results from the Monte Carlo tsunami simulation are useful for evaluating variability of tsunami simulation results at different locations and for developing stochastic tsunami hazard maps (Goda et al., 2014).

RESULTS AND DISCUSSION

The tsunami simulation results including the simulated tsunami wave height profiles and maximum tsunami heights along the coastal line are presented in this section by considering three magnitude scenarios (M_w 8.5, 8.75, and 9.0) and two cases ignoring and incorporating the uncertainty of the scaling relationships. The motivation to involve the uncertainty of the scaling relationships in the analysis is to assess the effect of incorporating the uncertainty of the scaling relationships to the tsunami simulation results. In addition, the height presenting in this section corresponds to the height of water flow above sea level. For each combination of magnitude scenario and uncertainty case, 100 stochastic source models are generated and used in Monte Carlo tsunami simulation. The stochastic tsunami simulation results from the M_w 9.0 scenario are used to investigate the sensitivity of the tsunami simulated wave profile and are compared with the reference results based on the Muhari et al. source model.

Tsunami Simulation Results: M_w 9.0 Scenario

Using the stochastic tsunami simulation results for the M_w 9.0 scenario, sensitivity analysis of the tsunami simulated wave profiles is carried out and presented in this section. The simulated tsunami wave profiles produced from Muhari et al. (2010) are used as a benchmark to demonstrate the tsunami simulation results. The earthquake source model considered by Muhari et al. (2010) is shown in **Figure 7A**. The model

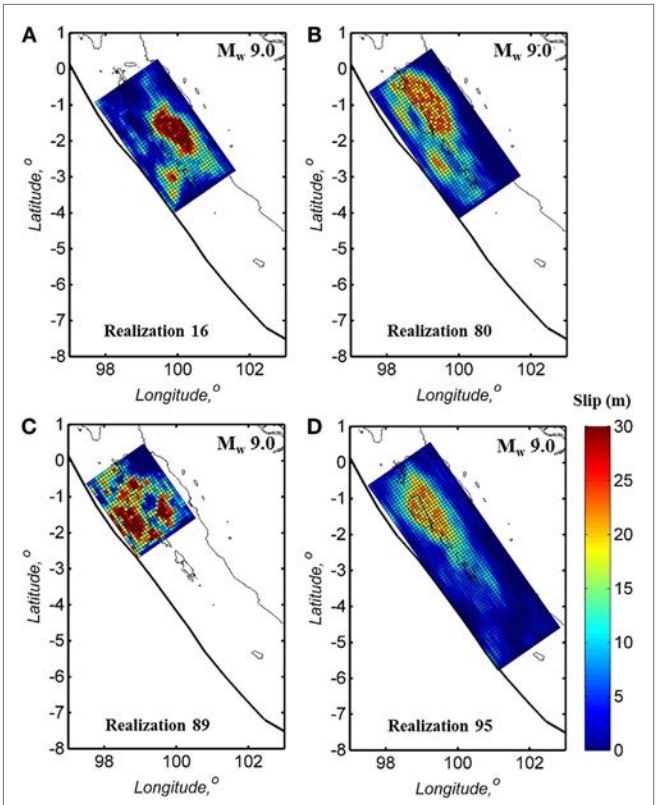

FIGURE 8 | **(A–D)** Stochastic source models for the future tsunamigenic earthquake scenario by considering the uncertainty of the scaling relationships.

was developed based on the slip accumulation of the current locked zone in the Mentawai segment with the total sub-fault number of 348 and the sub-fault size of 20 km by 20 km. Its moment magnitude was M_w 8.92. The comparison results show that the Muhari et al. model is in agreement with the global scaling relationships (**Figure 4**). For each tsunami simulation run, tsunami waveforms are recorded at three points with the water depth of 5 m: Tabing (0.85°S and 100.34°E), Purus (0.88°S and 100.345°E), and Teluk Bayur (1°S and 100.38°E) as shown in **Figure 9A**. These points are selected because they were also considered by Muhari et al. (2010). In addition, the maximum tsunami wave height contours are recorded to investigate the inundated area in Padang.

Two sets of 100 stochastic source models are generated for the M_w 9.0 earthquake scenario to carry out the Monte Carlo tsunami simulation. The first set takes into account the uncertainty of the scaling relationships of the source models, while the second set does not. **Figures 7** and **8** illustrate four realizations of the stochastic source models for the cases of including and excluding the uncertainty of the scaling relationships, respectively. The figures show that neglecting the uncertainty of the scaling relationships leads to identical dimensions (L and W) of the generated earthquake source models and the same slip statistics values for different realizations. For example, the generated values of D_a and D_m for the M_w 9.0 scenario are 8 and 30 m, respectively, while the spatial slip distribution and location of the fault rupture within the overall source zone are varied. By contrast, incorporating the uncertainty of the scaling relationships results in variability of dimensions and slip statistics.

The tsunami wave profiles at three recording points produced from the 100 stochastic source models for the M_w 9.0 scenario generated without considering the uncertainty of the scaling relationships (**Figure 7**) are shown in the middle panels of **Figures 9B–D**, whereas similar results obtained based on the Muhari et al. source model are shown in the top panels of **Figures 9B–D**. The raw simulated data are shown with gray color and the median and 10th/90th percentiles of the simulated tsunami waveforms are illustrated with red line and blue line, respectively. Large variations in the temporal tsunami wave profiles are observed at the recording points 1 to 3 (P1 to P3). For instance, at the Teluk Bayur station (P3), the variations in the simulated results range from −5 to 15 m, while the range between the 10th and 90th percentiles varies from −5 to 12.5 m. These trends are also observed at the other two stations. The medians of the simulated tsunami wave profiles recorded at three stations demonstrate results that are comparable to the Muhari et al. model with the maximum tsunami height of about 5 m. In addition, the tsunami arrival time to the coastal areas of Padang based on the median simulation results and Muhari et al. results are also consistent, i.e., 20–25 min after the event. Furthermore, the tsunami simulation results based on the 100 stochastic source models generated by incorporating the uncertainty of the scaling relationships for the M_w 9.0 (**Figure 8**) are presented. The simulated tsunami wave profiles at three recording points are shown in the bottom panels of **Figures 9B–D**. In general, the medians of tsunami wave profiles are similar to those produced without considering the uncertainty of the scaling relationships. Large variations in tsunami wave heights are observed at those three points with the maximum tsunami height of 15 m. From the medians of the tsunami waveforms at three recording points, consistent tsunami waveforms compared to the Muhari et al. results are also demonstrated.

To evaluate the differences of tsunami simulation results between excluding and including the uncertainty of the scaling relationships, 150 points are selected to record the maximum tsunami wave height along the coastal line of Padang starting from Tabing to Teluk Bayur (see **Figure 10A**). The median and the 10th/90th percentiles of maximum tsunami wave height profiles along the coastal line of Padang are shown in **Figure 10B**. In addition, the maximum tsunami wave height profiles from the 200 stochastic models excluding the uncertainty and including the uncertainty are presented in **Figures 10C,D**, respectively. The ranges between the 10th/90th percentiles of the maximum tsunami heights from those two cases show that the models with the uncertainty have greater variability in comparison to the models without the uncertainty. The range of the maximum tsunami wave height of the models considering the uncertainty is between 2.5 and 20 m, while the corresponding range for the models excluding the uncertainty is between 5 and 17.5 m.

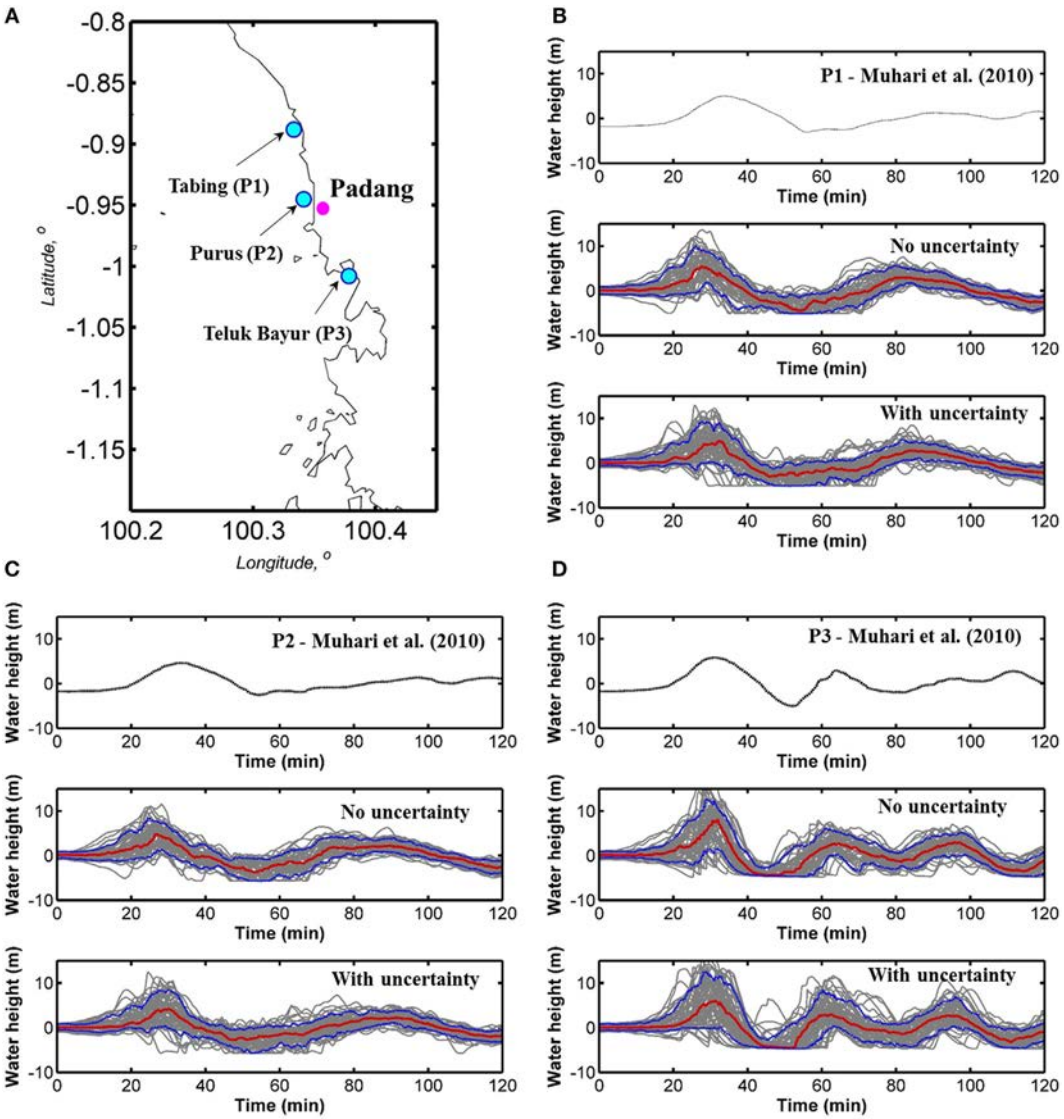

FIGURE 9 | **(A)** Site location. **(B)** Tsunami wave profiles at the Tabing station (P1). **(C)** Tsunami wave profiles at the Purus station (P2). **(D)** Tsunami wave profiles at the Teluk Bayur station (P3).

However, as observed from the tsunami wave profiles at the three recording stations, i.e., Tabing, Purus, and Teluk Bayur stations, the median of maximum tsunami wave profiles produced from these two calculation cases are similar (see black and green lines in **Figure 10A**).

Tsunami Hazard Assessment in Padang: All Magnitude Scenarios

The tsunami simulation results produced from different magnitude scenarios are presented in this section. **Figures 11–13** show the tsunami waveform results based on the stochastic source models for three scenario magnitudes, i.e., M_w 8.5, M_w 8.75, and M_w 9.0, both including and excluding the uncertainty of the scaling relationships recorded in Tabing, Purus, and Teluk Bayur stations, respectively. One hundred stochastic source models are used to run the tsunami simulation for each magnitude and uncertainty consideration (600 cases in total). In general, the large variation of wave amplitudes from the 10th and 90th percentile curves suggests that the earthquake slip model is an important source of uncertainty for the tsunami prediction. In addition, the tsunami waveforms from all three locations exhibit that the variation of tsunami wave heights increases with the magnitude. It can be seen that the 10th and 90th percentile curves vary significantly from the M_w 8.5 scenario to the M_w 9.0 scenario. For instance, at the Tabing station (P1), the percentiles range from −2 to 2 m for the M_w 8.5 scenario and the range increases to −5 to 10 m for the M_w 9.0 scenario. The median of the tsunami waveforms

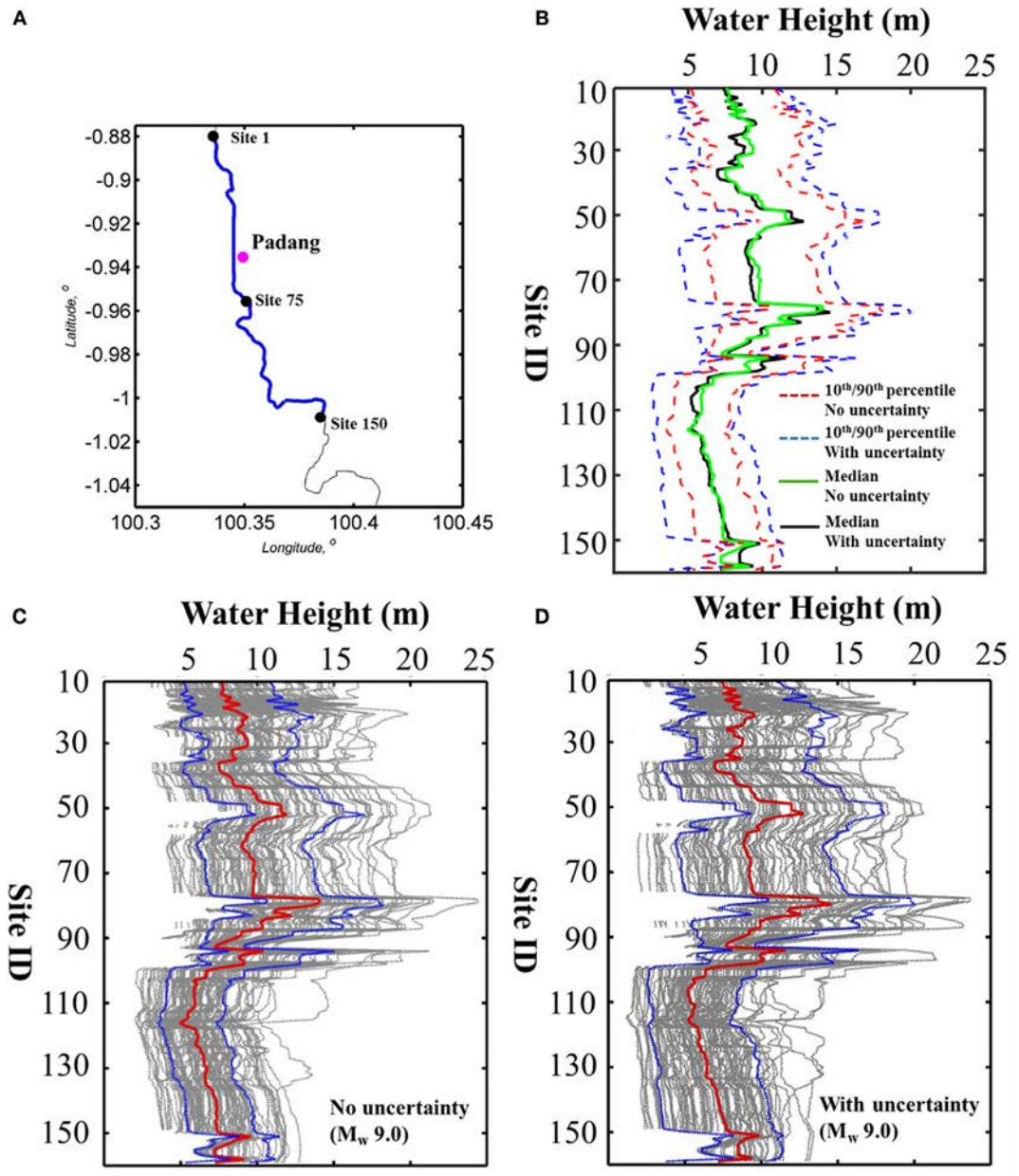

FIGURE 10 | **(A)** Site location. **(B)** 10th/90th percentile of maximum tsunami wave height along the coastal line. **(C)** Maximum tsunami wave height profile along the coastal line without incorporating uncertainty. **(D)** Maximum tsunami wave height profile along the coastal line by incorporating uncertainty.

shows that the tsunami wave height increases by a factor of 2 for the increasing magnitude by 0.25 U. Additionally, the tsunami hazard in Padang areas can also be assessed from the maximum tsunami wave height along the coastal line of Padang areas (see **Figure 10**). These data show that the maximum tsunami wave height in Padang can reach 20 m in urban areas (Tabing–Purus) where many important public facilities exist (e.g., school, hospital, and gas station). Therefore, the economic and social losses can be significant.

Another important characteristic illustrated from the tsunami wave profiles for all scenarios is the feature of secondary waves (second and third waves) which are important to design an evacuation plan for the areas of interest. As presented at P1 and P3, the secondary wave heights for the scenarios of M_w 8.5 and M_w 8.75 are insignificant with the heights of below 1 m. However, the heights increase significantly when the M_w 9.0 scenario are considered. The medians of the second waves in Tabing and Purus areas (P1 and P2) reach ~3 m for both uncertainty considerations with

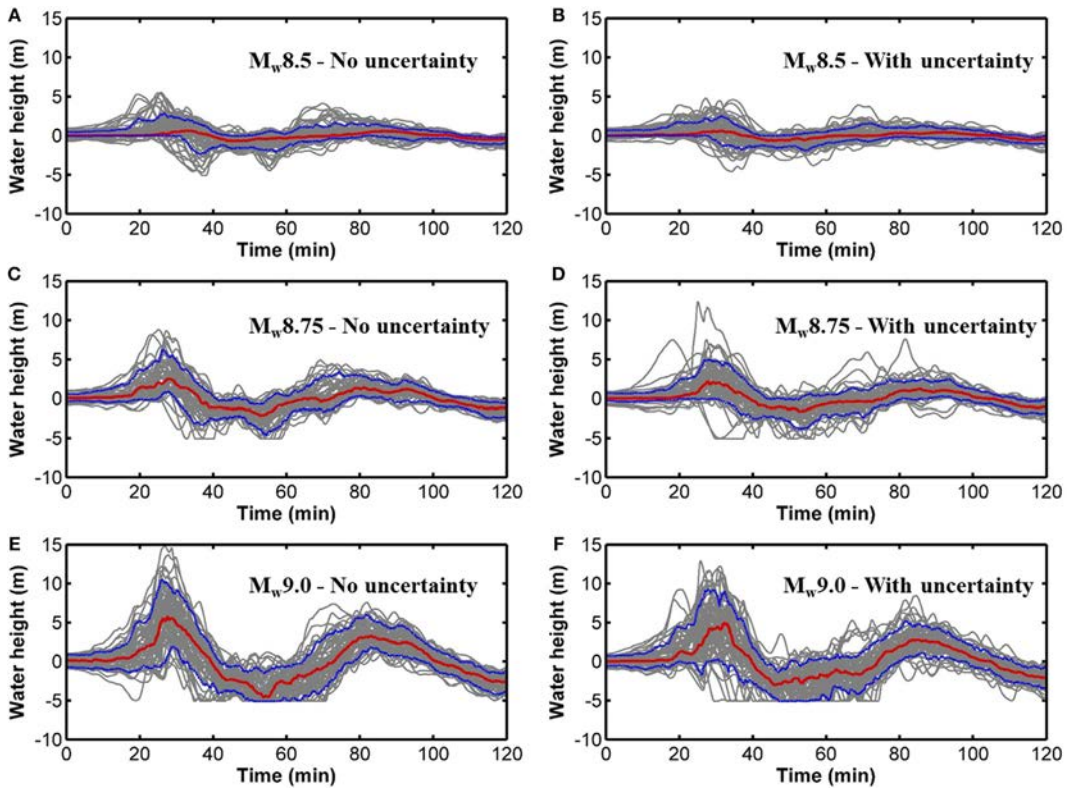

FIGURE 11 | Tsunami wave profiles at the Tabing station (P1). **(A)** M_w 8.5 scenario without considering uncertainty. **(B)** M_w 8.5 scenario considering uncertainty. **(C)** M_w 8.75 scenario without considering uncertainty. **(D)** M_w 8.75 scenario considering uncertainty. **(E)** M_w 9.0 scenario without considering uncertainty. **(F)** M_w 9.0 scenario considering uncertainty.

the maximum height of 5 m for the 90th percentile. In the Teluk Bayur region (P3), the second and third waves increase drastically with the increasing magnitude. For instance, the maximum height from the 90th percentile of the second and third waves for the M_w 9.0 scenario without considering the uncertainty is ~5 m, while it is ~7.5 m for the case considering the uncertainty of the scaling relationships. The striking times of the second and third waves in those three locations are in the range of 60–90 min, respectively. With the expected maximum height of the secondary waves as much as 7.5 m within the period of 90 min after the earthquake, people living within the coastal region of Padang must evacuate earlier and stay out of the inundated areas otherwise the secondary waves may cause additional human loses. Moreover, by neglecting the uncertainty of the scaling relationships in generating the earthquake scenarios for the worst case (M_w 9.0), the tsunami hazard in terms of the maximum secondary wave heights is underestimated and hence, may oversimplify the evacuation plan in the target region.

The tsunami hazard evaluations using multiple scenarios show that Padang may face a significant risk due to the future tsunamigenic event from the Mentawai segment. In comparison to the multiple-earthquake scenario approach, a deterministic scenario is not complex and requires a less computational effort. Although the single scenario approach is straightforward to communicate with the hazard results with emergency officers and relevant stakeholders, the multiple-scenario approach can produce a greater range of tsunami scenarios and therefore, more informed decisions regarding evacuation and mitigation actions can be made. In addition, for the risk assessment, the worst scenarios may be more relevant for critical facilities, such as public evacuation facilities. It is critically important to capture the most devastating effect that may occur in the target region. Using the stochastic tsunami simulation approach, the worst scenario ($M_w > 9.0$ at different percentile levels) can be considered to predict the future tsunamigenic earthquake impact, and therefore, a probabilistic approach is recommended to be implemented for preparing a better tsunami mitigation system for the future event.

CONCLUSION

The main objective of this study was to assess the tsunami hazard in Padang due to the future tsunamigenic event from the Mentawai source region in terms of near-shore tsunami wave profiles and maximum tsunami wave height data along the coastal of Padang using a novel method namely stochastic tsunami simulation. Extensive tsunami simulation for the future tsunamigenic earthquakes was conducted by developing a large number of

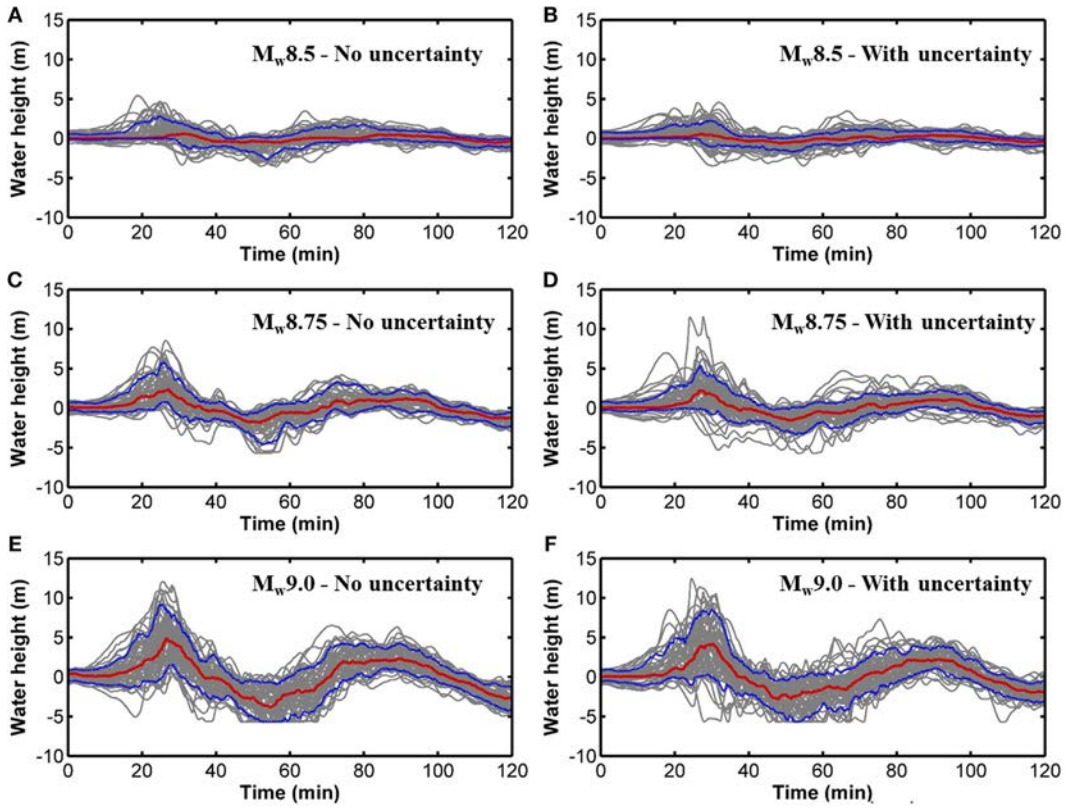

FIGURE 12 | Tsunami wave profiles at the Purus station (P2). **(A)** M_w 8.5 scenario without considering uncertainty. **(B)** M_w 8.5 scenario considering uncertainty. **(C)** M_w 8.75 scenario without considering uncertainty. **(D)** M_w 8.75 scenario considering uncertainty. **(E)** M_w 9.0 scenario without considering uncertainty. **(F)** M_w 9.0 scenario considering uncertainty.

stochastic earthquake slip models for different magnitude ranges. The earthquake source parameters from the finite-fault models of the past Sunda subduction earthquakes were firstly calculated and then compared with the corresponding scaling relationships for global tsunamigenic earthquakes developed by Goda et al. (2016). The verified scaling relationships were further used to build the earthquake source models for tsunami simulation. Uncertainty and dependency of earthquake source parameters were taken into account in producing earthquake source models stochastically. In total, 600 synthetic earthquake slip models were generated to obtain multiple realizations of maximum tsunami wave heights at various locations in Padang areas. Three scenarios magnitudes, i.e., M_w 8.5, M_w 8.75, and M_w 9.0, were considered to generate the stochastic earthquake source models, while the asperity zone was based on the significant slip areas from the 1797 tsunamigenic event. The simulated tsunami wave profiles from the M_w 9.0 scenario were compared with the results from Muhari et al. (2010) that predicted the tsunami hazard in Padang areas using the earthquake source models developed from the slip accumulation. The tsunami hazard in Padang was further evaluated using the tsunami wave profiles and maximum tsunami wave height data based on 600 stochastic tsunami simulations.

The stochastic earthquake source models for the future tsunamigenic earthquake in the Mentawai segment of the Sunda subduction zone have been successfully developed and further used in stochastic tsunami simulation. The estimated median of the simulated tsunami wave profiles produced from stochastic tsunami simulation is acceptable in comparison to the results from Muhari et al. (2010). Incorporating the uncertainty of the scaling relationships results in a larger variability of tsunami hazard parameters in comparison to excluding the uncertainty of the scaling relationships. The magnitude of earthquake scenarios has significant influence on the hazard assessment. In particular, the tsunami hazard assessment in Padang indicated that this region may experience a significant tsunami event with the maximum inundation height of 20 m in main urban areas (Tabing-Purus). Therefore, it can be concluded that the tsunami risk potential in Padang is high due to the future tsunamigenic event from the Mentawai segment of the Sunda subduction zone. Importantly, multiple scenarios of tsunami simulation using the stochastic methodology can produce a greater range of tsunami scenarios and hence, can inform emergency officers and stakeholders of the tsunami risk for improving the better tsunami mitigation system in the target region.

AUTHOR CONTRIBUTIONS

The three co-authors contributed equally to this work.

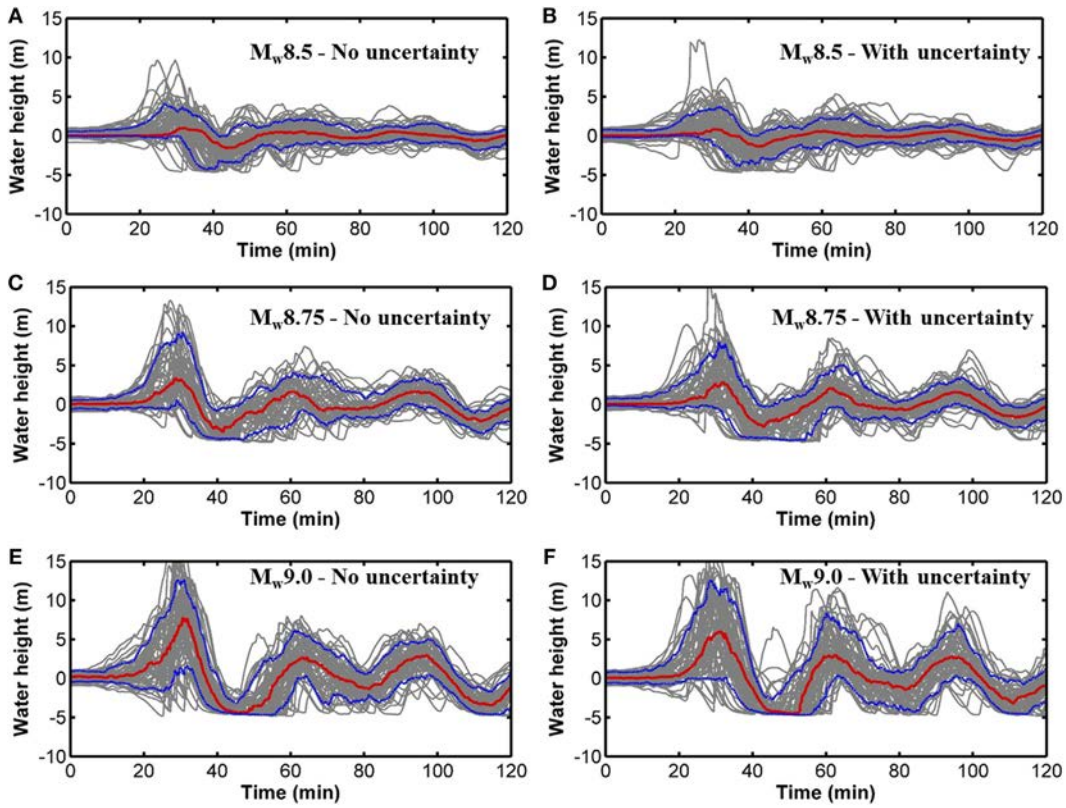

FIGURE 13 | Tsunami wave profiles at the Teluk Bayur station (P3). **(A)** M_w 8.5 scenario without considering uncertainty. **(B)** M_w 8.5 scenario considering uncertainty. **(C)** M_w 8.75 scenario without considering uncertainty. **(D)** M_w 8.75 scenario considering uncertainty. **(E)** M_w 9.0 scenario without considering uncertainty. **(F)** M_w 9.0 scenario considering uncertainty.

ACKNOWLEDGMENTS

The first author is grateful to the Directorate General of Resources for Science, Technology and Higher Education, Ministry of Research, Technology and Higher Education of Indonesia which sponsor his PhD study. This work is also funded by the Engineering and Physical Sciences Research Council (EP/M001067/1). The bathymetry and elevation data for the Sumatra region were obtained from the GEBCO2014 database (http://www.gebco.net/data_and_products/gridded_bathymetry_data/) and the GDEM2 database (https://asterweb.jpl.nasa.gov/gdem.asp), respectively. The authors are grateful to Abdul Muhari, Hilman Natawidjaja, and Widjo Kongko who provide an earthquake source model for the future tsunamigenic event in the Mentawai segment and the bathymetry and elevation data for Padang.

REFERENCES

Aydan, O. (2008). Seismic and tsunami hazard potentials in Indonesia with a special emphasis on Sumatra Island. *J. Sch. Mar. Sci. Tech.* 6, 19–38.

Banerjee, P., Nagarajan, B., Burgmann, R., and Pollitz, F. (2007). Coseismic slip distributions of the 26 December 2004 Sumatra-Andaman and 28 March 2005 Nias earthquakes from GPS static offsets. *Bull. Seismol. Soc. Am.* 97, S86–S102. doi:10.1785/0120050609

Borrero, J. C., Sieh, K., Chlieh, M., and Synolakis, C. E. (2006). Tsunami inundation modeling for western Sumatra. *Proc. Natl. Acad. Sci. U.S.A.* 103, 19673–19677. doi:10.1073/pnas.0604069103

Briggs, R. W., Sieh, K., Meltzner, A. J., Natawidjaja, D., Galetzka, J., Suwargadi, B., et al. (2006). Deformation and slip along the Sunda megathrust in the great 2005 Nias-Simeulue earthquake. *Science* 311, 1897–1901. doi:10.1126/science.1122602

Chlieh, M., Avouac, J. P., Sieh, K., Natawidjaja, D. H., and Galetzka, J. (2008). Heterogeneous coupling of the Sumatran megathrust constrained by geodetic and paleogeodetic measurements. *J. Geophys. Res.* 113, 1–31. doi:10.1029/2007JB004981

Collings, R., Lange, D., Rietbrock, A., Tilmann, F., Natawidjaja, D., Suwargadi, B., et al. (2012). Structure and seismogenic properties of the Mentawai segment of the Sumatra subduction zone revealed by local earthquake traveltime tomography. *J. Geophys. Res.* 117, B01312. doi:10.1029/2011JB008469

Collings, R., Rietbrock, A., Lange, D., Tilmann, F., Nippress, S., and Natawidjaja, D. (2013). Seismic anisotropy in the Sumatra subduction zone. *J. Geophys. Res. Solid Earth.* 118, 5372–5390. doi:10.1002/jgrb.50157

Gallovič, F., and Brokešová, J. (2004). On strong ground motion synthesis with k^{-2} slip distributions. *J. Seismol.* 8, 211–224. doi:10.1023/B:JOSE.0000021438.79877.58

Goda, K., Mai, P. M., Yasuda, T., and Mori, N. (2014). Sensitivity of tsunami wave profiles and inundation simulations to earthquake slip and fault geometry for the 2011 Tohoku earthquake. *Earth Planet Space* 66, 105. doi:10.1186/1880-5981-66-105

Goda, K., Yasuda, T., Mori, N., and Mai, P. M. (2015). Variability of tsunami inundation footprints considering stochastic scenarios based on a 2 single rupture

model: application to the 2011 Tohoku earthquake. *J. Geophys. Res. Oceans* 120, 4552–4575. doi:10.1002/2014JC010626

Goda, K., Yasuda, T., Mori, N., and Maruyama, T. (2016). New scaling relationships of earthquake source parameters for stochastic tsunami simulation. *Coastal Eng. J.* 58, 40. doi:10.1142/S0578563416500108

Goto, C., Ogawa, Y., Shuto, N., and Imamura, F. (1997). *Numerical Method of Tsunami Simulation with the Leap-Frog Scheme. IOC Manual*. Paris, France: UNESCO. UNESCO, No. 35.

Griffin, J. D., Pranantyo, I. R., Kongko, W., Haunan, A., Robiana, R., Miller, V., et al. (2016). "Assessing tsunami hazard using heterogeneous slip models in the Mentawai Islands, Indonesia," in *Geohazards in Indonesia: Earth Science for Disaster Risk Reduction*, eds P. R.Cummins and I.Meilano (London: Geological Society). Special Publications, 441.

Gusman, A. R., Tanioka, Y., Kobayashi, T., Latief, H., and Pandoe, W. (2010). Slip distribution of the 2007 Bengkulu earthquake inferred from tsunami waveforms and InSAR data. *J. Geophys. Res.* 115, B12316. doi:10.1029/2010JB007565

Hayes, G. P. (2010a). *Updated Result of the Apr 6, 2010 Northern Sumatra Earthquake*. Available at: http://equake-rc.info/SRCMOD/

Hayes, G. P. (2010b). *Preliminary Result of the May 9, 2010 Mw 7.2 Northern Sumatra Earthquake*. Available at: http://equake-rc.info/SRCMOD/

Hayes, G. P. (2010c). *Result of the Oct 25, 2010 Mw 7.7 Southern Sumatra Earthquake*. Available at: http://equake-rc.info/SRCMOD/

Hayes, G. P., and Ji, C. (2008). *Preliminary Result of the Feb 20, 2008 Mw 7.4 Simeulue Earthquake*. Available at: http://equake-rc.info/SRCMOD/

Hayes, G. P., Wald, D. J., and Johnson, R. L. (2012). Slab1.0: a three-dimensional model of global subduction zone geometries. *J. Geophys. Res.* 117, B01302. doi:10.1029/2011JB008524

Hayes, G. P., Wald, D. J., and Keranen, K. (2009). Advancing techniques to constrain the geometry of the seismic rupture plane on subduction interfaces a priori – higher order functional fits. *Geochem. Geophys. Geosyst.* 10, Q09006. doi:10.1029/2009GC002633

Hsu, Y. J., Simons, M., Avouac, J. P., Galetzka, J., Sieh, K., Chlieh, M., et al. (2006). Frictional afterslip following the 2005 Nias-Simeulue earthquake. *Sumatra. Sci.* 312, 1921–1926. doi:10.1126/science.1126960

Ji, C. (2005a). *Preliminary Rupture Model for the December 26, 2004 Earthquake, off the West Coast of Northern Sumatra, Magnitude 9.1*. Available at: http://neic.usgs.gov/neis/eq_depot/2004/eq_041226/neic_slav_ff.html

Ji, C. (2005b). *Preliminary Result 05/03/28 (Mw 8.7), Sumatra Earthquake*. Available at: http://www.tectonics.caltech.edu/slip_history/2005_sumatra/sumatra.html

Ji, C. (2007). *Rupture Process of the Sep 12, 2007 Mw 8.4 Sumatra Earthquake: Phase II*. Available at: http://www.geol.ucsb.edu/faculty/ji/big_earthquakes/2007/09/sumatra_seismic.html

Ji, C., and Zeng, Y. (2007). *Preliminary Result of the Sep 12, 2007 Mw 7.9 Kepulauan Earthquake*. Available at: http://equake-rc.info/

Konca, A. O., Avouac, J. P., Sladen, A., Meltzner, A. J., Sieh, K., Fang, P., et al. (2008). Partial rupture of a locked patch of the Sumatra megathrust during the 2007 earthquake sequence. *Nature* 456, 631–635. doi:10.1038/nature07572

Konca, A. O., Hjorleifsdottir, V., Song, T. A., Avouac, J. P., Helmberger, D. V., Ji, C., et al. (2007). Rupture kinematics of the 2005, Mw 8.6, Nias-Simeulue earthquake from the joint inversion of seismic and geodetic data. *Bull. Seismol. Soc. Am.* 97, S307–S322. doi:10.1785/0120050632

Li, L., Huang, Z., Qiu, Q., Natawidjaja, D. H., and Sieh, K. (2012). Tsunami-induced coastal change: scenario studies for Painan, West Sumatra, Indonesia. *Earth Planet Sp.* 64, 2. doi:10.5047/eps.2011.08.002

Mai, P. M., and Beroza, G. C. (2000). Source scaling properties from finite-fault-rupture models. *Bull. Seismol. Res. Lett.* 85, 1348–1357. doi:10.1785/0220140077

Mai, P. M., and Beroza, G. C. (2002). A spatial random field model to characterize complexity in earthquake slip. *J. Geophys. Res. Solid. Earth* 107, ESE 10-1–ESE 10-21. doi:10.1029/2001JB000588

Mai, P. M., and Thingbaijam, K. K. S. (2014). SRCMOD: an online database of finite source rupture models. *Seismol. Res. Lett.* 85, 1348–1357. doi:10.1785/0220140077

McCloskey, J., Antonioli, A., Piatanesi, A., Sieh, K., Steacy, S., Nalbant, S., et al. (2008). Tsunami threat in the Indian Ocean from a future megathrust earthquake west of Sumatra. *Earth Planet. Sci. Lett.* 265, 61–81. doi:10.1016/j.epsl.2007.09.034

McCloskey, J., Nalbant, S. S., and Steacy, S. (2005). Earthquake risk from co-seismic stress. *Nature* 434, 291. doi:10.1038/434291a

Meltzner, A. J., Sieh, K., Abrams, M., Agnew, D. C., Hudnut, K. W., Avouac, J. P., et al. (2006). Uplift and subsidence associated with the great Aceh-Andaman earthquake of 2004. *J. Geophys. Res.* 111, B02407. doi:10.1029/2005JB003891

Monecke, K., Finger, W., Klarer, D., Kongko, W., McAdoo, B. G., Moore, A. L., et al. (2008). A 1,000-year sediment record of tsunami recurrence in northern Sumatra. *Nature* 455, 1232–1234. doi:10.1038/nature07374

Muhari, A., Imamura, F., Koshimura, S., and Post, J. (2011). Examination of three practical run-up models for assessing tsunami impact on highly populated areas. *Nat. Haz. Earth Syst. Sci.* 11, 3107–3123. doi:10.5194/nhess-11-3107-2011

Muhari, A., Imamura, F., Natawidjaja, D. H., Diposaptono, S., Latief, H., Post, J., et al. (2010). Tsunami mitigation efforts with pTA in West Sumatra Province, Indonesia. *J. Earthq. Tsunami* 4, 341–368. doi:10.1142/S1793431110000790

Nalbant, S. S., Steacy, S., Sieh, K., Natawidjaja, D., and McCloskey, J. (2005). Seismology: earthquake risk on the Sunda trench. *Nature* 435, 756–757. doi:10.1038/nature435756a

Natawidjaja, D. H., Sieh, K., Chlieh, M., Galetzka, J., Suwargadi, B. W., Cheng, H., et al. (2006). Source parameters of the great Sumatran megathrust earthquakes of 1797 and 1833 inferred from coral microatolls. *J. Geophys. Res.* 111, B06403. doi:10.1029/2005JB004025

Newcomb, K. R., and McCan, W. R. (1987). Seismic history and seismotectonics of the Sunda arc. *J. Geophys. Res.* 92, 421–439. doi:10.1029/JB092iB01p00421

Newman, A. V., Hayes, G., Wei, Y., and Convers, J. (2011). The 25 October 2010 Mentawai tsunami earthquake, from real-time discriminants, finite-fault rupture, and tsunami excitation. *Geophys. Res. Lett.* 38, 1–7. doi:10.1029/2010GL046498

Okada, Y. (1985). Surface deformation due to shear and tensile faults in a half-space. *Bull. Seismol. Soc. Am.* 75, 1135–1154.

Pardo-Iguzquiza, E., and Chica-Olmo, M. (1993). The Fourier integral method: an efficient spectral method for simulation of random fields. *Math. Geol.* 25, 177–217. doi:10.1007/BF00893272

Philibosian, B., Sieh, K., Avouac, J. P., Natawidjaja, D. H., Chiang, H., Wu, C., et al. (2014). Rupture and variable coupling behavior of the Mentawai segment of the Sunda megathrust during the super cycle culmination of 1797 to 1833. *J. Geophys. Res. Solid Earth* 119, 7258–7287. doi:10.1002/2014JB011200

Satake, K., Nishimura, Y., Putra, P. S., Gusman, A. R., Sunendar, H., Fujii, Y., et al. (2013). Tsunami source of the 2010 Mentawai, Indonesia earthquake inferred from tsunami field survey and waveform modeling. *Pure Appl. Geophys.* 170, 1567–1582. doi:10.1007/s00024-012-0536-y

Shao, G., and Ji, C. (2005). *Preliminary Result of the Mar 28, 2005 Mw 8.68 Nias Earthquake*. Available from: http://www.geol.ucsb.edu/faculty/ji/big_earthquakes/2005/03/smooth/nias.html

Sieh, K., and Natawidjaja, D. H. (2000). Neotectonics of the Sumatran fault. *Indonesia. J. Geophys. Res. Solid Earth.* 105, 28295–28326. doi:10.1029/2000JB900120

Sieh, K., Natawidjaja, D. H., Meltzner, A. J., Shen, C. C., Cheng, H., Li, K. S., et al. (2008). Earthquake super cycles inferred from sea-level changes recorded in the corals of West Sumatra. *Science* 322, 1674–1678. doi:10.1126/science.1163589

Sladen, A. (2008). *Preliminary Result 02/20/2008 (Mw 7.4), Simeulue Earthquake, Indonesia*. Available at: http://www.tectonics.caltech.edu/slip_history/2008_n_sumatra/simeulue.html

Sladen, A., and Konca, A. O. (2007). *Preliminary Result 09/12/2007 (Mw 7.9), Central Sumatra Earthquake*. Available at: http://www.tectonics.caltech.edu/slip_history/2007_c_sumatra/c-sumatra.html

Tanioka, Y., and Satake, K. (1996). Tsunami generation by horizontal displacement of ocean bottom. *Geophys. Res. Lett.* 23, 861–864. doi:10.1029/96GL00736

United States Geological Survey (USGS). (2015). *Latest Earthquakes*. Available at: http://earthquake.usgs.gov/earthquakes/map/

Yue, H., Lay, T., Rivera, L., Bai, Y., Yamazaki, Y., Cheung, K. F., et al. (2014). Rupture process of the 2010 Mw7.8 Mentawai tsunami earthquake from joint inversion of near-field hr-GPS and teleseismic body wave recordings constrained by tsunami observations. *J. Geophys. Res. Solid Earth.* 119, 5574–5593. doi:10.1002/2014JB011082

Zachariasen, J., Sieh, K., Taylor, F. W., Edwards, R. L., and Hantoro, W. S. (1999). Submergence and uplift associated with the giant 1833 Sumatran subduction earthquake: evidence from coral microatolls. *J. Geophys. Res.* 104, 895–919. doi:10.1029/1998JB900050

Conflict of Interest Statement: The authors declare that the research was conducted in the absence of any commercial or financial relationships that could be construed as a potential conflict of interest.

Copyright © 2016 Muhammad, Goda and Alexander. This is an open-access article distributed under the terms of the Creative Commons Attribution License (CC BY). The use, distribution or reproduction in other forums is permitted, provided the original author(s) or licensor are credited and that the original publication in this journal is cited, in accordance with accepted academic practice. No use, distribution or reproduction is permitted which does not comply with these terms.

frontiers in Built Environment

ORIGINAL RESEARCH
published: 13 June 2017
doi: 10.3389/fbuil.2017.00034

Probabilistic Tsunami Hazard Analysis of the Pacific Coast of Mexico: Case Study Based on the 1995 Colima Earthquake Tsunami

Nobuhito Mori[1], Ario Muhammad[2,3], Katsuichiro Goda[2], Tomohiro Yasuda[4] and Angel Ruiz-Angulo[5]*

[1] Disaster Prevention Research Institute, Kyoto University, Kyoto, Japan, [2] Department of Civil Engineering, University of Bristol, Bristol, United Kingdom, [3] Department of Civil Engineering, University of Narotama, Surabaya, Indonesia, [4] Department of Civil, Environmental and Applied System Engineering, Kansai University, Suita, Japan, [5] Centro de Ciencias de la Atmósfera, Universidad Nacional Autónoma de México, Mexico City, Mexico

This study develops a novel computational framework to carry out probabilistic tsunami hazard assessment for the Pacific coast of Mexico. The new approach enables the consideration of stochastic tsunami source scenarios having variable fault geometry and heterogeneous slip that are constrained by an extensive database of rupture models for historical earthquakes around the world. The assessment focuses upon the 1995 Jalisco–Colima Earthquake Tsunami from a retrospective viewpoint. Numerous source scenarios of large subduction earthquakes are generated to assess the sensitivity and variability of tsunami inundation characteristics of the target region. Analyses of nine slip models along the Mexican Pacific coast are performed, and statistical characteristics of slips (e.g., coherent structures of slip spectra) are estimated. The source variability allows exploring a wide range of tsunami scenarios for a moment magnitude (M_w) 8 subduction earthquake in the Mexican Pacific region to conduct thorough sensitivity analyses and to quantify the tsunami height variability. The numerical results indicate a strong sensitivity of maximum tsunami height to major slip locations in the source and indicate major uncertainty at the first peak of tsunami waves.

Keywords: tsunami, probabilistic tsunami hazard assessment, synthetic slip, slip spectra, 1995 Colima earthquake

OPEN ACCESS

Edited by:
Luigi Di Sarno, University of Sannio, Italy

Reviewed by:
Izuru Takewaki, Kyoto University, Japan
David De Leon, Universidad Autónoma del Estado de México, Mexico

****Correspondence:***
Nobuhito Mori
mori@oceanwave.jp

Specialty section:
This article was submitted to Earthquake Engineering, a section of the journal Frontiers in Built Environment

Received: *12 March 2017*
Accepted: *23 May 2017*
Published: *13 June 2017*

Citation:
Mori N, Muhammad A, Goda K, Yasuda T and Ruiz-Angulo A (2017) Probabilistic Tsunami Hazard Analysis of the Pacific Coast of Mexico: Case Study Based on the 1995 Colima Earthquake Tsunami. Front. Built Environ. 3:34. doi: 10.3389/fbuil.2017.00034

INTRODUCTION

An accurate assessment of tsunami hazards and quantification of uncertainty associated with the assessment are essential to mitigate and to control disaster risk exposures from a tsunami risk management point of view. Research on probabilistic tsunami hazard analysis/assessment (PTHA) has been improved after two mega seismic events, the 2004 Indian Ocean Tsunami (e.g., McCloskey et al., 2008) and the 2011 Tohoku Earthquake Tsunami (e.g., Mori et al., 2011). PTHA is a viable approach to evaluate the uncertainty of tsunami sources and related hazard modeling. One of the major challenges for tsunami impact assessment is to predict the earthquake source characteristics of future tsunamigenic events (e.g., location and geometric slip distribution), and then to quantify the uncertainty associated with the variability in earthquake rupture (tsunami generation) and tsunami inundation processes (e.g., Burbidge et al., 2008). In particular, tsunami generation is influenced by the complex and non-linear interaction of earthquake generation properties, while offshore tsunami

propagation, affected by changes in sea bathymetry, is generally considered as a solved problem (Geist, 2002; McCloskey et al., 2008; Goda et al., 2014).

There are many scientific studies related to PTHA, which have been conducted worldwide. The earliest study that considered the probabilistic nature of tsunami hazard was by Rikitake and Aida (1988). Although they did not consider a full PTHA methodology, they used historical records and a typical earthquake fault model to estimate the probability of tsunami height exceeding a certain level at the shoreline. After the 2004 Indian Ocean event, there were several PTHA studies for other areas worldwide (e.g., Geist and Parsons, 2006; Annaka et al., 2007; Thio et al., 2007) and it accelerated after the 2011 Tohoku Earthquake Tsunami (e.g., Goda et al., 2015; Park and Cox, 2016). There are three major approaches for PTHA, which are commonly used [see a review article by Mori et al. (2017)]. The first approach is to use a combination of many source scenarios based on expert opinion (e.g., González et al., 2009). The second approach is to use a logic-tree based on a combination of slip scenarios and geometric slip parameters with a weight function (e.g., Sánchez and Farreras, 1987; Annaka et al., 2007; Horspool et al., 2014; Fukutani et al., 2015; Lorito et al., 2015; Park and Cox, 2016). The third approach is to generate synthetic slip distributions, which are constrained by seismological theories and models, by slip wavenumber spectra assuming a random phase approximation (e.g., Geist and Oglesby, 2014; Goda et al., 2014, 2015; Davies et al., 2015). The latter two methods are widely used for PTHA. Moreover, PTHA for landslide-triggered tsunamis is challenging and involves significant uncertainty in the tsunami generation process (e.g., Geist and Lynett, 2014).

The Pacific States of Mexico, i.e., Jalisco, Michoacan, Guerrero, and Oaxaca, are positioned at the subduction interface between the Rivera–Cocos Plates and the North American Plate (Bird, 2003). The slip rate along the plate boundary is in the range between 50 and 70 mm/year (DeMets et al., 1994), and hence, the potential for hosting large earthquakes is high. Historically, many large subduction earthquakes have occurred, causing severe shaking along the coastline and inland areas (e.g., Mexico City), and tsunami damage in coastal areas. Particularly, for this region, one of the major earthquakes that have been studied in the literature is the 28 March 1787 Earthquake (Suárez and Albini, 2009). According to the historical records, tsunami wave heights at specific locations had exceeded 10 m, and extensive inundation had occurred along southern Pacific Mexican coast (Nunez-Cornu et al., 2008). The estimated magnitude for this event ranges from M_w 8.4 to M_w 8.6. More recently, many moderate-to-large earthquakes have occurred in the Mexican subduction zone (Ramírez-Herrera et al., 2012). The large ($>M_w$ 8) earthquakes in this zone include the 1932 Jalisco Earthquake (Farreras and Sánchez, 1991; Ramírez-Herrera et al., 2014), the 1985 Michoacan Earthquake (Mendoza, 1993), and the 1995 Jalisco–Colima Earthquake [denoted by the 1995 Colima Earthquake hereafter; Mendoza and Hartzell (1999)].

The offshore areas near Guerrero have not ruptured since 1911, which are prone to cause large earthquakes. This segment of the Cocos–North American Plate interface is referred to as the Guerrero seismic gap (Kostoglodov et al., 2003). The recent geophysical investigations by Perez-Campos et al. (2008) and Pacheco and Singh (2010) indicate that the Cocos Plate is subducting beneath the North American Plate with a dip angle of about 15°, and the slab reaches a depth of about 25 km at the distance of about 65 km from the Trench. In this region, both interface events and inslab events may be generated. Gradually, the subduction interface becomes flatter and becomes almost horizontal at the distance of about 120 km from the Trench (depth of about 40 km). The low coupling of the interface at the distance range beyond 100 km from the Trench results in low seismicity of inslab earthquakes. At the farther distance of about 300 km from the Trench, the subduction interface falls off sharply into the mantle. In the Guerrero seismic gap, some of the accumulated strain along the plate interface is also released as episodic slow slip events (Pacheco and Singh, 2010). Recently, one example of slow slip event sequences was triggered by the 2010 Maule, Chile Earthquake (Zigone et al., 2012).

Regarding future Earthquake–Tsunami events in the Guerrero region, major concerns are that (i) the segment has a potential to host large mega-thrust subduction events and (ii) no events greater than M_w 8 have not occurred in the segment in the recent history. In case of large subduction events, touristic places, such as Acapulco, will be devastated by earthquake and tsunami. Although Geist and Parsons (2006) showed PTHA results based on the logic-tree approach targeted Acapulco region, it is difficult to setup plausible scenarios in the Guerrero region due to lack of scientific data of historical events. A recent study by Perez-Campos et al. (2013) considered a scenario magnitude of M_w 8.2 for the Guerrero seismic gap, having the fault length and fault width of 210 and 90 km, respectively, and average slip of 4.0 m. Even when the magnitude of the scenario event can be defined for disaster risk mitigation purposes, geometry as well as slip distribution of the earthquake rupture may vary significantly. These rupture characteristics have significant influence on the earthquake ground motions as well as tsunamis. In addition, Jaimes et al. (2016) developed tsunami hazard maps in Mexico using several earthquake source scenarios and highlighted that it is essential to incorporate multiple earthquake source scenarios to produce reliable tsunami hazard maps. Therefore, it is important to take into account various earthquake rupture scenarios as part of disaster risk reduction strategy. Furthermore, there are many PTHA studies but the comparisons with historical records are limited. For benchmarking tsunami hazard predictions with past experience and future development of PTHA research, it is important to compare PTHA results to historical observations.

This study develops a stochastic source model for large tsunamigenic earthquakes in the Guerrero region. The stochastic source modeling approach is useful for generating synthetic realizations of realistic source models (Mai and Beroza, 2002). The generated rupture models can be implemented in Monte Carlo tsunami simulation to assess the uncertainty of tsunami propagation and shoaling characteristics (Goda et al., 2014), and such uncertainties can be further propagated in tsunami hazard and damage estimation to promote effective tsunami risk mitigation decisions (Goda and Song, 2016). Recently, new

scaling relationships of various earthquake source parameters, such as fault geometry and slip statistics, have been developed for tsunamigenic events (Goda et al., 2016). The new empirical scaling models are based on an extensive statistical analysis of numerous source inversion models of the past earthquakes obtained from the SRCMOD (Mai and Thingbaijam, 2014; see http://equake-rc.info/SRCMOD/), which is an online database of finite-fault rupture models of past earthquakes. Using these equations, source parameters can be predicted by taking into account uncertainty and dependency of other parameters (note: source parameters are physically inter-related and thus prediction errors of these parameters are correlated). In short, stochastic tsunami simulation is valuable for assessing the regional tsunami impact due to future large earthquakes in the Guerrero region.

The study is organized as follows. First, a summary of the finite-fault rupture models for Mexican subduction earthquakes is presented; nine source models are obtained from the SRCMOD database. Based on the characteristics of the source models, a generic fault model for stochastic source modeling in the Guerrero region is developed. In synthesizing earthquake source models, new scaling relationships are implemented in the Monte Carlo tsunami simulation. Then, a numerical procedure of the stochastic tsunami simulation is described for the Guerrero region. Finally, an application of the stochastic tsunami simulation for the 1995 Colima Earthquake is presented, which facilitates the retrospective investigation and comparison with observed tsunamis during the historical event.

ANALYSIS OF HISTORICAL SOURCES

Analysis of Fault Models

Numerous source models have been developed for historical Mexican subduction earthquakes. In the well-organized source database, such as SRCMOD (Mai and Thingbaijam, 2014), nine finite-fault models are available for the Mexican subduction zone. The locations of the nine finite-fault models are shown in **Figure 1** (see also **Table 1**). The strike angles of the finite-fault models range from 283° to 309°, which are consistent with the boundary between the Cocos Plate and the North American Plate (Bird, 2003). The dip angles of the source models are typically in the range of 12–14°, except for Model 7.

Using these finite-fault model data, Goda et al. (2016) evaluated the macro source parameters: fault length (L), fault width (W), mean slip (D_a), maximum slip (D_m), Box–Cox parameter (λ), correlation length along strike direction (A_z), correlation length along dip direction (A_x), and Hurst number (H) as a function of moment magnitude. The fault width and length, together with strike and dip, define the geometry of the fault plane. The mean slip, maximum slip, and Box–Cox parameter characterize the probability distribution of the slip values. The correlation lengths and Hurst number are used to model the spatial heterogeneity of the slip values. The obtained values of the source parameters for the Mexican subduction earthquakes are listed in **Table 1**, except for Model 6. Because the majority of the slip values of Model 6 are 0 (**Figure 1**), Model 6 was regarded as unsuitable for spectral analysis of the source model and thus excluded from further investigations in this study.

Based on the geometry of the Mexican finite-fault models, a generic fault model for the Guerrero region is defined for the synthetic source generation (**Figure 2**). It covers the offshore region of the Pacific Mexican coast. The length and width of the Guerrero source zone are 930 and 170 km, respectively. The top edge of the fault plane is positioned at a depth of 3 km. The fault plane has a constant strike of 293° and a constant dip of 13°. For stochastic source modeling and Monte Carlo tsunami simulation, the Guerrero source zone is discretized into 10/10 km sub-faults. In stochastic source modeling, slip values that are consistent with the considered spatial slip distribution characteristics are generated.

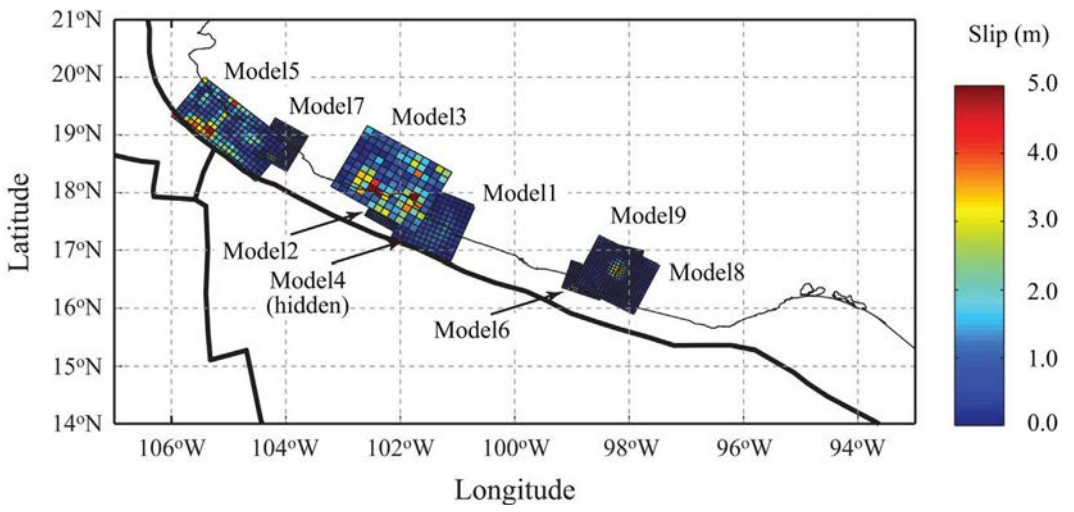

FIGURE 1 | Finite-fault models, along the Mexican Pacific coastline, available in the SRCMOD database (see details of parameters in **Table 1**).

TABLE 1 | Summary of the finite-fault source parameters for the Mexican subduction earthquakes.

Model	Date	M_w	W (km)	L (km)	Strike (°)	Dip (°)	Mean slip (m)	Maximum slip (m)	Box–Cox parameter	Correlation length along dip (km)	Correlation length along strike (km)	Hurst number	Reference
1: Petatlan	14/03/1979	7.39	120	120	293	14	0.288	1.225	0.40	30	25.20	0.96	Mendoza (1995)
2: Playa Azul	25/10/1981	7.25	55	45	300	14	0.784	4.044	0.10	16.5	14.30	0.68	Mendoza (1993)
3: Michoacan	19/09/1985	8.01	139	180	300	14	1.395	7.490	0.30	36	54	0.69	Mendoza and Hartzell (1989)
4: Zihuatanejo	21/09/1985	7.42	67.5	67.5	300	14	0.749	2.090	0.60	20.4	18.36	0.99	Mendoza (1993)
5: Colima	09/10/1995	7.96	100	170	309	14	1.354	4.771	0.30	28.9	57.80	0.54	Mendoza and Hartzell (1999)
6: Copala[a]	14/09/1995	7.30	55	75	289	11	–	–	–	–	–	–	Courboulex et al. (1997)
7: Colima	22/01/2003	7.50	85	70	300	22	0.606	3.143	0.10	17.85	12.75	0.85	Yagi et al. (2004)
8: Oaxaca (Pinotepa Nacional)	20/03/2012	7.40	66	72	297	12.32	0.579	4.525	0.0	10.8	11.52	0.99	Hayes (2012)
9: Oaxaca (Pinotepa Nacional)	20/03/2012	7.40	55	50	283	13	0.99	4.200	0.30	12.10	11	0.99	Wei (2012)

[a]*Model 6 is not analyzed because this model was judged as unsuitable for spectral analysis based on the criteria set in Goda et al. (2016). The gray shade in the table indicates target of this study.*

Scaling Relationships for Source Parameters for Guerrero Region

The stochastic source models are synthesized based on a set of new scaling relationships of source parameters developed by Goda et al. (2016). Equations 1–6 are the relationships for W, L, D_a, D_m, A_z, and A_x, respectively, and are given as a function of M_w. The error terms of the source parameters are correlated; **Table 2** lists the linear correlation coefficients of the prediction errors for Eqs 1–6.

$$\log_{10} W = -0.4877 + 0.3125M_w + 0.1464\varepsilon_W \quad (1)$$

$$\log_{10} L = -1.5021 + 0.4669M_w + 0.1717\varepsilon_L \quad (2)$$

$$\log_{10} D_a = -5.7933 + 0.7420M_w + 0.2502\varepsilon_{D_a} \quad (3)$$

$$\log_{10} D_m = -4.5761 + 0.6681M_w + 0.2249\varepsilon_{D_m} \quad (4)$$

$$\log_{10} A_z = -1.0644 + 0.3093M_w + 0.1592\varepsilon_{A_z} \quad (5)$$

$$\log_{10} A_x = -1.9844 + 0.4520M_w + 0.2204\varepsilon_{A_x} \quad (6)$$

The equations for the Box–Cox parameter and the Hurst number are independent of M_w (Goda et al., 2016). The Box–Cox parameter is modeled as a normal random variable with mean equal to 0.312 and SD equal to 0.278. On the other hand, the Hurst number is modeled as a random variable that takes a deterministic value of 0.99 with probability of 0.43 and a sampled (random) value from the normal distribution with mean equal to 0.714 and SD equal to 0.172 with probability of 0.57. See Goda et al. (2016) for further details of the probabilistic models of the source parameters. The prediction errors of the Box–Cox parameter/Hurst number are considered to be uncorrelated with those of other source parameters.

The consistency of the estimated source parameters for the eight finite-fault models of the Mexican subduction earthquakes (**Table 1**) with the prediction models of the source parameters mentioned above is examined, and the results are shown in **Figure 3**. In **Figure 3**, the results for the 1995 Colima Earthquake by Mendoza and Hartzell (1999) are represented by a different symbol. The stochastic tsunami simulation of the 1995 Colima Earthquake is carried out, in comparison with the field observations, in the latter part of this study. The results shown in **Figure 3** indicate that the estimated source parameters agree with the scaling relationships; for most cases, the estimated parameters fall within the 16th–84th percentile confidence interval of the prediction equations, Eqs 1–6. Therefore, the use of the developed scaling relationships by Goda et al. (2016) for Mexican subduction events in the Guerrero region can be justified by the historical slip models along the Pacific Mexican subduction zone.

OUTLINE OF NUMERICAL MODEL

Numerical Model for Tsunami Simulation

A series of numerical simulations for tsunami propagation from the source to coastline is performed by non-linear shallow water equations by Goto et al. (1997). The governing

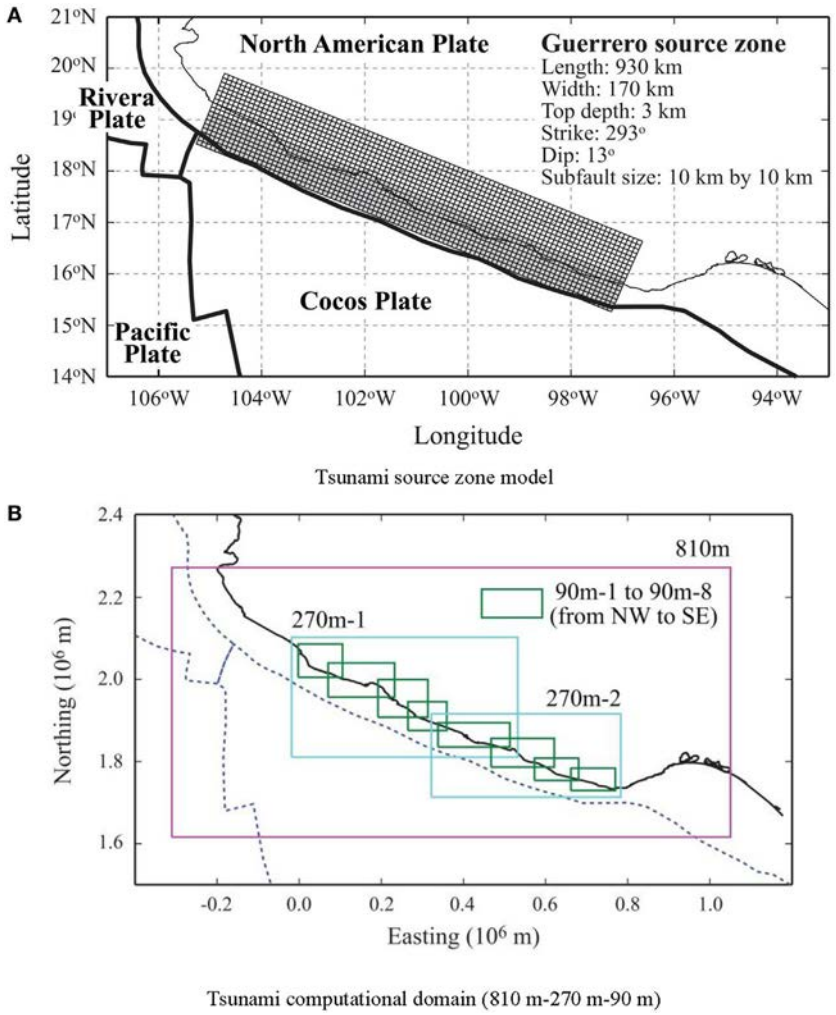

FIGURE 2 | Tsunami source zone model and tsunami propagation domain for the Guerrero region. **(A)** Tsunami source zone model. **(B)** Tsunami computational domain (810 m–270 m–90 m).

TABLE 2 | Linear correlation coefficients of regression residuals of the scaling relationships for the six earthquake source parameters.

Variables	ε_W	ε_L	ε_{D_a}	ε_{D_m}	ε_{A_z}	ε_{A_x}
ε_W	1.0	0.139	−0.680	−0.545	0.826	0.035
ε_L	0.139	1.0	−0.595	−0.516	0.249	0.734
ε_{D_a}	−0.680	−0.595	1.0	0.835	−0.620	−0.374
ε_{D_m}	−0.545	−0.516	0.835	1.0	−0.564	−0.337
ε_{A_z}	0.826	0.249	−0.620	−0.564	1.0	0.288
ε_{A_x}	0.035	0.734	−0.374	−0.337	0.288	1.0

equations are evaluated using a leap-frog staggered-grid finite difference scheme. The nesting grid systems that are implemented considering the size of continental shelf for the Guerrero region and nearshore bathymetry have three levels as shown in **Figure 2B**.

The grid discretization at the coarsest level is 810 m, while the finest level is 90 m; a factor of 3 is considered to connect individual grid systems with different resolutions. The coarsest 810 m region covers the entire Guerrero region, and the deformation due to fault rupture is computed at this resolution using Okada (1985) and Tanioka and Satake (1996) equations for the region shown in **Figure 2A**. There are two 270 m regions shown in **Figure 2B**; within the 270 m^{-1} and 270 m^{-2} regions, five 90 m regions are defined, respectively. The nested domains of 270 and 90 m resolutions are shown in **Figure 2B**. It is noted that at the same resolution, regions overlap with the nearby (same-resolution) regions. This is to ensure that the solutions of tsunami waves, especially edge wave, in simulation are propagated across different regions properly. The duration of each simulation is set to 2 h and the time step for the simulation is 0.25 s to satisfy the Courant–Friedrichs–Lewys condition, which is a necessary condition of time and space discretization for convergence when partial differential equations are numerically solved by the finite difference method. No tidal variation is taken into account.

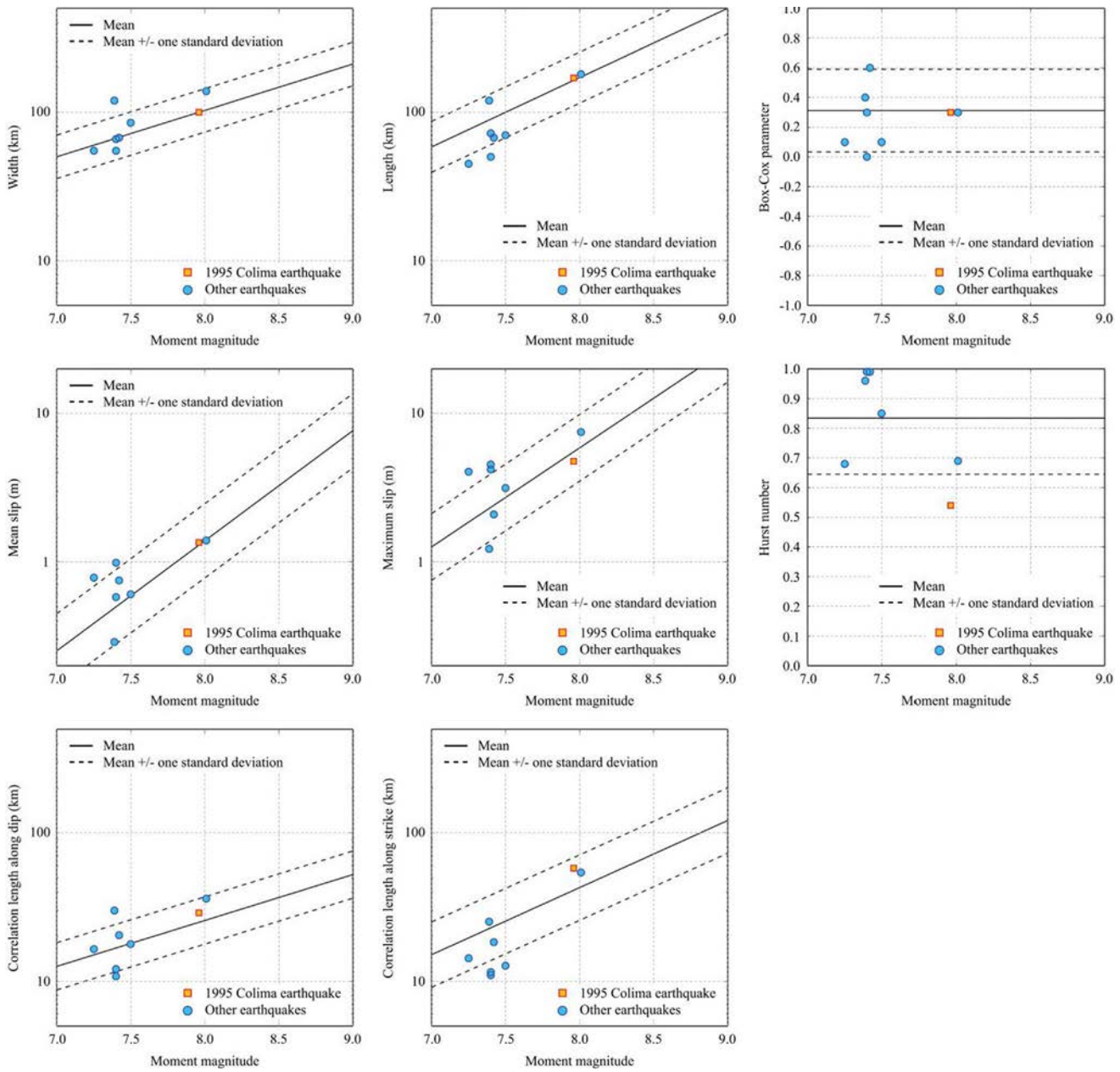

FIGURE 3 | Comparison of the estimated source parameters for the eight finite-fault models of the Mexican subduction earthquakes with the corresponding scaling relationships.

Bathymetry Data

To carry out tsunami modeling, bathymetry (i.e., measured water depth) data and digital elevation model for Mexico are collected. For bathymetry data, the General Bathymetric Chart of Oceans (GEBCO) Dataset (2014) whose grid spacing is about 900 m is used for deep to shallow water regions. The GEBCO2014 data for the Pacific Mexico and target area are shown in **Figure 4**. In **Figure 4**, the SRTM Water Body Data (SWBD, 2008) shoreline data SWBD of Shuttle Radar Topography Mission (SRTM) (2008) and plate boundary data by Bird (2003) are also displayed. The plate boundary between the Cocos Plate and the North American Plate coincides with the Trench based on the GEBCO2014 data.

An accurate inundation calculation is excluded in this study, although inland inundation is simulated during the computation. Therefore, the main results presented in this study focus on the tsunami heights along the coast. Note that the tsunami wave height that is discussed in this study is the height of water flow above mean sea level. It is important to emphasize that GEBCO2014 has bias in very shallow waters and the data also need to match with water

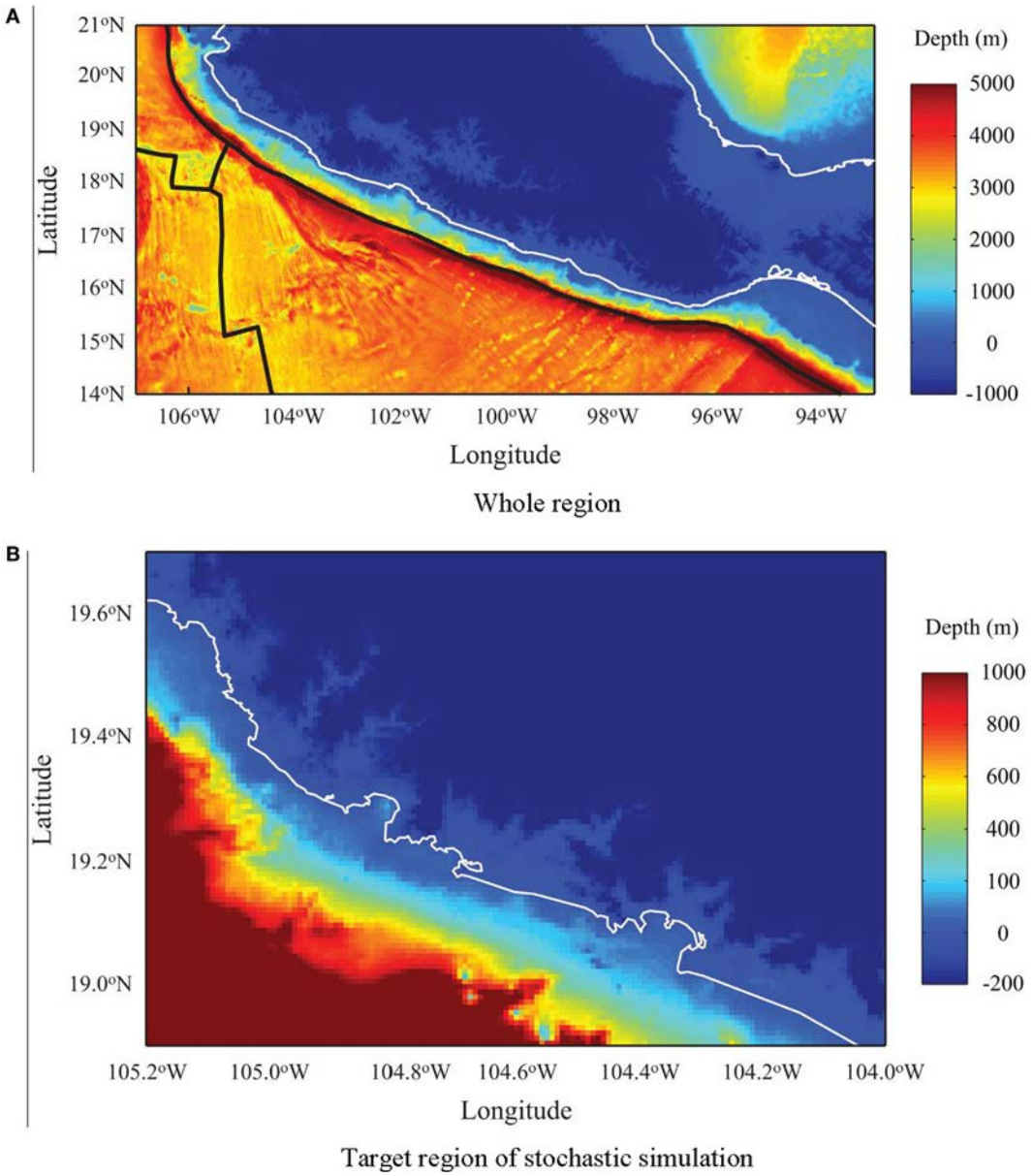

FIGURE 4 | Bathymetry data for the Guerrero region (GEBCO2014, unit: meters). **(A)** Whole region. **(B)** Target region of stochastic simulation.

depths along the shoreline. Thus, GDEM2 data (2011) are used for onshore topography. The integration of bathymetry data and elevation data are not trivial because the spatial resolutions of these data are very different. For the cases of GEBCO2014 and GDEM2, the resolutions differ by a factor of 30 (i.e., 900 versus 30 m). The effects of the interpolation are expected to be significant at shallow depths near the shoreline. In developing the "depth" data for tsunami simulation (i.e., combined elevation data for a given region), first, three datasets, namely GEBCO2014, GDEM2, and SWBD, are combined without interpolation. The points in the "combined" data are spaced neither regularly nor uniformly. Within the onshore areas, the corresponding GEBCO2014 data between 0 and 200 m in elevation are replaced by the counterparts of GDEM2 data. In addition, the SWBD shoreline data are overlaid as zero elevation data points. Once this composite dataset is developed, linear interpolation is carried out. In future studies, new bathymetry data (probably compiled from local sources) should be incorporated to improve the reliability and accuracy of the tsunami simulation, especially in the very shallow water environment.

Stochastic Tsunami Simulation

Stochastic tsunami simulation can be conducted by generating multiple stochastic source models for a given earthquake scenario and by performing tsunami forward modeling repeatedly.

A computational flowchart of stochastic tsunami simulation is shown in **Figure 5**. The detail of stochastic tsunami modeling is available in Goda et al. (2014, 2016) but it will be explained briefly in the following.

The first step of the method is to define a suitable tsunami source zone model. For the Guerrero region, the model shown in **Figure 2A** is adopted. The scenario magnitude should be selected according to the objective of the analysis. Within the fault plane, the so-called asperity zone is setup, together with the required slip concentration range. Essentially, the asperity zone works as crude constraints of the generated source model regarding the slip concentration within the fault plane. It requires that a certain amount of slip must be concentrated within the target region. One example is that more than 50% of the total slip should be concentrated in the shallow part of the fault plane (e.g., shallower than 20 km). The asperity zone parameters should reflect the seismological knowledge of earthquake rupture in the target region.

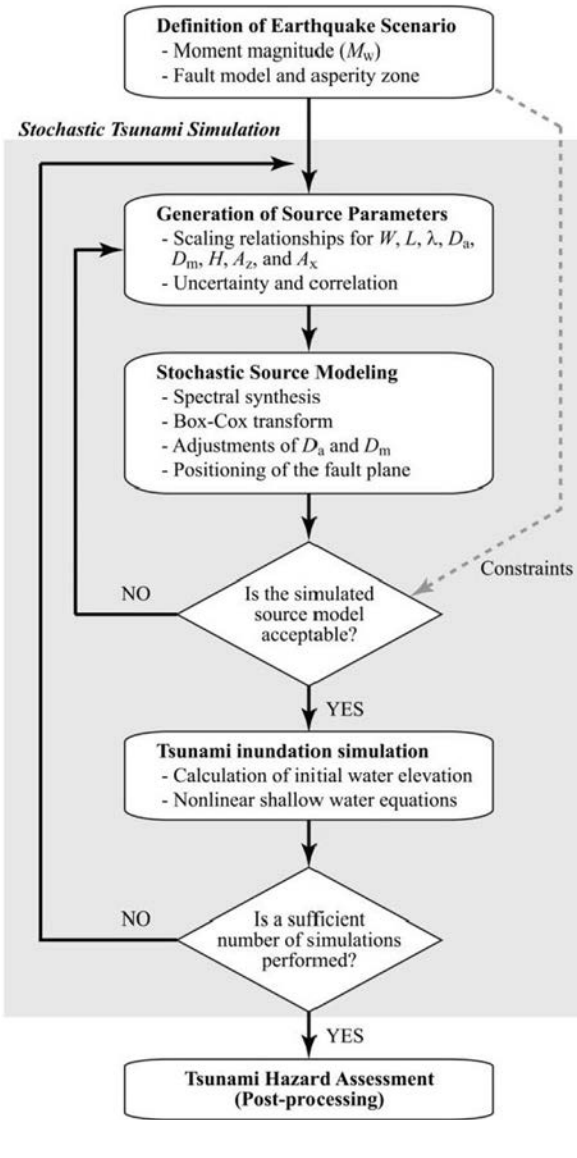

FIGURE 5 | Flowchart of stochastic tsunami simulation.

Second, the macro earthquake source parameters, such as W, L, D_a, D_m, λ, A_z, A_x, and H, are generated using the scaling relationships. Uncertainty as well as correlation associated with the regression models should be taken into account in sampling the values of the source parameters (Eqs 1–6 and **Table 2**). In the simulation, random variables for these residuals can be sampled from the multivariate normal distribution. In addition, at this stage, consistency among the simulated values of W, L, and D_a can be tested by comparing the target seismic moment (as specified by the given scenario magnitude) and the simulated seismic moment ($M_o = \mu WLD_a$, where μ is the rock rigidity). An inadequate combination of W, L, and D_a values is resampled until the scenario magnitude is satisfied.

Third, using the generated spatial slip distribution parameters, a random slip field is generated using a Fourier integral method (Pardo-Iguzquiza and Chica-Olmo, 1993). To achieve slip distribution with realistic positive skewness, the synthesized slip distribution is converted *via* Box–Cox transformation (Goda et al., 2014). The transformed slip distribution is then adjusted to achieve the target mean slip D_a and to avoid very large slip values exceeding the target maximum slip D_m. Subsequently, the position of the synthesized fault plane is determined randomly within the source region. To ensure that the synthesized slip distribution is realistic with respect to the seismotectonic characteristics of the region, two criteria/constraints are implemented to determine the final acceptance of the generated source model. The first constraint requires that the asperity area ratio of the candidate slip distribution falls between 0.2 and 0.3. The second constraint requires that the simulated earthquake slip is more concentrated in the designated asperity region. Multiple slip distributions are simulated repeatedly until an acceptable source model, which has all desirable characteristics, is obtained.

Fourth, for a given acceptable source model, the initial water surface elevation (i.e., initial boundary conditions for tsunami simulation) is evaluated based on formula by Okada (1985) and Tanioka and Satake (1996). Tsunami wave propagation is evaluated by solving non-linear shallow water equations (Goto et al., 1997). The run-up of tsunami is considered by the model but it is incomplete due to coarse grid size in this study. Finally, the above simulation procedure is repeated until a sufficient number of acceptable source models are generated and their tsunami inundation heights/depths at locations of interest are evaluated. The results from the Monte Carlo tsunami simulation are useful for evaluating variability of tsunami simulation results at different locations and for developing stochastic tsunami hazard maps along the coast.

RESULTS AND DISCUSSION: CASE STUDY OF THE 1995 COLIMA EARTHQUAKE

Synthetic Slips

A brief discussion of generated synthetic/stochastic tsunami sources for the Guerrero region is given before analyzing

synthetic tsunami characteristics. To demonstrate the stochastic tsunami simulation model for the Guerrero region, the 1995 Colima Earthquake is considered, which is one of the most major tsunami events in the northern part of the Guerrero region. More specifically, the selection of the 1995 Colima Earthquake is relevant because the size of the earthquake (M_w 8.0) is sufficiently large to cause tsunami waves and post-event tsunami survey data (e.g., Borerro et al., 1997; Trejo-Gómez et al., 2015) as well as an inverted slip model (Mendoza and Hartzell, 1999) are available for this event. Our aim in setting up the case study is to compare the results of stochastic tsunami simulations with the past survey data of the 1995 Colima Earthquake.

The moment magnitude of the event was M_w 8.0 and occurred near the junction of the Cocos–Rivera–North American Plates (Model 5 in **Figure 1**). Borerro et al. (1997) reported that the observed run-up heights along the Colima coast line (longitudes between 104 and 105°W) were mostly 2–3 m and was ranged up to 5 m (note: at one particular point, north end of Santiago Bay, the observed run-up height reached 10.9 m; this high run-up was likely to be caused by the very local topographical effect).

To setup the stochastic tsunami simulations for the 1995 Colima Earthquake, a separate source zone model is defined within the whole source zone model for the Guerrero region. The 1995 Colima Earthquake source zone model restricts ranges of slip along the subduction zone shorter than the Guerrero region and is based on the source model by Mendoza and Hartzell (1999), i.e., Model 5 in **Figure 1** and **Table 1**. A zoom-up of the Mendoza–Hartzell fault plane model (1999) is shown in **Figure 6A**. The maximum slip is 4.78 m, and it is located around 19°N in latitude and 106–105.5°W in longitude. To incorporate the variations of the fault plane size, the source zone model for the 1995 Colima Earthquake has the width equal to 150 km and the length equal to 310 km, which is larger than the original fault plane by Mendoza and Hartzell (1999) (note: the top edge of the fault plane model is identical). It is also noteworthy that the Mendoza–Hartzell model agrees with the scaling relationships developed by Goda et al. (2016) shown as the square marks in **Figure 3**.

Synthetic Tsunami Simulation

To carry out the stochastic tsunami simulation, two sets of 100 stochastic source models are generated for the M_w 8.0 scenario. The first set takes into account uncertainty of the scaling relationships of the source models, whereas the second set does not. The practical consequences of not incorporating the uncertainty of the scaling relationships are that the generated source models have identical dimensions and slip heterogeneity parameters, while the slip distribution and location of the source model are varied. On the other hand, when the uncertainty of the scaling relationships is considered, both dimensions and slip heterogeneity are varied. Note that such uncertainty sometimes is ignored, and scaling relationships are used as deterministic equations relating two source parameters. In addition to the two sets of 100 stochastic source models, a hindcast simulation for the 1995 Colima Earthquake Tsunami is performed by using the original Mendoza–Hartzell fault plane model (**Figure 6A**) as a benchmark. **Figure 6B** shows examples for four realizations of the stochastic source models for the cases where the uncertainty of the scaling relationships is accounted for. The synthetic slips in **Figure 6B** demonstrate that realistic locations of maximum slip along the Trench and coherent structure of sub-slips around the maximum slip given

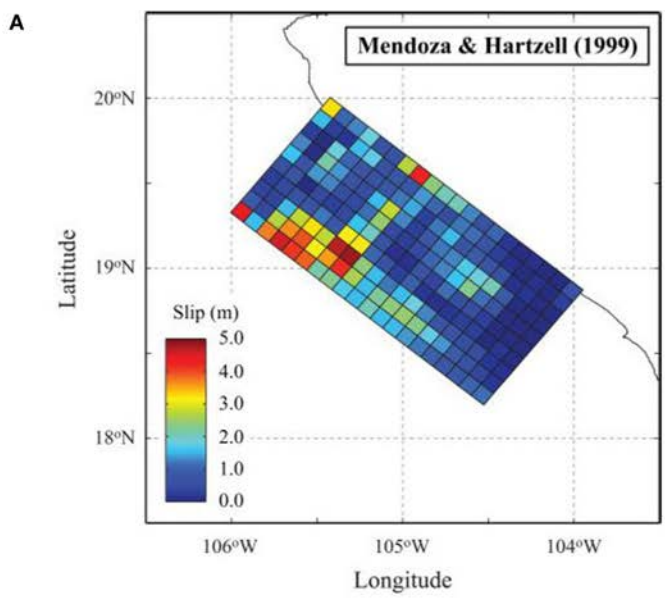

Mendoza-Hartzell model for the 1995 Colima Earthquake.

FIGURE 6 | Continued

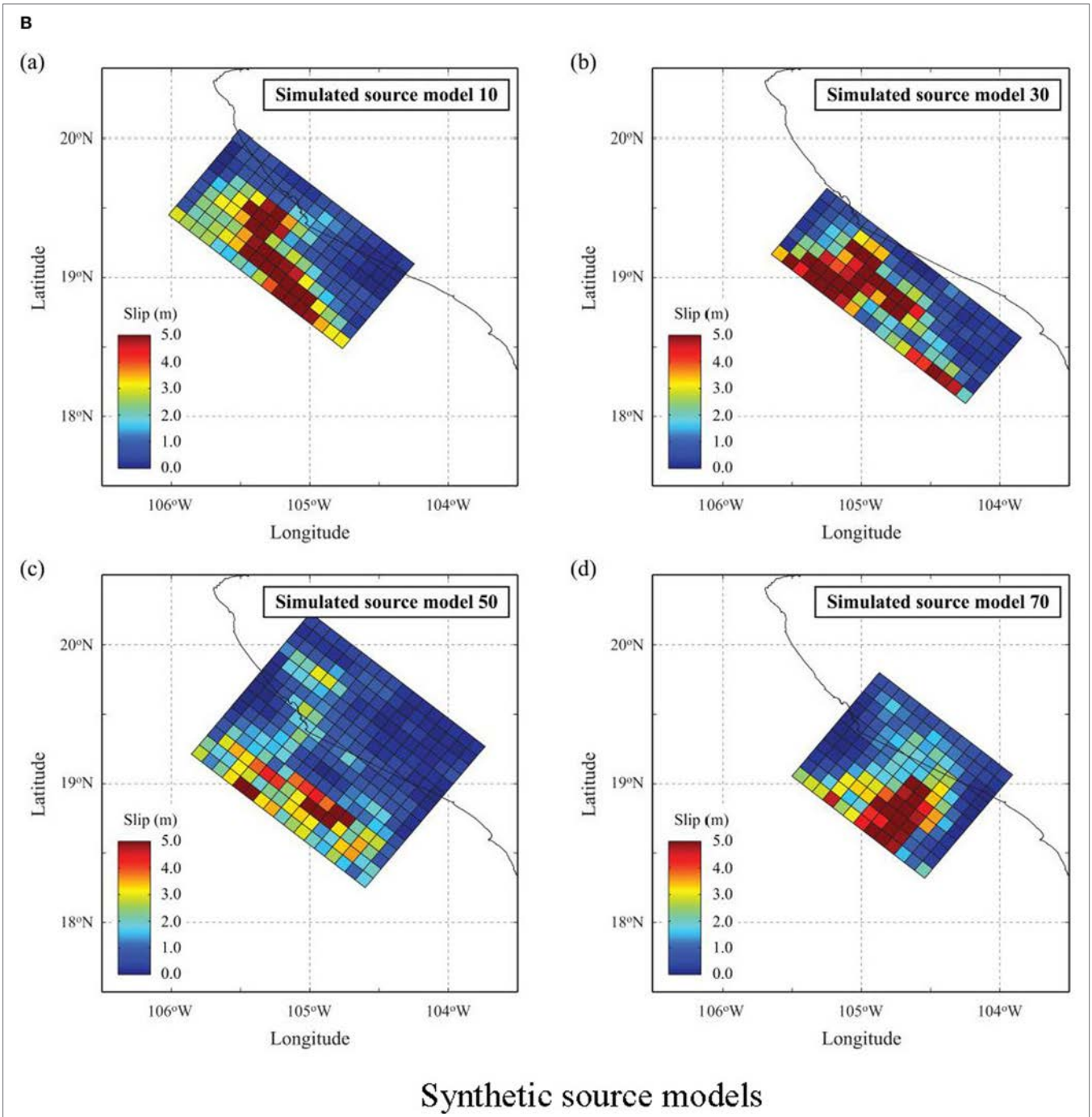

FIGURE 6 | Stochastic source models for the 1995 Colima Earthquake scenario by considering prediction errors of the scaling relationships. **(A)** Mendoza–Hartzell model for the 1995 Colima Earthquake. **(B)** Synthetic source models.

by spectral decomposition. Note that each realization has the similar tail of slip spectra, which are controlled by the spectral decomposition and Box–Cox parameter. The generation of arbitrary number of synthetic slips is one of advantages of using the random phase approach in PTHA, which is different from the logic-tree approach. Therefore, it is possible to discuss probabilistic tsunami heights along the coast. Although the examples of stochastic source models without the uncertainty of the scaling relationships are not shown due to limitation of space, the synthetic source models considering the uncertainty of the scaling relationships shown in **Figure 6B** change fault size, i.e., L and W, and the other slip characteristics due to the uncertainty terms ε in Eqs 1–6. Consequently, the rupture aspect ratios (i.e., L/W) become variable even when the same

magnitude is considered. To discuss the tsunami heights along the coast probabilistically and to investigate the uncertainty effects on earthquake source modeling, the tsunami simulation results are presented in two sections, i.e., sensitivity of tsunami simulated heights and effects of accounting for parameter uncertainty in earthquake source generation.

Sensitivity of Tsunami Simulated Heights

Figure 7 shows the maximum wave height of the 1995 Colima Earthquake Tsunami simulated by the Mendoza–Hartzell model. The large tsunami heights are located in the northern part of the domain due to the large slip concentration as shown in **Figure 7**. There is less significant tsunami amplification inside bays; however, the amplification of tsunami heights along the northern coast facing the Pacific due to shallow water shoaling effects is remarkable. The tsunami height in the southern part of the domain is less than 1 m, noting that this should be regarded one of realizations from ensemble events. The mean and SD of maximum tsunami heights based on the 100 stochastic models considering the uncertainty of scaling relationships are shown in **Figure 8**. Besides the southern end of the computational domain, the mean maximum tsunami height by the stochastic models are more uniformly distributed along the coast compared with other sites, although the wave deformation from the offshore to onshore are different especially in the middle of the domain. The SD of maximum tsunami heights along the coast is large outside of bays facing the Pacific but is not significant inside.

The comparison of the mean maximum tsunami heights from the stochastic tsunami simulations and the maximum tsunami height of the hindcast tsunami simulation is conducted by calculating the ratio between them. The results are shown in **Figure 9**. The ratio of the maximum tsunami heights, shown in **Figure 9**, is mostly larger than 1. Thus, the predicted tsunami hazards based on the inverted source model developed using actual observed geophysical data for the 1995 Colima Earthquake Tsunami are less than the averaged realization of the stochastic tsunami simulation. There are three major factors to amplify tsunami heights at particular coastal locations. The first is source characteristics (e.g., location of maximum slip), the second is wave shoaling and focusing due to large-scale bathymetry features, and the third is convergence of energy due to the shape of a bay. The second effects, i.e., wave shoaling, are proportional to $h^{-1/4}$ where h is water depth, if wave nonlinearity is negligible (i.e., Green's law). **Figure 10** shows the spatial distribution of $h^{-1/4}$ of GEBCO2014 data around the

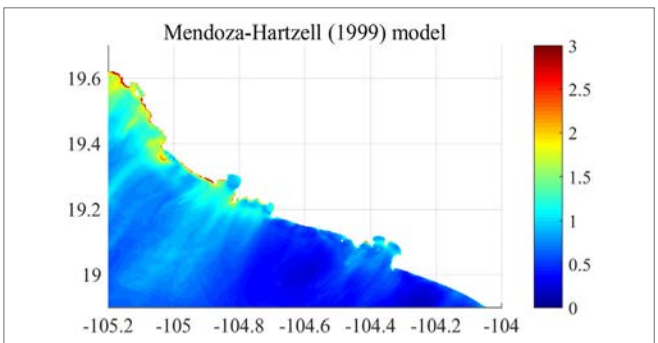

FIGURE 7 | Maximum surface elevation, in meters, of the 1995 Colima Earthquake Tsunami based on the Mendoza–Hartzell model.

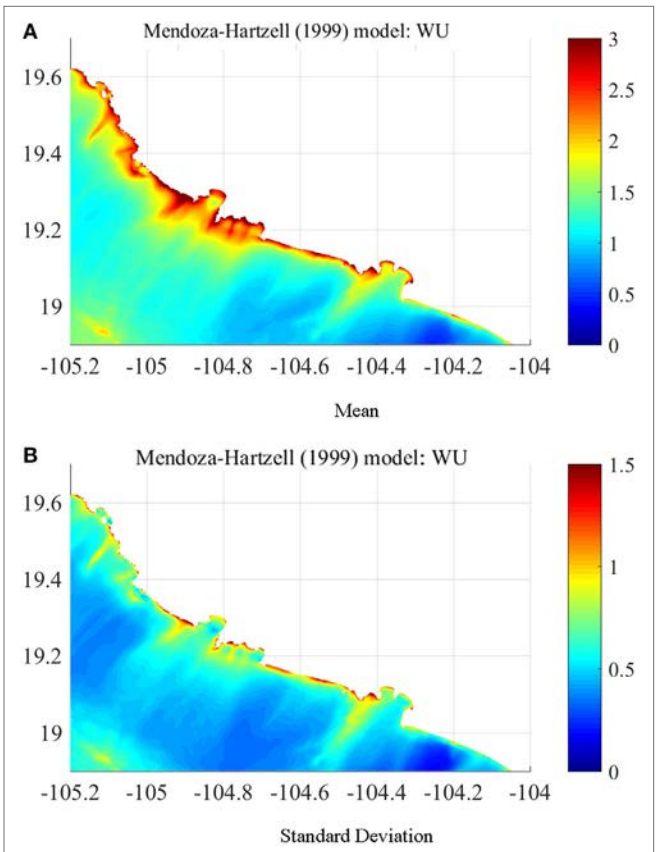

FIGURE 8 | Mean and SD of maximum surface elevation, in meters, by the stochastic models considering prediction errors of the scaling relationships. **(A)** Mean. **(B)** SD.

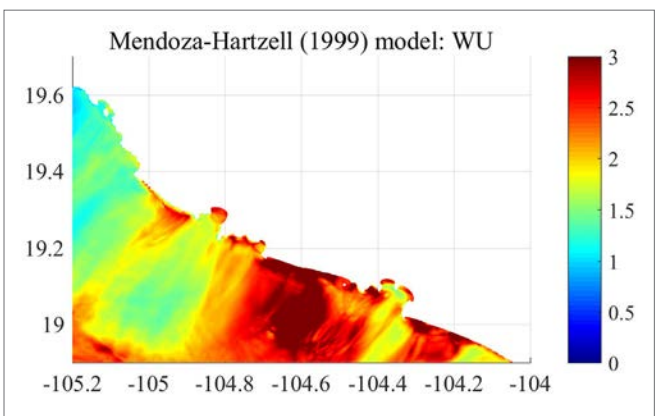

FIGURE 9 | Ratio of average maximum surface elevation by the stochastic model considering prediction errors of the scaling relationships to maximum surface elevation calculated based on the Mendoza–Hartzell model.

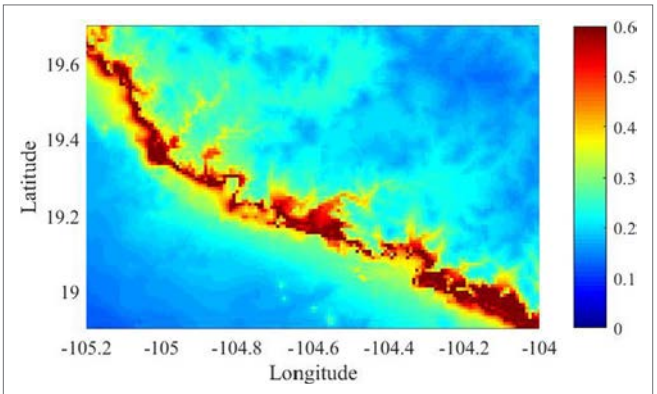

FIGURE 10 | Spatial distribution of $h^{-1/4}$ around target area (the areas correspond **Figure 4B**).

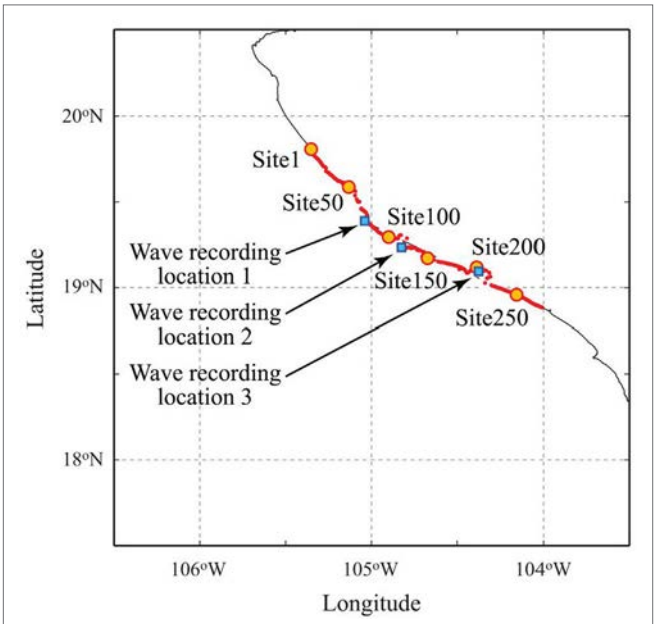

FIGURE 11 | Site locations (1–284) and wave recording locations (1–3) for the analysis of time series of tsunami surface elevation.

target area shown in **Figure 7**. The value of $h^{-1/4}$ constantly increases from offshore to onshore lower than 19.3°N in latitude. Therefore, the amplification of tsunami heights shown in **Figure 9** is not influenced by offshore bathymetry. It can be concluded that the source characteristics are the main cause of the observed spatial inhomogeneity of mean maximum tsunami height rather than the tsunami propagation processes.

The maximum tsunami heights along the coastal line (elevation is between –1.0 and 1.0 m) are then extracted for every 450 m (i.e., five grids) in the longitudinal direction to examine the spatial variation of the tsunami heights along the coast; the results can be compared with the tsunami survey results. The locations of the extracted points are shown in **Figure 11**. In total, there are 284 sites along the coast. In addition, tsunami waveforms (i.e., temporal profile) at three recording locations along the Colima coast are also focused on to investigate the temporal characteristics of the tsunami profiles for different source models. In relation to the surveyed locations by Borerro et al. (1997), the recording location 2 is in Tenacatita Bay, whereas the recording location 3 is in Manzanillo Bay. The depths at the recording locations 1–3 are 1.3, 10.1, and 36.2 m, respectively.

First, the maximum tsunami heights along the coast line from north to south are shown in **Figure 12**. The mean and the upper and lower 16th percentiles of the simulated tsunami heights with and without the uncertainty of the scaling relationships (red solid and dashed line) are shown in the figure. These results are also compared with the hindcast simulation of the 1995 Colima Earthquake Tsunami (blue solid line) and observed run-up heights (dots) by Trejo-Gómez et al. (2015). The past tsunami height profile of the 1995 Colima Earthquake shows that the wave heights for sites 1–100 are higher than others, which are consistent with the source model by Mendoza and Hartzell (1999), having large asperities in the north-western segment of its fault plane. The maximum tsunami profiles for the stochastic source models vary significantly along the coast; for instance, the median curve varies between 2.0 and 5.5 m, while the 84th percentile curve varies between 3.0 and 7.5 m. The spatial distributions of mean maximum tsunami heights from sites 0 to 70 are generally similar to the historical run as well as the measured tsunami run-up heights by Trejo-Gómez et al. (2015). On the other hand, the maximum tsunami height profile for the stochastic source models from the sites 100 and more (toward south-east) differs from the historical run and measured tsunami run-up heights, noting that the locations shown in **Figure 2** of Borerro et al. (1997) approximately correspond to sites 100–200. It emphasizes that the Mendoza–Hartzell source model is not based on the tsunami data; therefore, disagreement between the observed and the simulated tsunami results is not unexpected.

Effects of Accounting for Parameter Uncertainty in Earthquake Source Generation

Regarding the effects of the uncertainty of the scaling relationships (i.e., **Figure 12A** versus **Figure 12B**), it can be seen that the variability of the simulation results is significantly increased, especially for the maximum tsunami height profiles (although general trends of the results are similar for both cases). The mean and upper 16th percentile values of the simulated results with the uncertainty of the scaling relationships are larger than the results without the uncertainty of the scaling relationships. Especially, when the uncertainty of the scaling relationships is taken into account, the upper 16th percentile and upper bound of the maximum tsunami height, shown as background gray lines in **Figure 12**, become quite large and are related to the increase of the maximum slip due to the uncertainty by Eq. (4). Thereby, the estimation of scaling relationship for the maximum slip and its uncertainty by analyzing inversion slip models are important for tsunami hazard assessment.

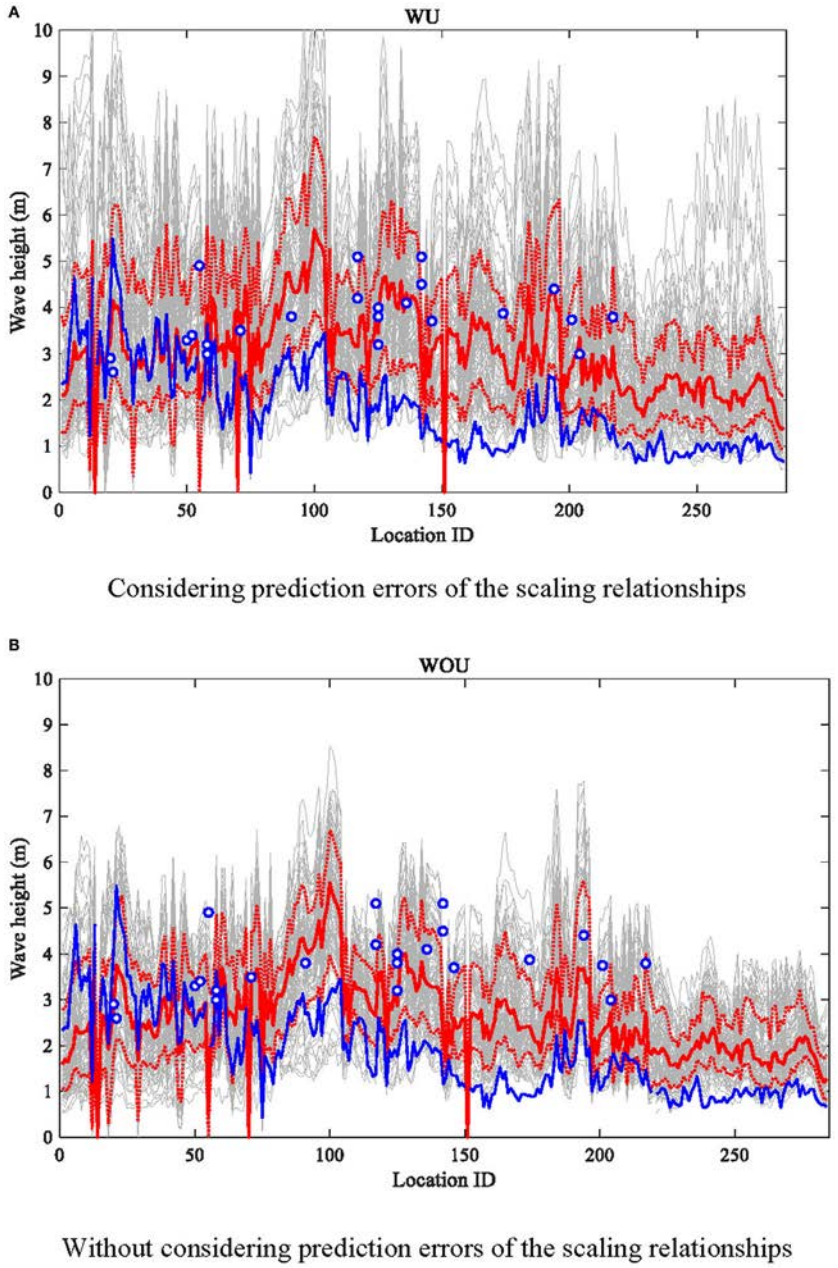

FIGURE 12 | Maximum tsunami wave height profile along the coastal line for the stochastic models with and without considering prediction errors of the scaling relationships [red solid line: mean, red dashed line: upper and lower 16%, gray line: individual stochastic run, blue solid line: historical run, circle: observed run-up height by Trejo-Gómez et al. (2015)]. **(A)** Considering prediction errors of the scaling relationships. **(B)** Without considering prediction errors of the scaling relationships.

The impact of stochastic modeling on time series of tsunami profile at the recording locations 1–3 (from north to south) are illustrated in **Figure 13**. The tsunami waveforms at the recording locations 1–3 show that the wave amplitudes are generally higher at the recording location 1 than those at the recording stations 2 and 3. The simulated tsunami waveforms for the recording locations 1–3 also exhibit large variations in the temporal tsunami profiles, indicating that tsunamis having amplitudes up to 5 m may be expected at offshore locations for the M_w 8.0 earthquake scenario. The largest variability due to different stochastic source models is found at the first peak of tsunami waves; such large variability is also observed for a few subsequent waves after the first one. However, the signs of the first wave do not change over the stochastic simulations, and the first waves always begin with positive change. Moreover, edge waves following continental shelf are mainly affected by large-scale nearshore bathymetry, which is

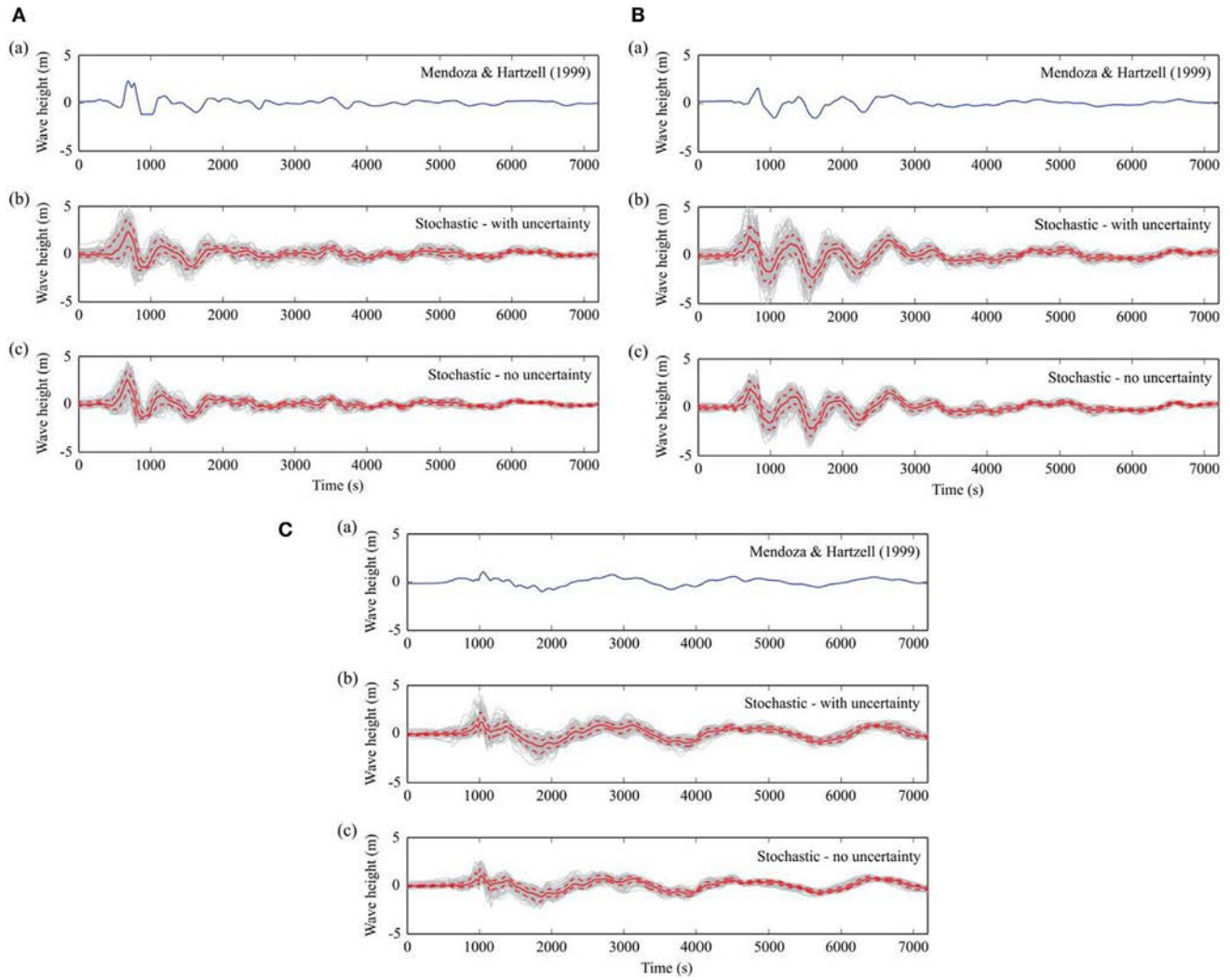

FIGURE 13 | Tsunami waveforms at the recording locations: top to bottom: location 1–3. **(A)** Mendoza–Hartzell model, **(B)** stochastic models by considering prediction errors of the scaling relationships, and **(C)** stochastic models without considering prediction errors of the scaling relationships (solid line: mean, dashed line: upper and lower 16%, gray line: individual run).

independent of slip source modeling. Consequently, there is less influence due to the stochastic source models on the later parts of the simulated waves.

CONCLUSION

PTHA for the Guerrero region, Mexico has been carried using the novel stochastic tsunami simulation method. The method takes into account uncertainty of the key source parameters and randomness of slip heterogeneity over the fault plane and, hence, is capable of quantifying the tsunami hazard probabilistically. Such a methodology has not been implemented in the previous PTHA studies for Mexico. The scaling relationships used in the stochastic earthquake source generation have been developed based on extensive statistical analyses of the source models parameters estimated from the SRCMOD database. The bathymetry and elevation data for the region were compiled based on the GEBCO2014 and GDEM2 to develop the nesting grid systems that are suitable for regional tsunami simulation studies. Finally, the developed stochastic tsunami simulation method was applied to the 1995 Colima Earthquake scenario. The results indicated that the effects of the source model characteristics on the simulation results are important. It was also found that the tsunami simulation results using the stochastic source models exhibit significant variability of tsunami profiles, while the results overall agree with the tsunami run-up survey results for the 1995 Colima event.

The extension of the source zone model to the Guerrero region by varying earthquake scenario magnitudes will be the focus of our future study. Such investigations have been carried out for Japan using the similar stochastic tsunami simulation method (Goda et al., 2017). It is also important to simulate tsunami inundation

and run-up and to assess tsunami damage to structures based on the stochastic tsunami simulations along the Pacific Mexican coast.

AUTHOR CONTRIBUTIONS

NM analyzed numerical results. He wrote half part in this manuscript. AM made bathymetry data. He wrote bathymetry setup part of this manuscript. KG setup stochastic slip model. He wrote another half part in this manuscript. TY setup numerical tsunami model. AR-A analyzed historical slips and tsunamis.

ACKNOWLEDGMENTS

The part of this research is supported by The Project for Hazard Assessment of Large Earthquakes and Tsunamis in the Mexican Pacific Coast for Disaster Mitigation, SATREPS funded by JICA-JST. This work was also supported by the Engineering and Physical Sciences Research Council (EP/M001067/1).

FUNDING

JICA/JST SATREPS 1500601 research program on earthquake and tsunami hazard assessment and implementation in Mexico.

REFERENCES

Annaka, T., Satake, K., Sakakiyama, T., Yanagisawa, K., and Shuto, N. (2007). Logic-tree approach for probabilistic tsunami hazard analysis and its applications to the Japanese coasts. *Pure Appl. Geophys.* 164, 577–592. doi:10.1007/s00024-006-0174-3

Bird, P. (2003). An updated digital model of plate boundaries. *Geochem. Geophys. Geosyst.* 4, 1027. doi:10.1029/2001GC000252

Borerro, J., Ortiz, M., Titov, V., and Synolakis, C. (1997). Field survey of Mexican tsunami produces new data, unusual photos. *EOS Trans. Am. Geophys. Union* 78, 85–88. doi:10.1029/97EO00054

Burbidge, D., Cummins, P. R., Mleczko, R., and Thio, H. K. (2008). A probabilistic tsunami hazard assessment for Western Australia. *Pure Appl. Geophys.* 165, 2059–2088. doi:10.1007/s00024-008-0421-x

Courboulex, F., Santoyo, M. A., Pacheco, J. F., and Singh, S. K. (1997). The 14 September 1995 (M=7.3) Copala, Mexico, earthquake: a source study using teleseismic, regional, and local data. *Bull. Seismol. Soc. Am.* 87, 999–1010.

Davies, G., Horspool, N., and Miller, V. (2015). Tsunami inundation from heterogeneous earthquake slip distributions: evaluation of synthetic source models. *J. Geophys. Res.* 120, 6431–6451. doi:10.1002/2015JB012272

DeMets, C., Gordon, R., Argus, D., and Stein, R. (1994). Effect of recent revisions to the geomagnetic reversal time scale and estimates of current plate motions. *Geophys. Res. Lett.* 21, 2191–2194. doi:10.1029/94GL02118

Farreras, S., and Sánchez, A. (1991). The tsunami threat on the Mexican West coast: a historical analysis and recommendations for hazard mitigation. *Nat. Hazards* 4, 301–316. doi:10.1007/BF00162795

Fukutani, Y., Suppasri, A., and Imamura, F. (2015). Stochastic analysis and uncertainty assessment of tsunami wave height using a random source parameter model that targets a Tohoku-type earthquake fault. *Stoch. Environ. Res. Risk Assess.* 29, 1763–1779. doi:10.1007/s00477-014-0966-4

GDEM2 data. (2011). *GDEM2: ASTER Global Digital Elevation Model Version 2. Summary of Validation Results*. Available at: https://asterweb.jpl.nasa.gov/gdem.asp

Geist, E., and Oglesby, D. D. (2014). Earthquake mechanism and seafloor deformation for tsunami generation. *Encycl. Earthquake Eng.* 1, 1–17. doi:10.1007/978-3-642-36197-5_296-1

Geist, E. L. (2002). Complex earthquake rupture and local tsunamis. *J. Geophys. Res.* 107, ESE2-1–ESE2-15. doi:10.1029/2000JB000139

Geist, E. L., and Lynett, P. J. (2014). Source processes for the probabilistic assessment of tsunami hazards. *Oceanography* 27, 86–93. doi:10.5670/oceanog.2014.43

Geist, E. L., and Parsons, T. (2006). Probabilistic analysis of tsunami hazards. *Nat. Hazards* 37, 277–314. doi:10.1007/s11069-005-4646-z

General Bathymetric Chart of Oceans (GEBCO) Dataset. (2014). *Gridded Bathymetry Data (General Bathymetric Chart of the Oceans) GEBCO2014 Dataset*. Available at: https://www.gebco.net/

Goda, K., Li, S., Mori, N., and Yasuda, T. (2015). Probabilistic tsunami damage assessment considering stochastic source models: application to the 2011 Tohoku earthquake. *Coast. Eng. J.* 57, 1–38. doi:10.1142/S0578563415500151

Goda, K., Mai, P. M., Yasuda, T., and Mori, N. (2014). Sensitivity of tsunami wave profiles and inundation simulations to earthquake slip and fault geometry for the 2011 Tohoku earthquake. *Earth Planets Space* 66, 105. doi:10.1186/1880-5981-66-105

Goda, K., and Song, J. (2016). Uncertainty modeling and visualization for tsunami hazard and risk mapping: a case study for the 2011 Tohoku earthquake. *Stoch. Environ. Res. Risk Assess.* 30, 2271–2285. doi:10.1007/s00477-015-1146-x

Goda, K., Yasuda, T., Mai, P. M., Maruyama, T., and Mori, N. (2017). "Tsunami simulations of mega-thrust earthquakes in the Nankai-Tonankai Trough (Japan) based on stochastic rupture scenarios," in *Tsunamis: Geology, Hazards and Risks*, 456 eds E. M. Scourse, N. A. Chapman, D. R. Tappin, and S. R. Wallis (London: Geological Society), 456.

Goda, K., Yasuda, T., Mori, N., and Maruyama, T. (2016). New scaling relationships of earthquake source parameters for stochastic tsunami simulation. *Coastal Eng. J.* 58. doi:10.1142/S0578563416500108

González, F. I., Geist, E. L., Jaffe, B., Kânoğlu, U., Mofjeld, H., Synolakis, C. E., et al. (2009). Probabilistic tsunami hazard assessment at seaside, Oregon, for near- and far-field seismic sources. *J. Geophys. Res.* 114, C11023-1–C11023-19. doi:10.1029/2008JC005132

Goto, C., Ogawa, Y., Shuto, N., and Imamura, F. (1997). "Numerical method of tsunami simulation with the leap-frog scheme," in *IOC Manual, No. 35* (Paris, France: UNESCO).

Hayes, G. (2012). *Preliminary Result of the March 20, 2012 M_w 7.4 Oaxaca, Mexico Earthquake*. Available at: https://earthquake.usgs.gov/archive/product/finite-fault/usp000jghj/us/1486510843869/p000jghj.html

Horspool, N., Pranantyo, I., Griffin, J., Latief, H., Natawidjaja, D. H., Kongko, W., et al. (2014). A probabilistic tsunami hazard assessment for Indonesia. *Nat. Hazards Earth Syst. Sci.* 14, 3105–3122. doi:10.5194/nhess-14-3105-2014

Jaimes, M. A., Reinoso, E., Ordaz, M., Silva, R., Mendoza, E., Huerta, B., et al. (2016). An earthquake-event-based method for mapping tsunami hazards. *Proc. Inst. Civ. Eng.* 169, 148–162. doi:10.1680/jmaen.2015.37

Kostoglodov, V., Singh, S. K., Santiago, J. A., Franco, S. I., Larson, K. M., Lowry, A. R., et al. (2003). A large silent earthquake in the Guerrero seismic gap, Mexico. *Geophys. Res. Lett.* 30, SD9-1–SD9-4. doi:10.1029/2003GL017219

Lorito, S., Selva, J., Basili, R., Romano, F., Tiberti, M. M., and Piatanesi, A. (2015). Probabilistic hazard for seismically induced tsunamis: accuracy and feasibility of inundation maps. *Geophys. J. Int.* 200, 574–588. doi:10.1093/gji/ggu408

Mai, P. M., and Beroza, G. C. (2002). A spatial random field model to characterize complexity in earthquake slip. *J. Geophys. Res.* 107, ESE10-1–ESE10-21. doi:10.1029/2001JB000588

Mai, P. M., and Thingbaijam, K. K. S. (2014). SRCMOD: an online database of finite source rupture models. *Seismol. Res. Lett.* 85, 1348–1357. doi:10.1785/0220140077

McCloskey, J., Antonioli, A., Piatanesi, A., Sieh, K., Steacy, S., Nalbant, S., et al. (2008). Tsunami threat in the Indian Ocean from a future megathrust earthquake west of Sumatra. *Earth Planet. Sci. Lett.* 265, 61–81. doi:10.1016/j.epsl.2007.09.034

Mendoza, C. (1993). Coseismic slip of two large Mexican earthquakes from teleseismic body waveforms: implications for asperity interaction in the Michoacan plate boundary segment. *J. Geophys. Res.* 98, 8197–8210. doi:10.1029/93JB00021

Mendoza, C. (1995). Finite-fault analysis of the 1979 March 14 Petatlan, Mexico, earthquake using teleseismic P-wave-forms. *Geophys. J. Int.* 121, 675–683. doi:10.1111/j.1365-246X.1995.tb06430.x

Mendoza, C., and Hartzell, S. H. (1989). Slip distribution of the 19 September 1985 Michoacan, Mexico, earthquake – near-source and teleseismic constraints. *Bul. Seismol. Soc. Am.* 79, 655–669.

Mendoza, C., and Hartzell, S. H. (1999). Fault-slip distribution of the 1995 Colima-Jalisco, Mexico, earthquake. *Bull. Seismol. Soc. Am.* 89, 1338–1344.

Mori, N., Goda, K., and Cox, D. T. (2017). "Recent process in probabilistic tsunami hazard analysis (PTHA) for mega thrust subduction earthquakes," in *Reconstruction and Restoration after the 2011 Japan Earthquake and Tsunami: Insights and Assessment after 5 Years* (Berlin: Springer).

Mori, N., Takahashi, T., Yasuda, T., and Yanagisawa, H. (2011). Survey of 2011 Tohoku earthquake tsunami inundation and run-up. *Geophys. Res. Lett.* 38, L00G14-1–L00G16-6. doi:10.1029/2011GL049210

Nunez-Cornu, F. J., Oritz, M., and Sanchez, J. J. (2008). The great 1787 Mexican tsunami. *Natural Hazards* 47, 569–576. doi:10.1007/s11069-008-9239-1

Okada, Y. (1985). Surface deformation due to shear and tensile faults in a half-space. *Bull. Seismol. Soc. Am.* 75, 1135–1154.

Pacheco, J. F., and Singh, S. K. (2010). Seismicity and state of stress in Guerrero segment of the Mexican subduction zone. *J. Geophys. Res.* 115, B01303. doi:10.1029/2009JB006453

Pardo-Iguzquiza, E., and Chica-Olmo, M. (1993). The Fourier integral method: an efficient spectral method for simulation of random fields. *Math. Geol.* 25, 177–217. doi:10.1007/BF00893272

Park, H., and Cox, D. T. (2016). Probabilistic assessment of near-field tsunami hazards: inundation depth, velocity, momentum flux, arrival time, and duration applied to Seaside, Oregon. *Coast. Eng.* 117, 79–96. doi:10.1016/j.coastaleng.2016.07.011

Perez-Campos, X., Kim, Y. H., Husker, A., Davis, P. M., Clayton, R. W., Iglesias, A., et al. (2008). Horizontal subduction and truncation of the Cocos Plate beneath central Mexico. *Geophys. Res. Lett.* 35, L18303. doi:10.1029/2008GL035127

Perez-Campos, X., Melgar, D., Singh, S. K., Cruz-Atienza, V., Iglesias, A., and Hjorleifsdottir, V. (2013). Rapid estimation of fault parameters for tsunami warning along the Mexican subduction zone: a scenario earthquake in the Guerrero gap. *Seismol. Res. Lett.* 84, 474–484. doi:10.1785/0220120156

Ramírez-Herrera, M. T., Corona, N., Lagos, M., Černý, J., Goguitchaichvili, A., Goff, J., et al. (2014). Unearthing earthquakes and their tsunamis using multiple proxies: the 22 June 1932 event and a probable fourteenth-century predecessor on the Pacific coast of Mexico. *Int. Geol. Rev.* 56, 1584–1601. doi:10.1080/00206814.2014.951977

Ramírez-Herrera, M. T., Lagos, M., Hutchinson, I., Kostoglodov, V., Machain, M. L., Caballero, M., et al. (2012). Extreme wave deposits on the Pacific coast of Mexico: tsunamis or storms? A multi-proxy approach. *Geomorphology* 139-140, 360–371. doi:10.1016/j.geomorph.2011.11.002

Rikitake, T., and Aida, I. (1988). Tsunami hazard probability in Japan. *Bull. Seismol. Soc. Am.* 78, 1268–1278.

Sánchez, A. J., and Farreras, S. F. (1987). Tsunami flooding extension for coastal zones of Mexico. *Mar. Geod.* 11, 127–135. doi:10.1080/15210608709379555

Suárez, G., and Albini, P. (2009). Evidence for great tsunamigenic earthquakes (M 8.6) along the Mexican subduction zone. *Bull. Seismol. Soc. Am.* 99, 892–896. doi:10.1785/0120080201

SWBD of Shuttle Radar Topography Mission (SRTM). (2008). *SRTM Water Body Data (SWBD) Shoreline Data*. Available at: https://lta.cr.usgs.gov/srtm_water_body_dataset

Tanioka, Y., and Satake, K. (1996). Tsunami generation by horizontal displacement of ocean bottom. *Geophys. Res. Lett.* 23, 861–864. doi:10.1029/96GL00736

Thio, H. K., Somerville, P., and Ichinose, G. (2007). Probabilistic analysis of strong ground motion and tsunami hazards in Southeast Asia. *J. Earthquake Tsunami* 1, 119–137. doi:10.1142/S1793431107000080

Trejo-Gómez, E., Ortiz, M., and Núñez-Cornú, F. J. (2015). Source model of the October 9, 1995 Jalisco-Colima Tsunami as constrained by field survey reports, and on the numerical simulation of the tsunami. *Geofísica Int.* 54, 149–159. doi:10.1016/j.gi.2015.04.010

Wei, S. (2012). *March/20/2012 (M_w 7.4), Oaxaca, Mexico Source Models of Large Earthquakes*. Available at: http://www.tectonics.caltech.edu/slip_history/2012_Mexico/index.html

Yagi, Y., Mikurno, T., Pacheco, J., and Reyes, G. (2004). Source rupture process of the Tecoman, Colima, Mexico earthquake of 22 January 2003, determined by joint inversion of teleseismic body-wave and near-source data. *Bull. Seismol. Soc. Am.* 94, 1795–1807. doi:10.1785/012003095

Zigone, D., Rivet, D., Radiguet, M., Campillo, M., Voisin, C., Cotte, N., et al. (2012). Triggering of tremors and slow slip event in Guerrero, Mexico, by the 2010 M_w 8.8 Maule, Chile, earthquake. *J. Geophys. Res.* 117, B09304-1–B09304-7. doi:10.1029/2012JB009160

Conflict of Interest Statement: The authors declare that the research was conducted in the absence of any commercial or financial relationships that could be construed as a potential conflict of interest.

The reviewer, IT, declared a shared affiliation, though no other collaboration, with one of the authors, NM, to the handling editor, who ensured that the process nevertheless met the standards of a fair and objective review.

Copyright © 2017 Mori, Muhammad, Goda, Yasuda and Ruiz-Angulo. This is an open-access article distributed under the terms of the Creative Commons Attribution License (CC BY). The use, distribution or reproduction in other forums is permitted, provided the original author(s) or licensor are credited and that the original publication in this journal is cited, in accordance with accepted academic practice. No use, distribution or reproduction is permitted which does not comply with these terms.

frontiers in Built Environment

REVIEW
published: 19 January 2017
doi: 10.3389/fbuil.2017.00002

Tsunami-Driven Debris Motion and Loads: A Critical Review

Ioan Nistor[1]*, *Nils Goseberg*[1,2] *and Jacob Stolle*[1]

[1] Department of Civil Engineering, University of Ottawa, Ottawa, ON, Canada, [2] Ludwig-Franzius-Institute for Hydraulic, Estuarine and Coastal Engineering, Leibniz Universität of Hannover, Hannover, Germany

Recent natural disasters, such as the 2004 Indian Ocean and 2011 Tohoku Tsunami, exhibited the importance of tsunami-resistant infrastructure in high-risk coastal areas. The failure of critical infrastructure in tsunami-stricken communities has led to a recent emphasis on extreme loading conditions associated with tsunami events. One of the critical loads identified by previous research was debris loads. Debris is defined as solid objects entrained within the inundating flows and can range from construction materials to shipping vessels. The emphasis of tsunami loading has led to recent progression in the understanding of debris loads and effects, particularly in evaluating the impact of a single debris piece on a structure. The following paper reviews state-of-the-art research in tsunami-driven debris motion and loads and identifies future directions of research into debris loads and effects to aid in the design of tsunami-resistant infrastructure.

Keywords: tsunami, debris, impact loads, debris damming, coastal engineering, hydraulic engineering

OPEN ACCESS

Edited by:
Katsuichiro Goda,
University of Bristol, UK

Reviewed by:
Andrew Foster,
University College London, UK
Takashi Tomita,
Nagoya University, Japan

***Correspondence:**
Ioan Nistor
inistor@uottawa.ca

Specialty section:
This article was submitted to Earthquake Engineering, a section of the journal Frontiers in Built Environment

Received: *30 November 2016*
Accepted: *04 January 2017*
Published: *19 January 2017*

Citation:
Nistor I, Goseberg N and Stolle J (2017) Tsunami-Driven Debris Motion and Loads: A Critical Review. Front. Built Environ. 3:2. doi: 10.3389/fbuil.2017.00002

INTRODUCTION

Tsunamis are among the most destructive and deadly natural disasters. Several recent events, such as the 2004 Indian Ocean Tsunami, the 2010 Chilean Tsunami, and the 2011 Tohoku Tsunami, have emphasized the importance of studying tsunami-induced loading conditions. The failure of critical infrastructure (Yeh et al., 2014) and the lack of a clear understanding of the tsunami-induced loading conditions highlighted the deficiency of current building design in tsunami-prone areas (Taubenböck et al., 2013). In the aftermath of tsunami events, reviews of current building standards have clearly shown that existing standards do not properly account for, or in some cases explicitly address, tsunami loads and effects (Palermo et al., 2009). These findings have led to an increased emphasis on the need to understand tsunami flow conditions and associated loads by researchers, engineers, and policy makers in an attempt to design tsunami-resilient infrastructure. In North America, this effort resulted in the addition of a new chapter in the upcoming ASCE *Minimum Design Loads for Buildings and Other Structures* (ASCE 7, 2016) for the design of structures in tsunami-prone areas of the United States: West Coast, Alaska, and Hawaii (Chock, 2016).

Tsunami engineering research has primarily focused on hydrodynamic loading, as generally field observations have identified hydrodynamic conditions as the critical load (Charvet et al., 2014). Additionally, information regarding critical flow features, such as maximum inundation and run-up, is available from post-tsunami field surveys. However, many field observations of tsunami-affected built areas have shown that debris loads and effects can play an important role in structural failure (Yeh et al., 2013). Until recently, existing guidelines have conservatively addressed debris impact recommending that all structures be designed for the impact of a single object (FEMA, 2012). Similarly, in research, the focus has been on quantifying the load of a single debris impact (Haehnel and Daly, 2004; Matsutomi, 2009; Aghl et al., 2015). Another aspect in the design of tsunami-resilient infrastructure is the identification of critical areas for debris impact. This aspect has been

significantly more difficult due to the random nature of debris motion (Matsutomi, 2009) and to the wide range of variables that affect debris motion (Naito et al., 2014).

The objective of this review is to (1) evaluate the current state-of-the-art research into tsunami-driven debris motion and loads, (2) indicate areas of research needs, (3) highlight results from a collaborative research effort by the University of Ottawa, Canada, the University of Hannover, Germany, and Waseda University, Japan, to develop new experimental methods to evaluate debris motion, and, finally, (4) evaluate debris impact loads on structures. These objectives have been reached by conducting a comprehensive literature review and further drawing conclusions regarding research gaps and outlining the methodological requirements and facilities to address current and future research needs.

LITERATURE REVIEW

Debris Transport

The focus of post-tsunami forensic engineering surveys of affected coastal communities has primarily evaluated the hydraulic conditions of the tsunami inflow, such as inundation depth, flow velocity, and spatial inundation limits (Saatcioglu et al., 2005; Borrero et al., 2006; Fritz et al., 2006). However, information regarding debris impact cannot easily be identified from the field data, aside from the fact that debris impact may have occurred. Critical information such as the flow conditions, debris velocity, and debris orientation at the time of impact cannot be determined without a video or images of the impact (Charvet et al., 2014). Therefore, very little information regarding debris dynamics within extreme hydrodynamic flows can be derived directly from field impact sites in the aftermath of a disaster.

Debris motion has been equally challenging to evaluate in the field, as the type of debris can vary significantly and few studies have performed a comprehensive survey of debris in the aftermath of a tsunami event. Any rigid or deformable objects entrained within the inundating flow, such as construction materials, vehicles, or shipping vessels, all common to many coastal communities, can become debris (Naito et al., 2014). Additionally, multiple potential debris sources make the identification of the source of debris challenging, particularly in the post-event site surveys. The work of Naito et al. (2014) was among the first field survey to examine overall transport of the debris after the 2011 Tohoku Tsunami. Naito et al. (2014) examined the position of displaced shipping containers and vessels after the 2011 Tohoku Tsunami as they originated from a clear source (the port area) for which substantial documentation of their position before the tsunami existed. From the survey, Naito et al. (2014) were able to develop a conservative estimate of the maximum spreading angle of the shipping vessels in relation to their original location.

Based on the identified sources and subsequent field investigations, Naito et al. (2014) proposed a method to determine the maximum spreading area of the debris. Their method considered the origin of the debris as the geometric center of the debris source (black dot in **Figure 1**). The debris was assumed to propagate in a shore normal direction (dashed line) and conservatively estimated to propagate within a $\pm 22.5°$ spreading sector in the inundation direction to the onshore extent of the tsunami inundation limit. From the point if maximum debris displacement, a similar $\pm 22.5°$ spreading sector was considered as a potential motion area a result of the outgoing flow. Based on the limited observations collected

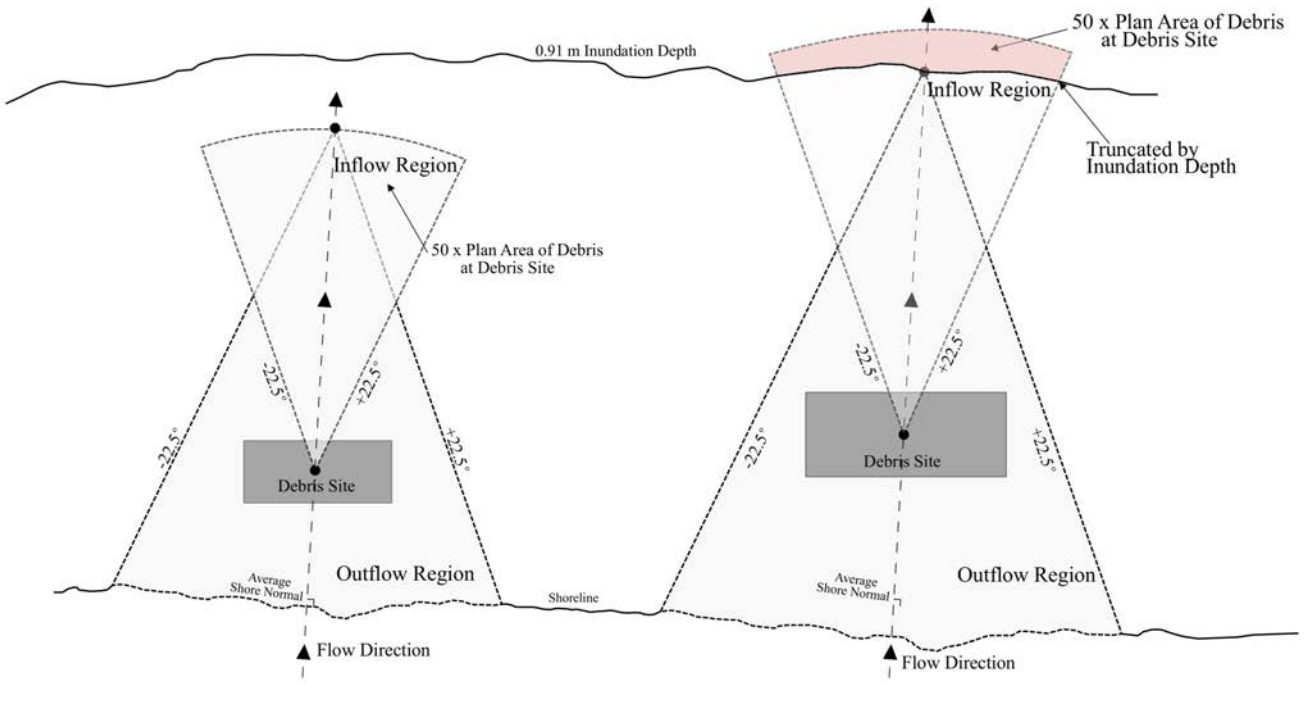

FIGURE 1 | Identification of area for potential debris impact [adapted from Naito et al. (2014)].

from field data, the majority of debris fell well within the proposed spreading angle.

The maximum displacement limit of the debris was calculated based on the debris concentration, which was defined as the plane area of the debris at the source divided by the spreading area of the debris. A conservative estimate was made to establish a debris concentration of 2% that would contain the majority of the debris. The debris limits for the inundating flow are defined by the $\pm 22.5°$ sector area defining a spreading area that gave a debris concentration of 2% (50 times the plane area of the debris), termed the *inflow region*. However, if the spreading area encroached on an area where the inundation depth is less than 0.91 m (the "prescribed" floatation threshold for debris), this area is not considered as it was expected that debris would ground and no longer propagate forward (red area in **Figure 1**). As a result, the maximum inundation limit of the debris would be truncated. Additionally, from the center of the inundation limit, a return spreading area can be again determined using the $\pm 22.5°$ conical area from the inundation limit toward the shoreline. The second area represents the potential spreading sector as a result of the outflow and is termed the *outflow region*. Based on the method outlined by Naito et al. (2014), any critical structures located within the two spreading areas (indicated by the light gray area in **Figure 1**) should be designed for debris impact. A detailed design example using this method can be found in Naito et al. (2016).

While the method of Naito et al. (2014) provided a conservative approach to evaluating the debris impact potential, several assumptions are associated with their proposed method. The topography of the spreading area has a substantial influence on the flow conditions and therefore the debris motion. Naito et al. (2016) indicated that, in cases with large topographical features that would divert flow, the spreading area should be shifted to account for these irregularities. Naito et al. (2014) also indicated that buildings could act as obstacles in the path of debris motion. In the case of industrial areas, large reinforced concrete buildings would act as a barrier to debris motion as long as the inundation depths were less than 0.91 m than the top of the building. However, in cases where the inundation depths' area greater than 0.91 m above the maximum height of the building or when the surrounding buildings are likely to be destroyed by the inundating flow (wooden structures), the buildings should not be considered as obstacles to the debris. Additionally, the method only examined one type of debris whereas debris are of wide variety of sizes and properties, such as buoyancy, that would influence their propagation distance.

To provide a larger dataset examining the spreading area of debris in tsunami-like flow conditions, Nistor et al. (2016) examined the transport of multiple scaled-down shipping containers in controlled laboratory conditions, over a flat horizontal topography and with no obstacles. The study found that the spreading angle of the debris increased as the number of debris increased. This was attributed to the inter-debris collisions and flow perturbations caused by the debris within the flow. Nevertheless, the motion trajectories of all debris occurred well within the spreading angle of $\pm 22.5°$ proposed by Naito et al. (2014). Nistor et al. (2016) determined that as the number of debris increased, the longitudinal displacement of the debris decreased. The latter conclusion counters the method proposed by Naito et al. (2014), which suggested that as the number of debris increased, the spreading area also increased. Additionally, Nistor et al. (2016) noted that the debris tended to propagate as an agglomeration which counters assumptions, made in the FEMA P646 (FEMA, 2012), that the likelihood of multiple debris impacts occurring is unlikely.

Goseberg et al. (2016b) built upon the study of Nistor et al. (2016) by including a scaled-down built environment, to act as obstacles to the propagating debris. Their study found that the obstacles acted as a macro-roughness feature for both the debris and inundating flow, resulting thus in significantly shorter longitudinal displacements of the debris. However, the obstacles appeared to have no influence on the spreading angle and the debris once again fell well within the $\pm 22.5°$ spreading angle proposed by Naito et al. (2014). Due to scaling issues related to debris transport in a scaled experimental environment, further work is needed to properly understand the momentum transfer for debris–debris and debris–fluid interactions to possibly amend the method proposed by Naito et al. (2014).

There are still multiple challenges that must be overcome to properly model debris motion in a reduced scale experimental setting. The foremost issue is the scaling of tsunami flow conditions (Madsen et al., 2008; Rossetto et al., 2011; Goseberg et al., 2013). Related to debris transport, the motion of debris was shown to be a highly variable process (Bocchiola et al., 2006; Matsutomi, 2009). Hence, extensive information is required to obtain meaningful results. To retrieve the necessary information, tracking of the debris' transient motion requires experimental methods that do not influence the debris motion while providing high-quality data regarding the debris' position, orientation, acceleration, and velocity.

Braudrick and Grant (2000) examined the entrainment of individual large woody debris (LWD) in steady flow conditions. Experiments were performed to test a simple entrainment model of a single piece of LWD based on a balance of forces as depicted in **Figure 2**. The original model considered the LWD as a smooth cylinder lying on a smooth bed; however, the debris cross-sectional geometry may also be rectangular. The initial movement of the LWD was by sliding, though Braudrick and Grant (2000) noted that the initial movement tends to be more complex with significant pivoting involved. **Figure 2** outlines the basic force balance used in the model considering a flow downstream with a channel of slope θ. The gravity force is the effective weight ($W_{\text{eff}} = F_g - F_{\text{Buoyant}}$) of the debris. The friction force ($F_f = F_N \mu$) acts in the upstream direction and is a function of the normal force (F_N) and the friction coefficient (μ) between the bed and the LWD. The drag force (F_d) is a function of the water velocity, flow depth, drag coefficient, and angle that the log is traveling in relation to the flow direction. The model performed reasonably well under experimental scrutiny though the pivoting, which was not captured by the model, was an important aspect of the LWD motion.

Imamura et al. (2008) experimentally evaluated the transport of boulders in a dam-break flow and developed a simple model for estimating their motion. Imamura et al. (2008) determined that the boulders tended to be transported by saltation or rolling

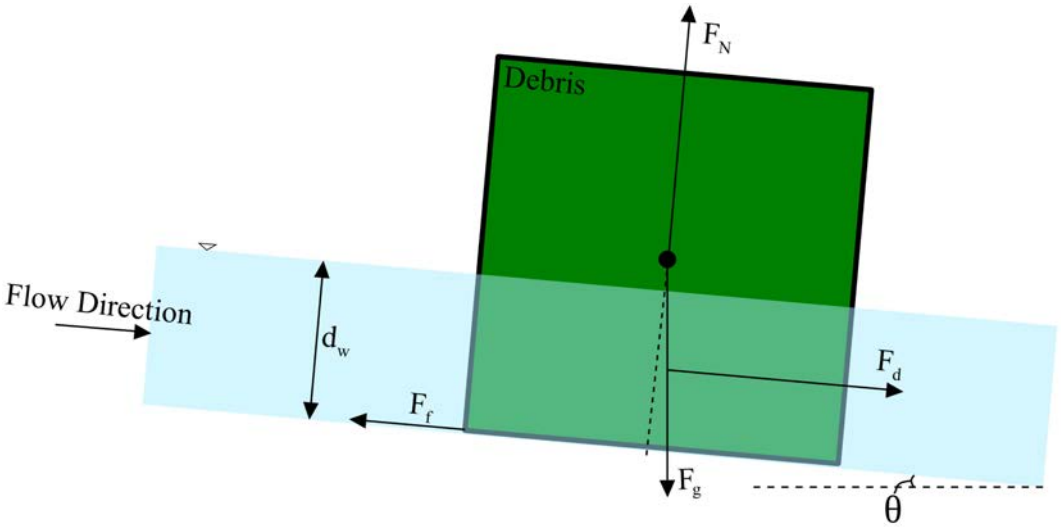

FIGURE 2 | Debris entrainment force balance [adapted from Braudrick and Grant (2000)].

initially (within the higher velocity flow). When flow velocity began to decrease, as the bore reached the point of maximum inundation and as the bore receded, the boulders would be transported by sliding. Their study also found that the debris orientation affected the motion of the boulder. The boulder would always pivot to have the long axis perpendicular to the flow direction, using some of the hydrodynamic energy, resulting thus in the boulder aligning with the long axis perpendicular to the flow and having thus a greater displacement under inflow conditions.

The model developed by Imamura et al. (2008) was based on a force balance of the boulder in contact with the ground. The forces to be considered for the boulder transport are the hydraulic force, the frictional force, and the component of the gravitational force on the slope. The balance of these forces resulted in:

$$\rho_s k_r d^3 X'' = \frac{1}{2} C_D \rho_f (U - v) |U - u| \left(k_r d^2\right) + C_M \rho_f U' \left(k d^3\right) - (C_M - 1)\, \rho_f u' \left(k_r d^3\right) - k_r F_b - k_r F_g, \quad (1)$$

$$F_b = \frac{\mu \left(\rho_s - \rho_f\right) k_r d^3 g \cos\theta\, X'}{|X'|}, \quad (2)$$

$$F_g = \left(\rho_s - \rho_f\right) k d^3 g \sin\theta, \quad (3)$$

where ρ_s is the density of the boulder, k_r is the ratio between the long axis and short axis of the boulder, d is the length of the short axis, u' is the acceleration of the boulder, C_D is the drag coefficient, ρ_f is the density of the fluid, U is the current velocity, u is the velocity of the boulder, θ is the angle of topographic slope, μ is the coefficient of friction, and C_M is the mass coefficient. This model tends to underestimate the propagation of the boulders, likely because the friction was always considered (even when saltation or rolling occurred) and the model does not consider the initial pivoting of the boulder, influencing thus the exposed surface area of the debris.

Matsutomi et al. (2008) examined the correlation between debris concentration and debris velocity as well as the hydrodynamic conditions in a dam-break flow. Debris concentration was expressed as the void ratio (1 − plan area of debris/area of flume bed). An increase in the debris concentration resulted in increased flow resistance in the bore front. The flow resistance in turn increased bore depth as well as decreased debris velocity and bore front propagation. The debris velocity was found to be always less than or equal to the bore front velocity.

Matsutomi (2009) evaluated the motion of driftwood pieces in steady-state, high-velocity flow to determine the probability of the driftwood colliding with a structure. The probability of impact was determined based on the lateral diffusion (y-direction) of the driftwood as the driftwood propagated downstream, therefore assuming that the structure would be in the center of the flume. The Gaussian probability distribution of the driftwood location (K_y) in the x- and y-direction was expressed as:

$$K_y(x, y) = \frac{1}{\sqrt{2\pi\overline{\delta}_y}} \exp\left(-\frac{(y - \bar{y})^2}{2\overline{\delta}_y^2}\right), \quad (4)$$

where $\overline{\delta}_y$ is the variance as a function of x (flow direction), roughly expressed as:

$$\frac{\overline{\delta}_y^2(x)}{L_w^2} = \frac{\frac{1}{n}\sum_{i=1}^{n}(y - \bar{y})}{L_w^2} = a\left(\frac{x}{L_w}\right)^b, \quad (5)$$

where L_w is the length of the driftwood, a and b are a function of the debris' physical properties and geometry. Extensive work is still needed in the classification of the a and b coefficients due to the variety of debris that are potentially present during a tsunami (Naito et al., 2014). The mere utilization of wooden debris with uniform draft restrains the validity of such approach in relation with different material debris.

As a preliminary investigation of debris motion in tsunami-like flow conditions, Yao et al. (2014) evaluated the motion of

scaled-down coastal house models in flow conditions developed by the shoaling and subsequent breaking of a solitary wave over a sloping bed. Their study examined the maximum debris inundation compared to the limit of the maximum flow inundation. The debris initially propagated within the overflow of the bore due to high flow velocities and water depths. As the overflow approached maximum inundation, the flow velocity and depth decreased, resulting in the debris contacting the bed and slowing down, falling thus behind the advancing bore front. In the case of smaller offshore waves, the debris fell behind the bore front earlier due to an earlier contact with the bed. For the most part, the debris were unaffected by the receding flow, except when they had grounded significantly earlier and were thus much closer to the coastline. The receding wave, in this case, pulled the debris further seaward than their initial position.

Recent improvements in non-intrusive laboratory techniques for tracking debris motion have allowed for more a more detailed evaluation of the intermediate variables important for debris motion, such as changes in their orientation during displacement as well as their velocity (Goseberg et al., 2016a; Stolle et al., 2016). Rueben et al. (2014) used a novel camera-based tracking algorithm to assess the repeatability of the motion of square boxes on a sloped bed. The camera-based tracking algorithm was developed to identify a pattern of dots painted on the top of each box. The number of dots drawn on the top of each box was the identifier of each box as well as the orientation. The algorithm performed well for experiments conducted at larger scale comparing to smaller scale experiments for which the algorithm failed to identify the pattern on the top of each box.

Rueben et al. (2014) found the motion of the debris was generally 1-D and repeatable during the onshore direction phase. However, once a debris reached its maximum inundation, it would then ground and be subsequently washed seaward by the receding flow. The trajectory of the debris in the receding stage was significantly more variable, possibly due to eddies induced by the grounded debris within the returning flow.

Rueben et al. (2014) additionally examined the effect of multiple debris and fixed obstacles on debris motion. For multiple debris, the motion remained qualitatively similar to that of the single debris case. However, the presence of more debris led to the grounding point being significantly closer to the shore and the peak onshore velocity also occurred later. Alternatively, in offshore direction, peak velocities were similar to the case of single debris experiments. This is likely due to less disturbance induced in the local flow fields by debris as they had already dispersed. To examine the effect of obstacles, a fixed box was placed in front of the debris to initiate a forced rotation. The rotation of the debris resulted in a significantly more random trajectory and grounding point. The obstacle also reduced the peak onshore velocity of the debris, likely as a result of the energy lost during their rotation.

Shafiei et al. (2016) used a sensor-based tracking system, which recorded the accelerations of debris within dam-break flow conditions. The acceleration was then integrated over time to obtain debris velocity. Using a force balance and based on the assumption that debris entrainment begins after the leading edge of the bore passes the debris and that average stream-wise velocity behind the bore is constant, the following equation can be derived regarding the velocity profile (u) of the debris propagation:

$$u(t) = U - \left(\frac{C_d \rho_f A_d}{2m_d} t + \frac{1}{U}\right)^{-1} \tag{6}$$

where U is the bore velocity, C_d is the drag coefficient, ρ_f is the density of fluid, A_d is the area of the debris projected to the incoming bore direction, m_d is the mass of the debris, and t is the debris travel time. The study showed that the debris velocity matched well to the proposed model and indicated the limit of Eq. 6 is the bore velocity.

Debris Impact

The primary approach to the modeling of debris loads has been on the impact force of a single debris on a structure (FEMA, 2012). As a result, the focus of current tsunami guidelines solely considers the impact of single debris; the likely occurrence of multiple, simultaneous debris impacts has not yet been evaluated. Nouri et al. (2010) examined the impact of a single wooden log on a structure. The debris impact resulted in an increase of the peak forces acting on the structure from 250 to 650 N. It was noted that while the debris impact load can be large, the dynamics of the impact are significantly different than those of the hydrodynamic loads, which are sustained. Nouri et al. (2010) also examined the impact duration of the debris and found that the impact duration was constant regardless of variation in log mass and velocity.

The majority of debris impact research has gone into determining maximum debris impact forces, as the maximum force will conservatively be included in the future design guidelines. The determination of the debris impact load has been based on the one-degree-of-freedom model proposed by Haehnel and Daly (2002) (**Figure 3**). Where the structure is considered to be rigid, the impact zone is considered to have a stiffness (k_i), the debris propagating at velocity (u_d) with a stiffness (k_d) impacts the zone causing a net displacement of x_0. Due to the relatively short duration of the impact, the damping has generally been ignored.

There are several methods of solving for the maximum impact force, the most common approach being the contact-stiffness method, which is the approach used by the FEMA P646 (FEMA, 2012). The basis for this prescription is given by a debris modeled as a log impacting a rigid structure (Haehnel and Daly, 2004). Maximum impact force is thus expressed as:

$$F_{i,\max} = u\sqrt{k\left(m_d + C_M m_f\right)}, \tag{7}$$

where u is the velocity of the debris, k is the effective contact stiffness ($k = \frac{1}{k_i} + \frac{1}{k_d}$), m_d is the mass of the debris, C_M is the added mass coefficient (dependent on debris geometry and density), and m_f is the mass of displaced fluid. In considering the maximum impact force, Matskevitch (1997), in a study of ice impacts, included a reduction in the impact force as a result of the eccentricity (e) and Haehnel and Daly (2004) considered the obliqueness (β) of the impact.

$$e = \frac{1}{\sqrt{1 + \left(\frac{\varepsilon_0}{r_i}\right)\left(1 + \mu\left(\frac{r_0}{\varepsilon_0}\right)\right)}}, \tag{8}$$

$$\beta = \sin\varphi, \tag{9}$$

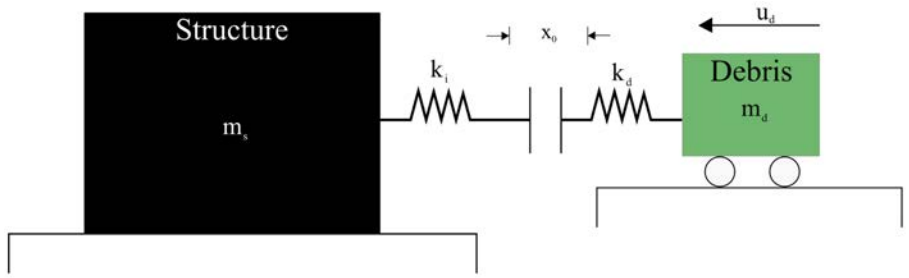

FIGURE 3 | Schematic of the one-degree-of-freedom model proposed by Haehnel and Daly (2002).

where ε_0 is the distance from the center of gravity of the debris to the point of impact, r_i is the radius of gyration of the debris, μ is the coefficient of friction between the debris and structure, r_0 is the radius of the log, and φ is the angle of impact relative to the log surface. Haehnel and Daly (2004) examined the effects of impact eccentricity, the distance from the impact axis to the center of gravity of the debris, and obliqueness, angle of the impact face to the structural face, on the impact force.

From the analysis of the impact force, Haehnel and Daly (2004) derived Eq. 10. The eccentricity of the debris impact results in a decrease in the impact force proportional to the distance of the impact away from the center of gravity of the debris. The obliqueness of impact generally decreased in a sine function from the 90° impact (long axis perpendicular to the structure). However, for a 0° angle of impact, the impact force was maximum. Although eccentricity resulted in a decrease in the maximum impact force, torque around the vertical axis of a structural member might be a side-product and no guidance exists at present to address such an additional load.

$$F_{i,\max} = e\beta u\sqrt{k\left(m_D + C_D m_f\right)}. \tag{10}$$

Riggs et al. (2014) evaluated the added mass coefficient by examining the impact of an aluminum box on a structure in-air and in-water. The in-water tests were performed by connecting an aluminum specimen to guidewires within a flume. The flume used a long wave generator to generate a wave that propagated the aluminum specimen along the guidewire toward the structure. The in-air tests were performed by connecting the aluminum specimen to a pendulum system that accelerated the specimen to a velocity matching the velocity in the in-water tests. The study found very little difference in the peak impact force between the in-air and in-water tests. Moreover, Riggs et al. (2014) determined that the difference in impact force between the in-air and in-water tests was unaffected by the debris impact velocity. Based on these findings, Riggs et al. (2014) did not support the use of the added mass coefficient in the evaluation of debris impact force. However, Shafiei et al. (2016) performed a similar study examining the effect of the added mass coefficient with denser debris and found the peak impact force to be up to 1.5 times greater in-water than in-air. More research is needed to determine if the added mass coefficient is necessary in the design for debris impact at full scale.

Aghl et al. (2014) expanded upon the work by Riggs et al. (2014) to develop a 1-D bar model that accurately estimated the impulse demand of a debris impact event. The model considered the structure to be rigid, therefore the impact force which was fully dependent on the properties of the debris. The impact force (F) was derived from the 1-D wave equation, assuming that the debris responds uniaxially to impact (Eq. 11). The impact force equation was very similar to that of the contact-stiffness approach (Eq. 7), without the added mass of the fluid. For the 1-D wave equation to be correctly evaluated, the stiffness of the debris must be considered as the equivalent stiffness of a 1-D bar (k_d) (Eq. 12).

$$F = u\sqrt{k_d m_d}, \tag{11}$$

$$k_d = \frac{EA_d}{L_d}, \tag{12}$$

where u is the impact velocity, m_d is the mass of the debris, E is the Young's modulus, A_d is the cross-sectional area of the debris, and L_d is the length of the debris. The derived formula also resulted in a constant impact force for the duration of the elastic impact, resulting in a rectangular impact pulse with a duration of t_d.

$$t_d = 2\sqrt{\frac{m_d}{k_d}}. \tag{13}$$

Aghl et al. (2014) evaluated the 1-D bar model with in-air experiments performed by accelerating debris (at full scale) to impact structures using a pendulum system. The experiments were performed with a wood pole, a steel tube, and shipping containers. The peak impact force was demonstrated to be within 5% for all the impact experiments when compared to the model equation. The impact duration was also well predicted in the cases of direct or close to direct impact of the shipping container. However, as the container impacted at the corners, the impact was not elastic, as was modeled, resulting in a significant difference between the analytical and experimental impact duration. Each debris impact force–time history had a characteristic impulse shape for the different debris types: half-sine (wood pole), rectangular (steel tube), and trapezoidal (shipping container). For all experiments, the impulse (area under the curve) for the impact model was less than the experimental results, indicating that the impact model is a conservative estimate of the impulse.

Ikeno et al. (2016) performed large-scale experiments evaluating the impact of large wood logs using a dam-break hydraulic boundary condition as well as in-air testing. The study compared the results of both test conditions to available debris impact models. The authors noted that the impact force using a hydraulic

boundary condition had a significantly lower impact force than the in-air experiments as well as the impact models. As a result, they considered the potential effects of water cushioning between the wood-log and the impact surface. Additionally, Ikeno et al. (2016) considered the effect of oblique collisions using the transformation of kinetic energy to rotational energy during oblique debris impacts by defining a reduction coefficient λ:

$$\lambda = \frac{1 + \left(\frac{\varepsilon_0}{r}\right)^2 \cos^2\theta}{1 + \left(\frac{\varepsilon_0}{r}\right)^2}, \tag{14}$$

where θ is the collision angle between the debris face and the impact surface. The authors noted that the improved equation still overpredicted the experimental results, though it did not reproduce the reduction in force observed in the experimental data.

The ASCE7–Chapter 6: Tsunami Loads and Effects is the first guideline which approaches the design of coastal structures in tsunami-prone areas in mandatory language (Chock, 2016). The code uses the approach outlined by Aghl et al. (2014) for calculating the maximum impact force and duration. In the event that the structure being designed is in close proximity to debris sources with large debris, such as shipping containers and shipping vessels, the code also uses the approach proposed by Naito et al. (2014) to determine if the structure must be designed for the larger debris impact loads.

Debris Damming

Debris entrained within the flow can result in additional loads and effects on structures, particularly when the debris forms a "dam" in front of the structure or between columns, referred to as debris damming or accumulation (Robertson et al., 2007). The hydrodynamic force on a structure can be estimated by using a similar equation to the drag force (F_D) (Bremm et al., 2015):

$$F_D = \frac{1}{2} C_D \rho_f A U^2, \tag{15}$$

where C_D is the drag coefficient, ρ_f is the density of the fluid, A is the cross-sectional area, and U is the flow velocity. The debris dam created by the debris will increase the cross-sectional area (A), which will in turn increase the hydrodynamic force linearly (Yeh et al., 2014). Alternatively, the properties of the dam will influence the drag coefficient as well as the surrounding hydrodynamic conditions (Parola, 2000).

While very little research has gone into debris damming in tsunami flows, research has been done within river engineering. Debris damming, in river flows, has been extensively studied due to the buildup of debris at bridge piers, depending on the shape of the structure the drag coefficient may vary as a result of the dam (Parola, 2000). The dam creates a blockage, further restring the flow path, the blockage results in a large increase in the flow depth. The debris dams also can result in increased scour as they tend to redirect the flow pattern resulting in increased scour underneath the debris dam (Pagliara and Carnacina, 2013). Due to the more diverse nature of debris in tsunami flows and due to different obstacle settings found in tsunami inundation areas, further research is expected to clarify whether river engineering findings on debris damming can be applicable to tsunami engineering.

Numerical Modeling of Debris

The numerical modeling of fluid–structure interactions (FSI) is a common topic in several fields of engineering. One of the main issues is that the numerical model needs to be able to reproduce all the physically relevant scales that affect the FSI (Canelas et al., 2015). However, the physical scales that affect the interaction are often not clear, resulting in these models requiring a high level spatial and temporal resolution. This difficulty has led to attempts to simplify the FSI by providing one-way coupling between model elements: fluid–structure or fluid–air–structure. One-way solid–fluid coupling considers the solids as massless marker particles that moved unconstrained on the water surface (Wu et al., 2014). One-way fluid–solid coupling causes the solids to move in relation to the fluid without the solids affecting the fluid. The one-way coupling methods can provide good results if the scale of the interaction between the phases is disproportionate in one direction, however, for many cases this is not the case. Two-way dynamic coupling of fluid and solid numerical solvers have become increasingly popular as computational resources are able nowadays to handle the significant computational demands of the two-way models. However, the development is still very much in its early stages.

Wu et al. (2014) used the Navier–Stokes equations coupled with the VOF free-surface tracking technique and a large eddy simulation turbulence model to calculate the flow field around the solids. Additionally, Wu et al. (2014) used partial cell treatment (PCT) to locate the faces of the solids. The basic principle of the PCT is similar to the VOF method where each cell was assigned a value between 0 and 1 indicating the phases present in the cell. When the solid phase was present within the cell, the cell is assigned a porosity that reduces the effective volume of the cell, and in the case where the cell was completely solid, the cell was removed from the Navier–Stokes equation calculations. The calculated porosity was used to adjust fluxing quantities, such as momentum and mass. The motion of the floating body was determined using the discrete element method (DEM) to calculate the translation and rotation. The translation was calculated using Newton's equations of motion, and the rotation was calculated using Euler's equations. The forces on the solid were calculated by integrating the fluid pressures on the surface of the solid.

The model from Wu et al. (2014) was validated using two laboratory experiments: a positively buoyant box in a tank of water (0.15 m × 0.14 m × 0.14 m) and a negatively buoyant box (0.02 m × 0.02 m × 0.02 m) in a tank of water. The boxes were released in the tank, and the motion of the box was tracked using cameras. Generally, good comparison between the numerical and experimental results was observed, with a maximum difference in displacement of 0.0044 m over a 0.06 m water column. The difference was due to the numerical simulation showing the negatively buoyant box rebounding off the bottom of the tank whereas the experimental results showed no such phenomena.

Smoothed-particle hydrodynamics (SPH) has been increasingly used in the modeling of free-surface flows (Gomez-Gesteira et al., 2012) and has been shown to be able to simultaneously deal with multiple body dynamics (Amicarelli et al., 2015). However, few current models can capably handle the transport of moving bodies in free-surface flow. Primarily, the current models have

modeled the moving bodies as a rigid body of moving particle simulations (MPS) fluid particles with an imposed rigidity (Canelas et al., 2013). While the models have achieved generally good results (Manenti et al., 2008; Rogers et al., 2009), the modeling of the interactions between the body and the fluid was not based on rigid body contact laws (Canelas et al., 2013).

Canelas et al. (2013) incorporated a DEM model where the interparticle rigid body forces are taken from rigid body contact laws. The boundary particles of the rigid body are taken as fluid particle allowing the DEM model to be coupled with the SPH model. The contact force between the fluid and rigid body particles is decomposed into a repulsion force, which also takes into consideration the deformation of the particle, and a damping force, which takes in consideration for energy lost during deformation. The coupled model was validated using a dam-break experiment entraining PVC cubes. While the model and the experimental results had qualitatively similar results, the study noted that that the bottom friction was not properly modeled resulting in the motion of the debris (particularly of the bottom box) to lag behind the experimental results. Moreover, due to the high computational cost associated with the coupled model resulted in the particle resolution being too low to properly resolve the water surface and bore profile.

Amicarelli et al. (2015) modeled the moving bodies using the MPS method. However, the authors used a modified boundary condition, originally proposed by Adami et al. (2012), for a more stable pressure gradient around the moving bodies. The solid–solid interactions were also adjusted by the addition of a coefficient to the repulsive boundary conditions proposed by Monaghan (2005) to better preserve global momentum and kinetic energy through the body–body interactions. The SPH model was validated using a 2D wedge falling into a water tank. The study compared the acceleration of the experimental and numerical model with generally good accuracy. Pressure fluctuations were common throughout the experimental runs, which is a commonly noted problem with SPH models (Gomez-Gesteira et al., 2012; St-Germain et al., 2013).

The numerical model used in Amicarelli et al. (2015) was also used to qualitatively examine 3-D test cases where debris interacted with a bore front and two sets of obstacles. The bore was developed using a dam-break, and the debris was tracked using cameras. The numerical model resulted in good results when comparing both the trajectory and the orientation of the debris was also relatively well reproduced. The presence of the obstacles resulted in the formation of recirculation zones in front of the obstacles furthest downstream, and the body dynamics were maintained through this highly non-linear zone.

Canelas et al. (2015) presented the most recent version of the DualSPHysics with its many improvements on current modeling of fluid–solid interactions. The primary difference in the model presented by Canelas et al. (2015) was the addition of a δ-SPH term to the continuity equation which helps in the interface description between the solid and fluid phase. The rapid change in the density at the interface results in the pressure and density fluctuations that can be seen in many SPH fluid–solid modeling. The SPH model showed promising results when examining the rising of a submerged positively buoyant cylinder. The SPH model compared well to the analytical solution for the linear acceleration when the Reynold's number was laminar and showed a noticeable shift in acceleration as the boundary layer transitioned to turbulent flow. The model also showed the stabilization of the density fields indicating that the δ-SPH term helping handle that particular common problem.

While the work by Canelas et al. (2015) and Amicarelli et al. (2015) showed a lot of promise in the SPH fluid–solid modeling, there are still many issues that have yet to be thoroughly evaluated. Amicarelli et al. (2015) presented a method of handling solid–solid interactions, yet, the contact mechanics were not fully evaluated. Canelas et al. (2013) coupled the SPH model with a DEM; however, the large computational cost associated with the coupling makes the use of the coupled model unfeasible for many studies. The addition of solid deformation and inelastic collisions would also greatly improve the applicability of the model throughout coastal and hydraulic engineering.

CRITICAL REVIEW AND FUTURE RESEARCH DIRECTIONS

The above presented literature review outlines the state-of-the-art knowledge on debris-induced loading and associated effects in the context of extreme hydrodynamic flows as arising from natural disasters, such as storm surges, tsunami, and flash floods. The current body of literature covers fundamental processes of impacts on vertical structures, either derived from experimental or analytical strategies. To date, this knowledge has started to improve guidelines and standards written in mandatory language, yet many aspects of the problem of debris exerting forces on or interacting with the build environment remain unclear.

The study of debris within the context of tsunami engineering has been difficult due to the random nature of debris transport (Matsutomi, 2009). Determining aspects of debris dynamics from post-event engineering survey has been challenging due to a lack of documentation regarding potential debris sources (Naito et al., 2014). Moreover, determining impact forces without the flow conditions at the time of impact makes drawing conclusions from impact sites equally challenging. Due to these challenges, along with the relative rare occurrence of tsunami events, available field data to be compared to experimental and numerical modeling results are limited to few post-tsunami forensic engineering surveys. Therefore, the determination of debris dynamics and impact loads has primarily been performed in an experimental setting.

The study of tsunami flows and their interaction with coastal infrastructure in a laboratory setting has fundamental scaling issues related to the period of a tsunami wave. Historically, the study of tsunami loads was performed using a broken solitary wave as the hydrodynamic boundary condition (Arnason et al., 2009). However, Madsen et al. (2008) showed that the spatial and temporal duration of a solitary wave was not on the same order of magnitude of observed tsunamis. Despite these observations, broken solitary waves have still be used to examine the near-shore impact of tsunami waves as well as incipient debris transport (Arnason et al., 2009; Chinnarasri et al., 2013; Yao et al., 2014; Nistor et al., 2016). Chanson (2006) indicated that the dam-break

solution was a good representation of tsunami surge profile over a coastal plain. The application of the dam-break in an experimental setting has shown better results representing the period of a tsunami wave (Imamura et al., 2008; Al-Faesly et al., 2012; Shafiei et al., 2016), though large experimental facilities are needed to achieve these flow durations at an appropriate scale. Other techniques, such as the use of N-waves (Tadepalli and Synolakis, 1994), cnoidal waves (Synolakis et al., 1988), and pump-driven long wave generation (Goseberg et al., 2013), have been shown to better represent tsunami inundation temporal features in a variety of cases. However, these experiments were performed at small scales. In determining maximum debris loads, the hydrodynamic boundary conditions must be carefully considered within the experimental procedure; it is generally recommended to aim at scales as large as possible to accurately model debris impact processes (Chock, 2016).

The problem of experimental scales extends to debris dynamics and impact loads, where little research has been done to determine minimum scales at which experiments can be performed. Studies of debris transport have mentioned the effects of turbulent eddies on debris transport (Rueben et al., 2014; Yao et al., 2014). However, as with most coastal physical models, studies are often scaled using the Froude number. The scaling of a model using the Froude number often does not adequately scale turbulent length scales (She and Leveque, 1994), resulting in an unproportioned effect of turbulence on the debris transport. Another scaling concern for debris transport is the effect of viscosity on the transport of debris at small scales. Similar to the modeling of dam-breaks (Lauber and Hager, 1998), there is likely a scale at which the viscosity of the fluid will have a significant effect on debris transport, and hence, the scaling of physical properties using Froude would no longer be adequate. A determination of the minimum scales required would help evaluate the applicability of studies to debris transport problems.

Additionally, the scaling of the debris for impact loads must also be taken into consideration. Studies of impact loads have often focused on scaling the physical properties of the debris, such as length, width, height, and mass; however, little research has been performed in examining the scaling of mechanical properties, such as stiffness and elasticity, which is critical in determining maximum impact loads. The minimum scales at which these experiments can be performed would be dependent on the material as the study must consider the loads at which the debris maintains elastic properties. A determination of the minimum scales would help identify experimental facilities capable of modeling debris impact loads. Moreover, the scaling of the plastic region of impact needs to consider the effect of debris deformation on maximum impact forces, building upon the studies by Aghl et al. (2015). Other physical properties, such as the draft of the debris, also need to be considered, as was shown in Shafiei et al. (2016) where the draft of the debris had a significant effect on the added mass coefficient.

In overcoming scaling issues related to debris dynamics, the physical modeling of debris is essential to provide benchmarking data for the numerical models, particularly due to the lack of available field or prototype data. Numerical modeling has made recent strides in the development of two-way coupled fluid–solid interactions. The availability of high temporal and spatial resolution of the various drivers of debris transport and impact would allow for numerical models to be accurately validated and calibrated. In particular, the momentum transfer between the fluid and free-floating solids needs to be thoroughly evaluated to be applied to numerical models. The momentum transfer between the fluid and the solid objects, as well as the reciprocal effects, is critical in resolving the entrainment and transport of debris within extreme hydrodynamic events.

In the determination of debris impact loads and effects, the primary objective is to apply the findings of the research to propose accurate methods of determining design loads on structures in extreme hydrodynamic events. One of the difficult aspects in designing for extreme hydrodynamic events, like tsunamis, is determining the design conditions and maximum loads associated with such rare events. Commonly, the design conditions for tsunamis are taken from historical maximum tsunamis (Okada et al., 2005). However, as observed during the 2011 Tohoku Tsunami, historical maximums may not always provide a measure of maximum conditions (Esteban et al., 2015). As a result, recent efforts have been made to implement probabilistic tsunami hazard analysis and tsunami-resistant design (Chock, 2015).

Assessing debris impact is currently considered as a deterministic design condition (Chock, 2016), despite the motion of debris being a random process (Matsutomi, 2009). The FEMA P-55 and FEMA P-646 (2012) guidelines maintain a conservative approach where debris impact should always be considered. The upcoming ASCE7 Chapter 6 also maintains a conservative approach when referring to debris ubiquitous to coastal areas, such as hydro poles and concrete debris (Chock, 2016). However, for larger debris, the ASCE7 uses the empirical approach proposed by Naito et al. (2014), based on a limited data set. The limited data set was due to difficulties in assessing debris sources in the aftermath of the 2011 Tohoku Tsunami, limiting the data set to debris with clearly defined debris sources, such as shipping vessels and shipping containers.

To better design structures for debris impact within the probabilistic assessment of tsunami hazard and account for the random nature of debris motion, the probabilistic assessment of debris motion would improve the quantification of debris loads. Considering the effect of the proximity of the debris site, the debris' physical properties, local topography, surround obstructions, and potential flow conditions on debris dynamics and entrainment would also help assess the likelihood of debris impact, as well as identify the type of debris impacting a structure.

Additional consideration is needed to quantity of debris entrained within the flow. Currently, design guidelines only consider the possibility of single debris impacts. However, in a study of the transport of shipping containers in extreme hydrodynamic events, Nistor et al. (2016) determined that the debris often tended to propagate as an agglomeration. Based on this finding, an assessment of multiple debris impact needs to be studied to determine if building standards need to consider multiple debris impacts as the critical load. Additionally, the agglomeration of debris would also increase the risk of debris accumulating at the upstream face of structures, therefore increasing the risk of debris damming.

CONCLUSIONS

Several post-tsunami forensic field surveys over the past decade have led to increased awareness about loads associated with tsunami-induced coastal inundation. One of the loads identified from these field surveys is debris loads, where objects entrained within the flow can impact and accumulate onto structures, causing supplementary loads in addition to the previously considered hydraulic ones. Due to the random nature of debris motion and the relative rarity of tsunami events, the assessment of debris motion loads in the field has been limited. However, recent advancements in the determination of debris dynamics using an experimental setting have allowed for improvements in the methods available for the assessment of mechanisms of debris load as well as of the potential maximum impact loads. Based on an extensive literature review of debris dynamics in extreme hydrodynamic conditions, the following conclusions can be drawn:

1. An assessment of the lower bounds for experimental scales and conditions is needed to determine the type of experimental facilities necessary to accurately assess debris loading conditions. Consideration is needed in scaling of the debris mechanical properties, such as their stiffness and/or elasticity. This is particularly necessary when assessing their plastic deformation, as these properties vary widely and would have to be accounted for in scaled models.
2. As there are several means of reproducing hydrodynamic boundary conditions used in tsunami engineering, the hydrodynamic forcing factor in an experimental setting needs to consider what the critical condition is when assessing debris loads.
3. Rigorous, high-resolution studies are needed to provide detailed, tailored benchmark data sets to aid in the calibration and validation of numerical models developed for debris impact.
4. Fundamental research is needed on the various factors governing the actual debris entrainment and the solid–solid/solid–fluid momentum transfer which are critical for validating numerical models.
5. Due to the random nature of debris motion and recent consideration to probabilistic tsunami hazards design, a probabilistic design approach is needed to assess the likelihood of debris loads occurring, which would be a function of the proximity of debris sources, debris properties, and surrounding environment.
6. It is important to evaluate of multiple impact events, as well as the increased likelihood of debris damming as they propagate as an agglomeration.

AUTHOR CONTRIBUTIONS

IN–lead author, leader of the research project, and wrote the critical discussion. NG–author, part of collaboration, and helped in the writing of both the review and critical discussion. JS–author, graduate student working on debris project, and helped in writing of the review and critical discussion.

FUNDING

The authors acknowledge the financial support by the Strategic Research Foundation Grant-aided Project for Private Universities (No. S1311028) from Japanese Ministry of Education and by Waseda University, of the NSERC Discovery Grant (Canada) and of the Kajima Foundation (Japan). NG acknowledges that this research was supported by a Marie Curie International Outgoing Fellowship within the 7th European Community Framework Programme (No. 622214).

REFERENCES

Adami, S., Hu, X., and Adams, N. (2012). A generalized wall boundary condition for smoothed particle hydrodynamics. *J. Comput. Phys.* 231, 7057–7075. doi:10.1016/j.jcp.2012.05.005

Aghl, P., Naito, C., and Riggs, H. (2014). Full-scale experimental study of impact demands resulting from high mass, low velocity debris. *J. Struct. Eng.* 140, 04014006. doi:10.1061/(ASCE)ST.1943-541X.0000948

Aghl, P. P., Naito, C., and Riggs, H. (2015). Estimation of demands resulting from inelastic axial impact of steel debris. *Eng. Struct.* 82, 11–21. doi:10.1016/j.engstruct.2014.10.021

Al-Faesly, T., Palermo, D., Nistor, I., and Cornett, A. (2012). Experimental modeling of extreme hydrodynamic forces on structural models. *Int. J. Protect. Struct.* 3, 477–506. doi:10.1260/2041-4196.3.4.477

Amicarelli, A., Albano, R., Mirauda, D., Agate, G., Sole, A., and Guandalini, R. (2015). A smoothed particle hydrodynamics model for 3D solid body transport in free surface flows. *Comput. Fluids* 116, 205–228. doi:10.1016/j.compfluid.2015.04.018

Arnason, H., Petroff, C., and Yeh, H. (2009). Tsunami bore impingement onto a vertical column. *J. Disaster Res.* 4, 391–403. doi:10.20965/jdr.2009.p0391

Bocchiola, D., Rulli, M., and Rosso, R. (2006). Transport of large woody debris in the presence of obstacles. *Geomorphology* 76, 166–178. doi:10.1016/j.geomorph.2005.08.016

Borrero, J. C., Sieh, K., Chlieh, M., and Synolakis, C. E. (2006). Tsunami inundation modeling for western Sumatra. *Proc. Natl. Acad. Sci. U.S.A.* 103, 19673–19677. doi:10.1073/pnas.0604069103

Braudrick, C. A., and Grant, G. E. (2000). When do logs move in rivers? *Water Resour. Res.* 36, 571–583. doi:10.1029/1999WR900290

Bremm, G. C., Goseberg, N., Schlurmann, T., and Nistor, I. (2015). Long wave flow interaction with a single square structure on a sloping beach. *J. Mar. Sci. Eng.* 3, 821. doi:10.3390/jmse3030821

Canelas, R. B., Dominguez, J. M., Crespo, A. J., ómez-Gesteira, M. G., and Ferreira, R. M. (2015). A smooth particle hydrodynamics discretization for the modelling of free surface flows and rigid body dynamics. *Int. J. Numer. Methods Fluids* 78, 581–593. doi:10.1002/fld.4031

Canelas, R. B., Ferreira, R. M., Crespo, A., and Domínguez, J. M. (2013). "A generalized SPH-DEM discretization for the modelling of complex multiphasic free surface flows," in *Proceedings of the 8th International SPHERIC Workshop*, Trondheim.

Chanson, H. (2006). Tsunami surges on dry coastal plains: application of dam break wave equations. *Coast. Eng. J.* 48, 355–370. doi:10.1142/S0578563406001477

Charvet, I., Suppasri, A., and Imamura, F. (2014). Empirical fragility analysis of building damage caused by the 2011 Great East Japan tsunami in Ishinomaki city using ordinal regression, and influence of key geographical features. *Stoch. Environ. Res. Risk Assess.* 28, 1853–1867. doi:10.1007/s00477-014-0850-2

Chinnarasri, C., Thanasisathit, N., Ruangrassamee, A., Weesakul, S., and Lukkunaprasit, P. (2013). The impact of tsunami-induced bores on buildings. *P I Civil Eng-Mar. En.* 166, 14–24.

Chock, G. Y. (2015). "The ASCE 7 tsunami loads and effects design standard," in *Structures Congress 2015* (Portland, OR: ASCE), 1446–1456.

Chock, G. Y. (2016). Design for tsunami loads and effects in the ASCE 7-16 standard. *J. Struct. Eng.* 142, 04016093. doi:10.1061/(ASCE)ST.1943-541X.0001565

Esteban, M., Takagi, H., and Shibayama, T. (2015). *Handbook of Coastal Disaster Mitigation for Engineers and Planners*, Waltham, MA: Butterworth Heinemann, Elsevier.

FEMA. (2012). *P646 Guidelines for Design of Structure for Vertical Evacuation from Tsunamis*. Redwood City, CA: Federal Emergency Management Agency.

Fritz, H. M., Borrero, J. C., Synolakis, C. E., and Yoo, J. (2006). 2004 Indian Ocean tsunami flow velocity measurements from survivor videos. *Geophys. Res. Lett.* 33, L24605. doi:10.1029/2006GL026784

Gomez-Gesteira, M., Rogers, B. D., Crespo, A. J., Dalrymple, R., Narayanaswamy, M., and Dominguez, J. M. (2012). SPHysics – development of a free-surface fluid solver – part 1: theory and formulations. *Comput. Geosci.* 48, 289–299. doi:10.1016/j.cageo.2012.02.029

Goseberg, N., Nistor, I., Mikami, T., Shibayama, T., and Stolle, J. (2016a). Nonintrusive spatiotemporal smart debris tracking in turbulent flows with application to debris-laden tsunami inundation. *J. Hydraul. Eng.* 142, 04016058. doi:10.1061/(ASCE)HY.1943-7900.0001199

Goseberg, N., Stolle, J., Nistor, I., and Shibayama, T. (2016b). Experimental analysis of debris motion due the obstruction from fixed obstacles in tsunami-like flow conditions. *Coast. Eng.* 118, 35–49. doi:10.1016/j.coastaleng.2016.08.012

Goseberg, N., Wurpts, A., and Schlurmann, T. (2013). Laboratory-scale generation of tsunami and long waves. *Coast. Eng.* 79, 57–74. doi:10.1016/j.coastaleng.2013.04.006

Haehnel, R. B., and Daly, S. F. (2002). *Maximum Impact Force of Woody Debris on Floodplain Structures*. Hanover: USACE.

Haehnel, R. B., and Daly, S. F. (2004). Maximum impact force of woody debris on floodplain structures. *J. Hydraul. Eng.* 130, 112–120. doi:10.1061/(ASCE)0733-9429(2004)130:2(112)

Ikeno, M., Takabatake, D., Kihara, N., Kaida, H., Miyagawa, Y., and Shibayama, A. (2016). Improvement of collision force formula for woody debris by airborne and hydraulic experiments. *Coast. Eng. J.* 58, 1640022. doi:10.1142/S0578563416400222

Imamura, F., Goto, K., and Ohkubo, S. (2008). A numerical model for the transport of a boulder by tsunami. *J. Geophys. Res. Oceans* 197, 113. doi:10.1029/2007JC004170

Lauber, G., and Hager, W. H. (1998). Experiments to dambreak wave: horizontal channel. *J. Hydraul. Eng.* 36, 291–307. doi:10.1080/00221689809498601

Madsen, P. A., Fuhrman, D. R., and Schäffer, H. A. (2008). On the solitary wave paradigm for tsunamis. *J. Geophys. Res. Oceans* 113, 1–22. doi:10.1029/2008JC004932

Manenti, S., Panizzo, A., Ruol, P., and Martinelli, L. (2008). "SPH simulation of a floating body forced by regular waves," in *Proceedings of 3rd SPHERIC Workshop* (Lausanne: Swiss Federal Institute of Technology), 38–41.

Matskevitch, D. (1997). Eccentric impact of an ice feature: linearized model. *Cold Reg. Sci. Technol.* 25, 159–171. doi:10.1016/S0165-232X(96)00009-2

Matsutomi, H. (2009). Method for estimating collision force of driftwood accompanying tsunami inundation flow. *J. Disaster Res.* 4, 435–440. doi:10.20965/jdr.2009.p0435

Matsutomi, H., Fujii, M., and Yamaguchi, T. (2008). "Experiments and development of a model on the inundated flow with floating bodies," in *Proceedings of the 31st International Conference on Coastal Engineering* (Hamburg: ASCE), 1458–1470.

Monaghan, J. J. (2005). Smoothed particle hydrodynamics. *Rep. Progr. Phys.* 68, 1703. doi:10.1088/0034-4885/68/8/R01

Naito, C., Cercone, C., Riggs, H. R., and Cox, D. (2014). Procedure for site assessment of the potential for tsunami debris impact. *J. Waterw. Port Coast. Ocean Eng.* 140, 223–232. doi:10.1061/(ASCE)WW.1943-5460.0000222

Naito, C., Riggs, H., Wei, Y., and Cercone, C. (2016). Shipping-container impact assessment for tsunamis. *J. Waterw. Port Coast. Ocean Eng.* 142, 05016003. doi:10.1061/(ASCE)WW.1943-5460.0000348

Nistor, I., Goseberg, N., Mikami, T., Shibayama, T., Stolle, J., Nakamura, R., et al. (2016). Hydraulic experiments on debris dynamics over a horizontal plane. *J. Waterw. Port Coast. Ocean Eng.* 04016022. doi:10.1061/(ASCE)WW.1943-5460.0000371

Nouri, Y., Nistor, I., Palermo, D., and Cornett, A. (2010). Experimental investigation of tsunami impact on free standing structures. *Coast. Eng. J.* 52, 43–70. doi:10.1142/S0578563410002117

Okada, T., Sugano, T., Ishikawa, T., Ohgi, T., Takai, S., and Hamabe, C. (2005). *Structural Design Method of Buildings for Tsunami Resistance (Proposed)*. Tokyo: Building Technology Research Institute, Building Centre for Japan, 15.

Pagliara, S., and Carnacina, I. (2013). Bridge pier flow field in the presence of debris accumulation. *P I Civil Eng-Water Manag.* 187–198.

Palermo, D., Nistor, I., Nouri, Y., and Cornett, A. (2009). Tsunami loading of near-shoreline structures: a primer. *Can. J. Civ. Eng.* 36, 1804–1815. doi:10.1139/L09-104

Parola, A. C. (2000). *Debris Forces on Highway Bridges*. Washington, DC: Transportation Research Board.

Riggs, H., Cox, D., Naito, C., Kobayashi, M., Aghl, P. P., Ko, H.-S., et al. (2014). Experimental and analytical study of water-driven debris impact forces on structures. *J. Offshore Mech. Arctic Eng.* 136, 041603. doi:10.1115/1.4028338

Robertson, I., Riggs, H. R., Yim, S. C., and Young, Y. L. (2007). Lessons from Hurricane Katrina storm surge on bridges and buildings. *J. Waterw. Port Coast. Ocean Eng.* 133, 463–483. doi:10.1061/(ASCE)0733-950X(2007)133:6(463)

Rogers, B. D., Dalrymple, R. A., and Stansby, P. K. (2009). "SPH modeling of floating bodies in the surf zone," in *Proc. 31st Int. Conf. Coastal Eng. 2008*. 204–215.

Rossetto, T., Allsop, W., Charvet, I., and Robinson, D. I. (2011). Physical modelling of tsunami using a new pneumatic wave generator. *Coast. Eng.* 58, 517–527. doi:10.1016/j.coastaleng.2011.01.012

Rueben, M., Cox, D., Holman, R., Shin, S., and Stanley, J. (2014). Optical measurements of tsunami inundation and debris movement in a large-scale wave basin. *J. Waterw. Port Coast. Ocean Eng.* 141, 04014029. doi:10.1061/(ASCE)WW.1943-5460.0000267

Saatcioglu, M., Ghobarah, A., and Nistor, I. (2005). Effects of the December 26, 2004 Sumatra earthquake and tsunami on physical infrastructure. *ISET J. Earthq. Technol.* 42, 79–94.

Shafiei, S., Melville, B. W., Shamseldin, A. Y., Beskhyroun, S., and Adams, K. N. (2016). Measurements of tsunami-borne debris impact on structures using an embedded accelerometer. *J. Hydraul. Res.* 54, 435–449. doi:10.1080/00221686.2016.1170071

She, Z.-S., and Leveque, E. (1994). Universal scaling laws in fully developed turbulence. *Phys. Rev. Lett.* 72, 336. doi:10.1103/PhysRevLett.72.336

St-Germain, P., Nistor, I., Townsend, R., and Shibayama, T. (2013). Smoothed-particle hydrodynamics numerical modeling of structures impacted by tsunami bores. *J. Waterw. Port Coast. Ocean Eng.* 140, 66–81. doi:10.1061/(ASCE)WW.1943-5460.0000225

Stolle, J., Nistor, I., and Goseberg, N. (2016). Optical tracking of floating shipping containers in a high-velocity flow. *Coast. Eng. J.* 58, 1650005. doi:10.1142/S0578563416500054

Synolakis, C. E., Deb, M. K., and Skjelbreia, J. E. (1988). The anomalous behavior of the runup of cnoidal waves. *Phys. Fluids* 31, 3–5. doi:10.1063/1.866575

Tadepalli, S., and Synolakis, C. E. (1994). The run-up of N-waves on sloping beaches. *Proc. R. Soc. Lond. A Math. Phys. Eng. Sci.* 445, 99–112. doi:10.1098/rspa.1994.0050

Taubenböck, H., Goseberg, N., Lämmel, G., Setiadi, N., Schlurmann, T., Nagel, K., et al. (2013). Risk reduction at the "last-mile": an attempt to turn science into action by the example of Padang, Indonesia. *Nat. Hazards* 65, 915–945. doi:10.1007/s11069-012-0377-0

Wu, T.-R., Chu, C.-R., Huang, C.-J., Wang, C.-Y., Chien, S.-Y., and Chen, M.-Z. (2014). A two-way coupled simulation of moving solids in free-surface flows. *Comput. Fluids* 100, 347–355. doi:10.1016/j.compfluid.2014.05.010

Yao, Y., Huang, Z., Lo, E. Y. M., and Shen, H.-T. (2014). A preliminary laboratory study of motion of floating debris generated by solitary waves running up a beach. *J. Earthq. Tsunami* 8, 1440006. doi:10.1142/S1793431114400065

Yeh, H., Barbosa, A. R., Ko, H., and Cawley, J. G. (2014). Tsunami loadings on structures: review and analysis. *Coast. Eng. Proc.* 34, 1–13. doi:10.9753/icce.v34.currents.4

Yeh, H., Sato, S., and Tajima, Y. (2013). The 11 March 2011 East Japan earthquake and tsunami: tsunami effects on coastal infrastructure and buildings. *Pure Appl. Geophys.* 170, 1019–1031. doi:10.1007/s00024-012-0489-1

Conflict of Interest Statement: The authors declare that the research was conducted in the absence of any commercial or financial relationships that could be construed as a potential conflict of interest.

Copyright © 2017 Nistor, Goseberg and Stolle. This is an open-access article distributed under the terms of the Creative Commons Attribution License (CC BY). The use, distribution or reproduction in other forums is permitted, provided the original author(s) or licensor are credited and that the original publication in this journal is cited, in accordance with accepted academic practice. No use, distribution or reproduction is permitted which does not comply with these terms.

frontiers in Built Environment

ORIGINAL RESEARCH
published: 03 August 2017
doi: 10.3389/fbuil.2017.00036

Estimating Tsunami-Induced Building Damage through Fragility Functions: Critical Review and Research Needs

Ingrid Charvet[1,2], *Joshua Macabuag*[2]* *and Tiziana Rossetto*[2]

[1]Risk Management Solutions, London, United Kingdom, [2]Department of Civil, Environmental and Geomatic Engineering, University College London, London, United Kingdom

Tsunami damage, fragility, and vulnerability functions are statistical models that provide an estimate of expected damage or losses due to tsunami. They allow for quantification of risk, and so are a vital component of catastrophe models used for human and financial loss estimation, and for land-use and emergency planning. This paper collates and reviews the currently available tsunami fragility functions in order to highlight the current limitations, outline significant advances in this field, make recommendations for model derivation, and propose key areas for further research. Existing functions are first presented, and then key issues are identified in the current literature for each of the model components: building damage data (the response variable of the statistical model), tsunami intensity data (the explanatory variable), and the statistical model that links the two. Finally, recommendations are made regarding areas for future research and current best practices in deriving tsunami fragility functions (see Discussion, Recommendations, and Future Research). The information presented in this paper may be used to assess the quality of current estimations (both based on the quality of the data, and the quality of the models and methods adopted) and to adopt best practice when developing new fragility functions.

Keywords: tsunami, vulnerability, fragility functions, damage, stochastic model

OPEN ACCESS

Edited by:
Ioannis Anastasopoulos, ETH Zurich, Switzerland

Reviewed by:
Siau Chen Chian, National University of Singapore, Singapore
Filippos Vallianatos, Technological Educational Institute of Crete, Greece

***Correspondence:**
Joshua Macabuag
macabuag@gmail.com

Specialty section:
This article was submitted to Earthquake Engineering, a section of the journal Frontiers in Built Environment

Received: *20 March 2017*
Accepted: *12 June 2017*
Published: *03 August 2017*

Citation:
Charvet I, Macabuag J and Rossetto T (2017) Estimating Tsunami-Induced Building Damage through Fragility Functions: Critical Review and Research Needs. Front. Built Environ. 3:36. doi: 10.3389/fbuil.2017.00036

INTRODUCTION

Tsunami are long propagating waves generated by large scale underwater displacements (eg. earthquake, underwater explosions), or aerial impacts (eg. landslides), which travel at high speeds across large bodies of water. When they reach coastal areas, large tsunami can inundate up to several kilometers inland causing many deaths and costly damage or destruction to buildings and infrastructure in the coastal region.

Figure 1 shows a widely accepted definition of risk to natural hazards in the built environment (Crichton, 1999) applied to tsunami. Following recent large tsunamis (e.g., Indian Ocean, 2004; Chile, 2010 and Japan, 2011) significant resources have been dedicated worldwide to improve tsunami hazard models (Suppasri et al., 2016). This has resulted in significant advances being made in the identification of tsunamigenic earthquake sources and their activity (Yamazaki and Cheung, 2011; Satake et al., 2013), and in the modeling of tsunami propagation and inundation both numerically (Synolakis et al., 2008) and experimentally (Rossetto et al., 2011; Goseberg et al., 2013; Foster et al., 2017). Less effort has been dedicated to the prediction of damage to the built environment from tsunami inundation and the accurate evaluation of tsunami risk.

TSUNAMI RISK = TSUNAMI HAZARD X **VULNERABILITY** X EXPOSURE

Tsunami hazard =	The probability of a potentially damaging tsunami occurring at a site within a given period of time.
Vulnerability =	The likelihood of losses (financial and casualty) given a tsunami of a particular intensity.
Exposure =	Quantification of the number of people and buildings at risk.

VULNERABILITY = **FRAGILITY** X LOSS MODEL

Fragility =	The probability of building damage given a tsunami of a particular intensity.
Loss Model =	Probable losses (financial and casualty) for a given level of building damage.

FIGURE 1 | The components of tsunami risk. Fragility is highlighted as it is the focus of this paper.

While some vulnerability assessment methods may directly relate probable losses to tsunami intensity (direct vulnerability), more detailed assessments (indirect vulnerability) separate the assessment of likely building damage (fragility assessment) from the estimation of losses due to that damage (the loss model), as shown in **Figure 2**. Fragility (sometimes referred to as "physical vulnerability") relates an indicator of building damage to a measure of the tsunami intensity at the location of each considered building.

Fragility functions are a family of cumulative distribution functions that provide the probability of a given type of building exceeding specified damage states (where each individual curve represents a specific damage state, such as "collapse" or "heavy damage") over a range of values of a tsunami intensity measure (TIM, e.g., inundation depth). In order to derive fragility functions, three components are required: damage data, tsunami inundation data, and the statistical model linking them (i.e., a representation of the mean damage exceedance probabilities and the associated uncertainty). There are in the literature a small number of tsunami damage functions, which relate a TIM directly to mean damage (Ruangrassamee et al., 2006; Valencia et al., 2011); however, these do not consider aleatoric uncertainty at a given TIM value so can be considered superseded by fragility functions, and so they will not be considered further. Vulnerability functions relate a TIM directly to financial loss or casualties (Berryman, 2005; Reese et al., 2007; Masuda et al., 2012) though very few exist in the literature (due partly to challenges in obtaining financial data), and so the remainder of this paper will focus only on fragility functions.

Functions can be classified according to how the damage data are gathered (regardless of how the inundation data are gathered) (D'Ayala et al., 2013; Rossetto et al., 2014). Empirical fragility functions derive damage data from post-tsunami assessments (or physical experiments); judgment-based functions derive damage estimates from expert elicitation; analytical functions use numerical simulations of structural damage (Dias et al., 2009; Park et al., 2013; Kircher and Bouabid, 2014; Macabuag and Rossetto, 2014); and hybrid functions use a combination of these techniques.

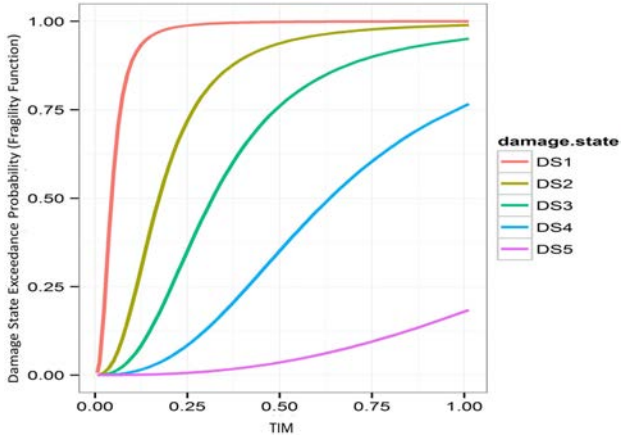

FIGURE 2 | Example fragility functions. IM, intensity measure; DS, damage state. The *y*-axis represents the probability of damage exceedance for each damage state ($P\{ds < DS\}$ versus IM).

Empirical fragility functions make up the overwhelming majority of the available functions, and so will be the focus of this paper.

The field of tsunami fragility assessment is relatively new when compared to seismic fragility, and there are, therefore, many lessons that can be learned from the seismic field. However, tsunami fragility assessment has access to damage data of better quality (primarily from the 2011 Great East Japan Earthquake and Tsunami) and so new statistical approaches have been developed that would not have been feasible using currently available earthquake damage datasets.

Tarbotton et al. (2015) give a review of existing literature on tsunami fragility curves, noting trends and comparing existing fragility curves in order to highlight variability in the mean function across a range of studies. However, they do not provide guidance on how to interpret and tackle such variability, nor draw on literature from other fields (such as earthquake engineering), nor include the most recent research that has made significant leaps forward in areas such as critical assessment of the statistical

models, multivariate methods, treatment of missing data, and quantification of uncertainty in both the explanatory and response variables of the fragility functions. Note that the terminology used by Tarbotton et al. (2015) to classify fragility functions is different to that of the Global Earthquake Model (GEM), though to be consistent with best practice functions will be classified as empirical or analytical as per the GEM guidance throughout this paper.

The present review provides the most comprehensive review of existing studies to-date and provides a deeper understanding of what drives the epistemic (systematic) uncertainty in existing models, and how to practically reduce it, focusing on sources of uncertainty which can be addressed. Key empirical fragility models from existing literature have been chosen for this purpose, representing a variety of locations, events, statistical approaches, intensity measures, and building stocks most commonly investigated. Drawing upon experience of a similar exercise for the development of the GEM compendium, this paper formulates recommendations consistent with the established best-practice in the seismic field (PAGER, GEM).

The aim of this paper is to collate and summarize existing empirical tsunami fragility functions for buildings, to outline limitations and significant advances in the field, and to propose key areas for further development. The information presented in this paper will allow the reader to assess the quality of current estimations (both based on the quality of the data, and the quality of the models and theories adopted), and to adopt best practice when developing new fragility functions and, therefore has significant implications for those using, assessing, or developing empirical tsunami fragility functions.

EXISTING EMPIRICAL TSUNAMI FRAGILITY FUNCTIONS

Empirical fragility functions are based on observed damage data from tsunami events. **Table 1** shows existing empirical tsunami fragility functions for the 1993 Japan tsunami, 2004 Indian Ocean tsunami, 2009 Samoa Tsunami, and 2010 Chilean Tsunami. **Table 2** shows existing empirical tsunami fragility functions for the 2011 Japan tsunami.

In **Tables 1** and **2**, TIM indicates the TIM assigned to each building, discussed in detail in Section "The Explanatory Variables: Tsunami Intensity Measures" (h, inundation depth; v, velocity; F, drag force; MF, momentum flux; MMF, moment of momentum flux, F_{QS}, a new proposed quasi-steady force estimate). The explanatory variable data-source describes how the TIM was determined for each building (sim., numerical inundation simulation). The response-variable data-points indicate the number of buildings in the study (− = data not given in the reference, Aggr. = aggregated, note that all data are aggregated when used in OLS models, see Model Quality). Response variable data-source indicates how damage data were collected (remote = satellite or aerial imagery, survey = visual inspection in the field). #DS indicates number of damage states (including DS0, so that #DS = 2 indicates 1 fragility curve, generally collapse). The model column indicates the statistical model describing the fragility function (OLS = standard linear model with parameters estimated via ordinary least squares (OLS), generalized linear model (GLM) using maximum likelihood parameter estimation with various link functions, see Section "Model Quality").

It can be seen that there are many more fragility functions derived from data for the 2011 Japan tsunami (19 fragility functions) than for all previous tsunamis combined (11 fragility functions), which is indicative of the unprecedented quantity and quality of data that have become available following the 2011 Japan tsunami. Furthermore, it can also be seen that the majority of damage data from the 2011 Japan tsunami which has been used in fragility functions is from field surveys, again due to the unprecedented scale of the surveys conducted, such as that conducted by Japan's Ministry of Land Infrastructure Tourism and Transport (MLIT) which provided a database of all of the houses (over 200,00) within the tsunami inundation zone.

Existing fragility functions cover several construction types, including engineered structures in Japan (RC, steel, masonry, and timber), and primarily non-engineered structures of Thailand, Indonesia, and Samoa. Some studies consider construction year (Amakuni and Terazono, 2011; Suppasri et al., 2014) and number of stories (Suppasri et al., 2013, 2014), though most do not make this distinction. The majority of studies use normal or lognormal models with OLS parameter estimation, with improved models (e.g., GLM) becoming more widely used in more recent studies.

Alongside the published studies presented in **Tables 1** and **2**, there are also substantial proprietary investigations carried out by commercial catastrophe risk modeling companies using confidential insurance loss information. While these cannot be included in this paper, the comprehensive review and recommendations presented here are of significance to modelers and model developers interrogating or developing these proprietary functions.

A critical review of this literature is now presented according to the three fundamental components of tsunami fragility functions. Building damage data are discussed in Section "The Response Variable: Building Damage Data," tsunami intensity data in Section "The Explanatory Variables: Tsunami Intensity Measures," and the statistical model that links the two in Section "Model Quality." Finally, recommendations are made regarding areas for future research and current best practices in deriving tsunami fragility functions.

THE RESPONSE VARIABLE: BUILDING DAMAGE DATA

Fragility functions express the probability that a building may reach or exceed a set of damage states, for a given value of a TIM (e.g., inundation depth). Damage states represent the response variable in regression analysis, and each curve of a family of fragility functions represents a different damage state. This section sets out the criteria that an optimal damage scale should meet for fragility function derivation and discusses the current literature in relation to these criteria, highlights shortcomings in damage data collection, and highlights that currently used building classifications miss features of the building that make it vulnerable to tsunami.

TABLE 1 | Published empirical fragility functions for the 1993 Japan tsunami, 2004 Indian Ocean tsunami, 2009 Samoa Tsunami, and 2010 Chilean Tsunami.

	Reference	Explanatory variable			Response variable			Model	Comments
		Tsunami event	Tsunami intensity measure	Data-source	Data-points	#DS	Data-source		
EF1	Koshimura and Kayaba (2010)	Japan 1993	*h*,*v*,*F*	sim.	769	2	Remote	Ordinary least squares (OLS)	In Japanese. Curves for Hokkaido, Japan
EF2	Pomonis and Peiris (2005)	Indian Ocean 2004	*h*	Survey	45,714	4	Survey	OLS	Curves for SW and SE coast of Sri Lanka
EF3	Dias et al. (2009)				33,900	2			Curves for Sri Lanka, compared with analytically derived curves
EF4	Koshimura et al. (2009b)		*h*,*v*,*F*	sim.	48,910				Curves for Banda Aceh, Indonesia
EF5	Suppasri et al. (2009)				–		Remote		Curves for Phang Nga, Thailand
EF6	Murao and Nakazato (2010)		*h*		1,535	4	Survey		Compares curves with other authors'
EF7	Suppasri et al. (2011)		*h*,*v*,*F*		4,596	2	Remote		Compares curves for Phang Nga and Phuket, Thailand
EF8	Valencia et al. (2011)		*h*	Survey	2,576	6	Survey, Remote		Error about datapoints and mean curve indicated (Banda Aceh, Indonesia)
EF9	Gokon et al. (2009)	Samoa 2009	*h*,*v*	sim.	902	2	Remote	OLS	Curves for Tutuila Island, American Samoa
EF10	Reese et al. (2011)		*h*, debris	Survey	201	5	Survey	Generalized linear model (GLM)	First use of GLM (American Samoa). Considers curves w/wo debris and sheltering.
EF11	Mas et al. (2012)	Chile 2010	*h*	sim.	915	2	Remote	OLS	Curves for Dichato, Chile. Visually compares curves from various countries

TABLE 2 | Published empirical fragility functions derived from data for the 2011 Great East Japan Earthquake and Tsunami.

	Reference	Explanatory variable		Response variable			Model	Comments
		Tsunami intensity measure (TIM)	Data-source	Data-points	#DS	Data-source		
EF12	Amakuni and Terazono (2011)	*h*,*v*,*F*	Survey	8,653	2	Remote	OLS	Compares multiple locations (Miyagi, Japan) and multiple construction years
EF13	Nihei et al. (2012)	*h*		~5,000		Survey, Remote		Curves for Natori, Japan (in Japanese)
EF14	Koshimura and Gokon (2012)			157,640				Compares curves for various locations across Japan (in Japanese)
EF15	Yanagisawa and Yanagisawa (2012)			202		Survey		Curves for Sendai, Japan (in Japanese)
EF16	Suppasri et al. (2012b)			189	5			Visually compares curves from Sri Lanka and Miyagi (Sendai and Ishinomaki), Japan
EF17	Suppasri et al. (2012a)			251,301 (aggr.)	6			Uses aggregated government survey data
EF18	Maruyama et al. (2013)	*h*,*v*,*F*		>335	2			Curves using data for Chiba prefecture, Japan. Does not specify number of non-collapsed buildings in survey
EF19	Hayashi et al. (2013)			8,244				Flow velocities validated against observations
EF20	Suppasri et al. (2014)	*h*		63,605	6			Compares topography, number of floors, building use, construction year, material (Ishinomaki, Japan), using disaggregated data
EF21	Charvet et al. (2014a)			178,448 (aggr.)			Generalized linear model (GLM)	Compares ordered and partially ordered models, various link functions, and quantifies inclusion of building class, for aggregated data
EF22	Charvet et al. (2014b)			56,950				Separates data by terrain type: plain, narrow coast (backed up by high topography), and river, for Ishinomaki, Japan, for disaggregated data
EF23	Narita and Koshimura (2015)			64,860	2	Survey	OLS	Damage data for each curve collated according to topographic features, building distribution, sea defenses, ground elevation and slope
EF24	Charvet et al. (2015)	*h*, *v*, debris	sim.	19,815	6		GLM	Kesennuma, Japan (disaggregated data). Concludes that debris has significant effect on fragility functions. Fragility surfaces also presented
EF25	Tanaka and Kondo (2015)	MF, MMF		–	2		OLS	Recommends switching between fragility functions for high and low Froude cases. Does not specify the number of buildings surveyed
EF26	Tanaka et al. (2015)	*h*, MF, MMF						
EF27	Macabuag et al. (2016a)	*h*, *v*, MF, *F*, Fr, F_{QS}	Survey sim.	67,125	6		OLS GLM General additive models (GAM)	Treatment of missing data. Proposed TIM and model optimization method. First use of GAMs for tsunami fragility
EF28	Macabuag et al. (2016b)	*h*, *v*, MF, *F*, Fr, F_{QS}, debris					GLM GAM	Inclusion of debris has large effect on fragility, which can be quantified.
EF29	De Risi et al. (2017a,b)	*h*	Survey	147,668			OLS GLM	First use of Bayesian methods to investigate the effect of uncertainty in inundation observations. Effect on loss estimates also considered
EF30	De Risi et al. (2017a,b)	*h*,*v*	sim.	>200,000			GLM	Fragility surfaces. Show velocity important in coastal plains

Damage Scale

Damage scales define the set of damage states into which tsunami-affected buildings are classified. McCullagh and Nelder (1983) states fundamental rules that damage scales must follow, and Hill and Rossetto (2008) proposed a ranking system for "scoring" existing seismic damage scales based on the key characteristics required for use in loss modeling. The rules and characteristics relevant for tsunami fragility function derivation are shown in **Table 3** and the damage mechanisms to be captured by fragility functions are defined and characterized in **Table 4**. All of the fragility functions derived from data for the Great East Japan Earthquake and Tsunami (**Table 2**) use the damage scale proposed by the Japan Cabinet Office (2013) shown in **Table 5**.

The damage scale in **Table 5** (and many of the scales presented in **Table 1**) violates the first rule set out by McCullagh and Nelder (1983) (CH1.1, **Table 3**). For example, buildings with inundation below the ground floor ceiling (DS3) could also experience collapse (DS5). Therefore, surveyors inspecting a building that falls into multiple damage state categories is presented with a subjective choice as to which damage state to assign. Charvet et al. (2014a,b) highlight that the descriptions of DS5 and DS6 also violate the second rule (CH1.2, **Table 3**). The damage scale in **Table 5** also does not directly address global and local damage nor distinguish between structural and non-structural damage but instead shows an assumed direct correlation between the hazard intensity (inundation depth in this case) and damage in that depth is specified directly in the damage state descriptions for DS1-DS4, and so structural response is not actually considered by these definitions.

The shortcomings of the damage scale in **Table 5** have implications for the uncertainty in the observations for empirical studies and, therefore, raises questions about the reliability of existing functions derived from data for the Great East Japan Earthquake and Tsunami (**Table 2**). Furthermore, the remaining building damage scales that can be found in the literature for tsunami (**Table 1**) are often not consistent, having different damage state definitions and a varying number of damage states, or otherwise fail to meet the criteria set out above. An improved and unified damage scale is, therefore, required for future studies.

TABLE 3 | Important characteristics of a damage scale for tsunami fragility function derivation.

	Characteristic		Description
Damage	CH1.1	Mutual exclusivity	Levels of response (i.e., the damage states) are mutually exclusive
	CH1.2	Damage progression	Each new damage state corresponds to an increase in intensity (i.e., an increase in the TIM)
	CH1.3	Ease of measurement	States are clearly distinguishable and can be easily applied to populations of buildings
	CH1.4	Coverage	Descriptions capture the full range of damage to the building type
	CH1.5	Global	Global damage is considered
	CH1.6	Local	Local damage is considered
	CH1.7	Non-structural	Non-structural damage is considered and distinguished from structural damage

Adapted from McCullagh and Nelder (1983) (CH1.1 and CH1.2) and Hill and Rossetto (2008) (all other characteristics). The definitions of "global," "local," and "non-structural," damage are given in ***Table 4****.*

Damage Data: Quality and Collection Method

Empirical building damage data post-tsunami is collected either via ground survey (visual inspection), or remotely (aerial or satellite photography). Remote sensing allows for the rapid collection of large amounts of data. However, the limitation on satellite remote sensing damage surveys is that the only detectable damage state is often "total collapse" (and where intermediate damage

TABLE 4 | Tsunami-induced damage and failure mechanisms (photos: EEFIT).

Damage mechanisms

Non-structural Damage

DM1: flooding damage

DM2: damage to cladding/finishes

Local Structural Damage

DM3: member failure

DM4: load-bearing wall failure

Global Structural Failure

DM5: global lateral deflection/failure

DM6: progressive collapse

DM7: foundation Failure

Note that all of these failures may have been caused by a combination of several tsunami effects (lateral fluid forces, buoyancy, debris impact and foundation effects) and ground shaking.

states are included, their accuracy is low), meaning that accurate fragility functions cannot be formed for partial collapse states (e.g., all studies in **Table 1** utilizing remote sensing consider only two damage states). Construction material can often not be determined remotely. Ground surveys can determine material and intermediate damage states, though they take more time than remote sensing. Ground surveys can be conducted by surveyors with different levels of training and expertise. They are commonly carried out for purposes other than the construction of fragility functions (e.g., for safety evaluations) hence they may not record appropriate damage. Further sources of uncertainty are introduced due to the typical issues highlighted in **Table 6**.

TABLE 5 | Damage state definitions used by the Japanese Ministry of Land Infrastructure Tourism and Transport following the 2011 Great East Japan Earthquake and Tsunami.

Damage State		Description	Use	Image
DS1	Minor damage	Inundation below ground floor. The building can be reused by removing mud below the floor boards	Possible to use immediately after minor floor and wall cleanup	
DS2	Moderate damage	The building is inundated less than 1 m above the floor	Possible to use after moderate repairs	
DS3	Major damage	The building is inundated more than 1 m above the floor (below the ceiling)	Possible to use after major repairs	
DS4	Complete damage	The building is inundated above the ground floor level	Major work is required for re-use of the building	
DS5	Collapsed	The key structure is damaged, and difficult to repair to be used as it was before	Not repairable	
DS6	Washed away	The building is completely washed away except for the foundation	Not repairable	

Descriptions from Japan Cabinet Office (2013), usage descriptions from Suppasri et al. (2014). This damage scale violates several of the rules set out in McCullagh and Nelder (1989), so it is not proposed that this scale be used in future studies.

In the case of an earthquake-generated tsunami where damage is surveyed in the near-field regions, it is likely that the earthquake has damaged buildings before the tsunami's arrival. Park et al. (2013) considered previous seismic damage in an analytical study of tsunami fragility. However, for empirical studies, it is difficult to separate tsunami-induced damage from earthquake-induced damage, which creates bias in the data (Rossetto et al., 2012) and so likely affects the applicability to estimating tsunami-only risk (e.g., for far-field tsunamis) for all of the fragility functions derived from the 2011 Japan tsunami to some degree.

Empirical fragility functions can be very specific to the location from where the damage data were gathered. Suppasri et al. (2014) and Charvet et al. (2014b) compare fragility functions formed using data from areas within the same city (Ishinomaki, Japan) but with different topographies. Narita and Koshimura (2015) separate building damage data by location according to four broad factors: bathymetric features, distribution of buildings, coastal protection facilities, topographic features. Such studies show that fragility functions cannot typically be generalized or applied to similar structures in a different geographical location.

Empirical fragility studies based on field measurements all face the issue of data analysis with missing attributes, and existing studies [e.g., Suppasri et al. (2013)] generally conduct complete-case analysis, i.e., they remove any partial data, such as buildings of unknown material, from their fragility analysis. However, this may lead to a loss of statistical power, loss of precision, and introduction of bias if the missing data are informative. Missing data can be assigned to one of three categories [Ware et al. (2012)]: Missing Completely At Random (MCAR), Missing At Random (MAR), or Missing Not At Random (MNAR). MCAR refers to the case where the data are missing purely by chance. MNAR refers to the case where the missing information is related to the reason that the information is missing (e.g., if wooden buildings had been removed from the dataset because they were wooden). MAR refers to the case where the information is not MCAR but can be accounted for by using other attributes. The only study to analyze and treat missing data before conducting fragility function derivation is Macabuag et al. (2016a). All other studies that produce fragility functions for various building classifications based on data from existing fragility functions may be susceptible to bias introduced by the removal of incomplete data-entries.

TABLE 6 | Database typologies and their main characteristics [adapted from Rossetto et al. (2014)].

Survey method	Typical sample sizes	Typical building classes	Typical no. of damage states	Reliability of observations	Typical issues
Rapid Surveys	Large	All buildings	2–3	Low	Safety, not damage evaluations
Detailed "Engineering"	Large to small	Detailed classes	5–6	High	Possibility of unrepresentative samples
Surveys by Reconnaissance Teams	Very small	Detailed classes	5–6	High	Possibility of unrepresentative samples
Remotely Sensed	Very large	All buildings	3–5	Low	Only collapse or very heavy states may be reliable. Misclassification errors

Building Classification

In order for the fragility results to be representative of the different structural responses to tsunami loading, typically buildings are classified according to structural properties and analysis is carried out on each class separately. Suppasri et al. (2014) considers structural material, height, occupancy, and date of construction (concluding that date of construction did not greatly affect tsunami performance). All other existing studies consider structural material only. However, the building classifications are not consistent between studies. For example, Tinti et al. (2011) divides masonry buildings into five sub-classes of structures with varying construction materials and numbers of stories, and Valencia et al. (2011) consider two types of masonry-structures (class B and C). Fragility functions from different studies can often not be compared for this reason.

The purpose of a building classification system is to allow buildings to be grouped according to their likely performance in the case of tsunami, i.e., so that they can be represented by a single set of fragility curves. Current building classes that have been used in tsunami fragility studies are based on classification systems for earthquakes and do not take into account the building characteristics that make buildings susceptible to damage from tsunami (e.g., openings, soil type, foundation type, cladding system). This means that they may cluster together buildings that will perform differently in tsunami, into the same building class. For example, an RC structure with and without large openings will behave very differently in tsunami, or a structure founded on piles verses one on raft foundations may behave very differently even if it has the same superstructure. Therefore, a building classification system that accounts for the features of the building that make it vulnerable to tsunami (so grouping buildings of similar performance together) is presented in Section "Assessment/Improvement of the Quality of Building Damage Data."

THE EXPLANATORY VARIABLES: TIMs

Tsunami intensity measures (represented as the x-axis of fragility curves) should provide the best possible representation of the damage potential of the tsunami. In this respect, they can be considered as trying to represent the structural demand that a given tsunami places on the building being investigated. However, existing studies vary in their selection of TIMs and derivation of intensity data. This section, therefore, compares the various TIMs used in the literature, highlights challenges in their methods of derivation, and highlights that the optimal TIM depends on the particular dataset being used.

Summary of Intensity Parameters

Tsunami-induced building damage can arise due to hydrostatic forces (including buoyancy), hydrodynamic effects (drag and bore impact), and debris (impact and damming), and the severity of these effects are determined by a number of flow parameters.

The majority of existing tsunami fragility curves adopt only the local maximum inundation depth as the TIM (**Tables 1** and **2**), often because it is the most readily definable parameter from post-tsunami surveys [e.g., residue lines in houses, Suppasri et al. (2012a,b)] and can be calculated from numerical inundation simulations more accurately than other flow parameters (discussed below, Section "Determination of Inundation Parameters"). Flow depth is indeed the main parameter driving lateral hydrostatic forces, buoyancy forces, and it also determines the size of debris that can be carried by the flow. However, a wide range of velocities (and so hydrodynamic forces) can exist for a given inundation depth, and indeed various studies have indicated that the sole use of inundation depth does not adequately describe observed damage at higher damage states (Charvet et al., 2014a; Macabuag et al., 2016a,b). Note also that various definitions and names for inundation depth can be found in the literature [water level (Reese et al., 2007), inundation depth (Inoue et al., 2007), tsunami depth, or water depth (Tanaka et al., 2007)], and so caution should be exercised when referring to these studies.

Flow velocity influences the hydrodynamic force, the surge force, the debris impact, and damming forces. Studies that have compared TIMs have generally concluded that velocity alone is less effective than depth as an indicator of damage for buildings for the datasets investigated (Koshimura et al., 2009a,b; Macabuag et al., 2016a). However, velocity is often used to calculate the fluid force TIMs shown in **Table 7**.

Froude number indicates the flow regime such that $Fr < 1$ indicates sub-critical flow (where the flow velocity is less than the wave velocity and so behaves in a slow or stable way) and $Fr > 1$ indicates choked or supercritical flow (where flow is dominated by inertia forces, so behaving as a rapid or unstable flow). Macabuag et al. (2016a) is the only study to consider Froude Number as a TIM and found it to be a poor indicator of building damage when used alone, for the dataset considered. However, Froude Number is used to calculate the quasi-steady force discussed below (Qi et al., 2014; Foster et al., 2017), and Tanaka and Kondo (2015) recommend using different fragility curves for flow conditions characterized by high and low Froude numbers.

Momentum flux is proportional to hydrodynamic form-drag (**Table 7**) and so they can be considered equivalent TIMs [i.e., fragility functions derived from momentum flux and drag force will give identical goodness-of-fit results, Macabuag et al. (2016a)]. Park et al. (2014) compares damage estimates for a case-study town in the USA using fragility functions for depth, velocity, and momentum flux, concluding that velocity and momentum flux provide the most realistic damage estimates, though this is only based on a qualitative visual assessment of damage locations and the authors acknowledge that this conclusion must be verified with field data. Tanaka and Kondo (2015) are the only empirical study to consider moment of momentum flux in their fragility curves. Note that nearly all current studies that consider force are using the standard drag equation (all except Macabuag et al. (2016a), below, and Tanaka and Kondo (2015) who additionally consider moment of momentum flux), however, this does not account for alternative estimations, such as equivalent hydrostatic methods (MLIT, 2011), bore impact (Robertson and Riggs, 2011), or changes in flow regime (Qi et al., 2014; Foster et al., 2017).

Macabuag et al. (2016a) derived fragility functions using an equivalent quasi-steady force proposed by Qi et al. (2014) and

TABLE 7 | Tsunami Intensity Measures (TIMs) used in the current literature.

	TIM	Description
	Inundation depth	Peak observed or simulated inundation depth (h_{peak}) at each building location.
Flow velocity	Peak velocity	Peak velocity (v_{peak}), generally calculated from numerical simulation as the vector sum of the velocity components in the directions of the two orthogonal axes of the 2D flow calculation.
	Froude number	A measure of flow velocity non-dimensionalized by the gravity-wave velocity: $$Fr = \left(\frac{v}{\sqrt{gh}}\right)_{peak}$$
Fluid forces	Momentum flux	A vector in the direction of flow, of magnitude equal to the mass-flow per unit area: $$MF = \left(hv^2\right)_{peak}$$
	Form drag	The force exerted on an object (per unit width perpendicular to the direction of flow) due to the movement of a surrounding fluid of density ρ: $$F_{drag} = \frac{1}{2}\rho C_d \left(hv^2\right)_{peak}$$ . . .where the drag coefficient (C_D) is a function of the object shape and orientation
	Moment of momentum flux	The product of momentum flux and inundation depth, considered a proxy for the overturning moment induced by the flow: $$MMF = \left(h.hv^2\right)_{peak}$$
	Quasi-steady Tsunami force	Alternative steady-state force estimation considering choked and sub-critical flow for a body of width b in a channel of width w: $$F_{QS} = \begin{cases} \frac{1}{2}\left[C_{D0}\left(1 + \frac{C_{D0}}{2}\left\{\frac{b}{w}\right\}\right)\right]\rho v^2 h, & Fr < Fr_c \\ \lambda \rho g^{1/3} v^{4/3} h^{4/3}, & Fr \geq Fr_c \end{cases}$$ . . .where: – λ is a function of hydrostatic and form drag coefficients, and up- and down-stream Froude Numbers. – Fr_c is a function of drag coefficient and blockage ratio (b/w). See Foster et al. (2017) for calculation procedure.
	In-flow debris	A measure of whether a building is thought to have been struck by large debris.

All TIMs represent a peak value measured at each building location. ***Tables 1*** *and* ***2*** *show which existing studies use each TIM.*

shown by Foster et al. (2017) to represent the force of a tsunami inundation on buildings. It is evaluated via two different flow regimes determined by Froude number. The equations relate depth, velocity, and blockage ratio (building width/channel width) to the force. Increasing the blockage ratio generally has the effect of increasing the force on the structure, and readers are referred to Qi et al. (2014) for the calculation procedure. Macabuag et al. (2016a) found that measures of force appear to provide the most efficient TIMs, if the inundation simulation from which they are derived is sufficiently accurate, or simulated velocity can be validated, and, furthermore, that flow regime (indicated by Froude number) appears to be a significant consideration when conducting fragility assessments, or quantifying tsunami-induced forces on structures.

Debris impact has been shown to have a significant influence on tsunami-induced damage and has been considered in fragility function derivation by Charvet et al. (2015), Macabuag et al. (2016b), Reese et al. (2011). However, all current studies simply use a binary indicator defining whether a building is thought to have been impacted or not, and further work is needed in order to more fully capture the characteristics of the likely forces imposed by debris on the structure.

Overall, the literature does not show a consensus as to which flow parameter is the most appropriate TIM to estimate fragility, though Macabuag et al. (2016a) proposed a rigorous methodology for determining the optimum TIM for any given dataset.

Tsunami magnitude is not considered a TIM as it is a function of offshore wave characteristics only and is not building specific. Run-up is also not considered a TIM as it is not building-specific, though it can be used to estimate building-specific inundation depths.

Not all tsunami loads and effects are necessarily captured by any single TIM used in the current literature (**Table 7**). For example, duration of immersion (and number of waves) is not captured in existing TIMs. This is significant as additional waves provide multiple impulsive impacts on the structure, the structure experiences load-reversal due to both the inflow and draw-down, and increases degradation of non-engineered structural materials (e.g., wood). Scott and Mason (2017) propose multi-hazard intensity measures considering both seismic and tsunami demand in a single parameter, though this concept has not been explored for fragility analysis. In fluvial flood modeling, Kreibich et al. (2009) compare Flood Intensity Measures of depth, velocity, momentum flux, and energy head according to the Bernoulli Equation, concluding that for fluvial flooding depth and energy head have the strongest correlation with observed damage, although it is acknowledged that a much larger sample size is required in order to draw conclusive results.

Froude Number and all of the force TIMs presented in **Table 7** are all complex TIMs that represent information of both depth and velocity. However, even a complex TIM may not capture all the relevant tsunami information necessary to predict structural damage, and so it would be beneficial to consider additional intensity measures simultaneously. Multiple regression techniques allow for several intensity measures to be included in the model simultaneously. Charvet et al. (2015) and De Risi et al. (2017a,b) generate fragility surfaces considering depth and velocity simultaneously (**Figure 3**), both concluding that such multiple regression models are more accurate than considering either TIM in isolation. However, surfaces are currently seldom used in practice for quantitative loss estimation and it is always the aim to develop a "parsimonious model" (the best model for the fewest predictors) as using additional intensity measures requires more data points and difficulties of obtaining these additional tsunami parameters must be overcome.

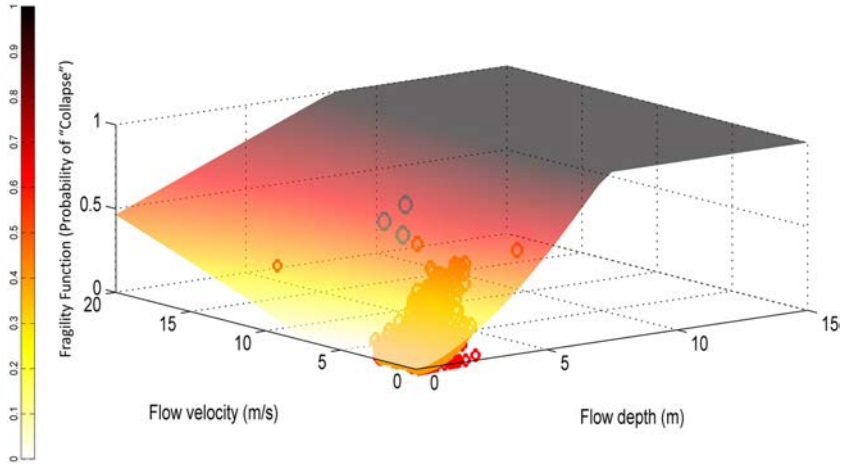

FIGURE 3 | Example tsunami fragility surface showing building collapse probability conditional on two key intensity measures, flow depth and velocity. Adapted from Charvet et al. (2015).

Determination of Inundation Parameters

For the derivation of fragility functions, the flow conditions at each building location (i.e., the TIM values) must be measured or estimated. These flow conditions may be obtained from post-tsunami field surveys, or they can be calculated using empirical flow estimation methods or numerical inundation modeling techniques. Calculation of onshore flow, by either empirical or numerical methods, requires information of offshore conditions obtained by modeling propagation from source to the coastline. Source and deep-sea propagation modeling is beyond the scope of this study, but methods of inundation estimation based on offshore conditions will be briefly discussed here, as the accuracy of the resulting TIM values directly impacts the reliability of the final fragility functions.

Field Surveys

In post-tsunami field surveys, flow depth can be measured using for example local water marks, or debris hanging on trees. If flow depth cannot be measured directly from an affected building (for example, the building has been washed away) various interpolation methods can be employed to estimate parameters between observation location (Mas et al., 2012; De Risi et al., 2017a,b), though there will be error introduced by the interpolation. Note that run-up may also be obtained from field surveys in order to validate numerical inundation results, either by direct observation immediately post-tsunami or by examining tsunami deposits, particularly for historic tsunamis.

Flow velocity is difficult to determine from observations in sufficient accuracy and resolution (EEFIT, 2006; Reese et al., 2007), and so is always calculated numerically for fragility function derivation. However, observation methods are often used to validate numerical results (Adriano et al., 2016).

Tsunami-induced forces on buildings have never been directly measured, and although some studies have attempted to estimate tsunami forces from observed damage to onshore structures (Tokyo University and BRI, 2011; Chock et al., 2013), force-related TIMs for fragility analysis have always been based on numerical inundation modeling.

Empirical Flow Estimation

Several studies and guidelines provide empirically based approaches for the estimation of onshore depth, velocity, and force.

Inundation depth values used in existing empirical fragility studies have all been derived using either field surveys or numerical modeling, and all velocity values obtained from numerical modeling. However, empirical methods may be used to verify numerical results in specific locations. These empirical methods include, for example, empirical formulae to estimate run-up from off-shore flow parameters [Charvet et al. (2013)], formulae provided by FEMA (2012) for determining the peak depth and velocity field from the run-up, or the energy grade-line method proposed by ASCE 7-16 (Kriebel et al., 2017) using offshore tsunami amplitude and run-up maps to define peak onshore depth and velocity fields.

However, depths and velocities are obtained, all of the fragility studies using any measure of force as a TIM generally use empirical formulations to estimate forces (**Table 7**) based on the peak depth and velocity flow-fields.

Numerical Inundation Modeling

Numerical modeling of tsunami inundation can provide estimates of onshore flow conditions across large areas as well as at single sites but poses a complex problem in computational fluid dynamics. Inundation models can vary in complexity from detailed 3D models considering flow around individual buildings to simplified 2D models modeling built-up areas using a roughness factor and making assumptions regarding the depth distribution of velocities and pressures (**Table 8**).

Tables 1 and **2** show which existing fragility studies obtain TIMs from numerical inundation. Where simulation has been used, simplified 2D models have been utilized as detailed topographical data are often lacking, and more complex models are still prohibitively costly in computation time and the required resources in accurately modeling a location with all buildings and obstacles to the required resolution. The required TIMs are calculated for each grid, and for each timestep, though over a large

TABLE 8 | A summary of numerical methods that have been used to define tsunami-induced forces on structures.

Inundation modeling methodology	Model complexity	Formulation	Modeling of buildings	Force resolution	Advantages	Disadvantages	Example software/ applications
2D model (no buildings)	Simplest	Non-linear shallow water equations, or Boussinesq equation. Calculate depth-averaged flow properties.	Model topography only. Model urban areas as roughness factor, either one factor for whole zone.	2 methods: – Difference in hydrostatic pressures on front face (calculated using Bernoulli's equation assuming stagnation at the face) and rear face of building (undisturbed flow depth). – Form drag equation using undisturbed flow depth and velocity.	Simplest method (therefore, most used in practice)	Accuracy of velocity calculation difficult to verify/validate in practice. Cannot capture any vertical components of flow. Cannot capture flow over/under structures.	Software: TUNAMI, MOST, COMCOT. Force resolution method 2 is that advocated in FEMA 646 and new ASCE 7-16.
2D model (with buildings)		As above	Buildings included in the model. Modify roughness factor per grid square based on the presence/absence of buildings	Difference in hydrostatic pressures on front face and rear face of building (depths taken directly from the model)	Effects of urban environment on inundation more accurately captured	Above cons of 2D modeling apply. Time-consuming to input individual buildings. Difficult to obtain accurate shape-size data for all buildings. Modeling grid resolution required to be adequately fine to allow individual buildings to be resolved	Muhari et al. (2011) Software: as above.
Hybrid 2D-3D analysis		As above, for several vertical layers. Calculated quantities at the boundary of each layer, is used as the boundary condition for adjacent layer	Both 2D methods above can be utilized	As in 2D methods, for each vertical layer	More vertical resolution of flow parameters. Flow over-under structures can be captured given sufficient vertical layer resolution.	More complex (set-up and computation) than 2D models	Pringle and Yoneyama (2013)
3D model using Navier–Stokes equations	Most complex	Navier–Stokes equations	Buildings/structures in model	Pressure distributions at structure surfaces taken directly from model	Removal of 2D assumptions. Can capture turbulence complexities. Can capture flow over/under/through structure.	Computation prohibitively expensive for all but small-specific areas of interest (not practical for large-scale inundation calculation)	Software: DELFT 3D, STOC.

inundation area this would represent a prohibitively large dataset, and so only peak TIM values are retained.

Existing studies using a force-related TIM (and Froude Number) all rely on empirical formulae to calculate force from depth and velocity. Peak depth and peak velocity generally do not occur at the same time (Chock, 2016), so peak force should not be calculated from the peak values of depth and velocity, but instead force should be calculated at each timestep with the peak force value over the inundation duration being retained for each calculation grid.

Numerical inundation estimates are seen to be highly sensitive to the uncertainties/inaccuracies in the initial properties of the tsunami (shape and total energy), the near-shore bathymetry, the effect of wave breaking, the on-shore topography, the effect of buildings and other obstacles, which may move or alter throughout the inundation period. Furthermore, while it is possible to validate simulated inundation depth results, there is generally insufficient velocity observation data to conduct a meaningful validation (Macabuag et al., 2016a,b). Park et al. (2013) compare simulated depth, velocity, and momentum flux values to experimental results, and Park et al. (2014) conduct a sensitivity analysis of the same TIMs to friction coefficient and modeling software. Both studies find that a change in simulation parameters can lead to small changes in depth, but result in much greater changes in velocity and momentum flux (e.g., they report a 15% change in depth corresponded to a change in velocity and momentum flux of 95% and 208%, respectively).

Therefore, the reliability of the existing fragility functions based on velocity or force is very dependent on the accuracy of those inundation models, which is determined by a number of factors. such as quality/reliability/resolution of the topography/bathymetry data, quality/reliability of the source and propagation models, the software used, the resolution of the calculation grid, and so on.

MODEL QUALITY

Fragility functions are derived by applying statistical model fitting techniques on building damage data. They are expressed as a function of the chosen TIMs for the purpose of making damage predictions under future tsunamis. In this context, statistical model fitting assumes that the probability of damage exceedance P_{DS} is a function of the TIM:

$$P_{DS} = P(ds \geq DS|TIM) = f(TIM) \tag{1}$$

In Eq. 1, *ds* is the observed damage state and *DS* the classification label given by the damage scale.

Three types of statistical models have been used in the literature:

- Linear models that utilize linear least squares regression—most commonly applied in fragility studies (**Tables 1** and **2**),
- GLM (e.g., Reese et al., 2011; Charvet et al., 2014a; Muhari et al., 2015; Macabuag et al., 2016a,b; De Risi et al., 2017a,b),
- Generalized Additive Models (Macabuag et al., 2016a,b).

This section describes methods of statistical model fitting and model diagnostics used in tsunami fragility studies to date, highlighting potential shortcomings of each method as well as potential solutions and proposed best-practice.

Traditional Fragility Estimation: Simple Linear Regression

Lognormal cumulative distribution functions have been the most popular form of tsunami fragility functions in the literature. This approach is typically attractive given the following three properties of this distribution (Ioannou et al., 2012):

- The lognormal distribution is constrained in the *y*-axis between [0, 1] which is suitable for fitting data points expressing aggregated probabilities,
- Values of the dependent variable are constrained in $[0, +\infty]$, which is sensible when considering parameters such as flow depths,
- This distribution appears to be skewed to the left, thus, it can provide a better estimate for the smaller intensities, where typically the majority of the data lie.

This has become a standard assumption, however, not well justified in the literature [e.g., "The capacity of the structure is generally assumed to be lognormally distributed" (Valencia et al., 2011); "(. . .) we develop the fragility functions for structural damage and casualties throughout the statistical analysis under the assumption that they can be represented by normal or lognormal distribution functions (. . .)" (Koshimura et al., 2009a,b)].

However, this distribution applies to a continuous response and, therefore, is not a suitable representation of discrete, classified outcomes such as a damage scale.

Simple linear regression applies when only one explanatory variable at a time can be considered as the TIM (i.e., for defining curves rather than functions of multiple TIMs, such as fragility surfaces). When a lognormal distribution is assumed, the fragility function or expected probability of damage exceedance $\hat{P}_{DS}$ is expressed as follows:

$$\hat{P}_{DS}(IM) = \Phi\left[\frac{\log(IM) - \mu}{\sigma}\right] \tag{2}$$

The parameters μ and σ of the distribution can be estimated using least squares regression by linearizing equation (2), where Φ is the normal distribution function:

$$\log(IM) = \sigma\Phi^{-1} + \mu \tag{3}$$

Unfortunately, this model is unable to deal with probabilities of 0 and 1 (the inverse normal distribution function does not converge for those values), thus disaggregated data cannot be analyzed directly. The data need to be aggregated into bins across the TIM to define a total number of buildings (across all damage states), and the number of buildings corresponding to each damage state *DS*. The observed probability of damage is then calculated as follows:

$$P_{DS}(IM) = \frac{n_{DS}}{n_{Total}} \tag{4}$$

However, aggregation introduces uncertainty: for example, the distribution of the TIM within each bin is unknown, which may

affect the shape of the curve, or the number of points in all bins may not be equal. In addition, data aggregation does not prevent some bins from having either a very low or a very high number of damaged buildings, which means that probabilities of 0 and 1 may still exist in the dataset. This issue is usually overcome by dismissing the corresponding data points and has consequences on model performance (Charvet et al., 2014a; Macabuag et al., 2016a).

New Fragility Estimation: GLM

Overview

The aforementioned issues associated with linear models have been addressed in recent research, by using a different class of models, namely GLM. GLMs relax many of the assumptions associated with linear regression and allow the response variable to follow various distributions (McCullagh and Nelder, 1989). Contrary to linear models, GLMs provide a better representation of the post-tsunami data because:

1. Discrete probability distributions (binomial or multinomial) can be used directly to model discrete outcomes, such as a damage level.
2. The linearity assumption (which may not hold) between the response and the explanatory variable (TIM) is relaxed through the use of a linear predictor.
3. More than one TIM can be included in the linear predictor, thus the model is not limited to one explanatory variable.
4. Model fitting does not require aggregation of the observations.
5. If only aggregated data are available, the binomial distribution can be used directly, without the need of a weighting system.

Parameter Estimation

In GLM regression, the assumption that the explanatory variable x is linearly related to the probability of damage $\hat{P}_{DS}$ is relaxed by using a linear predictor η, which relates the probability of damage to all J available explanatory variables x_j through a link function g:

$$g\left(\hat{P}_{DS_k} = \mu_k\right) = \eta_k = \theta_{0,k} + \sum_{j=1}^{J} \theta_{j,k} x_j \tag{5}$$

Equation 5 is the *systematic component* of the model, where μ_k represents the expected damage probability function (i.e., fragility function) for each k non-zero damage level. $\theta_{0,k}$ and $\theta_{j,k}$ are the parameters of the model to be estimated through maximum likelihood estimation (McCullagh and Nelder, 1989; Myung, 2003), commonly abbreviated as MLE.

In Eq. 5, g is the link function relating the linear predictor to the mean of the chosen distribution and can take one of the following forms for discrete outcomes:

$$\text{Probit} \quad g(\mu_k) = \Phi^{-1}(\mu_k) \tag{6}$$

$$\text{Logit} \quad g(\mu_k) = \log\left(\frac{\mu_k}{1-\mu_k}\right) \tag{7}$$

$$\text{Cloglog} \quad g(\mu_k) = \log(-\log(1-\mu_k)) \tag{8}$$

This model requires the response to be expressed in terms of the counts of buildings that have been damaged to a level equal or exceeding a predetermined damage state. The response can be considered to follow either a binomial or multinomial distribution for every level of intensity, and the *random component* of the model is the chosen distribution.

Logistic regression is the name given to GLM regression when the distribution is assumed binomial and the link function is the logit. It is appropriate when we assume the response variable is binary. However, the ordered nature of damage states is not represented. This may lead to inconsistent results, such as fragility functions that cross (**Figure 4**, left panel), implying DS_{k+1} is reached before DS_k as the intensity measure increases. Multinomial or Ordinal regression are both used when the response variable is defined as a categorical outcome, or classification; however, ordinal regression is a method specific to cases where such outcome is ordered (1, 2, 3. . .etc.), resulting in the so-called cumulative link model. In ordinal regression, $\theta_{j,k}$ (the rate of change of response probability for a unit increase in x_j) is fixed across damage levels ($\theta_{1,k} = \theta_1$), which preserves response ordering. **Figure 4**, right panel shows the fragility curves obtained using an ordinal model on the same sample data as in **Figure 4**, right panel. **Table 9** summarizes the components and concepts behind GLM regression.

Generalized Additive Models and Non-Parametric Models

One key assumption made in GLMs is that all explanatory variables are linearly related through the predictor (Eq. 5), which may not be the case. If rigorous diagnostics reveal that the chosen GLM do not provide a satisfactory fit to the data, alternative methods such as general additive models (GAM) or non-parametric regression can be used (Macabuag et al., 2016a).

Generalized additive models [developed by Hastie and Tibshirani (1990)] are semi-parametric models that fit GLMs in a piecewise regression system with a number of separation points (or knots). While there are dangers in using non-parametric and semiparametric methods for prediction purposes due to overfitting (Chandler, 2014), methods for overcoming this issue are demonstrated in Macabuag et al. (2016a). Rossetto et al. (2014) recommend that GAMs can be used if the data do not have a strictly monotonic trend which can be captured by GLMs, and when the data are densely distributed in the available TIM range (>100 data points). The reader is referred to Wood (2006) for detailed instruction on the fitting of GAMs.

When all assumptions cannot be met, an alternative approach is to use non-parametric regression, as non-parametric regression does not require a set of assumptions to be met for the results to be accurate and meaningful. The local polynomial kernel method is presented in Rossetto et al. (2012), this approach consists in using a well-known function (kernel) which is successively centered on each data point and uses a number of surrounding data points (bandwidth) to estimate the resulting function. Kernels are typically used as smoothers in signal processing (Schuenemeyer and Drew, 2011). The issue with this approach is the final, curve is very sensitive to the choice of bandwidth if the latter is too small, the resulting function will pick up unnecessary local variations in the data, if it is too large, the trend might be too general. Therefore, if all parametric alternatives fail to provide a satisfactory

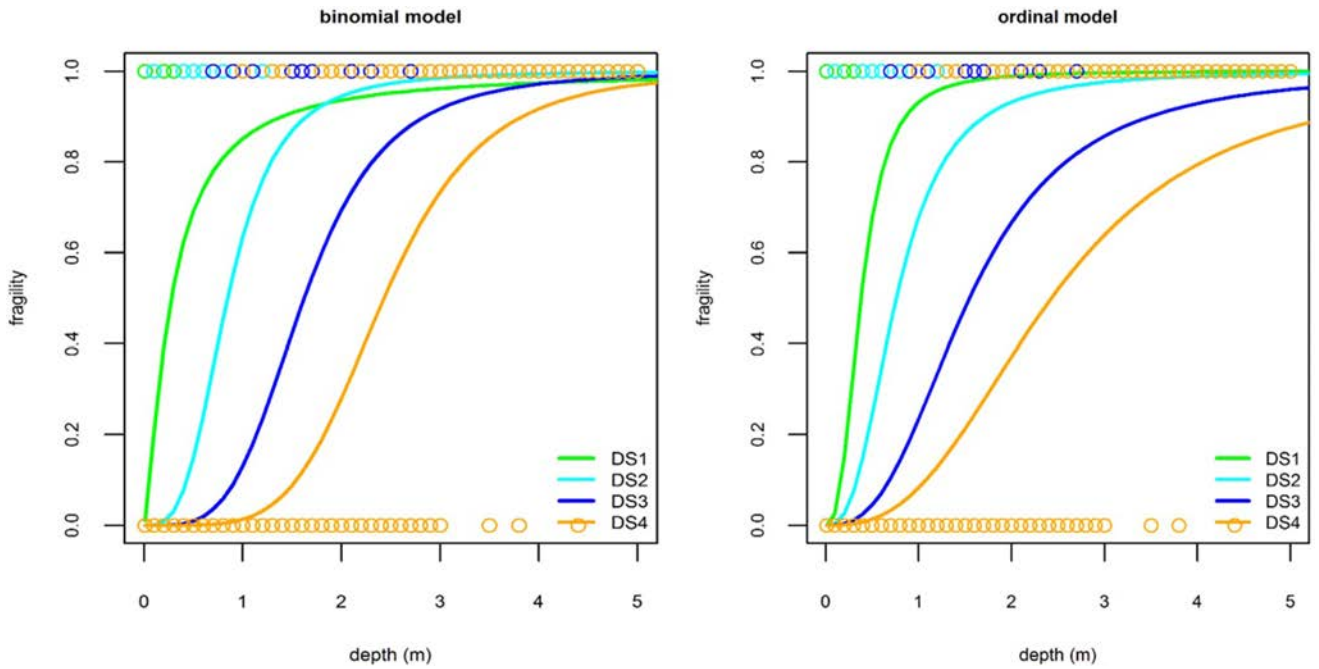

FIGURE 4 | *Left*—Crossing Fragility Functions—An unrealistic result which can be rectified by using ordinal regression. Here, the binomial logistic model has been fitted to a representative sub-sample of the data used in Charvet et al. (2014b) for illustrative purposes. *Right*—The same data analyzed using ordinal regression. The cross-over cannot take place.

TABLE 9 | GLMs used for fragility function derivation.

Number of damage levels	**0 to *K* damage states ⇔ *K* + 1 damage levels (*k* = {1, . . . ,*K* + 1})**	
Type of damage response	Binary $Y_k = \begin{cases} 1 & if\ ds \geq DS_k \\ 0 & if\ ds < DS_k \end{cases}$	Multi-level classification* $Y_k = \begin{cases} 1 & if\ ds \leq DS_1 \\ 2 & if\ DS_1 < ds \leq DS_2 \\ \ldots & \ldots \\ K+1 & if\ DS_k < ds \leq DS_{k+1} \end{cases}$
Random component (i.e., statistical distribution)	Binomial distribution $P(Y_k = 1) = \binom{n_{trials}}{n_{success}} p_s^{n_{success}} (1 - p_s)^{n_{trials} - n_{success}}$	Multinomial distribution $P(Y_1 = 1, \ldots, Y_{k+1} = K+1) = n_{trials}! \prod_{i=1}^{K+1} \frac{p_s^{n_{success}}}{n_{success}!}$
Linear Predictor η	$\eta_k = \theta_{0,k} + \sum_{j=1}^{J} \theta_{j,k} x_j$	Ordinal regression: $\eta_k = \theta_{0,k} + \sum_{j=1}^{J} \theta_j x_j$ Multinomial regression: $\eta_k = \theta_{0,k} + \sum_{j=1}^{J} \theta_{j,k} x_j$
Explanatory variables (TIMs) *x*	x_j	
Link function *g* (see also Eq. 6 to 8)	Logit (canonical link), probit or complementary loglog	
Fragility Function μ	$\hat{P}_{DS_k} = \mu_k = g^{-1}(\eta_k)$	

*Note that in existing literature J (the number of TIMs) is generally 1, with the exception of Charvet et al. (2014a), for which J = 3 [x_1 = tsunami flow depth, x_2 = velocity, and x_3 = building class (dummy coded variables {0,1})]. * Note also that because the theoretical multinomial response gives the probability of damage being smaller than or equal to a given level, the exceedance damage probability will be obtained by using the complimentary cumulative distribution, i.e., $P(ds \geq DS_k) = 1 - P(ds \leq DS_k)$.*

fit to the data non-parametric regression can be a useful alternative.

Model Diagnostics

Unfortunately, the evolution of fragility studies applied to tsunami induced damage is still at an early stage and adequate model assessment is seldom carried out. This leads to the impossibility of identifying sources of uncertainty in the probability estimations, thus preventing model improvement. In order for fragility results to be exploited further, it is necessary to perform model diagnostics to reveal if the model used gives a satisfactory representation of the data, identify sources of uncertainty, and assess the adequacy of the systematic and random components.

Diagnostics of Linear Models

For such models, the goodness-of-fit is typically assessed by reporting the value of the coefficient of determination, or R^2 [e.g., Gokon et al. (2010) and Suppasri et al. (2011)]. However, this assessment of model performance is insufficient in the light of the shortcomings previously outlined in this section.

In addition, when using any form of parametric regression, assumptions should be systematically validated as part of the analysis, as they can be easily violated (Charvet et al., 2013). Linear regression requires several assumptions to be met (Chatterjee and Hadi, 2006), which are typically not checked in practice.

Diagnostics of GLM

For *binomial models*, it is necessary to graphically examine the model errors (or Pearson residuals, McCullagh and Nelder, 1989) for each curve, which may reveal:

- The non-linear contribution of an additional variable/effect on the model (identification of a trend in the errors),
- Potential inadequacy of the link function,
- Influential points or outliers,
- Over-dispersion (the values of the residuals or errors are more than two standard deviations away from the mean, thus indicating a potential issue in the choice of distribution),

For *ordinal and multinomial models*, expected versus observed probabilities or counts graphs can be used [**Figure 5**: Expected versus observed probabilities after fitting an ordinal model to the building damage data, as per Charvet et al. (2014b)—Figure].

Model *accuracy* (the proportion of correctly classified outcomes) can be used as a quantitative indicator of the performance of the model. It is directly related to the *prediction error rate* (the proportion of incorrectly classified outcomes). Charvet et al. (2015) propose a penalized accuracy measure (accounting for the distance between observed and expected outcomes) estimated through 10-fold cross-validation, which provides a quantitative assessment of goodness-of-fit of the model and an indication of predictive power. This methodology was applied by Macabuag et al. (2016a) to assess model performance, as well as prevent overfitting with the use of GAMs.

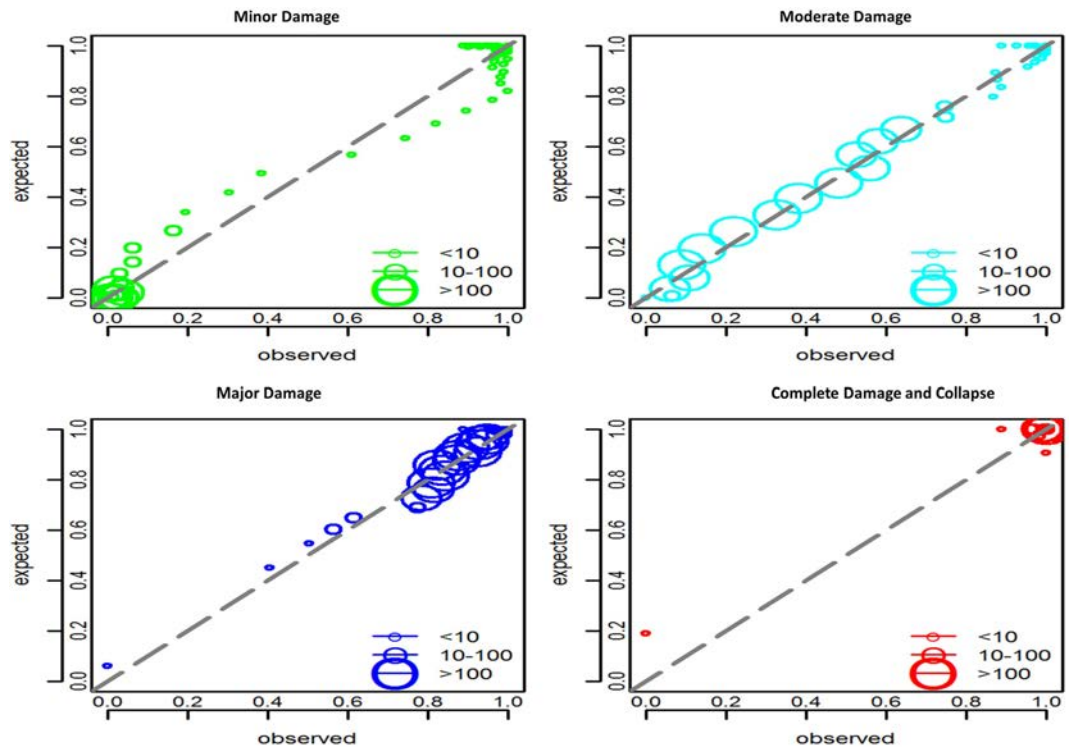

FIGURE 5 | Expected versus observed probabilities after fitting a multinomial model to the building damage data used in Charvet et al. (2014b), for 1 storey timber buildings. The green, light blue, dark blue, and red color codes correspond respectively to DS1, DS2, DS3, DS4 and over, as per damage descriptions in **Table 6**. A good fit is indicated by counts following closely the 45 line.

Measures such as the AIC (Akaike Information Criterion) or likelihood ratio tests based on deviance for nested models are useful measures for model comparison. These can only be used to compare two models that have been fitted on the same data and with the same choice of statistical distribution:

- The *likelihood ratio test* (Rossetto et al., 2014) can be used to assess whether a model with more parameters provides a significantly better fit in comparison to a simpler model with less parameters (i.e., *nested* models). For example, it can be used to assess whether a model with an additional explanatory variable fits the data significantly better. It can also be used to test the relative goodness-of-fit of the multinomial model compared to the ordinal model, its simpler alternative. Indeed, in an ordinal model, the free parameters for each class are fixed, which leads to a smaller number of parameters in comparison with the multinomial alternative (see **Table 9**).
- The AIC (Akaike, 1974) can be used, for example, to compare two identical models but differing only by their link function. It can also be used for nested models. The AIC can be calculated as follows:

$$AIC = 2p - 2\log(L) \tag{9}$$

$$L(\theta, \phi|DS) = P(ds = DS|\theta, \phi) \tag{10}$$

In Eq. (9), $-2\ln(L)$ is the model's deviance (a measure of the model error), p is the number of parameters in the model, ϕ is the dispersion parameter (a function of the model's variance), and L is the likelihood function (McCullagh and Nelder, 1983). The model that provides the best fit to the data is the model with the smallest AIC.

Various options for model configuration and selection method are presented in **Table 10**.

Further Considerations for Statistical Modeling

Sample Size

A low number of data points may lead to a spuriously well-fitted model (over-prediction). While a minimum sample size must be used to yield reliable results, little guidance is available on its determination (Rossetto et al., 2012).

Comprehensive studies on the topic of sample size have been carried in the context of linear regression, although these considerations also apply to the context of generalized linear modeling. In the context of simple or multiple regression such as linear regression, a rule of thumb states there should be no less than 50 data points for a regression, with the number increasing with larger numbers of independent variables. VanVoorhis and Morgan (2007) and Green (1991) provide a more detailed guidance in the context of regression analysis, based on power considerations.

Leveraging on the results from Cohen (1988), Green (1991) provides power tables that give the required sample size according to the number of predictors and expected *effect size*, i.e., the strength of the relationship between the predictor(s) and the response. If we assume that, for example, the damage state of a building is strongly related to the tsunami flow depth (i.e., the effect size is large), and flow depth is the only available predictor variable, the aforementioned power table recommends a minimum of 24 points. It should be noted that this study focused on the analysis of data for behavioral sciences, such thresholds should be investigated in the context of the typical relationships expected in physical sciences. Other studies have recommended to use anything from a minimum of 10 (Miller and Kunce, 1973; Harrell et al., 1985; Bartlett et al., 2001; Babyak, 2004) to a minimum of 100 (the case of small effect size or large number of predictors in Green, 1991) or even 200 data points (Guadagnoli and Velicer, 1988; Nunnally and Bernstein, 1994). Ideally, the analyst should carry out their own sensitivity study prior to fitting a statistical model, the minimum number of data points required to construct a vulnerability or fragility function depending on the level of uncertainty the analyst is willing to accept.

However, the scarcity of data is often a limitation and current rules-of-thumb have to be used.

In the case of fragility curves for earthquakes, a minimum of 100 observations is recommended (Rossetto et al., 2014) and at least 30 of them should have reached or exceeded a given damage state (Noh et al., 2014), with the data points spanning a wide range of TIM values. Although there is a reasonable starting point to

TABLE 10 | Statistical model types and model comparison methodologies [adapted from Macabuag et al. (2016a)].

Class	Model	Configuration options	Selection method	Reference
Parametric		(OLS not suitable for fragility function derivation)		Suppasri et al. (2012a); Suppasri et al. (2009); Tanaka and Kondo (2015)
	Generalized Linear Model (GLM) or Cumulative Link Model	Transformation of explanatory variables	AIC[a]	Charvet et al. (2015); Leelawat et al. (2014); Muhari et al. (2015); Reese et al. (2011)
		Link function	AIC	
		Ordered or partially ordered models	LRT	
Semi-parametric	Generalized Additive Model (GAM)	Transformation of explanatory variables	AIC[a]	Wood (2006)
		Link function	AIC	
		Number of knots	KFCV error rates[b]	
Non-parametric	Kernal Smoother	(See reference for information on fitting these models)		Noh et al. (2014)

[a] *It is noted that fragility functions are generally fit to the natural logarithm of the explanatory variable.*
[b] *If conducting trend analysis using GAMs it is recommended to simply select a preliminary number of knots (e.g., four knots).*
AIC, Akaike Information Criteria; LRT, Likelihood Ratio Test; KFCV, K-Fold Cross-Validation.

guide tsunami fragility function derivation, research is needed to assess the minimum sample size for tsunami fragility.

Aggregation of Data

When data are aggregated over bins of the TIM (such as flow depth), it is assumed that the distribution in each bin is normal or uniform (as the value of TIM for each bin is taken as its median). This definition affects both the shape of the function and the confidence intervals. For instance, Valencia et al. (2011) generated 0.1 m wide bins from minimum to maximum flow depth recorded. Similarly Koshimura et al. (2009b) generated 0.2 m bins in order to separate the building damage data into groups of roughly equal size. The definition of bins of arbitrary sizes (x-axis) typically leads to an inconsistent number of buildings in each sample, without the model accounting for points of different weights. This issue may be addressed by weighting the N_i data points in each sample. However, if both a large and small number of data points are used, i.e., $10 < N_i < 100$; the smaller samples will not have any influence on the curve and may have to be removed (Ioannou et al., 2012).

Data are also aggregated, at the collection stage, by location, by damage level, or by building class. Aggregation of data over real areas, including variable inundation depths introduces significant uncertainty in the TIM (x-value) at any specific location (Koshimura et al., 2009a). Charvet et al. (2014a,b) found the analysis of the 2011 Japan tsunami damage data aggregated over Japan led to a significant amount of uncertainty in the results, and Macabuag et al. (2016a) quantified the uncertainty related to data aggregation by showing a clear reduction in predictive accuracy of the model.

Finally, data from different sources (for example, different events or survey teams) are often grouped and analyzed as a single entity. This practice does not account properly for all sources of uncertainty. In such cases, it is appropriate to use generalized linear mixed models. These models introduce a random intercept for each group in Eq. (5) to explicitly account for the group (event or survey) as an explanatory variable (Rossetto et al., 2014).

Missing Data

Macabuag et al. (2016a) demonstrate techniques to classify missing data and complete the database accordingly (**Table 11**). Where data are identified as MCAR complete-case analysis may be conducted without introducing bias in the results. For data that are MNAR, complete-case analysis would introduce bias and missing data cannot be estimated, and so the dataset must be supplemented with additional information to address this issue before fragility analysis can be conducted. For data that are MAR, the missing data may be estimated by Multiple Imputation (MI) techniques. MI involves replacing missing observed data with substituted values estimated multiple times via stochastic regression models built on the other attributes (used as explanatory variables), with all of the imputations being combined in order to derive the final estimate (Rubin, 1987).

Figure 6 demonstrates the effect of bias due to complete-case analysis on fragility function derivation. Macabuag et al. (2016a), therefore, recommends that existing fragility assessments should be re-examined for potential bias if they have been based on complete-case analysis of data subsets (e.g., construction material).

TABLE 11 | Classification and treatment of missing data (adapted from Macabuag et al., 2016a).

Classification	Method of identification	Recommended action
Missing Completely At Random (MCAR)	Test whether the missing data distribution is the same as for the complete dataset (Kolmogorov–Smirnov test for disaggregated data, or χ^2-test for aggregated data)	Conduct Complete-Case Analysis (i.e., remove datapoints with missing information and perform regression analysis on the remaining dataset), or estimate missing data using Multiple Imputations (MIs) techniques
Missing Not at Random (MNAR)	Is the missing information related to the reason that the information is missing?	Fragility analysis cannot be conducted without introducing bias. Revisit data-collection process to complete missing data.
Missing at Random	Not MCAR or MNAR	Estimate missing data using MIs techniques

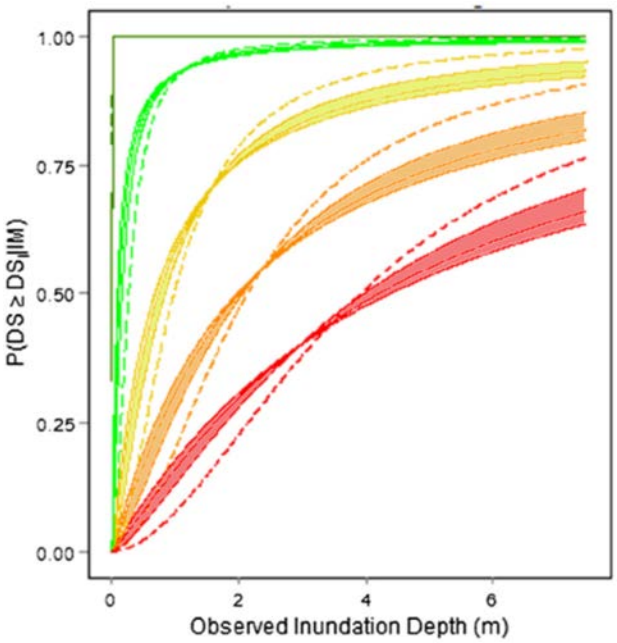

FIGURE 6 | The effect of ignoring incomplete datasets. Dashed-lines show curves formed using complete-case analysis for steel and RC buildings from the 2011 Japan Tsunami (i.e., ignoring all buildings for which the construction material was unknown). Solid lines show a range of mean curves for the imputed dataset (i.e., with building material for "unknown" buildings estimated using MI). Colours indicate the individual damage states, from light damage (dark green) to collapse (red). (Adapted from Macabuag et al., 2016a).

DISCUSSION, RECOMMENDATIONS, AND FUTURE RESEARCH

Existing tsunami fragility functions are concisely presented in **Tables 1** and **2**, which summarize the key features of the damage datasets, inundation datasets, and statistical models used by each

TABLE 12 | Issues with current fragility functions, organized by model component.

	Issues Identified in Existing Fragility Functions
Damage data (response variable)	• Inconsistency in building classes • Inconsistency in damage scales • Separation of structural and non-structural damage in damage scales • Specificity of the derived function to the area and environmental conditions being surveyed • Incomplete data omitted
Intensity measures (explanatory variable)	• Some inconsistencies in definitions of flow depth • Depth is generally the only intensity measure used in existing studies • Velocity and force-related TIMs are difficult to validate • Limitations of empirical tsunami data (measuring Inundation) • Limitations of physical inundation modeling (experiment-derived tsunami data) • Limitations of numerical inundation modeling (simulation-derived tsunami data)
Model quality (statistical treatment)	• Before model fitting: ○ Inadequate distribution assumptions ○ Inadequate sample size ○ Data aggregation ○ Dismissal of data and improper treatment of missing data ○ Improper treatment of multiple data sources • After model fitting: ○ Lack of model diagnostics ○ No comparison of different regression techniques ○ Limited quantification of model performance ○ No representation of uncertainty

function. Generally, there is considerable variability in terminology within the studies presented in **Table 1**. In order to compare and combine fragility functions it is important that consistent terminology is used, and so recommended terminology has been presented for tsunami risk and vulnerability (**Figure 1**), and the various methods for presenting damage and loss estimates.

The key issues with existing studies, as identified in previous sections, are summarized in **Table 12**. This section provides recommendations on both the assessment of existing fragility functions and the derivation of new fragility functions.

Assessment/Improvement of the Quality of Building Damage Data

In order to compare and combine fragility functions, a unification of building classifications for tsunami fragility analysis is needed. Following the example of the seismic building classifications recommended by the GEM (Brzev et al., 2013), it is recommended that tsunami building classifications follow the building attributes that govern performance under tsunami loading as summarized in **Table 13**.

Similarly, unification of tsunami damage scales is required and many of the issues highlighted with existing damage scales have been addressed by Fraser et al. (2013) [adapted from EEFIT (2006)] who propose improved damage scales, based on the familiar EMS-98 damage scales, for RC, steel, and timber. This damage scale only goes part way to fulfilling the needs of a damage scale suitable for use in the future development of tsunami fragility functions from both empirical and analytical approaches. Specifically, it includes descriptions of visual damage but does not define a set of engineering demand parameter thresholds that can be used to determine a building's damage state from an analysis of its tsunami response using software. Hence, research is still required in order to deliver an appropriate damage scale, adhering to the rules set out in **Table 3**, for use in fragility function derivation.

Typical issues associated with post-tsunami damage data collection have been summarized in **Table 6**. To obtain more reliable field-survey, data measures must be taken to limit uncertainties due to combining data from surveyors of differing experience, errors in survey forms, or combination of data from different surveys. It is, therefore, necessary to develop universal guidance for tsunami damage data collection. Consistent and adequate training for surveyors is required but may be difficult to achieve for large-scale disasters where a large number of surveyors from different professional backgrounds will be deployed rapidly in the immediate aftermath of the disaster. An example of guidance used for Japanese surveyors following the 2011 Tohoku earthquake and tsunami is presented in EEFIT (2013).

So as not to introduce biases in the data, it is also important to include all buildings in a survey and not segregate data collected to damaged buildings only. Aggregation of data (by location) must also be limited where possible, so as to reduce uncertainty when pairing damage and inundation data. It is recommended that incomplete data are investigated and treated as per Macabuag et al. (2016a).

As empirical fragility functions have been shown to be very sensitive to the location from where their damage data were collected, in order to quantify fragility in the many at-risk locations around the world without available damage data, analytical methods for fragility function derivation based on structural analysis are required.

Assessment/Improvement of the Quality of Tsunami Intensity Data

Although inundation depth is used as the only TIM for the majority of existing tsunami fragility functions, this does not capture all of the relevant tsunami information necessary to predict structural damage. Therefore, for future studies numerical modeling should be conducted in order to obtain TIMs other than depth (validated against values measured or inferred from observations). If the inundation simulation from which they are derived is sufficiently accurate, then force estimates often provide the most efficient TIMs. These and other additional TIMs should be compared and the optimal defined for a given dataset according to the methodology set out in Macabuag et al. (2016a).

Fragility functions incorporating multiple TIMs (e.g., fragility surfaces), should be considered also.

Debris has been shown to significantly affect the fragility of buildings, and further research is needed to fully capture the damage potential that debris presents.

The reliability of the existing fragility functions based on velocity or force is very dependent on the accuracy of the inundation models on which those TIMs are based. Reviewing current best-practice for numerical inundation modeling is outside the scope of this paper, but it is recommended that the quality of inundation models used in existing studies be examined against

TABLE 13 | Building attributes which govern tsunami performance (BA1-BA10).

Building Attribute		Description	Example
BA1	Material of the Lateral Load-Resisting System	Structural material	RC
BA2	Lateral Load-Resisting System	Structural system for resisting lateral loads	Shear-wall
BA3	Redundancy of Vertical Load Paths	When a building is only supported by a limited number of structural elements (e.g., four columns), floating debris damaging one or two columns may trigger disproportionate collapse of the structure	3% wall-density on plan
BA4	Building Height	Number of stories. Will govern member sizes (Suppasri et al., 2013)	Low-rise
BA5	Openings (and break away walls)	Reduce the visible cross-sectional area to oncoming flow, so allows for the hydrostatic and hydrodynamic pressures not to accumulate on the front face of the building (EEFIT, 2006; Ruangrassamee et al., 2006; Suppasri et al., 2012a,b)	10% openings
BA6	Shape and Orientation	Building orientation has a direct effect on induced drag forces (Dominey-Howes and Papathoma, 2006; Lloyd, 2014) with bluff bodies experiencing a greater force than those with leading walls that are not orthogonal to the flow	Bluff
BA7	Foundations	Deep foundations will reduce the vulnerability of the structure to scour around the base (Jackson et al., 2005; Ghobarah et al., 2006; Ruangrassamee et al., 2006; EEFIT, 2011)	Shallow
BA8	Soil Conditions	Uplift forces will develop more quickly for buildings founded on porous soils (Yeh et al., 2014). Scour will be enhanced by erodible soils such as sand, and a lack of protection such as pavements (EEFIT, 2011)	Sand
BA9	Date of Construction	Affects the design standards followed during construction (e.g., pre/post seismic codes) and the likelihood that materials have degraded during the lifetime of the building	Pre-code
BA10	Occupancy	Building use or line of business (for insurance modeling).	Commercial
BA11	Material of External Envelope	Lower damage states are generally defined by water ingress into the building footprint. Some building enveloped are more permeable (e.g., light cladding panels) than others (e.g., solid masonry)	Timber cladding

Note that material is the only attribute considered in existing studies, with the exception of Suppasri et al. (2014).

a number of factors, such as quality/reliability/resolution of the topography/bathymetry data, quality/reliability of the source and propagation models, the software used, the resolution of the calculation grid, and so on.

In order to improve the accuracy of numerical inundation models, better understanding is needed of tsunami near and onshore processes and on the determination of actions on structures. Physical experiments can give an insight into the complex processes involved in flow–structure interactions onshore, however, most large-scale laboratory facilities to-date do not allow for the reproduction of some keys characteristics of tsunami, such as their wavelengths. Some work on tsunami forces has been done using solitary waves or similar, but results involving long (shallow water) waves is limited. This leads to a lack of experimental validation of current fragility and damage relationships. There are several studies to address this gap (Rossetto et al., 2011; Charvet, 2012; Lloyd and Rossetto, 2012; Foster et al., 2017), and this area should be the focus of further research to improve the accuracy of inundation models and the understanding of tsunami-effects on buildings, both crucial for accurate fragility function derivation.

Assessment/Improvement of the Quality of Statistical Modeling

It is recommended that data aggregation be avoided and that missing data be classified and treated prior to regression analysis, as set out in section "Model Quality."

A case is made to show that existing fragility studies using GLMs are more reliable than those employing linear models with linear least squares parameter estimation. The optimal model configurations for a given dataset can be determined using the tests shown in **Table 10**. Semi-parametric GAMs may also be used if overfitting is avoided using the cross-validation methods outlined in Macabuag et al. (2016a). If all parametric alternatives fail to provide a satisfactory fit to the data non-parametric regression can be a useful alternative.

For new studies, missing data should be analyzed and treated as set out in **Table 11** and it is recommended that existing fragility assessments should be re-examined for potential bias if they have been based on complete-case analysis of data subsets (e.g., construction material).

It is recommended that uncertainty of the mean fragility curves should always be presented and one such technique is to confidence intervals derived by bootstrap methods as outlined in Charvet et al. (2014b). Furthermore, rigorous diagnostics of the final model should be employed in order to assess likely model accuracy.

Multivariate regression can be achieved using GLM regression techniques and any number of intensity measures can be included in the model. However, it is always the aim to develop a "parsimonious model" (the best model for the fewest predictors) as using additional intensity measures requires more data points, and difficulties of obtaining these additional tsunami parameters must be overcome. In addition, the representation of a fragility surface

in more than three dimensions (i.e., with more than two TIMs) is challenging and it is necessary to find a representation method giving interpretable and useful results.

CONCLUSION

This paper collates and summarizes existing empirical tsunami fragility functions for buildings, to outline limitations and significant advances in the field, and to propose key areas for further development. A number of key issues and recommendations for each component of tsunami fragility functions have been presented (damage data, tsunami intensity data, and the statistical model).

The information presented in this paper may be used to assess the quality of current estimations (both based on the quality of the data, and the quality of the models and theories adopted), and to adopt best practice when developing new fragility functions. This paper, therefore, has implications for those using, assessing, or developing tsunami fragility functions.

AUTHOR CONTRIBUTIONS

IC, early original draft of paper. Author of section on model quality. JM, author of all other sections building on IC's early draft. Editor of final paper. TR, Reviewer.

ACKNOWLEDGMENTS

TR's time is funded by the European Research Council funded URBAN WAVES Starting Grant (reference: 336084). JM's time is funded by the EPSRC Engineering Doctorate Programme and the Willis Research Network. We would also like to acknowledge the many years of successful collaboration between EPICentre, UCL (UK) and IRIDeS, Tohoku University (Japan) which has made this work possible.

REFERENCES

Adriano, B., Hayashi, S., Gokon, H., Mas, E., and Koshimura, S. (2016). Understanding the extreme tsunami inundation in Onagawa town by the 2011 Tohoku earthquake, its effects in urban structures and coastal facilities. *Coast. Eng. J.* 58, 19. doi:10.1142/S0578563416400131

Akaike, H. A. I. (1974). A new look at the statistical model identification. *IEEE Trans. Automat. Contr.* 19, 716–723. doi:10.1109/TAC.1974.1100705

Amakuni, K., and Terazono, N. (2011). "Basic analysis on building damages by tsunami due to the 2011 Great East Japan earthquake disaster using," in *15 World Conference on Earthquake Engineering*. Available at: http://www.iitk.ac.in/nicee/wcee/article/WCEE2012_3628.pdf

Babyak, M. A. (2004). What you see may not be what you get: a brief, nontechnical introduction to overfitting in regression-type models. *Psychosom. Med.* 66, 411–421. doi:10.1097/00006842-200405000-00021

Bartlett, J. E., Kotrlik, J. W., and Higgins, C. C. (2001). Organizational research: determining appropriate sample size in survey research. *Info. Technol. Learn. Perform. J.* 19, 43–50.

Berryman, K. (2005). *Review of Tsunami Hazard and Risk in New Zealand*. Prepared for (September). Institute of Geological & Nuclear Sciences client report 2005/104, GNS Limited. Available at: http://www.civildefence.govt.nz/assets/Uploads/publications/GNS-CR2005-104-review-of-tsunami-hazard.pdf

Brzev, S., Charleson, A. W., and Jaiswal, K. (2013). *GEM Basic Building Taxonomy Report Produced in the Context of the GEM Ontology and Taxonomy Global Component Project*. Available at: http://www.nexus.globalquakemodel.org/gem-building-taxonomy/posts/updated-gem-basic-building-taxonomy-v1.0

Chandler, R. (2014). "Classical approaches for statistical inference in model calibration with uncertainty," in *Applied Uncertainty Analysis for Flood Risk Management*, eds K. Beven and J. Hall (London: Imperial College Press), 60–67.

Charvet, I. (2012). *Experimental Modelling of Long Elevated and Depressed Waves Using a New Pneumatic Wave Generator*. PhD thesis, University College London. Available at: http://discovery.ucl.ac.uk/1343903/1/1343903.pdf

Charvet, I., Eames, I., and Rossetto, T. (2013). New tsunami runup relationships based on long wave experiments. *Ocean Model.* 69, 79–92. doi:10.1016/j.ocemod.2013.05.009

Charvet, I., Suppasri, A., Kimura, H., Sugawara, D., and Imamura, F. (2015). Fragility estimations for Kesennuma City following the 2011 Great East Japan Tsunami based on maximum flow depths, velocities and debris impact, with evaluation of the ordinal model's predictive accuracy. *Nat. Hazards* 79, 2073–2099. doi:10.1007/s11069-015-1947-8

Charvet, I., Ioannou, I., Rossetto, T., Suppasri, A., and Imamura, F. (2014a). Empirical fragility assessment of buildings affected by the 2011 Great East Japan tsunami using improved statistical models. *Nat. Hazards* 73, 951–973. doi:10.1007/s11069-014-1118-3

Charvet, I., Suppasri, A., and Imamura, F. (2014b). Empirical fragility analysis of building damage caused by the 2011 Great East Japan tsunami in Ishinomaki city using ordinal regression, and influence of key geographical features. *Stoch. Environ. Res. Risk Assess.* 28, 1853–1867. doi:10.1007/s00477-014-0850-2

Chatterjee, S., and Hadi, A. (2006). *Regression Analysis by Example*, 4th Edn. Hoboken, NJ, USA: Wiley & Sons.

Chock, G., Carden, L., Robertson, I., Olsen, M., and Yu, G. (2013). Tohoku tsunami-induced building failure analysis with implications for U.S. tsunami and seismic design codes. *Earthq. Spectra* 29, S99–S126. doi:10.1193/1.4000113

Chock, G. Y. K. (2016). Design for tsunami loads and effects in the ASCE 7-16 standard. *J. Struct. Eng.* 142, 1–12. doi:10.1061/(ASCE)ST.1943-541X.0001565

Cohen, J. (1988). *Statistical Power Analysis for the Behavioral Sciences*, 2nd Edn. Hillsdale, NJ: Lawrence Erlbaum Associates.

Crichton, D. (1999). *The Risk Triangle*. Available at: http://scholar.google.com/scholar?hl=en&btnG=Search&q=intitle:The+risk+triangle#0

D'Ayala, D., Meslem, A., Vamvatsikos, D., Porter, K., Rossetto, T., Crowley, H., et al. (2013). *Guidelines for Analytical Vulnerability Assessment*. Available at: http://www.nexus.globalquakemodel.org/gem-vulnerability/posts/guidelines-for-analytical-vulnerability-assessment

De Risi, R., Goda, K., Mori, N., and Yasuda, T. (2017a). Bayesian tsunami fragility modeling considering input data uncertainty. *Stoch. Environ. Res. Risk Assess.* 31, 1253–1269. doi:10.1007/s00477-016-1230-x

De Risi, R., Goda, K., Yasuda, T., and Mori, N. (2017b). Is flow velocity important in tsunami empirical fragility modeling? *Earth Sci. Rev.* 166, 64–82. doi:10.1016/j.earscirev.2016.12.015

Dias, W. P. S., Yapa, H. D., and Peiris, L. M. N. (2009). Tsunami vulnerability functions from field surveys and Monte Carlo simulation. *Civ. Eng. Environ. Syst.* 26, 181–194. doi:10.1080/10286600802435918

Dominey-Howes, D., and Papathoma, M. (2006). Validating a tsunami vulnerability assessment model (the PTVA model) using field data from the 2004 Indian Ocean tsunami. *Nat. Hazards*. 40, 113–36. doi:10.1007/s11069-006-0007-9

EEFIT. (2006). *The Indian Ocean Tsunami of 26 December 2004: Mission Findings in Sri Lanka and Thailand*. Field Report by the Earthquake Engineering Field Investigation Team (EEFIT), Institution of Structural Engineers. Available at: http://www.istructe.org/webtest/files/74/74b66946-020a-430d-a684-0f71ff0d2a23.pdf

EEFIT. (2011). *Field Report: Earthquake and Tsunami of 11th March 2011*. Field Report by the Earthquake Engineering Field Investigation Team (EEFIT), Institution of Structural Engineers.

EEFIT. (2013). *Field Report (Return Mission): Earthquake and Tsunami of 11th March 2011*. Field Report by the Earthquake Engineering Field Investigation Team (EEFIT), Institution of Structural Engineers.

FEMA. (2012). *FEMA P-646: Guidelines for Design of Structures for Vertical Evacuation from Tsunamis*, 2nd Edn, Federal Emergency Management Report. Availabale at: https://www.fema.gov/media-library/assets/documents/14708

Foster, A. S. J., Rossetto, T., and Allsop, W. (2017). An experimentally validated approach for evaluating tsunami inundation forces on rectangular buildings. *Coast. Eng.* (in press).

Fraser, S., Raby, A., Pomonis, A., Goda, K., Chian, S. C., Macabuag, J., et al. (2013). Tsunami damage to coastal defences and buildings in the March 11th 2011 M w 9.0 Great East Japan earthquake and tsunami. *Bull. Earthq. Eng.* 11, 205–239. doi:10.1007/s10518-012-9348-9

Ghobarah, A., Saatcioglu, M., and Nistor, I. (2006). The impact of the 26 December 2004 earthquake and tsunami on structures and infrastructure. *Eng. Struct.* 28, 312–326. doi:10.1016/j.engstruct.2005.09.028

Gokon, H., Koshimura, S., and Matsuoka, M. (2009). Developing tsunami fragility curves for structural destruction in American Samoa. *J. Jpn. Soc. Civ. Eng.* Available at: http://www.enveng.titech.ac.jp/midorikawa/rsdm2010_pdf/04_gokon_paper.pdf

Gokon, H., Koshimura, S., and Matsuoka, M. (2010). "Developing tsunami fragility curves for structural destruction in American Samoa," in *8th International Workshop on Remote Sensing for Disaster Response*, Tokyo.

Goseberg, N., Wurpts, A., and Schlurmann, T. (2013). Laboratory-scale generation of tsunami and long waves. *Coast. Eng.* 79, 57–74. doi:10.1016/j.coastaleng.2013.04.006

Green, S. (1991). How many subjects does it take to do a regression analysis? *Multivariate Behav. Res.* 26, 499–510. doi:10.1207/s15327906mbr2603_7

Guadagnoli, E., and Velicer, W. F. (1988). Relation to sample size to the stability of component patterns. *Psychol. Bull.* 103, 265–275. doi:10.1037/0033-2909.103.2.265

Harrell, F. E. Jr., Lee, K. L., Matchar, D. B., and Reichert, T. A. (1985). Regression models for prognostic prediction: advantages, problems, and suggested solutions. *Cancer Treat. Rep.* 69, 1071–1077.

Hastie, T., and Tibshirani, R. (1990). *Generalized Additive Models, Chapman & Hall/CRC Monographs on Statistics & Applied Probability.* Available at: http://www.amazon.co.uk/Generalized-Additive-Monographs-Statistics-Probability/dp/0412343908

Hayashi, S., Narita, Y., and Koshimura, S. (2013). Developing tsunami fragility curves from the surveyed data and numerical modeling of the 2011 Tohoku earthquake tsunami (in Japanese). *J. Jpn. Soc. Civ. Eng. Coast. Eng.* 69, 1–5. doi:10.2208/kaigan.69.I_386

Hill, M., and Rossetto, T. (2008). Comparison of building damage scales and damage descriptions for use in earthquake loss modelling in Europe. *Bull. Earthq. Eng.* 6, 335–365. doi:10.1007/s10518-007-9057-y

Inoue, S., Wijeyewickrema, A. C., and Matsumoto, H. (2007). "Field survey of tsunami effects in Sri Lanka due to the Sumatra-Andaman earthquake of December 26, 2004," in *Tsunami and Its Hazards in the Indian and Pacific Ocean* (Basel: Springer), 395–411.

Ioannou, I., Rossetto, T., and Grant, D. N. (2012). "Use of regression analysis for the construction of empirical fragility curves," in *15 World Conference on Earthquake Engineering*. Available at: http://www.iitk.ac.in/nicee/wcee/article/WCEE2012_2143.pdf

Jackson, L. E., Vaughn Barrie, J., Forbes, D. L., Shaw, J., Manson, G. K., and Schmidt, M. (2005). *Effects of the 26 December 2004 Indian Ocean Tsunami in the Republic of Seychelles. Report of the Canada-UNESCO Indian Ocean Tsunami Expedition 19 January–5 February 2005*. Available at: http://www.unisdr.org/files/2193_VL323132.pdf

Japan Cabinet Office. (2013). *Residential Disaster Damage Accreditation Criteria Operational Guideline*. Available at: http://www.bousai.go.jp/taisaku/unyou.html

Kircher, C. A., and Bouabid, J. (2014). "New building damage and loss functions for Tsunami," in *10th International Conference on Urban Earthquake Engineering* (Tokyo).

Koshimura, S., and Gokon, H. (2012). Structural vulnerability and tsunami fragility curves from the 2011 Tohoku earthquake tsunami disaster. *J. Jpn. Soc. Civ. Eng. Ser. B2 (Coast. Eng.)* 68, I_336–I_340. doi:10.2208/kaigan.68.I_336

Koshimura, S., and Kayaba, S. (2010). Tsunami fragility inferred from the 1993 Hokkaido Nansei-oki earthquake tsunami disaster. *J. Jpn. Assoc. Earthq. Eng.* 10, 87–101. doi:10.5610/jaee.10.3_87

Koshimura, S., Namegaya, Y., and Yanagisawa, H. (2009a). Tsunami fragility – a new measure to identify tsunami damage. *J. Disaster Res.* 4, 479–488. doi:10.20965/jdr.2009.p0479

Koshimura, S., Oie, T., Yanagisawa, H., Imamura, F. (2009b). Developing fragility functions for tsunami damage estimation using numerical model and post-tsunami data from Banda Aceh, Indonesia. *Coast. Eng. J.* 51, 243–273. doi:10.1142/S0578563409002004

Kreibich, H., Piroth, K., Seifert, I., Maiwald, H., Kunert, U., Schwarz, J., et al. (2009). Is flow velocity a significant parameter in flood damage modelling? *Nat. Hazards Earth Syst. Sci.* 9, 1679–1692. doi:10.5194/nhess-9-1679-2009

Kriebel, D. L., Lynett, P. J., Cox, D. T., Petroff, C. M., Robertson, I. N., and Chock, G. Y. K. (2017). Energy method for approximating overland tsunami flows. *J. Waterw. Port Coast. Ocean Eng.* 143. Available at: http://ascelibrary.org/doi/abs/10.1061/%28ASCE%29WW.1943-5460.0000393

Leelawat, N., Suppasri, A., Charvet, I., and Imamura, F. (2014). Building damage from the 2011 Great East Japan tsunami: quantitative assessment of influential factors. *Nat. Hazards* 73, 449–471. doi:10.1007/s11069-014-1081-z

Lloyd, T. O. (2014). *An Experimental Investigation of Tsunami Forces on Coastal Structures*. London: University College London.

Lloyd, T. O., and Rossetto, T. (2012). "A comparison between existing tsunami load guidance and large-scale experiments with long-waves," in *15 World Conference on Earthquake Engineering* (Lisbon).

Macabuag, J., and Rossetto, T. (2014). "Towards the development of a method for generating analytical tsunami fragility functions," in *2nd European Conference on Earthquake Engineering and Seismology*.

Macabuag, J., Rossetto, T., and Ioannou, I. (2016a). "Investigation of the effect of debris-induced damage for constructing tsunami fragility curves for buildings," in *1st International Conference on Natural Hazards & Infrastructure* (Chania, Greece).

Macabuag, J., Rossetto, T., Ioannou, I., Suppasri, A., Sugawara, D., Adriano, B., et al. (2016b). A proposed methodology for deriving tsunami fragility functions for buildings using optimum intensity measures. *Nat. Hazards* 84, 1257–1285. doi:10.1007/s11069-016-2485-8

Maruyama, Y., Kitamura, K., and Yamazaki, F. (2013). "Tsunami damage assessment of buildings in Chiba Prefecture, Japan using fragility function developed after the 2011 Tohoku-Oki earthquake," in *Safety, Reliability, Risk and Life-Cycle Performance of Structures & Infrastructures* (Taylor & Francis). Available at: http://ares.tu.chiba-u.jp/~papers/paper/2013/2013ICOSSAR_Maruyama.pdf

Mas, E., Koshimura, S., Suppasri, A., Matsuoka, M., Matsuyama, M., Yoshii, T., et al. (2012). Developing Tsunami fragility curves using remote sensing and survey data of the 2010 Chilean Tsunami in Dichato. *Nat. Hazards Earth Syst. Sci.* 12, 2689–2697. doi:10.5194/nhess-12-2689-2012

Masuda, M., Williams, C., Shahkarami, A., and Bryngelson, F. R. J. (2012). "Tsunami vulnerability function development based on the 2011 Tohoku earthquake in Japan," in *15 World Conference on Earthquake Engineering* (Lisbon).

McCullagh, P., and Nelder, J. A. (1983). *Generalized Linear Models*, 2nd Edn. Available at: https://books.google.co.uk/books/about/Generalized_Linear_Models_Second_Edition.html?id=h9kFH2_FfBkC&pgis=1

McCullagh, P., and Nelder, J. A. (1989). *Generalized Linear Models*, 2nd Edn, Chapman & Hall/CRC.

Miller, L. E., and Kunce, J. T. (1973). Prediction and statistical overkill revisited. *Meas. Eval. Guid.* 6, 157–163.

MLIT. (2011). *Concerning Setting the Safe Structure Method for Tsunamis Which Are Presumed When Tsunami Inundation Occurs – Public Notice 1318*. Ministry of Land, Infrastructure, Transportation and Tourism (in Japanese).

Muhari, A., Charvet, I., Tsuyoshi, F., Suppasri, A., and Imamura, F. (2015). Assessment of tsunami hazards in ports and their impact on marine vessels derived from tsunami models and the observed damage data. *Nat. Hazards* 78, 1309–1328. doi:10.1007/s11069-015-1772-0

Muhari, A., Imamura, F., Koshimura, S., and Post, J. (2011). Examination of three practical run-up models for assessing tsunami impact on highly populated areas. *Nat. Hazards Earth Syst. Sci.* 11, 3107–3123. doi:10.5194/nhess-11-3107-2011

Murao, O., and Nakazato, H. (2010). "Vulnerability functions for buildings based on damage survey data in Sri Lanka after the 2004 Indian Ocean tsunami," in *International Conference on Sustainable Built Environment (ICSBE-2010) Kandy*, 371–378.

Myung, I. J. (2003). Tutorial on maximum likelihood estimation. *J. Math. Psychol.* 47, 90–100. doi:10.1016/S0022-2496(02)00028-7

Narita, Y., and Koshimura, S. (2015). Classification of tsunami fragility curves based on regional characteristics of tsunami damage. *J. Jpn. Soc. Civ. Eng. Coast. Eng.* 71, 331–336. doi:10.2208/kaigan.71.I_331

Nihei, Y., Maekawa, T., Ohshima, R., and Yanagisawa, M. (2012). Evaluation of fragility functions for tsunami damage in coastal district in Natori City, Miyagi

Prefecture and mitigation effects of coastal dune. *J. Jpn. Soc. Civ. Eng.* 68, I_276–I_280. doi:10.2208/kaigan.68.I_276

Noh, H. Y., Lallemant, D., and Kiremidjian, A. S. (2014). Development of empirical and analytical fragility functions using kernel smoothing methods. *Earthq. Eng. Struct. Dyn.* Available at: http://faculty.ce.cmu.edu/noh/files/2016/02/Noh_EESD2_published_eqe2505.pdf

Nunnally, J. C., and Bernstein, I. H. (1994). *Psychometric Theory*, 3rd Edn. USA: McGraw-Hill, Inc.

Park, H., Wiebe, D., and Cox, D. T. (2014). Tsunami inundation modeling: sensitivity of velocity and momentum flux to bottom friction with application to building damage at Seaside, Oregon. *Coast. Eng.* 1–12. Available at: https://icce-ojs-tamu.tdl.org/icce/index.php/icce/article/view/7557/pdf_985

Park, S., van de Lindt, J. W., Cox, D., and Gupta, R. (2013). Concept of community fragilities for tsunami coastal inundation studies. *Nat. Hazards Rev.* 14, 220–228. doi:10.1061/(ASCE)NH.1527-6996.0000092

Pomonis, A., and Peiris, N. (2005). "December 26, 2004 Indian Ocean tsunami: vulnerability functions for loss estimation in," in *International Conference on Geotechnical Engineering for Disaster Mitigation & Rehabilitation* (Singapore), 411–416.

Pringle, W., and Yoneyama, N. (2013). The application of a hybrid 2D/3D numerical tsunami inundation-propagation flow model to the 2011 off the Pacific Coast of Tohoku earthquake tsunami. *J. Jpn. Soc. Civ. Eng. Coast. Eng.* 63, 3–7. doi:10.2208/kaigan.69.I_306

Qi, Z. X., Eames, I., and Johnson, E. R. (2014). Force acting on a square cylinder fixed in a free-surface channel flow. *J. Fluid Mech.* 756, 716–727. doi:10.1017/jfm.2014.455

Reese, S., Bradley, B. A., Bind, J., Smart, G., Power, W., and Sturman, J. (2011). Empirical building fragilities from observed damage in the 2009 South Pacific tsunami. *Earth Sci. Rev.* 107, 156–173. doi:10.1016/j.earscirev.2011.01.009

Reese, S., Cousins, W. J., Power, W. L., Palmer, N. G., Tejakusuma, I. G., and Nugrahadi, S. (2007). Tsunami vulnerability of buildings and people in South Java – field observations after the July 2006 Java tsunami. *Nat. Hazards Earth Syst. Sci.* 7, 573–589. doi:10.5194/nhess-7-573-2007

Robertson, I. N., and Riggs, H. R. (2011). "OMAE2011-49487 tsunami bore forces on walls," in *Proceedings of the ASTM 2011 30th Internal Conference on Ocean, Offshore and Arctic Engineering* (Rotterdam).

Rossetto, T., Allsop, W., Charvet, I., and Robinson, D. I. (2011). Physical modelling of tsunami using a new pneumatic wave generator. *Coast. Eng.* 58, 517–527. doi:10.1016/j.coastaleng.2011.01.012

Rossetto, T., Ioannou, I., Grant, D. N., and Maqsood, T. (2014). *Guidelines for Empirical Vulnerability Assessment: Report Produced in the Context of the Vulnerability Global Component Project*. Pavia: GEM Technical Report 2014-08, GEM Foundation.

Rossetto, T., Ioannou, I., and Grant, D. (2012). *Guidelines for Empirical Vulnerability Assessment – Phase I: Single Surveys*. Pavia: GEM Technical Report 2012-X, GEM Foundation.

Ruangrassamee, A., Yanagisawa, H., Foytong, P., Lukkunaprasit, P., Koshimura, S., and Imamura, F. (2006). Investigation of tsunami-induced damage and fragility of buildings in Thailand after the December 2004 Indian Ocean tsunami. *Earthq. Spectra* 22, 377–401. doi:10.1193/1.2208088

Rubin, D. (1987). *Multiple Imputation for Nonresponse in Surveys*. John Wiley & Sons.

Satake, K., Fujii, Y., Harada, T., and Namegaya, Y. (2013). Time and space distribution of coseismic slip of the 2011 Tohoku earthquake as inferred from tsunami waveform data. *Bull. Seismol. Soc. Am.* 103, 1473–1492. doi:10.1785/0120120122

Schuenemeyer, J., and Drew, L. (2011). *Statistics for Earth and Environmental Scientists*. John Wiley & Sons.

Scott, M. H., and Mason, H. B. (2017). Constant-ductility response spectra for sequential earthquake and tsunami loading. *Earthq. Eng. Struct. Dyn.* 46, 1549–1554.

Synolakis, C. E., Bernard, E. N., Titov, V. V., Kânoglu, U., and González, F. I. (2008). Validation and verification of tsunami numerical models. *Pure Appl. Geophys.* 165, 2197–2228. doi:10.1007/s00024-004-0427-y

Suppasri, A., Charvet, I., Imai, K., and Imamura, F. (2014). Fragility curves based on data from the 2011 Great East Japan tsunami in Ishinomaki city with discussion of parameters influencing building damage. *Earthq. Spectra* 31, 841–868. doi:10.1193/053013EQS138M

Suppasri, A., Koshimura, S., Imai, K., Mas, E., Gokon, H., Muhari, A., et al. (2012a). Damage characteristic and field survey of the 2011 Great East Japan tsunami in Miyagi Prefecture. *Coast. Eng. J.* 54, 30. doi:10.1142/S0578563412500052

Suppasri, A., Koshimura, S., and Imamura, F. (2009). "Tsunami fragility curves and structural performance of building along the Thailand coast," in *8th International Workshop on Remote Sensing for Disaster Management* (Tokyo), 3–8.

Suppasri, A., Koshimura, S., and Imamura, F. (2011). Developing tsunami fragility curves based on the satellite remote sensing and the numerical modeling of the 2004 Indian Ocean tsunami in Thailand. *Nat. Hazards Earth Syst. Sci.* 11, 173–189. doi:10.5194/nhess-11-173-2011

Suppasri, A., Latcharote, P., Bricker, J. D., Leelawat, N., Hayashi, A., Yamashita, K., et al. (2016). Improvement of tsunami countermeasures based on lessons from the 2011 Great East Japan earthquake and tsunami – situation after five years. *Coast. Eng. J.* 58, 1640011. doi:10.1142/S0578563416400118

Suppasri, A., Mas, E., Charvet, I., Gunasekera, R., Imai, K., Fukutani, Y., et al. (2013). Building damage characteristics based on surveyed data and fragility curves of the 2011 Great East Japan tsunami. *Nat. Hazards* 66, 319–341. doi:10.1007/s11069-012-0487-8

Suppasri, A., Mas, E., Koshimura, S., et al. (2012b). Developing tsunami fragility curves from the surveyed data of the 2011 Great East Japan tsunami in Sendai and Ishinomaki plains. *Coast. Eng. J.* 54, 16. doi:10.1142/S0578563412500088

Tanaka, N., and Kondo, K. (2015). Numerical analysis considering the effect of trapping the floatage by coastal forests and fragility curve of houses. *J. Jpn. Soc. Civil Eng. Ser. B1 (Hydraul Eng)*. 71, I_727–I_732. doi:10.2208/jscejhe.71.I_727

Tanaka, N., Onai, A., and Kondo, K. (2015). Fragility curve of different damage of wooden building due to tsunami based on tsunami fluid force and its moment (in Japanese). *J. Jpn. Soc. Civ. Eng. Coast. Eng.* 71, 1–11. doi:10.2208/kaigan.71.1

Tanaka, N., Sasaki, Y., Mowjood, M. I. M., Jinadasa, K. B. S. N., and Homchuen, S. (2007). Coastal vegetation structures and their functions in Tsunami protection: experience of the recent Indian Ocean Tsunami. *Landscape Ecol. Eng.* 33–45.

Tarbotton, C., Dall'Osso, F., Dominey-Howes, D., and Goff, J. (2015). The use of empirical vulnerability functions to assess the response of buildings to tsunami impact: comparative review and summary of best practice. *Earth Sci. Rev.* 142, 120–134. doi:10.1016/j.earscirev.2015.01.002

Tinti, S., Tonini, R., Bressan, L., Armigliato, A., Gardi, A., Guillande, R., et al. (2011). *Handbook of Tsunami Hazard and Damage Scenarios (EUR 24691 EN)*. Available at: http://publications.jrc.ec.europa.eu/repository/bitstream/111111111/16149/1/lbna24691enc.pdf

Tokyo University and BRI. (2011). *Interim Report of the Building Standards Improvement Promotion Project No. 40, A Study of Improvement of Building Standards etc in the Tsunami Critical Areas*.

Valencia, N., Gardi, A., Gauraz, A., Leone, F., and Guillande, R. (2011). New tsunami damage functions developed in the framework of SCHEMA project: application to European-Mediterranean coasts. *Nat. Hazards Earth Syst. Sci.* 11, 2835–2846. doi:10.5194/nhess-11-2835-2011

VanVoorhis, C. R. W., and Morgan, B. (2007). Understanding power and rules of thumb for determining sample sizes. *Tutorials Quant. Methods Psychol.* 3, 43–50. doi:10.20982/tqmp.03.2.p043

Ware, J. H., Harrington, D., Hunter, D. J., and D'Agostino, R. B. (2012). Missing data. *N. Engl. J. Med.* 367, 1353–1354. doi:10.1056/NEJMsm1210043

Wood, S. (2006). *Generalized Additive Models: An Introduction with R*. London: CRC Press.

Yamazaki, Y., and Cheung, K. (2011). Shelf resonance and impact of near-field tsunami generated by the 2010 Chile earthquake. *Geophys. Res. Lett.* 38. doi:10.1029/2011GL047508

Yanagisawa, H., and Yanagisawa, H. (2012). Fragility function of house damage by the 2011 off the Pacific Coast of Tohoku earthquake tsunami. *J. Jpn. Soc. Civ. Eng. Ser. B2 Coast. Eng.* 68, I_1401–I_1405. doi:10.2208/kaigan.68.I_1401

Yeh, H., Barbosa, A. R., Ko, H., and Cawley, J. G. (2014). Tsunami loadings on structures: review and analysis. *Coast. Eng. Proc.* 34. Available at: https://icce-ojs-tamu.tdl.org/icce/index.php/icce/article/view/7955

Conflict of Interest Statement: The authors declare that the research was conducted in the absence of any commercial or financial relationships that could be construed as a potential conflict of interest.

Copyright © 2017 Charvet, Macabuag and Rossetto. This is an open-access article distributed under the terms of the Creative Commons Attribution License (CC BY). The use, distribution or reproduction in other forums is permitted, provided the original author(s) or licensor are credited and that the original publication in this journal is cited, in accordance with accepted academic practice. No use, distribution or reproduction is permitted which does not comply with these terms.

frontiers in Built Environment

ORIGINAL RESEARCH
published: 16 March 2017
doi: 10.3389/fbuil.2017.00016

Possible Failure Mechanism of Buildings Overturned during the 2011 Great East Japan Tsunami in the Town of Onagawa

Panon Latcharote[1], Anawat Suppasri[1], Akane Yamashita[2], Bruno Adriano[1], Shunichi Koshimura[1], Yoshiro Kai[3] and Fumihiko Imamura[1]*

[1] International Research Institute of Disaster Science, Tohoku University, Sendai, Japan, [2] Earthquake Research Institute, University of Tokyo, Tokyo, Japan, [3] Department of Infrastructure Systems Engineering, Kochi University of Technology, Kochi, Japan

Six buildings were overturned in the town of Onagawa during the 2011 Great East Japan tsunami. This study investigates the possible failure mechanisms of building overturning during tsunami flow. The tsunami inundation depth and flow velocity at each overturned building were recalculated by using a tsunami numerical simulation and verified using a recorded video. The overturning moment is a result of hydrodynamic and buoyancy forces, whereas the resisting moment is a result of building self-weight and pile resistance force. This study aimed to demonstrate that the building foundation design is critical for preventing buildings from overturning. The analysis results suggest that buoyancy force can generate a larger overturning moment than hydrodynamic force, and the failure of a pile foundation could occur during both ground shaking and tsunami flow. For the pile foundation, pile resistance force plays a significant role due to both tension and shear capacities at the pile head and skin friction capacity between the pile and soil, which can be calculated from 18 soil boring data in Onagawa using a conventional method in the AIJ standards. In addition, soil liquefaction can reduce skin friction capacity between the pile and soil resulting in a decrease of the resisting moment from pile resistance force.

Keywords: building overturning, Onagawa, tsunami flow, pile foundation, soil liquefaction

OPEN ACCESS

Edited by:
Solomon Tesfamariam, University of British Columbia, Canada

Reviewed by:
Hossein Mostafaei, FM Global, USA
Tetsuya Hiraishi, Kyoto University, Japan

****Correspondence:***
Panon Latcharote
panon@irides.tohoku.ac.jp

Specialty section:
This article was submitted to Earthquake Engineering, a section of the journal Frontiers in Built Environment

Received: *12 December 2016*
Accepted: *17 February 2017*
Published: *16 March 2017*

Citation:
Latcharote P, Suppasri A, Yamashita A, Adriano B, Koshimura S, Kai Y and Imamura F (2017) Possible Failure Mechanism of Buildings Overturned during the 2011 Great East Japan Tsunami in the Town of Onagawa. Front. Built Environ. 3:16. doi: 10.3389/fbuil.2017.00016

INTRODUCTION

During the 2011 Great East Japan earthquake and tsunami, many buildings were seriously damaged by a combination of ground shaking, tsunami flow, debris impact, and soil liquefaction. After the 2011 Great East Japan tsunami, overturned buildings were found unexpectedly in two locations: (1) six buildings [i.e., five reinforced concrete (RC) buildings and one steel-frame building] in the town of Onagawa in Miyagi Prefecture and (2) two buildings in the city of Miyako in Iwate Prefecture. This study focused on the overturned buildings in Onagawa because of the comprehensiveness of the building-related information, soil information, and tsunami simulation results. These overturned buildings were built more than 30 years ago over filled soil foundations. A field survey revealed that one of the six overturned buildings in Onagawa was built on a shallow foundation, and the other buildings had a pile foundation; one of the buildings was overturned and moved 70 m from its original position (Suppasri et al.,

2012; Latcharote et al., 2014). Based on inundation data, these overturned buildings were fully (or at least nearly) submerged and overturned by the following possible causes: (a) hydrodynamic force, including debris effects; (b) buoyancy force; and (c) weakened foundation associated with soil instability (Yeh et al., 2013). Therefore, the maximum inundation depth exceeded the height of all overturned buildings in Onagawa, and it was assumed that those buildings were overturned during the overtopping tsunami flow.

The one famous instance of an overturned RC building occurred in 1946 following an Aleutian tsunami, in which an 18-m-tall lighthouse at a ground elevation of 10 m was overturned by a 30-m tsunami. In Japan, building overturning had not been reported in previous earthquakes and subsequent tsunamis and thus was not considered in building foundation design. However, building overturning is now considered in the design guidelines for building foundations (Architectural Institute of Japan, 2001), particularly for tsunami evacuation buildings. In recent years, the seismic performance design of pile foundations has considered the rocking of pile caps and the negative friction of piles to resist the uplift of buildings. During tsunami flow, building overturning can occur as a result of lateral force (hydrodynamic force) and uplift force (buoyancy force), the latter of which depends on the dimensions from the top of the window opening to the ceiling in buildings. Based on the surveyed data, most of the piles were likely broken by tension and shear failures at the pile head and insufficient friction between the pile and soil, including the effect of soil liquefaction, which caused the piles to be easily pulled out of the ground. During soil liquefaction, the soil shear strength is decreased, thereby decreasing the shaft resistance (skin friction) between the pile surface and soil around the pile (Fraser et al., 2013). This decreased shaft resistance would allow the greater vertical movement of the piles while in the ground. The piles would then be pulled from the ground more easily when the building is subjected to uplift and lateral forces from tsunami flow and debris impact, which were significant in Onagawa due to the extreme inundation depth (Fraser et al., 2013). Soil liquefaction changed the soil properties and caused a loss of skin friction capacity between the pile and soil because of the loosening of soil around the pile.

Therefore, the building foundation would be the main consideration of building overturning in Onagawa. The overturning mechanism of these overturned buildings has been thoroughly investigated in previous studies, such as Ishida et al. (2015), Tokimatsu et al. (2016), and Yeh and Sato (2016), and few design considerations have been suggested. This study investigates the overturning mechanism in different ways and also considers the effect of soil liquefaction, which can result in a decrease of skin friction capacity between the pile and soil. Based on experimental studies of geotechnical problems, this study suggests a conventional method to evaluate the approximate skin friction capacity when soil liquefaction occurs. The possible failure mechanism of the overturned buildings can then be investigated by comparing the overturning moment and resisting moment. The results of this study can be used to improve the recommendations for building foundation design in a building design code.

CHARACTERISTICS OF FIVE OVERTURNED BUILDINGS

Our survey team observed that most of six overturned buildings in Onagawa had shifted away from sea and thus appeared to be overturned by striking wave. The tsunami force is estimated to be many tons per square meter with a long-period wave (e.g., 30 min), which led to a prolonged interaction of tsunami flow acting on these overturned buildings. The water released from the uppermost floors of the buildings generated uplift force, which caused a large overturning moment with hydrodynamic force. Small openings were observed in these overturned buildings, which could also generate large uplift force. However, there was sufficient time for water to flow inside the buildings because of the long-period wave. Thus, only the accumulated air between the top of the windows and the ceiling generated buoyancy force (Suppasri et al., 2013). The survey team also stated that most of the piles were probably pulled out and broken at the pile head as a result of ground shaking, hydrodynamic force, buoyancy force, and soil liquefaction. Five overturned buildings (i.e., Buildings A, B, C, D, and E) in **Figure 1** were analyzed in this study, and the characteristics of each overturned building are provided below.

Building A

Building A is believed to have been built between 1965 and 1970 adjacent to the shoreline (Onagawa, 2013). It was used as a repair shop of fishing boats in the past but was being used as a commercial store before the tsunami (Onagawa, 2013). The building was submerged by 0.4 m of seawater at high tide for many months after the tsunami due to the residual subsidence from the earthquake. The building was a three-story RC structure with a mat foundation on hard ground, as shown in **Figure 2A**. Small openings were observed on the face of this building subject to tsunami flow. As shown in **Figure 1**, this building overturned seaward, but it is expected that the initial failure was landward (consistent with the other buildings) and this building was then moved during tsunami return flow to its final position (Fraser et al., 2013). On the other hand, the building may have been overturned seaward by the receding wave (Onagawa, 2013). Due to the mat foundation, only building self-weight could provide a resisting moment against the overturning moment from hydrodynamic and buoyancy forces.

Building B

Building B is believed to have been built between 1955 and 1975 based on its type of foundation (Nikkei BP Company, 2011). It was an accommodation building with a four-story RC structure and a pile foundation, as shown in **Figure 2B**. The pile foundation had 32 hollow concrete pipe piles with a pile diameter of 20 cm. This building was moved 70 m from its original position. As shown in **Figure 2B**, some piles were pulled from the ground, and some were broken under the foundation. Twelve of the 32 piles under the foundation appear to have been effective in resisting the overturning moment (Kabeyasawa et al., 2012). No spiral reinforcing bar was observed inside the piles, but six longitudinal reinforcing bars

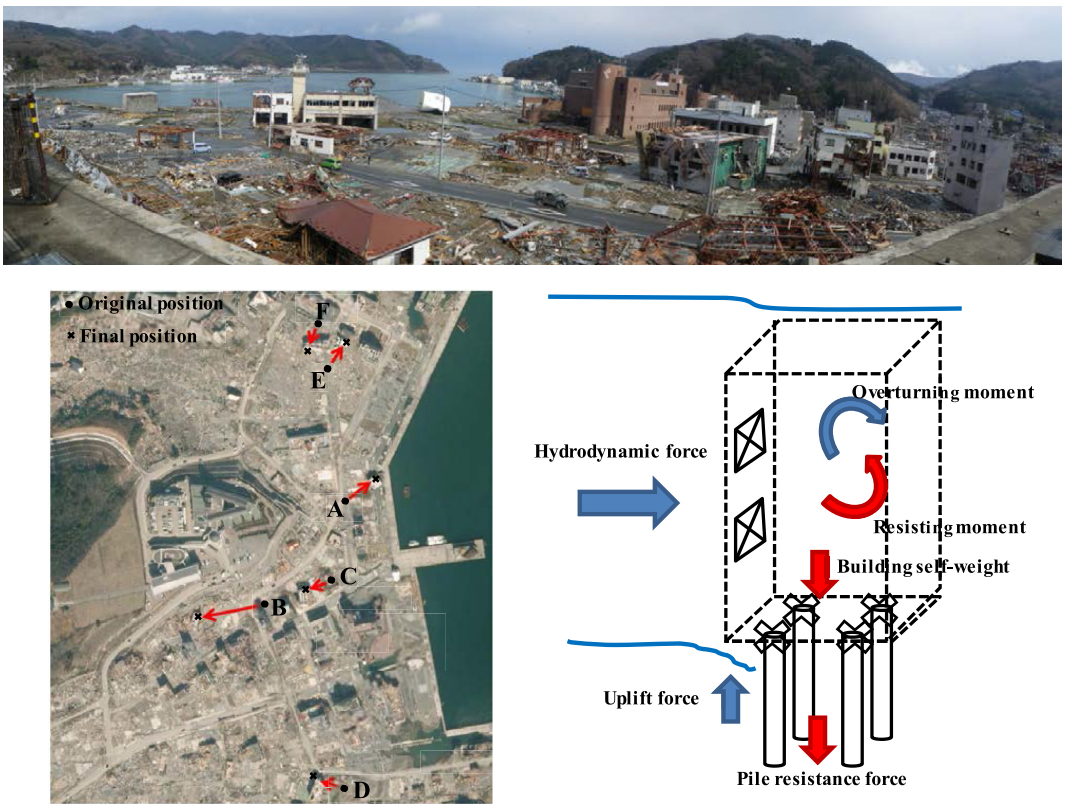

FIGURE 1 | Six overturned buildings in the town of Onagawa and free-body-diagram of building overturning. Note: taken by our survey team in March 29, 2011 at the town of Onagawa and Google Earth.

were observed inside each pile. The settled ground around a neighboring building indicated the occurrence of soil liquefaction (Tokimatsu et al., 2012).

Building C

Building C is believed to have been built between 1980 and 1985 (Onagawa, 2013). The building was used as an accommodation facility in the past but was being used as offices for private business and accommodations for sailors before the tsunami (Onagawa, 2013). The building was moved approximately 10–16 m from its original location by the tsunami (Onagawa, 2013). The building was submerged by 0.2 m of seawater at high tide for a short period after the tsunami. It was a four-story steel-frame building with a pile foundation, as shown in **Figure 2C**. The pile foundation had 8 pile caps with 20 piles having a diameter of 25 cm. Most hollow concrete pipe piles failed at the connection to the pile cap under the foundation unless one pile on the upper right was pulled out. A spiral reinforcing bar and six longitudinal reinforcing bars were observed inside each pile, and the six reinforcing bars had ruptured. This building was constructed from steel frames and ALC walls; thus, building self-weight was less than that of RC buildings. This building was floated, carried away and then overturned by tsunami flow, and most of the piles were broken at their joints with the pile caps (Tokimatsu et al., 2012).

Building D

Building D is believed to have been built between 1965 and 1975 (Nikkei BP Company, 2011). It was used as a refrigerated warehouse with a two-story RC structure and a pile foundation, as shown in **Figure 2D**. The pile foundation had six pile caps with four piles with a diameter of 20 cm in each pile cap. All piles were broken at the pile caps. No spiral reinforcing bar was observed inside the piles, but six longitudinal reinforcing bars were observed inside each pile. This building was floated more than 1 m and moved approximately 7 m, and all piles were ruptured at or near the joints (Tokimatsu et al., 2012). No pile remained connected to the pile caps, suggesting a higher level of shear in the overturning motion than was experienced in the other overturned building with a pile foundation (Fraser et al., 2013). This building was lifted by the hydrostatic buoyancy off of its pile foundation, which did not have tension capacity due to the minimal reinforcing steel (Chock et al., 2013). In addition, it was lifted off its original site and carried over a low wall before being deposited approximately 15 m inland from its original location (Chock et al., 2013).

Building E

Building E is believed to have been built in 1980 (Onagawa, 2013). It was a police box on the first floor and a rest area on the second floor (Onagawa, 2013). The building was overturned

FIGURE 2 | **Continued**

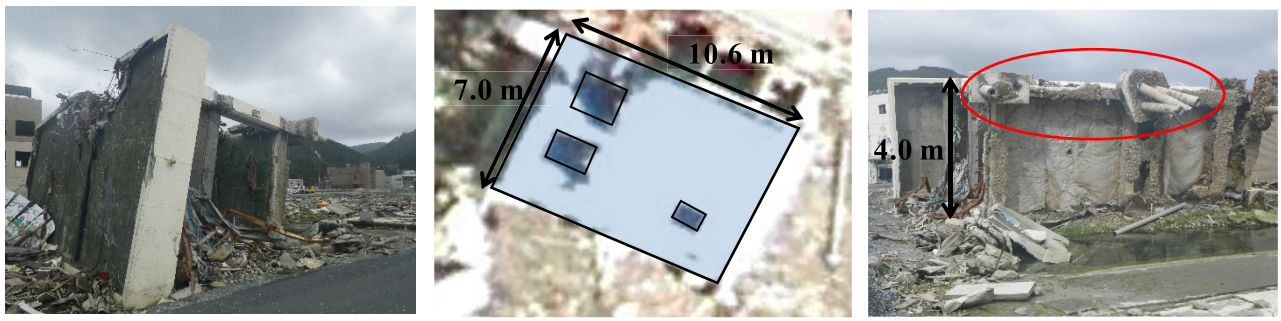

FIGURE 2 | **The characteristics of five overturned buildings in the town of Onagawa**. **(A)** Building A, **(B)** Building B, **(C)** Building C, **(D)** Building D, and **(E)** Building E. Note: taken by our survey team in March 29, 2011 and July 9, 2011 at the town of Onagawa.

near its present location and then moved to its present location by the receding wave (Onagawa, 2013). Some damage from floating debris can be observed on the upper part of the building. The building was submerged by 0.3 m of seawater at high tide for a short period after the tsunami. The building was a two-story RC building with a pile foundation, as shown in **Figure 2E**. The pile foundation had 6 pile caps with 14 piles having a diameter of 25 cm, and most of the piles were pulled out of the ground. No spiral reinforcing bar was observed inside the piles, but six longitudinal reinforcing bars were observed inside each pile. The settled ground near a neighboring building indicates that liquefaction occurred (Tokimatsu et al., 2012).

FACTORS INFLUENCING BUILDING OVERTURNING

Tsunami Inundation

Based on a video recorded from the rooftop of a building in Onagawa, a thorough analysis of the tsunami inundation was conducted using numerical modeling and measurements (Adriano et al., 2016). Numerical tsunami simulations were performed to reproduce the calculated time series of tsunami flow using the tsunami source model proposed by the Cabinet Office, Government of Japan. The simulations demonstrate that the maximum inundation depth due to the first incoming wave was over 16 m, and more than 500 buildings were washed away by this first wave, which is consistent with the video data (Adriano et al., 2016). The source model was verified with the observed tsunami inundation depth and flow velocity interpreted from the video record including the measured depth of maximum tsunami inundation of 30 points from tsunami watermark and the inundation area measured by field survey and satellite image analysis (Adriano et al., 2016). This study extended this reliable source model of tsunami numerical simulations to reproduce the waveforms of tsunami inundation depth and flow velocity at each overturned building. Then, these waveforms were used to estimate hydrodynamic and buoyancy forces in time series in order to investigate the possible mechanism of building overturning.

The tsunami inundation depth and flow velocity in the time series at each overturned building validated by the interpretation of the video data are shown in **Figure 3**. The peak inundation depth and peak flow velocity occurred at different times, which could result in the induction of large hydrodynamic force at any time during the striking or receding wave. **Figure 3A** shows the calculated time series of the tsunami inundation depth and flow velocity in 2014 (Adriano et al., 2014). In this 2014 simulation, the maximum inundation depth was not consistent with the video analysis, although the maximum flow velocity was somewhat consistent. **Figure 3B** shows the calculated time series of the tsunami inundation depth and flow velocity in 2016, including the crustal deformation (Adriano et al., 2016). In this 2016 simulation, the maximum inundation depth was consistent with the video analysis, whereas the maximum flow velocity was lower than that of the video analysis. However, these numerical tsunami simulations were generated by the tsunami source model, which is typically used to reproduce tsunami propagation for all affected areas in Japan after the 2011 Great East Japan tsunami. This source model is not specific to only the studied area in Onagawa, which makes it different from other reverse models that attempt to be consistent with the video evidence. In this study, sets of inundation depth and flow velocity from both 2014 and 2016 simulations were used to estimate hydrodynamic and buoyancy forces.

Hydrodynamic Force

The overturning moment is partially the result of hydrodynamic force, which can be calculated from the inundation depth and flow velocity, as shown in **Figure 3**. This study assumed that these overturned buildings were surrounded by water and had a minimum unbalanced hydrostatic force, i.e., a minimum tsunami load. For each overturned building, hydrodynamic force (F_d) was applied as a uniform load over the depth of tsunami flow (Federal Emergency Management Agency, 2011) as

$$F_d = \frac{1}{2}\rho_s C_d B\left(hu^2\right),$$

where ρ_s is the density of salt water with sediment (1,200 kg/m^3), C_d is the drag coefficient (2.0), B is the building width in the

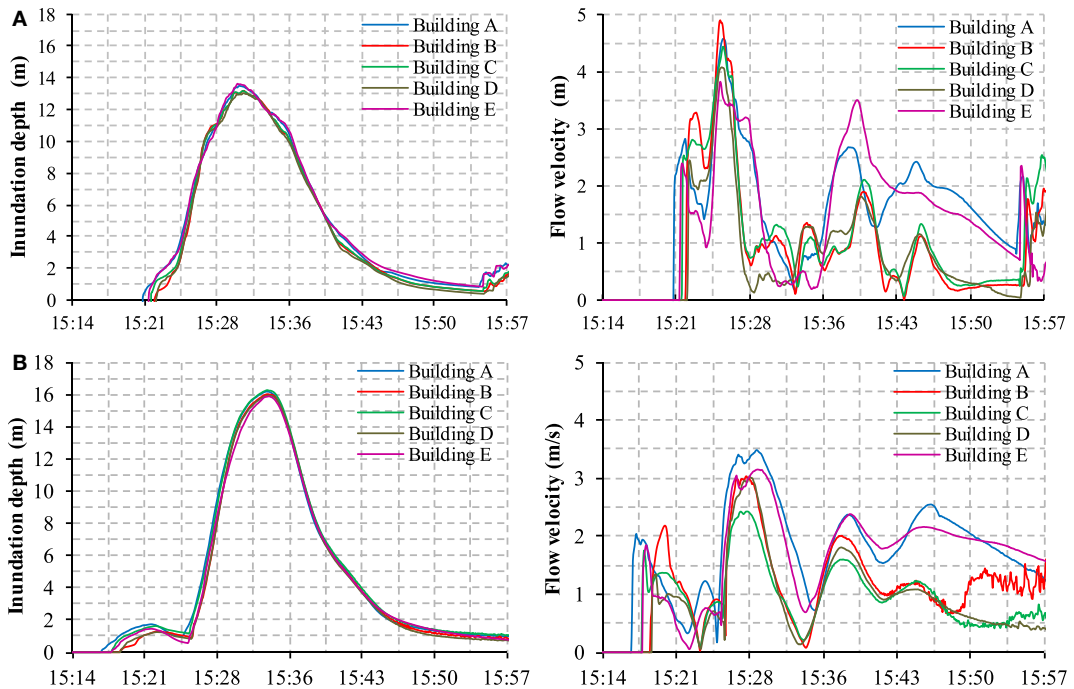

FIGURE 3 | **Tsunami inundation depth and flow velocity from 2014 and 2016 simulations**. **(A)** 2014 simulation and **(B)** 2016 simulation.

plane normal to the direction of flow, h is the inundation depth or building height, and u is the flow velocity.

Buoyancy Force

The overturning moment is also partially the result of buoyancy force, which can be calculated from the inundation depth shown in **Figure 3**. For each overturned building, buoyancy force (F_b) was set equal to the water weight of the residual air space inside it, which also depends on the opening ratio. A residual air space ratio (C_b) of 0 indicates that the entire building was filled with water, whereas a residual air space ratio of 1.0 indicates that no water entered the building, expressed as

$$F_b = \rho_s C_b g B D h,$$

where ρ_s is the density of salt water with sediment (1,200 kg/m^3), C_b is the residual air space ratio varying with the relative volume of entrapped air inside the building (0.0–1.0), g is the gravitational acceleration (9.81 m/s^2), B is the building width, D is the building depth, and h is the inundation depth or building height.

Building Self-Weight

The resisting moment is also partially the result of building self-weight, which can be calculated from the weight per unit area of the RC and steel buildings. The concrete density is typically 2,400 kg/m^3. In this study, the weight per unit area of the RC buildings is assumed to be 14 kPa, whereas the weight per unit area of the steel buildings is assumed to be 8 kPa.

Pile Resistance Force

The resisting moment is also partially the result of pile resistance force, which can be calculated from the pile and soil. From the damage observed in the overturned buildings with a pile foundation, two possible cases of pile damage were identified: tension or shear failure at the pile heads and pulling of the pile from the ground.

Tension and Shear Capacities

In the case of tension failure, pile resistance force (R_{TC}) can be calculated from the fracture strength of the PC steel wire (F_u) inside the pile and from the shear strength of the pile section (Q_u) for the case of shear failure. Tokimatsu et al. (2016) suggested the tension and shear capacities of piles in a pile foundation based on the catalog specifications.

Skin Friction Capacity

Eighteen soil boring data were obtained from the Onagawa office to represent the soil profiles of overturned buildings with pile foundations, as shown in **Figure 4**. The coastal area in **Figure 4A** (covered by the red-dashed line) was largely filled by soil (Onagawa, 1960). A soil boring data contains soil layers, such sand, gravel, silt, and clay, and N value, as shown in **Figure 4B**. In the case of pulling a pile out of the ground, pile resistance force (R_{TC}) is calculated from skin friction capacity (Q_s) between the pile and soil based on the recommendations for the design of building foundations (Architectural Institute of Japan, 2001) as

$$Q_s = \left(\sum \tau_{st} L_s + \sum \tau_{ct} L_c\right) \varphi_p,$$

where τ_{st} is the friction stress in a sand layer, L_s is the length of a sand layer, τ_{ct} is the friction stress in a clay layer, L_c is the length of a clay layer, and φ_p is the peripheral length of a pile. In this equation,

$$\tau_{st} = 2.0 \text{ N},$$

$$\tau_{ct} = \beta C_u,\ \beta = \alpha_p L_f,\ C_u = q_u / 2,\ q_u = \max\left(25 \text{ N}, 60\right),$$

where α_p is the adhesive factor (0.5–1.0), L_f is the length index (0.7–1.0), and C_u is the average undrained shear strength.

The adhesive factor (α_p) varies with the ratio of undrained shear strength and effective overburden pressure of silt and clay, whereas the length index (L_f) varies with the ratio of the layer thickness and the pile diameter.

Soil Liquefaction

In general, the evaluation of soil liquefaction during ground shaking and its effects on a pile foundation are highly complex because the seismic ground motion at the site must be considered. In addition, the dissipation of pore-water pressure and lateral ground spreading must be considered to investigate their effects on the soil–pile interaction, which could be caused

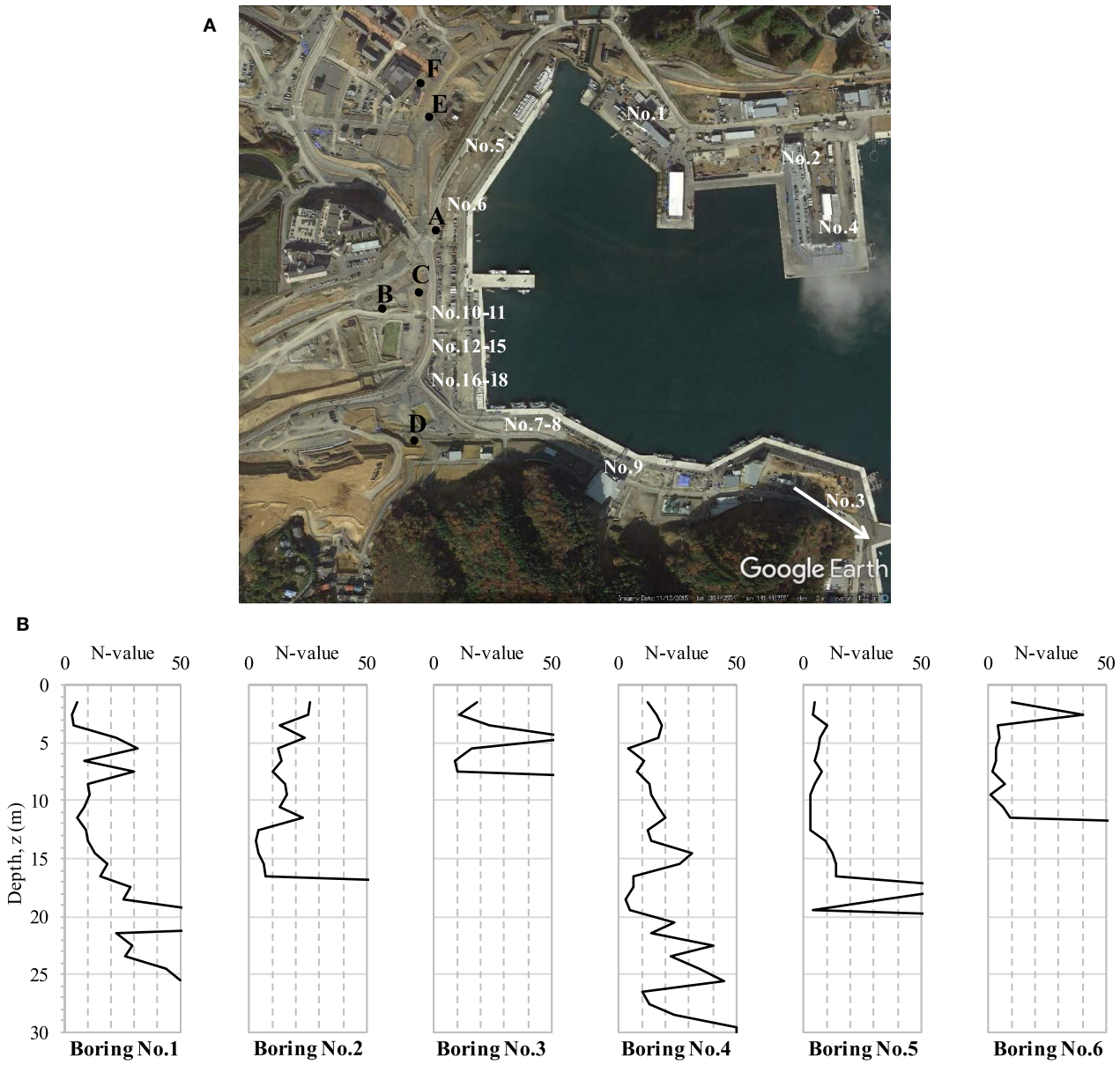

FIGURE 4 | **Continued**

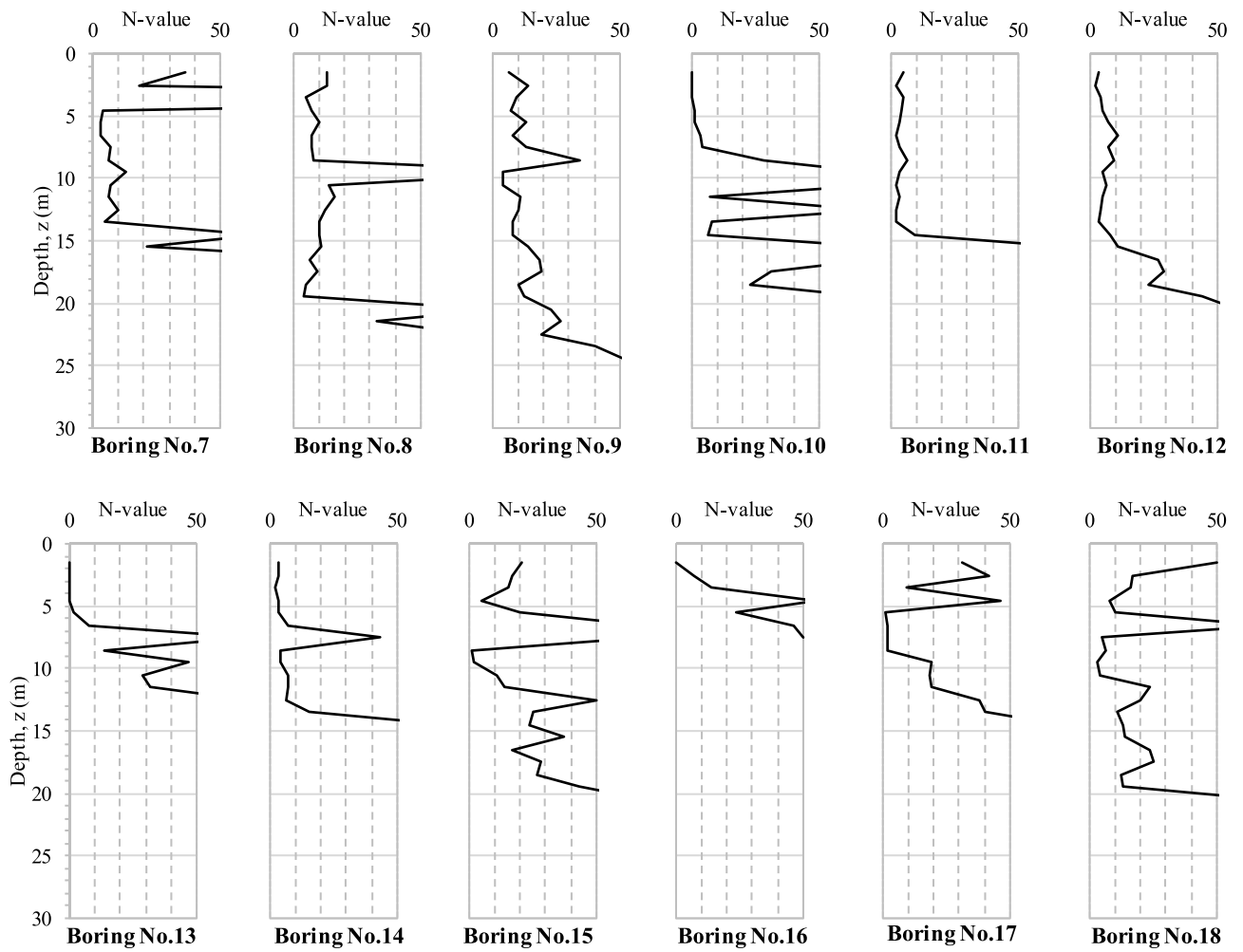

FIGURE 4 | 18 soil boring data in the town of Onagawa. **(A)** 18 boring locations (Google Earth). **(B)** Standard penetration test (SPT)-*N* value.

by the main shock before the tsunami arrival. Therefore, the liquefaction process might be completed before the tsunami arrival and the shear strength of the soil might have recovered by the dissipation of pore-water pressure. However, it may take longer for the soil to regain its shear strength so it might occur within the several tens of minutes between the main shock and tsunami arrival, such as with the repeated occurrence of soil liquefaction in New Zealand within a year due to the September 2010 Canterbury earthquake and the February 2011 Christchurch earthquake.

Because soil liquefaction is an interaction between soil and water, it takes time for the soil and water to slide out. Based on field surveys after two earthquakes in Japan, Mizutani (2008) reported that the soil liquefaction process took considerably longer than the ground shaking process. In the case of the 1964 Niigata earthquake, the sand boiling started after the ground shaking ended, and a large amount of soil boiling was observed for more than 10 to several tens of minutes. In the case of the 1983 Japan Sea earthquake, there was a report of a large sand boil hole with a diameter of 8 m and a depth of 1.5 m that sprayed soil with to a height of 10 m (Japanese Geotechnical Society, Tohoku Branch, 1986), and the outflow of water lasted for more than half a day. Therefore, the direct damage caused by strong ground shaking occurs over several tens of seconds, whereas the indirect damage caused by soil liquefaction requires much more time, and thus is responsible for minimal or no fatalities.

Yeh et al. (2013) suggested that soil liquefaction due to strong ground shaking of the earthquake that had occurred approximately 40 min prior to the tsunami arrival may have further promoted overturning failure. Fraser et al. (2013) also suggested that although any evidence of liquefaction was washed away in the tsunami, it may have contributed by loosening the soil around the piles prior to the overturning motion. Although, the liquefaction process in Onagawa is still not fully understood, it is worth considering the effect of soil liquefaction based on a building design standard because the 2011 tsunami arrived at Onagawa within approximately 40 min

of its initiation, when soil liquefaction could not have been negligible. In this study, cases with and without soil liquefaction will be analyzed and compared.

EFFECT OF SOIL LIQUEFACTION ON SKIN FRICTION CAPACITY

The possibility of soil liquefaction might not have been considered in the design of these overturned buildings because the effect of soil liquefaction on pile foundation had likely not been clearly described. Many factors influence the occurrence of soil liquefaction, such as the earthquake magnitude, peak ground acceleration, and soil condition. The Technical Standard Manual for Building [Building Center of Japan (BCJ), 2007] proposed the determination of soil conditions, such as liquefaction hazards. It suggested that soil liquefaction can occur in sandy soil based on four conditions, including alluvium within 20 m from the ground surface, saturated soil, less fine particles, and a lower *N* value. In this study, a conventional method based on the AIJ standards was used to evaluate the effect of soil liquefaction on the pile foundations. Based on the recommendations for design of building foundations (Architectural Institute of Japan, 2001), a description of the soil properties in this conventional method can be used to calculate the safety factor of each soil layer against the occurrence of soil liquefaction. This safety factor indicates the potential for soil liquefaction, which can cause a loss of skin friction between the soil and pile and result in a reduction of total pile resistance force.

Because boring data were not available at the exact location of each overturned building, skin friction capacity was evaluated from 18 boring data in an adjacent area. The majority of the filled soil at these 18 boring locations contains sand and gravel, which can cause a loss of skin friction between the pile and soil when soil liquefaction occurs. With this assumption, the conventional method was sufficient to calculate skin friction capacity when soil liquefaction occurs. Based on the report from field surveys after the 2011 Great East Japan tsunami (National Institute for Land and Infrastructure Management (NILIM) and Building Research Institute (BRI) in Japan, 2012), a sample calculation of skin friction capacity from this conventional method for boring No. 1 in **Figure 4** is shown in **Table 1**. Skin friction capacity (Q_s) can be calculated from the friction stress of the pile in sand and clay layers. The objective of this conventional method is to evaluate skin friction capacity when soil liquefaction occurs (Q_s'), as shown in **Table 1**. The soil parameters in **Table 1** are explained in **Table 2**. The cyclic resistance ratio (CRR) and cyclic stress ratio (CSR) were used to calculate the safety factor (FS), which can determine skin friction capacity during soil liquefaction as

$$\mathrm{FS} = \frac{\mathrm{CRR}}{\mathrm{CSR}},$$

$$\mathrm{CRR} = 0.041\left[\sqrt{N_a} + 0.00903\left(N_a/10\right)^7\right],$$

$$\mathrm{CSR} = \gamma_n \frac{\alpha_{max}}{g}\frac{\sigma_z}{\sigma_z'}\gamma_d,\ \gamma_n = 0.1\left(M-1\right),$$

where M is the earthquake magnitude, α_{max} is the peak ground acceleration, and γ_d is the stress reduction factor, which equal to $1 - 0.015z$.

The CRR can be estimated from the *N* value of the standard penetration test, and the CSR can be estimated from the peak ground acceleration and earthquake magnitude. As noted above, sand and gravel may cause a loss of skin friction capacity between the pile and soil when soil liquefaction occurs. As shown in **Table 1**, skin friction capacity becomes 0 if the safety factor is less than 1. Total pile resistance force of each pile was calculated by the summation of all soil layers multiplied by the peripheral length of a pile. To calculate the resisting moment from pile resistance forces, the load distribution on the pile group was considered for the summation of all piles. From these 18 boring data in the adjacent area, skin friction capacity in each pile length was evaluated, resulting in a decrease of total pile resistance force, as shown in **Table 3**. The overturning moment from hydrodynamic and buoyancy forces and the resisting moment from building self-weight and pile resistance force were considered to investigate possible overturning mechanisms in the next section.

POSSIBLE OVERTURNING MECHANISM

When investigating the possible mechanism of each overturned building, the overturning moment is the result of hydrodynamic and buoyancy forces, whereas the resisting moment is the result of building self-weight and pile resistance force. For a pile foundation, all of the piles could fail during the ground shaking due to large base shear force between the pile heads and pile caps; thus, the overturned buildings could resist tsunami flow using only their building self-weight. These overturned buildings floated and then moved from their original positions, so buoyancy force rapidly exceeded building self-weight after overturning. However, all piles may also have still been in good condition to resist tsunami flow after the ground shaking. Thus, two possible mechanisms of these overturned buildings with pile foundation are tension failure at the pile heads and pulling of the piles out of the ground.

Potential Shear Failure of Piles during Ground Shaking

For low-rise regular buildings, equivalent static seismic loads are sufficient to consider base shear force instead of dynamic loads during the ground shaking. The equivalent static seismic loads can be calculated based on a response spectrum analysis using natural period. Based on the AIJ Recommendations for Loads on Buildings (Architectural Institute of Japan, 2004), a simplified method can be used to evaluate the equivalent static seismic loads from the observed response spectrum at the site and an approximation of natural period (T_1) for each overturned building. Therefore, the approximate base shear force (V_B) can be calculated as

$$V_B = 0.816\frac{S_a}{g}W,$$

$$T_1 = \left(0.02 + 0.01\alpha_h\right)h,$$

TABLE 1 | Evaluation of skin friction capacity for boring No. 1.

z (m)	h (m)	Soil type	N	γ (kg/m^3)	σ'_z (kPa)	σ_z (kPa)	F_C (%)	D_{50} (m)	N_a	CRR	CSR (500 gal)	FS (500 gal)	Q_s/φ_p (kN/m)	Q'_s/φ_p (kN/m)
1.00	1.00	Sandy gravel mixed	–	–	–	–	–	–	–	–	–	–	–	–
1.60	0.60	with clay (fill)	5	2,100	6.47	12.36	15	0.03	16	0.17	0.76	0.23	6.00	0.00
2.00	0.40	Silty fine sand (fill)	5	1,800	9.61	19.42	15		23	0.32	0.80	0.39	4.00	0.00
2.70	0.70		3	1,800	15.11	31.78	15		15	0.16	0.82	0.20	4.20	0.00
3.00	0.30	Sandy silt (fill)	3	1,800	17.46	37.08							3.94	3.94
3.25	0.25		4	1,800	19.42	41.50							4.38	4.38
4.00	0.75	Silty sand (fill)	4	1,800	25.31	54.74	15		15	0.16	0.83	0.20	6.00	0.00
4.50	0.50		22	1,800	29.23	63.57	15		47	18.80	0.83	22.72	22.00	22.00
5.00	0.50	Sandy gravel mixed	22	2,100	34.63	73.87		0.005	26	0.48	0.81	0.60	22.00	0.00
6.00	1.00	with pebble (fill)	31	2,100	45.42	94.47		0.005	32	1.39	0.77	1.80	62.00	62.00
7.00	1.00		8	2,100	56.21	115.07		0.005	7	0.11	0.75	0.15	16.00	0.00
7.95	0.95		30	2,100	66.46	134.64		0.005	25	0.45	0.73	0.62	57.00	0.00
8.00	0.05	Sandy silt mixed with	30	1,800	66.86	135.53							6.56	6.56
8.60	0.60	gravel	10	1,800	71.56	146.12							26.25	26.25
9.00	0.40	Sandy gravel	10	2,100	75.88	154.36		0.002	9	0.12	0.72	0.17	8.00	0.00
10.00	1.00		11	2,100	86.67	174.96		0.002	9	0.13	0.70	0.18	22.00	0.00
10.40	0.40		8	2,100	90.99	183.20		0.002	7	0.11	0.69	0.15	6.40	0.00
11.00	0.60	Silty clay	8	1,500	93.93	192.03							21.00	21.00
11.45	0.45		5	1,500	96.14	198.65							9.84	9.84
12.00	0.55	Sandy gravel	5	2,100	102.07	209.98		0.002	4	0.08	0.69	0.12	5.50	0.00
13.00	1.00		9	2,100	112.86	230.58		0.002	7	0.11	0.67	0.16	18.00	0.00
13.90	0.90		10	2,100	122.58	249.12		0.002	7	0.11	0.66	0.17	18.00	0.00
14.00	0.10	Fine sand mixed	10	1,950	123.51	251.04			9	0.12	0.66	0.19	2.00	0.00
14.50	0.50	with silt	13	1,950	128.17	260.60			11	0.14	0.65	0.21	13.00	0.00
14.80	0.30	Clay mixed with gravel	13	1,500	129.64	265.02							17.06	17.06
15.00	0.20	Sandy gravel	13	2,100	131.80	269.14		0.002	9	0.12	0.65	0.19	5.20	0.00
16.00	1.00		18	2,100	142.59	289.74		0.002	12	0.14	0.63	0.23	36.00	0.00
17.00	1.00		15	2,100	153.38	310.34		0.002	10	0.13	0.62	0.21	30.00	0.00
18.00	1.00		28	2,100	164.17	330.94		0.002	17	0.19	0.60	0.31	56.00	0.00
19.00	1.00		25	2,100	174.96	351.54		0.002	15	0.16	0.59	0.28	50.00	0.00
20.00	1.00		50	2,100	185.75	372.14		0.002	29	0.83	0.57	1.45	100.00	100.00
21.00	1.00		50	2,100	196.54	392.74		0.002	28	0.72	0.56	1.28	100.00	100.00
22.00	1.00		22	2,100	207.33	413.34		0.002	12	0.14	0.55	0.26	44.00	0.00
23.00	1.00		29	2,100	218.13	433.95		0.002	15	0.17	0.53	0.32	58.00	0.00
24.00	1.00		26	2,100	228.92	454.55		0.002	13	0.15	0.52	0.30	52.00	0.00
24.35	0.35		44	2,100	232.69	461.76		0.002	23	0.31	0.51	0.60	30.80	0.00
–	–	Bedrock	–	–	–	–	–	–	–	–	–	–	–	–

R'_{TC}: pile resistance force in case of soil liquefaction.

φ_p: peripheral length of a pile.

The red color represents that the safety factor (FS) is less than 1.0, so that Qs become zero.

*The bold font represents the pile length of 4.0 m, 6.0 m, and 8.0 m in **Table 3**.*

TABLE 2 | Description of each parameter (Architectural Institute of Japan, 2001).

Symbol	Soil properties	Determination method
N	Standard penetration test (SPT)-N value	Obtained from SPT
γ	Unit weight of soil	Assumed from each soil type
σ'_z	Effective stress	$(\gamma - \gamma_w)h$
σ_z	Absolute stress	γh
F_C	Fine particle ratio	Estimated from each soil type (only sand and gravel)
D_{50}	50% Particle size	Estimated from each soil type (only sand and gravel)
N_a	Corrected N value	$N_a = N_1 + N_f$
N_1	Conversed value of N	$N_1 = C_N N$, $C_N = \sqrt{1/\sigma'_z}$
N_f	Correction factor for fine content	Varied with fine particle ratio

where S_a is the acceleration response at the base of the foundation, g is the gravitational acceleration (9.81 m/s^2), W is building self-weight, and α_h is the ratio of steel-frame height to total building height (h).

The base shear force was compared with total shear capacity of the piles in Section "Tension and Shear Capacities" to investigate the potential shear failure of the piles during ground shaking using a safety factor between total shear capacity ($\sum Q_u$) and base shear force (V_B). **Table 4** shows the calculation of total shear capacity and base shear force for Buildings B, C, D, and E. The acceleration response (S_a) was obtained from the response spectrum in Ishinomaki city that was provided by NIED, which is the nearest available data to Onagawa [National Research Institute for Earth Science and Disaster Resilience (accessed 2016)]. Based on the safety factor, all piles of Building D failed during the ground shaking due to large base shear force between the pile heads and

pile caps, whereas all piles of Buildings C and E were still in a sufficiently good condition to resist tsunami. In addition, some piles of Building B could have failed during the ground shaking because the safety factor is close to 1.00, as shown in **Table 4**.

Overturned Buildings Resisted by Only Building Self-Weight

The possible overturning mechanism of Buildings A and D was investigated by comparing the overturning moment calculated from hydrodynamic force (F_d) and buoyancy force (F_b) to the resisting moment calculated from building self-weight (W). Building A had a mat foundation, and all piles of Building D failed during the ground shaking, as shown in **Figure 5**. **Figure 6A** shows the tsunami inundation depths and flow velocities at Buildings A and D in the 2014 and 2016 simulations. The residual air space ratio (C_b) was estimated based on the condition of larger buoyancy force than building self-weight, as shown in **Figure 6B**. The residual air space ratios for Buildings A and D were approximately 0.6 and 0.4, respectively. **Figure 6C** shows the time series of the overturning moment (M_d and M_b) and the resisting moment (M_w).

As shown in **Table 5**, a comparison of Building A based on the 2014 simulation reveals that the peak overturning moment ($M_d + M_b$) that occurred at 15:28 was 1.59 times higher than the resisting moment (M_w), whereas a comparison based on the 2016 simulation suggests that the peak overturning moment that occurred at 15:29 was 1.84 times higher than the resisting moment. The peak overturning moment in the 2014 simulation occurred when the inundation depth was 10.60 m and the flow velocity was 2.83 m/s^2, whereas the maximum depth and velocity of 13.50 m and 4.57 m/s^2, respectively, occurred at different times, as shown in **Figure 6A**. The peak overturning moment in the 2016 simulation occurred when the inundation depth was 11.43 m and the flow velocity was 3.48 m/s^2, whereas the maximum depth of 16.18 m occurred at different times, as shown in **Figure 6A**. Building A was only 10.5 m tall; thus, it was overturned when the tsunami flow exceeded the top of the building.

All piles of Building D failed during the ground shaking by shear failure between the pile heads and pile caps, in which the shear strength of a pile (Q_u) was 65 kN, as shown in **Table 4**. As shown in **Table 5**, a comparison of Building D

TABLE 3 | Skin friction capacity of 18 soil boring data for each pile length.

Boring data	Pile length 4.0 m		Pile length 6.0 m		Pile length 8.0 m	
	Q_s/φ_p	Q'_s/φ_p	Q_s/φ_p	Q'_s/φ_p	Q_s/φ_p	Q'_s/φ_p
No. 1	28.51	8.31	134.51	92.31	214.08	98.88
No. 2	128.00	102.00	200.00	102.00	248.00	102.00
No. 3	106.00	36.00	238.00	136.00	276.00	136.00
No. 4	92.00	0.00	134.00	0.00	172.00	0.00
No. 5	38.00	0.00	64.00	0.00	118.50	52.50
No. 6	117.50	117.50	152.50	152.50	176.13	176.13
No. 7	231.75	231.753	262.38	262.38	303.06	303.06
No. 8	62.00	31.20	90.00	31.20	124.00	31.20
No. 9	66.55	43.75	106.55	43.75	148.55	43.75
No. 10	31.50	31.50	52.50	52.50	79.33	76.13
No. 11	24.00	0.00	38.00	0.00	48.00	0.00
No. 12	18.00	0.00	42.00	0.00	78.00	0.00
No. 13	31.50	31.50	49.90	48.30	165.90	148.30
No. 14	16.00	0.00	32.93	6.13	238.55	211.75
No. 15	106.00	42.00	156.00	42.00	356.00	242.00
No. 16	102.38	102.38	426.13	426.13	736.75	736.75
No. 17	164.00	146.00	262.25	243.25	283.25	264.25
No. 18	166.00	100.00	202.00	100.00	312.00	200.00

Unit (kN/m): force per peripheral length of pile.
*Pile length: depth (z) from ground in **Table 1**.*

TABLE 4 | Total shear capacity ($\sum Q_u$) and base shear force (V_B) at pile foundation.

Building	Number of piles	F_u (kN)	Q_u (kN)	$\sum Q_u$ (kN)	T_1 (s)	S_a (gal)	W (kN)	V_B (kN)	Safety factor
B	32	153	65	2,080	0.28	1,050	2,320	2,030	1.02
C	20	306	177	3,540	0.43	1,000	3,340	2,780	1.27
D	24	153	65	1,560	0.21	1,400	7,240	8,430	0.18
E	14	306	177	2,478	0.14	1,100	1,780	1,630	1.52

FIGURE 5 | Mat foundation of Building A and pile foundation of Building D. Note: taken by our survey team in March 29, 2011 at the town of Onagawa.

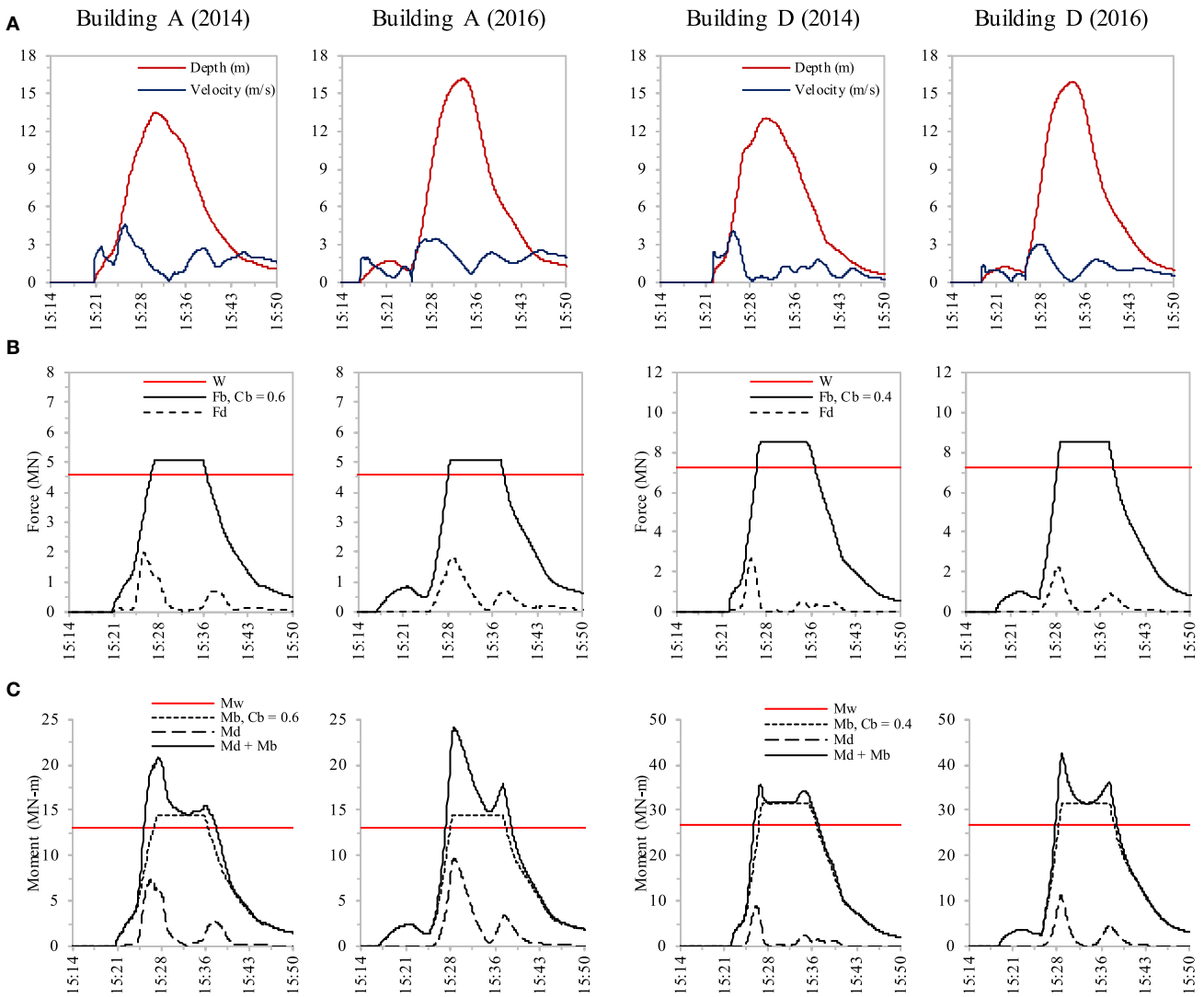

FIGURE 6 | Analysis results of Buildings A and D from 2014 and 2016 simulations. **(A)** Tsunami inundation depth and flow velocity. **(B)** Building self-weight, buoyancy force, and hydrodynamic force. **(C)** Resisting moment from building self-weight and overturning moment from hydrodynamic and buoyancy forces.

TABLE 5 | Analysis results of all overturned buildings.

Analysis results	Building A		Building B		Building C		Building D		Building E	
	2014	2016	2014	2016	2014	2016	2014	2016	2014	2016
Maximum inundation depth (m)	13.50	16.18	13.19	16.02	13.18	16.27	13.05	15.93	13.63	15.88
Maximum flow velocity (m/s²)	4.57	3.48	4.90	3.03	4.43	2.43	4.07	3.02	3.82	3.15
Residual air space ratio (C_b)	0.6	0.6	0.7	0.7	0.5	0.5	0.4	0.4	0.6	0.6
Max depth (m) at peak overturning moment	10.60	11.43	8.71	12.45	8.61	12.14	9.98	10.43	7.06	10.57
Max vel. (m/s²) at peak overturning moment	2.83	3.48	3.73	2.10	3.77	1.95	2.02	2.71	3.48	3.15
Time at peak overturning moment	15:28	15:29	15:27	15:30	15:27	15:30	15:27	15:29	15:26	15:29
Overturning ratio (OR)	1.59	1.84	1.61	1.59	1.17	1.24	1.33	1.59	1.47	1.34

based on the 2014 simulation reveals that the peak overturning moment ($M_d + M_b$) that occurred at 15:27 was 1.33 times higher than the resisting moment (M_w), whereas a comparison based on the 2016 simulation suggests that the peak overturning moment that occurred at 15:29 was 1.59 times higher than the resisting moment. The peak overturning moment in the 2014

FIGURE 7 | Pile foundation of Building C (one pile pulled out of ground). Note: taken by our survey team in March 29, 2011 at the town of Onagawa.

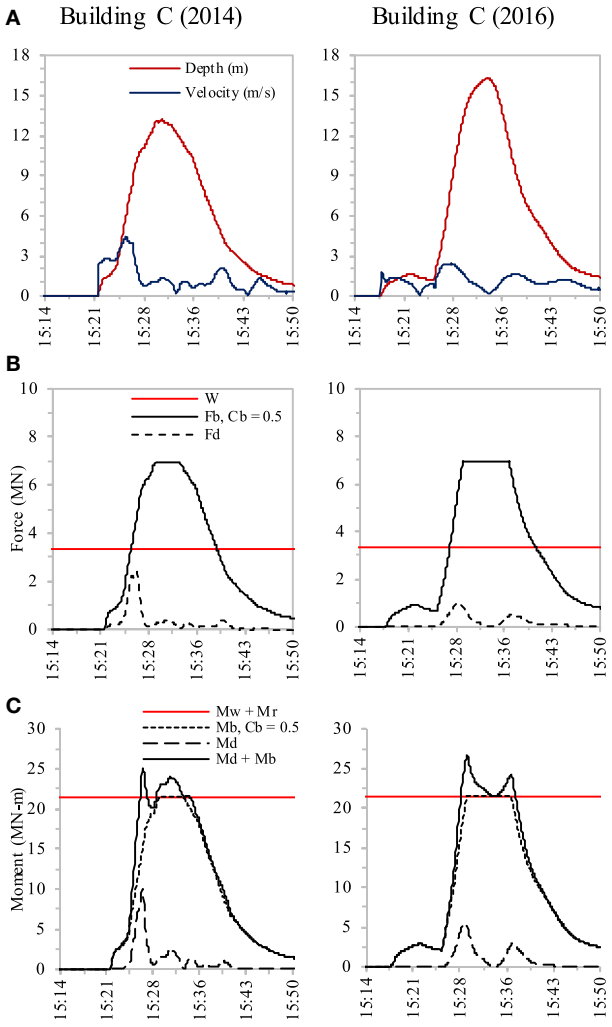

FIGURE 8 | Analysis results of Building C from 2014 and 2016 simulations. **(A)** Tsunami inundation depth and flow velocity. **(B)** Building self-weight, buoyancy force, and hydrodynamic force. **(C)** Resisting moment from building self-weight and pile resistance force, and overturning moment from hydrodynamic and buoyancy forces.

simulation occurred when the inundation depth was 9.98 m and the flow velocity was 2.02 m/s^2, whereas the maximum depth and velocity of 13.05 m and 4.07 m/s^2, respectively, occurred at different times, as shown in **Figure 6A**. The peak overturning moment in the 2016 simulation occurred when the inundation depth was 10.43 m and the flow velocity was 2.71 m/s^2, whereas the maximum depth and velocity of 15.93 m and 3.02 m/s^2, respectively, occurred at different times, as shown in **Figure 6A**. Building D was 10.5 m tall; thus, it was overturned when the tsunami flow was lower than the top of the building.

Another observation is that buoyancy force could generate an overturning moment larger than hydrodynamic force, particularly for Building D, as shown in **Figure 6C**. After building overturning occurred at 15:28, these buildings floated and then moved from their original positions such that buoyancy force was immediately greater than building self-weight, as shown in **Figure 6B**.

Tension Failure of Piles Caused by Overturning Moment

The overturning mechanism of Building C was investigated by comparing the overturning moment calculated from hydrodynamic force (F_d) and buoyancy force (F_b) to the resisting moment calculated from building self-weight (W) and pile resistance force (R_{TC}). Building C had a pile foundation and all of the piles failed by tension failure at the pile heads, except for one pile at the top-right pile cap, as shown in **Figure 7**. **Figure 8A** shows the tsunami inundation depth and flow velocity at Building C in the 2014 and 2016 simulations. The residual air space ratio (C_b) was approximately 0.5, as estimated based on the condition of larger buoyancy force than building self-weight, as shown in **Figure 8B**. **Figure 8C** shows the time series of the overturning moment (M_d and M_b) and the resisting moment (M_w and M_r).

For Building C, the pile foundation failed during tsunami flow through the observed tension failure between the pile heads and pile caps in which the tensile strength of a pile (F_u) was 307 kN, as shown in **Table 4**. The effective piles out of the 20 piles were used

to calculate the resisting moment (M_r), with 4.0-m moment arm on the pile group equal to the pile length, as shown in **Figure 7**. As shown in **Table 5**, a comparison of Building C based on the 2014 simulation reveals that the peak overturning moment ($M_d + M_b$) that occurred at 15:27 was 1.17 times higher than the resisting moment ($M_w + M_r$), whereas a comparison based on the 2016 simulation suggests that the peak overturning moment that occurred at 15:30 was 1.24 times higher than the resisting moment. The peak overturning moment in the 2014 simulation occurred when the inundation depth was 8.61 m and the flow velocity was 3.77 m/s^2, whereas the maximum depth and velocity of 13.18 m and 4.43 m/s^2, respectively, occurred at different times, as shown in **Figure 8A**. The peak overturning moment in the 2016 simulation occurred when the inundation depth was 12.14 m and the flow velocity was 1.95 m/s^2, whereas the maximum depth and velocity of 16.27 m and 2.43 m/s^2, respectively, occurred at different times, as shown in **Figure 8A**. Building C was 14.2 m tall; thus, it was overturned when tsunami flow was lower than the top of the building.

Buoyancy force could generate an overturning moment equal to the resisting moment, as shown in **Figure 8C**. Therefore, although hydrodynamic force could generate a smaller overturning moment than buoyancy force, the additional overturning moment from hydrodynamic force had a significant impact on building overturning.

Pulling out of Piles including Effect of Soil Liquefaction

The overturning mechanisms of Buildings B and E were investigated by comparing the overturning moment calculated from hydrodynamic force (F_d) and buoyancy force (F_b) to the resisting moment calculated from building self-weight (W) and pile resistance force (R_{TC}). Building B had a pile foundation, and 12 piles were pulled out of the ground, as shown in **Figure 9**, whereas 20 piles might have failed as a result of base shear force during the ground shaking because the safety factor was close to 1.00, as shown in **Table 4**. Building E had a pile foundation, and all piles were pulled out of the ground except for one pile that failed in tension, as shown in **Figure 9**. **Figure 10A** shows the tsunami inundation depths and flow velocities at Buildings B and E in the 2014 and 2016 simulations. The residual air space ratio (C_b) was estimated based on the condition of larger buoyancy force than building self-weight, as shown in **Figure 10B**. The residual air space ratios for Buildings B and E were approximately 0.7 and 0.6, respectively. **Figure 10C** shows the time series of the overturning moment (M_d and M_b) and the resisting moment (M_w and M_r).

For Building B, boring No. 11 at the nearest location and the assumed pile length of 6 m were used to calculate skin friction capacity (Q_s) of a pile, which was 38 kN/m, for a pile diameter of 20 cm, as shown in **Table 3**. As shown in **Table 5**, the comparison of Building B based on the 2014 simulation reveals that the peak overturning moment ($M_d + M_b$) that occurred at 15:27 was 1.61 times higher than the resisting moment ($M_w + M_r$), whereas the comparison based on the 2016 simulation suggests that the peak overturning moment that occurred at 15:30 was 1.59 times higher than the resisting moment. The peak overturning moment in the 2014 simulation occurred when the inundation depth was 8.71 m and the flow velocity was 3.73 m/s^2, whereas the maximum depth and velocity of 13.19 m and 4.90 m/s^2, respectively, occurred at different times, as shown in **Figure 10A**. The peak overturning moment in the 2016 simulation occurred when the inundation depth was 12.45 m and the flow velocity was 2.10 m/s^2, as the maximum depth and velocity of 16.02 m and 3.03 m/s^2, respectively, occurred at different times, as shown in **Figure 10A**. Building B was 14.0 m tall; thus, it was overturned when tsunami flow was lower than the top of the building.

For Building E, boring No. 5 at the nearest location and the assumed pile length of 6 m were used to calculate skin friction

FIGURE 9 | Pile foundation of Buildings B and E. (A) Red circles are 12 piles pulled out of ground, and gray circles are 20 piles broken during ground shaking. **(B)** Only one pile failed in tension. Note: taken by our survey team in March 29, 2011 at the town of Onagawa.

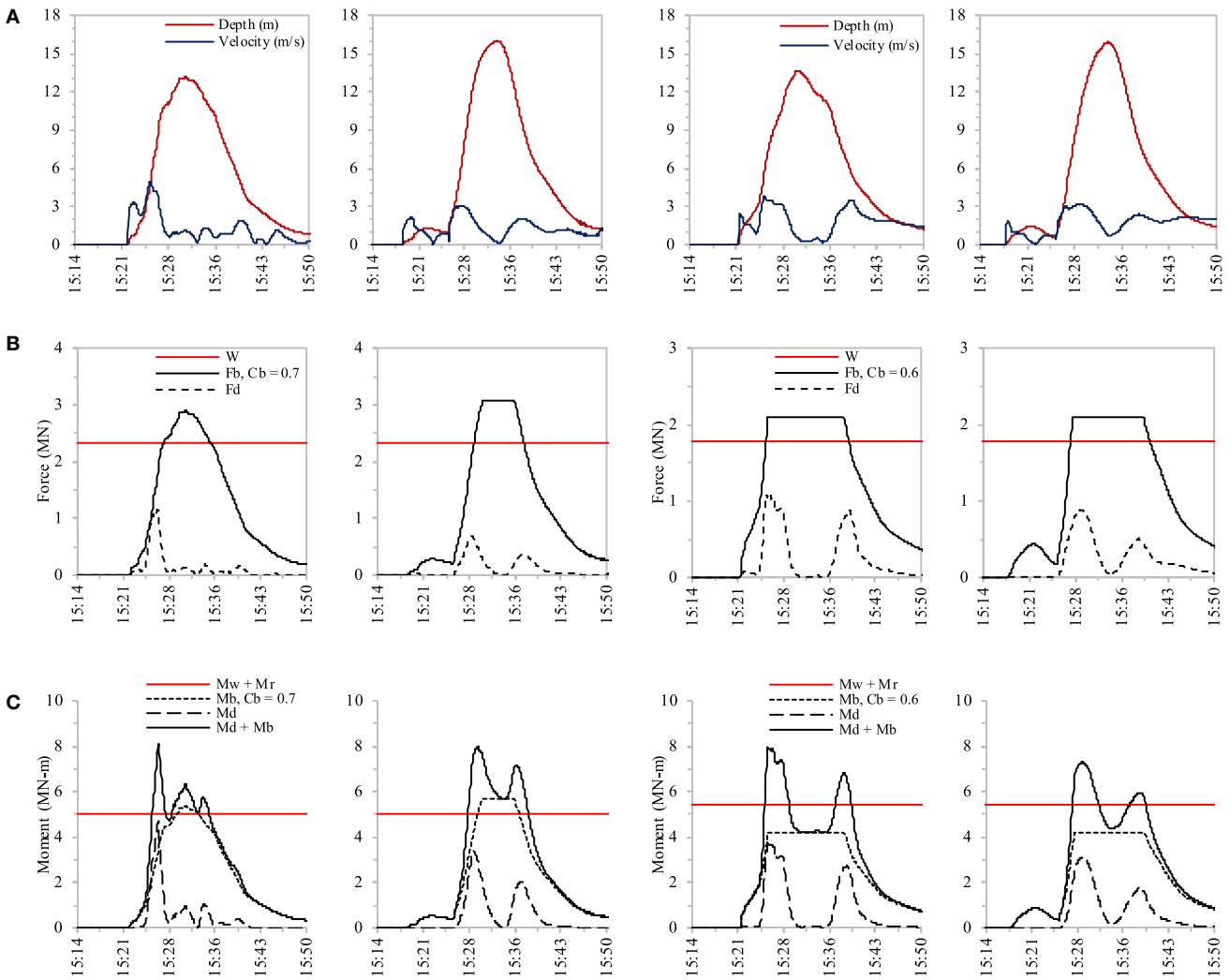

FIGURE 10 | Analysis results of Buildings B and E from 2014 and 2016 simulations. **(A)** Tsunami inundation depth and flow velocity. **(B)** Building self-weight, buoyancy force, and hydrodynamic force. **(C)** Resisting moment from building self-weight and pile resistance force, and overturning moment from hydrodynamic and buoyancy forces.

capacity (Q_s) of a pile, which was 64 kN/m, for a pile diameter of 25 cm, as shown in **Table 3**. As shown in **Table 5**, the comparison of Building B based on the 2014 simulation in reveals that the peak overturning moment ($M_d + M_b$) that occurred at 15:26 was 1.47 times higher than the resisting moment ($M_w + M_r$), whereas the comparison based on the 2016 simulation suggests that the peak overturning moment that occurred at 15:29 was 1.34 times higher than resisting moment. The peak overturning moment in the 2014 simulation occurred when the inundation depth was 7.06 m and the flow velocity was 3.48 m/s^2, whereas the maximum depth and velocity of 13.63 m and 3.82 m/s^2, respectively, occurred at different times, as shown in **Figure 10A**. The peak overturning moment in 2016 occurred when the inundation depth was 10.57 m and the flow velocity was 3.15 m/s^2, whereas the maximum depth and velocity were 15.88 m and 3.15 m/s^2, respectively, occurred at different times, as shown in **Figure 10A**. Building E was 7.0 m tall; thus, it was overturned when tsunami flow exceeded the top of the building.

The overturning ratio (OR) in **Table 5** can be calculated from the ratio between the peak overturning moment and the peak resisting moment. For each of 18 soil boring data, skin friction capacity (Q_s) is shown in **Table 3** for pile lengths of 4.0, 6.0, and 8.0 m and including the effect of soil liquefaction (Q_s'). However, the conventional method to evaluate the effect of soil liquefaction tends to overestimate liquefaction hazards (Chen et al., 2016). These 18 boring data were used to evaluate the potential of overturning for Buildings B and E based on the ORs, which can be classified as no possibility, low possibility, medium possibility, or high possibility.

Table 6 shows the ORs of Buildings B and E in the 2014 and 2016 simulations considering the pile length and soil

TABLE 6 | Overturning ratio (OR) of Buildings B and E for each soil boring data.

	Boring data	Pile length 4.0 m		Pile length 6.0 m		Pile length 8.0 m	
		OR	OR'	OR	OR'	OR	OR'
Building B 2014	No.1	1.67	1.80	1.21	1.36	1.00	1.33
	No.2	1.23	1.32	1.03	1.32	0.93	1.32
	No.3	1.31	1.62	0.95	1.20	0.89	1.20
	No.4	1.36	1.86	1.21	1.86	1.10	1.86
	No.5	1.61	1.86	1.48	1.86	1.26	1.54
	No.6	1.27	1.27	1.16	1.16	1.09	1.09
	No.7	0.97	0.97	0.91	0.91	0.84	0.84
	No.8	1.49	1.65	1.37	1.65	1.24	1.65
	No.9	1.47	1.58	1.30	1.58	1.17	1.58
	No.10	1.65	1.65	1.54	1.54	1.41	1.42
	No.11	1.69	1.86	1.61	1.86	1.56	1.86
	No.12	1.73	1.86	1.59	1.86	1.42	1.86
	No.13	1.65	1.65	1.55	1.56	1.12	1.17
	No.14	1.75	1.86	1.64	1.81	0.95	1.01
	No.15	1.31	1.59	1.15	1.59	0.77	0.95
	No.16	1.32	1.32	0.69	0.69	0.47	0.47
	No.17	1.12	1.17	0.91	0.94	0.87	0.91
	No.18	1.12	1.33	1.03	1.33	0.83	1.03

	Boring data	Pile length 4.0 m		Pile length 6.0 m		Pile length 8.0 m	
		OR	OR'	OR	OR'	OR	OR'
Building B 2016	No.1	1.65	1.77	1.19	1.34	0.99	1.32
	No.2	1.22	1.30	1.02	1.30	0.92	1.30
	No.3	1.29	1.60	0.94	1.19	0.87	1.19
	No.4	1.34	1.83	1.20	1.83	1.09	1.83
	No.5	1.59	1.83	1.46	1.83	1.25	1.52
	No.6	1.25	1.25	1.14	1.14	1.08	1.08
	No.7	0.95	0.95	0.90	0.90	0.83	0.83
	No.8	1.47	1.63	1.35	1.63	1.23	1.63
	No.9	1.45	1.56	1.29	1.56	1.15	1.56
	No.10	1.63	1.63	1.52	1.52	1.39	1.41
	No.11	1.67	1.83	1.59	1.83	1.54	1.83
	No.12	1.71	1.83	1.57	1.83	1.40	1.83
	No.13	1.63	1.63	1.53	1.54	1.10	1.15
	No.14	1.72	1.83	1.62	1.79	0.94	1.00
	No.15	1.29	1.57	1.13	1.57	0.76	0.93
	No.16	1.30	1.30	0.68	0.68	0.47	0.47
	No.17	1.11	1.16	0.90	0.93	0.86	0.89
	No.18	1.10	1.31	1.02	1.31	0.82	1.02

	Boring data	Pile length 4.0 m		Pile length 6.0 m		Pile length 8.0 m	
		OR	OR'	OR	OR'	OR	OR'
Building E 2014	No.1	1.88	2.10	1.22	1.42	0.96	1.38
	No.2	1.25	1.37	1.00	1.37	0.89	1.37
	No.3	1.35	1.81	0.91	1.21	0.83	1.21
	No.4	1.42	2.20	1.22	2.20	1.08	2.20
	No.5	1.79	2.20	1.59	2.20	1.29	1.67
	No.6	1.29	1.29	1.15	1.15	1.07	1.07
	No.7	0.92	0.92	0.86	0.86	0.78	0.78
	No.8	1.61	1.85	1.43	1.85	1.26	1.85
	No.9	1.57	1.74	1.34	1.74	1.16	1.74
	No.10	1.85	1.85	1.67	1.67	1.49	1.51
	No.11	1.92	2.20	1.79	2.20	1.71	2.20
	No.12	1.99	2.20	1.76	2.20	1.50	2.20
	No.13	1.85	1.85	1.69	1.71	1.10	1.17
	No.14	2.01	2.20	1.84	2.12	0.91	0.97
	No.15	1.35	1.76	1.14	1.76	0.70	0.90
	No.16	1.36	1.36	0.62	0.62	0.41	0.41
	No.17	1.11	1.17	0.86	0.90	0.82	0.85
	No.18	1.10	1.38	1.00	1.38	0.77	1.00

	Boring data	Pile length 4.0 m		Pile length 6.0 m		Pile length 8.0 m	
		OR	OR'	OR	OR'	OR	OR'
Building E 2016	No.1	1.72	1.92	1.12	1.30	0.88	1.26
	No.2	1.14	1.25	0.92	1.25	0.81	1.25
	No.3	1.23	1.66	0.83	1.11	0.76	1.11
	No.4	1.30	2.01	1.12	2.01	0.99	2.01
	No.5	1.64	2.01	1.46	2.01	1.18	1.53
	No.6	1.18	1.18	1.05	1.05	0.98	0.98
	No.7	0.84	0.84	0.78	0.78	0.72	0.72
	No.8	1.47	1.70	1.31	1.70	1.16	1.70
	No.9	1.44	1.60	1.23	1.60	1.07	1.60
	No.10	1.69	1.69	1.53	1.53	1.37	1.38
	No.11	1.76	2.01	1.64	2.01	1.56	2.01
	No.12	1.82	2.01	1.61	2.01	1.37	2.01
	No.13	1.69	1.69	1.55	1.56	1.01	1.07
	No.14	1.84	2.01	1.68	1.94	0.83	0.89
	No.15	1.23	1.61	1.04	1.61	0.64	0.82
	No.16	1.25	1.25	0.57	0.57	0.37	0.37
	No.17	1.02	1.07	0.78	0.82	0.75	0.78
	No.18	1.01	1.26	0.91	1.26	0.70	0.92

NO	OR < 1.00	LOW	1.00 ≤ OR < 1.20
MEDIUM	1.20 ≤ OR < 1.50	HIGH	OR ≥ 1.50

liquefaction. For all pile lengths, only boring No. 7 can provide safety from building overturning because the OR was less than 1.00 and including the effect of soil liquefaction. On the other hand, boring No. 11 provided the high possibility of building overturning for all pile lengths and including the effect of soil liquefaction. For borings No. 16 and No. 17, safety can be obtained using pile lengths of 6.0 and 8.0 m instead of 4.0 m, as was used in boring No. 3. However, building overturning could occur at boring No. 3 with pile lengths of 6.0 and 8.0 m in the case of soil liquefaction. Nevertheless, increasing the pile length can reduce the OR when neglecting the effect of soil liquefaction. In particular, for boring No. 14, increasing the pile length from 4.0 and 6.0 m to 8.0 m can prevent building overturning by changing the classification from high possibility to no possibility.

The effect of soil liquefaction generally increased the ORs for most of 18 soil boring data. However, the ORs for borings No. 6 and No. 16 were the same with and without soil liquefaction because soil liquefaction could not decrease of skin friction capacity. In the case of soil liquefaction, increasing the pile length could not affect the potential for building overturning in several borings, such as No. 2, No. 4, No. 8, No. 9, No. 11, and No. 12, because skin friction capacity is constant for all pile lengths, as shown in **Table 3**. In some borings, such as No. 2 and No. 3 with a pile length of 8.0 m, the OR exceeded 1.00 when soil liquefaction occurred because skin friction force was small and decreased significantly, as shown in **Table 3**.

CONCLUSION

Based on the surveyed data, the overturning mechanism of buildings in tsunami can be investigated by comparing the overturning moment induced by hydrodynamic and buoyancy forces and the resisting moment induced by building self-weight and pile resistance force. For a pile foundation, the potential for the shear failure of the piles at the pile head during the ground shaking can be analyzed based on the simplified method in a building design

standard. In this study, building overturning was investigated based on three possible mechanisms:

1. Building overturning due to hydrodynamic and buoyancy forces that were resisted by only building self-weight, such as in Buildings A and D.
2. Tension failure of piles at the pile head caused by the overturning moment, such as in Building C.
3. Pulling of the piles from the ground including the effect of soil liquefaction, including in combination with shear failure during the ground shaking in Building B and combination with tension failure during tsunami flow in Building E.

The analysis results of all overturned buildings indicated that buoyancy force could generate a larger overturning moment than hydrodynamic force, particularly for Buildings C and D. Previous studies indicated that the opening ratio had a significant effect on buoyancy force. However, the criterion that uses opening ratio should not be proposed in building design codes because it is difficult to estimate the volume of water inside the building during tsunami flow based on the size of the opening. This study focused on the performance of building foundations during earthquake and subsequent tsunami, including ground shaking, soil liquefaction, and tsunami inundation. The possible failure mechanism of these overturned buildings was investigated based on the residual performance from the earthquake and the sequential damage from the tsunami. The results suggested that a new criterion of building foundation design should be proposed in a building design guideline to prevent building overturning. In this criterion, the building performance should be evaluated from sequential scenarios of an earthquake and tsunami. The building foundation design should consider the states of the art of both earthquake and tsunami engineering. Otherwise, the evaluation of building performance will be misleading.

Soil liquefaction is a consequence of the earthquake that may reduce the performance of building foundation to resist building overturning during the tsunami. Due to soil liquefaction, the loss of skin friction capacity between the pile and soil could occur in most of 18 soil boring data, resulting in a decrease of the resisting moment calculated from pile resistance force. However, these 18 soil boring data are located near the shoreline and not in the precise locations of the overturned buildings, which contain a considerable amount of sand from filling and sediment. This might be a reason why there was a possibility of building overturning at most of 18 soil boring data. In addition, skin friction capacity including the effect of soil liquefaction was calculated by the conventional method in a building design standard. The accuracy of the evaluation of the effect of soil liquefaction could be improved by using a more advanced method, such as soil dynamic analysis.

AUTHOR CONTRIBUTIONS

PL did a contribution on investigating the possible mechanisms of overturned buildings in Onagawa based on the surveyed and simulated data. He wrote all parts in this manuscript. AS did a contribution on collecting the surveyed data of the characteristics of overturned buildings in Onagawa after the 2011 Great East Japan earthquake and tsunami. He wrote some part of the building characteristics. AY did a contribution on studying on building design codes. She suggested a method to evaluate pile resistance force from the Japanese standard for building foundation design and the survey report after the 2011 earthquake and tsunami. BA did a contribution on performing tsunami inundation simulation. He calculated the waveform at each overturned building to evaluate hydrodynamic and buoyancy forces during tsunami flow. SK has supported Bruno for tsunami inundation simulation in Onagawa. He provided the video evidence that was used for verifying the simulation. YK has supported AY because of his expertise in building design engineering. FI has supported PL for overall images of this manuscript and gave very useful comments.

ACKNOWLEDGMENTS

The authors express their sincere gratitude to the anonymous reviewers for their valuable suggestions, Prof. Nobuo Shuto of Tohoku University and the government office in the town of Onagawa for providing soil boring data, and the cooperation of other members of our survey team, including Dr. Erick Mas and Dr. Hideomi Gokon. This research was funded by the Reconstruction Agency of the Government of Japan, JSPS Grant-in-Aid for Young Scientists (B) "Applying developed fragility functions for the Global Tsunami Model (GTM)" (No. 16K16371), the Willis Research Network, and Tokio Marine & Nichido Fire Insurance Co., Ltd. through IRIDeS, Tohoku University.

REFERENCES

Adriano, B., Hayashi, S., Gokon, H., Mas, E., and Koshimura, S. (2016). Understanding the extreme tsunami inundation in Onagawa town by the 2011 Tohoku earthquake, its effects in urban structures and coastal facilities. *Coast. Eng. J.* 58, 1640013. doi:10.1142/S0578563416400131

Adriano, B., Mas, E., and Koshimura, S. (2014). "Tsunami inundation features verification through numerical modeling and video analysis: case study of Onagawa town on the 2011 Tohoku earthquake," in *Proc., Asia Oceania Geosciences Society 11th Annual Meeting*, Sapporo.

Architectural Institute of Japan. (2001). *Recommendations for Design of Building Foundations*. Tokyo, Japan: Architectural Institute of Japan, 486.

Architectural Institute of Japan. (2004). *Chapter 7 Seismic Loads*. Tokyo: AIJ Recommendations for Loads on Buildings, 652.

Building Center of Japan (BCJ). (2007). *Technical Standard Manual for Building (In Japanese)*. Tokyo, Japan: Building Center of Japan.

Chen, J., Takeyama, T., Otani, H., Fujita, K., and Hori, M. (2016). A framework for assessing liquefaction hazard for urban areas based on soil dynamics. *Int. J. Comput. Methods* 13, 1641011–1641011. doi:10.1142/S0219876216410115

Chock, G., Carden, L., Robertson, I., Olsen, M., and Guangren, Y. (2013). Tohoku tsunami-induced building failure analysis with implications for U.S. tsunami and seismic design codes. *Earthquake Spectra* 29, S99–S126. doi:10.1193/1.4000113

Federal Emergency Management Agency. (2011). *Guidelines for Design of Structures for Vertical Evacuation from Tsunamis*. Washington: FEMA, 158.

Fraser, S., Raby, A., Pomonis, A., Goda, K., Chian, S. C., Macabuag, J., et al. (2013). Tsunami damage to coastal defences and buildings in the March 11th

2011 Mw9.0 Great East Japan earthquake and tsunami. *Bull. Earthquake Eng.* 11, 205–239. doi:10.1007/s10518-012-9348-9

Ishida, M., Tokimatsu, K., and Inoue, S. (2015). "Overturning of buildings induced by tsunami run-up at Onagawa in the 2011 Great Tohoku Earthquake," in *Proc., 6th International Conference on Earthquake Geotechnical Engineering*, Christchurch.

Japanese Geotechnical Society, Tohoku Branch. (1986). *Damage Survey Report of the 1983 Sea of Japan Earthquake (In Japanese)*. Sendai, Japan: Japanese Geotechnical Society, 297.

Kabeyasawa, T., Okuda, Y., Fukai, A., Fukuyama, H., Kato, H., Ishihara, T., et al. (2012). "Evaluation of lateral and buoyant forces on reinforced concrete buildings by the tsunami of the 2011 East Japan earthquake," in *Proc., 15th World Conference in Earthquake Engineering*, Lisbon.

Latcharote, P., Suppasri, A., Yamashita, A., Adriano, B., Koshimura, S., Kai, Y., et al. (2014). "Mechanism and stability analysis of overturned buildings by the 2011 Great East Japan earthquake and tsunami in Onagawa town," in *Proc., 14th Japan Earthquake Engineering Symposium*. Chiba, 108–117.

Mizutani, T. (2008). "Lesson 13 soil liquefaction, principle of natural disaster: disaster case studies (In Japanese)," in *National Research Institute for Earth Science and Disaster Resilience (NIED)*. Available at: http://dil.bosai.go.jp/workshop/

National Institute for Land and Infrastructure Management (NILIM) and Building Research Institute (BRI) in Japan. (2012). Report on field surveys and subsequent investigations of building damage following the 2011 off the pacific coast of Tohoku earthquake. *Build. Res. Data* 136, 6.2–32–6.2–40.

National Research Institute for Earth Science and Disaster Resilience (NIED). (n.d.). *Strong-Motion Seismograph Networks (K-NET, KiK-net)*. Available at: http://www.kyoshin.bosai.go.jp/ (accessed November 24, 2016).

Nikkei BP Company. (2011). Lessons from the Great East Japan earthquake disaster: city and architecture part (In Japanese). *Nikkei Archit. Sect.* 207, 32–38.

Onagawa. (1960). *Onagawa Magazine (In Japanese)*. Onagawa, Miyagi Prefecture, 1010.

Onagawa. (2013). *Onagawa Guide: Industrial Promotion Division of Onagawa (In Japanese)*. Onagawa Tourism Association.

Suppasri, A., Koshimura, S., Imai, K., Mas, E., Gokon, H., Muhari, A., et al. (2012). Damage characteristic and field survey of the 2011 Great East Japan tsunami in Miyagi prefecture. *Coastal Eng. J.* 54, 1250005. doi:10.1142/S0578563412500052

Suppasri, A., Shuto, N., Imamura, F., Koshimura, S., Mas, E., and Yalciner, A. C. (2013). Lesson learned from the 2011 Great East Japan tsunami: performance of tsunami countermeasures, coastal buildings, and tsunami evacuation in Japan. *Pure Appl. Geophys.* 170, 993–1018. doi:10.1007/s00024-012-0511-7

Tokimatsu, K., Ishida, M., and Inoue, S. (2016). Tsunami-induced overturning of buildings in Onagawa during 2011 Tohoku earthquake. *Earthquake Spectra* 32, 1989–2007. doi:10.1193/101815EQS153M

Tokimatsu, K., Tamura, S., Suzuki, H., and Katsumata, K. (2012). Building damage associated with geotechnical problems in the 2011 Tohoku Pacific Earthquake. *Soils Found.* 52, 956–974. doi:10.1016/j.sandf.2012.11.014

Yeh, H., and Sato, S. (2016). Tsunami effects on buildings and coastal structures. *J. Disaster Res.* 11, 662–669. doi:10.20965/jdr.2016.p0662

Yeh, H., Sato, S., and Tajima, Y. (2013). The 11 march 2011 East Japan earthquake and tsunami: tsunami effects on coastal infrastructure and buildings. *Pure Appl. Geophys.* 170, 1019–1031. doi:10.1007/s00024-012-0489-1

Conflict of Interest Statement: The authors declare that the research was conducted in the absence of any commercial or financial relationships that could be construed as a potential conflict of interest.

Copyright © 2017 Latcharote, Suppasri, Yamashita, Adriano, Koshimura, Kai and Imamura. This is an open-access article distributed under the terms of the Creative Commons Attribution License (CC BY). The use, distribution or reproduction in other forums is permitted, provided the original author(s) or licensor are credited and that the original publication in this journal is cited, in accordance with accepted academic practice. No use, distribution or reproduction is permitted which does not comply with these terms.

frontiers in Built Environment

ORIGINAL RESEARCH
published: 25 October 2016
doi: 10.3389/fbuil.2016.00025

Probabilistic Earthquake–Tsunami Multi-Hazard Analysis: Application to the Tohoku Region, Japan

Raffaele De Risi and Katsuichiro Goda*

Department of Civil Engineering, University of Bristol, Bristol, UK

This study develops a novel simulation-based procedure for the estimation of the likelihood that seismic intensity (in terms of spectral acceleration) and tsunami inundation (in terms of wave height), at a particular location, will exceed given hazard levels. The procedure accounts for a common physical rupture process for shaking and tsunami. Numerous realizations of stochastic slip distributions of earthquakes having different magnitudes are generated using scaling relationships of source parameters for subduction zones and then using a stochastic synthesis method of earthquake slip distribution. Probabilistic characterization of earthquake and tsunami intensity parameters is carried out by evaluating spatially correlated strong motion intensity through the adoption of ground motion prediction equations as a function of magnitude and shortest distance from the rupture plane and by solving non-linear shallow water equations for tsunami wave propagation and inundation. The minimum number of simulations required to obtain stable estimates of seismic and tsunami intensity measures is investigated through a statistical bootstrap analysis. The main output of the proposed procedure is the earthquake–tsunami hazard curves representing, for each mean annual rate of occurrence, the corresponding seismic and inundation tsunami intensity measures. This simulation-based procedure facilitates the earthquake–tsunami hazard deaggregation with respect to magnitude and distance. Results are particularly useful for multi-hazard mapping purposes, and the developed framework can be further extended to probabilistic earthquake–tsunami risk assessment.

Keywords: earthquake, tsunami, probabilistic hazard analysis, stochastic rupture models, scaling relationships of earthquake source parameters, mega-thrust subduction earthquake

OPEN ACCESS

Edited by:
Luigi Di Sarno,
University of Sannio, Italy

Reviewed by:
Maria Rota,
European Centre for Training and Research in Earthquake Engineering, Italy
Ali Koçak,
Yıldız Technical University, Turkey

****Correspondence:***
Raffaele De Risi
raffaele.derisi@bristol.ac.uk

Specialty section:
This article was submitted to Earthquake Engineering, a section of the journal Frontiers in Built Environment

Received: *30 July 2016*
Accepted: *26 September 2016*
Published: *25 October 2016*

Citation:
De Risi R and Goda K (2016) Probabilistic Earthquake–Tsunami Multi-Hazard Analysis: Application to the Tohoku Region, Japan. Front. Built Environ. 2:25. doi: 10.3389/fbuil.2016.00025

INTRODUCTION

Earthquake and tsunami can be concurrent threats in many coastal regions around the world. In the last 2500 years, more than 2500 major tsunami events occurred globally (NGDC, 2016), and more than a half of those were triggered by seismic events. Other events were generated by volcanic eruptions (Latter, 1981), submarine landslides (Satake, 2001; Ward, 2001; Watts, 2004), or potentially by asteroid/meteorite impacts (Ward and Asphaug, 2000). **Figure 1** shows the distribution of tsunami events triggered by seismic events at a global scale (NGDC, 2016). Tsunamis are particularly likely in active subduction zones surrounding the Pacific and Indian Oceans and are less expected in crustal seismogenic regions surrounding the Mediterranean Sea. Nonetheless, devastating tsunami disasters can occur in the Mediterranean areas, as exemplified by two historical disasters, i.e., the 1303 Crete Island tsunami (Guidoboni and Comastri, 1997) and the 1908 Messina event (Billi et al., 2008).

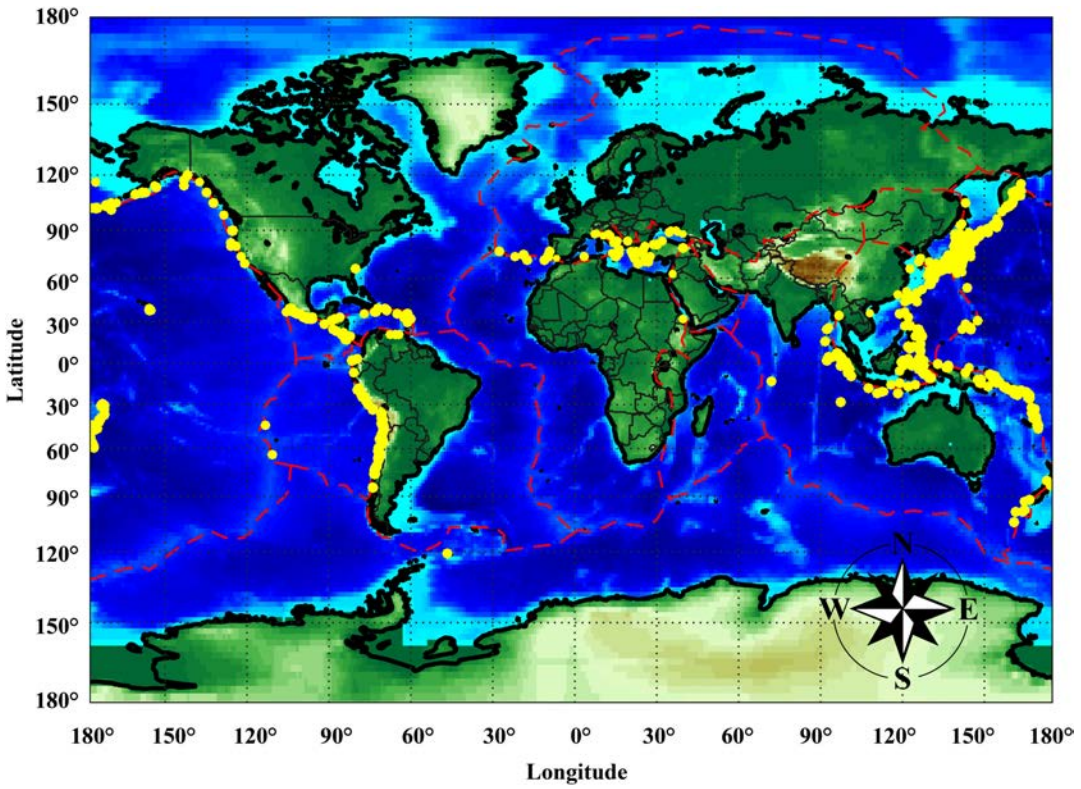

FIGURE 1 | Locations of tsunamis triggered by seismic events. The red lines represent the global plate margins.

It is therefore evident that simultaneous earthquake–tsunami hazard represents an urgent global issue and may cause catastrophic loss, affecting communities along coastal regions from economic and social viewpoints (Løvholt et al., 2014).

Seismic sources close to the shoreline can trigger tsunamis that cause devastating damage, especially due to the lack of sufficient reaction time (Monastersky, 2012). Thus, tsunamis triggered by near-field seismic sources can be regarded as the main contributors of the tsunami risk impact, and they should be studied in detail. Moreover, in comparison to local tsunamis, a simpler parameterization is usually sufficient for far-field tsunamis because seismic moment, source mechanism, and radiation pattern are more influential in comparison with slip distribution within a rupture plane (Geist and Parsons, 2006). For the above reasons, this work will focus on near-field scenarios by considering detailed features of the earthquake rupture.

Probabilistic hazard analysis is the fundamental prerequisite for assessing disaster risk accurately and for deciding effective risk mitigation strategies. Both probabilistic earthquake and tsunami analyses involve various uncertain parameters that are related to geophysical processes and geological characteristics [e.g., slip rate, slip distribution, dip, and strike (Goda et al., 2014)], propagating media, local site conditions (e.g., soil type, roughness, and topography), and sea conditions [e.g., tidal level (Mofjeld et al., 2007)]. Conventional probabilistic seismic hazard analysis [PSHA (Cornell, 1968; McGuire, 2008)] can incorporate all major uncertain parameters in a comprehensive manner, with a potentially high computational effort. The computation becomes prohibitive when a logic tree with numerous branches (to capture full extent of epistemic uncertainty) is adopted for the assessment. In order to reduce this effort, a simulation-based probabilistic procedure can be implemented (Atkinson and Goda, 2013; Akkar and Cheng, 2015).

In the current probabilistic tsunami hazard analysis (PTHA), a comprehensive treatment of these uncertainties is rarely considered due to the lack of high-resolution/accuracy data and to the great computational effort involved in tsunami simulations. There are mainly three methodologies for tsunami hazard assessment in the literature (González et al., 2009): (a) probabilistic hazard analysis; (b) worst-case scenario approach, typically a deterministic method used for the development of practical emergency management products, such as evacuation maps and coastal infrastructure design (Cheung et al., 2011); and (c) sensitivity analysis, where the most influential model parameters are identified (Geist, 2002; Goda et al., 2014). The existing PTHA methods can be grouped in three broad categories. In the first category, PTHA is conducted by using tsunami catalogs (Burroughs and Tebbens, 2005; Tinti et al., 2005; Orfanogiannaki and Papadopoulos, 2007); in the second category, different scenario-based PTHA methods are suggested (Geist and Dmowska, 1999; Downes and Stirling, 2001; Farreras et al., 2007; Liu et al., 2007; Power et al., 2007; Yanagisawa et al., 2007; Burbidge et al., 2008; González et al., 2009; Løvholt et al., 2012). In the third category, a combination of the two previous categories is considered (Geist, 2005; Geist and Parsons, 2006; Annaka et al., 2007; Thio et al., 2007; Burbidge et al., 2008; Parsons and Geist, 2008; Grezio

et al., 2010, 2012; Horspool et al., 2014; Fukutani et al., 2016). Specifically, for near-source subduction zones, Fukutani et al. (2016) extended the methodology of Annaka et al. (2007) for a Tohoku-type (*M*9) earthquake with fixed rupture geometry. They considered several cases for earthquake magnitude, slip pattern, and occurrence probability. However, the numbers of magnitudes and slip patterns are limited and thus not sufficient to capture a wide range of possible tsunami scenarios for this type of mega-thrust subduction earthquakes (Goda et al., 2014).

Building on the previous research, a new probabilistic earthquake and tsunami hazard assessment methodology for near-field seismic sources is presented. The novelty of the proposed methodology is the adoption of a single physical process for concurrent earthquake and tsunami threats; thus, dependency between ground-shaking and tsunami hazard parameters can be investigated probabilistically. On the one hand, the proposed methodology overcomes some of the previous limitations, such as inappropriate scaling relationships, simplistic slip distributions, subjective weights of the logic tree's branches, and simplified inundation models. On the other hand, some simplification, such as the adoption of discrete values of magnitude, and the fixed geometry and predefined meshing of the main subduction region, are maintained. This methodology can be extended to consider all possible sources in a region and can be applied to other subduction zones.

The first step is to define a suitable occurrence model; classical occurrence models in literature are the memory-less Poisson model, generally used for long-term hazard assessments, and the renewal model [e.g., Brownian passage time model (Matthews et al., 2002)] applied for short-term forecasting based on the seismic activity observed in the recent past. In this study, a classical Poisson model is adopted. Assuming a Poissonian inter-arrival time process, the probability of occurrence of an earthquake–tsunami event with specific characteristics in a given time window depends on the mean annual occurrence rate alone. A magnitude–frequency distribution of major seismic events that may potentially trigger tsunamis is then defined. For each value of earthquake magnitude, geometry of the rupture areas and other key source parameters (mean slip and spatial correlation parameters of slip distribution) are determined using new global scaling relationships for tsunamigenic earthquakes (Goda et al., 2016). In this step, both aleatory and epistemic uncertainties of the model parameters (i.e., position and geometry) are incorporated based on probabilistic information available in literature. Therefore, for each value of magnitude, multiple realizations of potential earthquake slip distribution are generated from a theoretical wavenumber spectrum model (Mai and Beroza, 2002). The incorporation of stochastic slip models in probabilistic earthquake–tsunami hazard analysis is another important novelty of this work with respect to the previous studies; conventionally, the slip distributions within a fault plane are considered as uniform or randomly distributed (without realistic spatial distribution of the slip).

Subsequently, simulations of the two hazard processes, i.e., ground shaking and tsunami, are carried out simultaneously. Specifically, for each slip distribution: (a) spatially correlated strong motion intensity measures are evaluated using ground motion prediction equations (GMPEs) for interface subduction events (Morikawa and Fujiwara, 2013; Abrahamson et al., 2016); and (b) the seafloor vertical displacement is calculated using analytical formulae (Okada, 1985; Tanioka and Satake, 1996), and tsunami simulation is performed by solving non-linear shallow water equations (Goto et al., 1997). By repeating the joint assessment of earthquake–tsunami hazards a sufficient number of times for each magnitude, a sample of spectral accelerations at multiple locations can be obtained by simulating a seismic intensity random field, while maximum tsunami wave heights/velocities can be obtained from tsunami hazard analysis. For each magnitude, the results obtained from the simulations are used to build the complementary cumulative distribution functions (CCDFs) for individual hazards, representing the conditional probability of reaching or exceeding a given intensity value. The CCDFs are provided with a confidence interval around the central estimates.

The site-specific earthquake–tsunami hazard curves can be derived by integrating the earthquake–tsunami simulation results and the magnitude–frequency distribution for the discrete values of magnitude, and by multiplying the result by the occurrence rate of earthquakes from the subduction zone. The result will be a triplet of CCDFs (central estimate and confidence interval curves), representing the mean annual rate of exceedance of specific values of seismic intensity or tsunami hazard parameters. The developed methodology is applied to the Tohoku region of Japan, where the subduction fault plane is well defined and information on regional seismicity is available. Finally, the hazards for a site in Sendai City, Miyagi Prefecture, are calculated.

METHODOLOGY

Formulation

The formulation presented herein is aimed at developing the earthquake–tsunami hazard curves for a specific location. Let **IM** represent the intensity measures of interest, such as spectral acceleration (S_a), inundation height (h), flow velocity (v), flux momentum, and tsunami force. Assuming a Poissonian arrival time process, the probability to observe an earthquake–tsunami sequence having intensity measure values **IM** equal to or greater than the specific values **im** in t years is

$$P(\mathbf{IM} \geq \mathbf{im}|t) = 1 - \exp[-\lambda(\mathbf{IM} \geq \mathbf{im}) \cdot t] \tag{1}$$

where $\lambda(\mathbf{IM} \geq \mathbf{im})$ is the mean annual rate at which the intensity measures **IM** will exceed specific values **im** at a given location. The rate $\lambda(\mathbf{IM} \geq \mathbf{im})$ can be expressed as a filtered Poisson process [e.g., Parsons and Geist (2008)]:

$$\lambda(\mathbf{IM} \geq \mathbf{im}) = \lambda(M \geq M_{\min}) \cdot \int P(\mathbf{IM} \geq \mathbf{im}|\boldsymbol{\theta}) \cdot S(\boldsymbol{\theta}|M) \cdot f(M) \cdot dM \tag{2}$$

$\lambda(M \geq M_{\min})$ is the mean annual rate of occurrence of the seismic events with magnitudes greater than the minimum magnitude considered in the magnitude–frequency distribution. $P(\mathbf{IM} \geq \mathbf{im}|\boldsymbol{\theta})$ is the probability that the joint intensity measures

IM will exceed prescribed values **im** at a given coastal location for a given set of source parameters $\boldsymbol{\theta}$. $S(\boldsymbol{\theta}|M)$ represents the scaling relationships (or prediction models) of the uncertain earthquake source parameters conditioned on the magnitude. $f(M)$ is the magnitude–frequency distribution.

Five phases are defined: Phase 1 – fault model and earthquake occurrence, Phase 2 – source parameter characterization and stochastic slip synthesis, Phase 3 – earthquake simulation, Phase 4 – tsunami simulation, and Phase 5 – development of earthquake–tsunami hazard curves. Detailed descriptions for each of these phases are presented in the following. **Figure 2** shows the computational framework of the methodology.

Fault Model and Earthquake Occurrence

The first step is the identification of all seismic sources capable of producing damaging ground motions and tsunami inundation at a site. In this study, a curved surface is considered. Specifically, a 2011 Tohoku-type fault is analyzed with a source zone of 650 km along the strike and 250 km along the dip (**Figure 3A**); such geometry is capable of accommodating a $M9$ earthquake that is consistent with the maximum magnitude adopted for the magnitude–frequency distribution. The fault plane geometry is the extended version of the source model by Satake et al. (2013). Note that extremely large earthquakes that span across multiple seismotectonic segments are not considered (e.g., simultaneous rupture of the off-the-Tohoku subduction region and the off-the-Hokkaido subduction zone). To implement the stochastic synthesis method of earthquake slip distribution, the fault plane is discretized into many sub-faults; a 10-km mesh with variable dip based on Satake et al. (2013) is generated. Such a discretization allows simulating accurately the slip distribution corresponding to a seismic event with $M7.5$ (i.e., the smallest central magnitude value considered for the magnitude–frequency distribution, as shown later), involving at least 5-by-5 sub-faults.

To describe the earthquake sizes in the target region, i.e., the term $f(M)$ in Eq. 2, a truncated Gutenberg–Richter relationship

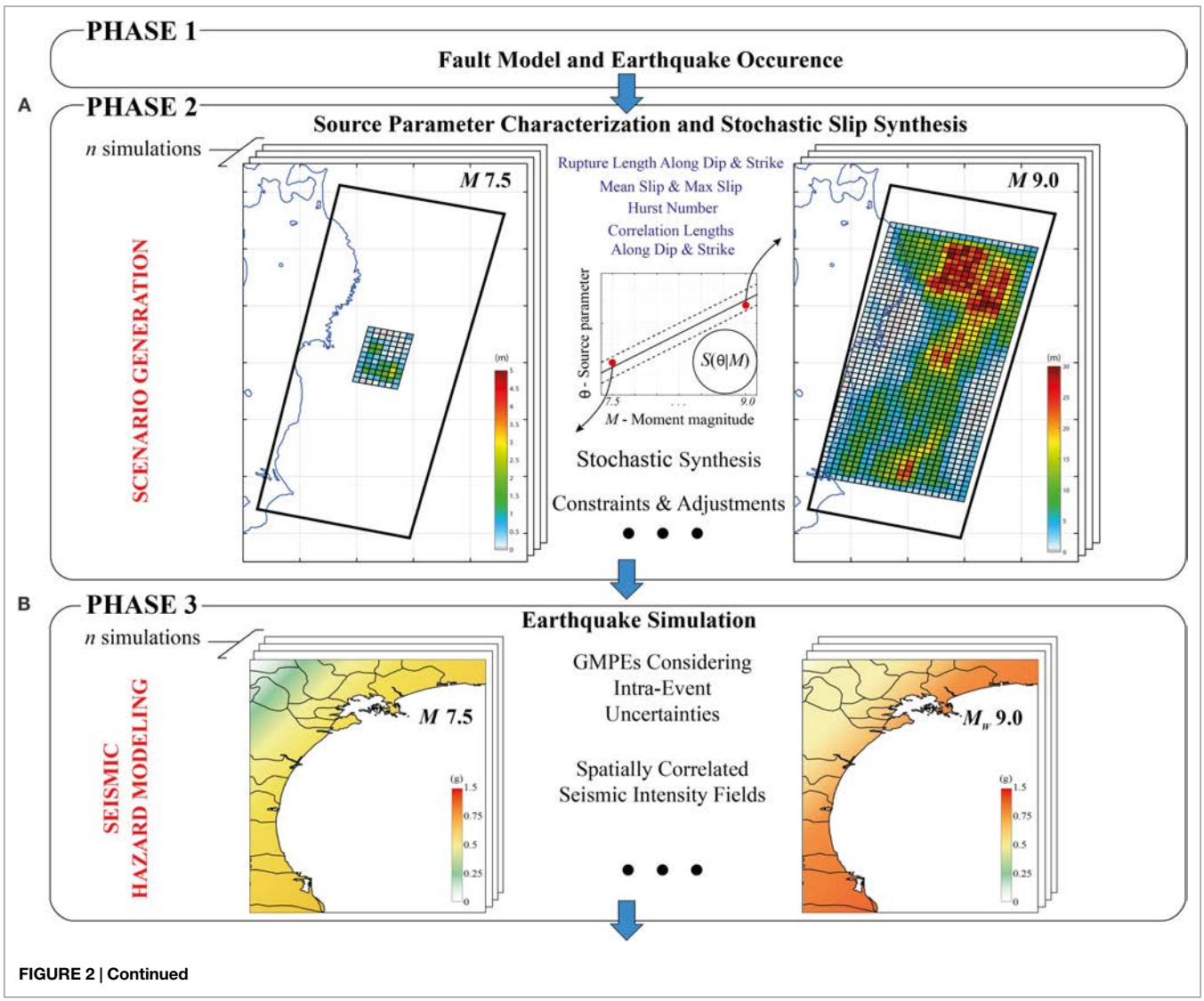

FIGURE 2 | Continued

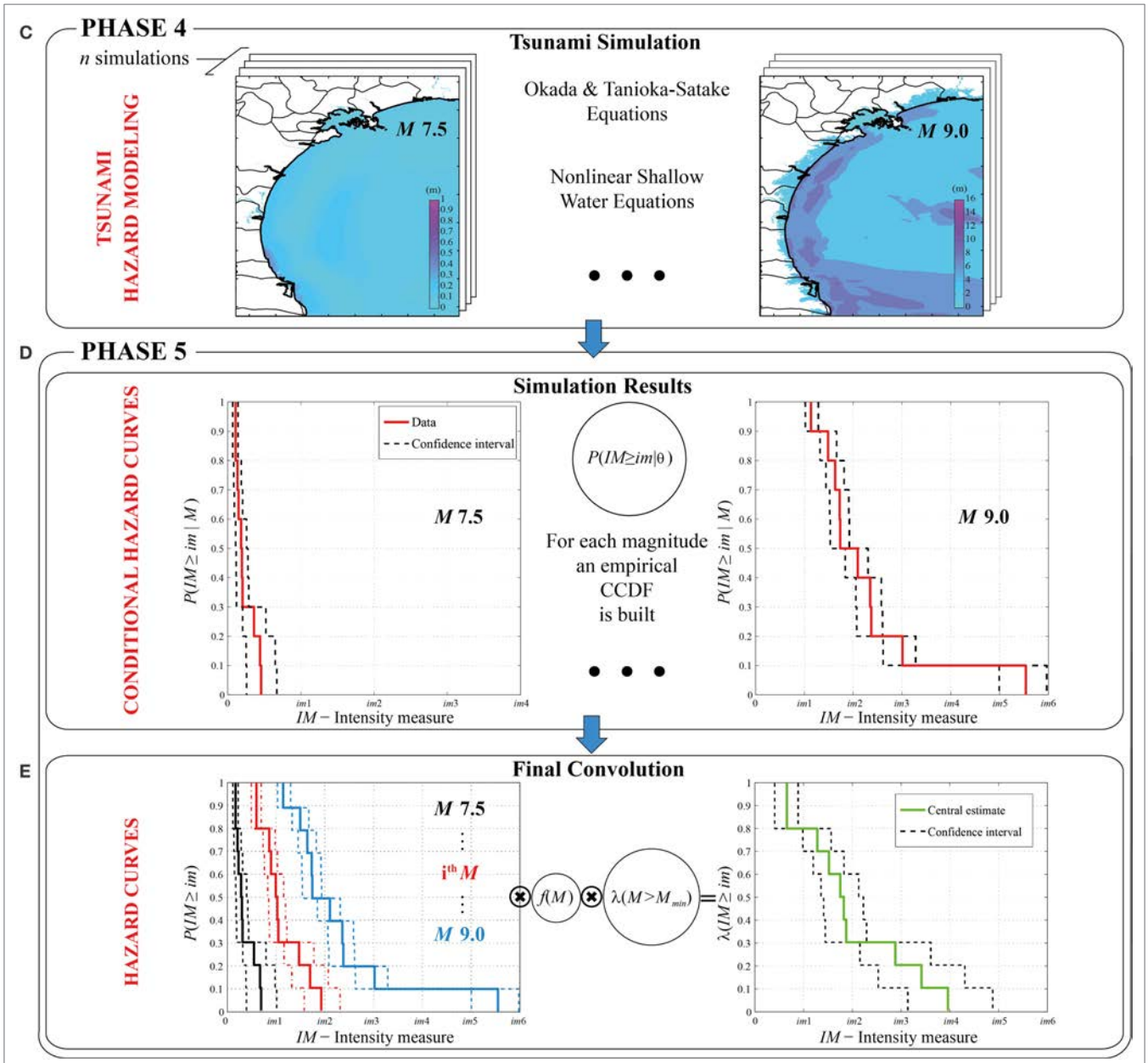

FIGURE 2 | Computational framework for probabilistic earthquake–tsunami hazard analysis. **(A)** Scenario generation. **(B)** Seismic hazard modeling. **(C)** Tsunami hazard modeling. **(D)** Conditional hazard curves. **(E)** Hazard curves.

(Gutenberg and Richter, 1956) is adopted, and its CCDF is given by

$$G(M) = \frac{1 - 10^{-b(M - M_{\min})}}{1 - 10^{-b(M_{\max} - M_{\min})}} M_{\min} < M < M_{\max} \qquad (3)$$

where $M_{\min}$ and $M_{\max}$ are the minimum and maximum moment magnitudes, respectively. For the simulation, it is convenient to convert the continuous distribution of magnitudes into a discrete set of values $(M_{\min}, \ldots, M_i, \ldots, M_{\max})$, assuming that they are the only possible magnitudes; such probabilities are computed as follows:

$$P(M_i) = G(M_i + 0.5 \cdot \Delta M) - G(M_i - 0.5 \cdot \Delta M) \qquad (4)$$

where ΔM is the discretization interval. The discrete term presented in Eq. 4 is used in Eq. 2 instead of $f(M)$.

For the analyses, $M_{\min}$ and $M_{\max}$ are set to 7.375 and 9.125, and a discretization interval of 0.25 is adopted. This means that seven central magnitude values, i.e., 7.5, 7.75, 8.0, 8.25, 8.5, 8.75, and 9.0, are considered to calculate the corresponding conditional probabilities as in Eq. 4. The minimum magnitude value is chosen, since small-to-moderate earthquakes rarely generate significant tsunamis, and their contributions to the tsunami hazard are negligible (Annaka et al., 2007). For the Tohoku case study, a b-value equal to 0.9 is adopted (Headquarters for Earthquake Research Promotion, 2013).

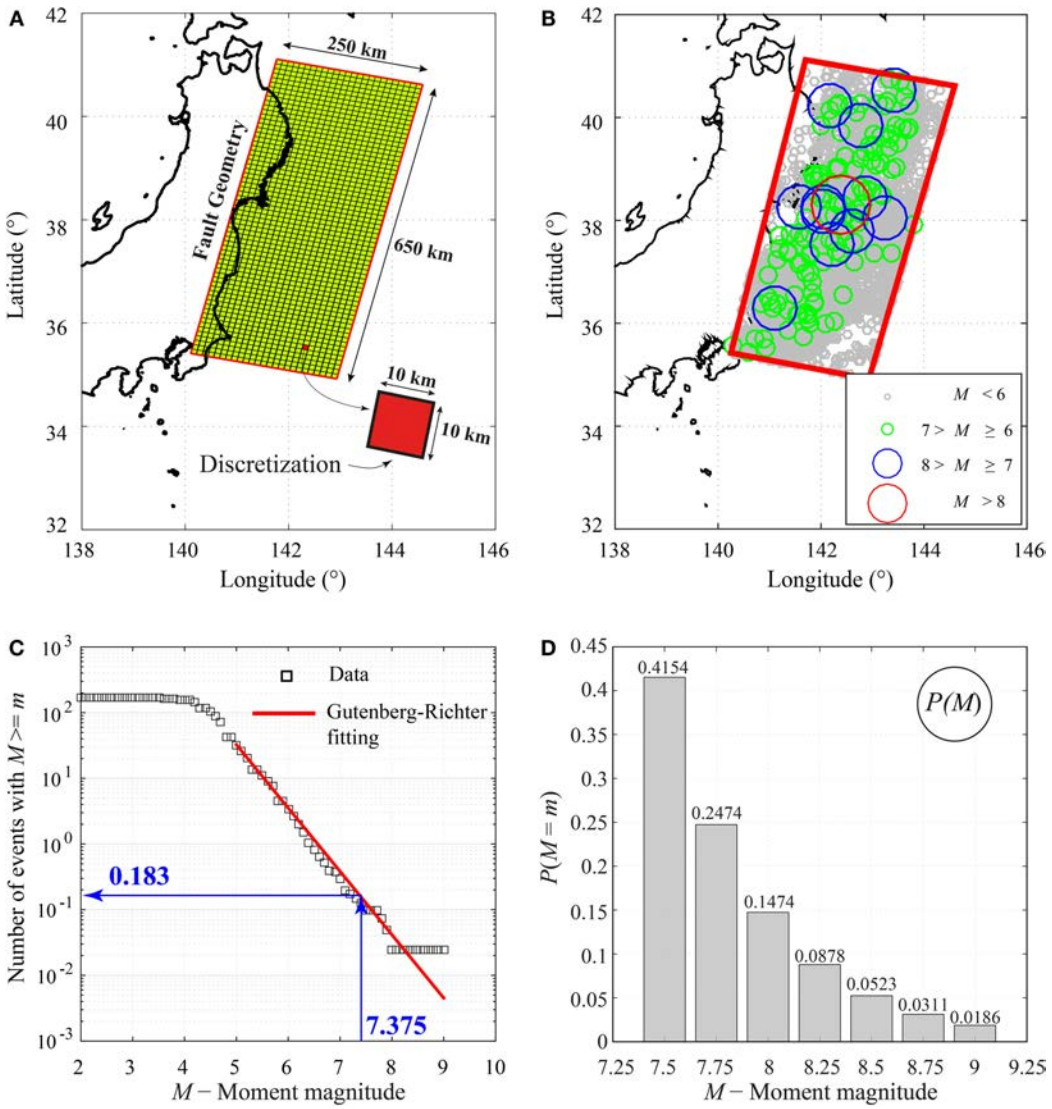

FIGURE 3 | (A) Fault plane model and discretization. **(B)** Spatial distribution of earthquakes in the source region using the NEIC catalog. **(C)** Gutenberg–Richter relationship. **(D)** Discrete probability mass based on the fitted Gutenberg–Richter relationship.

Once the magnitude interval is selected and the major source area containing all possible rupture scenarios is defined, the mean annual rate of occurrence of earthquakes with magnitudes greater than or equal to 7.375 falling in that area, i.e., the term $\lambda(M \geq M_{\min})$ in Eq. 2, can be calculated. In order to perform such a calculation, the NEIC earthquake catalog (http://earthquake.usgs.gov/earthquakes/search/) is used. **Figure 3B** shows the events reported in the database that fall in the considered rupture area, recorded in the period between 1976 and 2012, having a depth varying between 0 km and 60 km, and considering a magnitude range between 5 and 9. According to the data analysis (**Figure 3C**), the estimated rate $\lambda(M \geq 7.375)$ is equal to 0.183. **Figure 3D** shows the occurrence probabilities for the discrete set of magnitude values (i.e., 7.5, 7.75, 8.0, 8.25, 8.5, 8.75, and 9.0). Note that the probability mass function shown in **Figure 3D** is normalized (conditional) with respect to the occurrence rate for the minimum magnitude event.

Source Parameter Characterization and Stochastic Slip Synthesis

To take into account uncertainties related to the rupture process, multiple random slip fields are simulated (**Figure 2A**). The simulation procedure is based on a spectral synthesis method (Goda et al., 2014; Fukutani et al., 2016), where the earthquake slip distribution is characterized by wavenumber spectra (Mai and Beroza, 2002; Lavallée et al., 2006). Scaling relationships that evaluate the source parameters as a function of moment magnitude are needed for stochastic tsunami simulation (e.g., rupture size and spectral characteristics of the rupture).

In this study, new global scaling relationships for tsunamigenic earthquakes are employed. These relationships are obtained on the basis of 226 inverted source models in the SRCMOD database (Mai and Thingbaijam, 2014). The details of the adopted scaling laws can be found in Goda et al. (2016).

The following relationships are employed to obtain the rupture width (W) and length (L):

$$\log_{10} W = -0.4877 + 0.3125M + 0.1464 \times \varepsilon_W \quad (5)$$

$$\log_{10} L = -1.5021 + 0.4669M + 0.1717 \times \varepsilon_L \quad (6)$$

where the numbers multiplying by the ε terms are the SDs of the regression errors. The two geometrical dimensions are used to create the rupture area, which is randomly located inside the predefined subduction fault plane. Subsequently, a slip distribution realization with desired properties is obtained using a stochastic synthesis method (Goda et al., 2014). First, a random field, having quasi-normal distribution with a desired spatial correlation structure, is generated using a Fourier integral method (Pardo-Iguzquiza and Chica-Olmo, 1993). The amplitude spectrum of the target slip distribution is specified by a theoretical power spectrum, while the phase spectrum is represented by a random phase matrix. For the amplitude spectrum, the von Kármán model is considered (Mai and Beroza, 2002):

$$P(k) \propto \frac{\mathrm{CL}_z \mathrm{CL}_x}{\left(1 + k^2\right)^{\mathrm{HN}+1}} \quad (7)$$

where k is the wavenumber (i.e., reciprocal of the wavelength). The correlation lengths (CL_z along the dip and CL_x along the strike) are important source parameters that define the spatial heterogeneity of small wavenumber components in the spectrum and are determined from the following scaling relationships:

$$\log_{10} \mathrm{CL}_z = -1.0644 + 0.3093M + 0.1592 \times \varepsilon_{\mathrm{CL}_z} \quad (8)$$

$$\log_{10} \mathrm{CL}_x = -1.9844 + 0.4520M + 0.2204 \times \varepsilon_{\mathrm{CL}_x} \quad (9)$$

On the other hand, the Hurst number NH determines the spectral decay in the large wavenumber range and can be modeled as a bimodal random variable that takes a value of 0.99 with probability of 0.43 or a value sampled from the normal distribution with mean equal to 0.714 and SD equal to 0.172 with probability of 0.57 (Goda et al., 2016). The obtained complex Fourier coefficients are transformed into the spatial domain *via* 2-D inverse fast Fourier transform. The synthesized slip distribution is then scaled nonlinearly to achieve suitable right-tail characteristics, in agreement with those observed in the finite-fault models, using the Box–Cox parameter λ (Box and Cox, 1964). It can be modeled as a normal random variable with mean equal to 0.312 and SD equal to 0.278.

Finally, the generated slip distribution is further adjusted in order to have a mean slip (D_a) and maximum slip (D_m), according to the values calculated from the scaling relationships for the given magnitude:

$$\log_{10} D_\mathrm{a} = -5.7933 + 0.7420M + 0.2502 \times \varepsilon_{D_\mathrm{a}} \quad (10)$$

$$\log_{10} D_\mathrm{m} = -4.5761 + 0.6681M + 0.2249 \times \varepsilon_{D_\mathrm{m}} \quad (11)$$

It is important to note that the error terms of the source parameters W, L, CL_z, CL_x, D_a, and D_m mentioned above are distributed according to a multivariate normal distribution (Goda et al., 2016). The linear correlation matrix of the regression errors ε is given by

$$\rho_\varepsilon = \begin{array}{c} \\ \varepsilon_W \\ \varepsilon_L \\ \varepsilon_{\mathrm{CL}_z} \\ \varepsilon_{\mathrm{CL}_x} \\ \varepsilon_{D_\mathrm{a}} \\ \varepsilon_{D_\mathrm{m}} \end{array} \begin{array}{c} \begin{array}{cccccc} \varepsilon_W & \varepsilon_L & \varepsilon_{\mathrm{CL}_z} & \varepsilon_{\mathrm{CL}_x} & \varepsilon_{D_\mathrm{a}} & \varepsilon_{D_\mathrm{m}} \end{array} \\ \begin{bmatrix} 1.000 & 0.139 & 0.826 & 0.035 & -0.680 & -0.545 \\ & 1.000 & 0.249 & 0.734 & -0.595 & -0.516 \\ & & 1.000 & 0.288 & -0.620 & -0.564 \\ & & & 1.000 & -0.374 & -0.337 \\ & & & & 1.000 & 0.835 \\ & & & & & 1.000 \end{bmatrix} \end{array} \quad (12)$$

Therefore, values of W, L, CL_z, CL_x, D_a, and D_m can be simulated jointly in the stochastic source simulation. The central estimates and the confidence interval (16th and 84th percentiles) of the scaling relationships are shown in **Figure 4**. The same figure also shows simulated data (green dots) and associated statistics (colored circles), which are obtained from the stochastic source modeling. Magnitude values for simulated data are not perfectly aligned at the seven discrete values; in fact, the simulation algorithm allows a tolerance band of ±0.05 around each magnitude value.

The preceding procedure of earthquake source characterization is innovative with respect to the literature. In particular, a common physical process for concurrent earthquake and tsunami threats is considered, i.e., the common fault rupture scenario that is modeled through the generic stochastic slip scenario on the subduction fault plane. The adoption of a common physical process facilitates the probabilistic investigation of the dependency between shaking and tsunami hazard parameters.

Earthquake Simulation

Ground motion prediction equations are extensively used as an effective way to predict seismic intensity measures for a given earthquake scenario (Wald et al., 2006). To account for seismic intensities at multiple locations that occur simultaneously for a given event, GMPEs together with spatial correlations in the regression residuals can be treated as statistical prediction models (Goda and Atkinson, 2010; Goda, 2011). This feature is particularly important in extending the seismic hazard assessment into a risk assessment of a portfolio of buildings/infrastructures. In this study, only the intra-event SD is propagated through the simulation procedure; such a choice is consistent with the simulation scenario of a single fault plane.

Two GMPEs that are applicable to subduction zones are used for the seismic simulations (**Figure 2B**). The first GMPE (Abrahamson et al., 2016) was developed with a global dataset of earthquakes in subduction zones and has been modified by adding the 2010 Maule Chile and 2011 Tohoku Japan earthquakes to the initial database. The basic functional form of the model for interface subduction events is

$$\begin{aligned} \ln(S_\mathrm{a}) = {} & \theta_1 + \theta_4 \cdot \Delta C_1 + [\theta_2 + \theta_3 \cdot (M - 7.8)] \\ & \cdot \ln\{R + C_4 \cdot \exp[\theta_9 \cdot (M - 6)]\} + \theta_6 \cdot R \\ & + f_\mathrm{MAG}(M) + f_\mathrm{FABA}(R) + f_\mathrm{SITE}\left(\mathrm{PGA}_{1000}, V_{S30}\right) + \sigma \cdot \varepsilon \end{aligned} \quad (13)$$

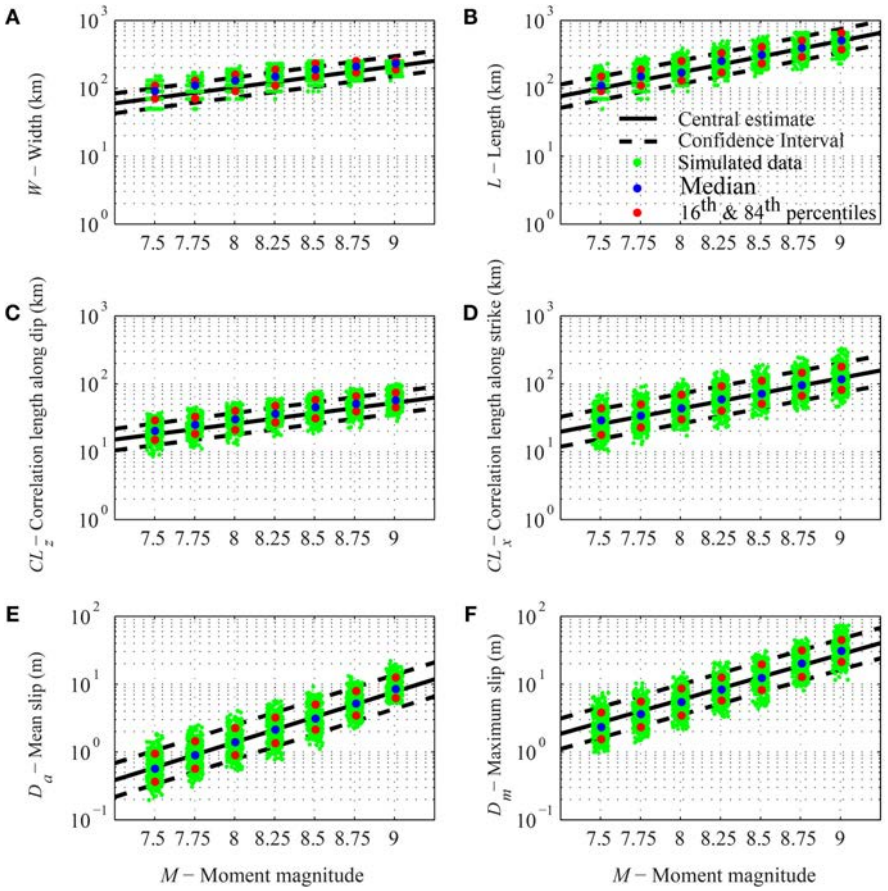

FIGURE 4 | Scaling relationships for tsunamigenic earthquakes. **(A)** Rupture width versus moment magnitude. **(B)** Rupture length versus moment magnitude. **(C)** Correlation length along dip versus moment magnitude. **(D)** Correlation length along strike versus moment magnitude. **(E)** Mean slip versus moment magnitude. **(F)** Maximum slip versus moment magnitude. The simulated values (green dots) and the corresponding percentiles (colored circles) are also shown.

where ln is the natural logarithm, R is the closest distance to the rupture area, V_{S30} is the shear wave velocity in the uppermost 30 m of soil column, PGA_{1000} is the median peak ground acceleration (PGA) value corresponding to $V_{S30} = 1000$ m/s, σ is the total SD, and ε is the Gaussian error term, represented by 0 mean and unit SD. The SD is period-dependent; it is obtained by the combination of intra-event (ϕ) and inter-event (τ) SDs. The magnitude function is

$$f_{\mathrm{MAG}}(M) = \begin{cases} \theta_4 \cdot [M - (7.8 + \Delta C_1)] \\ \quad + \theta_{13} \cdot (10 - M)^2 & \text{for } M \leq 7.8 + \Delta C_1 \\ \theta_5 \cdot [M - (7.8 + \Delta C_1)] \\ \quad + \theta_{13} \cdot (10 - M)^2 & \text{for } M > 7.8 + \Delta C_1 \end{cases} \tag{14}$$

where ΔC_1 is the term representing the epistemic uncertainty in the break of the magnitude scaling and allows adjusting the GMPE for large interface events that were not originally considered in the earthquake database. $f_{\mathrm{FABA}}(R)$ represents the forearc/backarc scaling term; it is equal to 0 for forearc or unknown site, and this is applicable to the case of this study. Finally, the model for site response scaling is given by

$$\begin{aligned} f_{\mathrm{SITE}} &= \theta_{12} \cdot \ln\left(\frac{\min(V_{S30}, 1000)}{V_{\mathrm{lin}}}\right) - b \cdot \ln(\mathrm{PGA}_{1000} + c) \\ &\quad + b \cdot \ln\left[\mathrm{PGA}_{1000} + c \cdot \left(\frac{\min(V_{S30}, 1000)}{V_{\mathrm{lin}}}\right)^n\right] \quad V_{S30} < V_{\mathrm{lin}} \\ f_{\mathrm{SITE}} &= \theta_{12} \cdot \ln\left(\frac{\min(V_{S30}, 1000)}{V_{\mathrm{lin}}}\right) \\ &\quad + b \cdot n \cdot \ln\left(\frac{\min(V_{S30}, 1000)}{V_{\mathrm{lin}}}\right) \quad V_{S30} \geq V_{\mathrm{lin}} \end{aligned} \tag{15}$$

All the model coefficients for Eqs 13–15 can be found in Abrahamson et al. (2016).

The second GMPE by Morikawa and Fujiwara (2013) is suitable for $M9$ earthquakes in Japan. Two formulations are proposed: one is expressed with a quadratic magnitude term, while the other considers a linear magnitude term. In this study, the quadratic formulation is used since the correction factors (presented in the following) that are included in the quadratic formulation reduce

the regression SD. The functional form for interface events is

$$\log(S_a) = a_1 \cdot (\min(M, 8.2) - M)^2 + b_1 \cdot R + c_1 - \log\left(R + d_1 \cdot 10^{e_1 \cdot \min(M, 8.2)}\right) + \sigma \cdot \varepsilon \quad (16)$$

where log is the base-10 logarithm, a_1, b_1, c_1, d_1, e_1, and σ are period-dependent regression coefficients and can be found in Morikawa and Fujiwara (2013). In Morikawa and Fujiwara (2013), no distinction is made between intra-event and inter-event SDs. The two SDs ϕ and τ can be determined by splitting the total variance into the intra-event and inter-event components based on the ratios of intra-event and inter-event variances to the total variance presented in Zhao et al. (2006). The estimate of the prediction equation is further modified using three additional correction terms: amplification due to the deep sedimentary layers (G_d), amplification due to shallow soft soils (G_s), and anomalous seismic intensity distribution due to the position of the site of interest with respect to the volcanic front (AI). In this study, only the second correction term is taken into account and is given by

$$\log(G_s) = p_s \cdot \log\left[\frac{\min(V_{S_{max}}, V_{S30})}{350}\right] \quad (17)$$

where $V_{S_{max}}$ is a period-dependent regression parameter that can be found in Morikawa and Fujiwara (2013).

Figures 5A–D compare the two GMPEs for three seismic intensity parameters [i.e., PGA, $S_a(T = 0.3\,s)$, and $S_a(T = 3\,s)$], for M equal to 7.5 and 9.0 and for V_{S30} equal to 300 m/s. **Figure 6** shows the acceleration response spectra obtained using the two GMPEs, considering two values of closest distance (i.e., 50 and 200 km), and the same values of magnitude and V_{S30} described before. Significant differences between the two GMPEs can be observed, especially for the large value of magnitude. Moreover, the Morikawa–Fujiwara GMPE tends to attenuate PGA and short-period spectral acceleration faster than the Abrahamson et al. GMPE with the distance, while the opposite trend occurs for the long-period spectral accelerations.

For seismic simulations, three main inputs are required: event magnitude, distance from the rupture, and shear wave velocity for the considered site. Regarding the distance from the rupture, the GMPEs presented above are both based on the closest distance between the location of interest and the rupture area (**Figure 7A**). To optimize the computation of the shortest distance, the distances between the coastline location and each

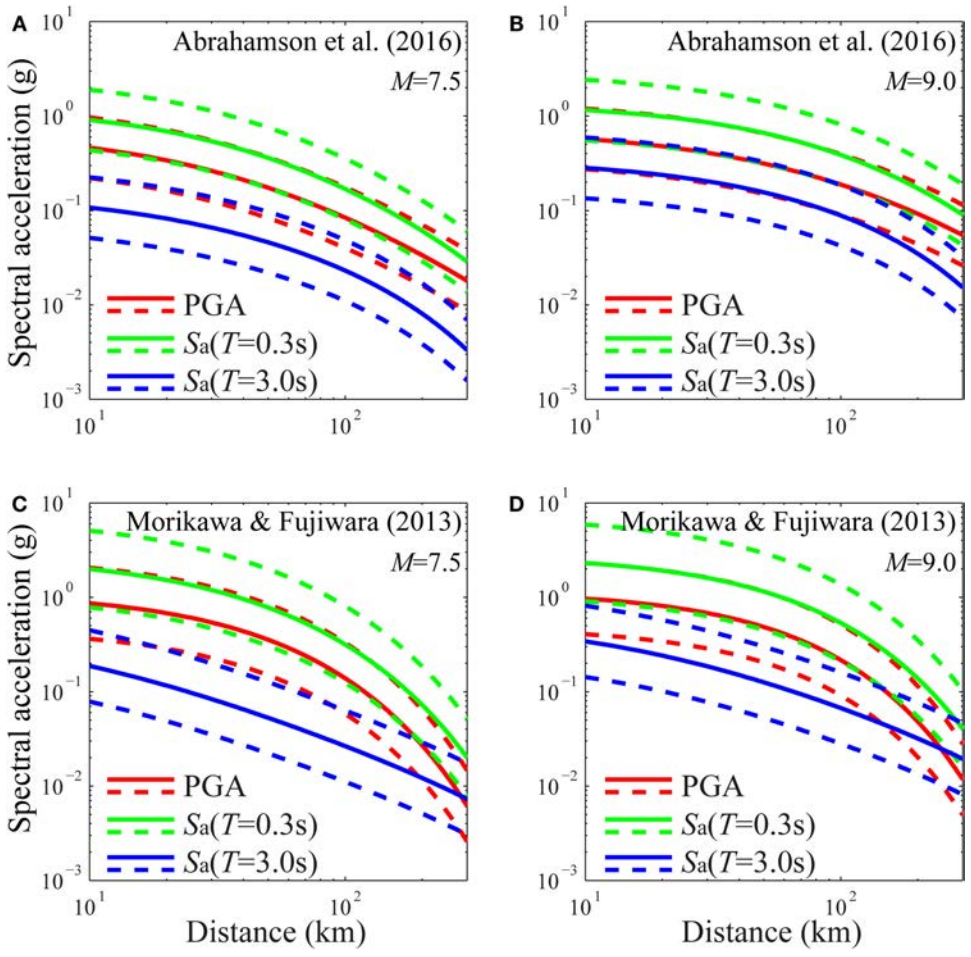

FIGURE 5 | Comparison of GMPEs. **(A)** Abrahamson et al. GMPE for $M = 7.5$ and $V_{S30} = 300$ m/s. **(B)** Abrahamson et al. GMPE for $M = 9.0$ and $V_{S30} = 300$ m/s. **(C)** Morikawa–Fujiwara GMPE for $M = 7.5$ and $V_{S30} = 300$ m/s. **(D)** Morikawa–Fujiwara GMPE for $M = 9.0$ and $V_{S30} = 300$ m/s.

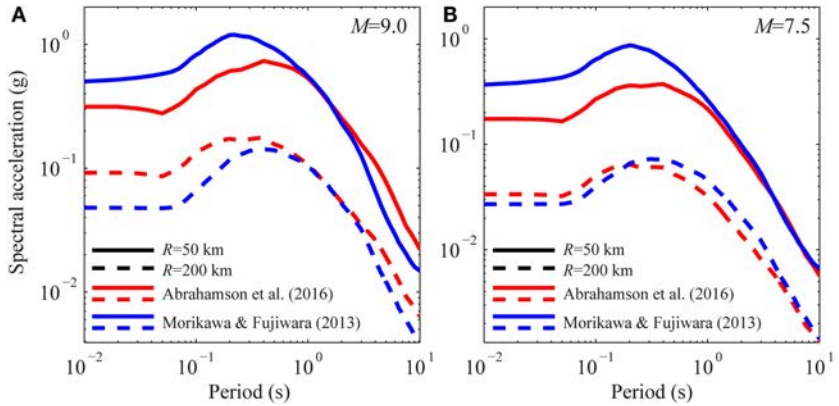

FIGURE 6 | Response spectra obtained considering the Abrahamson et al. and Morikawa–Fujiwara GMPEs, $V_{S30} = 300$ m/s, and two shortest distances ($R = 50$ and 200 km). (A) $M = 7.5$. **(B)** $M = 9.0$.

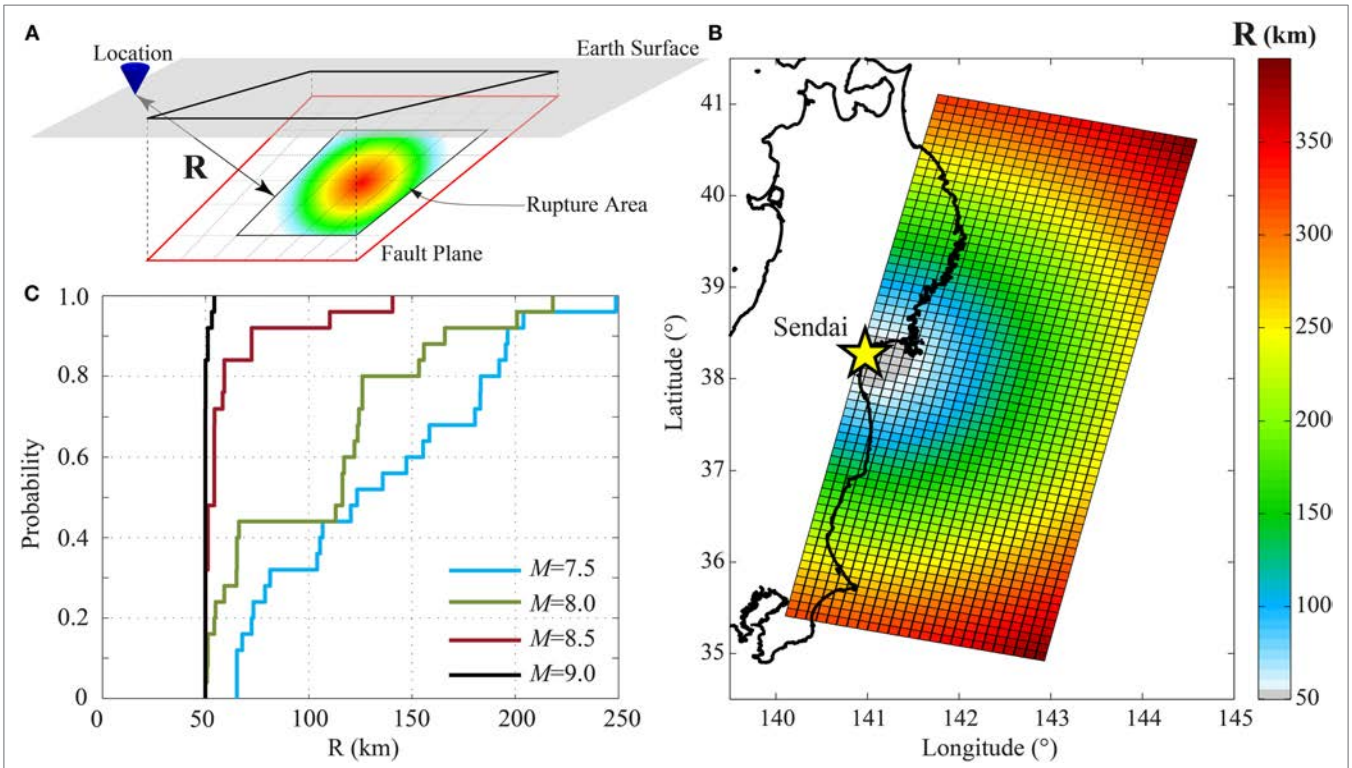

FIGURE 7 | (A) Schematic representation of the shortest distance from the rupture. **(B)** Precalculated distance for each sub-fault from a site in Sendai City. **(C)** Distribution of the distances for 500 stochastic simulations associated with 4 values of magnitude.

discretized element of the 2011 Tohoku-type fault are precomputed and stored (**Figure 7B**). As an example, **Figure 7C** shows the distances computed for 500 stochastic scenarios, which are considered in Section "Results." It is worth noting that the minimum distance is circa 50 km, corresponding to the depth of the fault plane under the considered location. As observed in Goda and Atkinson (2014), the source-to-site distance is affected by the location and size of the fault plane, which in turn is determined by the magnitude of the event. In **Figure 7C**, it can be observed that the greater magnitude value results in smaller variability of the closest distance (i.e., distribution function has a steeper slope). This is because the rupture plane can move more freely within the overall fault plane (**Figure 2A**) when the earthquake magnitude is small. For the shear wave velocity, the USGS global V_{S30} map server is used (Wald and Allen, 2007).

Finally, to generate shake maps of intensity measures **IM**, the multivariate lognormal distribution can be adopted. The median values of **IM** at sites of interest are calculated from the GMPE, whereas their variances are based on the intra-event components. The prediction errors ε in the GMPE are spatially correlated; the

correlation coefficient matrix has diagonal elements equal to 1 and off-diagonal elements equal to the correlation coefficient ρ. The correlation coefficient can be calculated using the following equation (Goda and Atkinson, 2010):

$$\rho_{i,j}(\Delta) = \max\left[\gamma \cdot \exp\left(-\alpha \cdot \Delta^{\beta}\right) - \gamma + 1, 0\right] \quad (18)$$

where Δ is the distance between the points *i* and *j*, while α, β, and γ are period-dependent model parameters that can be found in Goda and Atkinson (2010).

Tsunami Simulation

For each stochastic event, a tsunami simulation is carried out in order to compute the maximum inundation intensity measure (**Figure 2C**). To optimize the computational time, the subduction plane is discretized into sub-faults of 10 km × 10 km (**Figure 3A**), and for each sub-fault, the seafloor displacement corresponding to 1 m of slip is calculated using analytical equations by Okada (1985) and Tanioka and Satake (1996). Subsequently, for each simulated earthquake slip (i.e., event), the overall seafloor displacement field is estimated by scaling and summing the seafloor deformation fields of all individual sub-faults that make up the event.

Tsunami modeling is then carried out using a well-tested numerical code of Goto et al. (1997) that is capable of generating offshore tsunami propagation and inundation profiles by evaluating non-linear shallow water equations, with run-up using a leapfrog staggered-grid finite difference scheme. The run-up calculation is based on a moving boundary approach, where a dry/wet condition of a computational cell is determined based on total water depth relative to its elevation. The numerical tsunami calculation is performed for duration sufficient to model the most critical phases of tsunami waves (i.e., 2 h). The integration time step is determined by satisfying the CFL condition; it depends on the bathymetry/elevation data, and their grid sizes and is typically between 0.1 and 0.5 s. For the simulation, it is possible to obtain the maximum tsunami intensity measures of interest (i.e., tsunami height, tsunami velocity, etc.) for one or more specific locations along the coast. The results can also be used to evaluate aggregate tsunami hazard parameters, such as inundation areas above a certain depth.

A complete dataset of bathymetry/elevation, coastal/riverside structures (e.g., breakwater and levees), and surface roughness is obtained from the Miyagi prefectural government. The data are provided in the form of nested grids (1350 m–450 m–150 m–50 m), covering the geographical regions of Tohoku. The ocean-floor topography data are based on the 1:50,000 bathymetric charts and JTOPO30 database developed by Japan Hydrographic Association and based on the nautical charts developed by Japan Coastal Guard. The tidal fluctuation is not taken into account in this study. The elevation data of the coastal/riverside structures are primarily provided by municipalities. In the tsunami simulation, the coastal/riverside structures are represented by a vertical wall at one or two sides of the computational cells. To evaluate the volume of water that overpasses these walls, Homma's overflowing formulae are employed. In the tsunami simulation, the bottom friction is evaluated using the Manning's formula. The Manning's coefficients are assigned to computational cells based on national land use data in Japan: 0.02 $m^{-1/3}s$ for agricultural land, 0.025 $m^{-1/3}s$ for ocean/water, 0.03 $m^{-1/3}s$ for forest vegetation, 0.04 $m^{-1/3}s$ for low-density residential areas, 0.06 $m^{-1/3}s$ for moderate-density residential areas, and 0.08 $m^{-1/3}s$ for high-density residential areas.

Development of Earthquake–Tsunami Hazard Curves

For each value of magnitude, the simulations are used to evaluate the term $P(\mathbf{IM} \geq \mathbf{im}|M)$ for the location of interest. Such probability is represented by the CCDF of the **IM** (**Figure 2D**). Specifically, the CCDF of the **IM** (i.e., spectral acceleration or tsunami inundation) is obtained as the Kaplan–Meier estimator (Kaplan and Meier, 1958), for which the variance can be calculated through the Greenwood's formula (Greenwood, 1926), and therefore, a confidence interval around the central estimate can be obtained. In this study, the 95% confidence interval is considered.

The curves obtained in the previous step for each magnitude are then multiplied by the probabilities corresponding to the related magnitude and eventually are summed up (**Figure 2E**). Also in this case, three curves are obtained, one corresponding to the central value and two for the confidence interval. The final hazard curves, representing the mean annual rate of occurrence of specific values of earthquake–tsunami intensity measures, are obtained by multiplying the previous three conditional curves (for each hazard) by the occurrence rate of events with magnitudes greater than the minimum magnitude considered in the magnitude–frequency distribution.

RESULTS

The developed methodology is applied to calculate the earthquake and tsunami hazard curves for a site along the coast line of Sendai City, Miyagi Prefecture (the yellow star in **Figure 7B**), for which $V_{S30} = 240$ m/s is obtained based on the USGS data. It is interesting to note that during the 2011 Tohoku earthquake, PGA of 0.8 g (Wald et al., 2006; USGS ShakeMap Archive, 2016) and tsunami wave height of 7 m [Ministry of Land, Infrastructure, and Transportation (MLIT), 2014] were observed in the vicinity of this site. The main results that are discussed in this section focus on (a) sensitivity of seismic and tsunami hazard estimates to the number of stochastic simulations, and (b) development of earthquake–tsunami multi-hazard curves for the target site and the deaggregation of the seismic and tsunami hazards. The former provides useful information regarding the stability of the simulation-based hazard assessments.

Sensitivity of Seismic and Tsunami Hazard Parameters to the Number of Simulations

Short or incomplete records lead to biased estimation of the hazard parameters, especially when conventional statistical methods are used (Lamarre et al., 1992). To investigate the effect of the number of simulations on the final hazard estimation, a bootstrap procedure is carried out by randomly sampling *m* values from the original sample containing *n* elements (with $m \leq n$). This provides a pool of different samples of independent and identically distributed random variables, whose distribution function is the

same as that of the original sample. For each generated sample, statistics of the parameter of interest (e.g., mean, median, and different percentiles) are then computed. The ensemble of such estimates can be used to quantify the uncertainty in the parameter value.

Figures 8 and **9** show five percentiles (i.e., 5th, 25th, 50th, 75th, and 95th) of the spectral acceleration and wave height, respectively; such intensity measures are calculated for the site in Sendai by considering different magnitude values (i.e., 7.5, 8.0, 8.5, and 9.0) as a function of the number of simulations. Moreover,

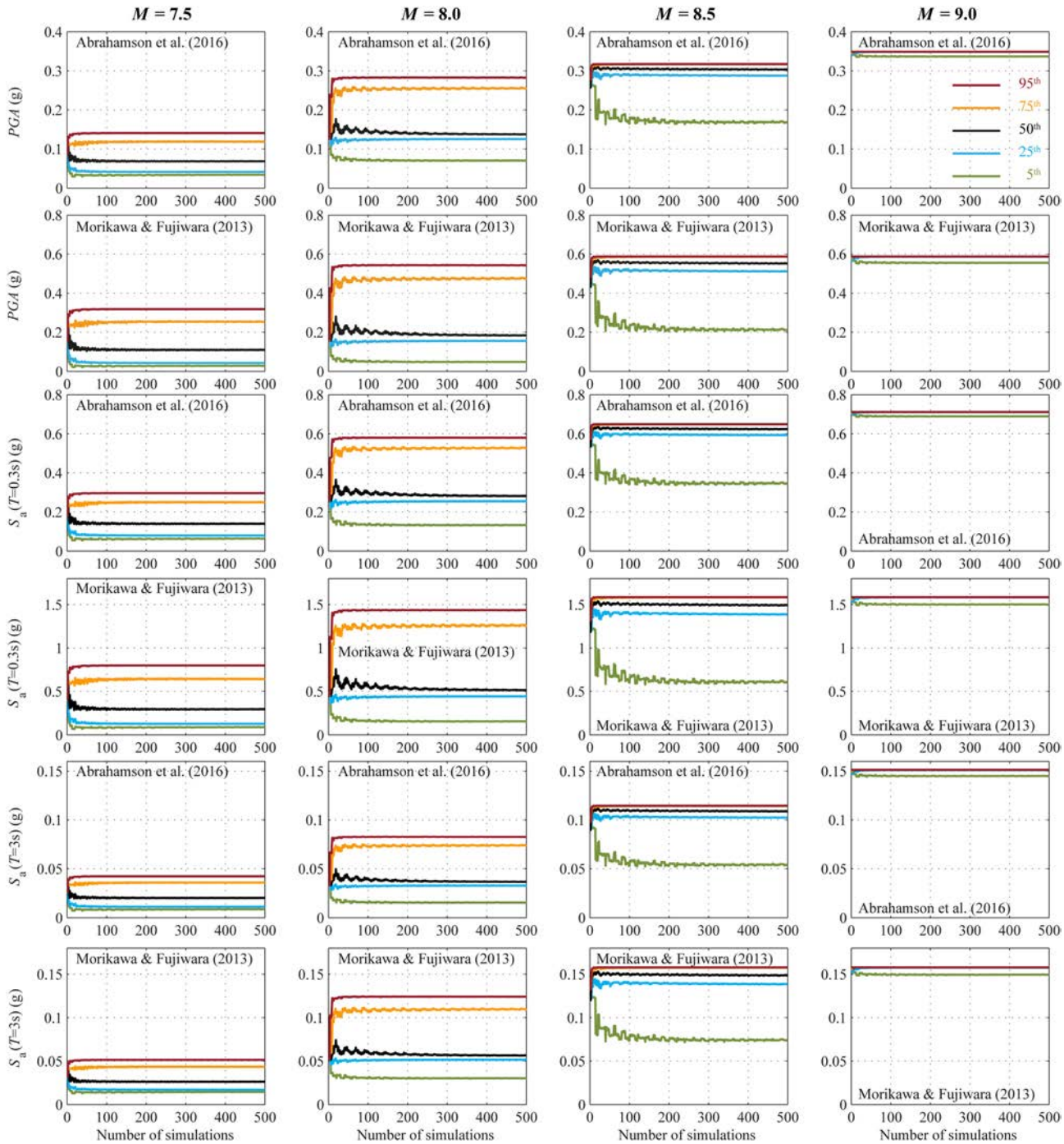

FIGURE 8 | Convergence of estimated seismic intensity measures [i.e., PGA, $S_a(T = 0.3\,s)$ and $S_a(T = 3\,s)$] as a function of the number of simulations by considering the Abrahamson et al. and Morikawa–Fujiwara GMPEs and four moment magnitudes ($M = 7.5$, 8.0, 8.5, and 9.0). Different colors represent different percentiles.

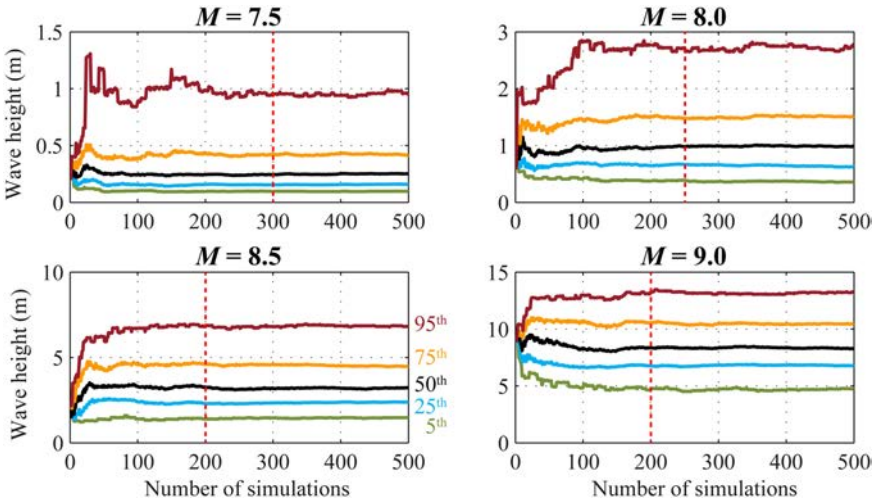

FIGURE 9 | Convergence of estimated tsunami intensity measures (wave height) as a function of the number of simulations by considering four moment magnitudes ($M = 7.5$, 8.0, 8.5, and 9.0).

Figure 8 shows bootstrap results for the seismic case considering two different GMPEs. The analysis is carried out for the maximum sample size of $n = 500$ simulations. The bootstrap procedure is then applied considering the number of simulations m varying between 1 and 500. For each trial number of simulations m, 1000 Monte Carlo samples are generated, and then the percentile curves are obtained as the mean value of such simulations. Based on **Figure 8**, it can be concluded that for the considered seismic case, 200 simulations is sufficient to observe stable percentiles for all magnitude values and for both GMPEs considered. Also in this case, for increasing values of magnitude, there is a decreasing trend of variability of the simulated values due to the reduction in variability of the closest distance (**Figure 7C**).

Tsunami simulation results show that the 50th percentile curves are stable after 100 simulations for all the considered magnitude values. To obtain stable estimates of the high percentiles, a larger number of simulations are needed (the red dotted line in **Figure 9**). In particular, 300 simulations are necessary for M7.5, 250 simulations for M8.0, and 200 simulations for M8.5 and M9.0. Such a decreasing trend with the magnitude is consistent with what was observed for the rupture distance (**Figure 7C**), i.e., when the magnitude is relatively small, the variability of the inundation intensity measures are increased because the rupture area can move more freely within the fault plane. In turn, when the magnitude is large, the fluctuation of the rupture area is more constrained.

Considering the results shown in **Figures 8** and **9**, 300 stochastic simulations are carried out for the final coupled multi-hazard simulation process in the following. The calculation can be completed in less than 1 week using a conventional workstation with parallel processing.

Earthquake–Tsunami Hazard Curves

For each value of 7 magnitudes (i.e., 7.5, 7.75, 8.0, 8.25, 8.5, 8.75, and 9.0), 300 sets of the source parameters $\boldsymbol{\theta}$ are generated using the scaling relationships by Goda et al. (2016). **Figure 4** shows the simulated source parameters (the green dots). Simulated data are in agreement with the source parameter distributions (i.e., green dots are well clustered within the confidence interval of the scaling relationships). Then, 300 simulations are carried out for the earthquake hazard and tsunami hazard analysis, starting from the same stochastic source models.

The CCDFs (**Figure 2D**) in terms of PGA, $S_a(T = 0.3\,\text{s})$, and $S_a(T = 3\,\text{s})$ are shown in **Figures 10A,C,E**, respectively, for all the magnitude values analyzed. The analogous CCDFs for the tsunami wave height are presented in **Figure 11A**. **Figures 10B,D,F** and **11B** show the CCDFs, weighted by the probability values obtained from the discretized Gutenberg–Richter relationship (**Figure 3D**).

As shown in **Figure 2E**, for each IM [i.e., PGA, $S_a(T)$, h, etc.], the summation of the curves presented in **Figures 10B,D,F** and **11B**, multiplied by $\lambda(M \geq 7.375) = 0.183$, leads to the final hazard curves. **Figures 12A–C** shows the final hazard curves, and the 95% confidence interval, for PGA, $S_a(T = 0.3\,\text{s})$, and $S_a(T = 3\,\text{s})$ obtained using the two GMPEs, i.e., Abrahamson et al. (2016), represented with blue lines, and Morikawa and Fujiwara (2013), represented with red lines. In the same figures, the mean seismic hazard curves are represented with black lines. Similarly, **Figure 12D** shows the final tsunami hazard curve and its 95% confidence interval that is very tight around the central estimate curve. It is noteworthy that the steep slope of the final tsunami hazard curve for wave heights greater than 10 m is because the tsunami height cannot be so high in the Sendai plain areas unlike ria-type coastal areas (e.g., Onagawa and Kesennuma), where the wave amplification due to topographical effects is significant.

Seismic Uniform Hazard Spectra and Earthquake–Tsunami Deaggregation

The proposed procedure also facilitates the construction of uniform hazard spectra (UHS) for seismic hazard. By repeating the seismic simulations for several spectral accelerations

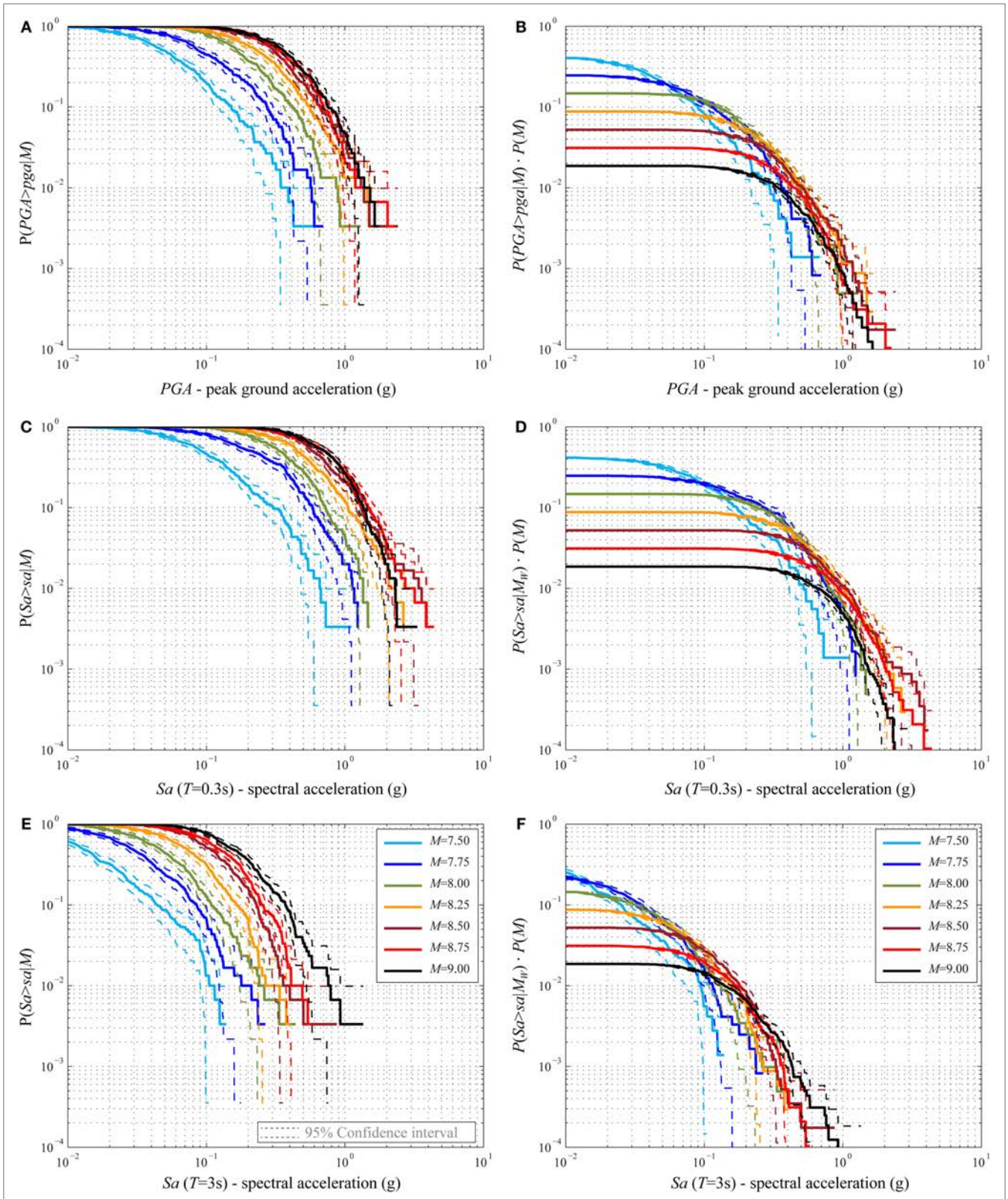

FIGURE 10 | (A) Conditional hazard curve for PGA. **(B)** Weighted conditional hazard curves for PGA. **(C)** Conditional hazard curve for $S_a(T = 0.3\,s)$. **(D)** Weighted conditional hazard curves for $S_a(T = 0.3\,s)$. **(E)** Conditional hazard curve for $S_a(T = 3\,s)$. **(F)** Weighted conditional hazard curves for $S_a(T = 3\,s)$.

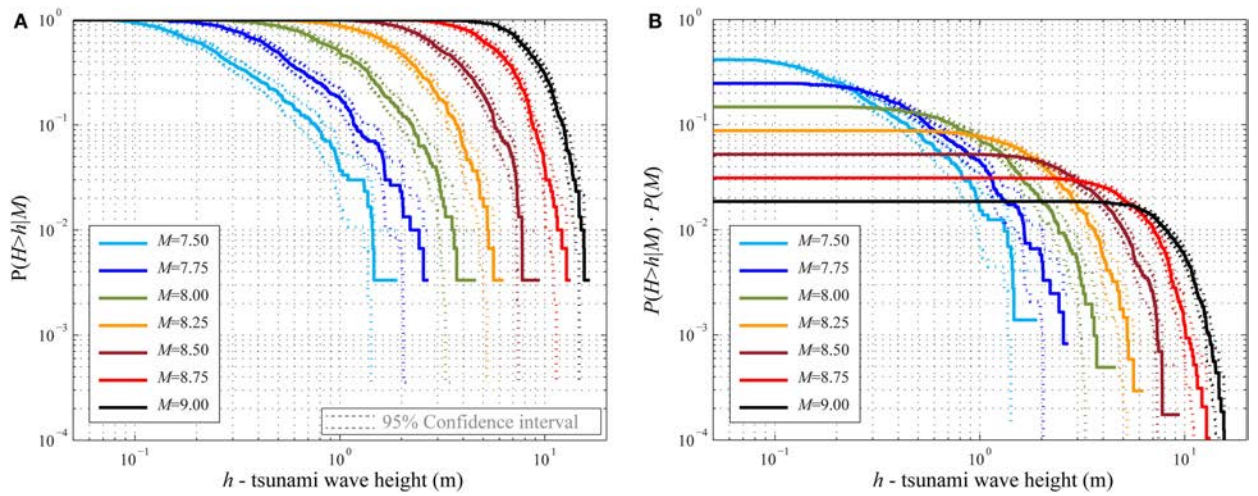

FIGURE 11 | (A) Conditional hazard curve for tsunami wave height. **(B)** Weighted conditional hazard curves for tsunami wave height.

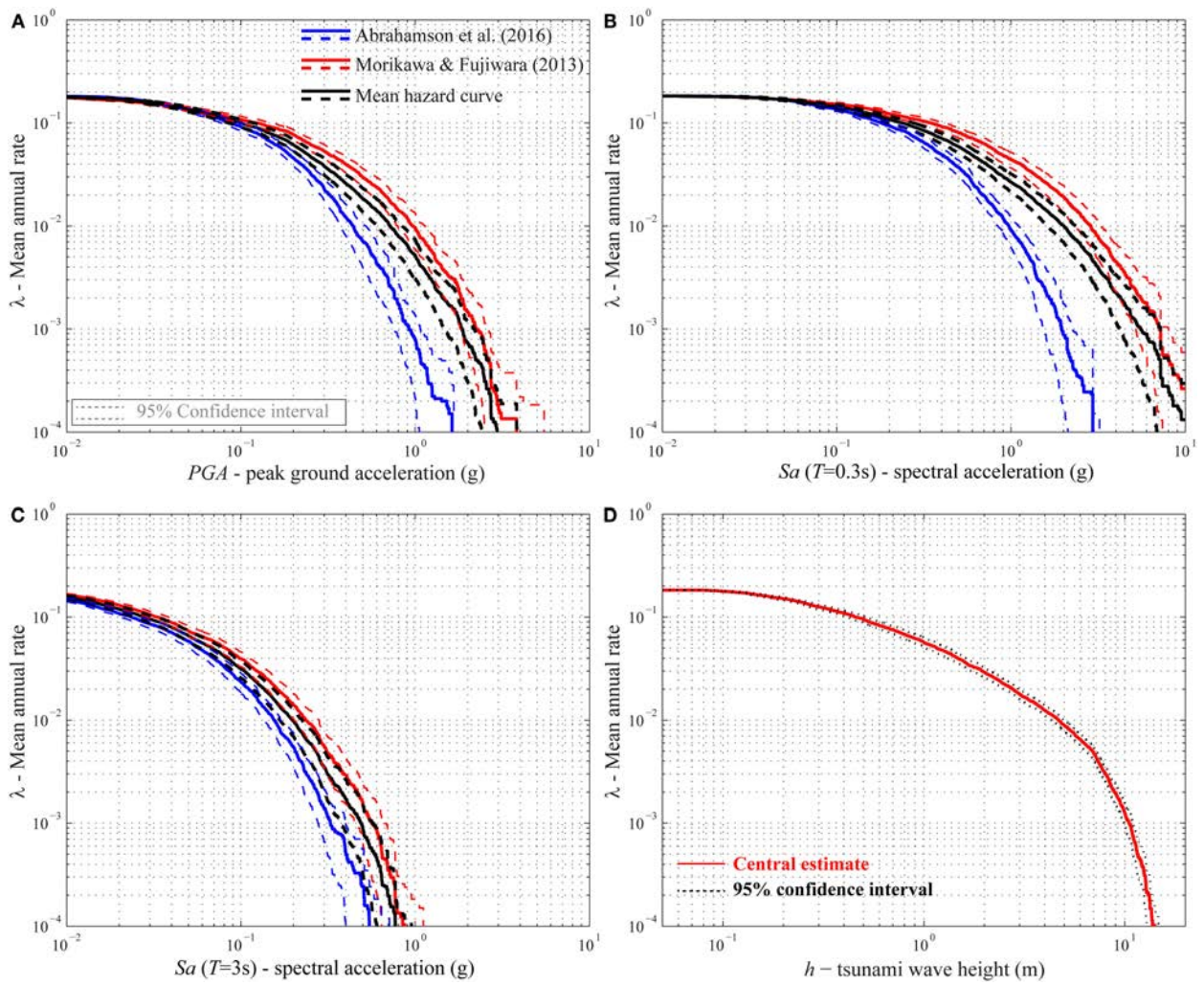

FIGURE 12 | (A) Final seismic hazard curves for PGA. **(B)** Final seismic hazard curves for $S_a(T = 0.3\,s)$. **(C)** Final seismic hazard curves for $S_a(T = 3\,s)$. **(D)** Final tsunami hazard curves.

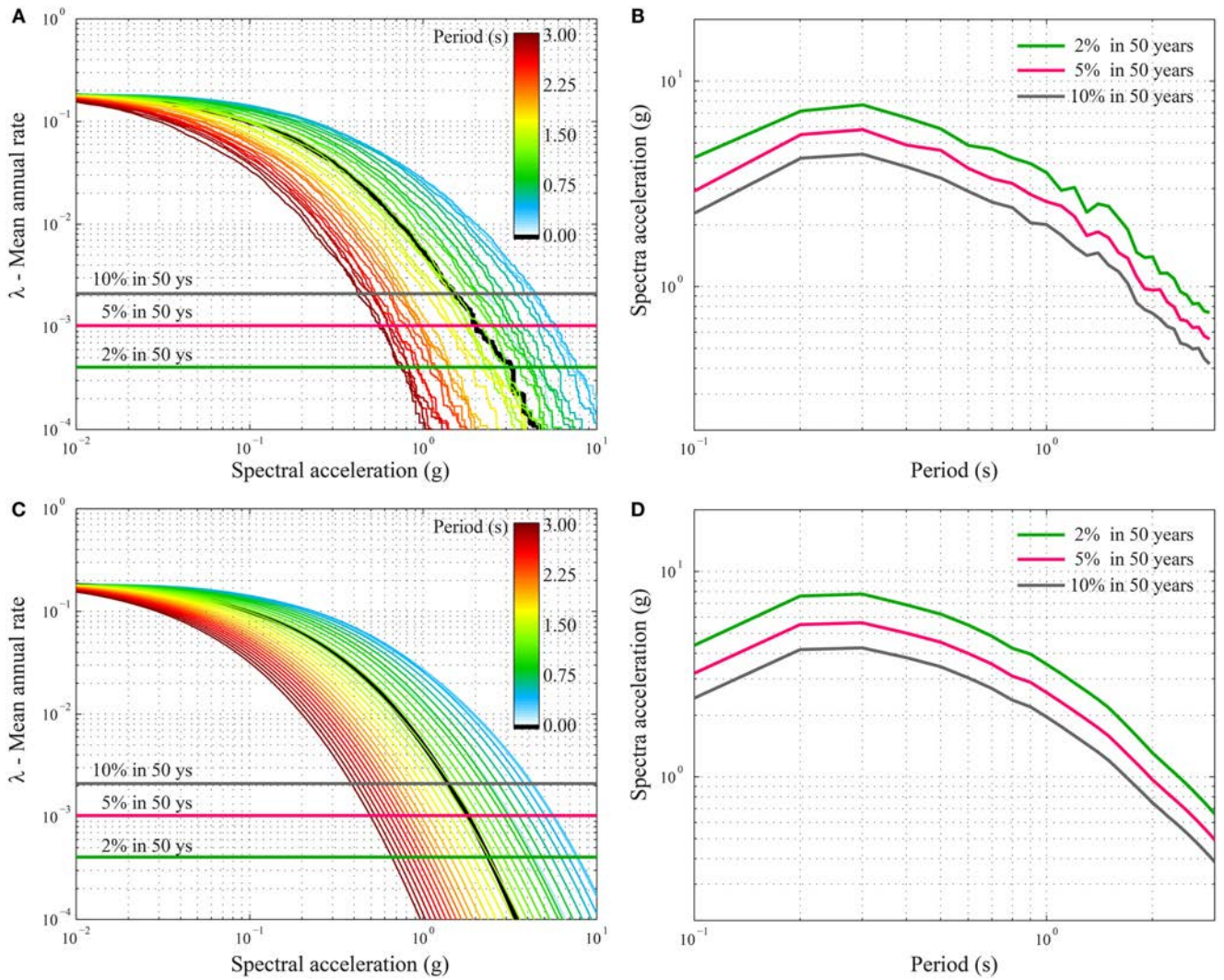

FIGURE 13 | (A) Final seismic hazard curves for intensity parameters from PGA (the black line) to $S_a(T = 3\,s)$ based on 300 simulations. **(B)** Uniform hazard spectra based on 300 simulations. **(C)** Final seismic hazard curves for intensity parameters from PGA (the black line) to $S_a(T = 3\,s)$ based on 300 × 5000 simulations. **(D)** Uniform hazard spectra based on 300 × 5000 simulations.

(**Figure 13A**) and considering specific values of the mean annual rate (e.g., 2, 5, and 10% in 50 years), it is possible to obtain the UHS, as shown in **Figure 13B**. The hazard curves and spectra are jagged because of the limited number of simulations (i.e., 300). Since the seismic simulations are less time consuming with respect to the tsunami simulations, it is possible to increase the number of simulations; in particular, for each scenario, several thousands of simulations can be conducted with a low additional computational effort. **Figure 13C** shows the seismic hazard curves obtained by performing 300 × 5000 simulations (i.e., 5000 simulations for each stochastic simulation). By increasing the number of simulations, the UHS become smooth (**Figure 13D**), and the confidence intervals around the central estimate hazard curves become narrow.

As a byproduct of the procedure, the earthquake–tsunami hazard deaggregation is obtained. Deaggregation shows the relative contributions of dominant seismic scenarios to the specified hazard levels and can be represented in terms of distance and magnitude. The deaggregation of the two hazards for the same mean annual rate of occurrence is demonstrated. **Figure 14** shows the deaggregation results for Sendai by considering PGA (**Figures 14A,C**) and tsunami inundation height (**Figures 14B,D**) corresponding to two values of mean annual rate of occurrence (i.e., 63 and 10% in 50 years). The 10% in 50-year hazard level (corresponding to an event with 475-year return period) is commonly used to describe the life safety limit state, whereas the 63% in 50-year hazard level (corresponding to an event with 50-year return period) corresponds to the damage control limit state (CEN, 2004). It is worth noting that only large magnitude events contribute to higher values of **IM**s. Moreover, as observed before, the larger the magnitude is, the less the distance is influential. Finally, it is interesting to observe that the combinations of magnitude and distance that affect the seismic hazard and tsunami hazard differ significantly.

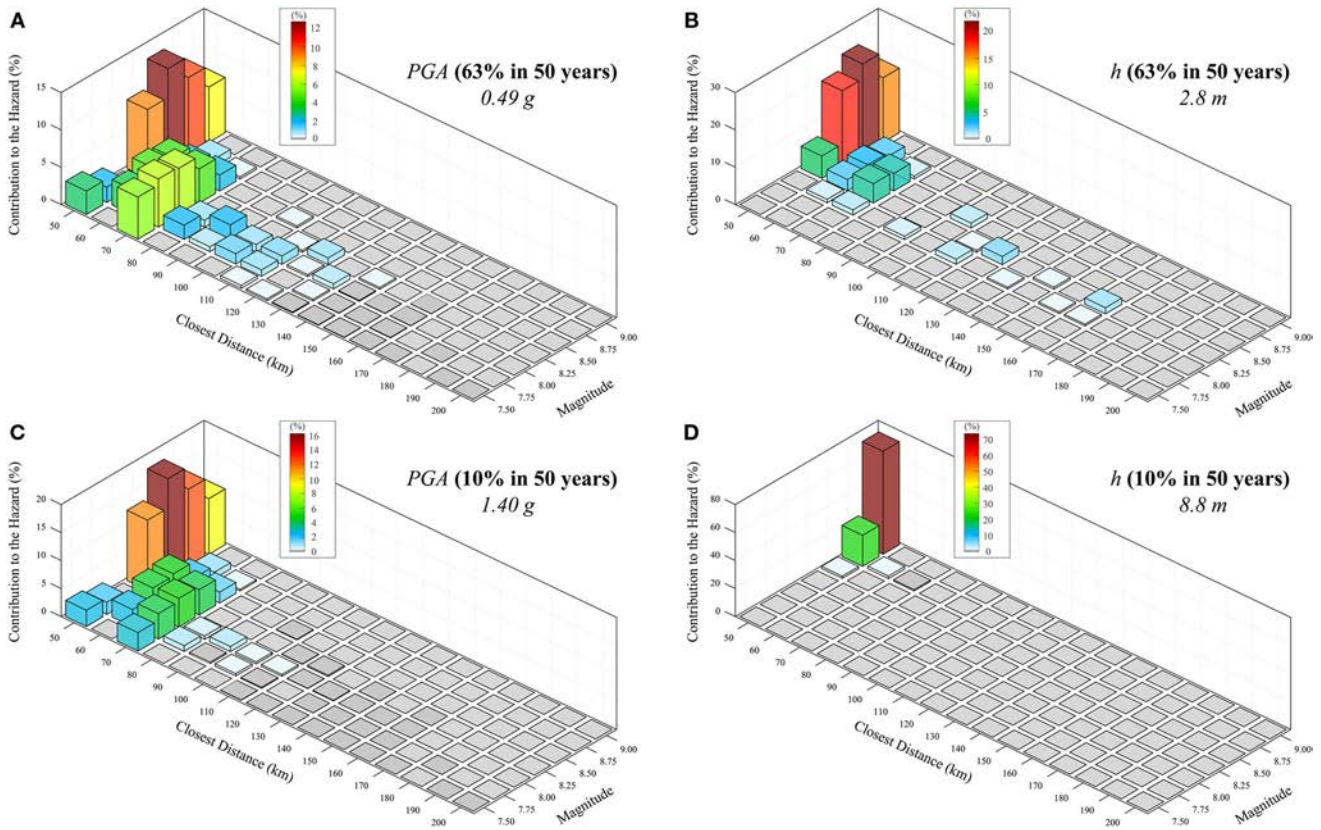

FIGURE 14 | (A) Seismic hazard deaggregation for PGA corresponding to the hazard level of 63% in 50 years. **(B)** Tsunami hazard deaggregation for wave height corresponding to the hazard level of 63% in 50 years. **(C)** Seismic hazard deaggregation for PGA corresponding to the hazard level of 10% in 50 years. **(D)** Tsunami hazard deaggregation for wave height corresponding to the hazard level of 10% in 50 years.

CONCLUSION

A new simulation-based procedure to probabilistically calculate the earthquake–tsunami multi-hazard for specific locations was presented. The simulation framework allows implementing all potential sources of uncertainties, both epistemic and aleatory. The slip distribution on the fault plane was characterized in detail since it represents the major source of uncertainty. To generate a wide range of earthquake scenarios, new global scaling relationships of earthquake source parameters for tsunamigenic events were used. For each discrete magnitude value, multiple realizations of possible earthquake slip distributions were generated. The procedure was applied to the Tohoku region (Japan), and a single point located on the coastline in Sendai City was considered for assessing the concurrent earthquake–tsunami hazard. Three hundred simulations were performed for both seismic and tsunami intensity estimations at each discrete magnitude value. Data obtained from simulations were used to calculate the CCDFs of the considered intensity measures (i.e., spectral acceleration and tsunami inundation height) and their confidence intervals. Finally, such curves were combined with the magnitude–frequency distribution and were summed up in order to obtain the final triplets of earthquake–tsunami hazard curves: one representative of the central estimate and the others corresponding to the 95% confidence interval.

Based on the analysis results, the following conclusions can be drawn:

(a) For the considered case study, 300 simulations were sufficient to obtain a reliable and stable representation of both earthquake and tsunami hazard parameters at a single location, both in terms of central estimates and high percentiles.
(b) Given the same number of simulations and passing from small magnitude to large magnitude, a decrease in the dispersion of the simulation results was observed. This is due to the decreased variability of the earthquake location on the fault, and it also implies a reduction of the confidence interval.
(c) The procedure facilitates the calculation of UHS for seismic hazard and the deaggregation of both seismic and tsunami hazards.

The presented work can be considered a first step toward an earthquake–tsunami multi-hazard performance-based framework; in fact, a multi-risk assessment can be carried out by convoluting the obtained multi-hazard curves with seismic and tsunami

fragility curves. The work can be extended using a Bayesian robust methodology (Cheung and Beck, 2010) to make more reliable estimations of earthquake–tsunami hazards. The proposed method can be further integrated into an operational tool for real-time earthquake–tsunami forecast (Tsushima et al., 2011) using data from offshore buoy and ocean-bottom pressure gauges. Furthermore, the methodology can be expanded to obtain the conditional tsunami or seismic hazard curve, given that a specific value of the counterpart hazard has been selected.

AUTHOR CONTRIBUTIONS

The two co-authors contributed equally to this work.

ACKNOWLEDGMENTS

This work is funded by the Engineering and Physical Sciences Research Council (EP/M001067/1).

REFERENCES

Abrahamson, N., Gregor, N., and Addo, K. (2016). BC hydro ground motion prediction equations for subduction earthquakes. *Earthquake Spectra* 32, 23–44. doi:10.1193/051712EQS188MR

Akkar, S., and Cheng, Y. (2015). Application of a Monte-Carlo simulation approach for the probabilistic assessment of seismic hazard for geographically distributed portfolio. *Earthquake Eng. Struct. Dyn.* 45, 525–541. doi:10.1002/eqe.2667

Annaka, T., Satake, K., Sakakiyama, T., Yanagisawa, K., and Shuto, N. (2007). Logic-tree approach for probabilistic tsunami hazard analysis and its applications to the Japanese coasts. *Pure Appl. Geophys.* 164, 577–592. doi:10.1007/s00024-006-0174-3

Atkinson, G. M., and Goda, K. (2013). "Probabilistic seismic hazard analysis of civil infrastructure: chapter 1, 3–28," in *Handbook of Seismic Risk Analysis and Management of Civil Infrastructure Systems*, eds S. Tesfamariam and K. Goda (Cambridge: Woodhead Publishing), 912.

Billi, A., Funiciello, R., Minelli, L., Faccenna, C., Neri, G., Orecchio, B., et al. (2008). On the cause of the 1908 Messina tsunami, southern Italy. *Geophys. Res. Lett.* 35, L06301. doi:10.1029/2008GL033251

Box, G. E. P., and Cox, D. R. (1964). An analysis of transformations. *J. R. Stat. Soc. Ser. B* 26, 211–252.

Burbidge, D., Cummins, P. R., Mleczko, R., and Thio, H. K. (2008). A probabilistic tsunami hazard assessment for Western Australia. *Pure Appl. Geophys.* 165, 2059–2088. doi:10.1007/s00024-008-0421-x

Burroughs, S. M., and Tebbens, S. F. (2005). Power-law scaling and probabilistic forecasting of tsunami runup heights. *Pure Appl. Geophys.* 162, 331–342. doi:10.1007/s00024-004-2603-5

CEN. (2004). *Eurocode 8: Design of Structures for Earthquake Resistance – Part 1: General Rules, Seismic Actions and Rules for Buildings*. Brussels: Comite International de Normalization.

Cheung, K. F., Wei, Y., Yamazaki, Y., and Yim, S. C. (2011). Modeling of 500-year tsunamis for probabilistic design of coastal infrastructure in the Pacific Northwest. *Coast. Eng. J.* 58, 970–985. doi:10.1016/j.coastaleng.2011.05.003

Cheung, S. H., and Beck, J. L. (2010). Calculation of posterior probabilities for Bayesian model class assessment and averaging from posterior samples based on dynamic system data. *Comput. Aided Civil Infrastruct. Eng.* 25, 304–321. doi:10.1111/j.1467-8667.2009.00642.x

Cornell, C. A. (1968). Engineering seismic risk analysis. *Bull. Seismol. Soc. Am.* 58, 1583–1606.

Downes, G. L., and Stirling, M. W. (2001). "Groundwork for development of a probabilistic tsunami hazard model for New Zealand," in *Proceedings of International Tsunami Symposium, Session 1* (Seattle, USA: National Oceanic and Atmospheric Administration), 293–301.

Farreras, S., Ortiz, M., and Gonzalez, J. I. (2007). Steps towards the implementation of a tsunami detection, warning, mitigation and preparedness program for southwestern coastal areas of Mexico. *Pure Appl. Geophys.* 164, 605–616. doi: 10.1007/s00024-006-0175-2

Fukutani, Y., Suppasri, A., and Imamura, F. (2016). Stochastic analysis and uncertainty assessment of tsunami wave height using a random source parameter model that targets a Tohoku-type earthquake fault. *Stoch. Environ. Res. Risk Assess.* 29, 1763–1779. doi:10.1007/s00477-014-0966-4

Geist, E. L. (2002). Complex earthquake rupture and local tsunamis. *J. Geophys. Res. Solid Earth* 107, ESE 2-1–ESE 2-15. doi:10.1029/2000JB000139

Geist, E. L. (2005). *Local Tsunami Hazards in the Pacific Northwest from Cascadia Subduction Zone Earthquakes*. Reston: U.S. Geological Survey, 17. Professional Paper 1661-B.

Geist, E. L., and Dmowska, R. (1999). Local tsunamis and distributed slip at the source. *Pure Appl. Geophys.* 154, 485–512. doi:10.1007/s000240050241

Geist, E. L., and Parsons, T. (2006). Probabilistic analysis of tsunami hazards. *Nat. Hazards* 37, 277–314. doi:10.1007/s11069-005-4646-z

Goda, K. (2011). Interevent variability of spatial correlation of peak ground motions and response spectra. *Bull. Seismol. Soc. Am.* 101, 2522–2531. doi:10.1785/0120110092

Goda, K., and Atkinson, G. M. (2010). Intraevent spatial correlation of ground-motion parameters using SK-net data. *Bull. Seismol. Soc. Am.* 100, 3055–3067. doi:10.1785/0120100031

Goda, K., and Atkinson, G. M. (2014). Variation of source-to-site distance for megathrust subduction earthquakes: effects on ground motion prediction equations. *Earthquake Spectra* 30, 845–866. doi:10.1193/080512EQS254M

Goda, K., Mai, P. M., Yasuda, T., and Mori, N. (2014). Sensitivity of tsunami wave profiles and inundation simulations to earthquake slip and fault geometry for the 2011 Tohoku earthquake. *Earth Planets Space* 66:105. doi:10.1186/1880-5981-66-105

Goda, K., Yasuda, T., Mori, N., and Maruyama, T. (2016). New scaling relationships of earthquake source parameters for stochastic tsunami simulation. *Coast. Eng. J.* 58:1650010. doi:10.1142/S0578563416500108

González, F. I., Geist, E. L., Jaffe, B., Kânoglu, U., Mofjeld, H., Synolakis, C. E., et al. (2009). Probabilistic tsunami hazard assessment at Seaside, Oregon, for near- and far-field seismic sources. *J. Geophys. Res. Oceans* 114, C11023. doi:10.1029/2008JC005132

Goto, C., Ogawa, Y., Shuto, N., and Imamura, F. (1997). *Numerical Method of Tsunami Simulation with the Leap-Frog Scheme (IUGG/IOC Time Project), IOC Manual*. Paris, France: UNESCO.

Greenwood, M. (1926). *The Natural Duration of Cancer. Reports on Public Health and Medical Subjects*, Vol. 33. London: Her Majesty's Stationery Office, 1–26.

Grezio, A., Gasparini, P., Marzocchi, W., Patera, A., and Tinti, S. (2012). Tsunami risk assessments in Messina, Sicily – Italy. *Nat. Hazards Earth Syst. Sci.* 12, 151–163. doi:10.5194/nhess-12-151-2012

Grezio, A., Marzocchi, W., Sandri, L., and Gasparini, P. (2010). A Bayesian procedure for probabilistic tsunami hazard assessment. *Nat. Hazards* 53, 159–174. doi:10.1007/s11069-009-9418-8

Guidoboni, E., and Comastri, A. (1997). The large earthquake of 8 August 1303 in Crete: seismic scenario and tsunami in the Mediterranean area. *J. Seismol.* 1, 55–72. doi:10.1023/A:1009737632542

Gutenberg, B., and Richter, C. F. (1956). Magnitude and energy of earthquakes. *Ann. Geophys.* 9, 1–15.

Headquarters for Earthquake Research Promotion. (2013). *Investigations of Future Seismic Hazard Assessment*. Tokyo: Japanese Govern, 217.

Horspool, N., Pranantyo, I., Griffin, J., Latief, H., Natawidjaja, D. H., Kongko, W., et al. (2014). A probabilistic tsunami hazard assessment for Indonesia. *Nat. Hazards Earth Syst. Sci.* 14, 3105–3122. doi:10.5194/nhess-14-3105-2014

Kaplan, E. L., and Meier, P. (1958). Nonparametric estimation from incomplete observations. *J. Am. Stat. Assoc.* 53, 457–481. doi:10.1080/01621459.1958.10501452

Lamarre, M., Townshend, B., and Shah, H. C. (1992). Application of the bootstrap method to quantify uncertainty in seismic hazard estimates. *Bull. Seismol. Soc. Am.* 82, 104–119.

Latter, J. H. (1981). Tsunamis of volcanic origin: summary of causes, with particular reference to Krakatoa, 1883. *Bull. Volcanol.* 44, 467–490. doi:10.1007/BF02600578

Lavallée, D., Liu, P., and Archuleta, R. J. (2006). Stochastic model of heterogeneity in earthquake slip spatial distributions. *Geophys. J. Int.* 165, 622–640. doi:10.1111/j.1365-246X.2006.02943.x

Liu, Y., Santos, A., Wang, S. M., Shi, Y., Liu, H., and Yuen, D. A. (2007). Tsunami hazards along Chinese coast from potential earthquakes in South China Sea. *Phys. Earth Planet. Inter.* 163, 233–244. doi:10.1016/j.pepi.2007.02.012

Løvholt, F., Glimsdal, S., Harbitz, C. B., Horspool, N., Smebye, H., de Bono, A., et al. (2014). Global tsunami hazard and exposure due to large co-seismic slip. *Int. J. Disaster Risk Reduct.* 10, 406–418. doi:10.1016/j.ijdrr.2014.04.003

Løvholt, F., Glimsdal, S., Harbitz, C. B., Zamora, N., Nadim, F., Peduzzi, P., et al. (2012). Tsunami hazard and exposure on the global scale. *Earth-Sci. Rev.* 110, 58–73. doi:10.1016/j.earscirev.2011.10.002

Mai, P. M., and Beroza, G. C. (2002). A spatial random field model to characterize complexity in earthquake slip. *J. Geophys. Res. Solid Earth* 107, ESE 10-1–ESE 10-21. doi:10.1029/2001JB000588

Mai, P. M., and Thingbaijam, K. K. S. (2014). SRCMOD: an online database of finite-fault rupture models. *Seismol. Res. Lett.* 85, 1348–1357. doi:10.1785/0220140077

Matthews, M. V., Ellsworth, W. L., and Reasenberg, P. A. (2002). A Brownian model for recurrent earthquakes. *Bull. Seismol. Soc. Am.* 92, 2233–2250. doi:10.1785/0120010267

McGuire, R. K. (2008). Probabilistic seismic hazard analysis: early history. *Earthquake Eng. Struct. Dyn.* 37, 329–338. doi:10.1002/eqe.765

Ministry of Land, Infrastructure, and Transportation (MLIT). (2014). *Survey of Tsunami Damage Condition*. Available at: http://www.mlit.go.jp/toshi/toshi-hukkou-arkaibu.html

Mofjeld, H. O., González, F. I., Titov, V. V., Venturato, A. J., and Newman, J. C. (2007). Effects of tides on maximum tsunami wave heights: probability distributions. *J. Atmos. Oceanic Technol.* 24, 117–123. doi:10.1175/JTECH1955.1

Monastersky, R. (2012). The next wave. *Nature* 483, 144–146. doi:10.1038/483144a

Morikawa, N., and Fujiwara, H. (2013). A new ground motion prediction equation for Japan applicable up to M9 mega-earthquake. *J. Disaster Res.* 8, 878–888. doi:10.20965/jdr.2013.p0878

NGDC. (2016). *National Geophysical Data Center (NGDC WDS) Global Historical Tsunami Database*. Boulder, CO, USA. Available at: https://www.ngdc.noaa.gov/hazard/tsu_db.shtml

Okada, Y. (1985). Surface deformation due to shear and tensile faults in a half-space. *Bull. Seismol. Soc. Am.* 75, 1135–1154.

Orfanogiannaki, K., and Papadopoulos, G. A. (2007). Conditional probability approach of the assessment of tsunami potential: application in three tsunamigenic regions of the Pacific Ocean. *Pure Appl. Geophys.* 164, 593–603. doi:10.1007/s00024-006-0170-7

Pardo-Iguzquiza, E., and Chica-Olmo, M. (1993). The Fourier integral method: an efficient spectral method for simulation of random fields. *Math. Geol.* 25, 177–217. doi:10.1007/BF00893272

Parsons, T., and Geist, E. L. (2008). Tsunami probability in the Caribbean region. *Pure Appl. Geophys.* 165, 2089–2116. doi:10.1007/s00024-008-0416-7

Power, W., Downes, G., and Stirling, M. (2007). Estimation of tsunami hazard in New Zealand due to South American earthquakes. *Pure Appl. Geophys.* 164, 547–564. doi:10.1007/s00024-006-0166-3

Satake, K. (2001). "Tsunami modeling from submarine landslides," in *Proceedings of the International Tsunami Symposium, Session 6* (Seattle, USA: National Oceanic and Atmospheric Administration), 665–674.

Satake, K., Fujii, Y., Harada, T., and Namegaya, Y. (2013). Time and space distribution of coseismic slip of the 2011 Tohoku earthquake as inferred from tsunami waveform data. *Bull. Seismol. Soc. Am.* 103, 1473–1492. doi:10.1785/0120120122

Tanioka, Y., and Satake, K. (1996). Tsunami generation by horizontal displacement of ocean bottom. *Geophys. Res. Lett.* 23, 861–864. doi:10.1029/96GL00736

Thio, H. K., Somerville, P., and Ichinose, G. (2007). Probabilistic analysis of strong ground motion and tsunami hazards in Southeast Asia. *J. Earthquake Tsunami* 1, 119–137. doi:10.1142/S1793431107000080

Tinti, S., Armigliato, A., Tonini, R., Maramai, A., and Graziani, L. (2005). Assessing the hazard related to tsunamis of tectonic origin: a hybrid statistical-deterministic method applied to southern Italy coasts. *ISET J. Earthquake Technol.* 42, 189–201.

Tsushima, H., Hirata, K., Hayashi, Y., Tanioka, Y., Kimura, K., Sakai, S. I., et al. (2011). Near-field tsunami forecasting using offshore tsunami data from the 2011 off the Pacific coast of Tohoku earthquake. *Earth Planets Space* 63, 821–826. doi:10.5047/eps.2011.06.052

USGS ShakeMap Archive. (2016). *The 2011 Tohoku Earthquake*. Available at: http://earthquake.usgs.gov/earthquakes/shakemap/global/shake/c0001xgp/

Wald, D. J., Worden, B. C., Quitoriano, V., and Pankow, K. L. (2006). *ShakeMap Manual: Technical Manual, User's Guide, and Software Guide*. Reston: United States Geological Survey, 156.

Wald, D. J., and Allen, T. I. (2007). Topographic slope as a proxy for seismic site conditions and amplification. *Bull. Seismol. Soc. Am.* 97, 1379–1395. doi:10.1785/0120060267

Ward, S. N. (2001). Landslide tsunami. *J. Geophys. Res. Solid Earth* 106, 11201–11215. doi:10.1029/2000JB900450

Ward, S. N., and Asphaug, E. (2000). Asteroid impact tsunami: a probabilistic hazard assessment. *Icarus* 145, 64–78. doi:10.1006/icar.1999.6336

Watts, P. (2004). Probabilistic predictions of landslide tsunamis off Southern California. *Mar. Geol.* 203, 281–301. doi:10.1016/S0025-3227(03)00311-6

Yanagisawa, K., Imamura, F., Sakakiyama, T., Annaka, T., Takeda, T., and Shuto, N. (2007). Tsunami assessment for risk management at nuclear power facilities in Japan. *Pure Appl. Geophys.* 164, 565–576. doi:10.1007/s00024-006-0176-1

Zhao, J. X., Zhang, J., Asano, A., Ohno, Y., Oouchi, T., Takahashi, T., et al. (2006). Attenuation relations of strong ground motion in Japan using site classification based on predominant period. *Bull. Seismol. Soc. Am.* 96, 898–913. doi:10.1785/0120050122

Conflict of Interest Statement: The authors declare that the research was conducted in the absence of any commercial or financial relationships that could be construed as a potential conflict of interest.

Copyright © 2016 De Risi and Goda. This is an open-access article distributed under the terms of the Creative Commons Attribution License (CC BY). The use, distribution or reproduction in other forums is permitted, provided the original author(s) or licensor are credited and that the original publication in this journal is cited, in accordance with accepted academic practice. No use, distribution or reproduction is permitted which does not comply with these terms.

frontiers in Built Environment

ORIGINAL RESEARCH
published: 15 June 2017
doi: 10.3389/fbuil.2017.00032

Probabilistic Seismic and Tsunami Hazard Analysis Conditioned on a Megathrust Rupture of the Cascadia Subduction Zone

Hyoungsu Park, Daniel T. Cox, Mohammad Shafiqual Alam and Andre R. Barbosa*

School of Civil and Construction Engineering, Oregon State University, Corvallis, OR, United States

This paper presents a methodology for probabilistic hazard assessment for the multi-hazard seismic and tsunami phenomena [probabilistic seismic and tsunami hazard analysis (PSTHA)]. For this work, a full-rupture event along the Cascadia subduction zone is considered and the methodology is applied to a study area of Seaside, Oregon, which is located on the US Pacific Northwest coast. In this work, the annual exceedance probabilities (AEPs) of the tsunami intensity measures (*IM*s) are shown to be qualitatively dissimilar to the *IM*s of the seismic ground motion in the study area. Specifically, the spatial gradients for the tsunami *IM* are much stronger across the length scale of the study area owing to the physical differences of wave propagation and energy dissipation of the two mechanisms. Example results of probabilistic seismic hazard analysis and probabilistic tsunami hazard analysis are shown for three observation points in the study area of Seaside. For the seismic hazard, the joint mean annual rate of exceedance of *IM*s shows similar trends for the three observation points, even though for a given observation point there is a large scatter between two ground-motion *IM*s analyzed, which were peak ground acceleration (PGA) and spectral acceleration at a period of vibration of 0.3 s, i.e., PGA and S_a ($T_1 = 0.3$ s). For the tsunami hazard, the joint AEP of maximum flow depth (h_{max}) and maximum momentum flux ((M_F)$_{max}$) shows a high correlation between the two *IM*s in the study area. The joint AEP at each of the three observation points follows a particular Froude number (*Fr*) due to the local site-specific conditions rather than the distributions of fault slip distributions used to generate the scenarios that are the basis of the AEP maps developed. The joint probability distribution of h_{max} and (M_F)$_{max}$ throughout the study region falls between $0.1 \leq Fr < 1.0$ (i.e., the flow is subcritical), regardless of return interval (500-, 1,000-, and 2,500-year). However, the peak of the joint probability distribution with respect to h_{max} and (M_F)$_{max}$ varies with the return interval, and the largest values of h_{max} and (M_F)$_{max}$ were observed with the highest return intervals (2,500 years) as would be expected. The results of the PSTHA can be the basis for a probabilistic multi-hazard damage and loss assessment and help to evaluate the uncertainties of the multi-hazard assessments.

Keywords: seismic hazard analysis, tsunami hazard analysis, multi-hazard risk, Cascadia subduction zone, community resilience

OPEN ACCESS

Edited by:
Katsuichiro Goda,
University of Bristol, United Kingdom

Reviewed by:
Panon Latcharote,
Tohoku University, Japan
Andreas Maximilian Schaefer,
Karlsruhe Institute of Technology, Germany

****Correspondence:***
Hyoungsu Park
hyoungsu.park@gmail.com

Specialty section:
This article was submitted to Earthquake Engineering, a section of the journal Frontiers in Built Environment

Received: *17 March 2017*
Accepted: *11 May 2017*
Published: *15 June 2017*

Citation:
Park H, Cox DT, Alam MS and Barbosa AR (2017) Probabilistic Seismic and Tsunami Hazard Analysis Conditioned on a Megathrust Rupture of the Cascadia Subduction Zone. Front. Built Environ. 3:32. doi: 10.3389/fbuil.2017.00032

INTRODUCTION

Over the past decade and a half, megathrust earthquakes accompanied by near-field tsunamis have devastated coastal regions throughout the world, including the 2004 Indian Ocean tsunami (e.g., Jaffe et al., 2006; Rossetto et al., 2007), events in Chile in 2010 (e.g., Mas et al., 2012), and the 2011 Tohoku tsunami (e.g., Mori et al., 2013). These events remind us that when assessing for life safety, it is often desirable to plan for a "worst case" or "most credible" scenario. However, when considering damage to the built environment, it is often more practical to employ risk-informed decision-making to help minimize the overall damage, annualized financial loss, and increase the rate of recovery. In other words, risk-based decisions can increase the overall resilience of a community to earthquake and tsunami events. However, risk-based methods require a probabilistic understanding of the hazard. The case of subduction zone (SZ) earthquakes and tsunamis is particularly challenging because of the multi-hazard phenomena. A large building located in the megathrust earthquake region and in a potentially tsunami prone zone, for example, will first experience intense ground shaking followed by the subsequent hydrodynamic demands imposed by the tsunami. Liquefaction, local scour, landslides, debris, and other cascading consequences further exacerbate the problem. This paper marks one of the first attempts to provide a methodology for conducting a joint hazard analysis, which is termed as probabilistic seismic and tsunami hazard analysis (PSTHA), by combining probabilistic seismic hazard analysis (PSHA) with probabilistic tsunami hazard analysis (PTHA) based on a consistent process for concurrent earthquake occurrence and tsunami generation. As an illustrative example, the PSTHA is applied to a coastal community based on a conditional rupture of the Cascadia subduction zone (CSZ) along the northwest coast of North America.

Background and Literature Review

Probabilistic seismic hazard analysis provides the evaluation of annual frequencies of exceedance of ground motion intensity measures (*IMs*) [typically designated by peak ground acceleration (PGA) or by linear elastic damped response spectral ordinates at specific periods of vibration] at a site. The result of a PSHA is a seismic hazard curve [annual frequency of exceedance versus ground-motion intensity measure (*IM*) amplitude], a uniform hazard spectrum (spectral amplitude versus structural period, for a fixed annual frequency of exceedance), or conditional mean spectrum (Baker, 2011; Lin et al., 2013). First reports of PSHA date back to the 1960s. Since then, PSHA has become the basis for seismic assessment and design of new and existing engineered facilities ranging from civil structures, such as buildings and bridges, to critical facilities, such as nuclear power plants. In PSHA, all possible earthquake fault sources contributing to the hazard need to be characterized first. Second, ground-motion prediction equations (GMPEs) are used to relate ground-motion *IM*s to variables describing earthquake source, path, and site effects. Extensive research has been performed on GMPEs for use in PSHA. Douglas (2003, 2011, 2016) summarized over 400 GMPEs that were developed since 1964–2016 for estimation of PGA and over 250 GMPEs for estimation of spectral ordinates at a site. Douglas and Edwards (2016) provides a recent discussion of current and future trends in ground-motion prediction. Stewart et al. (2015) provides a discussion of the selection of GMPEs for hazard assessments for the three principal tectonic regimes: active crustal regions, SZs, and stable continental regions for a global earthquake model. Of interest to this paper, Stewart et al. (2015) recommended the use of three models for SZ ground-motion predictions, "BC Hydro" model of Abrahamson et al. (2016), the global earthquake model described in Atkinson and Boore (2003), and the model in the study by Zhao et al. (2006). The BC Hydro model was developed using different data sets of SZ strong-motion recordings (e.g., Crouse et al., 1988; Crouse, 1991; Youngs et al., 1997; Atkinson and Boore, 2003, 2008; Zhao et al., 2006; Lin and Lee, 2008). While GMPEs are most often used for PSHA, it is worth noting that other methods for generating the *IM*s that involve the generation of synthetic ground motions have also been recently proposed, however, all involving extremely computational intensive methods. These methods that could serve as alternatives to the GMPEs include kinematic earthquake models (e.g., Olsen et al., 2008; Frankel et al., 2014; Pulido et al., 2015; Iwaki et al., 2016), stochastic finite-fault ground-motion methods (e.g., Atkinson et al., 2009), or hybrid broadband ground-motion methods (e.g., Atkinson et al., 2011; Skarlatoudis et al., 2015).

Relative to PSHA, only recently has there been much work on PTHA. Mori et al. (submitted)[1] summarized 30 PTHA studies conducted worldwide, all but one of which were conducted after the 2004 Indian Ocean tsunami. Prior to the 2004 event, tsunami hazards were generally characterized by "worst credible" or "worst case" scenarios. Rikitake and Aida (1988) were the first to use historical records of past run-up events to characterize the probability of the tsunami run-up hazard in Japan. Subsequent to the 2004 event and with the more recent SZ tsunami events in Chile in 2010 and in Japan in 2011, there has been an increasing interest in developing PTHA. Studies have focused on regions throughout the Pacific Rim, including Japan (Burroughs and Tebbens, 2005; Annaka et al., 2007; Yanagisawa et al., 2007; Fukutani et al., 2015; and Goda and Song, 2016), the US Pacific Coast and Canada (Geist and Parsons, 2006; González et al., 2009; Thio and Somerville, 2009; Priest et al., 2010; Witter et al., 2013; Leonard et al., 2014; and Park and Cox, 2016), South China Sea (Liu et al., 2007; Li et al., 2016), New Zealand, and Australia (Power et al., 2007, 2013; Burbidge et al., 2008; and Mueller et al., 2015), as well as places in Europe (Tinti et al., 2005; Grezio et al., 2010; Anita et al., 2012) and the Northwestern Indian Ocean (Thio et al., 2007; Heidarzadeh and Kijko, 2011). As explained in the study by see text footnote 1, the PTHA generally uses one of three approaches for the tsunami generation: (1) historical record approach, (2) logic-tree approach, and (3) random phase approach. Generally, the historical record of tsunamis is not sufficient to build a credible probabilistic model. Therefore, the second two approaches are favored. The logic-tree approach (e.g., Park and Cox, 2016) is based on combinations of slip conditions (e.g., magnitude, peak slip location, and slip distribution), and these combinations are given a weighting based on expert opinion, historical record, or

[1]Mori, N., Goda, K., and Cox, D. T. (submitted). "Recent progress in probabilistic tsunami hazard analysis (PTHA) for mega thrust subduction earthquakes," in *Reconstruction and Restoration after the 2011 Japan Earthquake and Tsunami* (Springer).

equal weighting in some cases. For the random phase approach (e.g., Goda et al., 2014), the slip distributions are created by an assumed slip wavenumber spectrum using random phases. For this paper, the logic-tree approach is used since it is straightforward to combine PTHA with the PSHA. In general, the output of the PTHA focuses on the flow depth at the shoreline, the maximum extent of inundation for planning, the evaluation of annual exceedance probabilities (AEPs), or the estimation of the extent of damage through a probabilistic tsunami damage analysis (e.g., Wiebe and Cox, 2014; Park et al., 2017).

The authors are aware of only one study by De Risi and Goda, 2016 (DG16 hereafter), which considers the combined PSTHA. In that paper, the authors present a consistent method to account for a common rupture process. They use GMPEs based on magnitude and rupture distance to quantify the shaking intensity at a particular location subjected to a SZ earthquake, and then solve the shallow water wave equations for tsunami propagation and inundation from the source to the site of interest. The main output of their work is seismic hazard curves and tsunami hazard curves that represents the mean annual rate (MAR) of exceedance of a given *IM*. Their generalized framework was applied for assessing combined earthquake and tsunami hazard at a single location on the coast line of Sendai City based on the subduction fault plane in the Tohoku region of Japan.

Study Objectives and Outline

Similar to the work of DG16, the objective of this work is to develop a consistent framework for a multi-hazard analysis considering large magnitude SZ earthquakes and a subsequent near-field tsunami. However, the study performed herein is developed for a different site with a different methodology to define earthquake and tsunami sources when compared to DG16. The long-term objective is to be able to use the PSTHA as the basis for a probabilistic multi-hazard damage assessment to quantify the separate contributions of seismicity and tsunami hazards in the estimation of damage to the built environment at a community scale or for design of specific infrastructure elements such as a critical facility. A general methodology is first presented in Section "Methodology," with a general review of the combined probabilistic hazard analysis (PHA) methodology proposed (see General PHA Methodology), the earthquake fault source models and their characteristics (see Earthquake Fault Source Models and Their Characteristics), the GMPEs used (see Earthquake Simulation), and the tsunami generation, propagation, and inundation (see Tsunami Generation, Propagation, and Inundation). Then, the multi-hazard logic-tree model is presented (see Multi-Hazard Logic-Tree Model), and the methods to estimate the AEP (see Estimates of the AEP) are presented next. In Section "Application: Full-Rapture Event of the CSZ Impacting the City of Seaside, OR," the methodology is applied to an application example in which the combined seismic and tsunami hazard are quantified for the City of Seaside on the Oregon Coast of the US Pacific Northwest, conditional on a full rupture of the CSZ. In this application, the CSZ earthquake source model, and the geological, geographic, and morphological features of the City of Seaside, Oregon, are characterized first (see Characterization of the Source) and then details of the CSZ fault model and tsunami model (see CSZ Fault Modeling) are provided. In Section "Results," results are presented in terms of the seismicity (see Seismicity) and tsunami intensity (see Tsunami Intensity) estimated for the area of interest. A spatial representation of both the seismic and tsunami intensity is presented, including the study of the granularity needed to characterize the hazards and joint distribution for different vector-valued *IM*s (see Spatial Representations Seismic and Tsunami Hazard). Finally, in Section "Summary, Conclusion, and Future Work," discussion and summary of the results are provided, followed by the conclusion and recommendations for future research.

METHODOLOGY

The methodology for consistent PSTHA is presented in this section. The methodology behind PSHA is well known (e.g., McGuire, 2004). However, a few adaptations are required for performing the combined PSTHA. The statistical earthquake model behind PSTHA is the same for PSHA and PTHA, although in PSHA the earthquakes generated solely inland do not contribute to the tsunami hazard. Even though the statistical earthquake model may be the same, the methods used in PSHA and PTHA for propagation of the effects of a fault slip to a specific site of interest vary. For PSHA, GMPEs are most often used. The GMPEs relate a certain moment release on an earthquake source (a line source or an area source) and the source-to-site rupture distance (or in a few instances, the hypocentral distance) to the ground-motion *IM*s. For the tsunami hazards, and due to the way tsunamis are generated, instead of using equations analogous to GMPEs, the conscientious decision is made herein of using the waveform excitation and propagation approach by solving non-linear shallow water equations [e.g., the "Method of Splitting Tsunami" (MOST) model, Titov et al., 2011] in which an earthquake, transoceanic propagation, and inundation of dry land are modeled. This type of detailed modeling of the tsunami propagation is analogous to computationally intensive recent trends in PSHA, which involves the use of methods for generating ensembles of synthetic ground-motion time histories as described above.

General PHA Methodology

The general formulation presented here is aimed at developing the probabilistic earthquake and tsunami hazard at a site. In this formulation, the first topic that has to be addressed is the definition of an *IM* for the hazard. For example, with respect to earthquake ground shaking, typical measures of interest are spectral acceleration (S_a), while common *IM*s used for the tsunami hazard are the inundation flow depth (h), flow velocity (V), and specific momentum flux ($M_F = hV^2$). Since there is great uncertainty in the quantification of the earthquake that induces ground shaking and possible tsunamis, be it in the focal mechanism including definition of the location (e.g., location of the epicenter, extension of fault rupture), size (magnitude), and resulting intensity of a future earthquake at a specific site of interest, PSHA (e.g., Cornell, 1968; McGuire, 1995; Kramer, 1996) was developed as an analytical tool to characterize the seismic hazard probabilistically. PSHA has become the most widely used method for assessing seismic hazard at a specific site. More recently, PTHA has also been developed (PTHA—e.g., Geist and Parsons, 2006; Annaka et al., 2007; Power

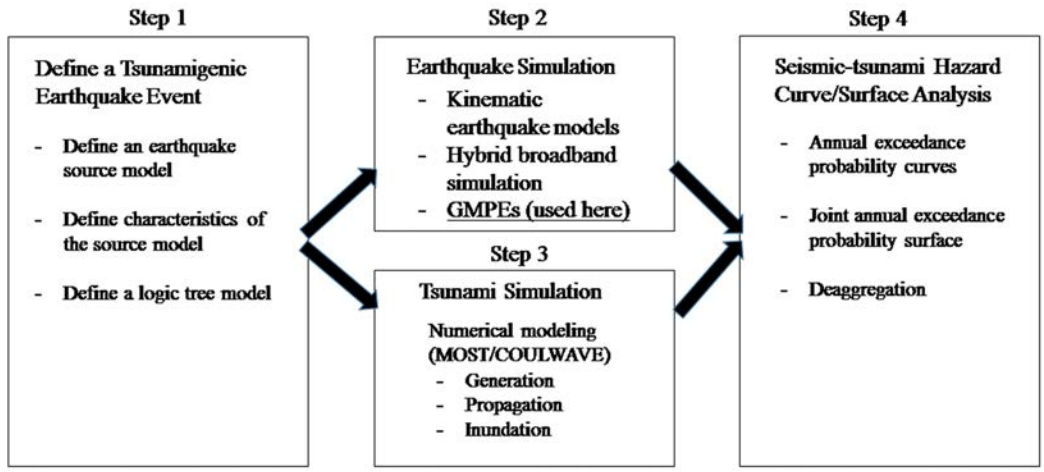

FIGURE 1 | Flow chart of methodology used for probabilistic seismic and tsunami hazard analysis.

et al., 2007) as reviewed by see text footnote 1 and summarized in Section "Background and Literature Review."

The general PHA provides the MAR(λ) of *IM* exceeding an intensity measure value *im* that is computed using the Total Probability Theorem (Benjamin and Cornell, 1970), by integrating the contributions of all possible tsunami-seismogenic sources, and for each of the sources, all possible values of earthquake magnitude as

$$\lambda_{IM>im}(im) = \sum_{i=1}^{N_{\text{sources}}} \lambda_i(M \geq m_{\min}) \times \int_{\boldsymbol{\Theta}} \int_{m_{\min}}^{m_{\max}} P(IM > im|\,\boldsymbol{\Theta}, M) s_{\boldsymbol{\Theta}_i}(\boldsymbol{\Theta}|\,M) f_{M_i}(m) dm\, d\boldsymbol{\Theta} \quad (1)$$

where N_{sources} denotes the total number of seismic sources contributing to the hazard at the site, $\lambda_i(M \geq m_{\min})$ is the MAR of occurrence of earthquakes with magnitude greater than a lower bound threshold value, $m_{\min}$, of seismic source *i*, $P\,(IM > im|\boldsymbol{\Theta},M)$ represents the probability that intensity measure *IM* will exceed a given intensity value *im* at the site conditional on a given magnitude *M* and source parameters $\boldsymbol{\Theta}$, $s_{\boldsymbol{\Theta}_i}(\boldsymbol{\Theta}|\,M)$ represents the characteristic probability density function (PDF) of earthquake source parameters $\boldsymbol{\Theta}$ obtained from a hazard parameter prediction model conditional on the magnitude of the earthquake, and the function $f_{M_i}(m)$ denotes the PDF of the magnitude *M* given the occurrence of an earthquake on seismic source *i*.

In Eq. 1, it is assumed that earthquake occurrences at different seismic sources are statistically independent (in terms of occurrence time, scaling relationship, *M*, etc.), implying that earthquake occurrences from all possible sources can be assumed to follow a Poisson process. It is also assumed that within each seismic source *i*, the magnitude M_i earthquake events are statistically independent. Thus, the summation in Eq. 1 considers the contributions from all seismic sources while the integrations over M_i and source parameters account for earthquakes of all possible magnitudes and source parameters conditional on the magnitude for each seismic source, respectively. In Eq. 1, the conditional probability $P(IM > im|\boldsymbol{\Theta},M)$, with $im > 0$, represents the complementary cumulative distribution function (CCDF) of the *IM* conditional on *M* and $\boldsymbol{\Theta}$. **Figure 1** illustrates the steps that can be used to compute the probabilistic seismic and tsunami hazard relationships. In Step 1, the earthquake fault source models and characteristics of the earthquake source models are defined. In Step 2, the ground-motion *IM*s at a given site are obtained through the earthquake simulation, performed through either explicit source-to-site wave propagation models and synthetic ground-motion generation or, most commonly, with GMPEs. In Step 3, the tsunami is simulated, including tsunami generation, propagation and inundation modeling. In Step 4, the seismic-tsunami hazard curves and surfaces are determined. It is notable that Step 2 (seismic simulations) and Step 3 (tsunami simulations) are produced from a consistent earthquake event.

Earthquake Fault Source Models and Their Characteristics

To describe the distribution of earthquake magnitudes in a given region of interest, the Gutenberg–Richter relationship (GR) is widely adopted. The GR relationship is given by

$$\log \boldsymbol{\lambda}_m = a - bm \quad (2)$$

where $\boldsymbol{\lambda}_m$ is the MAR of exceedance of an earthquake of magnitude *m*, *a* represents the overall rate of earthquakes in a region of interest, and *b* represents the relative ratio of small and large magnitudes. The parameters *a* and *b* are estimated based on statistical analysis of the database of seismicity for the seismic source zone of interest. The GR relationship is developed from a regional dataset of seismicity accounting for many different source zones and has been found to be inadequate to represent the earthquake recurrence relationship for the tail-end of the magnitude–frequency distribution representing large magnitude earthquakes (Schwartz

and Coppersmith, 1984; Wesnousky, 1994). Several models have been proposed to address the shortcomings of the GR recurrence law (Kagan, 1997, 2002a; Bird and Kagan, 2004). For SZs, such as the CSZ used as an example in this paper, a Tapered Gutenberg–Richter (TGR) distribution has been shown to be a robust model (Rong et al., 2014). The TGR is expressed as a function of the seismic moment M_0, instead of magnitude m and an exponential taper is applied to the number of events with very large seismic moment. The TGR CCDF is given by Kagan (2002a)

$$F(M_0) = \left(\frac{M_{0t}}{M_0}\right)^{\beta} \exp\left(\frac{M_{0t} - M_0}{M_{0c}}\right), \text{ for } M_{0t} \le M_0 < \infty \quad (3)$$

where β is the index parameter of the distribution, and $\beta = (2/3)b$, M_{0c} is the corner moment, and M_{0t} is the threshold moment above which the earthquake catalog is assumed to be complete. The conversion between seismic moment M_0 and moment magnitude m is given by

$$M_0 = 10^{1.5m+C} \quad (4)$$

where $C = 9 - 9.1$. The corner moment M_{0c} can be estimated using the seismic moment conversion principle (Kagan, 2002b) and given approximately by

$$M_{0c} = \left[\frac{\chi \dot{M}_T (1-\beta)}{\alpha_t M_{0t}^{\beta} \Gamma(2-\beta)}\right]^{1/(1-\beta)} \quad (5)$$

where χ is the seismic coupling coefficient, $\dot{M}_T$ is the tectonic moment rate, α_t is the recurrence rate for earthquake with moment M_{0t} and greater, and Γ is the gamma function. Equation 5 can be used to derive the recurrence interval as

$$T(M_{0t}) = \left[\frac{1}{1-\beta}\right] \frac{M_{0t}^{\beta} M_{0c}^{1-\beta}}{\dot{M}_T} \Gamma(2-\beta) \exp\left(\frac{M_{0t}}{M_{0c}}\right) \quad (6)$$

The TGR CCDF can be rewritten in terms of magnitude m and given as

$$F(m) = \left[10^{1.5(m_t - m)}\right]^{\beta} \exp\left[10^{1.5(m_t - m_c)} - 10^{1.5(m - m_c)}\right] \quad (7)$$

Rong et al. (2014) estimated the probable maximum earthquake that is likely to occur within a given time for circum-Pacific SZs using TGR distributions. For the CSZ, using maximum likelihood estimation method, the values of $\beta = 0.59$ and $m_c = 9.02$ were estimated considering the 10,000-year paleoseismic record based on the turbidite studies by Goldfinger et al. (2012), coupled with the limited number of instrumental earthquake data. In the implementation performed, it is convenient to convert the continuous distribution of magnitudes into a discrete set of possible magnitudes m_j, which are given by

$$P[M = m_j] = G(m_j + 0.5\Delta m) - G(m_j - 0.5\Delta m) \quad (8)$$

where the $G(m) = 1 - F(m)$ is the cumulative density function and Δm is the adopted discretization interval.

Figure 2 shows the median earthquake recurrence relationship developed for the CSZ using a TGR distribution (Eqs 3–7) and

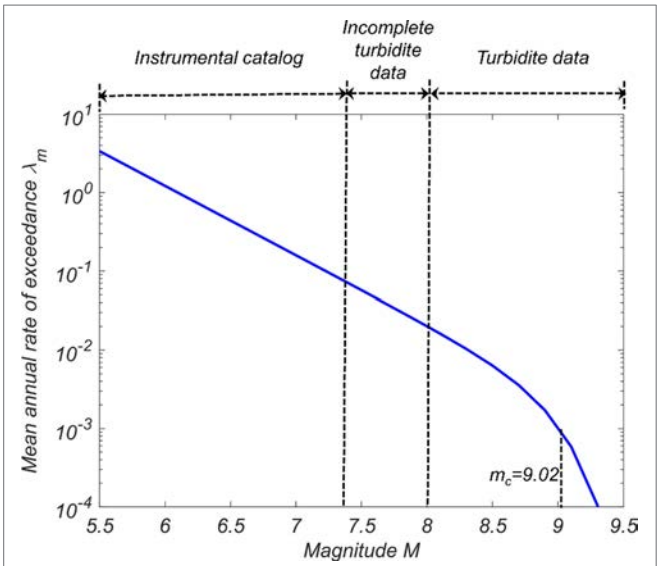

FIGURE 2 | Tapered Gutenberg–Richter relationship for Cascadia subduction zone.

with $\beta = 0.59$ and $m_c = 9.02$, as recommended by Rong et al. (2014) for the CSZ. According to the TGR distribution shown in **Figure 2**, $m \ge 8.8$ earthquakes are expected with a return period of 500 years ($\boldsymbol{\lambda}_m = 0.002$), while $m \ge 9.0$ earthquakes are expected with a return period of 1,000 years ($\boldsymbol{\lambda}_m = 0.001$). Goldfinger et al. (2012) reconstructed the large earthquake history of the CSZ for approximately10,000 years based on strong shaking-induced turbidite deposits in marine sediments and onshore paleoseismic records. The study suggested four types of earthquake rupture along the CSZ based on the interpretation of the turbidite data during the past 10,000 years: (1) 19–20 full-margin or nearly full-margin ruptures, (2) 3–4 ruptures along the 50–70% of the southern margins, (3) 10–12 southern ruptures from central Oregon southward, and (4) 7–8 southern Oregon/northern California ruptures. Though the turbidite data do not provide direct indication of the probable earthquake magnitudes, Goldfinger et al. (2012) estimated the earthquake magnitudes of different rupture events based on the relations observed among the rupture length (distance between offshore core sites containing turbidites from same events), turbidite thickness, and turbidite mass and estimated that full-rupture events constituted $m = 8.7$~9.3. Considering 20 full rupture over the past 10,000 years, the MAR of full-rupture events $\boldsymbol{\lambda}_{full-rupture} \approx \frac{20}{10{,}000} = 0.002$, which is consistent with the $\boldsymbol{\lambda}_{m \ge 8.8} = 0.002$ estimated by Rong et al. (2014) using TGR distribution shown in **Figure 2**.

Earthquake Simulation

Near-field ground motions are strongly affected by the heterogeneity of earthquake rupture processes, such as slip distribution, rupture directivity, and the acceleration and deceleration of the rupture front. To estimate the ground motion quantitatively for a seismic hazard assessment, characterization of this heterogeneity is essential, and usually accounted for in ground-motion hybrid broadband simulation procedures (e.g., Somerville et al., 2012) or 3D simulations of earthquake event scenarios (e.g., Olsen et al.,

2008; Delorey et al., 2014). While these explicit source-to-site wave propagation models and synthetic ground-motion generation models are extremely useful, especially in generating synthetic waveforms, these typically involve very large number of computations in large parallel computing centers, which is currently still not feasible when performing probabilistic seismic hazard analyses. Instead, when performing PSHA, GMPEs are still typically used today.

In this study, GMPEs, which are dependent on the local and regional site conditions, are used to simulate the ground-motion *IM*s. The recently developed Abrahamson et al. (2016) GMPE, which is based on the global datasets on SZ earthquakes described in Section "Background and Literature Review" is used. The functional form of this GMPE for interface SZ earthquakes is given by:

$$\begin{aligned}\ln(Sa_{\text{interface}}) = {} & \theta_1 + \theta_4 \Delta C_1 + (\theta_2 + \theta_3 (M - 7.8)) \ln(R_{\text{rup}} \\ & + C_4 \exp(\theta_9 (M - 6))) + \theta_6 R_{\text{rup}} + f_{\text{MAG}}(M) \\ & + f_{\text{FABA}}(R_{\text{rup}}) + f_{\text{site}}(\text{PGA}_{1,000}, Vs_{30}) + \sigma\epsilon \quad (9)\end{aligned}$$

where $\boldsymbol{\theta}_i$ are regression parameters, R_{rup} is the closest distance to the rupture area from site, Vs_{30} is the shear wave velocity of the uppermost 30 m of soil, $\text{PGA}_{1,000}$ is the median PGA corresponding to $Vs_{30} = 1{,}000$ m/s, σ is the total SD, which is obtained combining intra-event uncertainty $\boldsymbol{\phi}$ and inter-event uncertainty $\boldsymbol{\tau}$, and $\boldsymbol{\epsilon}$ is the standard normal error term. In this study, only the intra-event uncertainty $\boldsymbol{\phi}$ is considered since only the CSZ is used for hazard analysis. The magnitude scaling term is given by

$$f_{\text{MAG}}(M) = \begin{cases} \theta_4 (M - (C_1 + \Delta C_1)) + \theta_{13} (10 - M)^2, & \text{for } M \le C_1 + \Delta C_1 \\ \theta_5 (M - (C_1 + \Delta C_1)) + \theta_{13} (10 - M)^2, & \text{for } M > C_1 + \Delta C_1 \end{cases} \quad (10)$$

where $C_1 = 7.8$, and the ΔC_1 term represents the epistemic uncertainty around the distinct break in magnitude scaling between frequent smaller magnitudes events and rare large interface events. The forearc and backarc scaling term in Eq. 9 is given by

$$f_{\text{FABA}}(M) = \left[\theta_{15} + \theta_{16} \ln\left(\frac{\max(R_{\text{rup}}, 100)}{40}\right)\right] F_{\text{FABA}};$$
$$F_{\text{FABA}} = \begin{cases} 0, & \text{for forearc or unknow sites;} \\ 1, & \text{for backarc sites.} \end{cases} \quad (11)$$

The model for site response scaling is given by

$$f_{\text{site}}(\text{PGA}_{1,000}, Vs_{30}) = \begin{cases} \left[\theta_{12} \ln\left(\frac{V_S^*}{V_{\text{lin}}}\right)\right] - b \ln(\text{PGA}_{1,000} + c) & \text{for } V_{s30} < V_{\text{lin}} \\ \quad + b \ln\left(\text{PGA}_{1,000} + c\left(\frac{V_S^*}{V_{\text{lin}}}\right)^n\right), & \\ \left[\theta_{12} \ln\left(\frac{V_S^*}{V_{\text{lin}}}\right)\right] + b \ln\left(\frac{V_S^*}{V_{\text{lin}}}\right), & \text{for } V_{s30} \ge V_{\text{lin}} \end{cases}$$
$$V_S^* = \begin{cases} 1{,}000, & \text{for } V_{s30} > 1{,}000; \\ V_{s30}, & \text{for } V_{s30} \le 1{,}000. \end{cases} \quad (12)$$

All other model coefficients in Eqs 9–12 are listed in the study by Abrahamson et al. (2016).

Tsunami Generation, Propagation, and Inundation

In general terms, the tsunami hazard at a particular site requires the three steps of (1) tsunami generation, (2) propagation, and (3) inundation. For most modeling efforts, tsunami generation is given as an initial surface water displacement along the fault. The Okada (1985) model, which is based on the linear co-seismic dislocation of fault slips, is often used for simplicity, and the initial displacement is assumed to occur simultaneously along the fault.

Tsunami propagation is generally considered a solved problem in that the equations are well defined for long wave propagation in the open ocean. Of course, the propagation phase requires accurate knowledge of the underlying bathymetry which affects the wave through refraction, diffraction, and shoaling. The third phase, tsunami inundation, considers the flow of water over dry land. This is considered a difficult problem to solve because of the complex interaction of the flow with the built and natural environment that is also changing due to the destructive nature of the flow. However, most inundation models assume "bare earth" conditions, that is a digital elevation model (DEM) in which the natural and built environments are removed. Typically, the effects of the vegetation and structures are replaced by a suitable friction factor, although there are additional uncertainties in this step (e.g., Park et al., 2013; Bricker et al., 2015).

In this study, the logic-tree model by Park and Cox (2016) is applied for tsunami generation to characterize the fault slip. The slip model from the study by Park and Cox (2016) characterizes the randomness of fault slip distribution at the CSZ as a Gaussian shape, parameterized in terms of the moment magnitude, peak slip location, and a fault slip shape as

$$f(Y'/dL|\alpha, \beta) = \frac{1}{\beta\sqrt{2\pi}} \exp\left(\frac{-\left(Y'/dL - \alpha\right)^2}{2\beta^2}\right) \quad (13)$$

where α and β are the slip distribution parameters along a rupture strike direction (Y'), and dL is the unit length of sub-fault utilized in the slip model. Each parameter α and β controls the location of the peak slip and the shape of slips. A total of 72 scenarios from the three seismic moments, three slip shapes, and eight peak slip locations are proposed for the full-length rupture CSZ event. The occurrence rate of each seismic moment estimated from the paleoseismic data at CSZ (Goldfinger et al., 2012). Each of the fault slip distributions are determined from the slip model and applied to the ComMIT/MOST model (Titov et al., 2011) as an input to simulate the tsunami generation and propagation parts. Although MOST can also be used for the inundation phase, the software COULWAVE (Lynett et al., 2002) is used to model this final step (Park and Cox, 2016).

Multi-Hazard Logic-Tree Model

The generic multi-hazard logic tree is presented in **Figure 3**. The first step is to identify all tsunamigenic earthquakes that could potentially affect the site of interest. These earthquakes are then classified as near-field or far-field earthquakes depending on the source location with respect to the site. For each of the potential fault sources, the next step is to use an appropriate recurrence

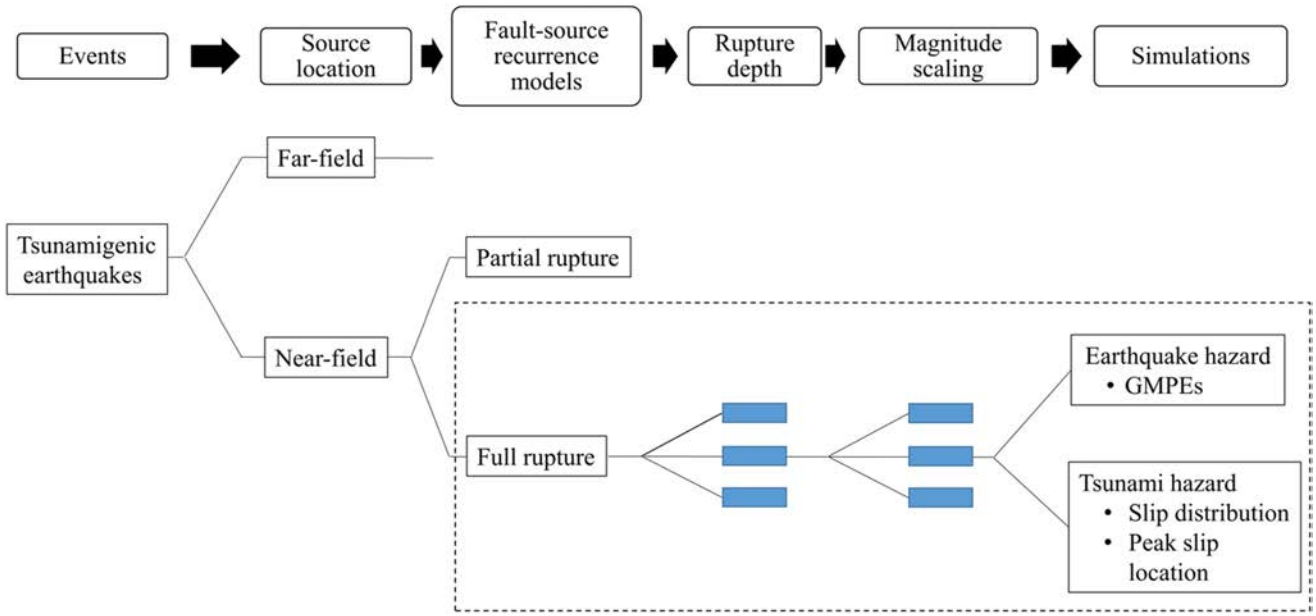

FIGURE 3 | Generic logic tree for the probabilistic seismic and tsunami hazard analysis. The dashed box shows the full-rupture event considered in the example applied to the Cascadia subduction zone.

model. As mentioned in Section "Earthquake Fault Source Models and Their Characteristics," the widely used modified-GR underpredicts the recurrence rate for large magnitude tsunamigenic earthquakes and hence TGR (Kagan, 2002a) and other characteristic moment–frequency distributions (e.g., Wesnousky, 1994) are preferred. Since most of the GMPEs use a distance metric of closest distance from the site to the rupture plane (R_{rup}), the depth of rupture which determines the position of the rupture edge close to the site of interest can have significant effect on the ground-motion intensity observed. Several geophysical models are available to determine the rupture depth and can be used for a specific fault of interest. As for example, for 2014 National Seismic Hazard Map of United States, three geophysical models were used to constrain the eastern edge of the CSZ rupture zone (Frankel et al., 2015).

Reliable magnitude scaling relationships for subduction earthquakes is a prerequisite for accurate estimation of earthquake and tsunami hazard intensities. There are several magnitude scaling relationships available in the literature that are derived from global observation of earthquakes on the plate interface of SZ (Papazachos et al., 2004; Strasser et al., 2010; Murotani et al., 2013; Goda et al., 2016; Skarlatoudis et al., 2016). Of these, Skarlatoudis et al. (2016) compiled an updated database of interface earthquakes that occurred worldwide in last decade in the major SZs (e.g., 2004 M 9.1 Sumatra, 2010 M 8.8 Chile, 2011M 9.0 Japan earthquake) and proposed new and improved source scaling laws with reduced uncertainty compared to other currently available source scaling laws for subduction earthquakes. Once the appropriate source magnitude and scaling laws are identified, the final step is to perform the earthquake and tsunami simulations for a multiple logic-tree branch. In the case of earthquakes, GMPEs are utilized, which typically make use of the M and R_{rup} as the input parameter to compute the ground-motion *IM*s at the site. On the other hand, for tsunamis, the details of the slip distribution (e.g., slip shape, peak slip location within rupture zones) and seismic moment for a given rupture are critical input parameters needed to compute the tsunami hazard intensity at a given site.

Estimates of the AEP

Four *IM*s were selected for the PSTHA, including the PGA, the 5% damped linear elastic spectral acceleration at a fundamental period of vibration of 0.3 s [$S_a(T_1) = 0.3$ s], the maximum flow depth ($h_{\max}$), and the specific maximum momentum flux $(M_F)_{\max}$ because these *IM*s are often linked with structural damage at a structure scale (e.g., Faggella et al., 2013; Gidaris et al., 2016). Here, the flow depth is the net elevation of the free surface elevation above the local land elevation, and the specific momentum flux is given by the product of the flow depth with the square of the flow velocity ($M_F = hV^2$).

The Poisson process (Cornell, 1968) is used to estimate the AEP of both earthquake and tsunami hazard curves at a specific location. The probability of *IM*s exceeding a certain level of that hazard conditional on a given time t is equal to the probability of at least one event occurring in time t, and is given by

$$P[IM > im|t] = 1 - e^{-\lambda t} \tag{14}$$

where λ is the mean occurrence rate at which the *IM* will exceed a specific *im* at a given location during the time t. The MAR exceedance of each *IM* is computed using Eq. 1.

The AEP surfaces for the joint seismic-tsunami hazard can be computed using the formulation presented next, designated here as vector-valued probabilistic seismic and tsunami hazard analysis (VPSTHA). The presentation starts from the definition

of the joint mean rate density (MRD) of the hazard (e.g., Bazzurro, 1998; Barbosa, 2011), here expanded to account for *IM*s related to ground-motion shaking intensity as well as tsunami *IM*s. For a vector of ground-motion and/or tsunami intensity parameters $\mathbf{IM} = \{IM_1, IM_2\}$, the joint MRD of the hazard is given by

$$\mathrm{MRD}_{IM_1,IM_2}(im_1, im_2) = \sum_{i=1}^{N_{\mathrm{sources}}} \lambda_i(M \geq m_{\min}) \times \int_{\boldsymbol{\Theta}} \int_{M} f_{IM_1,IM_2}(im_1, im_2 | \boldsymbol{\Theta}, M) s_{\boldsymbol{\Theta}_i}(\boldsymbol{\Theta} | M) f_{M_i}(m) dm \, d\boldsymbol{\Theta} \quad (15)$$

where $f_{IM_1,IM_2}(im_1, im_2 | \boldsymbol{\Theta}, M)$ is the joint PDF of IM_1 and IM_2 conditional on earthquake of magnitude M and source parameters $\boldsymbol{\Theta}$. Once the MRD is defined, the MAR of events at the site with IM_1 and IM_2 being between $im_{1,1} < IM_1 \leq im_{1,2}$ and $im_{2,1} < IM_2 \leq im_{2,2}$, respectively, is given by:

$$\lambda_{IM_1 \in]im_{1,1}, im_{1,2}], IM_2 \in]im_{2,1}, im_{2,2}]} = \int_{im_{1,1}}^{im_{1,2}} \int_{im_{2,1}}^{im_{2,2}} \mathrm{MRD}(im_1, im_2) \, dim_2 dim_1 \quad (16)$$

It is worth highlighting that the vector of intensity parameters $\mathbf{IM} = \{IM_1, IM_2\}$ may contain ground-motion scalar *IM*s and/or tsunami scalar *IM*s. Examples are vector-valued *IM*s such as $\mathbf{IM} = \{S_a(T_1), h_{\max}\}$, $\mathbf{IM} = \{\mathrm{PGA}, S_a(T_1)\}$, $\mathbf{IM} = \{h_{\max}, (M_F)_{\max}\}$ The formulation in Eqs 15 and 16 is generic, but its implementation requires the computation of joint MRDs, which can be computationally expensive.

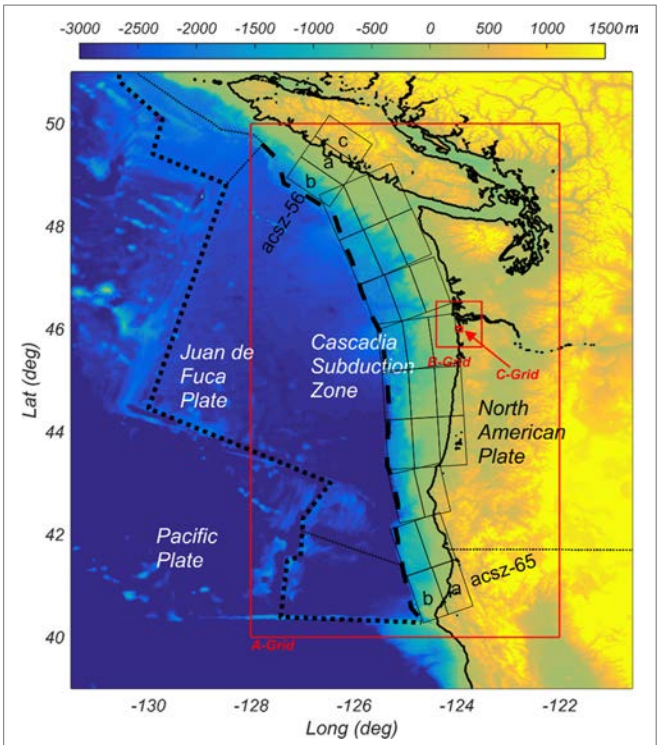

FIGURE 4 | Cascadia subduction zone (CSZ) formed by the Juan de Fuca Plane and the North American Plate. The red boxes indicate the nested grids used in the tsunami modeling. The rectangular boxes along the CSZ show the slip locations used in the tsunami generation model and in the prediction of the ground-motion intensities. The study area of Seaside, Oregon, is located in the C-Grid.

APPLICATION: FULL-RAPTURE EVENT OF THE CSZ IMPACTING THE CITY OF SEASIDE, OR

Characterization of the Source

The northern coast of the North American continent from Northern California in the United States to Vancouver Island in Canada is facing the threat of a megathrust earthquake event with near-field tsunami from the CSZ along the converging plate boundary between Juan de Fuca Plate and North American Plate. The Juan de Fuca Plate is sinking beneath the North American Plate with the mean rate of 0.04 m/year (Heaton and Hartzell, 1987) to the northeast direction (**Figure 4**). The accumulated potential energy between two plates is released in the megathrust earthquake events and can cause ground shaking and rapid displacement of the seafloor which generates the initial deformation of surface water. Each megathrust rupture of the converging plate boundary triggers the earthquake and tsunami event in both offshore and onshore directions. The last full-rupture event occurred on January 26, 1700, with moment magnitude estimated between 8.7 and 9.2 (Satake et al., 2003). It was also reported that there were smaller but more frequent partial rupture events on the north or south margins of the CSZ (Atwater and Griggs, 2012; Goldfinger et al., 2012). However, in this application example of the proposed multi-hazard assessment, the partial rupture events are not considered to reduce the number of computations needed for the tsunami inundation.

Seaside, Oregon, is the study area chosen to demonstrate the proposed PSTHA methodology. **Figure 5A** shows an aerial view of Seaside with approximately 4 km of shoreline facing the Pacific Ocean and two small rivers, the Necanicum River and Neawanna Creek, that run parallel to the shoreline. The city has a population of approximately 6,500 residents, and the number of people in the city can increase to over 20,000 during the summer tourist season. There are over 5,700 buildings in Seaside with the larger hotels constructed out of steel and reinforced concrete in the center of the city (highlighted by the red box in **Figure 5A**) and surrounded by mostly wooden residential structures to the north and south of the city center. **Figure 5B** shows the bathymetry and topography of the study area. The remnant coastal dune on which the city was built can be seen running parallel to the shoreline with a secondary rise between the Necanicum River and Neawanna Creek. To the east of the Neawanna Creek, there is a steep gradient leading to the foot hills and a large headland to the south west. **Figure 5C** shows the distribution of the soil classes for this region. The steeper mountain areas are considered as Class C, and a majority of the city area is Class D (ASCE, 2010). The soil class distribution is also aligned approximately in the shore parallel direction.

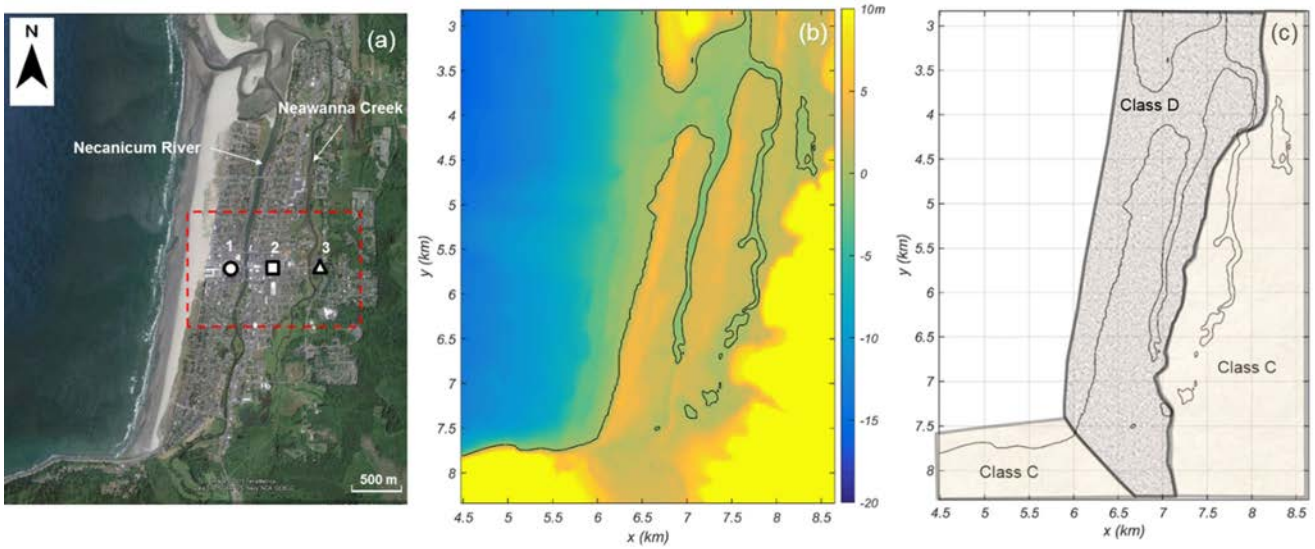

FIGURE 5 | Study area of Seaside, Oregon, at the landward side of the C-Grid shown in **Figure 4**. **(A)** Satellite image of the City of Seaside area with Necanicum River and Neawanna Creek bisecting the city. Areas marked by 1 (circle), 2 (square), and 3 (triangle) are example locations used in later figures. Red box highlights detailed area in later figures. **(B)** Bathymetry/topography for study area. Note that waterfront area of the city is built on a remnant dune and has higher elevation than river areas. **(C)** Soil classes assumed based on DOGAMI Oregon Department of Geology and Mineral Industries (2017) maps.

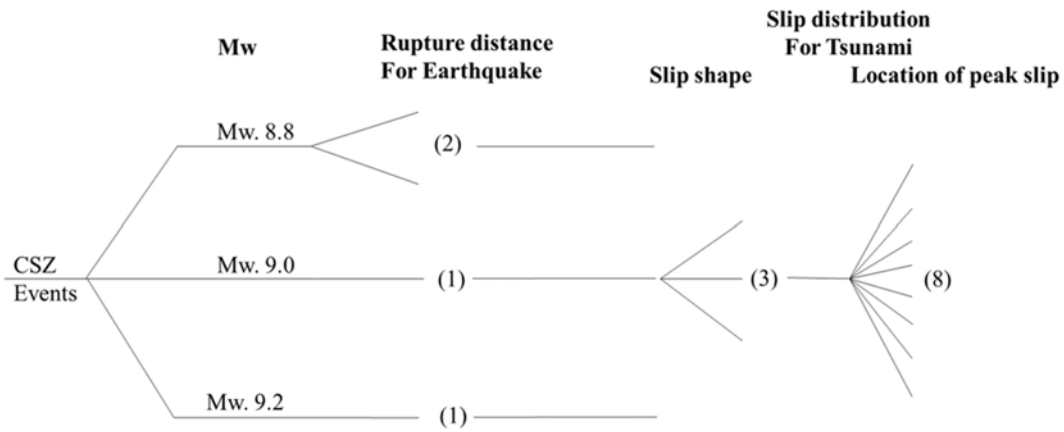

FIGURE 6 | Logic-tree model for full-rupture event at Cascadia subduction zone (CSZ). Each number in parenthesis provides the number of branches (scenario cases) considered depending on the characteristics of the rupture events (see details in the study by Park and Cox, 2016).

Seaside has been the subject of multiple tsunami studies in the past because it is considered to be one of the most vulnerable locations to a CSZ event. As reported by Wood et al. (2010), the low lying city has approximately 87% of its land within the inundation zone of a CSZ full-rupture event, and 89% of the employees work within this zone. Because of the high vulnerability of Seaside to a CSZ event, there have been several recent studies in this area as reviewed by Park and Cox (2016) and Park et al. (2017), including the work by González et al. (2009) that conducted a PTHA using 14 historic tsunami far-field scenarios and 12 scenarios of the CSZ event.

CSZ Fault Modeling

Figure 6 shows the logic-tree model utilized for both earthquake and tsunami for CSZ full-rupture event (Park and Cox, 2016). This logic-tree model characterizes the randomness of the fault slip in terms of the moment magnitude, peak slip location, and a fault slip shape. To simplify the scenarios, 27 sub-faults distributed along the CSZ were considered, which are the default sub-fault setup for the ComMIT model (Titov et al., 2011). The sub-faults are distributed from the northern Vancouver Island to Northern California. Each sub-fault is 100 km long by 50 km wide, as shown in **Figure 4**. The detailed geologic information of the location and slip information is summarized in **Table 1**. Each of the 27 sub-faults has a constant rake of 90° and has varied strike, dip, and depth conditions along the entire fault. The x and y coordinates indicate the middle point on the right edge boundary of each sub-faults in **Figure 4**.

The full-rupture event at the CSZ is discretized as three moment magnitude scenarios (M 8.8, 9.0, and 9.2), and the corresponding

TABLE 1 | Geologic sub-faults information at Cascadia subduction zone.

Sub-faults	Longitude (°E)	Latitude (°N)	Strike (°)	Dip (°)	Depth (m)
acsz-56a	234.0588	49.1702	315	11	12.82
acsz-56b	233.5849	48.8584	315	9	5.00
acsz-56c	234.5230	49.4727	315	18	22.36
acsz-57a	234.9041	48.2596	341	11	12.82
acsz-57b	234.2797	48.1161	341	9	5.00
acsz-57c	235.5249	48.4018	341	14	22.36
acsz-58a	235.3021	47.3812	344	11	12.82
acsz-58b	234.6776	47.2597	344	9	5.00
acsz-58c	235.9298	47.5029	344	11	22.36
acsz-59a	235.6432	46.5082	345	11	12.82
acsz-59b	235.0257	46.3941	345	9	5.00
acsz-59c	236.2591	46.6216	345	13	22.36
acsz-60a	235.8640	45.5429	356	11	12.82
acsz-60b	235.2363	45.5121	356	9	5.00
acsz-60c	236.4860	45.5734	356	14	22.36
acsz-61a	235.9106	44.6227	359	11	12.82
acsz-61b	235.2913	44.6150	359	9	5.00
acsz-61c	236.5211	44.6303	359	15	22.36
acsz-62a	235.9229	43.7245	359	11	12.82
acsz-62b	235.3130	43.7168	359	9	5.00
acsz-62c	236.5213	43.7321	359	16	22.36
acsz-63a	236.0220	42.9020	350	11	12.82
acsz-63b	235.4300	42.8254	350	9	5.00
acsz-64a	235.9638	41.9818	345	11	12.82
acsz-64b	235.3919	41.8677	345	9	5.00
acsz-65a	236.2643	41.1141	345	11	12.82
acsz-65b	235.7000	41.0000	345	9	5.00

rupture areas (S) were estimated using the relationship between seismic moment M_0 and rupture area provided by Murotani et al. (2013) and given by

$$S = 1.34 \times 10^{-10} M_0^{2/3} \tag{17}$$

Park and Cox (2016) added upper and lower limits to the surface area moment magnitude relationships of Eq. 17 by multiplying Eq. 17 with 2.0 and 0.5, respectively, and these limits bounded most of historic recent tsunami events at SZ around the Pacific Ocean which are generated by earthquake scenarios with $M > 8.5$. Including those two limits, a total of three slip shapes along the strike direction were utilized as possible scenarios per moment magnitude condition. Additionally, 8 possible peak locations are considered along the rupture length, giving rise to 24 scenarios applied for each moment magnitude condition. A total of 72 scenarios (3 moment magnitudes × 3 slip shapes × 8 peak slip locations) are proposed here to characterize the full-rupture CSZ event. Park and Cox (2016) applied 72 scenarios as inputs to the ComMIT/MOST (Titov et al., 2011) model, which considers the elastic dislocation model (Okada, 1985) for tsunami generation and solves the non-linear shallow water equations implemented with a finite difference scheme. The ComMIT/MOST model consists of three nested grids (A, B, and C-Grid) shown in **Figure 4**. For the inundation modeling, the results of COULWAVE (Lynett et al., 2002) were used, which solves a set of Boussinesq equations with a high-order finite-volume method by using the output of ComMIT/MOST modeling at B-Grid as the input of COULWAVE at C-Grid. All bathymetry data were originated from NOAA's National Geophysical Data Center and the DEM for the Seaside area whose resolution is 1/3 arc second was used for the C-Grid. Each A, B, and C-Grids has 1 min (400 × 400), 3 s (800 × 800), and 24 m (416 × 390) resolutions. As a tide condition, the mean high water level was fixed as conservative tsunami hazards estimation in this study. The model results provide surface elevation and velocity time series over the entire study area at the 24 m grid resolution. More details of fault slip distributions and tsunami simulations are available in the study by Park and Cox (2016). In case of earthquakes, the same fault model is used. However, the BC Hydro GMPE is utilized in this study, which is based on the closest rupture distance, R_{rup}, between the site of interest and rupture surface for the interface earthquakes considered.

RESULTS

Seismicity

Though larger magnitude earthquakes generally have higher damage potential compared to smaller magnitude earthquakes, smaller and frequent events can be dominant contributors to the structural damage risk measured in terms of mean annual frequency of exceeding a damage state such as the collapse damage state (e.g., Zareian and Krawinkler, 2007; Eads et al., 2013). **Figure 7A** shows the probability mass function (PMF) of the earthquakes in CSZ deemed capable of generating tsunamis. Tsunamigenic eartquakes with lowest magnitude of $m_{min} = 7.3$ is assumed and largest magnitude is assumed to be $m_{max} = 9.3$, consistent with the earthquake expected over a 10,000-year period in CSZ (Rong et al., 2014). A discretization interval of $\Delta m = 0.2$ is adopted to develop the PMF of **Figure 7**, resulting in 10 central magnitude values $m = 7.4$ to $m = 9.2$. The PMF for different magnitudes are computed based on the TGR distribution described in Section "Earthquake Fault Source Models and Their Characteristics" and using Eq. 8. Of these 10 magnitudes, $m \geq 8.8$ is assumed to produce the full rupture along the CSZ following the recommendations by Goldfinger et al. (2012), which is also consistent with Park and Cox (2016). These full-rupture events ($m = 8.8$, 9.0, 9.2) are only considered for earthquake-tsunami hazard analysis for Seaside. According to **Figure 7A**, $\boldsymbol{\lambda}_{m \geq 8.8} = 0.002$ results in 500-year return period for $m \geq 8.8$ representing full-rupture scenarios. To be consistent with 526-year return period used in Park and Cox (2016) for full-rupture CSZ events, $\boldsymbol{\lambda}_{m \geq 8.8} = 0.0019$ is used for the PSHA computations for the study area of City of Seaside.

One of the inputs required in the GMPEs for computing ground-motion intensities at a given site is the source-to-site distance. The BC Hydro GMPE used in this study is based on the closest rupture distance R_{rup} between the site of interest and the rupture surface for interface SZ earthquakes. To compute the R_{rup} for different locations in Seaside for different magnitude scenarios, the R_{rup} for all the C-grid locations are precomputed from the 27 sub-fault areas shown in **Figure 4**. The rupture surface for different magnitude scenarios of **Figure 7A** are then computed based on the magnitude scaling law by Murotani et al. (2013), which are randomly positioned along the 27 sub-faults corresponding to the approximately 1,000 km long by 150 m width fault plane. The randomly positioned rupture surfaces corresponding to different scenarios are subsequently used to interpolate the R_{rup} for each

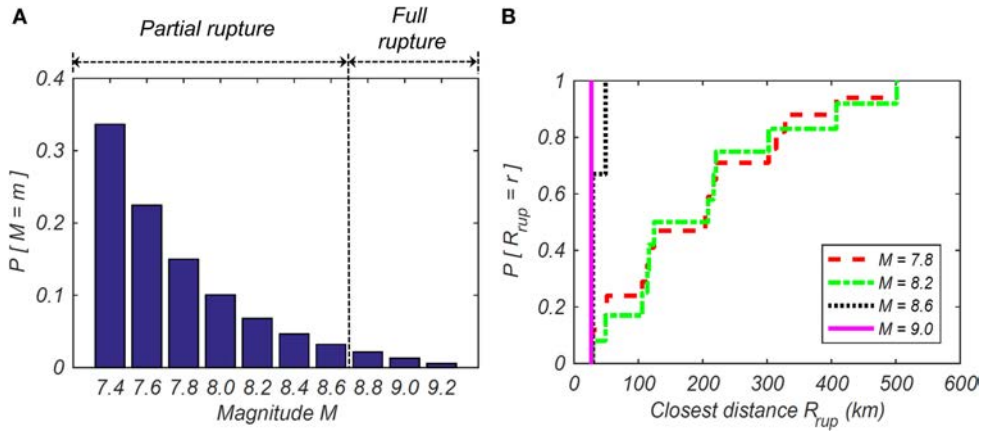

FIGURE 7 | Probability mass function (PMF) of the ground-motion basic random variables for different earthquake scenarios computed for observation Point 1 based on the Tapered Gutenberg–Richter recurrence relationship: **(A)** PMF of the magnitude and **(B)** PMF of closest rupture distance.

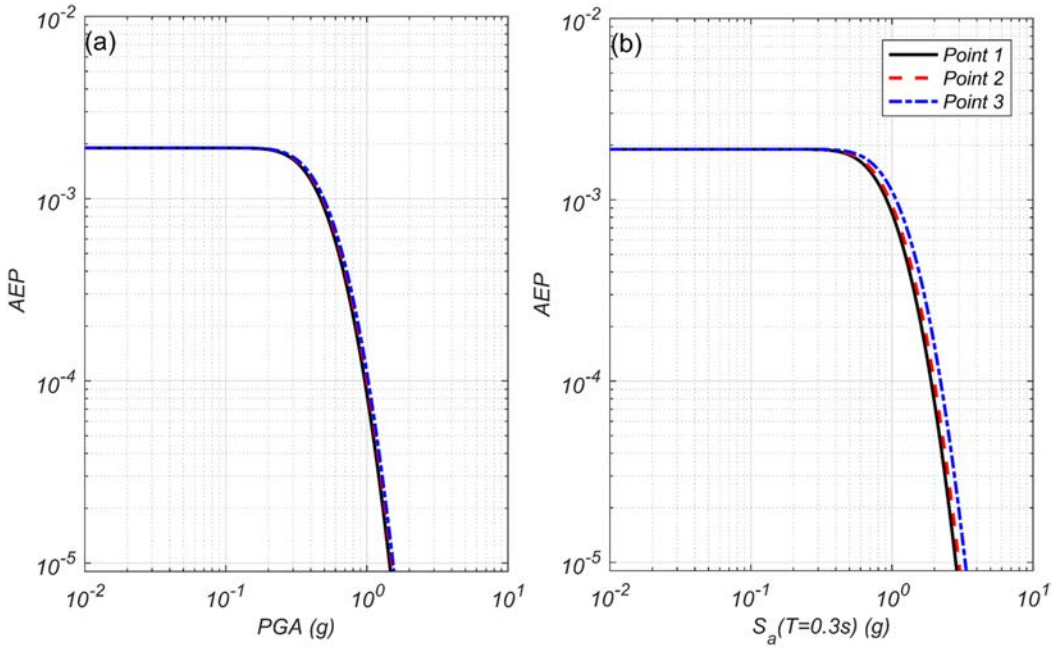

FIGURE 8 | Annual exceedance probability (AEP) for peak ground acceleration (PGA) **(A)** and $S_a(T_1 = 0.3\,\text{s})$ **(B)** at Points 1 (black solid), 2 (red dash), and 3 (blue dash-dot) for the full-rupture scenarios.

scenario from the precomputed closest distances. **Figure 7B** shows the PMF of R_{rup} computed for observation point 1 in **Figure 5A**. The closest distance computed for all the scenarios is 27.5 km, which is the distance computed from the fault area immediately below the C-grid. It can be observed in **Figure 7B** that smaller variability of R_{rup} is observed for larger magnitudes. For example, for $m = 9.0$ that is a full-rupture event results in a single source-to-site distance and the resulting R_{rup} can be considered as a deterministic event with $P[R_{\text{rup}} = 27.5\,\text{km}] = 1$. For the partial rupture events, the rupture surface is randomly positioned within the fault plane, which results in variability in the closest rupture distance computed as shown in **Figure 7B**.

AEP for two earthquake *IM*s, PGA and $S_a(T_1 = 0.3\,\text{s})$, are computed for three observation points (shown in **Figure 5A**) in Seaside. These points are aligned shore-normal along the urban center of Seaside with approximately 400 m distance apart from each other. The observation Points 1, 2, and 3 are located between shoreline and the Necanicum River, Necanicum River and the Neawanna Creek, and Neawanna Creek and the edge of inundation zone, respectively.

Figure 8 shows the AEP of PGA and $S_a(T_1 = 0.3\,\text{s})$ at three observation points computed for the full-rupture scenarios ($M = 8.8$, $M = 9.0$, $M = 9.2$) using the BC Hydro GMPE. As per the soil site class map of **Figure 5C**, point 1 and point 2 fall in

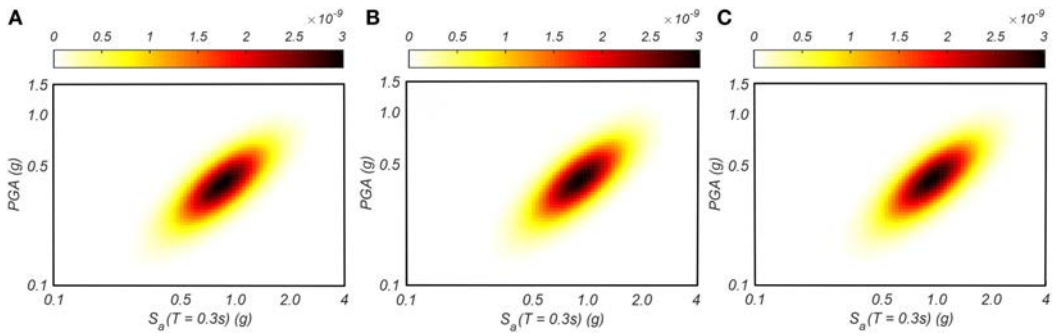

FIGURE 9 | Joint hazard curves of peak ground acceleration (PGA) and S_a at **(A)** Point 1, **(B)** Point 2, and **(C)** Point 3.

site class D where as point 3 is in site class C. The V_{s30} values assigned to Point 1, Point 2, and Point 3 are 300, 360, and 420 m/s, respectively. A value of $\boldsymbol{\lambda}_m = 0.0019$ corresponding to $M \geq 8.8$ is used for the hazard curves and subsequent AEP computations. In AEP computations, the PMF values considered for the three magnitudes is consistent with those used in the study by Park and Cox (2016), which were obtained from the study by Goldfinger et al. (2012). Since the weights assigned to the M 8.8, M 9.0, and M 9.2 are 5/19, 13/19, and 1/19, respectively, the M 9.0 is the dominant contributor to the hazard curves presented in **Figure 8** for both PGA and $S_a(T_1 = 0.3\,\text{s})$, followed by M 8.8, and M 9.2, respectively. As shown in **Figure 8**, AEP of PGA for three points are almost identical whereas slight variation in AEP for $S_a(T_1 = 0.3\,\text{s})$ is observed for those three points. The slight variation in AEP for $S_a(T_1 = 0.3\,\text{s})$ is due to the different V_{s30} values assigned to those points. Overall AEP of both *IM*s are insensitive to their geographical conditions at this 800 m distance between the three points, which are all approximately 27.5 km from the fault.

The joint MAR of exceedance of *IM*s contour plot of PGA and $S_a(T_1 = 0.3\,\text{s})$ is shown in **Figure 9** for the three points indicated in **Figure 5** for the 1,000-year event. The joint MAR of exceedance of *IM*s is computed based on the formulation presented in Eqs 15 and 16, in which the joint probability function of the two *IM*s conditional on the magnitude at a given site is computed assuming that the *IM*s follow a joint lognormal distribution. For the jont MAR of exceedance computation of PGA and $S_a(T_1 = 0.3\,\text{s})$, correlation between the two *IM*s are considered and computed based on the study by Baker and Jayaram (2008). It can be seen from **Figure 9** that for all three observation points, the most likely joint intensities occur for values of PGA = 0.5 g and $S_a(T_1 = 0.3\,\text{s}) = 1.0$ g. Moreover, there is no discernable difference in the joint hazard intensities among the observation points considered as can be observed in **Figure 9**, as expected.

Tsunami Intensity

Figure 10 shows the AEP of two tsunami *IM*s $h_{\max}$ and $(M_F)_{\max}$ at the three observation points similar to **Figure 8**. Generally, the tsunami *IM*s decrease as distance from the shoreline increases because of the dissipation of energy during the inundation process as shown for the AEP of $h_{\max}$ (**Figure 10A**) and $(M_F)_{\max}$ (**Figure 10B**). For example, the AEP of both $h_{\max}$ and $(M_F)_{\max}$ at Point 1 are higher than Points 2 and 3. However, for lower probability events in the range of $0 < h_{\max} \leq 3$ m, Points 2 and 3 have nearly the same AEP. Point 3 has higher $h_{\max}$ at the higher probability events in the range of $3 < h_{\max} \leq 10$ m and also has the highest $h_{\max}$ due to the local topographic effects, including effects of the river and the creek running parallel to the shoreline (**Figure 5A**), highlighting the sensitivity of the tsunami *IM* to site-specific conditions. On the other hand, $(M_F)_{\max}$ shown in **Figure 10B** has three distinct curves with a generally decreasing trend from the shoreline to inundation limits. Comparing **Figures 8** and **10**, it is noted that the variation of AEP of tsunami *IM*s among three observation points are qualitatively dissimilar to the results of earthquakes *IM*s in that there are strong spatial gradients for the tsunami *IM*s across the length scale of the city. This is somewhat expected because the AEP of both PGA and $S_a(T_1 = 0.3\,\text{s})$ depend primarily on the soil types and R_{rup} that have relatively small variations over the study region at Seaside, especially for the full-rupture scenarios considered. Moreover, this difference underscores the differences in the fundamental physics of the propagation of the seismic energy through the subsurface and the propagation of the hydrodynamic tsunami energy.

Figures 11A–C shows the joint AEP of $h_{\max}$ and $(M_F)_{\max}$ at Point 1, 2, and 3, respectively, where the same number of bins for both *IM*s are utilized to calculate the vector-valued **IMs** of the joint $h_{\max}$ and $(M_F)_{\max}$ from Eqs 15 and 16. **Figure 11** also includes the isolines for four Froude numbers ($Fr = 0.2$, 0.5, 1.0, and 2.0) to show the possible range of distributions of velocity fields at the given flow depth. In general, the results show the high correlation between $h_{\max}$ and $(M_F)_{\max}$ at all three observation points, and each joint AEP follows a particular *Fr* for that area. For example, at Point 1 when $h_{\max}$ is in the range $6 < h_{\max} < 7$ m, the corresponding range of $(M_F)_{\max}$ is $150 < (M_F)_{\max} < 200\ \text{m}^3/\text{s}^2$ and corresponds to a *Fr* range of approximately $0.6 < Fr < 0.7$. The *Fr* generally decreases shoreward, and seems to be everywhere subcritical ($Fr < 1.0$) which is physically realistic based on observed inundations following the 2011 Tohoku tsunami. This is not to say that the flow is always subcritical, just that at the point of maximum flow depth or momentum flux, that the flow can be expected to be subcritical.

Figure 11 reveals that the different distributions of the joint surface of the AEP following the specific *Fr* at three observation points originate from the local bathymetric/topographic conditions and not from the fault slip distributions. These results

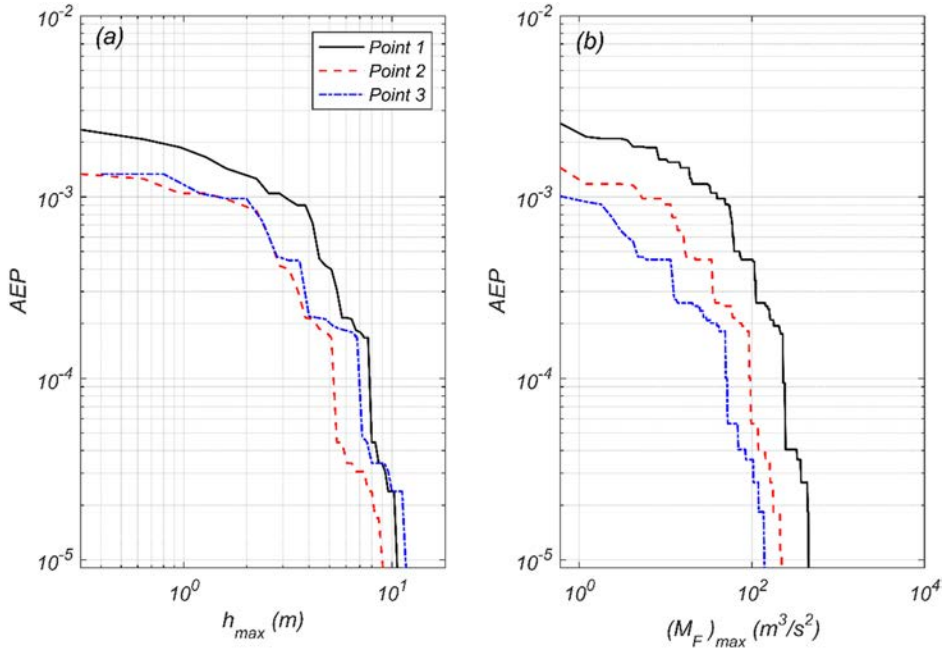

FIGURE 10 | Annual exceedance probability (AEP) of h_{max} **(A)** and $(M_F)_{max}$ **(B)** at Points 1 (black solid), 2 (red dash), and 3 (blue dash-dot).

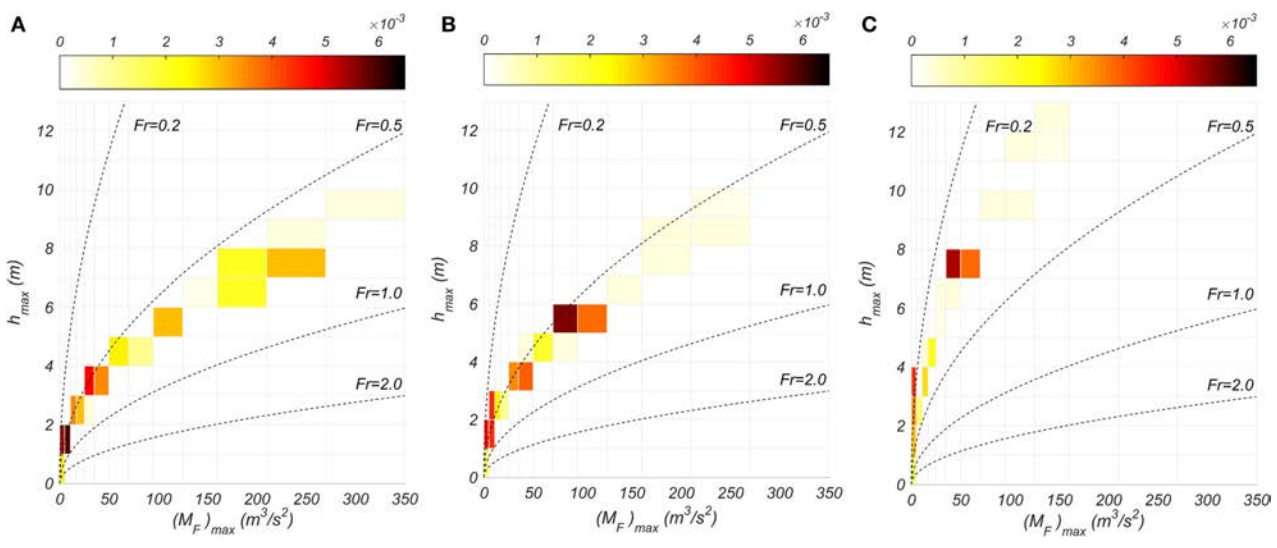

FIGURE 11 | Joint MAR of h_{max} and $(M_F)_{max}$ with Froude number (*Fr*) (dash lines) at **(A)** Point 1, **(B)** Point 2, and **(C)** Point 3.

are helpful to understand realistic input conditions of flow depth and velocity fields for different *Fr* regime that can be used to develop the tsunami fragility curves, which utilize the random combinations of h_{max} and flow velocity in the generation of fragility curves (Attary et al., 2017a; Attary et al., 2017b; Alam et al., submitted[2]). In addition, it is worth noting that the maximum flow depth and momentum flux typically do not occur at the same time (Park et al., 2013). Therefore, *Fr* at the maximum momentum flux and at the maximum flow depth can be expected to be slightly different. However, plots similar to **Figure 11** (not shown in the interest of brevity) in which the flow depth *h* at the instant of the maximum momentum flux $(M_F)_{max}$ or the instantaneous momentum flux is plotted against the corresponding maximum inundation flow depth lead to similar conclusions that the flow is generally subcritical for the maximum *IM*s.

[2]Alam, M. S., Barbosa, A. R., Scott, M. H., Cox, D., and van de Lindt, J. W. (submitted). Development of physics-based tsunami fragility functions considering structural member failures. *ASCE J. Struct. Eng.*

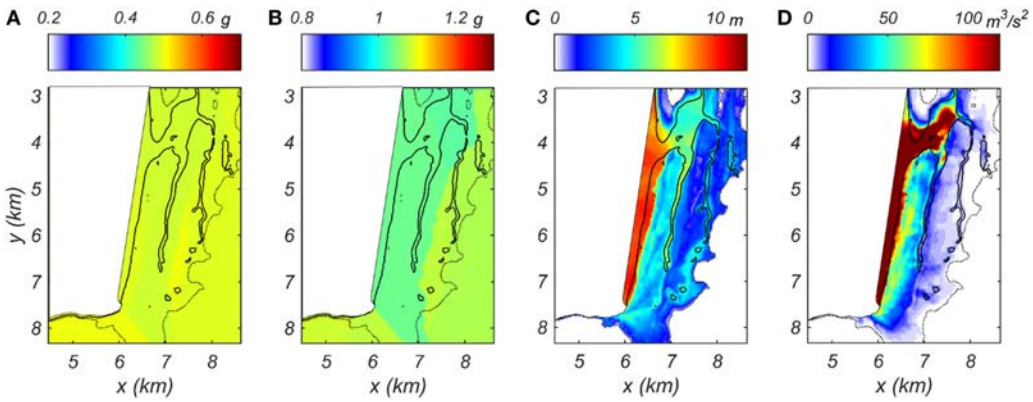

FIGURE 12 | Spatial hazard maps of **(A)** peak ground acceleration, **(B)** $S_a(T_1 = 0.3\,\text{s})$, **(C)** $h_{\max}$, and **(D)** $(M_F)_{\max}$ for 1,000-year event.

Spatial Representations Seismic and Tsunami Hazard

Figure 12 shows the spatial distributions of the earthquake and tsunami *IM*s at Seaside, Oregon, for the AEP = 0.001 (often referred to as the "1,000-year event") for the full-rupture scenario at CSZ. **Figures 12A–D** presents the spatial distribution of PGA, S_a ($T_1 = 0.3$ s), $h_{\max}$, and $(M_F)_{\max}$ respectively, and the dotted contour lines in each panel show the maximum inundation limits ($h_{\max} = 0.3$ m). Two distinct regions of earthquake *IM*s (PGA and S_a) are observed for the study area depending on the soil site class assumed in **Figure 5C** and within each region distributions of *IM*s are generally uniform. In the case of tsunami *IM*s ($h_{\max}$ and $(M_F)_{\max}$), irregular distributions are observed depending on the bathymetry conditions. However, both the *IM*s generally decreases from the shore toward inland (i.e., in the positive x-direction).

The range of PGA and $S_a(T_1 = 0.3\,\text{s})$ over the study region is 0.47–0.50 g and 1.03–1.08 g, respectively, while the $h_{\max}$ and $(M_F)_{\max}$ range from 0 to 12 m and 0 to 120 m^3/s^2, respectively for the 1,000-year event. The values of PGA and S_a are uniformly distributed over the entire study area, while the area affected by $h_{\max}$ and $(M_F)_{\max}$ are limited to the maximum inundation limits. To understand the granularity of both *IM*s of the earthquake and tsunami at the same event, the spatial mean and deviation of *IM*s conditional on varying unit block size is computed. This analysis is performed on the rectangle region, shown in **Figure 5A**, which is a 1,990 m length and 3,000 m wide rectangle near the center of the City of Seaside. The smallest unit block size, designated as reference or unit block size here forth, is equal to the Cartesian mesh grid size ($dx = dy = 24$ m) considered for tsunami inundation modeling in the C-grid. The ratio of block size $\left(r_B = \frac{\text{Block } size}{\text{reference mesh size}}\right)$ is increased systematically, keeping the same block shape and the mean and SD of the *IM*s are estimated as a function of the changes in the block size. The mean of normalized *IM* is given by

$$IM' = \frac{\sum_{j=1}^{N_b}\left(\sum_{i=1}^{N_g} im'_{i,j}\right)}{N_b N_g} \tag{18}$$

where N_b is the number of blocks depending on r_B conditions, and N_g is the number of grid points in a jth block ($N_g = {r_B}^2$). The im'_{ij} is the normalized *IM* of grid points of the jth block. The *IM*s in the jth block are normalized by the mean of the *IM*s for the jth blocks, and this calculation is performed for eight r_B conditions: $r_B = 1$, 2, 3, 5, 8, 13, 18, and 25. The corresponding block size and number of grid points per each block (N_g) are 24 m (1), 48 m (4), 72 m (9), 120 m (25), 192 m (64), 312 m (169), 432 m (324), and 600 m (625). For example, the total number of grid points in the study region is 10,625. For the case of $r_B = 5$, there are 425 block subsets over the study region, and each block is composed of $N_g = 25$ mesh grid points. The mean of *IM* at each of the 425 blocks is first computed, and then, each *IM* is normalized by the calculated mean.

Figure 13 shows the PDF of $\ln({h_{\max}}')$ over the study region for AEP = 0.001 (1,000-year event). **Figures 13A–D** show the PDFs at $r_B = 2$, 5, 13, and 25, respectively. The red line in each panel shows the natural log-normal fitting curve. When $\ln({h_{\max}}')$ is equal to zero, the mean of block subsets match exactly with the $h_{\max}$ of the unit grids, and each negative or positive value indicates an overestimation or underestimation of the block means. In the case of $h_{\max}$, the PDF shape becomes wider and shows a larger deviation as the block size increases. This process was extended to the three other *IM*s: PGA and S_a and $(M_F)_{\max}$.

Figure 14 summarizes the results of the four granularity tests for AEP = 0.001 (1,000-year event) by plotting the mean of the four normalized *IM*s with 90% confidence intervals for each unit block size. Both PGA and S_a ($T_1 = 0.3$ s) show almost insensitivity to the block sizes. All of the normalized means are essentially zero and the confidence intervals are small for all block sizes. However, both $h_{\max}$ and $(M_F)_{\max}$ results show significant variation with the 90% confidence intervals increasing as the block size increases. The largest deviation is found at $(M_F)_{\max}$, and relatively smaller deviation if found $h_{\max}$. The range of confidence interval of both $h_{\max}$ and $(M_F)_{\max}$ increases sharply with $r_B = 13$ (block size = 312 m). These results highlight the different sensitivity between two earthquake and tsunami *IM*s to the block size used to aggregate the *IM* results. In case of the PGA and S_a, the information of the site and location are less significant for determining each *IM* while $h_{\max}$ and $(M_F)_{\max}$ require detailed information of the site to minimize the uncertainty.

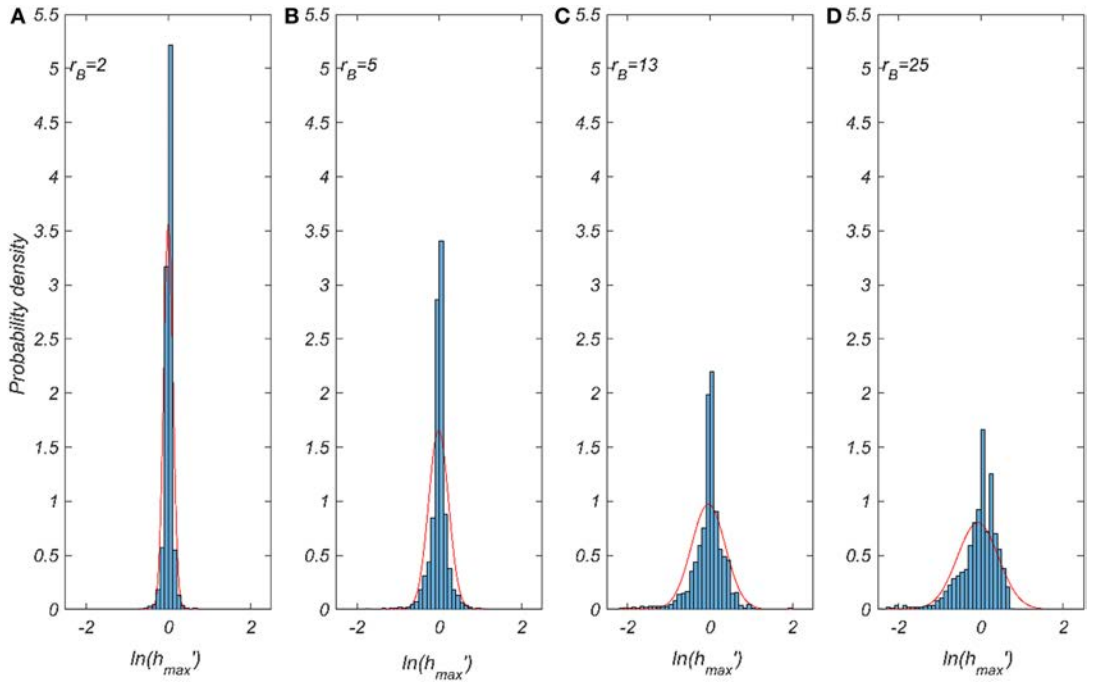

FIGURE 13 | Probability density function (PDF) of normalized h_{max} for 1,000-year event. **(A)** $r_B = 2$, **(B)** $r_B = 5$, **(C)** $r_B = 13$, and **(D)** $r_B = 25$. Each red line in the panel shows the fitted natural lognormal PDF curves.

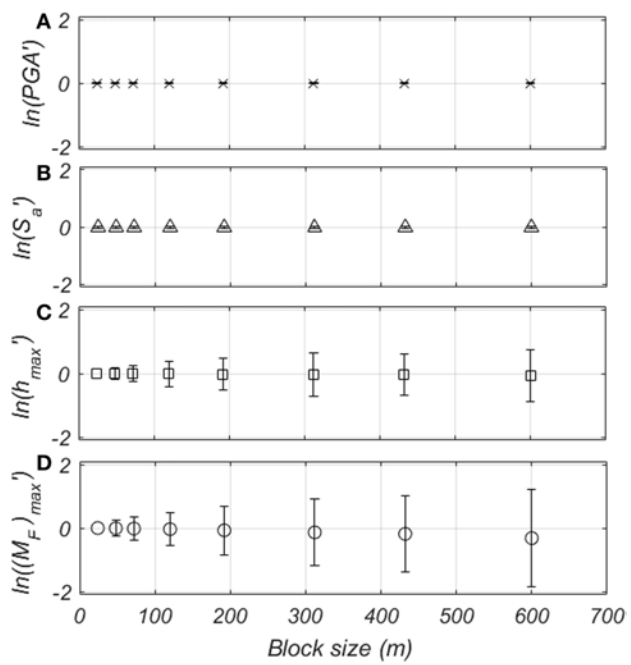

FIGURE 14 | Granularity of **(A)** peak ground acceleration (PGA), **(B)** $S_a(T_1 = 0.3\,\text{s})$, **(C)** h_{max}, and **(D)** $(M_F)_{max}$ for 1,000-year event.

Lastly, the spatial distribution of joint *IM*s is analyzed next. Only h_{max} and $(M_F)_{max}$ are considered herein since significant variations of tsunami *IM*s across the study area is observed in **Figure 12**. For the joint distribution computations uniform bins at 0.2 m interval are used for h_{max}, while a 4 m^3/s^2 interval is used for $(M_F)_{max}$. The probability (%) of the joint distribution is computed by counting number of grids which involved in the joint h_{max} and $(M_F)_{max}$ bin, for the whole study region, at the three AEP conditions, i.e., the 500, 1,000, and 2,500-year events, respectively. The results of spatial distributions of joint probability of h_{max} and $(M_F)_{max}$ are shown in **Figures 15A–C** for the 500, 1,000, and 2,500-year events, respectively, with four Froude numbers plotted on each figure in a manner similar to **Figure 11**.

In the case of the 500-year event (**Figure 15A**), more than 45% of the joint h_{max} and $(M_F)_{max}$ is distributed within $0.1 < Fr \leq 0.5$. The larger $(M_F)_{max}$ is observed within $0.5 < Fr \leq 1.0$. The joint peak of h_{max} and $(M_F)_{max}$ is located at $1.2 < h_{max} \leq 1.4$ m, and $0.0 < (M_F)_{max} \leq 4.0\ m^3/s^2$. Two distinct narrow banded regions of h_{max} are observed near $h_{max} = 3.8$ and $h_{max} = 5.8$ m, which correspond to different ranges of $(M_F)_{max}$ even at the similar flow depth conditions. In the case of the 1,000-year event (**Figure 15B**), more than 60% of the joint h_{max} and $(M_F)_{max}$ is distributed within $0.1 < Fr \leq 0.5$. Large $(M_F)_{max}$ values are observed at both $0.1 < Fr \leq 0.5$ and $0.5 < Fr \leq 1.0$. The joint peak is located at $1.6 \leq h_{max} < 1.8$ m, and $0.0 < (M_F)_{max} \leq 4.0\ m^3/s^2$ which is a slightly higher h_{max} condition than the 500-year event. Several isolated islands of joint distributions are observed that have relatively higher $(M_F)_{max}$ values. In the case of the 2,500-year event (**Figure 15C**), more than 68% of the joint h_{max} and $(M_F)_{max}$ is located within $0.1 < Fr \leq 0.5$. Large $(M_F)_{max}$ values are located primarily within $0.1 < Fr \leq 0.5$. The joint peak is located at $3.4 < h_{max} \leq 3.6$ m, and $16.0 < (M_F)_{max} \leq 20.0\ m^3/s^2$, which are significantly larger than the 500 and 1,000-year events. A few isolated points are observed for 2500-year event similar to that

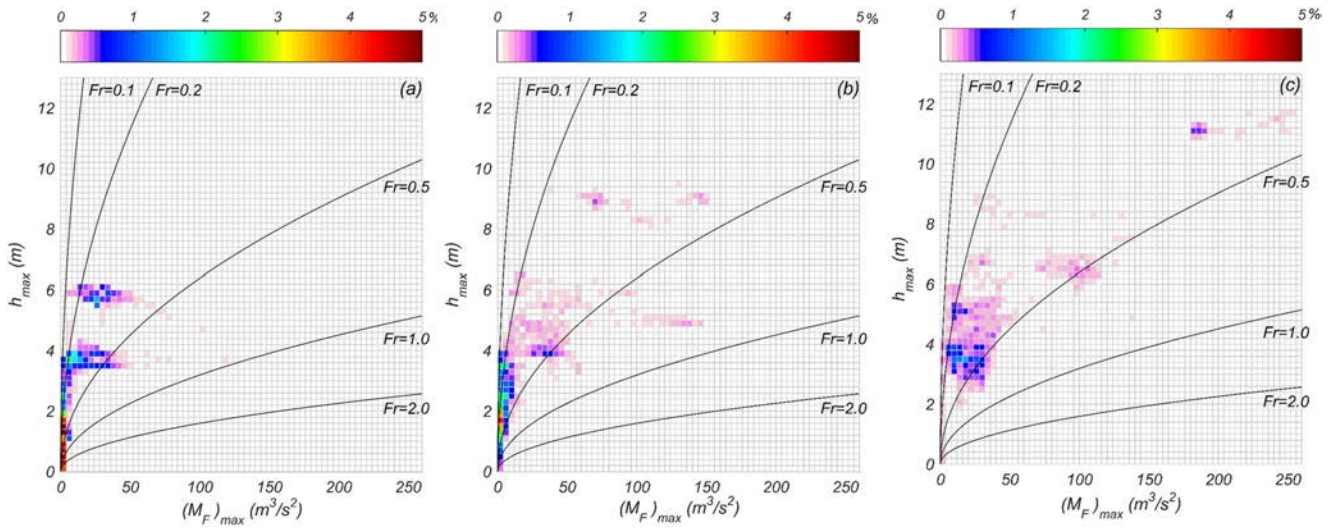

FIGURE 15 | Spatial distribution of joint h_{max} and $(M_F)_{max}$ with Froude number (Fr) for **(A)** 500, **(B)** 1,000, and **(C)** 2,500-year events.

observed in 1,000-year event. Overall, the joint h_{max} and $(M_F)_{max}$ is distributed within $0.1 \leq Fr < 1.0$ and are typically in the range $0.1 < Fr \leq 0.5$. It is also observed that each event has a different joint peak location. Further research is needed to understand the extent to which these are site-specific results, how this work can be generalized for other coastal archetypes (e.g., embayments), and how these results can be parameterized based on conditions offshore of the study area.

SUMMARY, CONCLUSION, AND FUTURE WORK

This paper presents a framework for a consistent probabilistic hazard assessment for the multi-hazard seismic and tsunami phenomena (PSTHA). For this work, full-rupture event along the CSZ is considered and the PSTHA methodology is applied to the study area of Seaside, Oregon, along the US Pacific Northwest coast. In this work, it is shown that:

1. The AEPs off the tsunami *IM*s are qualitatively dissimilar to the *IM*s of the seismic ground motion in the study area. Specifically, the spatial gradients for the tsunami *IM*s are much stronger across the length scale of the city owing to the physical differences of energy dissipation of the two mechanisms.
2. For the seismic hazard, similar trends were observed for the joint MAR of exceedance of the PGA and $S_a(T_1 = 0.3\,\text{s})$ at the three observation points, which may be attributed to the proximity of the observation points with respect to each other as well as from the source of the meag-thrust full rupture of CSZ.
3. For the tsunami hazard, the joint AEP of h_{max} and $(M_F)_{max}$ show a high correlation between h_{max} and $(M_F)_{max}$ in the study area. The joint AEP at each of the three observation points follows a particular Fr due to the local site-specific conditions at each location rather than the distributions of fault slips.
4. The joint probability distribution of h_{max} and $(M_F)_{max}$ throughout the study region falls between $0.1 \leq Fr < 1.0$ (i.e., the flow is subcritical), regardless of return interval (500-, 1,000-, and 2,500-year). However, the peak of the joint probability distribution with respect to h_{max} and $(M_F)_{max}$ varies with the return interval, and the largest values of h_{max} and $(M_F)_{max}$ were observed with the highest return intervals (2,500 year) as would be expected.

The tsunami inundation simulations were conducted with a bare earth DEM, and the effects of the natural and built environment were simply modeled using a single friction factor. It is known that the tsunami inundation velocity is sensitive to the choice of friction factor (e.g., Park et al., 2013) and that the friction factor can vary significantly for the built environment (e.g., Bricker et al., 2015). Therefore, future research should consider the effect of bottom friction uncertainty in modeling the probabilistic tsunami hazard assessment. Moreover, the difference in the types of models being used with respect to the approximation of the governing equations (e.g., non-linear shallow water equations or Boussinesq equations), solution techniques (finite element, finite difference), grid resolution, and so on introduce model source uncertainty and should be evaluated in a similar manner as bottom friction.

In terms of multi-hazards, future PSTHA frameworks should include additional sources such as other earthquake faults (on land), which would not produce tsunamis. Nonetheless, these would contribute to the seismic hazard in the region. Conversely, distance sources tsunamis should also be included, which may not produce ground shaking.

The results of the PSTHA can be the basis for a probabilistic multi-hazard damage assessment (PTSDA) to quantify the separate contributions of seismicity and tsunami hazards in the estimation of damage to the built environment over the community scale. In addition, it will be necessary to understand the propagation of uncertainties of the hazard assessments combined with the uncertainties of the damage estimates to evaluate the overall community risk to the multi-hazards. Moreover, the PTSDA should be evaluated considering the spatial gradients of the building damages at a

community scale due to the site information (e.g., building types) or fragility functions applied to each building for both earthquake and tsunami *IM*s across the length scale.

AUTHOR CONTRIBUTIONS

Each author contributed equally to the manuscript. HP and DC contributed to the tsunami hazard modeling. MA and AB contributed to the seismic hazard modeling.

FUNDING

Funding for this study was provided as part of the cooperative agreement 70NANB15H044 between the National Institute of Standards and Technology (NIST) and Colorado State University through a subaward to Oregon State University. The content expressed in this paper are the views of the authors and do not necessarily represent the opinions or views of NIST or the U.S. Department of Commerce.

REFERENCES

Abrahamson, N., Gregor, N., and Addo, K. (2016). BC Hydro ground motion prediction equations for subduction earthquakes. *Earthq. Spectra* 32, 23–44. doi:10.1193/051712EQS188MR

Anita, G., Sandri, L., Marzocchi, W., Argnani, A., Gasparini, P., and Selva, J. (2012). Probabilistic tsunami hazard assessment for Messina Strait Area (Sicily, Italy). *Nat. Hazards* 64, 329–358. doi:10.1007/s11069-012-0246-x

Annaka, T., Satake, K., Sakakiyama, T., Yanagisawa, K., and Shuto, N. (2007). Logic-tree approach for probabilistic tsunami hazard analysis and its applications to the Japanese coasts. *Pure appl. geophys.* 164, 577–592. doi:10.1007/s00024-006-0174-3

ASCE. (2010). *ASCE 7-10 Minimum Design Loads for Buildings and Other Structures*. Reston, VA: American Society of Civil Engineering.

Atkinson, G. M., Assatourians, K., Boore, D. M., Campbell, K., and Motazedian, D. (2009). A guide to differences between stochastic point-source and stochastic finite-fault simulations. *Bull. Seismol. Soc. Am.* 99, 3192–3201. doi:10.1785/0120090058

Atkinson, G. M., and Boore, D. M. (2003). Empirical ground-motion relations for subduction-zone earthquakes and their application to Cascadia and other regions. *Bull. Seismol. Soc. Am.* 93, 1703–1729. doi:10.1785/0120020156

Atkinson, G. M., and Boore, D. M. (2008). Erratum to empirical ground-motion relationships for subduction-zone earthquakes and their application to Cascadia and other regions. *Bull. Seismol. Soc. Am.* 98, 2567–2569.

Atkinson, G. M., Goda, K., and Assatourians, K. (2011). Comparison of nonlinear structural responses for accelerograms simulated from the stochastic finite-fault approach versus the hybrid broadband approach. *Bull. Seismol. Soc. Am.* 101, 2967–2980. doi:10.1785/0120100308

Attary, N., van de Lindt, J. W., Unnikrishnan, V. U., Barbosa, A. R., and Cox, D. T. (2017a). Methodology for development of physics-based tsunami fragilities. *J. Struct. Eng.* doi:10.1061/(ASCE)ST.1943-541X.0001715

Attary, N., Unnikrishnan, V. U., van de Lindt, J. W., Cox, D. T., and Barbosa, A. R. (2017b). Performance-based tsunami engineering methodology for risk assessment of structures. *Eng. Struct.* 141, 676–686. doi:10.1016/j.engstruct.2017.03.071

Atwater, B. F., and Griggs, G. B. (2012). "Deep-sea turbidites as guides to holocene earthquake history at the Cascadia subduction zone," in *Alternative Views for a Seismic-Hazard Workshop: U.S. Geological Survey Open-File Report 2012–1043*, Seattle, WA, 58.

Baker, J. W. (2011). Conditional mean spectrum: tool for ground-motion selection. *J. Struct. Eng.* 137, 322–331. doi:10.1061/(ASCE)ST.1943-541X.0000215

Baker, J. W., and Jayaram, N. (2008). Correlation of spectral acceleration values from NGA ground motion models. *Earthq. Spectra* 24, 299–317. doi:10.1193/1.2857544

Barbosa, A. R. (2011). *Simplified Vector-Valued Probabilistic Seismic Hazard Analysis and Probabilistic Seismic Demand Analysis: Application to the 13-Story NEHRP Reinforced Concrete Frame-Wall Building Design Example*. Ph.D. Dissertation, University of California San Diego, California.

Bazzurro, P. (1998). *Probabilistic Seismic Demand Analysis*. Ph.D. Dissertation. Stanford University, California.

Benjamin, J. R., and Cornell, C. A. (1970). *Probability, Statistics, and Decision for Civil Engineers*. New York: McGraw-Hill.

Bird, P., and Kagan, Y. Y. (2004). Plate-tectonic analysis of shallow seismicity: apparent boundary width, beta, corner magnitude, coupled lithosphere thickness, and coupling in seven tectonic settings. *Bull. Seismol. Soc. Am.* 94, 2380–2399. doi:10.1785/0120030107

Bricker, J. D., Gibson, S., Takagi, H., and Imamura, F. (2015). On the need for larger manning's roughness coefficients in depth-integrated tsunami inundation models. *Coast. Eng. J.* 57, 1550005. doi:10.1142/S0578563415500059

Burbidge, D., Cummins, P. R., Mleczko, R., and Thio, H. K. (2008). A probabilistic tsunami hazard assessment for Western Australia. *Pure appl. geophys.* 165, 2059–2088. doi:10.1007/s00024-008-0421-x

Burroughs, S. M., and Tebbens, S. F. (2005). Power-law scaling and probabilistic forecasting of tsunami runup height. *Pure Appl. Geophys.* 162, 331–342. doi:10.1007/s00024-004-2603-5

Cornell, C. A. (1968). Engineering seismic risk analysis. *Bull. Seismol. Soc. Am.* 58, 1583–1606.

Crouse, C. B. (1991). Ground-motion attenuation equation for earthquake on Cascadia Subduction-Zone earthquake. *Earthq. Spectra* 7, 210–236. doi:10.1193/1.1585626

Crouse, C. B., Yogesh, K. V., and Schell, B. A. (1988). Ground motions from subduction zone earthquakes. *Bull. Seismol. Soc. Am.* 78, 1–25.

De Risi, R., and Goda, K. (2016). Probabilistic earthquake–tsunami multi-hazard analysis: application to the Tohoku Region, Japan. *Front. Built Environ.* 2:25. doi:10.3389/fbuil.2016.00025

Delorey, A. A., Frankel, A. D., Liu, P., and Stephenson, W. J. (2014). Modeling the effects of source and path heterogeneity on ground motions of great earthquakes on the Cascadia subduction zone using 3D simulations. *Bull. Seismol. Soc. Am.* 104, 1430–1446. doi:10.1785/0120130181

DOGAMI Oregon Department of Geology and Mineral Industries. (2017). *Oregon HazVu: Statewide Geohazards Viewer*. Available at: http://www.oregongeology.org/sub/hazvu/

Douglas, J. (2003). Earthquake ground motion estimation using strong-motion records: a review of equations for the estimation of peak ground acceleration and response spectral ordinates. *Earth Sci. Rev.* 61, 43–104. doi:10.1016/S0012-8252(02)00112-5

Douglas, J. (2011). *Ground-Motion Prediction Equations 1964-2010*. Berkeley, CA: Pacific Earthquake Engineering Research Center, 444.

Douglas, J. (2016). *Ground-Motion Prediction Equations 1964-2016*. 564. Available at: http://gmpe.org.uk/gmpereport2014.pdf

Douglas, J., and Edwards, B. (2016). Recent and future developments in earthquake ground motion estimation. *Earth Sci. Rev.* 160, 203–219. doi:10.1016/j.earscirev.2016.07.005

Eads, L., Miranda, E., Krawinkler, H., and Lignos, D. G. (2013). An efficient method for estimating the collapse risk of structures in seismic regions. *Earthq. Eng. Struct. Dyn.* 42, 25–41. doi:10.1002/eqe.2191

Faggella, M., Barbosa, A. R., Conte, J. P., Spacone, E., and Restrepo, J. I. (2013). Probabilistic seismic response analysis of a 3-D reinforced concrete building. *Struct. Safety* 44, 11–27. doi:10.1016/j.strusafe.2013.04.002

Frankel, A., Chen, R., Petersen, M., Moschetti, M., and Sherrod, B. (2015). 2014 update of the Pacific northwest portion of the US national seismic hazard maps. *Earthq. Spectra* 31, S131–S148. doi:10.1193/111314EQS193M

Frankel, A., Paul, T., and Rohay, A. (2014). *Three-Dimensional Ground-Motion Simulations of Earthquakes for the Hanford Area, Washington*. U.S. Geological Survey Open-File Report 2013–1289, Reston, VA, 48.

Fukutani, Y., Suppasri, A., and Imamura, F. (2015). Stochastic analysis and uncertainty assessment of tsunami wave height using a random source parameter model that targets a Tohoku-type earthquake fault. *Stoch. Environ. Res. Risk Assess.* 29, 1763–1779. doi:10.1007/s00477-014-0966-4

Geist, E. L., and Parsons, T. (2006). Probabilistic analysis of tsunami hazards. *Nat. Hazards* 37, 277–314. doi:10.1007/s11069-005-4646-z

Gidaris, I., Padgett, J., Barbosa, A. R., Chen, S., Cox, D., Webb, B., et al. (2016). Multiple-hazard fragility and restoration models of highway bridges for regional

risk and resilience assessment in the U.S.: a state-of-the-art review. *ASCE J. Struct. Eng.* 143, 04016188-1–04016188-17. doi:10.1061/(ASCE)ST.1943-541X.0001672

Goda, K., Mai, P. M., Yasuda, T., and Mori, N. (2014). Sensitivity of tsunami wave profiles and inundation simulations to earthquake slip and fault geometry for the 2011 Tohoku earthquake. *Earth Planets Space* 66, 1–20. doi:10.1186/1880-5981-66-105

Goda, K., and Song, J. (2016). Uncertainty modeling and visualization for tsunami hazard and risk mapping: a case study for the 2011 Tohoku earthquake. *Stoch. Environ. Res. Risk Assess.* 30, 2271–2285. doi:10.1007/s00477-015-1146-x

Goda, K., Yasuda, T., Mori, N., and Maruyama, T. (2016). New scaling relationships of earthquake source parameters for stochastic tsunami simulation. *Coast. Eng. J.* 58, 1650010. doi:10.1142/S0578563416500108

Goldfinger, C., Nelson, C. H., Morey, A. E., Johnson, J. E., Patton, J. R., Karabanov, E., et al. (2012). "Turbidite event history: methods and implications for holocene paleoseismicity of the Cascadia subduction zone," in *U.S. Geological Survey Professional Paper 1661-F*, Corvallis, OR, 178.

González, F. I., Geist, E. L., Jaffe, B., Kânoglu, U., Mofjeld, H., Synolakis, C. E., et al. (2009). Probabilistic tsunami hazard assessment at seaside, Oregon, for near- and far-field seismic sources. *J. Geophys. Res. Oceans* 114, C11. doi:10.1029/2008JC005132

Grezio, A., Marzocchi, W., Sandri, L., and Gasparini, P. (2010). A Bayesian procedure for probabilistic tsunami hazard assessment. *Nat. Hazards* 53, 159–174. doi:10.1007/s11069-009-9418-8

Heaton, T. H., and Hartzell, S. H. (1987). Earthquake hazards on the Cascadia subduction zone. *Science* 236, 162–168. doi:10.1126/science.236.4798.162

Heidarzadeh, M., and Kijko, A. (2011). A probabilistic tsunami hazard assessment for the Makran subduction zone at the northwestern Indian Ocean. *Nat. Hazards* 56, 577–593. doi:10.1007/s11069-010-9574-x

Iwaki, A., Maeda, T., Morikawa, N., Aoi, S., and Fujiwara, H. (2016). Kinematic source models for long-period ground motion simulations of megathrust earthquakes: validation against ground motion data for the 2003 Tokachi-oki earthquake. *Earth Planets Space* 68, 95. doi:10.1186/s40623-016-0473-6

Jaffe, B. E., Borrero, J. C., Prasetya, G. S., Peters, R., McAdoo, B., Gelfenbaum, G., et al. (2006). Northwest Sumatra and offshore islands field survey after the December 2004 Indian Ocean tsunami. *Earthq. Spectra* 22, 105–135. doi:10.1193/1.2207724

Kagan, Y. Y. (1997). Seismic moment-frequency relation for shallow earthquakes: regional comparison. *J. Geophys. Res. Solid Earth* 102, 2835–2852. doi:10.1029/96JB03386

Kagan, Y. Y. (2002a). Seismic moment distribution revisited: I. Statistical results. *Geophys. J. Int.* 148, 520–541. doi:10.1046/j.1365-246x.2002.01594.x

Kagan, Y. Y. (2002b). Seismic moment distribution revisited: II. Moment conservation principle. *Geophys. J. Int.* 149, 731–754. doi:10.1046/j.1365-246X.2002.01671.x

Kramer, S. L. (1996). *Geotechnical Earthquake Engineering*. India: Pearson Education.

Leonard, L. J., Rogers, G. C., and Mazzotti, S. (2014). Tsunami hazard assessment of Canada. *Nat. Hazards* 70, 237–274. doi:10.1007/s11069-013-0809-5

Li, H., Yuan, Y., Xu, Z., Wang, Z., Wang, J., Wang, P., et al. (2016). The dependency of probabilistic tsunami hazard assessment on magnitude limits of seismic sources in the South China Sea and adjoining basins. *Pure Appl. Geophys.* 1–20.

Lin, P. S., and Lee, C. T. (2008). Ground-motion attenuation relationships for subduction-zone earthquakes in northeastern Taiwan. *Bull. Seismol. Soc. Am.* 98, 220–240. doi:10.1785/0120060002

Lin, T., Harmsen, S. C., Baker, J. W., and Luco, N. (2013). Conditional spectrum computation incorporating multiple causal earthquakes and ground-motion prediction models. *Bull. Seismol. Soc. Am.* 103, 1103–1116. doi:10.1785/0120110293

Liu, Y., Santos, A., Wang, S. M., Shi, Y., Liu, H., and Yuen, D. A. (2007). Tsunami hazards along Chinese coast from potential earthquakes in South China Sea. *Phys. Earth Planet. Inter.* 163, 233–244. doi:10.1016/j.pepi.2007.02.012

Lynett, P., Wu, T., and Liu, P. (2002). Modeling wave runup with depth-integrated equations. *Coast. Eng.* 46, 89–107. doi:10.1016/S0378-3839(02)00043-1

Mas, E., Koshimura, S., Suppasri, A., Matsuoka, M., Matsuyama, M., Yoshii, T., et al. (2012). Developing tsunami fragility curves using remote sensing and survey data of the 2010 Chilean tsunami in Dichato. *Nat. Hazards Earth Syst. Sci.* 12, 2689–2697. doi:10.5194/nhess-12-2689-2012

McGuire, R. K. (1995). Probabilistic seismic hazard analysis and design earthquakes: closing the loop. *Bull. Seismol. Soc. Am.* 85, 1275–1284.

McGuire, R. K. (2004). *Seismic Hazard and Risk Analysis*. Berkeley, CA: Earthquake Engineering Research Institute, 240.

Mori, N., Cox, D. T., Yasuda, T., and Mase, H. (2013). Overview of the 2011 Tohoku earthquake tsunami damage and its relation to coastal protection along the Sanriku coast. *Earthq. Spectra* 29, S127–S143. doi:10.1193/1.4000118

Mueller, C., Power, W., Fraser, S., and Wang, X. (2015). Effects of rupture complexity on local tsunami inundation: implications for probabilistic tsunami hazard assessment by example. *J. Geophys. Res. Solid Earth* 120, 488–502.

Murotani, S., Satake, K., and Fujii, Y. (2013). Scaling relations of seismic moment, rupture area, average slip, and asperity size for M 9 subduction-zone earthquakes. *Geophys. Res. Lett.* 40, 5070–5074. doi:10.1002/grl.50976

Okada, Y. (1985). Surface deformation due to shear and tensile faults in a half-space. *Bull. Seismol. Soc. Am.* 75, 1135–1154.

Olsen, K. B., Stephenson, W. J., and Geisselmeyer, A. (2008). 3D crustal structure and long-period ground motions from a M9.0 megathrust earthquake in the Pacific Northwest region. *J. Seismol.* 12, 145–159. doi:10.1007/s10950-007-9082-y

Papazachos, B. C., Scordilis, E. M., Panagiotopoulus, C. B., and Karakaisis, G. F. (2004). Global relations between seismic fault parameters and moment magnitudes of earthquakes. *Bull. Geol. Soc. Greece* 36, 1482–1489.

Park, H., and Cox, D. T. (2016). Probabilistic assessment of near-field tsunami hazards: inundation depth, velocity, momentum flux, arrival time, and duration applied to seaside, Oregon. *Coast. Eng.* 117, 79–96. doi:10.1016/j.coastaleng.2016.07.011

Park, H., Cox, D. T., and Barbosa, A. (2017). Comparison of inundation depth and momentum flux based fragilities for probabilistic tsunami damage assessment and uncertainty analysis. *Coast. Eng.* 122, 10–26. doi:10.1016/j.coastaleng.2017.01.008

Park, H., Cox, D. T., Lynett, P. J., Wiebe, D. M., and Shin, S. (2013). Tsunami inundation modeling in constructed environments: a physical and numerical comparison of free-surface elevation, velocity, and momentum flux. *Coast. Eng.* 79, 9–21. doi:10.1016/j.coastaleng.2013.04.002

Power, W., Downes, G., and Stirling, M. (2007). Estimation of tsunami hazard in New Zealand due to South American Earthquakes. *Pure Appl. Geophys.* 164, 547–564. doi:10.1007/s00024-006-0166-3

Power, W., Wang, X., Lane, E., and Gillibrand, P. (2013). A probabilistic tsunami hazard study of the Auckland region, part I: propagation modelling and tsunami hazard assessment at the shoreline. *Pure Appl. Geophys.* 170, 1621–1634. doi:10.1007/s00024-012-0543-z

Priest, G. R., Goldfinger, C., Wang, K., Witter, R. C., Zhang, Y., and Baptista, A. M. (2010). Confidence levels for tsunami-inundation limits in northern Oregon inferred from a 10,000-year history of great earthquakes at the Cascadia subduction zone. *Nat. Hazards* 54, 27–73. doi:10.1007/s11069-009-9453-5

Pulido, N., Aguilar, Z., Tavera, H., Chlieh, M., Calderon, D., Sekiguchi, T., et al. (2015). Scenario source models and strong ground motion for future mega-earthquakes: application to Lima, Central Peru. *Bull. Seismol. Soc. Am.* 105, 368–386. doi:10.1785/0120140098

Rikitake, T., and Aida, I. (1988). Tsunami hazard probability in Japan. *Bull. Seismol. Soc. Japan* 78, 1268–1278.

Rong, Y., Jackson, D. D., Magistrale, H., and Goldfinger, C. (2014). Magnitude limits of subduction zone earthquakes. *Bull. Seismol. Soc. Am.* 104, 2359–2377. doi:10.1785/0120130287

Rossetto, T., Peiris, N., Pomonis, A., Wilkinson, S. M., Del Re, D., Koo, R., et al. (2007). The Indian Ocean tsunami of December 26, 2004: observations in Sri Lanka and Thailand. *Nat. Haz.* 42, 105–124.

Satake, K., Wang, K., and Atwater, B. F. (2003). Fault slip and seismic moment of the 1700 Cascadia earthquake inferred from Japanese tsunami descriptions. *J. Geophys. Res. Solid Earth* 108, 2535. doi:10.1029/2003JB002521

Schwartz, D. P., and Coppersmith, K. J. (1984). Fault behavior and characteristic earthquakes: examples from the Wasatch and San Andreas fault zones. *J. Geophys. Res. Solid Earth* 89, 5681–5698. doi:10.1029/JB089iB07p05681

Skarlatoudis, A. A., Somerville, P. G., and Thio, H. K. (2016). Source-scaling relations of interface subduction earthquakes for strong ground motion and tsunami simulation. *Bull. Seismol. Soc. Am.* 106, 1652–1662. doi:10.1785/0120150320

Skarlatoudis, A. A., Somerville, P. G., Thio, H. K., and Bayless, J. R. (2015). Broadband strong ground motion simulations of large subduction earthquakes. *Bull. Seismol. Soc. Am.* 105, 3050–3067. doi:10.1785/0120140322

Somerville, P., Skarlatoudis, A., and Li, W. (2012). "Ground motions and tsunamis from large Cascadia subduction earthquakes based on the 2011 Tokoku, Japan Earthquake," in *USGS Report G12AP20081*.

Stewart, J. P., Douglas, J., Javanbarg, M., Bozorgnia, Y., Abrahamson, N. A., Boore, D. M., et al. (2015). Selection of ground motion prediction equations for the Global Earthquake Model. *Earthq. Spectra* 31, 19–45. doi:10.1193/013013EQS017M

Strasser, F. O., Arango, M. C., and Bommer, J. J. (2010). Scaling of the source dimensions of interface and intraslab subduction-zone earthquakes with moment magnitude. *Seismol. Res. Lett.* 81, 941–950. doi:10.1785/gssrl.81.6.941

Thio, H. K., and Somerville, P. (2009). "A probabilistic tsunami hazard analysis of California," in *TCLEE 2009: Lifeline Earthquake Engineering in a Multihazard Environment* (Oakland, CA: ASCE), 1–12.

Thio, H. K., Somerville, P., and Ichinose, G. (2007). Probabilistic analysis of strong ground motion and tsunami hazards in Southeast Asia. *J. Earthq. Tsunami* 1, 119–137. doi:10.1142/S1793431107000080

Tinti, S., Armigliato, A., Tonini, R., Maramai, A., and Graziani, L. (2005). Assessing the hazard related to tsunamis of tectonic origin: a hybrid statistical-deterministic method applied to southern Italy coasts. *ISET J. Earthq. Technol.* 42, 189–201.

Titov, V. V., Moore, C. W., Greenslade, D. J. M., Pattiaratchi, C., Badal, R., Synolakis, C. E., et al. (2011). A new tool for inundation modeling: community modeling interface for tsunamis (ComMIT). *Pure Appl. Geophys.* 168, 2121–2131. doi:10.1007/s00024-011-0292-4

Wesnousky, S. G. (1994). The Gutenberg-Richter or characteristic earthquake distribution, which is it? *Bull. Seismol. Soc. Am.* 84, 1940–1959.

Wiebe, D. M., and Cox, D. T. (2014). Application of fragility curves to estimate building damage and economic loss at a community scale: a case study of Seaside, Oregon. *Nat. Hazards* 71, 2043–2061. doi:10.1007/s11069-013-0995-1

Witter, R. C., Zhang, Y. J., Wang, K., Priest, G. R., Goldfinger, C., Stimely, L., et al. (2013). Simulated tsunami inundation for a range of Cascadia megathrust earthquake scenarios at Bandon, Oregon, USA. *Geosphere* 9, 1783–1803. doi:10.1130/GES00899.1

Wood, N., Burton, C. G., and Cutter, S. L. (2010). Community variations in social vulnerability to Cascadia-related tsunamis in the U.S. Pacific Northwest. *Nat. Hazards* 52, 369–389. doi:10.1007/s11069-009-9376-1

Yanagisawa, K., Imamura, F., Sakakiyama, T., Annaka, T., Takeda, T., and Shuto, N. (2007). Tsunami assessment for risk management at nuclear power facilities in Japan. *Pure Appl. Geophys.* 164, 565–576. doi:10.1007/s00024-006-0176-1

Youngs, R., Chiou, S., Silva, W., and Humphrey, J. (1997). Strong ground motion attenuation relationships for subduction zone earthquakes. *Seismic Res. Lett.* 68, 58–73. doi:10.1785/gssrl.68.1.58

Zareian, F., and Krawinkler, H. (2007). Assessment of probability of collapse and design for collapse safety. *Earthq. Eng. Struct. Dyn.* 36, 1901–1914. doi:10.1002/eqe.702

Zhao, J. X., Zhang, J., Asano, A., Ohno, Y., Oouchi, T., Takahashi, T., et al. (2006). Attenuation relations of strong ground motion in Japan using site classification based on predominant period. *Bull. Seismol. Soc. Am.* 96, 898–913. doi:10.1785/0120050122

Conflict of Interest Statement: The authors declare that the research was conducted in the absence of any commercial or financial relationships that could be construed as a potential conflict of interest.

Copyright © 2017 Park, Cox, Alam and Barbosa. This is an open-access article distributed under the terms of the Creative Commons Attribution License (CC BY). The use, distribution or reproduction in other forums is permitted, provided the original author(s) or licensor are credited and that the original publication in this journal is cited, in accordance with accepted academic practice. No use, distribution or reproduction is permitted which does not comply with these terms.

frontiers in Built Environment

ORIGINAL RESEARCH
published: 05 May 2017
doi: 10.3389/fbuil.2017.00027

A Framework for Seismic Design of Items in Safety-Critical Facilities for Implementing a Risk-Informed Defense-in-Depth-Based Concept

Tatsuya Itoi, Yuki Iita and Naoto Sekimura*

School of Engineering, The University of Tokyo, Tokyo, Japan

Recently, especially after the 2011 off the Pacific coast of Tohoku earthquake and the Fukushima Daiichi nuclear power plant accident, the need for treating residual risks and cliff-edge effects in safety-critical facilities has been widely recognized as an extremely important issue. In this article, the sophistication of seismic designs in safety-critical facilities is discussed from the viewpoint of mitigating the consequences of accidents, such as the avoidance of cliff-edge effects. For this purpose, the implementation of a risk-informed defense-in-depth-based framework is proposed in this study. A basic framework that utilizes diversity in the dynamic characteristics of items and also provides additional seismic margin to items important for safety when needed is proposed to prevent common cause failure and to avoid cliff-edge effects as far as practicable. The proposed method is demonstrated to be effective using an example calculation.

Keywords: seismic design, risk, safety-critical facility, defense in depth, cliff-edge effects

OPEN ACCESS

Edited by:
Katsuichiro Goda,
University of Bristol, UK

Reviewed by:
Taojun Liu,
United States Geological Survey, USA
Christian Málaga-Chuquitaype,
Imperial College London, UK

****Correspondence:***
Tatsuya Itoi
itoi@n.t.u-tokyo.ac.jp

Specialty section:
This article was submitted to Earthquake Engineering, a section of the journal Frontiers in Built Environment

Received: *17 January 2017*
Accepted: *13 April 2017*
Published: *05 May 2017*

Citation:
Itoi T, Iita Y and Sekimura N (2017) A Framework for Seismic Design of Items in Safety-Critical Facilities for Implementing a Risk-Informed Defense-in-Depth-Based Concept. Front. Built Environ. 3:27. doi: 10.3389/fbuil.2017.00027

INTRODUCTION

Natural hazards, including earthquakes, are considered to be one of several possible causes of major accidents in safety-critical facilities such as nuclear power plants. Conventionally, it had been required, when designing safety-critical facilities against earthquakes, that design ground motion must be determined so that risks, e.g., to public health, associated with ground motion hazards are negligible compared with those associated with accidents of internal origins (International Atomic Energy Agency, 1988). It has been occasionally misunderstood that seismic safety of safety-critical facilities can be achieved if design ground motion is set large enough so that seismic risks can be sufficiently reduced. Recently, however, especially after the 2011 off the Pacific coast of Tohoku earthquake and the Fukushima Daiichi nuclear power plant accident, the need for serious consideration and treatment of residual risks has been widely recognized as an extremely important issue. Although the accident was caused due to tsunami, it was also recognized that there exists a room for discussion also for a framework of earthquake engineering.

A framework of performance-based seismic design (Structural Engineers Association of California, 1995) is considered to be one of several reasonable approaches in the practice of seismic design of engineering facilities. Within this framework, as shown in **Figure 1**, the levels of design ground motion are specified so that several performance objectives are met, and these levels are specified based on the potential severity of consequences when facilities suffer from damage.

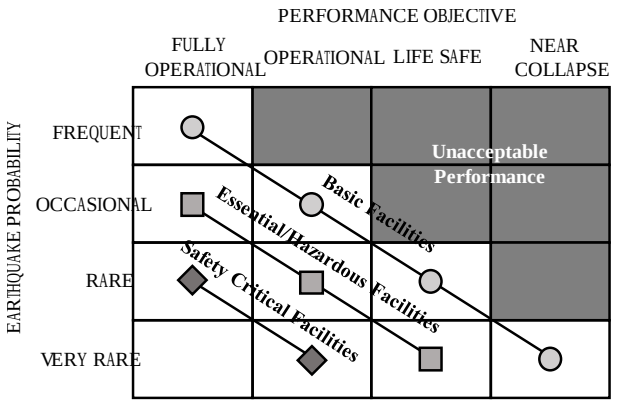

FIGURE 1 | Typical framework for performance-based seismic design (Structural Engineers Association of California, 1995).

For safety-critical facilities, it is required to be operational even in the case of very rare earthquakes, i.e., severe earthquakes, and a near collapse state is not acceptable for any level of earthquake. On the other hand, a near collapse state is acceptable for basic facilities in the event of very rare earthquakes. What should be emphasized here is that this framework does not imply that safety-critical facilities do not require a mitigation strategy in dealing with the consequences of failure to the extent where these facilities are severely damaged to the point of collapse. Such a strategy, nonetheless, is considered to be more important for safety-critical facilities than for basic facilities.

In the field of nuclear safety, the "defense-in-depth" concept is considered to be important when dealing with residual risks, i.e., remaining risks after safety measures are introduced, and it is the primary means to prevent and mitigate the consequences of accidents (International Atomic Energy Agency, 1996, 2006). For safety-critical facilities, the defense-in-depth concept is implemented through a combination of consecutive and independent levels of protection (International Atomic Energy Agency, 1996, 2006). The central feature of the defense in depth is the idea of multiple levels of protection of public and workers (International Atomic Energy Agency, 1996). Under seismic excitations, however, it is impossible and unrealistic to assume that each level of protection for defense in depth is completely independent of each other. This is because items corresponding to each level of defense are simultaneously excited by earthquake ground motion in space and time, and this could lead to simultaneous malfunction and/or damage that results in a common cause failure. If items that are important in preventing accidents and mitigating the consequences of accidents simultaneously malfunction and/or suffer from damage, accidents with serious consequences could occur. These kinds of effects in the event of accidents are also known as cliff-edge effects (International Atomic Energy Agency, 2003, 2016a,b). The term "cliff-edge effects" implies a sudden large variation in condition of the facilities in response to a small variation in an input. It is triggered by simultaneous malfunction of these items.

There appears to be, however, no widely accepted approach in implementing the defense-in-depth concept over a wide range of seismic excitations, because the concept of the defense in depth was originally developed for accidents of internal origins. Therefore, this article proposes a basic theoretical framework with respect to seismic design of items important to safety based on a risk-informed concept (United States Nuclear Regulatory Commission, 2012), so that the defense-in-depth concept can be appropriately implemented for the seismic safety of safety-critical facilities.

As mentioned earlier, multiple items in a facility are excited and some of them are damaged by earthquake ground motions simultaneously. Moreover, spatially distributed multiple facilities suffer from damage simultaneously. These characteristics should be taken into consideration when conducting seismic risk assessment (Bazzurro and Cornell, 2002; Wang et al., 2009). Ground motion modeling, which can be applied to such seismic probabilistic risk assessment, has also been developed (Wang and Takada, 2005; Baker and Jayaram, 2008). In this study, a basic implementation method to deal with such characteristics of ground motions, called "risk-informed defense-in-depth-based framework" (Miyano et al., 2015), is developed by using this risk-based framework. The proposed method combines the concepts of diversity and seismic margin for the framework to give a basic insight on how multiple items closely located to each other can be designed to cope with earthquakes by combining multiple barriers.

PROPOSED FRAMEWORK OF SEISMIC DESIGN OF ITEMS IMPORTANT TO SAFETY

Background and Assumption

Items important to safety can be simply categorized into items that are important in preventing accidents and items that are important in mitigating the consequences of accidents. Items important to mitigating the consequences of accidents are required to function only after the occurrence of an accident, which essentially means that items important in preventing accident, in the first place, are damaged and/or have malfunctioned. Conventional seismic design procedures, however, do not usually distinguish between the roles of these two items explicitly.

The strategy for items important for safety is considered to be developed by combining diversity, physical separation, and functional independence (International Atomic Energy Agency, 2016a). Implementation of physical separation and functional independence is considered to be straightforward, while implementation of diversity to seismic excitation needs to be discussed further. Therefore, implementation of diversity to seismic excitation is discussed in this article. Diversity is provided by different mechanisms to function. In the seismic design of facilities, diversity is considered to be provided through differences in location of items (such as a plan layout or elevation) and by different dynamic characteristics between items (such as structural type, natural period, and damping characteristics). Providing an additional seismic margin, such as differentiation in classes of required seismic margins to each item based on its role, is another means in avoiding cliff-edge effects (International Atomic Energy Agency, 2016a). Typically, conservative parameters are introduced in the

analysis of seismic design to deal with uncertainty, which are based on engineering judgment, the results of structural analysis, etc. These conservative parameters result in conservative designs. Quantification of such conservativeness is important to discuss the performance of facility to ground motions greater than the design ground motion (Budnitz et al., 1985; Haselton et al., 2011). In this study, an appropriate combination of seismic margin and diversity is discussed to implement the defense-in-depth concept to seismic design for safety-critical facility based on the risk-informed approach. A method to assign required additional seismic margins to each item is proposed depending on the characteristics of diversity introduced. As mentioned earlier, diversity is important to implement the defense-in-depth concept under seismic excitations. It is, however, not always possible to introduce it, because of the limitation due to the characteristics of item. Additional seismic margin is considered to be effective as a means of supplementing for such cases. Here, additional seismic margin means that seismic margin is required in addition to the seismic margin that is already introduced in the conventional seismic design.

A Method to Identify the Most Probable Source Characteristics and Associated Ground Motion Parameters That May Cause Accidents at Safety-Critical Facilities

Probabilistic Seismic Hazard Analysis and Ground Motion Prediction Equation

Probabilistic seismic hazard analysis is used to determine design ground motion and to analyze seismic risk of facilities. An example of the annual exceedance probability of design ground motion required for safety-critical facilities is usually $\sim 10^{-4}$ or smaller (Nuclear Regulatory Commission, 1997, 2007). Statistical equations, called ground motion prediction equations, are conventionally used to predict ground motions. In all, 5% damped acceleration response spectra are conveniently used to characterize a variety of frequency contents in different ground motions. A ground motion prediction equation for 5% damped spectral acceleration that is used in this study was initially developed for crustal earthquakes in Japan (Itoi et al., 2015). The functional form of the equation is as follows (Itoi et al., 2015):

$$\begin{aligned}\log_{10} S_{a\mathrm{GM}}(T) = {} & a(T) + b(T)M_W - c(T)X \\ & - \log_{10}\left(X + d(T)\cdot 10^{0.5M_W}\right) \\ & - e(T)\left(\log_{10} V_{S30}\right)^2 + f(T)\log_{10} V_{S30} \\ & + g(T)\log_{10}\left(\max\left(\min\left(Z_{1500}, h(T)\right), k(T)\right)\right) \\ & + \sigma_{\mathrm{INTER}}(T)E_{\mathrm{INTER}}(T) + \sigma_{\mathrm{INTRA}}(T)E_{\mathrm{INTRA}}(T)\end{aligned} \tag{1}$$

where $S_a(T)$ is the 5% damped spectral acceleration at period T. M_W, X (km), V_{S30} (m/s), and Z_{1500} (m) are the moment magnitude, the shortest distance from fault to site, the 30 m average shear wave velocity, and the depth to shear wave velocity, which is equal to 1,500 m/s, respectively. $E_{\mathrm{INTER}}(T)$ and $E_{\mathrm{INTRA}}(T)$ are standard normal variables for inter-event and intra-event residuals, respectively, while $\sigma_{\mathrm{INTER}}(T)$ and $\sigma_{\mathrm{INTRA}}(T)$ are their corresponding standard deviations. $a(T)$ to $k(T)$ are the coefficients obtained by the least-square regression. The coefficients $a(T)$ to $k(T)$, $\sigma_{\mathrm{INTER}}(T)$, and $\sigma_{\mathrm{INTRA}}(T)$ obtained based on the least-square regression are summarized in **Table 1**. Period-to-period correlations for inter-event residuals $\rho_{\mathrm{INTER}}(T_A, T_B)$ and intra-event residuals $\rho_{\mathrm{INTRA}}(T_A, T_B)$ are summarized in **Table 2**. Correlation of $E_{\mathrm{INTER}}(T)$ and $E_{\mathrm{INTRA}}(T)$ between different periods T is important when the possibility of simultaneous damage of multiple items, i.e., a common cause failure, is discussed. The applicable range of the equation is $5.1 \leq M_W \leq 6.9$, $X \leq 100$ km, $110\ \mathrm{m/s} \leq V_{S30} \leq 700$ m/s, and $Z_{1500} \leq 3{,}000$ m (Itoi et al., 2015).

A Method to Identify the Most Probable Source Characteristics

In this section, a framework is proposed to identify the most probable source characteristics and ground motion parameters that may result in accidents. The most probable source characteristics and ground motion parameters are defined here as the design point that can be obtained by the first-order reliability method (FORM) (Rackwitz and Fiessler, 1978). The design point is defined as the point with the highest probability density in the domain of accident. The FORM (Rackwitz and Fiessler, 1978), probabilistic seismic hazard deaggregation (McGuire, 1995; Takada et al., 2003), and the conditional mean spectrum (Baker, 2011) are used in the proposed framework.

A system that is considered for a simplified case is assumed to contain two items (items A and B) that are located at the same place. It is assumed that an accidental condition occurs if item A fails. Item B is then used to mitigate the consequences of the resulting accident. A fault tree representation of system failure defined by an occurrence of an accident with serious consequences is shown in **Figure 2** using the priority-AND gate. Item A is assumed to be a single-degree-of-freedom system that has a natural period T_A. The limit state function for failure of item A, G_A, is defined as follows:

$$G_A = R_A(T_A) - S_A(T_A) \tag{2}$$

where $R_A(T_A)$ is the capacity of item A as a function of the 5% damped spectral acceleration at $T = T_A$ and is assumed to have a log-normal distribution. $S_A(T_A)$ is the maximum seismic action on item A, i.e., 5% damped spectral acceleration at $T = T_A$. The probability distribution of $S_A(T_A)$ for a certain period of time, which is 1 year in this case, is obtained using the probabilistic seismic hazard analysis. Item A fails if G_A is negative, while item A survives if G_A is positive. The most probable level of spectral acceleration ${s_A}^*$ for $S_A(T_A)$ is obtained using FORM.

Then, the most probable earthquake source parameters and ground motion parameters that may result in accidents are identified. Similar to Eq. 2, a limit state function G_{HA} is defined as follows:

$$G_{\mathrm{HA}} = \log_{10}{s_A}^* - \log_{10} S_{\mathrm{CA}}(T_A) \tag{3}$$

TABLE 1 | The coefficients for the ground motion prediction equation (Itoi et al., 2015).

T(s)	*a*	*b*	*c* ($\times 10^{-3}$)	*d* ($\times 10^{-3}$)	*e*	*f*	*g*	*h*	*k*	σ_{INTER}	σ_{INTRA}
0.02	−8.202	0.5462	2.909	3.955	−1.508	7.226	–	–	–	0.2068	0.2446
0.04	−7.576	0.5154	3.218	4.631	−1.377	6.762	–	–	–	0.2197	0.2474
0.06	−7.076	0.4936	2.823	4.549	−1.267	6.376	–	–	–	0.2253	0.2639
0.11	−13.26	0.5285	2.428	3.851	−2.314	11.45	–	–	–	0.2195	0.2715
0.19	−14.40	0.5852	2.843	2.651	−2.644	12.60	–	–	–	0.2038	0.2795
0.32	−8.716	0.6585	3.213	1.982	−1.759	7.867	–	–	–	0.1948	0.2777
0.56	0.2375	0.7416	3.148	1.144	−0.263	0.116	0.1279	988.4	12.19	0.1926	0.2788
0.97	4.066	0.8234	3.728	1.238	0.512	−3.721	0.1909	968.8	7.664	0.1860	0.2718
1.7	0.6731	0.9358	4.644	2.493	0.193	−1.966	0.2135	–	9.785	0.1625	0.2501
2.9	0.4002	0.9731	3.809	3.421	0.380	−2.731	0.3573	–	100.9	0.1265	0.2257
5.0	−1.629	1.063	2.204	4.502	0.271	−2.028	0.3410	–	131.5	0.1047	0.2080

TABLE 2 | Period-to-period correlation for inter-event and intra-event residuals (Itoi et al., 2015).

T(s)	0.02	0.04	0.06	0.11	0.19	0.32	0.56	0.97	1.7	2.9	5.0
(A) Inter-event residuals $\rho_{INTER}(T_1, T_2)$											
0.02	1	0.9928	0.9811	0.9877	0.9841	0.9284	0.8333	0.7689	0.7007	0.2367	0.0716
0.04		1	0.9942	0.9867	0.9655	0.8868	0.7917	0.7345	0.6742	0.2200	0.0614
0.06			1	0.9867	0.9509	0.8569	0.7563	0.6971	0.6368	0.2222	0.0632
0.11				1	0.9740	0.8930	0.7830	0.7141	0.6503	0.2380	0.0706
0.19					1	0.9490	0.8436	0.7681	0.6887	0.2653	0.1013
0.32						1	0.9326	0.8540	0.7520	0.2703	0.1276
0.56							1	0.9596	0.8677	0.3285	0.1944
0.97				Sym.				1	0.9303	0.4126	0.3179
1.7									1	0.5987	0.4917
2.9										1	0.8011
5.0											1
(B) Intra-event residuals $\rho_{INTRA}(T_1, T_2)$											
0.02	1	0.9568	0.9022	0.8976	0.8048	0.6247	0.4673	0.3294	0.2541	0.2428	0.2865
0.04		1	0.9501	0.8570	0.7061	0.5133	0.3592	0.2294	0.1583	0.1555	0.1911
0.06			1	0.8362	0.6153	0.4158	0.2737	0.1524	0.0903	0.0990	0.1337
0.11				1	0.7007	0.4519	0.3054	0.1991	0.1458	0.1551	0.2050
0.19					1	0.7257	0.5306	0.3996	0.3188	0.2954	0.3372
0.32						1	0.7485	0.5702	0.4521	0.3779	0.3966
0.56							1	0.7764	0.6156	0.5218	0.4969
0.97				Sym.				1	0.7926	0.6457	0.5793
1.7									1	0.7920	0.6628
2.9										1	0.7956
5.0											1

where $S_{CA}(T_A)$ is the ground motion given the earthquake occurrence. Based on Eq. 1, $S_{CA}(T_A)$ is described as follows:

$$\begin{aligned}\log_{10} S_{CA}(T_A) = {} & a(T_A) + b(T_A) M_W - c(T_A) X \\ & - \log_{10}\left(X + d(T_A)\cdot 10^{0.5 M_W}\right) \\ & - e(T_A)\left(\log_{10} v_{S30S}\right)^2 + f(T_A)\log_{10} v_{S30S} \\ & + g(T_A)\log_{10}\left(\max\left(\min\left(z_{1500S}, h(T_A)\right), k(T_A)\right)\right) \\ & + \sigma_{INTER}(T_A) E_{INTER}(T_A) \\ & + \sigma_{INTRA}(T_A) E_{INTRA}(T_A)\end{aligned} \tag{4}$$

where M_W, X, $E_{INTER}(T_A)$, and $E_{INTRA}(T_A)$ are random variables representing the moment magnitude, the shortest distance from fault to site, the standard normal variable for inter-event residual, and the standard normal variable for intra-event residual, respectively. v_{S30S} and z_{1500S} are V_{S30} and Z_{1500} at the location of the system, respectively.

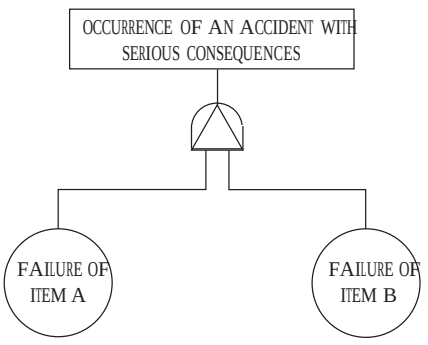

FIGURE 2 | Fault tree representation of the system considered.

The most probable values for M_W, X, $E_{INTER}(T_A)$ and $E_{INTRA}(T_A)$, $M_W{}^*$, x^*, $\varepsilon_{INTER}{}^*(T_A)$, and $\varepsilon_{INTRA}{}^*(T_A)$ are obtained given that $S_A(T_A) = s_A{}^*$ using FORM. The

methodology used is almost identical to that proposed by Takada et al. (2003) and similar to that proposed by McGuire (1995).

Item B is also assumed to be a single-degree-of-freedom system with a natural period T_B, which can be different from T_A. The most probable earthquake source characteristics under which item B is required to function is an earthquake of magnitude $M_W{}^*$, whose shortest distance from fault to site is x^*. The most probable spectral acceleration at period T_A is $s_A{}^*$, which is obtained from Eq. 3 using the abovementioned procedure. The most probable spectral acceleration at period T_B, $\bar{s}_B{}^*(T_B|T_A)$, given this condition, is calculated as follows:

$$\begin{aligned}\log_{10}\bar{s}_B{}^*(T_B|T_A) = {} & a(T_B) + b(T_B)\,M_W{}^* - c(T_B)\,x^* \\ & - \log_{10}\left(x^* + d(T_B)\cdot 10^{0.5M_W{}^*}\right) \\ & - e(T_B)\left(\log_{10}V_{S30S}\right)^2 + f(T_B)\log_{10}V_{S30S} \\ & + g(T_B)\log_{10}(\max(\min(Z_{1500S}, h(T_B)), k(T_B))) \\ & + \sigma_{\mathrm{INTER}}(T_B)\,\bar{\varepsilon}_{\mathrm{INTER}}{}^*(T_B|T_A) \\ & + \sigma_{\mathrm{INTRA}}(T_B)\,\bar{\varepsilon}_{\mathrm{INTRA}}{}^*(T_B|T_A)\end{aligned} \tag{5}$$

where $\bar{\varepsilon}_{\mathrm{INTER}}{}^*(T_B|T_A)$ and $\bar{\varepsilon}_{\mathrm{INTRA}}{}^*(T_B|T_A)$ are the conditional means of the bivariate normal distribution given $\varepsilon_{\mathrm{INTER}}{}^*(T_A)$ and $\varepsilon_{\mathrm{INTRA}}{}^*(T_A)$, respectively, as follows:

$$\bar{\varepsilon}_{\mathrm{INTER}}{}^*(T_B|T_A) = \frac{\rho_{\mathrm{INTER}}(T_A,\ T_B)\,\varepsilon_{\mathrm{INTER}}{}^*(T_A)}{\sqrt{1-\rho_{\mathrm{INTER}}(T_A,\ T_B)^2}} \tag{6}$$

$$\bar{\varepsilon}_{\mathrm{INTRA}}{}^*(T_B|T_A) = \frac{\rho_{\mathrm{INTRA}}(T_A,\ T_B)\,\varepsilon_{\mathrm{INTRA}}{}^*(T_A)}{\sqrt{1-\rho_{\mathrm{INTRA}}(T_A,\ T_B)^2}} \tag{7}$$

This concept is identical to that of the conditional mean spectrum proposed by Baker (2011). As can be understood from Eqs 6 and 7, $\bar{\varepsilon}_{\mathrm{INTER}}{}^*(T_B|T_A)$ and $\bar{\varepsilon}_{\mathrm{INTRA}}{}^*(T_B|T_A)$ respectively, approach asymptotically to 0 as the difference between T_A and T_B increases. This is because $\rho_{\mathrm{INTER}}(T_A, T_B)$ and $\rho_{\mathrm{INTRA}}(T_A, T_B)$ approach 0 as the difference between T_A and T_B increases as shown in **Table 2**.

Proposed Framework to Provide Additional Seismic Margins to Items Important in Mitigating the Consequences of Accidents

Item B should be designed based on a different concept from that of item A. It is because a role of item B is different from that of item A. Therefore, it has been proposed in this study that the seismic margin $m_B(T_B|T_A)$, which is additionally required for item B, is a function of the obtained spectral acceleration $\bar{s}_B{}^*(T_B|T_A)$ and is given as follows:

$$m_B(T_B|T_A) = \max\left(1,\ \frac{\bar{s}_B{}^*(T_B|T_A)}{s_{\mathrm{BD}}(T_B)}\right) \tag{8}$$

where $S_{\mathrm{BD}}(T_B)$ is the spectral acceleration at period T_B for the original seismic design obtained using the same concept as that for item A. From Eq. 5, it can be found that the additional seismic margin $m_B(T_B|T_A)$ is almost unity if the difference between T_A and T_B is large enough. This is justified because diversity with respect to dynamic characteristics, such as the natural period, is expected to work effectively. (This will be discussed in the next chapter.). On the other hand, a larger additional margin $m_B(T_B|T_A)$ is required if T_A and T_B are close to each other, i.e., if the diversity in the characteristics of items is not introduced in the seismic design. The proposed method combines the information on regional seismicity, the characteristics of ground motions, and the vulnerability of the facility to determine the additional seismic margin required for items that are important in mitigating the consequences of accidents.

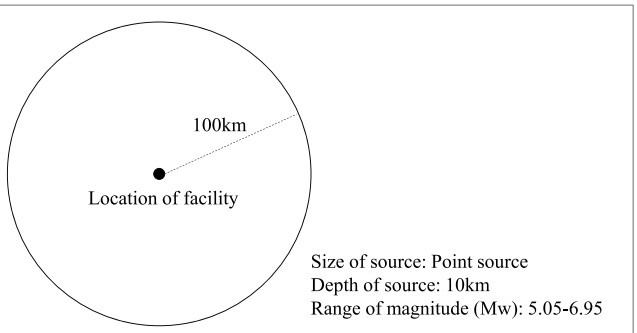

FIGURE 3 | Location of facility and the assumed area source. Size of source: point source; depth of source: 10 km; range of magnitude (M_w): 5.05–6.95.

SEISMIC MARGIN REQUIRED FOR ITEMS THAT ARE IMPORTANT IN MITIGATING THE CONSEQUENCES OF ACCIDENTS FOR AREA SOURCES

Simulation Conditions

An area source as shown in **Figure 3** is used as an example. Point sources are uniformly distributed within a radius of 100 km, whereby their focal depth is 10 km. The facility is assumed to be located on the ground surface above the center of the area source. The probability distribution of the earthquake magnitude is assumed to be in agreement with the Gutenberg–Richter law. The cumulative distribution function for the magnitude $F_M(m)$ is as follows:

$$F_M(m) = \frac{\exp(-b\cdot\ln 10\cdot m) - \exp(-b\cdot\ln 10\cdot m_{\min})}{\exp(-b\cdot\ln 10\cdot m_{\max}) - \exp(-b\cdot\ln 10\cdot m_{\min})} \tag{9}$$

where $m_{\max}$ (6.95) and $m_{\min}$ (5.05) are the maximum and minimum magnitudes, respectively. b is assumed to be 0.9. These values are typical for those used for earthquakes without specified source faults in Japan. v_{S30S} and z_{1500S} of Eq. 5 are assumed to be 700 m/s and 100 m, respectively. v_{S30S} and z_{1500S} are the 30 m average shear wave velocity and the depth to shear wave velocity, which is equal to 1,500 m/s at the site, respectively. Seismic hazard curves and uniform hazard response spectra calculated at the facility are shown in **Figure 4**. The design ground motion for a

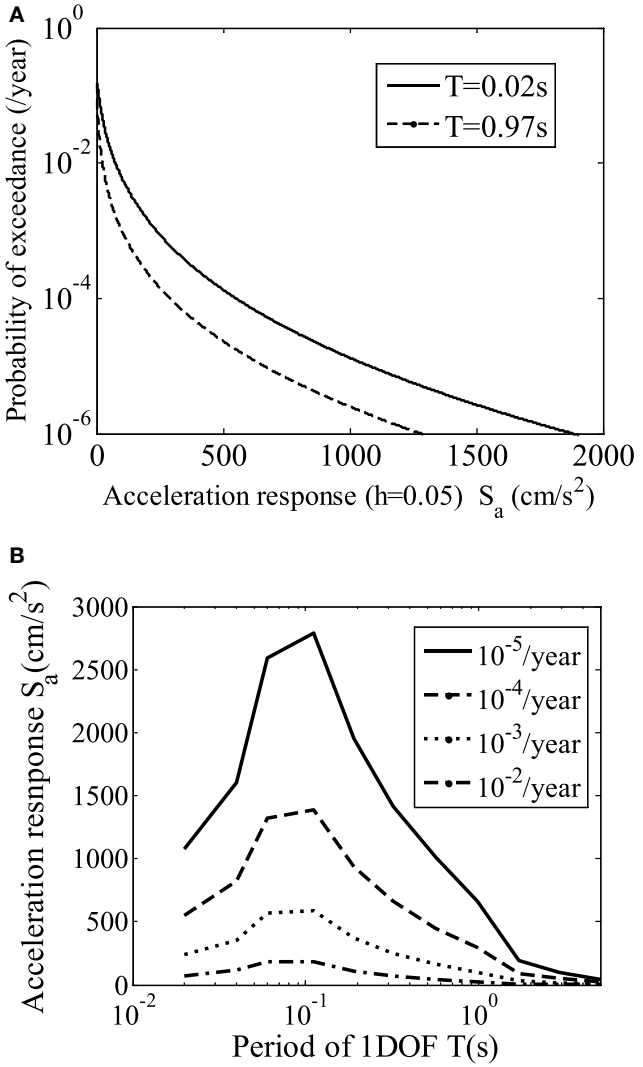

FIGURE 4 | Seismic hazard at the location of the facility. **(A)** $T = 0.02$ s and $T = 0.97$ s and **(B)** uniform hazard spectra.

TABLE 3 | Three alternative options for item B.

Case 0 (item B_0)	Natural period of item B is 0.02 s, which is identical to that of item A Item B is designed for design ground motion corresponding to the exceedance probability of 10^{-4}/year
Case S (item B_S)	Natural period of item B is 0.02 s, which is identical to that of item A Seismic margin is provided based on the proposed method (Eq. 8)
Case T (item B_T)	Natural period of item B is 0.97 s Seismic margin is provided based on the proposed method (Eq. 8)

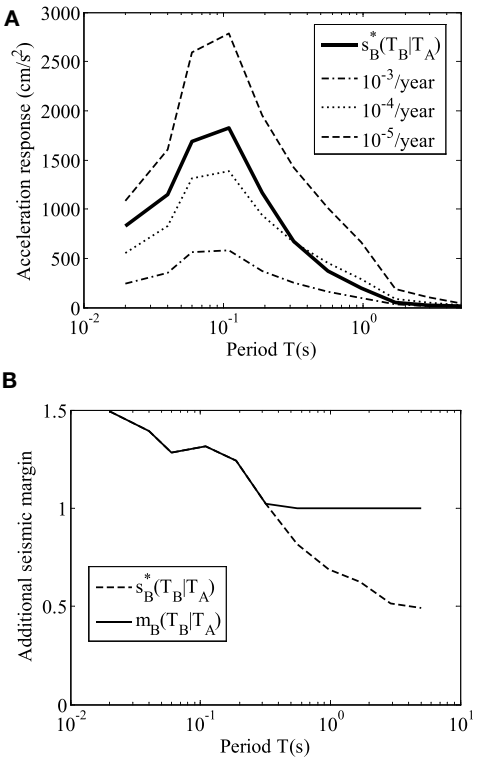

FIGURE 5 | Most probable acceleration response spectrum and the required additional seismic margin required for items important in mitigating the consequences of accidents. **(A)** Comparison between the most probable acceleration response spectrum and uniform hazard spectra and **(B)** required additional seismic margin.

system is assumed to correspond to the exceedance probability of 10^{-4}/year.

The facility is modeled as a system that contains two items, items A and B, as is the case in Section "A Method to Identify the Most Probable Source Characteristics." The natural period of item A, T_A, is assumed to be 0.02 s. As for item B, three alternative options (items B_0, B_S, and B_T) are assumed as listed in **Table 3**. It is assumed as an example that the logarithmic standard deviation of the capacity of each item is 0.3, while the conditional probability of failure at the level of design ground motion is 0.01. The most probable spectral acceleration and additional seismic margin required for items that are important in mitigating the consequences of accidents (items B_S and B_T) are obtained based on the proposed method as shown in **Figure 5**. Seismic fragility curves that show the cumulative distribution function of the capacity as a function of 5% spectral acceleration at the natural period, assumed for items B_0, B_S, and B_T, are shown in **Figures 6A,B**. The most probable source characteristics and the most probable ground motion parameters that may cause accidents are shown in **Table 4**. An additional seismic margin of 1.49 for item B_S, as compared to item B_0, is obtained using Eq. 8 for this example, whereas an additional seismic margin is not required for item B_T. If two items have the similar mechanism to resist seismic forces, it is reasonable to assume that the capacities between them are correlated. Therefore, for cases 0 and S, the correlation coefficient ρ between the capacities of A and B is assumed to be 0, 0.3, and 0.6, i.e., for items B_0 and B_S, where $\rho = 0$ for reference. Independence between items A and B_T is assumed for case T.

Monte Carlo simulations are conducted where the number of samples for the simulation is 10^8. Samples of hypocenter and magnitude of earthquakes, 5% damped acceleration response spectra, and capacity of items are generated to calculate the fragility curve

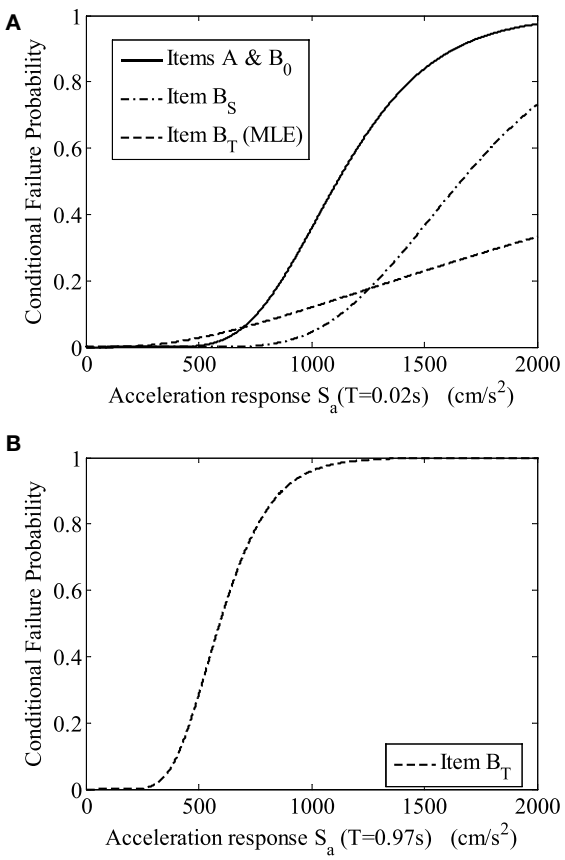

FIGURE 6 | Seismic fragility curves for items B_0, B_S, and B_T. As a function of 5% damped spectral acceleration at **(A)** 0.02 s (items B_0, B_S, and B_T) and **(B)** 0.97 s (item B_T).

TABLE 4 | Most probable source characteristics and the most probable ground motion parameters that may cause accidents.

s_A* (cm/s^2)	M_W*	x* (km)	ε_{INTER}*(T_A)	ε_{INTRA}*(T_A)
824	6.47	15	0.283	0.396

for failure of the system, i.e., simultaneous malfunction of both items.

Results and Discussions

Seismic fragility curves for item B_T as a function of 5% damped spectral acceleration at 0.02 s are estimated based on the simulated samples using the maximum likelihood estimation (Shinozuka et al., 2000), as shown in **Figure 6A**. The logarithmic standard deviation obtained is 0.93, which includes the effects of uncertainties in the shape of acceleration response spectra and the capacity of the item.

Seismic fragility curves of the system representing the cumulative distribution as a function of 5% damped spectral acceleration at 0.02 s, for the occurrence of a simultaneous malfunction of two items, are also obtained using the maximum likelihood estimation (Shinozuka et al., 2000). These are shown in **Figure 7**. As for case 0, i.e., item B_0, the median capacity of the system is 1.2 times larger than that of item A when $\rho = 0$, while it is 1.1 times larger when $\rho = 0.6$. The median capacity decreases as the correlation coefficient ρ increases because of simultaneous damage of two items. As for case S where an additional seismic margin is provided to item B, the median capacity of the system is 1.5 times larger than that of item A when $\rho = 0$, 0.3, and 0.6. The difference between ρ can be observed for ground motion <2,000 cm/s^2. As for case T, the case that the natural period of item B is elongated, the median capacity of the system is 2.1 times larger than that of item A, while the logarithmic standard deviation is 0.47, and this is larger than those in case 0 (0.24–0.28) and case S (0.26–0.30). Case T is more effective for larger ground motion levels as compared to cases 0 and S.

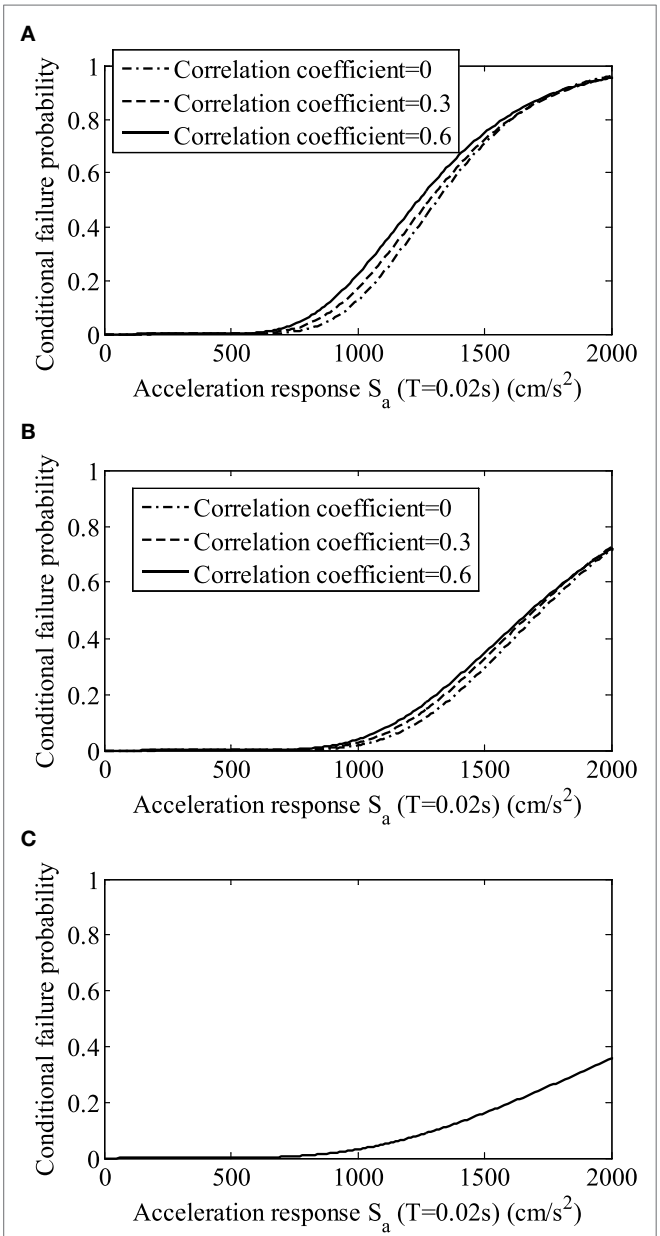

FIGURE 7 | Seismic fragility curves for occurrence of accident with serious consequences. **(A)** Case 0, **(B)** Case S, and **(C)** Case T.

TABLE 5 | Calculated failure probabilities for the system.

Case	Failure probability of the system (per year)	Ratio to failure probability of item A
Item A (reference)	1.54×10^{-5}	–
Case 0	6.91×10^{-6} ($\rho = 0.0$) 8.16×10^{-6} ($\rho = 0.3$) 9.86×10^{-6} ($\rho = 0.6$)	0.449 ($\rho = 0.0$) 0.530 ($\rho = 0.3$) 0.640 ($\rho = 0.6$)
Case S	2.54×10^{-6} ($\rho = 0.0$) 2.91×10^{-6} ($\rho = 0.3$) 3.28×10^{-6} ($\rho = 0.6$)	0.165 ($\rho = 0.0$) 0.189 ($\rho = 0.3$) 0.213 ($\rho = 0.6$)
Case T	2.08×10^{-6}	0.135

The annual failure probability of the system is numerically calculated to discuss the effectiveness of diversity in the natural period of items and additional seismic margins. The annual failure probability of the system, P_{fsys}, is calculated as follows:

$$P_{fsys} = \int_0^\infty f_S(s)\, F_{Sys}(s)\, ds \tag{10}$$

where $f_s(s)$ is the probability density function of the annual maximum 5% damped spectral acceleration at 0.02 s, while $F_{Sys}(s)$ is the cumulative distribution function of the capacity of the system.

The results are tabulated in **Table 5**. For case 0, item B_0 is not so much effective to mitigate the consequences of accidents, because the failure probability of the system does not decrease <0.449–0.640 times as compared to that of item A. The failure probability of the system decreases 0.165–0.213 times as compared to that of item A for case S, and it decreases 0.14 times as compared to that of item A for case T. Both cases T and S are effective in mitigating the consequences of accidents, while case 0 is not because of the effects of common cause failure.

It still remains a room for discussion how this framework can be applied to the design of actual safety-critical facility. One of typical examples where the framework can be applied is the case when an emergency operations facility is additionally constructed in the vicinity of the facility. Whether a base-isolated structure is better than an earthquake-resistant structure for the emergency operations facility should be discussed not only by the performance of a single facility but also based on the performance of a group of facilities. The proposed framework can be used to discuss the latter case.

CONCLUSION

In this article, the sophistication of seismic design of safety-critical facilities was discussed from the viewpoint of seismic design of items that are important in mitigating the consequences of accidents to avoid cliff-edge effects. The proposed approach is considered to be related to an implementation of risk-informed and performance-based defense in depth.

First, it was pointed out that a strategy in mitigating the consequences of severe accidents to the point of near collapse is more important for safety-critical facilities than for basic facilities. Therefore, a basic framework for ensuring diversity in dynamic characteristics of items and providing additional seismic margin, such as a differentiation in classes of required seismic margins to each item based on its role, was proposed. This framework is meant to prevent a common cause failure and to avoid cliff-edge effects based on a risk-informed systems approach. The framework is proposed by utilizing the concepts of the FORM, probabilistic seismic hazard deaggregation, and the conditional mean spectrum. An appropriate combination of seismic margin and diversity was discussed to implement the defense-in-depth concept to seismic design based on the risk-informed approach. An example was demonstrated to prove that the proposed method was effective. The proposed method is considered to be useful because a defense-in-depth concept can be appropriately implemented under a wide range of seismic excitations.

Further applicability of the proposed method should be discussed using a more realistic system in future study. An actual safety-critical facility is composed of a large number of items and is much more complicated, although cases with two items are investigated in this article as a simplified example. Increasing the redundancy ensures higher level of safety, while total cost increases, including initial and maintenance costs. A framework of cost–benefit analysis should be developed to discuss how safe is safe enough. The effects of diversity in location of items in addition to diversity in dynamic characteristics are also needed to be discussed in the future study.

AUTHOR CONTRIBUTIONS

TI contributed to develop the framework and to conduct part of simulation study. YI contributed to conduct simulation. NS contributed to develop and elaborate the proposed framework of nuclear safety.

FUNDING

Part of this study is supported by The Center of World Intelligence Project for Nuclear S&T and Human Resource Development of the Ministry of Education, Culture, Sports, Science and Technology (MEXT), Japan (Grant Number: 271104).

REFERENCES

Baker, J. W. (2011). Conditional mean spectrum: tool for ground motion selection. *J. Struct. Eng.* 137, 322–331. doi:10.1061/(ASCE)ST.1943-541X.0000215

Baker, J. W., and Jayaram, N. (2008). Correlation of spectral acceleration values from NGA ground motion models. *Earthq. Spectra* 4, 299–317. doi:10.1193/1.2857544

Bazzurro, P., and Cornell, C. A. (2002). "Vector-valued probabilistic seismic hazard analysis (VPSHA)," in *Proceedings of 7th U.S. National Conference on Earthquake Engineering* (Boston, MA).

Budnitz, R. J., Amico, P. J., Cornell, C. A., Hall, W. J., Kennedy, R. P., Reed, J. W., et al. (1985). *An Approach to the Quantification of Seismic Margins in Nuclear Power Plants, NUREG/CR-4334*. Washington, DC: Lawrence Livermore National Laboratory, U.S. Nuclear Regulatory Commission.

Haselton, C. B., Liel, A. B., Deierlein, G. G., Dean, B. S., and Chou, J. H. (2011). Seismic collapse safety of reinforced concrete buildings. I: assessment of ductile moment frames. *J. Struct. Eng.* 137, 481–491. doi:10.1061/(ASCE)ST.1943-541X.0000318

International Atomic Energy Agency. (1988). *Code on the Safety of Nuclear Power Plants: Siting, Safety Series, No. 50-C-S*. Vienna: International Atomic Energy Agency.

International Atomic Energy Agency. (1996). *Defence in Depth in Nuclear Safety, INSAG-10*. Vienna: International Atomic Energy Agency.

International Atomic Energy Agency. (2003). *Seismic Design and Qualification for Nuclear Power Plants, Safety Guide No. NS-G-1.6*. Vienna: International Atomic Energy Agency.

International Atomic Energy Agency. (2006). *Fundamental Safety Principles, No. SF-1*. Vienna: International Atomic Energy Agency.

International Atomic Energy Agency. (2016a). *Safety of Nuclear Power Plants: Design, Specific Safety Requirements No. SSR-2/1 (Rev. 1)*. Vienna: International Atomic Energy Agency.

International Atomic Energy Agency. (2016b). *Considerations on the Application of the IAEA Safety Requirements for the Design of Nuclear Power Plants, IAEA-TECDOC-1791*. Vienna: International Atomic Energy Agency.

Itoi, T., Murakami, M., and Sekimura, N. (2015). Statistical equations of response spectra of crustal earthquake for assessment of multiple facilities seismic risk. *J. Jpn. Assoc. Earthq. Eng.* 15, 126–141; (in Japanese with English abstract). doi:10.5610/jaee.15.6_126

McGuire, R. K. (1995). Probabilistic seismic hazard analysis and design earthquakes – closing the loop. *Bull. Seismol. Soc. Am.* 85, 1275–1284.

Miyano, H., Takada, T., and Itoi, T. (2015). Tsunami resistant engineering for nuclear safety: (No.2) integrated risk-informed earthquake-tsunami protection framework for nuclear safety. *J. Atom. Energy Soc. Jpn.* 57, 639–645; (in Japanese).

Nuclear Regulatory Commission. (1997). *Regulatory Guide 1.165 Identification and Characterization of Seismic Sources and Determination of Safe Shutdown Earthquake Ground Motion (RG 1.165)*. Washington, DC: United States Nuclear Regulatory Commission.

Nuclear Regulatory Commission. (2007). *Regulatory Guide 1.208 A Performance-Based Approach to Define the Site-Specific Earthquake Ground Motion (RG 1.208)*. Washington, DC: United States Nuclear Regulatory Commission.

Rackwitz, R., and Fiessler, B. (1978). Structural reliability under combined random load sequences. *Comput. Struct.* 9, 489–494. doi:10.1016/0045-7949(78)90046-9

Shinozuka, M., Feng, M. Q., Lee, J., and Naganuma, T. (2000). Statistical analysis of fragility curve. *J. Eng. Mech.* 126, 1224–1231. doi:10.1061/(ASCE)0733-9399(2000)126:12(1287)

Structural Engineers Association of California. (1995). *Vision 2000 – A Framework for Performance-Based Design*. Sacramento, CA: Vision 2000 Committee.

Takada, T., Ochi, S., and Kanda, J. (2003). Basic study on determination of probabilistic controlling earthquakes. *J. Struct. Constr. Eng.* 68, 53–59; (in Japanese with English abstract). doi:10.3130/aijs.68.App53

United States Nuclear Regulatory Commission. (2012). *A Proposed Risk Management Regulatory Framework, NUREG-2150*. Washington, DC.

Wang, M., and Takada, T. (2005). Macrospatial correlation model of seismic ground motions. *Earthq. Spectra* 21, 1137–1156. doi:10.1193/1.2083887

Wang, M., Tanaka, K., and Takada, T. (2009). "Probabilistic seismic risk analysis for building portfolio," in *Proceeding of 10th International Conference on Structural Safety and Reliability, 13–17 September 2009* (Osaka, Japan: CRC Press Book).

Conflict of Interest Statement: The authors declare that the research was conducted in the absence of any commercial or financial relationships that could be construed as a potential conflict of interest.

Copyright © 2017 Itoi, Iita and Sekimura. This is an open-access article distributed under the terms of the Creative Commons Attribution License (CC BY). The use, distribution or reproduction in other forums is permitted, provided the original author(s) or licensor are credited and that the original publication in this journal is cited, in accordance with accepted academic practice. No use, distribution or reproduction is permitted which does not comply with these terms.

frontiers in Built Environment

ORIGINAL RESEARCH
published: 15 February 2018
doi: 10.3389/fbuil.2018.00001

Application of High Performance Computing to Earthquake Hazard and Disaster Estimation in Urban Area

Muneo Hori[1,2], Tsuyoshi Ichimura[1], Lalith Wijerathne[1], Hideyuki Ohtani[2], Jiang Chen[2], Kohei Fujita[2] and Hiroyuki Motoyama[2]*

[1] Earthquake Research Institute, The University of Tokyo, Tokyo, Japan, [2] Advanced Institute for Computational Science, RIKEN, Kobe, Japan

Integrated earthquake simulation (IES) is a seamless simulation of analyzing all processes of earthquake hazard and disaster. There are two difficulties in carrying out IES, namely, the requirement of large-scale computation and the requirement of numerous analysis models for structures in an urban area, and they are solved by taking advantage of high performance computing (HPC) and by developing a system of automated model construction. HPC is a key element in developing IES, as it needs to analyze wave propagation and amplification processes in an underground structure; a model of high fidelity for the underground structure exceeds a degree-of-freedom larger than 100 billion. Examples of IES for Tokyo Metropolis are presented; the numerical computation is made by using K computer, the supercomputer of Japan. The estimation of earthquake hazard and disaster for a given earthquake scenario is made by the ground motion simulation and the urban area seismic response simulation, respectively, for the target area of 10,000 m × 10,000 m.

Keywords: high performance computing, automated model construction, ground motion simulation, structural seismic response simulation, regional simulation

OPEN ACCESS

Edited by:
Katsuichiro Goda, University of Bristol, United Kingdom

Reviewed by:
Tatsuya Itoi, The University of Tokyo, Japan
Manolis S. Georgioudakis, National Technical University of Athens, Greece

****Correspondence:***
Muneo Hori
hori@eri.u-tokyo.ac.jp

Specialty section:
This article was submitted to Earthquake Engineering, a section of the journal Frontiers in Built Environment

Received: *21 June 2017*
Accepted: *05 January 2018*
Published: *15 February 2018*

Citation:
Hori M, Ichimura T, Wijerathne L, Ohtani H, Chen J, Fujita K and Motoyama H (2018) Application of High Performance Computing to Earthquake Hazard and Disaster Estimation in Urban Area. Front. Built Environ. 4:1. doi: 10.3389/fbuil.2018.00001

1. INTRODUCTION

Estimation of earthquake hazard and disaster has been a core theme of earthquake engineering, and, recently, some systems have been developed for this purpose; see HAZUS (2017) and GEM (2015). These systems share the following two core elements: (1) calculation of a ground motion intensity measure using an empirical attenuation equation and (2) estimation of a degree of structure damage applying fragility (or vulnerability) curves between the structure damage and the ground motion intensity measure. The attenuation equation and the fragility curves are obtained from the statistical analysis of the past records of earthquake hazards and disasters; the relations are often updated adequately (Masing, 1926; Architectural Institute of Japan, 2000; Sahin et al., 2016). We have to emphasize that the use of the empirical equations is a unique solution of the systems, because the estimation of earthquake hazard and disaster is made for an entire urban area of a few kilometers in which more than ten thousand structures are located.

The two core elements of the system, namely, the attenuation relation and the fragility curves, are not often used for other purposes except for the assessment of earthquake hazard and disaster for an urban area. For the first element, numerical analysis of earthquake wave propagation is used; the ground motion distribution is obtained for a given earthquake scenario. For the second

element, there are many numerical methods for structural seismic responses analysis which are used for the seismic design. Thus, arises a natural question, "why such numerical analysis methods are not used as alternative of the two core elements of the system?" Around the world, some research projects (Si and Midorikawa, 1999; Saad, 2003; Cimellaro et al., 2014; Jayasinghe et al., 2015; DesignSafe-CI, 2016) are conducted to answer this question. **Figure 1** presents a possible shift from the current empirical methods to a simulation-based method for the estimation of earthquake hazard and disaster in an urban area.

While the question made above is natural, it is not easy to replace the empirical equations with the numerical simulation for the estimation of earthquake hazard and disaster. This is because there are two major difficulties; see **Figure 2**. The first difficulty is that simulating the propagation and amplification processes of seismic waves requires large-scale numerical computation if it needs high temporal and spatial resolution. The degree-of-freedom (DOF) increases as proportional to the inverse of the cubic of the spatial resolution (i.e., if the spatial resolution becomes half, DOF increases eight times), and the time step increases linearly to the required temporal resolution. The second difficulty is that an analysis model has to be constructed for each structure which is located in a target urban area. The number of the structures is of the order of 100,000, and an analysis model ought to have sufficient fidelity. The work needed for the model construction cannot be underestimated.

The authors have been developing a system for the estimation of earthquake hazard and disaster that uses a set of numerical analysis methods. Developing such a system is a challenging problem even for modern computational science since the target is an urban area. The system is called *integrated earthquake simulation* (Hori, 2011) (IES), as it integrates numerical analysis methods, together with modules for the automated model construction with which the implemented numerical analysis methods are executable. Key numerical simulations of IES are the simulation for the ground motion and the urban area seismic response. The ground motion simulation analyzes a three-dimensional underground structure model in which seismic waves are amplified in soft ground, and the urban area seismic response simulation computes a set of non-linear analysis models for all structures which are located in a target area.

This paper is aimed at summarizing recent achievements of developing IES, which are made by applying HPC to IES and using a large-scale parallel computer such as K computer in Japan (Miyamura et al., 2016). The contents of the present paper are organized as follows: first, in Section 2, we briefly explain the two difficulties in using numerical analysis method as an alternative

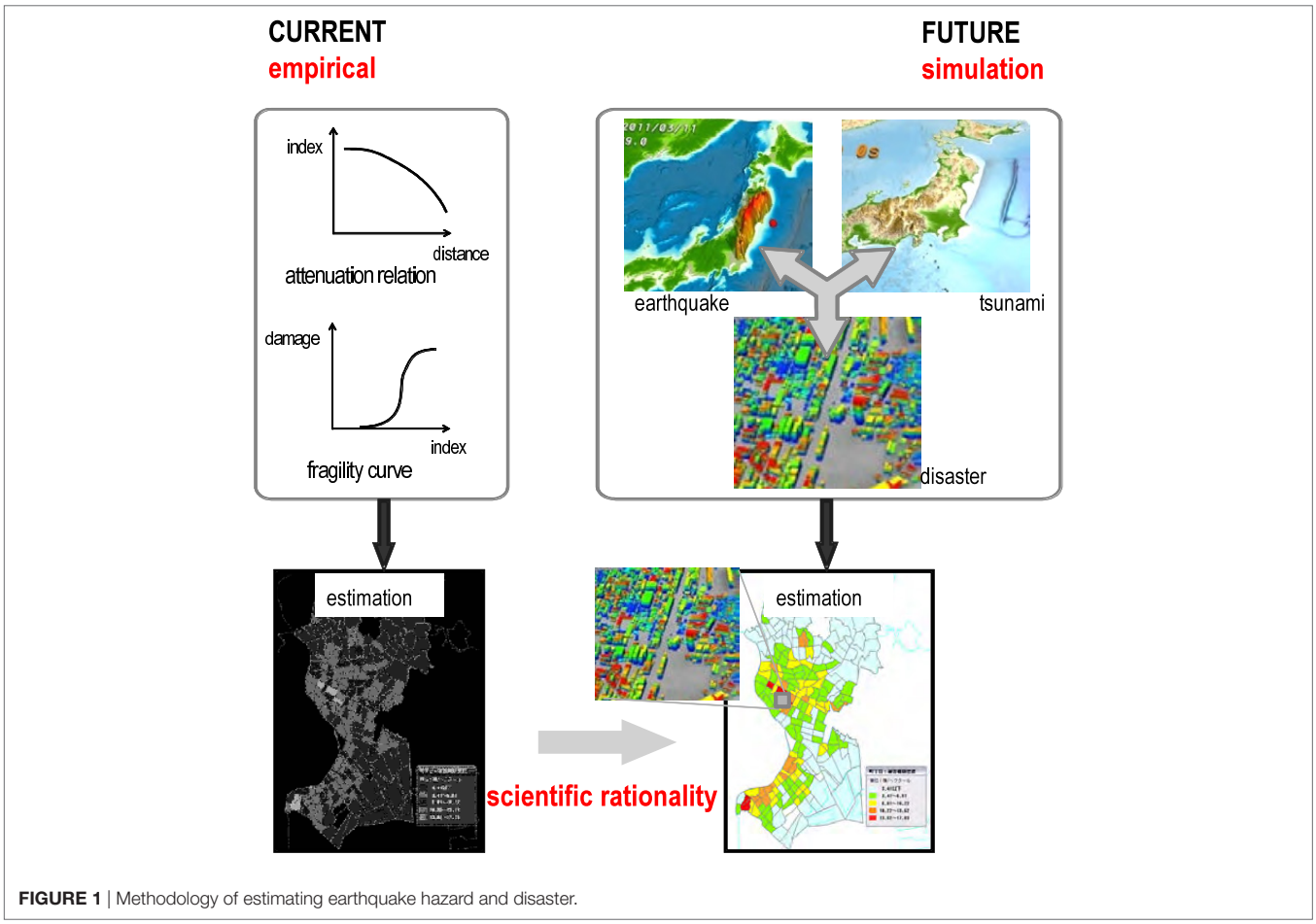

FIGURE 1 | Methodology of estimating earthquake hazard and disaster.

1. Requirement of large scale numerical computation
   - Large urban area: > 1,000 m order
   - High spatial and temporal resolution: < 1 m order
   - Degree-of-freedom: > 10,000,000
   - Number of time steps: > 10,000
2. Requirement of construction of numerous analysis models
   - Number of structures in urban area: > 100,000
   - Analysis model of high fidelity
   - Linear/non-linear model
   - Ensemble computing for uncertainty of material and structure properties

FIGURE 2 | Two requirements in applying numerical simulation to estimation of earthquake hazard and disaster.

of conventional empirical equations. The key features of IES are explained in Section 3; the architecture of IES for easier implementation of a third-party program is explained in detail. Examples of using IES for the earthquake hazard and disaster assessment are presented in Section 4. The target is Tokyo Metropolis, and the ground motion simulation and the urban area seismic response simulation made for this city by using K computer are explained.

In closing this section, we have to explain the quality of IES as numerical simulation. All the numerical methods that are implemented in IES are verified, but automatically constructed analysis models are not validated; literally no observed data are available for the purpose of validation. Highest quality is thus not expected for IES. The reliability of IES could be evaluated beside for the quality of the numerical simulation; IES employs the rational methodology of simulating the physical processes of earthquake hazard and disaster. No reduced models are used for the earthquake hazard estimation, and reduced but consistent models are sued for the earthquake disaster estimation. The resulting estimation of earthquake hazard and disaster made by IES is being compared with that made by the conventional method together with the observed data of 2011 Tohoku Earthquake.

2. TWO DIFFICULTIES OF NUMERICAL ANALYSIS FOR EARTHQUAKE HAZARD AND DISASTER

The progress of computers, both hardware and software, enables us to utilize advanced numerical analysis methods in various fields of science and engineering. For instance, in the field of seismology, available are advanced numerical analysis methods which are capable to compute the seismic wave propagation processes in a large domain the dimension of which is in the crustal length scale (Bao et al., 1996; Somerville et al., 2001; Ichimura et al., 2009, 2014b; Yifeng et al., 2010; Cui et al., 2013; Quinay et al., 2013; Heinecke et al., 2014; Society, 2016; Tanaka et al., 2016). In earthquake engineering, numerical analysis methods based on finite element method (FEM) are being used to analyze soil–structure interaction effects for more accurate evaluation of seismic performance of a structure (Hori, 2011); material nonlinearity of the structure and soil are considered in FEM.

The numerical analysis methods mentioned above are not capable to be used in the numerical simulation for the estimation of earthquake hazard and disaster in an urban area. As for the ground motion simulation, there is a limitation in the temporal resolution; the temporal resolution of currently available methods do not reach 10 Hz, which is needed for the accurate computation of structural responses since its major frequency components lie in the range of 1–10 Hz. Near the surface ground, the wave velocity is of the order of 100 m/s, and hence the required spatial resolution is 1 m in order to accurately compute frequency components of 10 Hz which has the wave length of 10 m; this fine resolution is in contrast of the spatial resolution of 100 m that is required for bedrock whose wave velocity is of the order of 1,000 m/s. Accurate computation is essential to estimate the topographical effects of irregular underground structures.

As for the urban area seismic response simulation, we have to construct an analysis model for all structures which are located in a target area. The quality of the constructed analysis model ought to be assured so that the results of the numerical analysis are reliable. Manual construction is not feasible for structures the number of which exceeds 100,000. Moreover, we have to be aware of the fact that perfect digital data about material and structural properties are not available for all the structures. For instance, high-rise buildings have a complete data set for the material and structure components for the construction, but the data set are not open to the public because the buildings are private asset.

We have to mention that the difficulty of constructing an analysis model is shared by the ground motion simulation. This is because the simulating needs a three-dimensional underground structure model which consists of a few soil layers of distinct configuration and material properties. The model must have high fidelity for the configuration of the soil layers, so that the topographical effects are evaluated accurately. However, the data of the soil layers are limited in the quality and quantity. We have to guess as well for the analysis model of the underground structures.

3. SOLUTIONS TO TWO DIFFICULTIES OF NUMERICAL ANALYSIS

The first difficulty, the requirement of large-scale numerical computation, is solved by making use of HPC. A model of more than 10,000,000 DOF can be analyzed by using a parallel computer of moderate class, and we need to develop a numerical analysis method which possesses sufficient performance or fast analysis of a model of such large DOF. In IES, we have developed an FEM that is capable to solve a model of 1,000,000,000,000 DOF. Numerically solving a mode of this scale is a challenge in the field of HPC; this is regarded as a challenge of capability computing that solves a problem of largest scale. The number of time steps that are needed for the ground motion simulation is of the order of 10,000, since the time increment and the time duration are 0.01 and 100 s, respectively. FEM of IES is fast in analyzing a model of large DOF in repeated times.

The second difficulty, the need of analysis model construction for a large number of structures located in a target urban area, is solved by developing a program of the automated model

construction. Automated model construction is regarded as data conversion, in the sense that digital data stored in several data resources are processed to form a set of digital data which correspond to an analysis model. Data resources available to the automated morel construction are of the form of Geographical Information System (GIS), and hence the data conversion is principally possible. As explained in the preceding section, however, there are no GIS's which have data of the material and structure properties for all structures. We have to guess these properties by interpreting data which are stored in several data resources of GIS.

In the following two subsections, we briefly explain FEM developed for the ground motion simulation and the automated model construction for the urban area response simulation. The points of the explanation are the key feature of FEM and the automated model construction, in order to solve the two difficulties.

3.1. FEM Developed for IES

We first mention that FEM, rather than finite difference method, is suitable to solve numerical problems of the ground motion simulation, since a major concern of the simulation for the estimation of earthquake hazard is the identification of sites at which larger ground motion is concentrated due to the topographical effects induced by the underground structures. An analysis model of high fidelity is thus needed to model complicated configuration of soil layers, and FEM is the unique solution to analyze such a model.

The major portion of the numerical computation of FEM is used in solving a matrix equation for unknown displacement. That is,

$$\left(\frac{4}{dt^2}[M]+\frac{2}{dt}[C^n]+[K^n]\right)[\delta u^n] = [f^n]-[q^{n-1}]+[C^n][v^{n-1}]+[M]\left([a^{n-1}]+\frac{4}{dt}[v^{n-1}]\right), \quad (1)$$

where $[u]$, $[v]$, $[a]$, $[f]$, and $[q]$ are displacement, velocity, acceleration, external force, and residual force vectors, respectively; $[M]$, $[C]$, and $[K]$ are mass, damping, and stiffness matrices, dt is the time increment, and superscript n stands for the n-th time step; $[C]$ and $[K]$ change due to non-linearity of soil. In the present paper, we employ a simple Ramberg–Osgood model and Masing rule (Ichimura et al., 2007; Lu and Guan, 2017) for the soil non-linearity. We compute $[K]$ using the non-linear constitutive relations at all the Gauss points and compute $[C]$ assuming a simple Rayleigh damping (Ichimura et al., 2015). The unknown is $[\delta u^n] = [u^n] - [u^{n-1}]$, and $[f^n]$ is given; the other matrices and vectors are determined. The ground motion simulation must solve a matrix equation the dimension of which is 1,000,000,000,000 for time steps of more than 10,000; for simplicity, $[C^n]$ and $[K^n]$ are fixed at the n-th time step, and the number of the time steps becomes a few times larger if $[C^n]$ and $[K^n]$ are changed at the same time step.

FEM of IES has developed a fast *solver* (Golub and Ye, 1997; Rietmann et al., 2012) which solves the matrix equation. The solver is tuned for K computer; the speed-up for the strong scalability is almost ideal, and the peak performance is 10 to 15% of the peak performance of K computer, depending on the number of compute nodes. Pre-conditioned conjugate gradient (CG) method is used as an algorithm of solving equation (1) for $[\delta u^n]$; denoting by N the dimension of $[\delta u^n]$, the computation time is $O(N^2)$ for ordinary algorithms, but $O(N \log N)$ for the CG method. Note that the CG method is an iterative solver, as it computes a series of improved solutions for the matrix equation until it reaches a suitable solution which does not produce a large error of the matrix equation.

The speed of solving equation (1) by the pre-conditioned CG method depends on the number of iteration at which a suitably accurate solution is obtained as well as the CPU time of solving each iteration. Applying suitable pre-conditioning and using a good initial solution makes most efficient combination of the number of iteration and the CPU time for each iteration. To this end, we have to make special tunings in order to increase the performance of the solver; see the related references (Ichimura et al., 2014a, 2015; Agata et al., 2016; Fujita and Ichimura, 2016; Fujita et al., 2016) for detailed explanations of the tunings made by our group. The following two major tunings are made: (1) the geometric multi-grid which uses coarse and fine solutions (a coarse solution of less DOF and serves an initial solution for a fine solution of full DOF) and (2) the mixed precision arithmetic which uses single and double precision for the coarse and fine solution, respectively. In general, single precision arithmetic makes faster computation, and hence using single precision for parts of numerical computation which do not need high accuracy makes efficient numerical computation.

The scalability of the solver that is implemented in FEM of IES is presented in **Figure 3**; K computer is used for this computation, and DOF of the models analyzed exceeds 100,000,000. As the number of CPU cores increase, the CPU time decreases linearly, which indicates good scalability of the developed solver. We have to mention that other tunings, such as element-by-element method for efficient memory usage, compressed row storage for efficient communication, or predictor of higher order, are made for FEM of IES. The use of the element-by-element method reduces the number of elements for which an element stiffness matrix computes is computed, and the compressed row storage is used for the global stiffness matrix that is made by assembling those element stiffness matrices.

3.2. Automated Model Construction Developed for IES

The automated model construction has two steps, namely, interpreting data stored in data resources, and converting data of the data resources to an analysis model (Architectural Institute of Japan, 2011); procedure (Idriss et al., 1978; Hori et al., 2015) of automatically constructing mutually consistent models for a target structure is proposed by our group, as well as procedure (Midorikawa et al., 2011; Taborda and Bielak, 2011; Miyamura et al., 2015) of constructing a highest fidelity model. A system of taking these steps for the automated model construction is being developed for IES. While the key simulations are the ground motion simulation and the urban area seismic response simulation, IES is implementing the seismic wave propagation

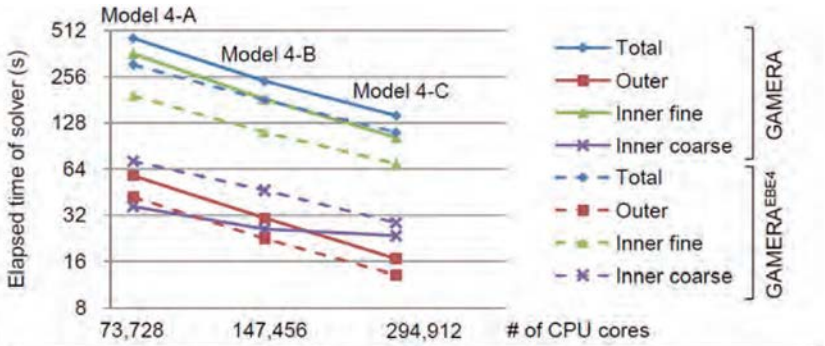

Method	GAMERA			GAMERA^{EBE4}		
Model	4-A	4-B	4-C	4-A	4-B	4-C
Elapsed time of solver (s)	456.6	239.4	143.0	306.3	180.0	111.0
FLOPS/Peak (%)	10.3	9.65	8.19	17.1	14.7	11.8

FIGURE 3 | Scalability of developed FEM: GAMERA and GAMERA^{EBE} designate the usage of the element-by-element method (GAMERA does not use it); Model 4-A, 4-B, and 4-C have different DOF; outer, inner fine, and inner coarse provide the breakdown of the developed multi-grid solver processes, with outer for the finest grid with double precision arithmetic's, inner fine and coarse for the coarse grid with single and double precision arithmetic's, respectively.

simulation, the tsunami inundation simulation, and the mass evacuation simulation, which also need the automated model construction. Hence, the system ought to be flexible so that it is able to handle various numerical analysis models.

Data resources which are currently available are commercial GIS or 3D maps, or a set of inventories operated by local government. The commercial GIS has configuration data for structures including residential buildings and road networks. The configuration data are the height and floor shape of the structure, together with the location information of a target of the data, which is given as a pair of latitude and altitude. There are some structures whose configuration data include minor errors, such as negative height. The inventories are made for specific purposes such as the registration of real estate. There are the inventories for the structure type and construction year. The location information of a target structure is given as a certain address; mailing address or lot number is mainly used, but some inventories are made as a map and the location information is specified as coordinates of the map.

Interpreting data stored in a data resource is made by understanding the data structure of the data resource. In general, the data resource has several attributes (or data) to each target item, and the data structure means the number of attributes and the property of each attribute; there are cases where an attribute consists of a few attributes. Location information is an attribute. If the data structure is understood, it is possible to make a program for reading a file of the data resource (which is often of binary format) and interpreting data. Since data resources share a similar data structure, aspect-oriented programming makes efficient and robust programming for the program for reading and interpreting, when not a small number of data resources are used.

The difficulty of converting interpreted data to an analysis model depends on the complexity of the model. That is, a fewer model parameters are converted from the interpreted data, as a simpler model is constructed. The simplest model for the structural seismic response analysis is a linear one-degree-of-freedom system, which has two model parameters, a mass and a stiffness. The quality of the model depends on the accuracy of the model parameters, and we have to make rational conversion from the interpreted data to the model parameters. A natural frequency is a key characteristic of a structure, and an empirical relation between the natural frequency and the structure height is available (Architectural Institute of Japan, 1978; NIED, 2016). In IES, the natural frequency computed for the analysis model using the model parameters is compared with the empirical relation, in order to verify the reliability of the model that is constructed in an automated manner.

Between the step of interpreting data stored in data resources and converting data to an analysis method, we have to combine data for a target structure which are stored in different data resources. If the data include the location information of a target structure in it, combining the data is principally straightforward. However, as explained above, we have to interpret the location information in order to accurately specify the location of a target; this could be understood as conversion of the local coordinate (that is relevant to each data resource) to the global coordinate. There are data resources which have errors about location information or cases where contracting location information is found in different data resources. Combining data of different data resources for one structure is thus difficult, and manual works are needed if data resources which do not have accurate location information in them are used. A flow of the automated model construction is presented in **Figure 4**.

We point out that the automated model construction system is designed for easy operation; the system is coded to take advantage of object-oriented programming together with the aspect-oriented programming. As shown in **Figure 5**, two built-infunctions, `MakeShape` and `MakeAttribute`, are used to interpret data stored in any data resource. `Shape` and

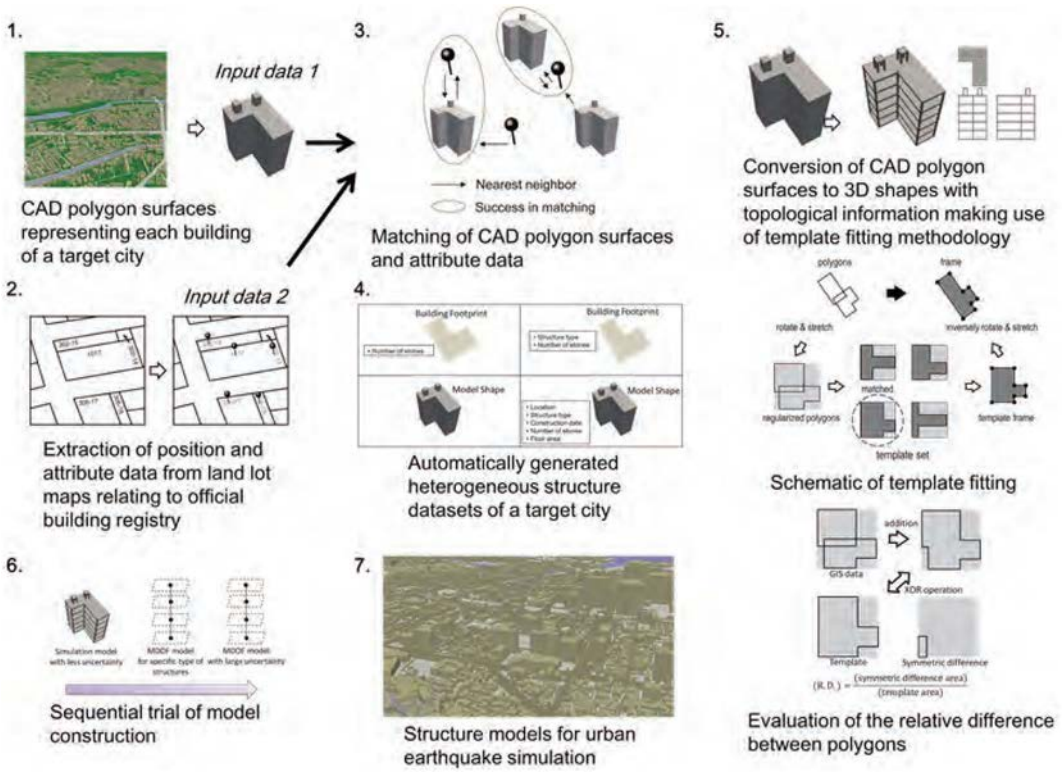

FIGURE 4 | Flow of automated model construction.

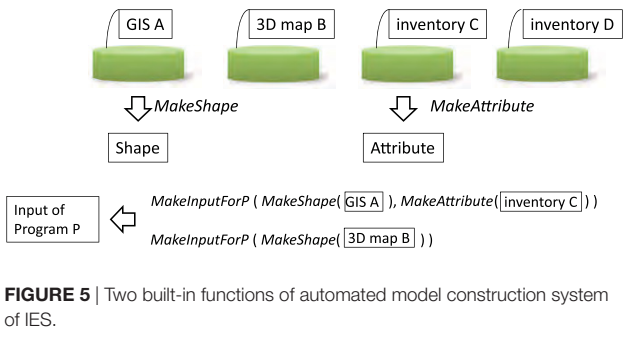

FIGURE 5 | Two built-in functions of automated model construction system of IES.

`Attribute` are an object for the structure configuration and the structure properties (such as structure type, construction year), respectively. Another built-in function, `MakeInputForP`, is used to construct an analysis model for a program `P` of the structural seismic response analysis. As is seen, an analysis model for `P` is constructed by using data resources for which `MakeShape` and `MakeAttribute` are programmed.

It is not expected that complete information that is needed to construct an analysis model is included in available data resources. To account for the limitation of the available data, IES is able to construct 10,000 or more analysis models for one structure, which are generated by the automated model construction system, suitably varying model parameters. It is another challenge of HPC in terms of capacity computing to construct and analyze numerous models for one target considering the uncertainty of the model parameters; note that the number of analysis models reaches 10,000,000,0000 if IES analyzed 1,000,000 structures located in a target area and constructs 10,000 analysis models for each structure.

3.3. Uncertainty Quantification of IES

As mentioned, all the numerical analysis methods implemented in IES are verified by comparing the numerical solution with analytical solution, but automatically constructed analysis models are not validated. This is because no data are available to fully validate high fidelity model for the underground structure or numerous analysis models of buildings. Thus, IES cannot have highest quality as numerical analysis. Uncertainty quantification is needed for IES.

The greatest uncertainty is an earthquake scenario. Since predicting fault mechanism (or rupture processes on a fault plane) is impossible at this moment, an alternative is to simulate earthquake hazard and disaster for numerous earthquake scenarios. Indeed, capacity computing of HPS is often used for this purpose. Strong ground motion and structural seismic responses change depending on the given scenario, but we can quantitatively estimate a range of possible ground motion and seismic responses which are obtained by capacity computing.

As for man-made structures, we can use capacity computing in which numerous analysis models are used for one structure by changing model parameters. We might use 10,000 models for

one structure. It should be noted that even when design data are available, actual structural properties are better than the design values since safety factors are included in the design. Monitoring or sensing is needed for the estimation of the actual structural properties; it is extremely difficult to estimate strength of a structure, compared with its stiffness, since strength is not identified until certain failure takes place in the structure.

4. EXAMPLES OF IES USING HIGH PERFORMANCE COMPUTING

In this section, we present examples of IES using capability computing and capacity computing. The target is Tokyo Metropolis, and commercial GIS's are used as data resources. The ground motion simulation is made for an underground structure consisting of three ground layers, and the urban area seismic response simulation is made by using a non-linear multi-degree-of-freedom system as an analysis model of a residential building. The last example presents the combination of the ground motion simulation and the urban area seismic response simulation.

4.1. Ground Motion Simulation

An analysis model of surface layers is presented in **Figure 6**; the domain is 1,250 m × 1,250 m, and consists of three layers including bedrock (Miyazaki et al., 2012; SimCenter, 2016). The number of nodes, elements, and degree-of-freedom are 340,876,783, 252,737,051, and 1,022,630,349, respectively; this large scale of this model is necessary in order to assure the numerical convergence of the solution with temporal resolution up to 10 Hz (Housner, 1952; Ichimura et al., 2015; Ohtani et al., 2014). This simulation is regarded as capability computing, as DOF of the model exceeds 100,000,000. As mentioned, a simple Ramberg–Osgood mode and Masing rule are employed as a non-linear constitutive relation of soil (Ichimura et al., 2007; Lu and Guan, 2017).

Figure 7 presents the distribution of SI (Tiankai et al., 2006), which is commonly used in earthquake engineering and defined as

$$SI = \frac{1}{2.4}\int_{0.1}^{2.5} S_v(T)\,\mathrm{d}T,$$

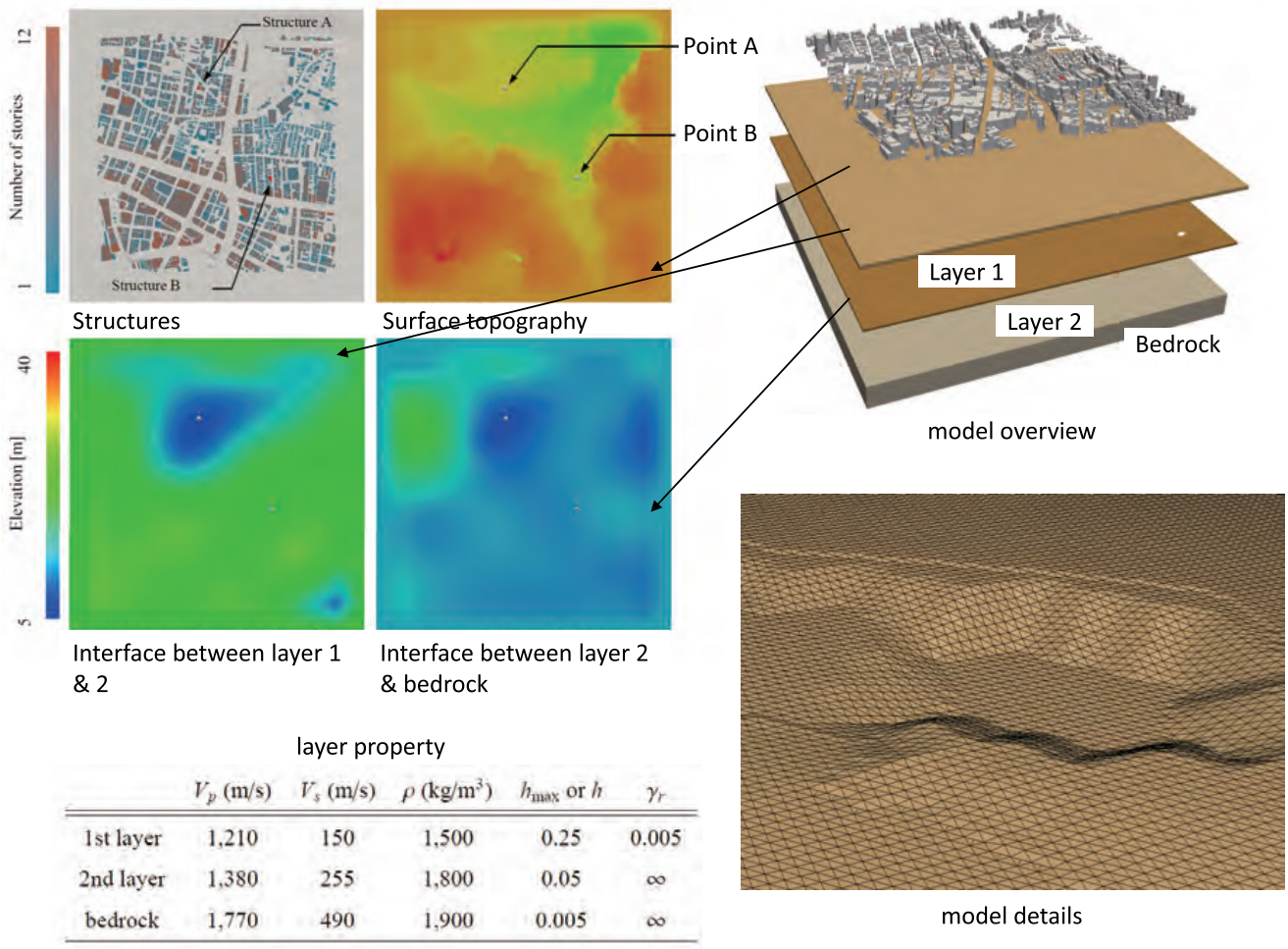

layer property

	V_p (m/s)	V_s (m/s)	ρ (kg/m^3)	h_{max} or h	γ_r
1st layer	1,210	150	1,500	0.25	0.005
2nd layer	1,380	255	1,800	0.05	∞
bedrock	1,770	490	1,900	0.005	∞

FIGURE 6 | A model for ground motion simulation.

with S_v being the velocity response spectra of the ground motion measured or synthesized at the site; as is seen, SI is the average of the velocity response taken over 0.1 and 2.4 s. Kobe Earthquake (JR Takatori) (Japan Meteorological Agency, 2016) is used as input seismic wave on the bed rock. The distribution of SI is far from being uniform in this area of around 1 km × 1 km. As well expected, this is due to the topographical effects of the three layers of complicated configuration; see **Figure 6**. Recall that the uniform seismic wave is input on the bottom of the bedrock layer. There are two sites at which SI is concentrated; the value of SI exceeds 200 kine.

It is of interest to compare the results of the above capability computing with the conventional analysis that uses a one-dimensional (1D) stratified model at a target site. In **Figure 8**, the waveform of acceleration in the EW and NS directions is presented; Points A and B indicated in **Figure 6** are used for the comparison. While the waveform at Point B computed by the conventional analysis appears similar to that of the 3D model analysis, with the largest difference being around 30 Gal, the difference in the waveform at Point A is substantial with the largest difference being around 100 Gal. The dependence of the difference on the site is well excepted since Point A is located near the valley of the underground structure and has larger topographical effects on the ground motion concentration. It should be emphasized that capability computing that uses a large-scale model of underground structures enable us to understand the site and degree of the ground motion concentration induced by the topographical effects.

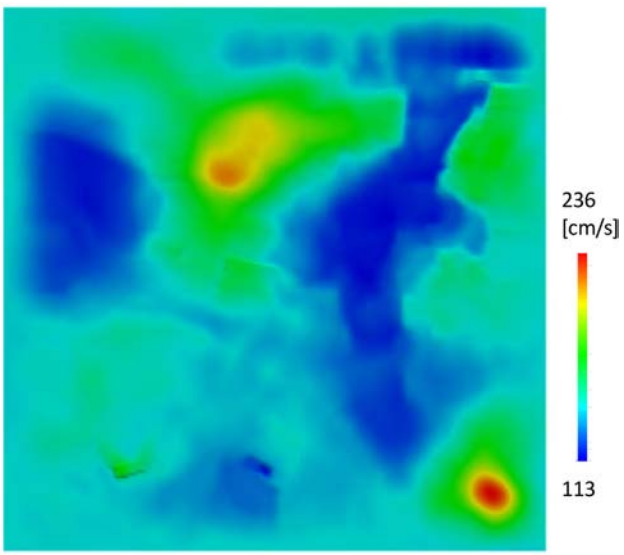

FIGURE 7 | Distribution of SI.

4.2. Urban Area Seismic Response Simulation

There are 4,066 residential buildings in the area presented in **Figure 6**. No inventory of the building type is available, and we assume that the structure type of all the buildings is reinforced concrete. A non-linear multi-degree-of-freedom system is made for each residential building; the number of the mass coincides with the floor number and a bi-linear spring is used to connect two neighboring masses. The mass is computed by using the floor area and an assumed floor thickness. The bi-linear spring has a linear relation between displacement and force until the force reaches the maximum value; the spring carries the same force even though its displacement increases. The stiffness for the linear relation is determined from an empirical equation between the first natural frequency and the building height.

The distribution of the maximum story drift angle (MSDA) is presented in **Figure 9**. It is difficult to see similarity in the distribution of SI and the distribution of MSDA, by comparing **Figures 7** and **9**. MSDA is relatively smaller at the two spots where SI is locally large and building models which have larger maximum drift angles stand at sites where SI is relatively smaller. The discrepancy between the ground motion concentration and the structural response is due to the difference in the dominant frequency of the ground motion input to the structure and the natural frequency of the structure. As for the earthquake hazard estimation, the distribution of MSDA is more important. We have to understand that relatively large MSDA is computed for a structure for which the coalesce of the input ground motion and its dynamic characteristic occurs.

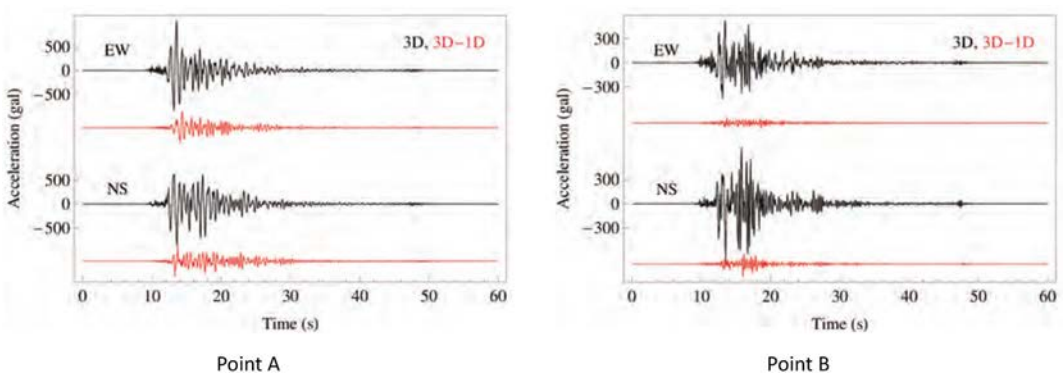

FIGURE 8 | Comparison of ground motion simulation and conventional 1D analysis.

Like the preceding subsection, we examine the necessity of making the 3D ground motion simulation, which provide ground motion that is amplified in ground layers and input to a structure on it. The identical analysis models are used for the residential buildings, but input ground motion is either the one computed by using the 3D ground motion simulation or the conventional 1D analysis. The results are presented in **Figure 10**; SI computed by the 3D ground motion simulation and the conventional 1D analysis, and the difference in SI are plotted in the top three figures, and MSDA based on the 3D ground motion simulation and the conventional 1D analysis, and the difference in MSDA are plotted in the bottom three figures. The difference reaches 40 kine for SI and 0.003 for MADA. This difference is critical; we need the ground motion simulation for the assessment of earthquake hazard and disaster at least in places which have larger topographical effects.

FIGURE 9 | Distribution of MSDA.

Due to the lack in relevant data resources, there is larger uncertainty in determining the strength of an analysis model for the residential buildings. While the stiffness can be determined by using empirical relations, it is not easy to determine the maximum force of the springs; the maximum force corresponds to the sum of the strength of walls and columns located on the floor which the spring represents. We apply capacity computing of generating 10,000 models for each residential building, assuming a normal distribution of the strength and assigning a randomly generated value to each spring; the mean of the maximum force is determined by using an empirical relation between the stiffness and the strength, and the SD is assumed to be 10% of the mean. Since the number of the buildings is 4,066, the total number of non-linear analysis models is 40,066,000.

A typical distribution of MSDA for 10,000 analysis models is shown in **Figure 11**. Three ground motions are used, and a wider distribution of MSDA is observed for larger ground motion. In **Figure 12**, the mean, the maximum, and the SD of MSDA is plotted. The effects of the model parameter uncertainty on the structural seismic response could be evaluated by studying the SD of MSDA. The SD of the model parameter (10% of the mean of

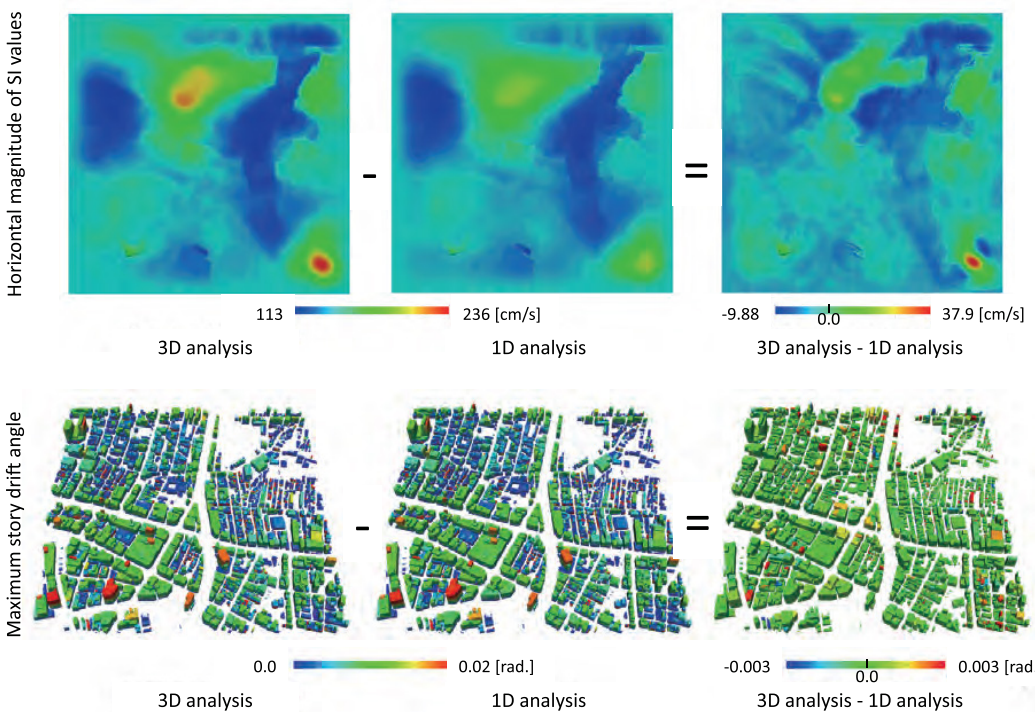

FIGURE 10 | Comparison of ground motion simulation and conventional 1D analysis for estimation of earthquake hazard and disaster.

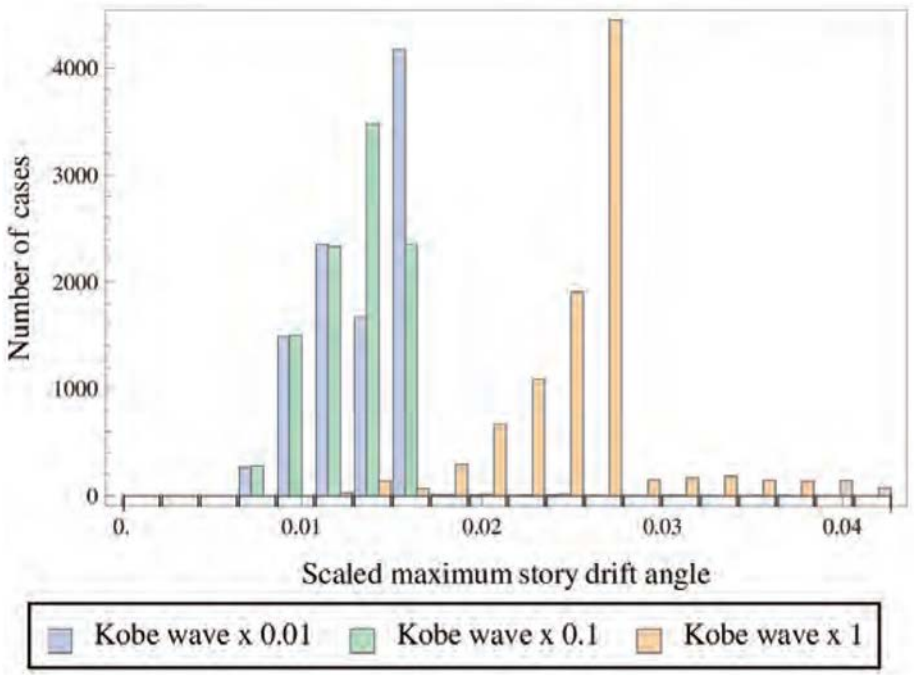

FIGURE 11 | Distribution of MSDA for 10,000 analysis models for one residential building.

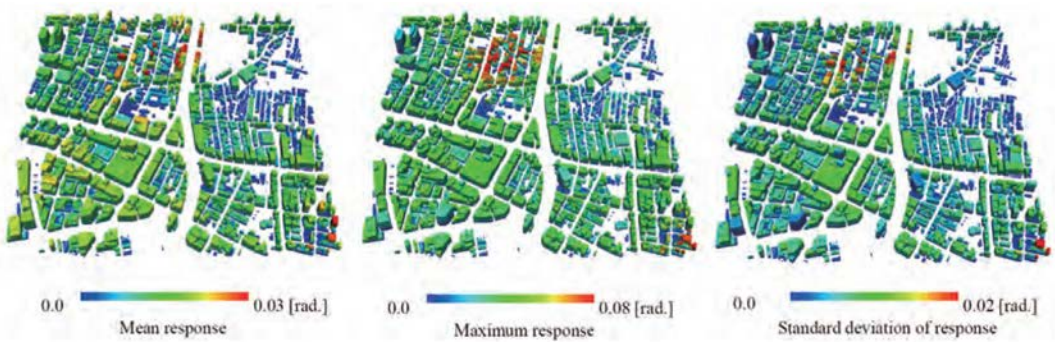

FIGURE 12 | Distribution of mean, maximum and SD of MSDA.

the strength) produces the standard deviation of around 0.01 for MSDA when the largest ground motion is input. For this case, the non-linearity of the present analysis model induces a wider range of a possible earthquake disaster, compared with the uncertainty of the model parameter.

4.3. Combined Simulation of Ground Motion and Urban Area Seismic Response Simulation for 10 km × 10 km Area

Using K computer, IES is able to mate the ground motion simulation and the urban area seismic response simulation for a domain of 10,250 m × 9,250 m (Ichimura et al., 2014a). This is the combined simulation in the sense that output of the ground motion simulation is used as input of the urban area seismic response simulation. It should be noted that the ground motion simulation is regarded as capability computing since it needs the whole 705,024 compute cores of K computer to finish the computation less than 12 h. An underground structure model similar to the one shown in **Figure 6** is considered; it consists of three surface layers, but the number of DOF is 133,000,000,000 and the number of time steps is 6,600. In this setting, the temporal resolution is 10 Hz, which is assured by examining the convergence of a solution with respect to the model size.

An example of the combined simulation is presented in **Figure 13**; there are 32,800 residential buildings in the target domain, and a multi-degree-of-freedom system is constructed as an analysis model for each building, based on an assumption that

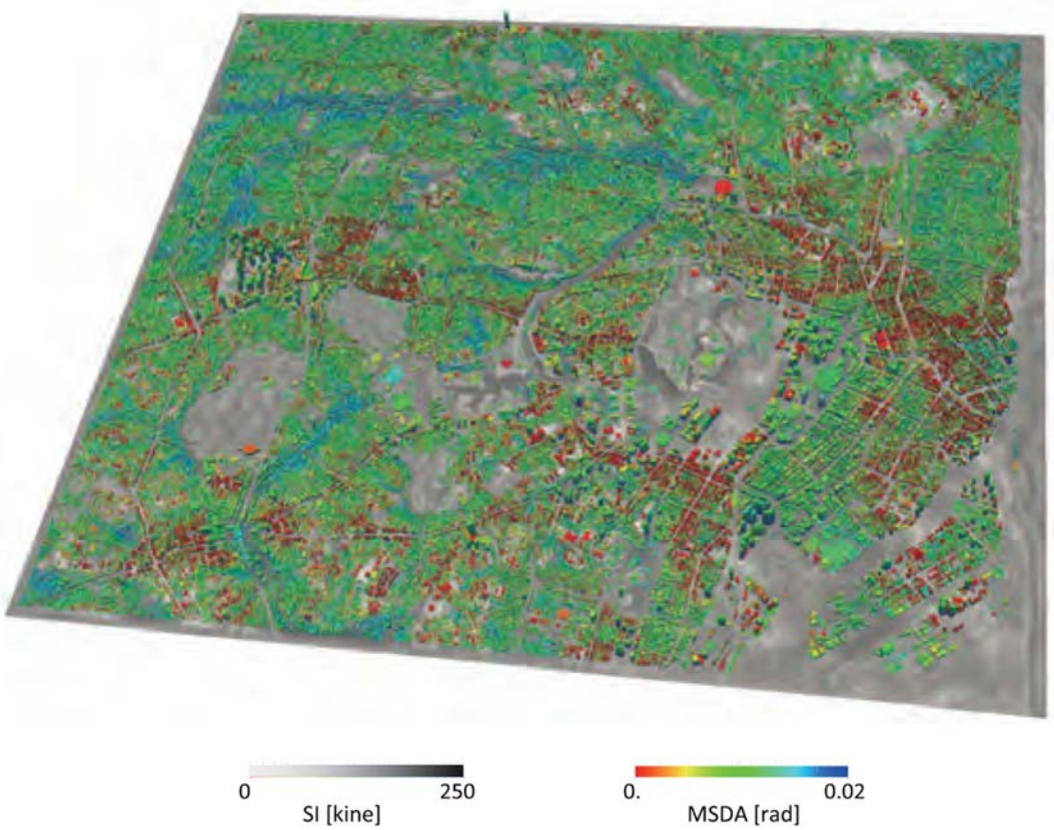

FIGURE 13 | Distribution of SI and MSDA computed by making combined simulation of ground motion and seismic response.

they are a reinforced concrete building. The input ground motion is actually computed by using FEM for an assumed earthquake scenario of Tokyo Metropolis Earthquake (Government of Japan Cabinet Office, 2016). In IES, the earthquake hazard and disaster are quantified in terms of SI and MSDA, respectively. The distribution of these two indices is computed by making the combined simulation.

It should be emphasized that new findings are never made in the combined simulation of IES. It simply combines ground motion simulation to well-established structural seismic response analysis. However, applying the combined simulation to a large area, we can surely identify spots at which SI takes on a larger value and other spots at which buildings of large MSDA's are more densely located. The results of the combined simulation are worth being examined as it produces more rational assessment of earthquake hazard and disaster in highest resolution. Such combined simulation made by IES is applicable to any other cities in the world if suitable data resources are available and the automated model construction system generates a suitable model for the city using the data resources.

5. CONCLUDING REMARKS

This paper presents recent achievement of developing Integrated Earthquake Simulation (IES), by taking advantage of High performance computing (HPC). Indeed, IES enhanced with HPC enables us to develop a method of making a rational estimation of earthquake hazard and disaster for Tokyo Metropolis when an earthquake scenario is given. Provided that suitable computational environment and data resources are available, IES is applicable to any urban area. The two difficulties of numerically simulating earthquake hazard and disaster processes are being solved by developing a finite element method (FEM) with a fast solver and by developing a system of automated model construction.

We are planning to extend IES to social science simulations, such as mass evacuation from tsunami, traffic simulation in damaged areas, or recovery of economic activities. This social science simulation needs numerous scenarios of earthquake disasters which are made by applying IES to a target area for various earthquake scenarios. Further spatial resolution will be needed to consider more details of earthquake disasters, and we have to improve FEM of IES. It is another challenge to apply HPC to realize the social science simulation that is needed to increase the resilience of a target area, as it helps us to consider a better recovery plan. Part of the results was obtained by using the K computer at the RIKEN Advanced Institute for Computational Science. We used KiK-net and Japan Seismic Hazard Information Station of National Research Institute for Earth Science and Disaster Prevention (NIED), and National Digital Soil Map provided by

Japanese Geotechnical Society. This work was supported by JSPS KAKENHI Grant Number 25220908, MEXT's program of Post-K project.

AUTHOR CONTRIBUTIONS

The first author is a primary investigator of this research. The second and third authors made numerical analysis programs for earthquake hazard and disaster assessment. The fourth, fifth, and sixth authors carried out numerical computations, constructing urban area models.

FUNDING

Part of the results was obtained by using the K computer at the RIKEN Advanced Institute for Computational Science. Results are obtained using the K computer at the RIKEN Advanced Institute for Computational Science. We used KiK-net and Japan Seismic Hazard Information Station of National Research Institute for Earth Science and Disaster Prevention (NIED), and National Digital Soil Map provided by Japanese Geotechnical Society. This work was supported by JSPS KAKENHI Grant Number 25220908, MEXT's program of Post-K project.

REFERENCES

Agata, R., Ichimura, T., Hirahara, K., Hyodo, M., Hori, T., and Hori, M. (2016). Robust and portable capacity computing method for many finite element analyses of a high-fidelity crustal structure model aimed for coseismic slip estimation. *Comput. Geosci.* 94, 121–130. doi:10.1016/j.cageo.2016.05.015

Architectural Institute of Japan. (1978). *Vibration Experiment of Building (in Japanese)*. Maruzen.

Architectural Institute of Japan. (2000). *Damping of Building (in Japanese)*. Maruzen.

Architectural Institute of Japan. (2011). *Prompt Report on the 2011 Off the Pacific Coast of Tohoku Earthquake Disaster*. Maruzen.

Bao, H., Bielak, J., Ghattas, O., O'Hallaron, D. R., Kallivokas, L. F., Shewchuk, J. R., et al. (1996). "Earthquake ground motion modeling on parallel computers," in *The 1996 ACM/IEEE Conference on SUPERCOMPUTING*, (Pittsburgh: IEEE Computer Society Press). doi:10.1145/369028.369053

Cimellaro, G. P., Renschler, C., and Bruneau, M. (2014). *Introduction to Resilience-Based Design, Computational Methods, Seismic Protection, Hybrid Testing and Resilience in Earthquake Engineering*. New York: Springer International Publishing AG.

Cui, Y., Poyraz, E., Olsen, K. B., Zhou, J., Withers, K., Callaghan, S., et al. (2013). "Physics-based seismic hazard analysis on petascale heterogeneous supercomputers," in *The International Conference on High Performance Computing, Networking, Storage and Analysis (SC'13)* (New York: IEEE Computer Society Press). doi:10.1145/2503210.2503300

DesignSafe-CI. (2016). *Nheri: A Natural Hazards Engineering Research Infrastructure*. Available at: https://www.designsafe-ci.org/about/designsafe/

Fujita, K., and Ichimura, T. (2016). Development of large-scale three-dimensional seismic ground strain response analysis method and its application to Tokyo using full k computer. *J. Earthq. Tsunami* 10:1640017. doi:10.1142/S1793431116400170

Fujita, K., Yamaguchi, T., Ichimura, T., Hori, M., and Maddegedara, L. (2016). "Acceleration of element-by-element kernel in unstructured implicit low-order finite-element earthquake simulation using openacc on pascal gpus," in *Third Workshop on Accelerator Programming Using Directives (WACCPD, WACCPD' 16)*, Salt Lake City. doi:10.1109/WACCPD.2016.6

GEM. (2015). *Openquake: Global Earthquake Model*. Available at: https://www.globalquakemodel.org/

Golub, G. H., and Ye, Q. (1997). Inexact preconditioned conjugate gradient method with inner-outer iteration. *SIAM J. Sci. Comput.* 21, 1305–1320. doi:10.1137/S1064827597323415

Government of Japan Cabinet Office. (2016). *Report of the Assumed Tokyo Large Earthquake Model Committee*. Available at: http://www.bousai.go.jp/kaigirep/chuobou/senmon/shutochokkajishinmodel/

HAZUS. (2017). *Hazus 4.0*. Available at: http://www.hazus.org/

Heinecke, A., Breuer, A., Rettenberger, S., Bader, M., Gabriel, A.-A., Pelties, C., et al. (2014). "Petascale high order dynamic rupture earthquake simulations on heterogeneous supercomputers," in *The International Conference on High Performance Computing, Networking, Storage and Analysis, (SC'14)* (New Orleans, LA: IEEE Computer Society Press), 3–14. doi:10.1109/SC.2014.6

Hori, M. (2011). *Introduction to Computational Earthquake Engineering*, 2nd Edn. London: Imperial College Press.

Hori, M., Wijerathne, L., Ichimura, T., and Tanaka, S. (2015). Meta-modeling for constructing model consistent with continuum mechanics. *J. Jpn. Soc. Civil Eng. Ser. A2* 71. doi:10.2208/journalofjsce.2.1_269

Housner, G. W. (1952). "Spectrum intensity of strong motion earthquakes," in *Proceedings of the Symposium on Earthquakes and Blast Effects on Structures* (California: Earthquake Engineering Research Institute), 20–36.

Ichimura, T., Fujita, K., Hori, M., Sakanoue, T., and Hamanaka, R. (2014a). Three-dimensional nonlinear seismic ground response analysis of local site effects for estimating seismic behavior of buried pipelines. *J. Press. Vessel Technol. Am. Soc. Mech. Eng.* 136:041702. doi:10.1115/1.4026208

Ichimura, T., Fujita, K., Tanaka, S., Hori, M., Lalith, M., Shizawa, Y., et al. (2014b). "Physics-based urban earthquake simulation enhanced by 10.7 BlnDOF x 30 k time-step unstructured fe non-linear seismic wave simulation," in *The International Conference on High Performance Computing, Networking, Storage and Analysis (SC'14)* (New Orleans, LA: IEEE Computer Society Press), 15–26. doi:10.1109/SC.2014.7

Ichimura, T., Fujita, K., Quinay, P. E. B., Maddegedara, L., Hori, M., Tanaka, S., et al. (2015). "Implicit nonlinear wave simulation with 1.08t DOF and 0.270t unstructured finite elements to enhance comprehensive earthquake Simulation," in *The International Conference for High Performance Computing, Networking, Storage and Analysis (SC'15)* (New Orleans, LA: IEEE Computer Society Press). doi:10.1145/2807591.2807674

Ichimura, T., Hori, M., and Bielak, J. (2009). A hybrid multiresolution meshing technique for finite element three-dimensional earthquake ground motion modeling in basins including topography. *Geophys. J. Int.* 177, 1221–1232. doi:10.1111/j.1365-246X.2009.04154.x

Ichimura, T., Hori, M., and Kuwamoto, H. (2007). Earthquake motion simulation with multi-scale finite element analysis on hybrid grid. *Bull. Seismol. Soc. Am.* 97, 1133–1143. doi:10.1785/0120060175

Idriss, I. M., Singh, R. D., and Dobry, R. (1978). Nonlinear behavior of soft clays during cyclic loading. *J. Geotech. Eng.* 104, 1427–1447.

Japan Meteorological Agency. (2016). *Strong Ground Motion of the Southern Hyogo Prefecture Earthquake in 1995 Observed at Kobe JMA Observatory*. Available at: http://www.data.jma.go.jp/svd/eqev/data/kyoshin/jishin/hyogo_nanbu/index.html

Jayasinghe, J. A. S. C., Tanaka, S., Wijerathne, L., Hori, M., and Ichimura, T. (2015). Automated construction of consistent lumped mass model for road network. *J. Jpn. Soc. Civil Eng.* 71, I_547–I_556. doi:10.2208/jscejseee.71.I_547

Lu, X., and Guan, H. (2017). *Earthquake Disaster Simulation of Civil Infrastructures, from Tall Buildings to Urban Areas*. New York: Springer.

Masing, G. (1926). "Eigenspannungen und verfestigung beim messing (in German)," in *The 2nd International Congress of Applied Mechanics*, 332–335.

Midorikawa, S., Ito, Y., and Miura, H. (2011). Vulnerability functions of buildings based on damage survey data of earthquakes after the 1995 kobe earthquake. *J. Jpn. Assoc. Earthq. Eng.* 11, 4_34–4_47. doi:10.5610/jaee.11.4_34

Miyamura, T., Akiba, H., and Hori, M. (2015). Large-scale seismic response analysis of super-high-rise steel building considering soil-structure interaction using k computer. *High Rise* 4, 75–83.

Miyamura, T., Tanaka, S., and Hori, M. (2016). Large-scale seismic response analysis of a super-high-rise-building fully considering the soil-structure interaction using a high-fidelity 3d solid element model. *J. Earthq. Tsunami* 10:1640014. doi:10.1142/S1793431116400145

Miyazaki, H., Kusano, Y., Shinjou, N., Shoji, F., Yokokawa, M., and Watanabe, T. (2012). *Overview of the k Computer System*, Vol. 48, FUJITSU Sci. Tech, J, 302–309.

NIED. (2016). *Japan Seismic Hazard Information Station, National Research Institute for Earth Science and Disaster Prevention*. Available at: http://www.j-shis.bosai.go.jp/en/

Ohtani, H., Chen, J., and Hori, M. (2014). Automatic combination of the 3D shapes and the attributes of buildings in different GIS data. *J. Jpn. Soc. Civil Eng. Ser. 70*, I_631–I_639. doi:10.2208/jscejam.70.I_631

Quinay, P. E. B., Ichimura, T., Hori, M., Nishida, A., and Yoshimura, S. (2013). Seismic structural response estimates of a high-fidelity fault-structure system model using multiscale analysis with parallel simulation of seismic wave propagation. *Bull. Seismol. Soc. Am.* 103, 2094–2110. doi:10.1785/0120120216

Rietmann, M., Messmer, P., Nissen-Meyer, T., Peter, D., Basini, P., Komatitsch, D., et al. (2012). "Forward and adjoint simulations of seismic wave propagation on emerging largescale GPU architectures," in *The International Conference on High Performance Computing, Networking, Storage and Analysis (SC' 12)* (Los Alamitos: IEEE Computer Society Press).

Saad, Y. (2003). *Iterative Methods for Sparse Linear Systems*, 2nd Edn. New York: SIAM.

Sahin, A., Sisman, R., Askan, A., and Hori, M. (2016). Development of integrated earthquake simulation system for Istanbul. *Earth Planets Space* 68, 115. doi:10.1186/s40623-016-0497-y

Si, H., and Midorikawa, S. (1999). New attenuation relationships for peak ground acceleration and velocity considering effects of fault type and site condition. *J. Struct. Construct. Eng.* 523, 63–70.

SimCenter. (2016). *Computational Mdoeling and Simulaiton Center*. Available at: https://www.designsafe-ci.org/facilities/simcenter/

Society, T. J. G. (2016). *National Digital Soil Map*. Available at: http://www.den-shi-jiban.jp/

Somerville, P., Collins, N., Abrahamson, N., Graves, R., and Saikia, C. (2001). *Ground Motion Attenuation Relations for the Central and Eastern United States, Final Report*. Available at: http://earthquake.usgs.gov/hazards/products/conterminous/2008/99HQGR0098.pdf

Taborda, R., and Bielak, J. (2011). Large-scale earthquake simulation: computational seismology and complex engineering systems. *Comput. Sci. Eng.* 13, 14–27. doi:10.1109/MCSE.2011.19

Tanaka, S., Hori, M., and Ichimura, T. (2016). Hybrid finite element modeling for seismic structural response analysis of a reinforced concrete structure. *J. Earthq. Tsunami* 10:1640015. doi:10.1142/S1793431116400157

Tiankai, T., Hongfeng, Y., Ramirez-Guzman, L., Bielak, J., Ghattas, O., Kwan-Liu, M., et al. (2006). "From mesh generation to scientific visualization: an End-to-end approach to parallel supercomputing," in *The 2006 ACMIEEE conference on Supercomputing (SCf06)* (New York: ACM). doi:10.1145/1188455.1188551

Yifeng, C., Cui, C., Olsen, K. B., Jordan, T. H., Lee, K., Zhou, J., et al. (2010). "Scalable earthquake simulation on petascale supercomputers," in *The 2010 ACM/IEEE International Conference for High Performance Computing, Networking, Storage and Analysis (SC'10)* (Washington: IEEE Computer Society), 1–20. doi:10.1109/SC.2010.45

Conflict of Interest Statement: The authors declare that the research was conducted in the absence of any commercial or financial relationships that could be construed as a potential conflict of interest.

The reviewer, TI, declared a shared affiliation, though no other collaboration, with several of the authors, MH, TI, and LW, to the handling editor.

Copyright © 2018 Hori, Ichimura, Wijerathne, Ohtani, Chen, Fujita and Motoyama. This is an open-access article distributed under the terms of the Creative Commons Attribution License (CC BY). The use, distribution or reproduction in other forums is permitted, provided the original author(s) and the copyright owner are credited and that the original publication in this journal is cited, in accordance with accepted academic practice. No use, distribution or reproduction is permitted which does not comply with these terms.

Advantages of publishing in Frontiers

OPEN ACCESS
Articles are free to read, for greatest visibility

COLLABORATIVE PEER-REVIEW
Designed to be rigorous – yet also collaborative, fair and constructive

FAST PUBLICATION
Average 85 days from submission to publication (across all journals)

COPYRIGHT TO AUTHORS
No limit to article distribution and re-use

TRANSPARENT
Editors and reviewers acknowledged by name on published articles

SUPPORT
By our Swiss-based editorial team

IMPACT METRICS
Advanced metrics track your article's impact

GLOBAL SPREAD
5'100'000+ monthly article views and downloads

LOOP RESEARCH NETWORK
Our network increases readership for your article

Frontiers
EPFL Innovation Park, Building I • 1015 Lausanne • Switzerland
Tel +41 21 510 17 00 • Fax +41 21 510 17 01 • info@frontiersin.org
www.frontiersin.org

Find us on